ON THE DESIGN, SYNTHESIS, AND RADIATION EFFECT PREVENTION OF A 6U DEEP SPACE CUBESAT

by

Michael Cullen Halvorson

A thesis submitted to the Graduate Faculty of Auburn University
in partial fulfillment of the requirements for the Degree of
Master of Science

Auburn, AL
December 12, 2020

Keywords: Deep Space CubeSat, Orbit Thermal Modeling, Electric Propulsion Optimization, Radiation Tolerance

Copyright 2020 by Michael Cullen Halvorson

Approved by

Dr. David G. Beale, Chair, Professor of Mechanical Engineering
Dr. Daniel K. Harris, Associate Professor of Mechanical Engineering
Dr. Thaddeus H. Roppel, Associate Professor of Electrical Engineering
Dr. Michael Fogle Jr., Associate Professor of Physics

Except where reference is made to the work of others, the work described in this thesis is my own or was done in collaboration of my advisory committee. This thesis does not include proprietary or classified information except where permission was given.

Michael Cullen Halvorson

Certificate of Approval:

David G. Beale, Chair
Professor
Mechanical Engineering

Thaddeus H. Roppel
Associate Professor
Electrical Engineering

Daniel K. Harris
Associate Professor
Mechanical Engineering

Michael Fogle Jr
Associate Professor
Physics

Jeffrey Suhling
Department Chair
Mechanical Engineering

Permission is granted to Auburn University to make copies of this thesis at its discretion,
upon request of individuals or institutions and at their expense.
The author reserves all publication rights.

Signature of Author

Date

VITA

Michael Halvorson is an Aeromechanical Engineer from Montgomery, AL. His mother, Melanie, is an internal medicine nephrologist, and his father, David, is an otolaryngological surgeon. With five generations of medical doctors in his immediate ancestry, academia was always the plan. Michael graduated with undergraduate degrees in both Aerospace and Mechanical Engineering from Auburn University in 2017 and is graduating from a Master's in Mechanical Engineering upon submission of this thesis.

Michael's background includes study in CubeSat technical engineering, radiation dose mitigation, aeroacoustics, convective and radiative heat transfer, composite material fabrication, spacecraft propulsion, and shape memory alloy application; he will transition into a Ph.D. in Aeromechanical Engineering in Spring 2021.

ABSTRACT

ON THE DESIGN, SYNTHESIS, AND RADIATION EFFECT PREVENTION OF A 6U DEEP SPACE CUBESAT

Michael C. Halvorson

Master of Science, November 5th, 2020
Department of Mechanical Engineering, Auburn University
(B.S. Mechanical Engineering, Auburn University, 2017)
(B.S. Aerospace Engineering, Auburn University, 2017)

The Alabama Space Grant Consortium initiated a workforce development program across seven universities to build a 6U CubeSat with an astrophysics payload. The science mission, an investigation on the efficacy of augmented lunar regolith as radiation shielding, required the CubeSat to be outside of the magnetosphere for maximal data return. Artemis II was the only launch vehicle capable of achieving the science distance requirement and released a solicitation for CubeSat secondary payloads. Significant research in deep space thermal modeling, electric propulsion optimization, and high frequency communications strategy was completed. Artemis II canceled its CubeSat opportunity, but the first comprehensive guide to deep space CubeSat design is conferred to the CubeSat development community.

ACKNOWLEDGEMENTS

The author would first and foremost like to thank Dr. David Beale, without whom he could not have had such a rewarding and extensive educational experience. Dr. Dan Harris is thanked for always having his door open for questions, and Dr. L. Dale Thomas is thanked for tirelessly supporting those who reach for the stars. Thank you to Drs. Melanie and David Halvorson for supporting the author's dream of becoming a leader in deep space satellite design, both emotionally and financially. Thank you to Amanda, who is always there to listen. Finally, thank you to all the faculty and students across the state of Alabama who made this work possible.

Alabama Space Grant Consortium

Dr. L. Dale Thomas
Debora Nielson
Brooke Graham

Alabama A&M

Cyean Johnson
Rodney Morgan
Aniekan Ruffin
Robert Bryant
Brevin Davis
Kashta Dozier-Muhammad
Andrew Glenn
Ja'Kira Jackson
Duane Johnson
Trevaughn Nettles
Derrius Plair
Micah Taylor
Tony White
Akeia Williams
Jalen Woodland
Aleya Hamilton
Kaylee Murrey
Jessalyn Peoples
De'Aires Scroggins
Joshua Seals

Tuskegee University

Jared Brown
Austin Harris
Tamunoenefaa Harry
Robyn King
Immanuel Momoh
Zarren Riley
Michael Rowe
Patrick Rozell
Maya York

University of South Alabama

Dr. Carlos Montalvo
Dr. Saeed Latif
Darcey D'Amato
Ruthie Hill
William Sherman
Maxwell Cobar
Vincent Oberkirch
Ismael Hamadou
Josh Berglund
Robert Clark
James Paul Elijah Saucier
Willie Ford
Benjamin Barnes
Fredrick Chuks
Tayjon Culley
Lawrence Oberkirch
Joshua Sewell

University of Alabama

Dr. Patrick Kung
Dr. Jaber Abu-Qahouq
Ricardo Avila
Adam Baker
Chase Barksdale
Caleb Cooper
Meagan DeNardo
Austin Steele
Bailey Adams
Ethan Brooks
Billy Deutsch
Lauren Faris
Zach Johnson
Bracken Jones
Tristan Phillips
Yuankun Zhao
Mason Blanke
Cassie DeSalvo
Spencer Davis

Garrett Giddings
Chuck Gehrdes
Jarrett Montgomery
Jody Davis
Hayden Roy
Julia Lisac
Palmer Swanson
Diego Beeker

University of Alabama in Huntsville

Dr. Michael Briggs
Jared Fuchs
Chandler Ellis
Alex Spalding
Victor Lopez
Alana Flint

Auburn University

Dr. David Beale
Dr. Dan Harris
Chris Gomes
Colin Holtkamp
Ryan Collins
Thad Hatcher
Michael Robins
Berk Adanur
Johannes Allen
Rory Alston
Trevor Garrison
Brian Lim
Jonathan Marquardt
Paul Minda
Lydia Mitchell
Austin Obanian
Andrew Parvino
Ryan Reeves
Matthew Sanford
Christian Smith
Noah Pitts
Zach Slemmons
Andrew Kozlowski
Matthew Entrekin
Divy Dishant
William Griffin
Brock Buchanan
Arkaradech Zornnetr
Austin McLendon
Joey Hoke
Nick Hope
Sydnee Shadoan
Tyler Jackson
Sierra Jacbos
Louis Buckalew
Tyler Evans
Connor Jones
Kendall Wichman
Walt Kelly
Colin Finnegan
Daniel Keith
Hunter Bernier
Philip Snitzer
Michael Prince
Aleha Crumpton
Jordan Cox
Kevin Hubbard
Luke Harvey
Cameron Baker
Jake Stamps
Nathan Brooks
Kowshik Vadlamudi
Matthew Bottom
Frank Brown
Bryan Hardaker
Eric Bradshaw
Evan Johnson
Jerry Kigerl
Hayden Patteson
Jonathan Coleman
Logan Williams
Nicolas Hoepfner
Noah Cargile
Ryan Mueller
Tiana Ramos
Ivan Garcia
Jake Houston
Mark Bentz
Alex Walker
Cam McLean
Colton Bevel
Drew Mullinax
Eddie Strickland
Grant Holbrook
Mikah Abbott
Scot Carpenter
Joseph Langan
Brandon Molyneaux
Grant Robertson
Houston Walley
Leah Lee
Theo Zinner
Blake Schilleci
Michael Johnson
Allen Barrett
Dakota Coffman

FOREWORD

This document is a guide on the design tasks required of a deep space CubeSat development program before Preliminary Design Review (PDR) using the Alabama Experiment on Galactic-ray In-situ Shielding (AEGIS) spacecraft as a case study. Many space mission design textbooks, reports, and presentations have been parsed for information most relevant to deep space CubeSat design, and several novel methodologies are introduced. The most prominent contributions to the field of deep space satellite design are an Earth to Moon thermal model and a modified electric propulsion optimization scheme for small spacecraft.

AEGIS was commissioned, organized, and developed by the Alabama Space Grant Consortium (ASGC), and the described program architecture can be emulated by any state or organization that encompasses multiple colleges or universities willing to contribute senior design teams or student groups to the cause. The present work was written by the Chief Engineer, Michael Halvorson, but it contains analyses by the Program Manager, Jared Fuchs, and the Lead Systems Engineer, Victor Lopez, along with undergraduate student contributions that were guided or assigned by the Chief Engineer. Work that does not come directly from the author is acknowledged where included.

Space hardware design and synthesis approaches are discussed at length, but limited information is provided on Systems Engineering (SE), Integration, Verification, and Testing (IV&T), and Command and Data Handling (C&DH). Flight Software provisions are specific to Concept of Operations (ConOps) development and radiation tolerance. Of the works cited, 15 are textbooks, 195 are scholarly papers or presentations, and 78 are websites, mostly NASA resources, online software tools, and satellite home pages. Complete overviews of radiation environments, effects of radiation on spacecraft, and radiation analysis procedures are detailed. Acronyms and nomenclature are provided at the end.

It is the hope of the author that this organized collection of knowledge, skills, and methods will be the first resource for undergraduate and graduate students who wish to design a deep space CubeSat.

TABLE OF CONTENTS

VITA....iv
ABSTRACT....v
ACKNOWLEDGEMENTS....vi
FOREWORD....viii
TABLE OF CONTENTS....ix
TABLE OF FIGURES....xiii
TABLE OF TABLES....xvi
1. Introduction....1
  1.1 What is a CubeSat?....1
    1.1.1 CubeSat History....1
    1.1.2 Classification....1
  1.2 Why CubeSats?....1
    1.2.1 Cost Savings....2
    1.2.2 Size....2
    1.2.3 Component Availability....4
  1.3 CubeSat Destinations....4
    1.3.1 LEO Missions....5
    1.3.2 Interplanetary Missions....5
    1.3.3 Asteroid Hunters....5
    1.3.4 A Word on Launch Vehicles....6
  1.4 The AEGIS Project....6
    1.4.1 Multi-University Collaborative Program....6
    1.4.2 Science Mission....10
    1.4.3 Educational Objectives and Metrics....11
    1.4.4 Timeline and Development Strategy....12
    1.4.5 Future of the Program....14
    1.4.6 Document Considerations....14
2. Mission and Spacecraft ConOps....15
  2.1 Cislunar Launch Vehicles....15
  2.2 Mission Orbit and Trajectory....17
  2.3 Mission Segment Definition: Structural....18
  2.4 Mission Segment Definition: Software....20
  2.5 Concept of Operations....21
3. Architecture and Subsystem Design....22
  3.1 Preliminary Considerations....22
    3.1.1 The Iterative Process....22
    3.1.2 Subsystem Architecture....22

3.1.3 Senior Design Teams 23
3.2 Structural Integrity 24
  3.2.1 Structural Design Objectives 24
  3.2.2 Satellite Architecture 26
  3.2.3 Structural Material and Fabrication 36
  3.2.4 Rail and Dispenser Considerations 39
  3.2.5 Design Qualification 41
  3.2.6 Solar Array Design 42
  3.2.7 Hold and Release Mechanisms 45
3.3 Thermal Control 46
  3.3.1 Thermal Design Objectives 46
  3.3.2 Historical Perspective 47
  3.3.3 Heat Sources in Space 47
  3.3.4 Orbit Beta Angle 55
  3.3.5 Coatings and Finishes 57
  3.3.6 Energy Balance Thermal Model 63
  3.3.7 Transient Finite Difference Analyses 77
3.4 Propulsion 86
  3.4.1 Propulsion Design Objectives 86
  3.4.2 Propulsion Overview 88
  3.4.3 Deep Space: High ΔV Maneuvers 89
  3.4.4 Legacy EP Optimization Procedure 91
  3.4.5 Modified EP Optimization Procedure 96
3.5 Electrical Power System 98
  3.5.1 EPS Design Objectives 98
  3.5.2 Power Generation 100
  3.5.3 Power Distribution 106
  3.5.4 Power Consumption 106
  3.5.5 Battery Considerations 109
  3.5.6 Maximum Power Point Trackers 111
3.6 Telemetry, Tracking, and Command 115
  3.6.1 TT&C Design Objectives 115
  3.6.2 Bandwidths and Frequency Selection 116
  3.6.3 Radio Hardware Evaluation 117
  3.6.4 Antennae 118
  3.6.5 Link Budget and Comparison 120
  3.6.6 FCC Licensing 122
  3.6.7 Optical Satellite Communication 122
  3.6.8 Networks 123

3.6.9 Signal Effects: Ranging, Tracking, and Doppler 124
3.6.10 System Block Diagram 125
3.6.11 Power Interface Comparison 126
3.7 Guidance, Navigation, and Control 127
3.7.1 GN&C Design Objectives 127
3.7.2 Spacecraft Disturbance Sources 128
3.7.3 GN&C and the Magnetosphere 128
3.7.4 Guidance Sensor Overview 132
3.7.5 Control Mechanisms Overview 135
3.7.6 Control Accuracy 139
3.7.7 Navigation Methodology 140
4. Radiation Effects, Shielding, and Redundancy 142
4.1 Space Radiation Environment 142
4.1.1 Radiation Parameters for Spacecraft Design 142
4.1.2 Galactic Cosmic Rays 146
4.1.3 Solar Energetic Particles 149
4.1.4 Electromagnetic Radiation 152
4.1.5 Particle Data Summary 153
4.2 Single Event Effects 153
4.2.1 Recoverable Effects 153
4.2.2 Destructive Effects 156
4.3 Radiation-Tolerant Electronics Design 157
4.3.1 Faults, Errors, and Tolerance 157
4.3.2 Fault Avoidance 158
4.3.3 Fault Masking and Redundancy 159
4.3.4 Process Error Detection 165
4.3.5 Containment of Error Propagation 169
4.3.6 Recovery of Operations 169
4.3.7 Additional Embedded System Design Guidance 170
4.4 Radiation-Tolerant Structural Design 171
4.4.1 Secondary Particles 171
4.4.2 Characterizing Secondary Particles 172
4.4.3 Types of Radiation Shielding 172
4.5 Radiation Effect Assessment 176
4.5.1 Radiation Characterization Flow 176
4.5.2 Simulation Tools 177
4.5.3 Finding Total Ionizing Dose 179
4.5.4 Finding Non-Ionizing Energy Loss 180
4.5.5 Finding Surface Charge 181

4.5.6 Finding SEE-Induced Upset Rates 183
5. Conclusion 185
REFERENCES 186
NOMENCLATURE 198
ACRONYMS 208
APPENDIX A: SOFTWARE STATE LOGIC FLOWS 217
APPENDIX B: SPACECRAFT FOR RADIATION CHARACTERIZATION 228
B.1 Solar Observation Spacecraft 228
B.1.1 Solar and Heliophysics Observatory 228
B.1.2 Comprehensive Solar Wind Laboratory 228
B.1.3 Cluster 228
B.1.4 Solar Dynamics Observatory 229
B.1.5 Solar Terrestrial Relations Observatory 229
B.1.6 Parker Solar Probe 229
B.1.7 SunRISE 230
B.2 Cislunar Observation Spacecraft 230
B.2.1 Lunar Reconnaissance Orbiter 230
B.2.2 LCROSS 230
B.3 Interplanetary Observation Spacecraft 231
B.3.1 Geostationary Operational Environment Satellite 231
B.3.2 Advanced Composition Explorer 231
B.3.3 Geotail 231
B.3.4 Mars Reconnaissance Orbiter 231
APPENDIX C: LINK BUDGET EXCEL CALCULATOR 233

TABLE OF FIGURES

Figure 1: CubeSats Launched by Mission Class, 2000-Present, No Constellations [2] 2
Figure 2: Tyvak Fit Check on Rocket Lab's Photon Platform, Used with Permission [14] 3
Figure 3: CubeSat Altitude Histogram. Values in Grey Indicate Decayed Orbits [2] 4
Figure 4: Success of First CubeSat Mission for University-Class Missions, 150 Universities [2] 5
Figure 5: AEGIS Science Payload 11
Figure 6: Integrated Master Plan 13
Figure 7: Artemis I CubeSat Bus Stops [31] 15
Figure 8: Orion Stage Adapter, Artemis I [31] 16
Figure 9: AEGIS Mission Altitude Over Proposed Lifetime 17
Figure 10: AEGIS Trajectory, Earth-Sun Rotating Frame. Red represents burn maneuvers, grey represents coast trajectories, blue represents science data collection orbit 18
Figure 11: AEGIS Mission Sequence 21
Figure 12: AEGIS Array View in Stowed Configuration with Coordinate System 27
Figure 13: AEGIS Array View in Deployed Configuration with Coordinate System 28
Figure 14: AEGIS Radiator View in Stowed Configuration with Coordinate System 28
Figure 15: AEGIS Science Aperture View with Solar Arrays Deployed 29
Figure 16: +Z View, Solar Array A Half-Deployed 30
Figure 17: -Z View, Solar Array C Stowed 30
Figure 18: +Z View, AEGIS Interior with Kapton-Wrapped Cabling Shown 31
Figure 19: +Z View, AEGIS Interior without Cabling 31
Figure 20: Science Instrument Mounting and Structure 32
Figure 21: -X View, Interior Cable Harnessing Design 32
Figure 22: +X View, Interior Star Tracker View 1 33
Figure 23: +X View, Interior Star Tracker View 2 33
Figure 24: +Z View, Component Mounting Strategy 34
Figure 25: IMU and Yaw RW Mounting Strategy 34
Figure 26: Science Instrument and Star Tracker FOV 35
Figure 27: +Z View, -X Direction Sun Sensor FOV Occultation by Solar Array B 35
Figure 28: Thread Locking Helicoil from Boellhoff, Used with Permission [45] 37
Figure 29: Belleville Washer Between Battery Pack and +Y Face 38
Figure 30: CubeSat Dispenser Rails on -X Direction Face 39
Figure 31: Plunger-Type Deployment Switch 40
Figure 32: Solar Panel Sandwich Representation [50] 43
Figure 33: Spectral Emissive Power Flux from a Blackbody at 5780 K 48
Figure 34: Lunar Emissivity as a Function of Lunar Surface Temperature 50
Figure 35: Lunar Albedo as a Function of Solar Zenith Angle 51
Figure 36: Lunar Emission Flux Model 51
Figure 37: Lunar Emission Flux Model Transposed Over the Lunar Surface 52
Figure 38: Histogram of Operational Internal Generation Wattage, Science State 54
Figure 39: Histogram of Operational Internal Generation Wattage, Burn State 54
Figure 40: Beta Angle Example Diagram 55
Figure 41: Scrutinized Earth Circular Orbit Solar Heat Flux Formulation, Altitude = 419 km. Atmospheric and charged particle heating not included 56
Figure 42: Corrected Earth Circular Orbit Solar Heat Flux Formulation, Altitude = 419 km. Atmospheric and charged particle heating not included 57
Figure 43: Spectral Reflectivity of Four Surface Materials for Solar Wavelengths 61
Figure 44: Reflection and Absorption of Solar Wavelengths, Four Materials 61
Figure 45: Varied AOI for a Surface of Bare Aluminum, No Coating 62
Figure 46: Varied AOI for a Surface of Kapton-Coated Aluminum, Kapton Thickness = 1 mm 62
Figure 47: Hohmann Transfer for Thermal Analysis. Red represents starting circular orbit and green represents transfer orbit. Earth and Moon size scaled by a factor of π 65
Figure 48: Heat Flux in Earth LEO, Hot and Cold Cases. Atmospheric and charged particle heating not included. Altitude = 419 km 68

Figure 49: Heat Flux in Earth GTO, Hot and Cold Cases. Charged particle heating not included. Altitude = 24,582 km 69
Figure 50: Heat Flux Near Equatorial Lunar Surface, Hot and Cold Cases. Altitude = 419 km 70
Figure 51: Heat Flux in Distant Lunar Orbit, Hot and Cold Cases. Altitude = 5,000 km 70
Figure 52: Heat Flux in Earth, Transfer, and Lunar Orbits. Hot Case. Earth Alt = 24,582 km, Lunar Alt = 5,000 km 71
Figure 53: Heat Flux in Earth, Transfer, and Lunar Orbits. Cold Case. Earth Alt = 24,582 km, Lunar Alt = 5,000 km 71
Figure 54: Heat Load, All Orbital Geometry Permutations. Hot Case. Earth Alt = 24,582 km, Lunar Alt = 5,000 km 73
Figure 55: Heat Load, All Orbital Geometry Permutations. Cold Case. Earth Alt = 24,582 km, Lunar Alt = 5,000 km 73
Figure 56: CubeSat Temperature, All Orbital Geometry Permutations. Hot Case, Earth Alt = 24,582 km, Lunar Alt = 5,000 km 74
Figure 57: CubeSat Temperature, All Orbital Geometry Permutations. Cold Case. Earth Alt = 24,582 km, Lunar Alt = 5,000 km 74
Figure 58: CubeSat Temperature, Power-Generating Orbital Geometry Permutations. Hot Case. Earth Alt = 24,582 km, Lunar Alt = 5,000 km 75
Figure 59: CubeSat Temperature, Power-Generating Orbital Geometry Permutations. Cold Case. Earth Alt = 24,582 km, Lunar Alt = 5,000 km 75
Figure 60: CubeSat Temperature, Relevant Orbital Geometry Permutations. Hot Case. Earth Alt = 24,582 km, Lunar Alt = 5,000 km 76
Figure 61: CubeSat Temperature, Relevant Orbital Geometry Permutations. Cold Case. Earth Alt = 24,582 km, Lunar Alt = 5,000 km 76
Figure 62: CubeSat Temperature Envelope, Earth Alt = 24,582 km, Lunar Alt = 5,000 km 77
Figure 63: AEGIS Radiator Structure. Thruster mounted to section near middle six fasteners 78
Figure 64: Transient Hot Case Temperature Distribution of the Radiator, Steady State Reached in 585 seconds 80
Figure 65: Transient Cold Case Temperature Distribution of the Radiator, Steady State Reached in 390 seconds 81
Figure 66: Geometry of Solar Array A 82
Figure 67: Transient Hot Case Temperatures of Solar Array A, Steady-State Reached at 3345 seconds 83
Figure 68: Transient Cold Case Temperatures of Solar Array A, Steady-State Reached at 6750 seconds 83
Figure 69: Geometry of Solar Array B 84
Figure 70: Transient Hot Case Temperatures of Solar Array B, Steady-State Reached at 3615 seconds 85
Figure 71: Transient Cold Case Temperatures of Solar Array B, Steady-State Reached at 19800 seconds 85
Figure 72: Thruster Capability Overview, Used with Permission [96] 88
Figure 73: Bipropellant Engine Converging/Diverging De Laval Nozzle [97] 89
Figure 74: Basic Tsiolkovsky's Equation Comparison for 6U CubeSat Masses, $\Delta V = 200$ m/s 90
Figure 75: Basic Tsiolkovsky's Equation Comparison for varied ΔV, Total Mass = 14 kg 90
Figure 76: Legacy Optimization Output, Specific Impulse and Propellant Mass Ratio vs. Payload Ratio. $\Delta V = 206$ m/s, $m_o = 14$ kg, We = 25 W 95
Figure 77: Legacy Optimization Output, Specific Impulse and Propellant Mass Ratio vs. Payload Ratio. $\Delta V = 20{,}000$ m/s, $m_o = 1{,}000$ kg, We = 100 W 96
Figure 78: Modified Optimization Procedure Specific Impulse. $\Delta V = 206$ m/s, m0 = 14 kg, We = 25 W 97
Figure 79: Modified Optimization Procedure Propellant Mass Ratio. $\Delta V = 206$ m/s, m0 = 14 kg, We = 25 W 97
Figure 80: Available Solar Power Flux vs. Planetary Distance 100
Figure 81: Basic EPS Block Diagram, Distributed MPPT System, Not All AEGIS Components Represented, Nothing to Scale 101
Figure 82: Solar Array A, Deployed Configuration 102
Figure 83: Body-Mounted Panels with Right Side of Solar Array A Deployed 102
Figure 84: Solar Array B, Deployed Configuration 103
Figure 85: Solar Array C, Deployed Configuration 103
Figure 86: Power Generation Per Solar Array Per Solar Angle of Incidence 104
Figure 87: Power-Transferring Winglet Hinges from Pumpkin, Used with Permission 106
Figure 88: Photovoltaic Power and Current vs. Voltage [108] 112
Figure 89: (a) TDRS Reflector Antenna Design [124] (b) RainCube Parabolic Reflector Antenna [123] 119
Figure 90: (a) MarCo Reflectarray Design [126] (b) ISARA Reflectarray Design [125] 119

Figure 91: HCT Shape Memory Alloy Deployable Travelling-Wave Antenna, Used with Permission [132] 120
Figure 92: EnduroSat X-band 2x2 Patch Antenna array, Used with Permission, [133] 120
Figure 93: (a) AEGIS TT&C Block Diagram (b) CU-E3 TT&C Block Diagram, Used with Permission [120] 126
Figure 94: Magnetosphere Shape and Field Lines [157] 128
Figure 95: Van Allen Belts with Satellite Positioning [168] 130
Figure 96: (a) SolarMEMS Nano-SSOC-A60 (b) SolarMEMS Nano-SSOC-D60. Used with permission [179] 133
Figure 97: Hyperion ST200 Shown Without Baffle. Baffles are commonly 30 or 45 degrees, used with permission [186] 133
Figure 98: Sensonor STIM318, Used with Permission [189] 134
Figure 99: Single-Axis RW Desaturation Thruster Configuration Possibilities 138
Figure 100: GCR Flux in Cislunar Space 400,000 km from Earth. Blue is H ions, red is He ions, green is heavy ion flux from Z = 3 to Z = 26 148
Figure 101: GCR Combined Flux per Ion Showing Relative Distribution of Flux vs. Z 148
Figure 102: SEP Peak Event Flux. Blue is H ions, red is He ions, and yellow is combined heavy ion flux from Z = 3 to Z = 26 150
Figure 103: SEP Peak Event Relative Flux 150
Figure 104: SEP Mission Fluence, Mission Duration 1 Year. Blue is H ions, red is He ions, and green is the combined heavy ion flux from Z=3 to Z=26 151
Figure 105: Gamma-ray Background Flux 152
Figure 106: Charged Particle Strike Example in a PN Junction 159
Figure 107: N-Version Programming Procedure [234] 166
Figure 108: Recovery Block Procedure [234] 167
Figure 109: Oxide Formation Between Dissimilar Bonded Materials [247] 173
Figure 110: VSRS Multi-Layer Conformal Shielding. Low-Z PEEK polymer (red) with layers containing high-Z tungsten (gray). Used with permission from Tethers Unlimited, Inc. [250] 175
Figure 111: Radiation Assessment Flow, Adapted with Permission from [166] 177
Figure 112: Differences in AP8/AE8 and AP9/AE9 [259] 178
Figure 113: TID Dose Depth Curve Example, Target Material Si, Shield Material Al, GCR Not Included. GEO 1 year. Used with permission from Zero-g Radiation 180
Figure 114: NIEL Dose Depth Curve Example, Target Material Si, Shield Material Al, GCR Not Included. ISS Orbit 3 year. Used with permission from Zero-g Radiation 181
Figure 115: Software State Architecture Flow 218
Figure 116: Deployment Software State Logic 219
Figure 117: Communications Software State Logic 220
Figure 118: Charge Software State Logic 221
Figure 119: Contingency Software State Logic 222
Figure 120: Warmup Software State Logic 223
Figure 121: Burn Software State Logic 224
Figure 122: Science Software State Logic 225
Figure 123: Safety 1 Software State Logic 226
Figure 124: Safety 2 Software State Logic 227
Figure 125: Parker Solar Probe Design and Instrumentation [280] 229
Figure 126: Frost-covered Dunes on the Martian Surface [288] 232

TABLE OF TABLES

Table 1: Senior Design Teams and their Engineering Disciplines....7
Table 2: NASA Mission Phases [28]....9
Table 3: UNP Mission Phases [29]....9
Table 4: AEGIS Merit and Feasibility Review SMEs....10
Table 5: ICPS Initial State Vectors....18
Table 6: AEGIS Structural Mission Segments....19
Table 7: Software Mission Segment Definition....20
Table 8: Structural Bus and Chassis Design Objectives, Adapted from [28]....24
Table 9: Component Selection and Vendor Recognition....26
Table 10: Standards for Deep Space CubeSat Structural Analysis [40]....27
Table 11: Material Factors of Safety for Stress Applications....41
Table 12: Structural Mission Segment Environment....42
Table 13: Solar Panel Material Properties [50]....43
Table 14: Solar Panel Natural Frequency Example....44
Table 15: Thermal Control Subsystem Design Objectives, Adapted from [28]....46
Table 16: Component Power Consumption Example per Software State....53
Table 17: Modified Fresnel Relation Overview....59
Table 18: Wavelength Range of Complex Spectral Refractive Indices for Selected Materials....61
Table 19: Integrated Absorbed and Reflected Heat Flux Values per Material....62
Table 20: TMM Hot and Cold Case Parameter Input Variation....64
Table 21: TMM Derivation Parameter Overview....66
Table 22: TMM Material Absorptivity and Emissivity Data....72
Table 23: TMM Surface Area, Absorptivity, and Emissivity Data....72
Table 24: Radiator Parameter Variation....78
Table 25: Gauss-Seidel Model Parameters, Radiator....79
Table 26: Gauss-Seidel Model Parameters, Solar Array A....82
Table 27: Gauss-Seidel Model Parameters, Solar Array B....84
Table 28: Maximum and Minimum Temperatures per Case....85
Table 29: Propulsion Subsystem Design Objectives, Adapted from [28]....86
Table 30: Electrical Power System Design Objectives, Adapted from [28]....98
Table 31: Solar Array Areas....104
Table 32: AEGIS Software State Power Consumption Breakdown. H = High Power Draw, N = Nominal Power Draw, L = Low Power Draw, S = Special Case, O = Off....107
Table 33: Comparison of Power Generation Values to Distribution and Consumption Values for Varied AOI....108
Table 34: LG MJ1 18650 Li-ion Battery Specifications [105]....109
Table 35: EnduroSat EPS II Parameter Overview [107]....111
Table 36: EnduroSat EPS II Input Ratings [107]....111
Table 37: Spectrolab XTE-SF Post 1 MeV e- Retention (US Standard AIAA S-111-2005) [91]....112
Table 38: EnduroSat EPS II Ratings Per MPPT Input Channel....113
Table 39: PV Configuration MPPT Calculations....114
Table 40: Telemetry, Tracking, and Command Subsystem Design Objectives, Adapted from [28]....115
Table 41: High Level Frequency Divisions [110]....116
Table 42: Widely Accepted Frequency Divisions [110]....116
Table 43: ITU Allocated Frequency Bands [112]....117
Table 44: Link Budget Analysis for UHF, S and X-band Uplink/Downlink Considering Various Ground Station Options. Orbital Altitude Assumed at 400,000 km....121
Table 45: Guidance, Navigation, and Control Subsystem Design Objectives, Adapted from [28]....127
Table 46: Flare Classification System....131
Table 47: Attitude Control Methods and Their Capabilities, Used with Permission [33]....135
Table 48: Estimates for AEGIS Reaction Wheel Sizing Parameters....136
Table 49: Effects of Control Accuracy Requirements on Sensor Selection, Used with Permission [33]....139
Table 50: Radiation Parameter Unit Definition....146
Table 51: GCR Model Inputs to SPENVIS....147

Table 52: SEP Peak Flux Model Inputs to SPENVIS 149
Table 53: SEP Fluence Model Inputs in SPENVIS 151
Table 54: ESD Component Sensitivity Classes, HBM 182
Table 55: ESD Component Sensitivity Classes, MM 182
Table 56: ESD Component Sensitivity Classes, CDM 182
Table 57: Band Gap and Ionization Energy of Semiconductors at Room Temperature, Used with Permission [166] 183
Table 58: Proton Upset Rate Predictions $\sigma 0 = 1.0 \cdot 10 - 12\ cm2, E0 = 20\ MeV, W = 50\ MeV,\ S = 2$. Used with permission [166]. 184
Table 59: Link Budget Excel Calculator 233

1. Introduction

1.1 What is a CubeSat?

A CubeSat is a type of small satellite characterized by a discretized range of volumetric increments. They are sometimes known as "Containerized Spacecraft." The primary advantage of CubeSats over larger satellite profiles is that they are decoupled from the launch vehicle more so than most other types of spacecraft in that the deployment of various types or sizes of CubeSat does not require the creation of a new ejector system [1]. CubeSat parameters are not currently defined by any government body, and standardization comes from strong developer community. Dr. Michael Swartwout has begun to categorize CubeSats by their mission type, mission status, orbit status, class, and builder type [2], but all CubeSats exhibit volumes in increments of "U", or roughly 10 cm x 10 cm x 10 cm. CubeSat property definitions, history, and classifications will be discussed in the introduction followed by a modernized review of CubeSat subsystems for deep space missions. All information provided will feature the Alabama Experiment on Galactic-Ray In-situ Shielding (AEGIS) mission as a case study.

1.1.1 CubeSat History

The first Small Satellite Conference in 1987 was organized by Bob Twiggs and Dr. Jordi Puig-Suari to discuss the idea of a satellite standardization format. Completed in 1999, the Orbiting Picosatellite Automatic Launcher (OPAL) out of Stanford University was the first system to realize the idea of launching six small spacecraft with defined volume criteria; it had a total mass of 25.5 kg [3]. Shortly after, California Polytechnic State University followed with the Poly Picosatellite Orbital Deployer (P-POD) [4]. On June 30th, 2003, four 1U CubeSats were launched on two P-PODS, and the first official CubeSat is widely considered to be the XI-IV (pronounced "ξ-four") mission by the University of Tokyo and the Tokyo Institute of Technology [5]. Amazingly, this satellite remained operational for over 15 years.

1.1.2 Classification

Satellite classes are defined as civil, commercial, military, or university; mission type may be communications, educational, Earth imaging, military, science, or technological demonstration [2]. The present work is intended for the design of science-type, university-class missions in deep space. Explicitly defining a CubeSat's attributes will provide ease in communicating with bandwidth license providers such as the Federal Communications Commission. While satellite developers can remain hopeful that regulatory definitions emerge from government participation in CubeSat development, for now a reliance on community-developed classifications is sufficient for data presentation and analysis. **Figure 1** depicts the surge of university-class missions since 2000.

1.2 Why CubeSats?

In the 2000s and early 2010s, the primary reasons to utilize CubeSat platforms over traditional satellite architectures were cost, size, and component availability. Accomplishing the same science missions for less mass and volume meant smaller, inexpensive launch vehicles, and relatively interchangeable parts in a consumer market grew the economy of scale. Due to that scaled CubeSat economy providing a wide variety of developers an array of new components to work with, a dramatic increase in launch opportunities will be both the driver and limiting factor for CubeSat launches in the 2020s.

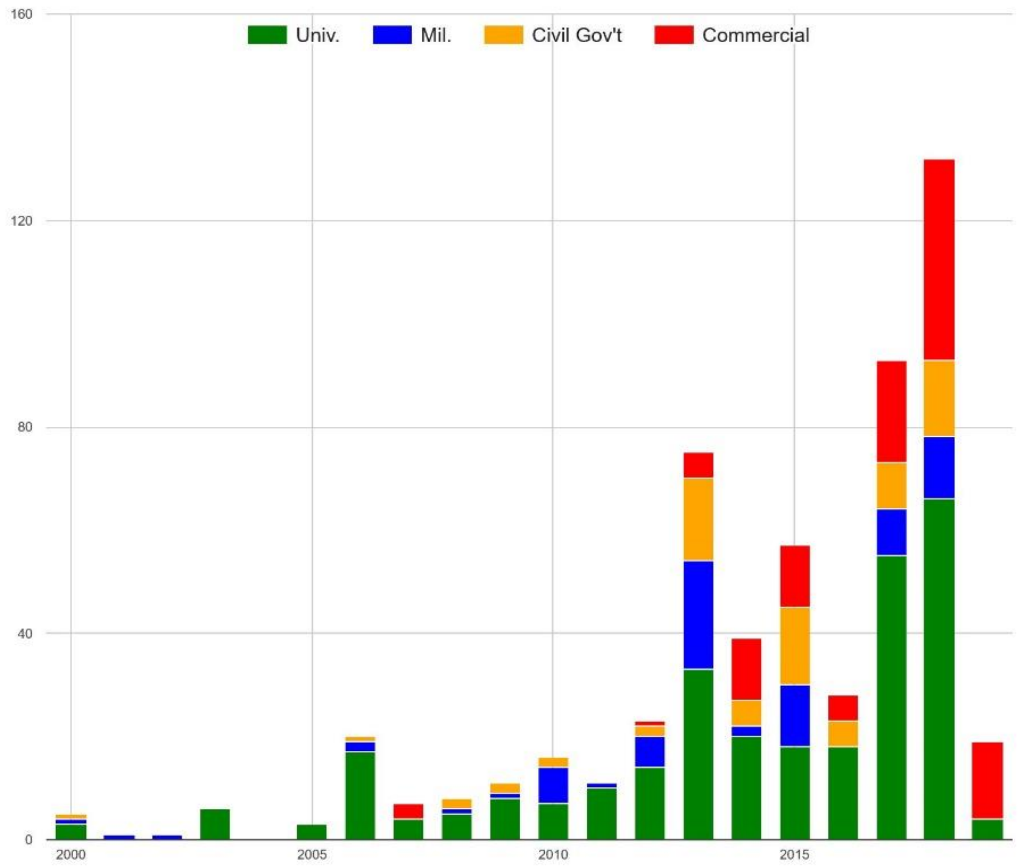

Figure 1: CubeSats Launched by Mission Class, 2000-Present, No Constellations [2]

1.2.1 Cost Savings

Building a satellite is expensive. The price tag for the Mars Reconnaissance Orbiter (MRO) hardware was $416,600,000, the Lunar Reconnaissance Orbiter (LRO) cost $583,000,000, and each of the first 10 GPS satellites cost $577,000,000 [6-8]. Obviously, these are not price points that universities can negotiate for satellites intended beyond LEO. The sources for those prices are not scholarly publications, and prices are not adjusted for inflation.

The Jet Propulsion Lab (JPL) was tasked in the 2010s with creating a CubeSat system to assist in a data relay from the Mars InSight lander. InSight was going to land on the opposite side of Mars as the MRO, and data needed to be transferred from InSight to the MRO during landing. JPL devised a two CubeSat data relay system called Mars Cube One (MarCO) consisting of two satellites affectionately coined Wall-E and Eva, and the total cost of the mission was $18,500,000. While this was a high-risk mission built by the best spacecraft designers in the business, MarCO opened the doors to affordable deep space CubeSat development. InSight itself cost $993,000,000 [9].

1.2.2 Size

There are a few obvious reasons smaller satellite platforms are desirable. Smaller frameworks are easier to handle in a clean room environment, reduced areas mean reduced risk of orbital collisions, and assembly line manufacturing principles are possible during fabrication for large quantities. However, the most prominent advantage in the 2020s that did not exist prior will be launch vehicle packing density.

When the LRO launched aboard the Atlas V-401 rocket in 2009, its total mass was 1846 kg, and it was one of two payloads on board. The second payload was the Lunar Crater Observation and Sensing Satellite (LCROSS) [10]. The InSight lander also launched aboard an Atlas V-401 in 2018 with a mass of 360 kg, except this deep space lander was accompanied by CubeSats Wall-E and Eva [11]. As CubeSat technology matured, a larger number of CubeSats were deployable from a single launch vehicle, even in deep space. For LEO insertions, Rocket Lab's Photon, shown in **Figure 2**, can carry 180 kg, or about fifteen 3U CubeSats. That mass approaches 40 kg for interplanetary missions [12]. While Tyvak dispensers are shown in **Figure 2**, selecting, procuring, and supplying dispensers is often the responsibility of the CubeSat program and not the Launch Vehicle (LV). For deep space, until commercial ventures start offering manifesting prices better than $1,000,000/kg, a CubeSat's best bet would be an Artemis-class vehicle. Artemis II's secondary payload stage, a precursor to Block 1B, can hold up to seventeen 6U and 12U payloads [13]. The United States has decided it wants to go back to the Moon, and the biggest beneficiaries may be CubeSats intended for cislunar space.

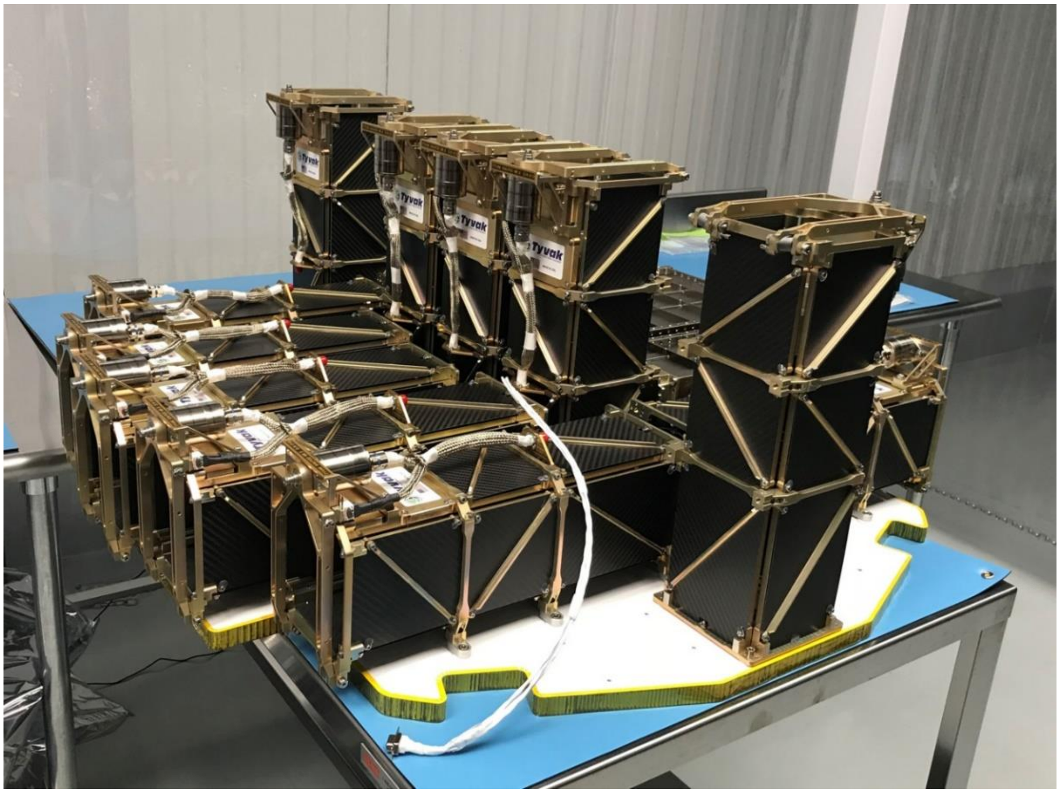

Figure 2: Tyvak Fit Check on Rocket Lab's Photon Platform, Used with Permission [14]

A less obvious benefit of containerized spacecraft is the ability to further divide their volume; the Technology Education Satellite (TechEdSat) series and ThinSat framework have proven this to be an effective platform for diminutive science payloads. TechEdSat is a line of CubeSats by University of Idaho and San Jose State University students in partnership with NASA Ames that includes multiple single-board science payloads from a variety of sources [15]. The ThinSat framework, developed by Virginia Space in partnership with Twiggs Space Lab, Northrup Grumman Innovation Systems, and NASA Wallops Flight Facility can house multiple single-board payloads and deploy those payloads as standalone satellites. A single ThinSat mission could house eighty-four 280 g payloads [16]. Students as early as elementary school have submitted successful science payloads on the ThinSat platform.

1.2.3 Component Availability

The CubeSat component market is a burgeoning field, and those working in it today may feel as if they are selling shovels during a gold rush. At the inception of CubeSat design and use, all components needed to be fabricated in-house or repurposed. Even now, specifically regarding flight software, certain subsystem components do not have plug-and-play usability, leading entire subsystems to be custom jobs with potentially high Non-Recurring Engineering (NRE) costs.

Every component vendor will have a catalog on their own website, but two resources may prove vital for first-time CubeSat designers: CubeSatShop and the Small Spacecraft Systems Virtual Institute (S3VI) Small Spacecraft Information Search [17,18]. CubeSatShop is a repository for CubeSat components where some, not all, companies will post their inventory. It may not have the perfect component for the job, but the specifications and datasheets can serve as baselines for component trade and selection. Parts cannot be purchased directly from CubeSatShop. The Small Spacecraft Information Search is like Google but for CubeSats. Hosted there is both technical information and a parts repository, but it will take more time to sift through than CubeSatShop. The team behind S3VI is exceptional, and their contribution to the Small Satellite community could not be overstated.

1.3 CubeSat Destinations

The number of successfully launched CubeSats was 1189 in November 2020, but that number does not speak to mission or deployment success [19]. A March 2020 dataset stated 1058 CubeSats had been launched and successfully deployed; 1056 of those have been to LEO [2]. A histogram of CubeSat altitude data for [2] is shown in **Figure 3**. Non-CubeSat deep space missions may be found in Appendix B.

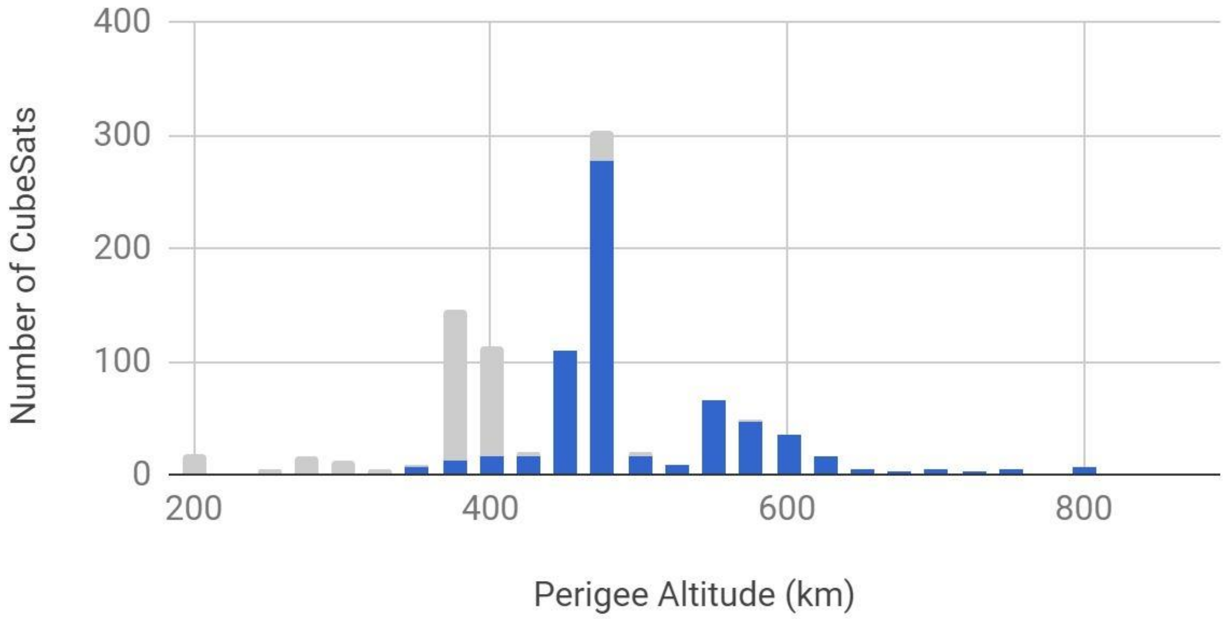

Figure 3: CubeSat Altitude Histogram. Values in Grey Indicate Decayed Orbits [2]

1.3.1 LEO Missions

A database of nearly every CubeSat launched, constellation or otherwise, may be found in [2], and the data elicits skepticism on the wisdom of university-class missions when compared to hobbyists and professionals. While professionals have a mission failure rate of 25-30 percent, **Figure 4** depicts mission success rates for first time university-class CubeSats.

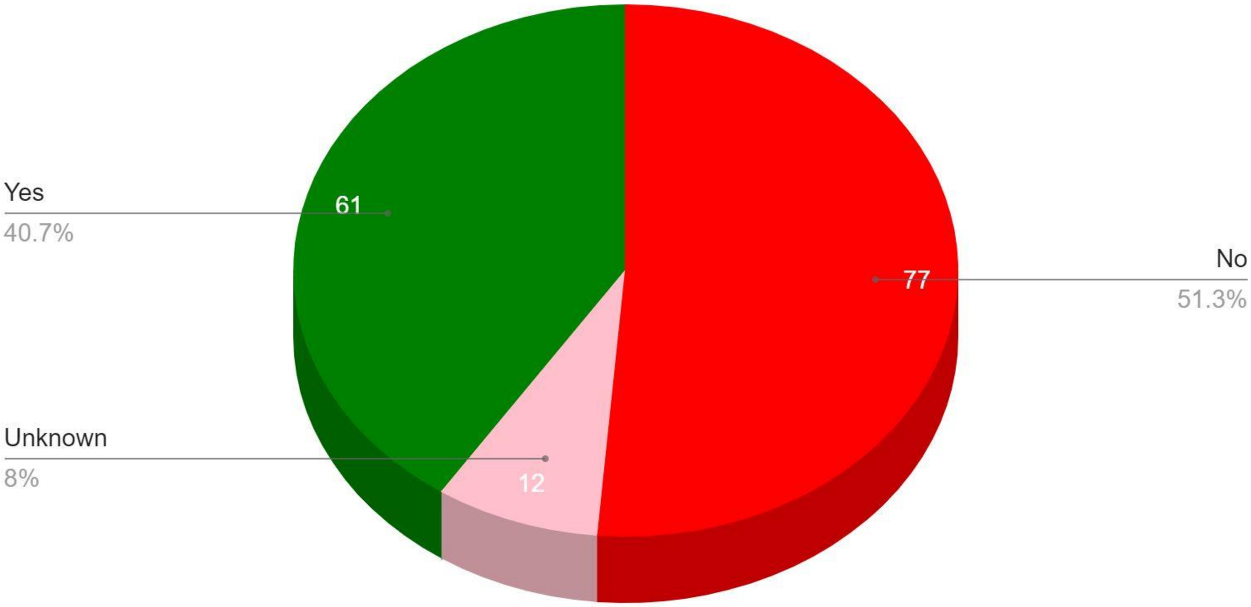

Figure 4: Success of First CubeSat Mission for University-Class Missions, 150 Universities [2]

It is evident student missions have a high rate of mission failure. Much of this has been blamed on student turnover increasing development time which leads to inadequate testing as well as insufficient flight software development time. Many case studies on what not to do in student-led programs may be found in the Small Satellite Conference archives [20].

1.3.2 Interplanetary Missions

Aside from the MarCO mission, deep space CubeSats with a currently set launch date will manifest aboard Artemis I. Thirteen CubeSats have been selected as secondary payloads, coined the “Lucky 13” by those in the community envious of their opportunity: LunIR, Lunar IceCube, NEAScout, BioSentinel, Lunar Flashlight, CuSP, LunaH-Map, Cislunar Explorers, CU-E^3, Team Miles, EQUULEUS, OMOTENASHI, and ArgoMoon [21]. CubeSat enthusiasts eagerly await their data return; some aspects of the Lucky 13 missions will be discussed further where relevant.

1.3.3 Asteroid Hunters

The Moon and Mars are not the only desirable destinations for CubeSats. Asteroids are valuable as both scientific specimina and physical resources, and two not-so-small satellites have already departed Earth with this purpose. The Origins, Spectral Interpretation, Resource Identification, Security, and Regolith Explorer (OSIRIS-REx) spacecraft launched in September 2017 with 2,110 kg wet mass to visit the B-type asteroid Bennu, and the Hayabusa2 launched in December 2014 with 609 kg wet mass to explore the C-type asteroid Ryugu [22,23].

The Asteroid Prospection Explorer (APEX) and Juventas 6U CubeSats, designed for the Hera mission as the European Space Agency's (ESA) contribution to the international Asteroid Impact and Deflection Assessment (AIDA), are probably the most exciting asteroid hunter CubeSats in the works at this time. The Didymos asteroid system is a binary system consisting of a larger and smaller asteroid termed Didymos and Dimorphos, or more affectionately Didymoon. NASA's Double Asteroid Redirection Test (DART) in 2022 will deliberately slam itself into the asteroid system to attempt to redirect its motion in the first demonstration of the kinetic impactor technique [24]. DART features Roll Out Solar Arrays (ROSA), which, while not discussed in this document due to technological infancy in CubeSat size, were proven to work aboard the ISS in 2017 and represent State of the Art technology options for CubeSats in the 2020s [25]. In 2027, Juventas and APEX will be deployed from Hera to characterize the impact site from DART. Juventas will later attempt to land (bounce slowly) on Didymoon to glean additional data from the binary system [26]. This is important because it represents the first time an international CubeSat quasi-constellation will be used as both a sensor and lander system. CubeSats will be effective at characterizing the moons of planets in Earth's solar system, and this could potentially involve sensor-lander hybrid missions. Any Near-Earth Object (NEO) is a viable target.

1.3.4 A Word on Launch Vehicles

CubeSats historically have not had an LV downselect process [27]. Launches have been manifested on a first come, first serve basis for those who could afford increasingly economical LEO manifesting costs, but this approach is not yet feasible for deep space CubeSat missions. There are only a handful of LVs intended for deep space, so secondary payload solicitation response writing becomes a key part of the manifesting procedure. Basing a mission on an uncertain launch opportunity can be dangerous, and caution is advised for missions dependent on a single LV.

1.4 The AEGIS Project

AEGIS is the brainchild of the Alabama Space Grant Consortium (ASGC). Universities within the consortium collaborate on a 6U CubeSat by synergizing senior design programs across multiple engineering disciplines. Five of the seven ASGC universities are currently party to the program: University of Alabama at Huntsville, Auburn University, University of Alabama, Alabama A&M, and the University of South Alabama. There are plans to bring on Tuskegee University and the University of Alabama at Birmingham. Disciplines involved include Aerospace, Electrical, Mechanical, Wireless, Industrial, and Software Engineering, and over 120 undergraduate students have been trained in satellite subsystem architecture design. As far as the program administration has seen in CubeSat technical conferences and literature, AEGIS is the largest intercollegiate satellite program in the world.

A distinction which has not been properly made lies between the AEGIS satellite and the ASGC program for student workforce development. At this time, both the program and the CubeSat are referred to as AEGIS. However, AEGIS will not be the final CubeSat fabricated by this program. The blurred nomenclature will continue in subsequent sections, and the author will attempt to ensure adequate context.

1.4.1 Multi-University Collaborative Program

This program aims to be the paragon for other Space Grant Consortia or university partnerships to emulate, and the practices defined here are intended as a manual. The work required to bring a satellite to Preliminary Design Review (PDR) should be examined by program administrators and delineated in a way that undergraduate senior design teams can tackle. Once the incipient Work Breakdown Structure (WBS) has been defined by a team with at least cursory familiarity of satellite operations, Requests For Proposals (RFP) may be sent out by the Space Grant Consortium or lead university.

1.4.1.1 Starting a Subsystem Design Team

RFPs are how the program will bring on new teams, and not all the work must or should be done at the same time. Component Trade and Selection (T&S) is an early design life task while Ground Control Station (GCS) operations definition should be reserved for later. It is not that the later work is unimportant or unnecessary; university-class missions must learn to use and schedule their limited resources effectively. An example list of Senior Design teams, which may not be the same for other programs, is Propulsion, Structures & Thermal, Science, Flight Software (FSW), Command & Data Handling (C&DH), Guidance, Navigation, & Control (GN&C), Telemetry, Tracking & Command (TT&C), Electrical Power System (EPS), Orbit, Mechanisms, Systems Engineering, Astrodynamics, and Ground Control Station (GCS). If subsystem teams are to be combined or divided, it should reflect the strengths of a university. To expound, Structural design and Thermal design should be considered separate disciplines. Auburn University has significant capabilities in both areas, so a large, singular Senior Design team was created to address both design spaces. Structural and Thermal design will be addressed later in separate sections. **Table 1** lists the AEGIS subsystems and their universities. As AEGIS has multiple design reviews before Integration, Verification and Testing (IV&T) would begin, not all subsystem RFPs have been released. Note that Propulsion was assigned to a Mechanical Engineering team because the technical advisor had expertise in this area; Propulsion should be considered for Aerospace Engineering students first. While some schools have distinct Aerospace and Mechanical colleges, some feature Aeromechanical departments.

Table 1: Senior Design Teams and their Engineering Disciplines

Subsystem	University	Engineering Discipline
Propulsion	Auburn University	Mechanical
Structures & Thermal	Auburn University	Mechanical
Science	University of Alabama at Huntsville	Physics, Aeromechanical
Flight Software	Auburn University	Software
Command & Data Handling	University of Alabama	Electrical
Guidance, Navigation, & Control	University of South Alabama	Mechanical
Telemetry, Tracking, & Command	University of South Alabama	Electrical
Electrical Power System	University of Alabama	Electrical
Orbit	University of Alabama at Huntsville	Aerospace
Mechanisms (2 teams)	Auburn University, Alabama A&M	Mechanical
Systems Engineering	University of Alabama at Huntsville	Industrial, Aeromechanical
Astrodynamics	Unreleased	N/A
Ground Control Station	Unreleased	N/A

1.4.1.2 Subsystem Management

Each subsystem should feature a graduate student or faculty member who serves as the Subsystem Lead for the program and the technical advisor for the senior design team. Ideally, this person is at the same university as the design team. This advisor will take requirements from the Systems Engineering team and turn those requirements into actionable items such as trade studies and code reviews. The Project Manager (PM) and Chief Engineer (CE) will communicate frequently with the subsystem lead to ensure they have everything they need to complete actionable items from the requirements and WBS.

1.4.1.3 Inter-University Communication

It was rapidly understood that email is not enough for the type of productivity a satellite program demands. At first, GroupMe was used within singular universities to facilitate internal communication, but this was equally insufficient for the required frequency of inter-university communication. Enter Software as a Service (SaaS). SaaS communications platforms such as Slack or Microsoft Teams are vital to the success of a geographically disperse design team. AEGIS uses Slack, but the purpose here is less a corporate endorsement and more an endorsement of the utility itself. Slack's free service allows for file sharing and a large number of channels, but it does not keep more than 10,000 messages across the workspace. Upgrading to the plan which keeps all data costs ~$7 per month per person, so a yearlong plan for 100+ people will cost upwards of $7,000. Functionally, there does not seem to be a difference other than the lack of message posterity, and the free service is recommended.

1.4.1.4 Design Reviews

Senior design is based around university academic calendars, and those cannot be eschewed entirely for the sake of a satellite program. AEGIS is structured so that programmatic reviews coincide with final reviews for the students. Generally, all universities need is some kind of formal review to serve as their university-level PDR, Critical Design Review (CDR), or Operational Readiness Review (ORR), but university programs differ by semester and requirement. Some universities have single-semester senior design programs, while other universities break it up over two semesters. Some disciplines, such as Mechanical Engineering, have university-level PDRs, while other disciplines, such as Software Engineering, have code review cycles. The approval of a satellite-level review functioning as a university-level review is handled by the Subsystem Lead at a given university.

Reviews vary by subject matter and relative importance. A Merit and Feasibility Review (MFR) is almost always required for a solicitation response wherein Subject Matter Experts (SMEs), mostly from NASA, evaluate a design's usefulness and readiness. A failure at this review is a significant setback which may preclude a program from applying as a launch vehicle secondary payload. A System Requirements Review (SRR), however, is a necessary internal review wherein mission and component requirements are refined as they relate to delivering mission success. This review has no formal consequence if things do not go as planned. The internal question to be answered is, *"How many students from a team should present?"* A counterintuitive rule of thumb may be applied here. The more important a review is to the continuance of a program, the fewer students should be presenting at that review. While it is important that students are exposed to formal SME reviews as part of their workforce development, budgetary concerns on the order of millions of dollars are at stake. Successful programs will schedule review timelines that ensure students have proper exposure to spacecraft engineering environments without jeopardizing the mission by forcing unprepared students to present.

Finally, review chronology among existing satellite programs is woefully inconsistent. NASA defines phases as conceptual study in Pre-Phase A, including Mission Concept Review (MCR), preliminary analysis in Phase A, including Initial Confirmation Review (ICR) and Mission Definition Review (MDR), system definition in Phase B, including PDR, design and development in Phases C and D, including CDR, Pre-Environmental Review (PER,) and Pre-Ship Review (PSR), and operations in Phase E, potentially including an Operational Readiness Review (ORR) or Flight Readiness Review (FRR) [28]. In contrast, the University Nanosatellite Program, a CubeSat workforce development program run jointly by the Air Force Office of Scientific Research (AFOSR), Air Force Research Laboratory (AFRL), and the American Institute of Aeronautics and Astronautics (AIAA), defines Phase A all the way through CDR and a Flight Selection

Review (FSR), Phase B into Pre-Integration Review (PIR) and a first PSR, Phase C from a Test Readiness Review (TRR) to a second PSR, and Phase D from launch to End Of Life (EOL) [29]. These are two entirely different design schedules for the same type of spacecraft, and both have desirable aspects that the other does not feature. The program phases are shown in **Tables 2** and **3**. Spacecraft mission designers are encouraged to begin with the phases outlined in [28], but the chosen review cycle should be finalized with a panel of SMEs for the program.

Table 2: NASA Mission Phases [28]

Phase	Work Definition	Review	Acronym
Pre-A	Conceptual Study	Mission Concept Review	MCR
A	Preliminary Analysis	Initial Confirmation Review	ICR
		Mission Definition Review	MDR
B	System Definition	Preliminary Design Review	PDR
C	Technical Design	Critical Design Review	CDR
D	System Coordination and Testing	Pre-Environmental Review	PER
		Pre-Ship Review	PSR
E	Flight Operations	Flight Readiness Review	FRR
		Launch	N/A

Table 3: UNP Mission Phases [29]

Phase	Work Definition	Review	Acronym
A	Conceptual Study, Preliminary Analysis, System Definition, and Technical Design	System Concept Review	SCR
		System Requirements Review	SRR
		Program Management Review	PMR
		Preliminary Design Review	PDR
		Critical Design Review	CDR
B	Technical Review and Qualification	Pre-Integration Review	PIR
		AFRL Pre-Ship Review	PSR
C	Environmental Testing	Test Readiness Review	TRR
		Mission Readiness Review	MRR
		LV Pre-Ship Review	PSR
D	Flight Operations	Launch & Early Ops Review	EOR

1.4.1.5 Subject Matter Experts

There are aspects of spacecraft architecture engineering that are gleaned only through years of experience. It is important that some, if not all, reviews are presided over by a panel of SMEs with this kind of experience, and reaching out to potential SMEs should happen prior to Phase A. Spacecraft designers at SME reviews should expect to feel like marshmallows. You are going to get roasted, but you will be more desirable after the experience. SMEs see aspects of the design that have gone previously unconsidered, and that is the point of inviting them. Listed in **Table 4** are the SMEs who were invited to the AEGIS MFR as an example for which and how many people to invite. To reiterate, an MFR is part of a solicitation response process, not a design phase review.

Table 4: AEGIS Merit and Feasibility Review SMEs

Name	Organization	Subsystem Expertise
Michelle Hui	MSFC-ST12	Science
Scott Craig	MSFC-EV42	Orbit
Stephen Elrod	MSFC-ST14	Systems Engineering
Lisa Roth	MSFC-ES22	Structures and Mechanisms
Stephanie Mauro	MSFC-ES22	Thermal Control
John Rakoczy	MSFC-EV41	Guidance, Navigation, & Control
Evan Anzalone	MSFC-EV41	Guidance, Navigation, & Control
Daniel Cavender	MSFC-ST24	Propulsion
Miguel Rodriguez-Otero	MSFC-ES36	Electrical Power System
Luster Ingram	MSFC-ES35	Command & Data Handling
Jeff Levinson	JPL US 348C	Flight Software
Michael Starch	JPL US 348C	Flight Software
Timothy Canham	JPL US 348C	Flight Software
Alex Few	MSFC-ES21	Mechanisms
Bert Gangl	MSFC-ES45	Telemetry, Tracking, & Command

1.4.2 Science Mission

The prime directive of AEGIS is to characterize the efficacy of compacted, augmented lunar regolith as radiation shielding in deep space. If a manned mission is to travel into deep space, dedicated radiation shielding on the human module must be present. That shielding is generally heavy, and it would require significant propellant mass to liftoff from Earth with heavy shielding attached. The science instrument will determine how effective the radiation shielding would be if a mission landed on the Moon, obtained lunar regolith, augmented it as radiation shielding, attached it to the spacecraft exterior, and departed from the lunar surface.

The science payload is a charged particle detector that uses silicon detector pairs with a scintillating crystal calorimeter to record background particles as they pass through a control and shielded volume. These measurements provide insight on particle interactions of the shield and calculation of dose reduction from the shield material. A depiction of the science instrument is found in **Figure 5.** The instrument would have the ability to distinguish ion charge and energy spectrum in the detector using a combination of energy measurements and coincidence triggering between the silicon detectors and calorimeter. Each side of the instrument operates independently to measure the shield and control volumes.

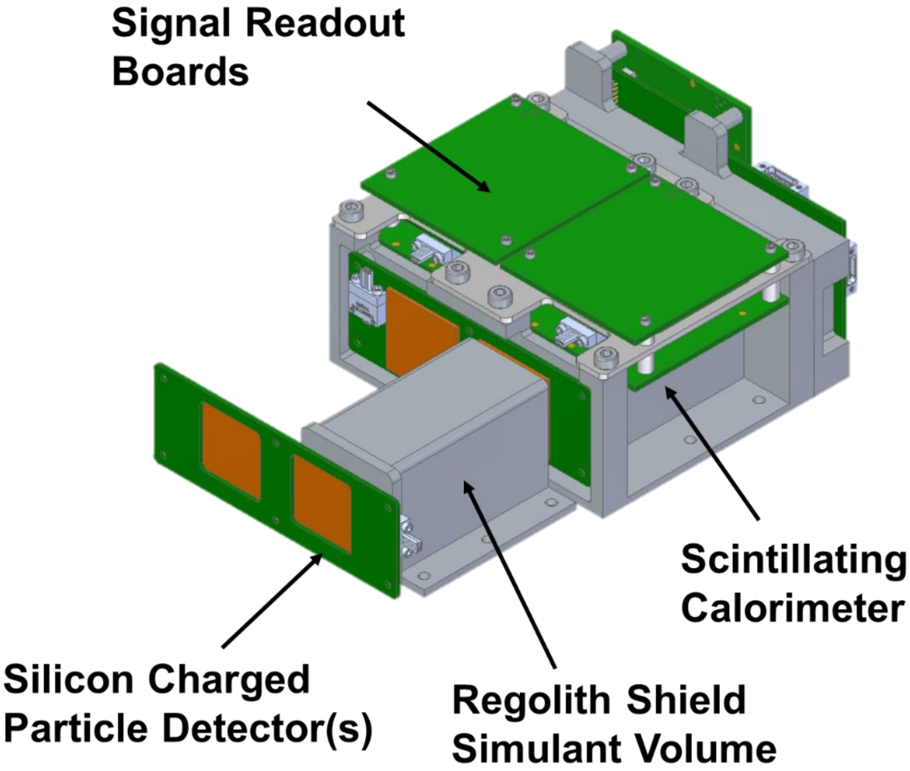
Signal Readout Boards
Scintillating Calorimeter
Silicon Charged Particle Detector(s)
Regolith Shield Simulant Volume

Figure 5: AEGIS Science Payload

1.4.3 Educational Objectives and Metrics

The scope of a geographically disperse, university-class mission and its focus on student involvement provides a unique environment for students to experience the challenges posed in the design life of space systems and collaborative large-scale projects. As stated in the NASA 2018 Strategic Plan, Strategic Objective 3.3 [30], NASA seeks to “inspire, engage, educate, and employ the next generation of explorers through NASA-unique Science, Technology, Engineering and Mathematics learning opportunities.” The AEGIS project includes three main STEM student learning objectives:

- **Learning Objective 1 (LO-1):** Provide students with the opportunity to participate in the design and development of an actual aerospace system to realize the benefits that only real project experience can provide.

- **Learning Objective 2 (LO-2):** Provide students with the skills and experience needed to work in collaborative and diverse teams that are geographically and organizationally dispersed, equipping the students to productively contribute to projects in today’s global development environment.

- **Learning Objective 3 (LO-3):** Provide students with the skills and experience needed to successfully contribute to projects that were initiated by and/or will be completed by others, equipping students to deal with the knowledge management challenges resulting from member turnover on development teams.

While LO-1 would have been as beneficial to students today as a generation prior to today, the second and third learning objectives are driven by the need to equip today's STEM graduates with the experience to function productively in a system development environment far different than Apollo-era missions. These learning objectives for the AEGIS project were endorsed by the ASGC Management Committee upon origination of the project in February 2018 and then by the ASGC Industrial Advisory Board in June 2019.

It is not enough to say that a program is teaching students just by initiating a CubeSat mission. The performance of the educational objectives will be quantifiable through metrics to be measured throughout the mission at internal reviews.

- **Educational Metric 1 (EM-1):** Number of students involved in the design effort; including undergraduate students, graduate students and K-12 students who are reached through classroom training, science fairs, Science Olympiad and campus visits (**LO-1**).

- **Educational Metric 2 (EM-2):** Meeting deadlines and milestone dates in a well-coordinated system engineering effort wherein success is ascertained by the team of SME reviewers (**LO-1,2,3**).

- **Educational Metric 3 (EM-3):** Numbers of female, minority and disabled students in the program (**LO-2**).

- **Educational Metric 4 (EM-4):** Measure of faculty and student incentives and opportunities provided through this program to keep them participating for knowledge retention. This would include funding from ASGC for scholarships/fellowships/internships/faculty fellowships, ASGC supplemental awarded grants, collective proposals for competitive grant opportunities, and funding of equipment for faculty laboratories assisting CubeSat capabilities (**LO-3**).

1.4.4 Timeline and Development Strategy

AEGIS began work in 2018 and, like everyone, experienced scheduling and development delays due to SARS-CoV-2 beginning in 2019. The excellent work of the PM and Lead Systems Engineer (LSE) kept the program on track with the help of Project Management Plans (PMP), Systems Engineering Management Plans (SEMP), Cost and Acquisition Plans, Funding Review Boards, Information Technology Plans, Risk Management Plans, and Quality Assurance Plans. Their contribution to the program could not be overstated. The culmination of these plans results in an Integrated Master Plan (IMP), generated primarily by the PM and LSE, depicted in **Figure 6**.

Development strategies and timelines are difficult to adhere to with the inherent turnover of a student workforce. While reviews force students to document their work and student-created documentation is retained, student knowledge bases are lost with each new student team. Some senior design programs are one semester, and some are two semesters. In either case, the creation of turnover documents is imperative. The goal is to reduce the learning curve from one student team to another while retaining the necessary satellite information.

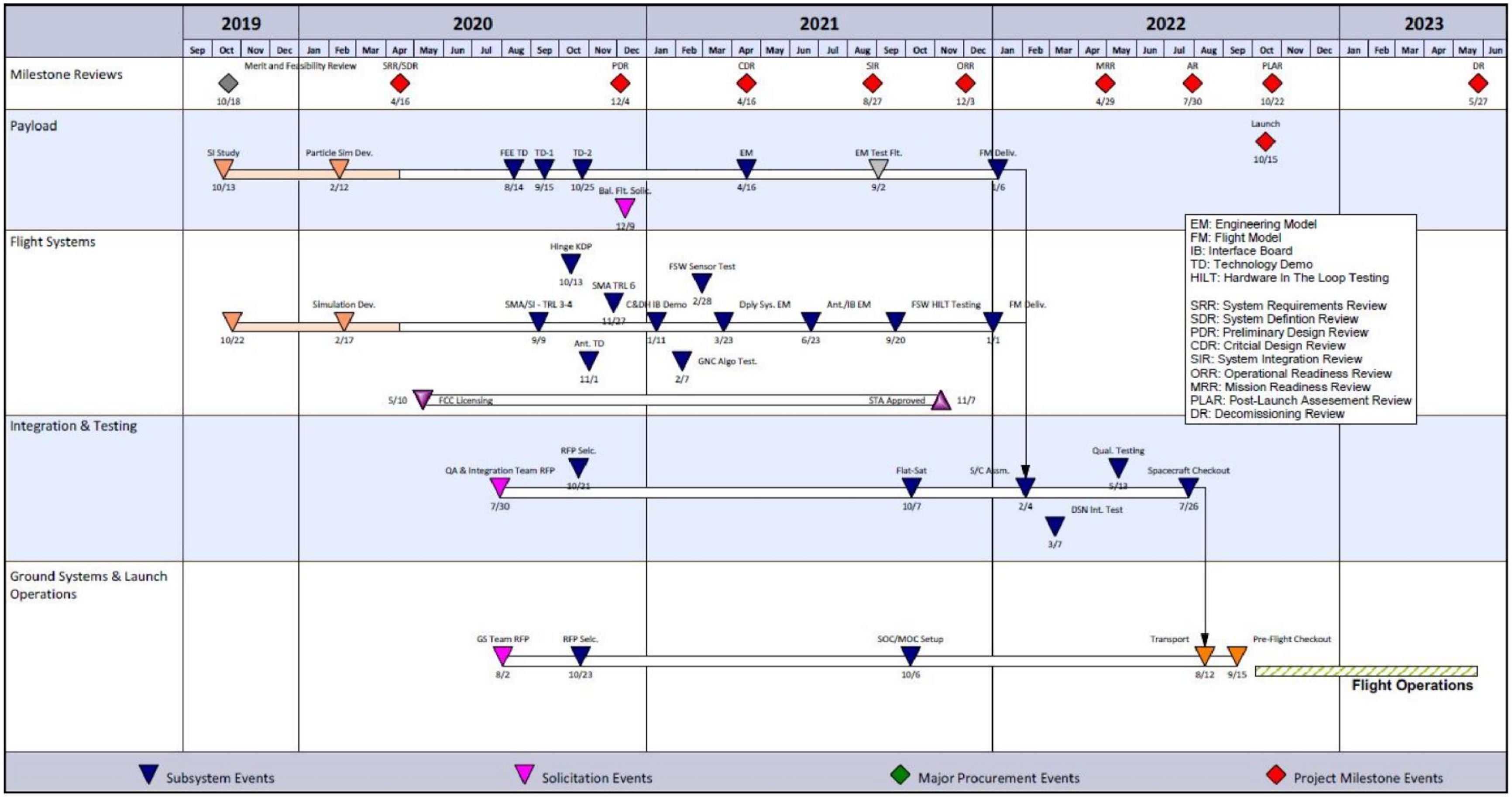

Figure 6: Integrated Master Plan

1.4.5 Future of the Program

AEGIS will be the first of many deep space CubeSats designed by the ASGC. Students across the state have gained knowledge, experience, and confidence in spacecraft design, and the program is structured to expect student turnover rather than be hindered by turnover’s negative effects. By structuring a program to play to the strengths of students’ experience levels and mindsets, a program can turn a historically negative effect into a positive one. There is no right way to build a university-class satellite, but universities involved in **Figure 4** will say there are plenty of wrong ways.

AEGIS applied to the Artemis II launch vehicle secondary payload solicitation released in August 2019. In August 2020, Artemis II announced that they would not be taking any secondary payloads or even travelling to the Moon. This was a debilitating outcome for the AEGIS mission, and the reason was that Artemis II was being forced to mitigate risk with the Orion spacecraft because it was deigned that Artemis III had to put humans on the Moon by 2024. Three days after Artemis II’s secondary payload opportunities were canceled NASA released a call for science proposals that astronauts could perform while on the Moon. So not only did NASA cancel the secondary payload opportunities because they were being forced to put astronauts on the Moon, they had no idea what the astronauts would do while they were there.

AEGIS has been working for two years on a mission that was proceeding to PDR in Fall 2020. The mission design and lessons learned are valid and are presented as a case study. As Artemis II never officially released a lunar orbit, an assumed orbit based on Artemis I was used for the mission Concept of Operations (ConOps) presented in Section 2. Lunar orbital considerations are included, and detailed analysis is presented for each subsystem. It is likely that the launch vehicle, orbit, science payload, and name of AEGIS will change for a new mission that builds upon this work.

1.4.6 Document Considerations

Before diving into the world of deep space satellite development, a few words must be said about this document itself. It is a collaboration of work by hundreds of students and university faculty organized by the author. Citations are copiously provided, student involvement is acknowledged, and investigative faculty are specified where applicable. Detailed material on the science payload will not be provided, and considerations for SE, IV&T, and C&DH will be limited.

When designing any engineering system, everything starts with requirements. Requirements are what dictate component viability, and components generally follow three pathways to requirement satisfaction. A designer can choose from existing components, modify an existing component, or develop a component from scratch to fit the need. Requirements for this mission are not explicitly stated, but this document is intended to facilitate the reproduction of the AEGIS process for other Space Grant Consortia or geographically disperse collections of universities. Thus, mission-specific requirements at the beginning of each subsystem section are replaced with Design Objectives directly stemming, in some cases verbatim, from the NASA Technical Standards System’s Rules for the Design, Development, Verification, and Operation of Flight Systems [28]. Many of the Design Objectives (DOs) are written for NASA Phase B or prior design, and Phase C or later design will likely include component-specific qualifications for a given mission. In short, attention was paid to applying a certain level of generalization to the DOs so that this document may be a steppingstone to ensuring mission success no matter what the mission may be, and DO verbiage is not original or from the author.

2. Mission and Spacecraft ConOps

Upon purchase of or selection to a deep space LV, a process called manifesting, a Mission Integrator (MI) is assigned to the program. The MI communicates the official volume, mass, umbilical location, access port location, and delivery date of the spacecraft unless a program is purchasing their own dispenser. The spacecraft is delivered to the MI up to four months before the launch date with limited additional work considerations from the development team. The spacecraft will be integrated into the LV dispenser with a full charge, but it does have the potential to sit on the launch pad for an extended period. From the time when the spacecraft is delivered to the MI to the time when the spacecraft is intended to be disposed of in space, the mission can be delineated into segments. Mission segments are subsystem-specific breakdowns of a larger spacecraft ConOps.

Mission segments are of primary importance to two subsystems: FSW and Structures, and the mission segments for those two subsystems are not the same. FSW mission segments will dictate the spacecraft operations, and structural mission segments will detail the static loads, dynamic loads, and fatigue implications for the design. For example, the structural mission segments must account for whether the spacecraft is transported to the LV by car or forklift, but the FSW would not need this information. Mission segments such as a thruster burn phase or dispenser deployment phase are the same for both subsystems. General mission concepts, FSW mission segments, and structural mission segments are presented; high-level mission ConOps is broken down into software state logic in Appendix A.

2.1 Cislunar Launch Vehicles

The primary benefit of deep space LV manifestation is avoiding unshielded crossings of the Van Allen Belts (VABs). The VABs, massive torii of trapped, deleterious, charged particles, are fully described in Sections 3.7.3.3 and 4.5.2.3, and spacecraft do their best to avoid them. Only super-heavy class LVs have the propulsive capability to reach bus stops, i.e. spacecraft dispensing zones, that begin outside of the VABs. A secondary benefit is reduced propulsive requirements on the CubeSat itself to reach an intended target. The trajectory and bus stops of Artemis I are shown in **Figure 7.**

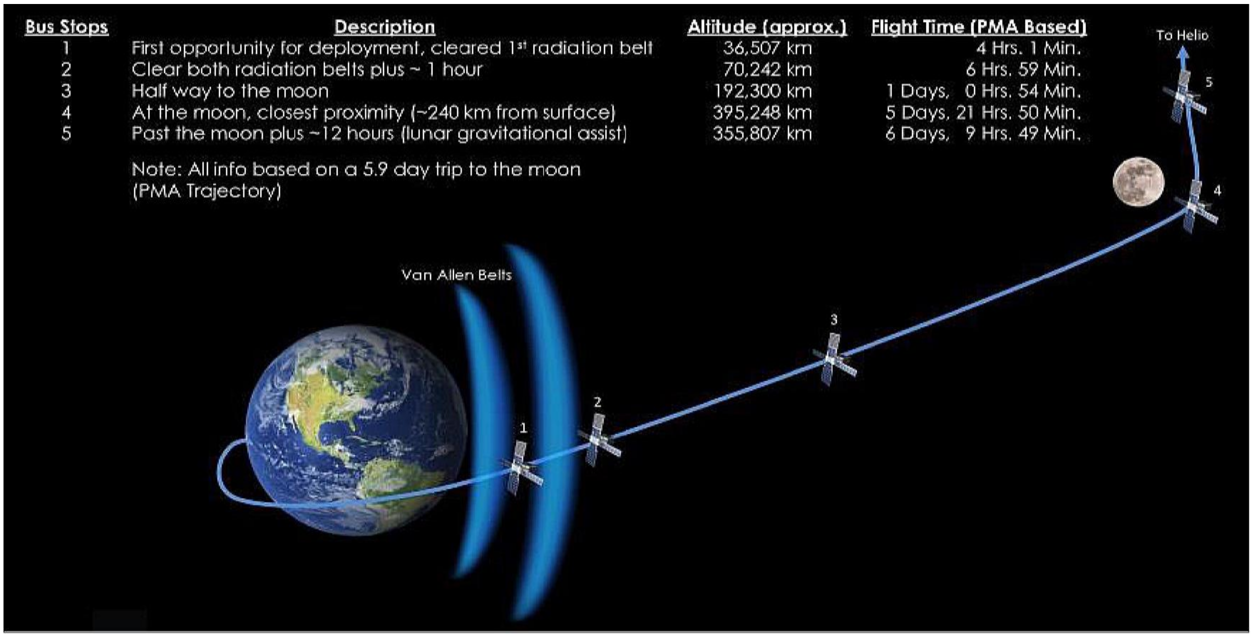

Bus Stops	Description	Altitude (approx.)	Flight Time (PMA Based)
1	First opportunity for deployment, cleared 1st radiation belt	36,507 km	4 Hrs. 1 Min.
2	Clear both radiation belts plus ~ 1 hour	70,242 km	6 Hrs. 59 Min.
3	Half way to the moon	192,300 km	1 Days, 0 Hrs. 54 Min.
4	At the moon, closest proximity (~240 km from surface)	395,248 km	5 Days, 21 Hrs. 50 Min.
5	Past the moon plus ~12 hours (lunar gravitational assist)	355,807 km	6 Days, 9 Hrs. 49 Min.

Note: All info based on a 5.9 day trip to the moon
(PMA Trajectory)

Figure 7: Artemis I CubeSat Bus Stops [31]

Some spacecraft designed to characterize aspects of the VABs may choose to depart from Artemis I at the first bus stop, but spacecraft for any other mission type should strive to avoid them. The module which houses the CubeSats themselves has been known as the Orion Stage Adapter (OSA), but current iterations of the OSA are known as Block 1 or Block 1-b. The OSA is seen in **Figure 8** and is mounted to the Interim Cryogenic Propulsion Stage (ICPS) of the Space Launch System (SLS).

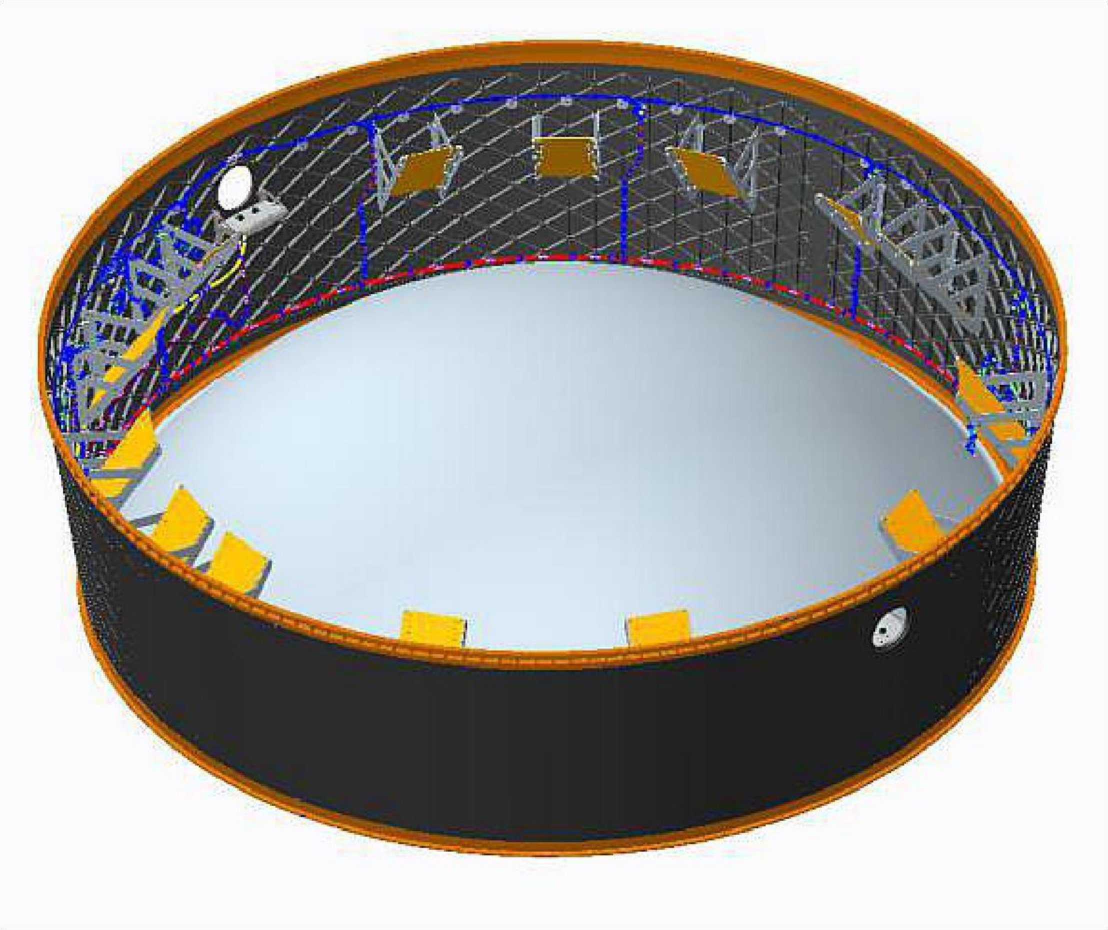

Figure 8: Orion Stage Adapter, Artemis I [31]

The OSA is designed to rotate as it deploys CubeSats, and no more than 1 CubeSat will be ejected per 60 seconds. The nominal design rotation is 1 rotation per 60 seconds as well. As the CubeSats are located on angled, sequenced housing structures that may or may not feature vibrational isolators depending on the dispenser vendor, the initial trajectory of the CubeSat ejection could be along any vector on a conic surface extending from the OSA. There is no way to determine what the exact initial trajectory would be. Therefore, one of the first mission operations upon receiving state vectors from the ground station is to perform any necessary trajectory corrections. As the velocity of Artemis I at the first two bus stops is estimated near 11.2 km/s, this may represent a sizable percent of total propellant mass. The takeaway is that the first burn after ejection is the most important, and ground teams should be ready to perform on-site trajectory correction maneuver calculations directly after deployment. AEGIS plans to depart at bus stop 2.

2.2 Mission Orbit and Trajectory

As the full orbit for Artemis II was never announced, AEGIS evaluated a set of potential orbits which included lunar distant retrograde orbits, the L4/L5 Lagrange points, near-rectilinear halo orbits, and a 400,000 km High Earth Orbit (HEO). HEO sometimes represents Highly Elliptical Orbit but does not here. It was found that a mild eccentricity HEO was optimal for both the mission ΔV, or required change in velocity to achieve a target orbit, and communications profile while providing the least amount of uncertainty. The orbit must be considered first because the propulsion and communications requirements are strictly dependent upon the ΔV and slant range, or distance that the spacecraft must communicate over. Orbit uncertainties propagate into component trade and selection uncertainties; it was determined that the communication slant range would be between 200,000 km and 800,000 km for the six-month science mission duration. A nominal altitude over the mission lifespan is considered and shown in **Figure 9**, where blue represents the spacecraft distance to Earth and orange represents the lunar distance to Earth. The initial state vectors are found in **Table 5**, and the three-dimensional trajectory is shown in **Figure 10**. **Figure 9** was made by the LSE using AGI's Systems Tool Kit [32] and Excel. The first lunar flyby occurs when the spacecraft approaches 400,000 km, and the science mission begins roughly 90 days into the flight.

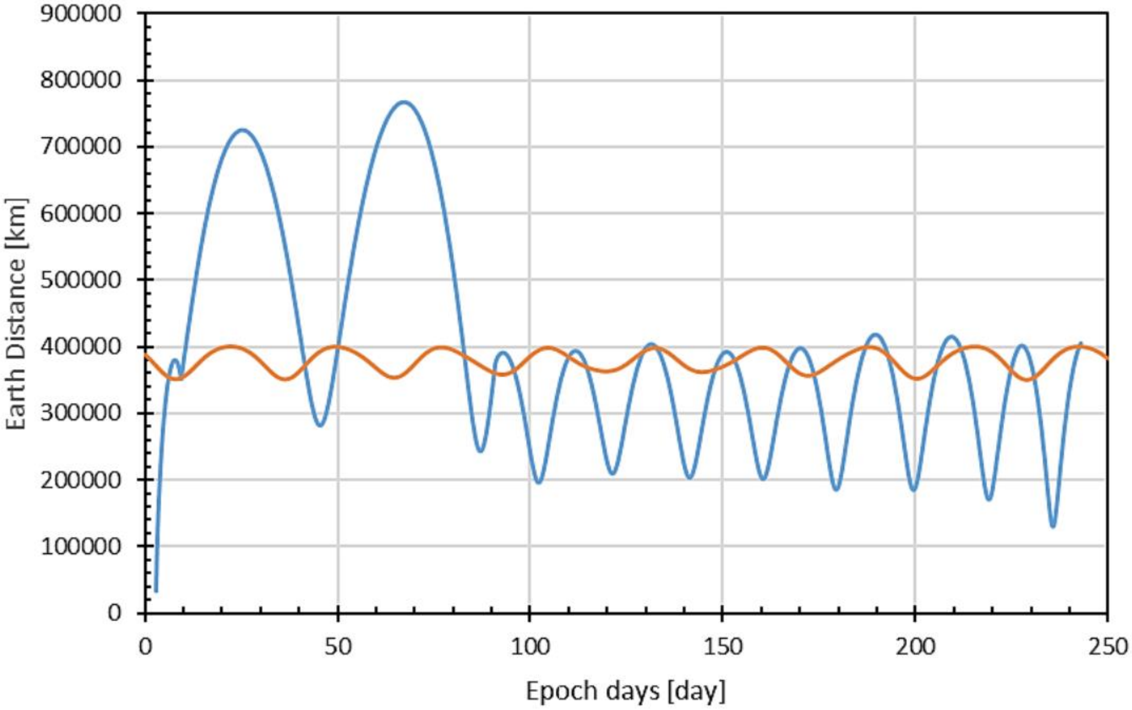

Figure 9: AEGIS Mission Altitude Over Proposed Lifetime

The ΔV required to achieve this orbit upon ejection from Artemis II at bus stop 2, assuming the same launch vehicle velocity values as Artemis I, is 134 m/s, broken into two separate burn maneuvers. The burn maneuvers are both retrothrusting maneuvers designed to bleed off velocity imparted to the spacecraft during initial ejection. If the spacecraft did not slow itself down, it could bypass the Moon entirely rather than utilize a gravitational assist to achieve a desired HEO. Therefore, the first burn would set up the gravitational assist and prevent a hyperbolic lunar trajectory while the second burn would stabilize the spacecraft in HEO. With a workable ΔV and slant range envelope defined, trade and selection can begin for specific subsystems, discussed at length in Section 3.

Table 5: ICPS Initial State Vectors

Cartesian Parameter, (J2000 ECI Frame)	Value	Unit
X	-1.8835789496E+04	km
Y	-2.8893210530E+04	km
X	-1.9149088979E+04	km
V_x	-1.3339449483E-01	km/s
V_y	-3.6408958514E+00	km/s
V_z	-2.2210640813E+00	km/s

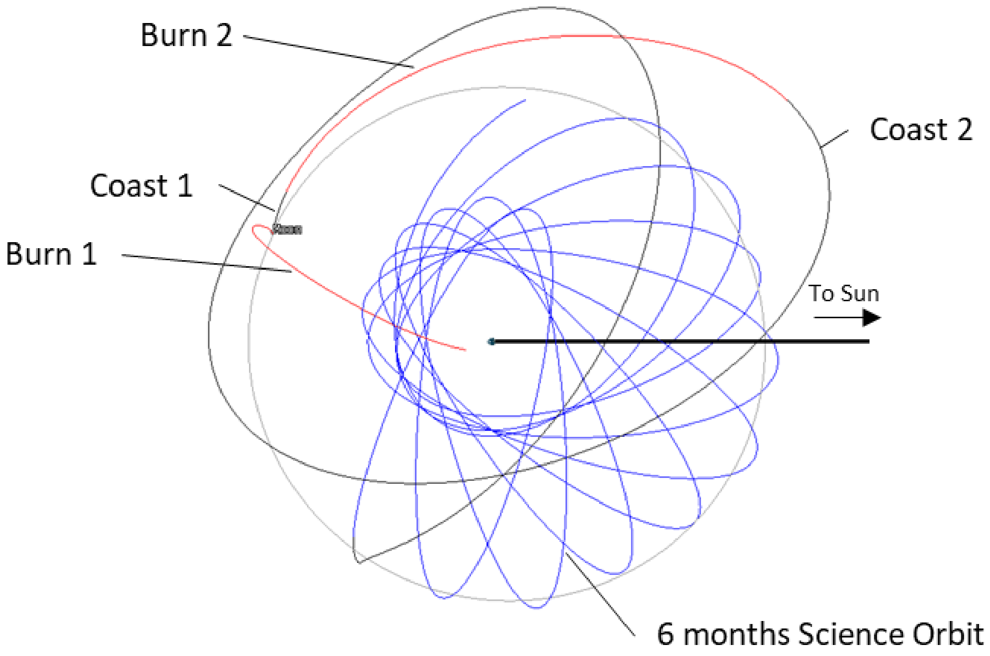

Figure 10: AEGIS Trajectory, Earth-Sun Rotating Frame. Red represents burn maneuvers, grey represents coast trajectories, blue represents science data collection orbit

2.3 Mission Segment Definition: Structural

Structural mission segments are defined to provide clear distinctions between static, dynamic, and thermal stress environments, and understanding them allows for a standardization of stress and fatigue calculations. For AEGIS, structural mission segments are broken down from terrestrial transport to disposal. Further discussion of structural mission phases is found in Section 3.2. Structural mission segments are enumerated in **Table 6**.

Table 6: AEGIS Structural Mission Segments

Segment Number	Segment Title
1	Terrestrial Transport
2	Vehicle Assembly Building Storage
3	Pre-Launch
4	Dynamic Ascent
5	Static Ascent
6	Launch Vehicle Coast
7	CubeSat Deployment
8	Commissioning
9	Burn 1
10	On-Orbit 1
11	Burn 2
12	On-Orbit 2
13	Science Orbit
14	Reaction Wheel Desaturation
15	Disposal

Segments 1-3 occur before launch but after providing the spacecraft to the MI, and all represent mild static or thermal stresses. Thermal stresses in this sense are temperature swings causing swelling and shrinking of fasteners in the bus chassis leading to structural fatigue. Dynamic and static ascent account for the difference between launch vehicle thruster ignition versus general thruster operation for ten seconds or more. Vibrational considerations for thruster ignition are severe, and the dynamic profile of constant operation is not the same as the ignition profile.

After the primary boosters have finished firing (during ground test they were fired for 122 seconds), the launch vehicle will burn out its primary engines and coast along its defined trajectory. While no static or dynamic loads are present in this period, a thermal profile must be analyzed as the LV comes into thermal equilibrium. A small but non-negligible dynamic load is imparted during CubeSat ejection, and a commissioning phase allows for thermal equilibrium to be reached outside of the launch vehicle. Commissioning also allows for any outgassing considerations to be resolved.

Burn phases are not necessary for every spacecraft mission, but certain thrusters exhibit substantial thermal soakback, or radiative emission from the thruster exhaust plume back to the spacecraft, which must be accounted for. Thermal soakback considerations are difficult to estimate and thruster-specific; they will not be covered in this work. The electric propulsion thruster utilized by AEGIS features a thrust on the order of 0.3 µN at a mass flow rate of 10^{-8} kg/s, so static, dynamic, and thermal soakback loads are negligible. The first burn period is for ~6.5 days, and the second is for ~20 days. Both burns will change the spacecraft orbit, and consequentially the thermal environment, thus the thermal cycling profile encountered by the chassis fasteners changes. Segments 9-13 represent only those thermal cycling considerations based on differing orbits, and segment 14 is meant to cover any reaction wheel desaturation maneuver, no matter if it occurs directly after segment 8, before segment 15, or anywhere in between. Disposal, the final mission segment, represents a final burn with no additional operations.

2.4 Mission Segment Definition: Software

Software mission segment definition is the precursor to formal, detailed ConOps definition, and it is more about anticipated operations of the spacecraft than the environment the spacecraft will encounter. While structural mission segments, other than reaction wheel desaturation, are sequential, defined by the amount of time spent within a given environment, software mission segments must be able to internally select which mission segment should ensue after the completion of another segment according to the logic of the FSW. Certain tenets remain the same in that reaction wheel desaturation occurs when required during nominal operations and disposal occurs last, but in-situ requirements play an enhanced role in the software logic flow. These mission segments are known as software states when logic flows are applied, which occurs after mission sequencing shown in **Figure 11**. A charge state may follow a communications state if the batteries display high Depth of Discharge (DoD), and safety states must be enterable at any time. Software mission segment titles are shown in **Table 7**. The order of the presented mission segments is immaterial, and software state logic flow is detailed in Appendix B.

Table 7: Software Mission Segment Definition

Segment Number	Segment Title
1	Deployment
2	Contingency
3	Charge
4	Communications
5	Warm-up
6	Burn
7	Science
8	Reaction Wheel Desaturation
9	Reset
10	Safety 1
11	Safety 2
12	Pre-Disposal
13	Disposal

The deployment software state is enacted by deployment switches registering that the spacecraft has exited the dispenser, described in Section 3.2.4.1. Deployment handles initialization of components, release of solar array Hold and Release Mechanisms (HRMs), and preliminary diagnostics. Contingency is analogous to a safety state but specifically for the recognition of a debilitating issue that occurs immediately following ejection from the dispenser during deployment operations. Charge finds the Sun and points the spacecraft solar arrays toward it while carefully monitoring battery levels and thermometer readings. Communications locates the Earth and engages in any ground station operations, described in Sections 3.6.8 and 3.6.9. Warm-up is a direct precursor to burn wherein the thruster propellant is being heated from a solid to a liquid, but burn operations are so critical that a planned hard reset is a part of the warm-up sequence to prevent any radiation-induced faults in volatile memory from manifesting as errors. Distinctions between faults and errors are described in Section 4.3.1. Non-deployment initialization is handled in the reset state but is not shown in Appendix B. Science represents nominal spacecraft operations, and reaction wheel desaturation handles the complex logic of coupling thrust vector control and feedback linearization schemes to drive reaction wheel angular velocities down to zero. Safety 1 represents non-emergency on-orbit errors that are assumed to be recoverable, and the spacecraft does not need to immediately contact Earth. Safety 2 represents an error that must be immediately addressed by the ground control team because the spacecraft either does not understand the error, or recovery operations in Safety 1 did not bring a faulty component back online. Transitions between software states often involve the powering on or off of spacecraft components. The science instrument would not be powered-on during burn phase, and the radio would not be attempting to downlink information during science data collection. Readers are encouraged to skim Appendix B to get a sense of software operations before proceeding to Section 3.

2.5 Concept of Operations

Tables 6 and 7 describe spacecraft ConOps breakdowns from distinct subsystem perspectives to get a sense of how subsystem design approaches react to mission goals. Mission success not including educational goals is defined as six months of valuable science data return, though structural fatigue is qualified for one year. A high-level ConOps developed by the PM, LSE, and CE is illustrated in **Figure 11**.

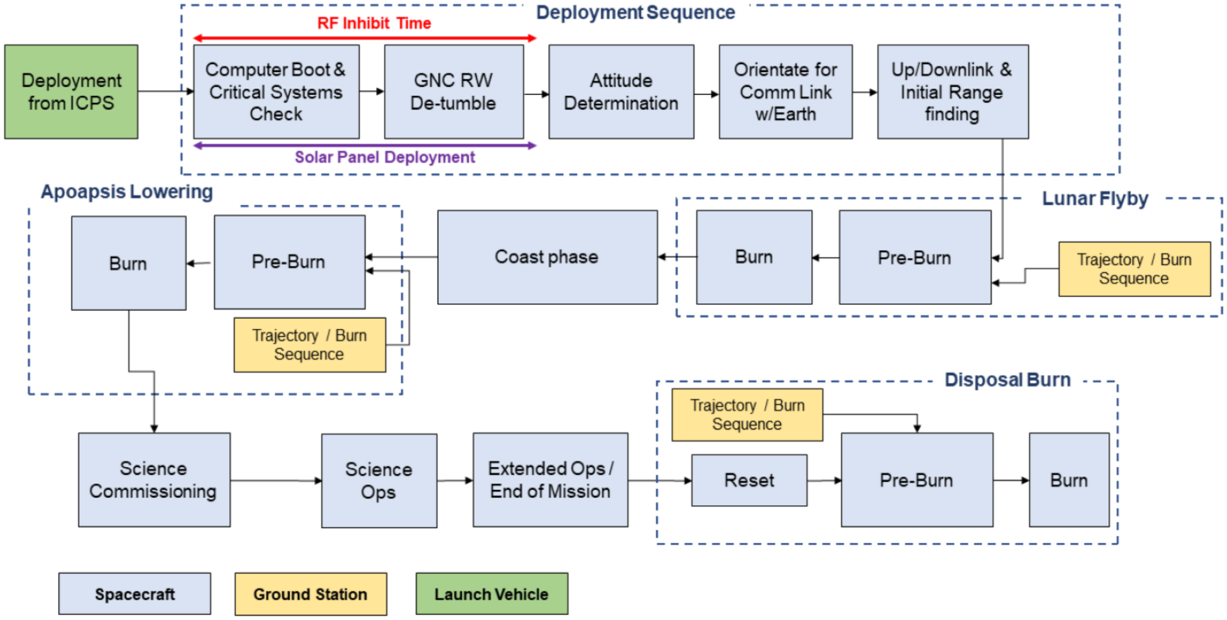
Deployment Sequence
RF Inhibit Time
Deployment from ICPS
Computer Boot & Critical Systems Check
GNC RW De-tumble
Attitude Determination
Orientate for Comm Link w/Earth
Up/Downlink & Initial Range finding
Solar Panel Deployment
Apoapsis Lowering
Burn
Pre-Burn
Trajectory / Burn Sequence
Coast phase
Lunar Flyby
Burn
Pre-Burn
Trajectory / Burn Sequence
Disposal Burn
Trajectory / Burn Sequence
Science Commissioning
Science Ops
Extended Ops / End of Mission
Reset
Pre-Burn
Burn
Spacecraft
Ground Station
Launch Vehicle

Figure 11: AEGIS Mission Sequence

A high-level framework such as **Figure 11** to achieve mission goals is conscientious but not prescient; it does little to describe how goals are achieved and is only useful in early mission planning. Software mission segments, or software states, were described as a precursor to **Figure 11**. This is true in the sense that generalized operations must be known before operations can be indexed, but the order of ConOps development should proceed as orbit definition, software operation organization, mission sequencing, and then formal software state development. Mission segment definition can occur after manifestation.

3. Architecture and Subsystem Design

3.1 Preliminary Considerations

CubeSat design is an arduous and rewarding task. It is a precarious balance of mass, volume, power consumption, cost, life expectancy, schedule, orbit, and reliability, and in many cases the designers are performing work done by NASA contractors or engineers in low-budget settings. Subsystem design doctrines presented here are organized to provide low-budget teams guidance to not only put a satellite into deep space but do it in a way that ensures the first organization project is not the last.

3.1.1 The Iterative Process

Everything starts from requirements. At the beginning, a program may only have a science payload and potential orbit. Mass, lifetime, ΔV, and payload operations may lead to more specific requirements like pointing accuracy and expected data rates, but it is possible an aspect of the science instrument or launch rideshare is altered in a way that significantly changes the operating requirements. Spacecraft engineers should foster an environment that expects, accommodates, and encourages change. If design space is constricted by program administration or inflexible requirements, frequent changes may lead designers to adopt a demoralizing "one step forward, two steps back" mentality. Spacecraft design programs must pave the way for an iterative approach that ensures designers consistently feel they are converging upon a solution. For a labor force that is not being paid, morale is a Key Performance Parameter (KPP).

3.1.2 Subsystem Architecture

Government regulation and official nomenclature have not kept pace with technology as the transition from bulky spinner satellite to streamlined CubeSat took place, and much of the available information comes from a wonderful community of small satellite developers. A myriad of texts is available regarding satellite design and operations [33-37], but not all the traditional definitions mesh when applied to CubeSats. Additionally, a shift is occurring where more attention is paid to the governance and operations of the FSW, also called On-Board Software (OBSW), than was given in the latter half of the 20th century, which is not reflected in texts until you get into niche subfields not specifically intended for CubeSats. Presented here is a methodology for delineating CubeSat subsystems from traditional subsystems which will hopefully allow readers to organize their programs to maximize development efficiency.

3.1.2.1 Traditional Satellite Subsystems

Large-scale satellites are historically comprised of Propulsion, Attitude Determination and Control Systems (ADCS or ADACS), Position and Orbit Determination, Command and Data Handling (C&DH), Telemetry, Tracking and Command (TT&C), Power, Structures and Mechanisms, and Thermal Control [33]. There may also be a science or payload subsystem. The subsystems are divided so that various disciplines may be applied effectively within a design program, but as the nature of these disciplines change, so must the subsystem definitions. For example, attention has been paid in the last decade to the application of Shape Memory Alloys (SMAs) on spacecraft. SMAs are specially alloyed metals that undergo a change in crystal geometry when thermally cycled that causes the alloy to constrict to recover residual strains upon heating and then elongate upon cooling in the presence of a preload [38]. They are metallic structures which change shape when exposed to heat, and mechanisms that employ the shape memory effect for actuation cannot allow for thermal and structural analysis to be decoupled. Additionally, CubeSat programmatics may be handled by universities or businesses which will have a GCS different than that of NASA, ESA, or JAXA.

3.1.2.2 CubeSat Subsystems

CubeSat subsystems are more difficult to define because they are dependent upon the orbit. CubeSats placed in LEO do not require propulsion or even orbit determination in some cases. A line which can be drawn between CubeSat subsystem definitions is whether or not the CubeSat intends to use electromagnetism for attitude control. For CubeSats within the magnetosphere, the subsystems may be defined as Structures, Thermal Control, Mechanisms, EPS, ADCS, TT&C, Science, FSW, C&DH, and GCS. In general, CubeSats that use magnetic attitude controls do not need or feature propulsion systems, but this is not always the case. Some CubeSats exhibit thruster payloads, and the science performed is thruster Technology Readiness Level (TRL) advancement. Defined subsystems for a given program should reflect the intended goals of a mission.

For CubeSats operating outside the magnetosphere, colloquially above Geostationary Equatorial Orbit (GEO) but realistically farther, the subsystems may be defined as Structures, Thermal Control, Mechanisms, EPS, Guidance, Navigation and Control (GN&C), TT&C, Science, FSW, C&DH, Propulsion, Astrodynamics, and GCS. The primary differences are the inclusion of a propulsion system and the transition from ADCS to GN&C. Until private entities offer X-band and above ground services, GCS may simply be the Deep Space Network (DSN). These subsystems are appropriately divided to allow teams of a given discipline to focus on a single aspect of the spacecraft with respect to given requirements.

3.1.2.3 Subsystem Resources

Many subsystems described above feature detailed component vendor comparison information found in the NASA State of the Art Small Spacecraft Technology Reports [39]. The information provided in Section 3 is not a full component review and instead focuses on the calculations required for component selection for a given mission. Calculation outputs are intended to be compared against components described in [39], and [39] is updated frequently.

3.1.3 Senior Design Teams

The AEGIS program is comprised of senior design students at the grassroots level and graduate students at the management level. What makes the program unique, and able to be emulated, is that the senior design teams span several engineering disciplines across multiple universities within a given Space Grant Consortium (SGC). Mechanical engineers evaluate structural, thermal, and mechanical considerations, aerospace engineers survey astrodynamic models, propulsion, and attitude control frameworks, electrical engineers design the EPS and C&DH subsystems, software engineers build the FSW, and wireless engineers characterize the link and communications strategy. The program architecture is flexible, and subsystem team locations should be based on the program strengths of constituent universities. Additionally, not all subsystems need to be initiated at once. Upper management should decide when teams should begin work on a subsystem based on the development schedule of the program. When work has been defined for a senior design team, the SGC can put out an RFP to be sent to each SGC university as discussed in Section 1.4.1.1. RFPs should be announced at least two semesters before the work is slated to begin.

3.2 Structural Integrity

The structural bus houses components, shields sensitive hardware, and provides electrostatic protection by means of electrically insulating surface treatments. It defines the layout constraints of component configurations and separates photovoltaic power generation mechanisms from internal components. Basic mechanisms, material selection, stress environment determination, and solar array structural design considerations are discussed.

3.2.1 Structural Design Objectives

Table 8: Structural Bus and Chassis Design Objectives, Adapted from [28]

Design Objective	Description	Rationale	Actionable Items
Hardware Definition (**ST-1**)	Identify and list heritage hardware used. Update hardware list and identify and assess applicability and qualification requirements of heritage designs.	All hardware needs to be qualified for its expected environment and operational uses.	A list of all components has been compiled in the mass and volume budget.
Visible Inspection (**ST-2**)	Demonstrate via inspection that subsystem concepts allow for full visibility of sensors, telemetry and command antennas.	The two highest priority post-separation activities are establishment of spacecraft communications and acquisition of safe attitude.	Arrange antennas and navigational components so that they have full visibility.
Design Safety Factors (**ST-3**)	Employ design safety factors in accordance with GEVS 2.2.5 and NASA-STD-5001.	This provides confidence that the hardware will not experience failure or detrimental permanent deformation under test, ground handling, launch, or operational conditions. Using minimum recommended test durations and factors developed over years of development experience will increase confidence in test adequacy and verification status.	Perform FEA and determine factor of safeties for all structural components.

Orbit and Life (**ST-4**)	Orbit and life requirements shall be used for assurance of material selection compatibility. Refine materials compatibility analysis.	Understanding trajectory and orbital environmental effects on the spacecraft eliminate costly redesign and fixes, and minimize the on-orbit failures due to environmental interaction with spacecraft materials.	Provide radiation shielding for all sensitive components.
Structural Qualification (**ST-5**)	Develop outline of structural qualification methodology. Update structural qualification methodology and develop strength qualification plan.	Demonstration of structural requirements is a key risk reduction activity during mission development.	Test structural components in accordance with GEVS Table 2.4-1 and NASA-STD-5001, 5002
Interface Identification (**ST-6**)	Begin to identify potential high precision interfaces. Refine identification of high precision interfaces.	The use of pinning or similar non-friction reliant method will help ensure alignment is maintained through all expected stresses.	Develop a coordinate system so that components can have accurate locations.

3.2.2 Satellite Architecture

The architecture of AEGIS is introduced and described first for continued reference. Subsequent sections will focus less on AEGIS and more on advanced pre-PDR analysis techniques. The structure of AEGIS was designed entirely by students. No single chassis style was emulated, and particular attention was paid to designing for machinability and accessibility. Chassis elements were mapped for science return optimization, mating structures were created where necessary, and fasteners were chosen for joining strategies over epoxies, welds, and friction bonds.

Structural housing for spacecraft should be built with a submarine mentality in that no internal component should be directly exposed to the space environment without a specified reason. Access ports, science instruments, and solar array structures have reasons for environmental exposure and are designed with increased thermal concern in mind. Many commercially available CubeSat busses for LEO do not feature enclosed outer surfaces, and some of the Lucky 13 also have exposed interior hardware. A submarine-type bus has increased mass and milder thermal control requirements compared to commercial LEO busses, and the decision to expose or enclose any given component is mission-specific.

AEGIS features one science instrument, one battery housing unit, one EPS unit, one On-Board Computer (OBC), one interface board, one Software-Defined Radio (SDR), one patch antenna, four Reaction Wheels (RW) with one Drive Control Electronics (DCE) unit, two Inertial Measurement Units (IMU), one Star Tracker (ST), five Sun sensors, three deployable solar arrays, three Hold and Release Mechanisms (HRM), one surface-mounted radiator, three patch heaters, one thruster, two deployment switches, a structural chassis with fasteners, a FSW system, and various thermal coatings and conductive paints. All components and selection criteria will be given discussion except for the OBC. CAD was provided from CubeSat component vendors and is included with permission except for the OBC, and all subsystems other than C&DH are copiously described. Selected components are found in **Table 9**. The science instrument, interface board, patch antenna, and structural chassis were designed in-house. No vendor was selected for solar array fabrication.

Table 9: Component Selection and Vendor Recognition

Component	Vendor Title	Vendor
Battery Housing & EPS	EPS II	EnduroSat
OBC	CubeSat Space Processor	Space Micro
Software-Defined Radio	XLink	IQ Spacecom
Reaction Wheels + DCE	RWP050 & RWP100	Blue Canyon Technologies
Inertial Measurement Unit	STIM318	Sensonor
Star Tracker	ST200	Hyperion (AAC Clyde Space)
Sun Sensors	NanoSSOC-A/D60	SolarMEMS
Solar Array Hinges	Winglet	Pumpkin
Hold and Release Mechanisms	Panel Release Mechanism (PRM)	Pumpkin
Solar Cells	XTE-SF	Spectrolab
Cabling	Varied	Omnetics
Patch Heaters	All-Polyimide Thermofoil	Minco
Thruster	NANO AR^3	Enpulsion
Deployment Switches	DB2C-A1AA	ZF Manufacturers

3.2.2.1 Applicable Standards

The first step to successful structural chassis design is an exhaustive review of applicable standards. NASA has made all standards and lessons learned from failed missions publicly available [40], and several stand out as directly relevant to deep space CubeSat design. NASA-STD-5001 and 5002 are directly relevant for structural component qualification; 5008, 5019, 5020, 6016, and NASA-STD-8739.14 are excellent resources for fastener design. **Table 10** provides all relevant standard material.

Table 10: Standards for Deep Space CubeSat Structural Analysis [40]

Numeric Designation	Title
MSFC-STD-3029	Guidelines for the Selection of Metallic Materials for Stress Corrosion Cracking Resistance in Sodium Chloride Environments
NASA-HDBK-7005	Dynamic Environmental Criteria
NASA-HDBK-8739.21	Workmanship Manual for Electrostatic Discharge Control
NASA-STD-5001	Structural Design and Test Factors of Safety for Spaceflight Hardware
NASA-STD-5002	Load Analyses of Spacecraft and Payloads
NASA-STD-5008	Protective Coating of Carbon Steel, Stainless Steel, and Aluminum on Launch Structures, Facilities, and Ground Support Equipment
NASA-STD-5017	Design and Development Requirements for Mechanisms
NASA-STD-5019	Fracture Control Requirements for Spaceflight Hardware
NASA-STD-5020	Requirements for Threaded Fastening Systems in Spaceflight Hardware
NASA-STD-6016	Standard Materials and Processes Requirements for Spacecraft
NASA-STD-8739.14	NASA Fastener Procurement, Receiving Inspection, and Storage Practices for NASA Mission Hardware

3.2.2.2 Layout and Configuration

A coordinate system is defined for continued use throughout this document, found in **Figures 12-13**. **Figure 12** displays a stowed configuration while **Figure 13** depicts the CubeSat with solar panels deployed. Solar panels are stationary upon deployment and do not feature a Solar Array Drive Assembly (SADA). Colton Bevel and Arkaradech Zornnetr are thanked for their spacecraft structural modeling efforts.

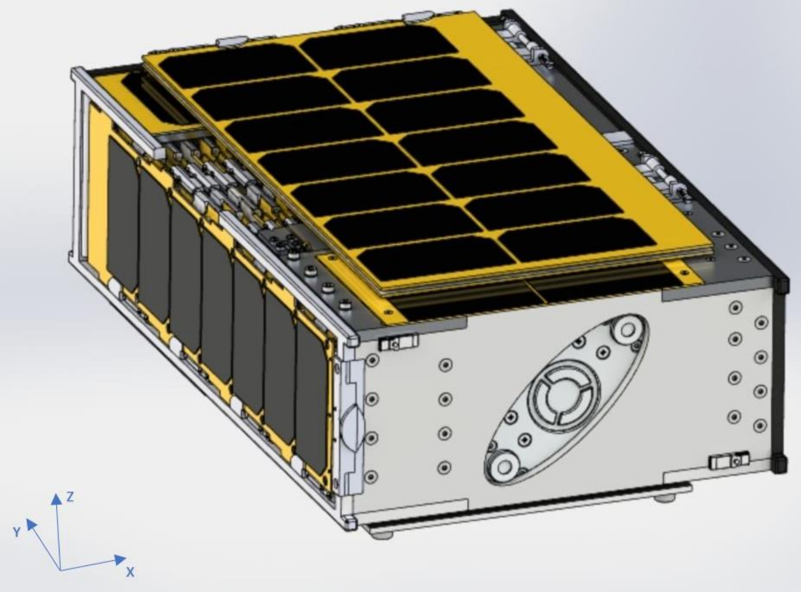

Figure 12: AEGIS Array View in Stowed Configuration with Coordinate System

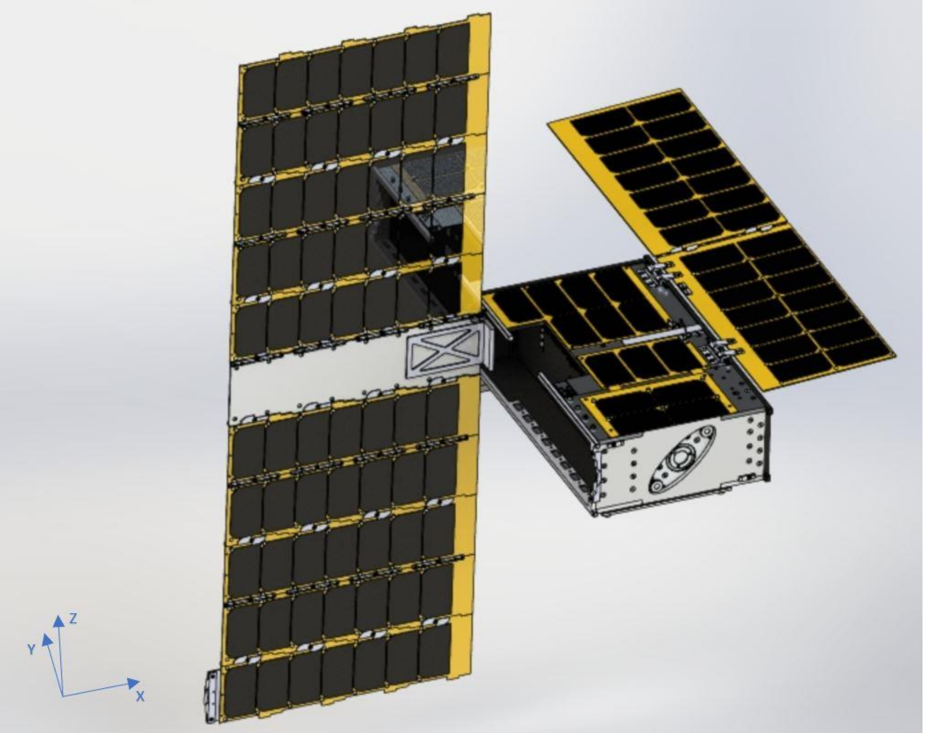

Figure 13: AEGIS Array View in Deployed Configuration with Coordinate System

Direction -Y represents the thruster face, +Y represents the science instrument aperture face, shown momentarily. Direction +Z represents solar array A and the body panels, while -Z represents the radiator face. Direction +X represents a blank chassis wall and -X represents solar array B’s stowage and deployment side. The underside and science aperture face of AEGIS is shown in **Figure 14** with the same coordinate system.

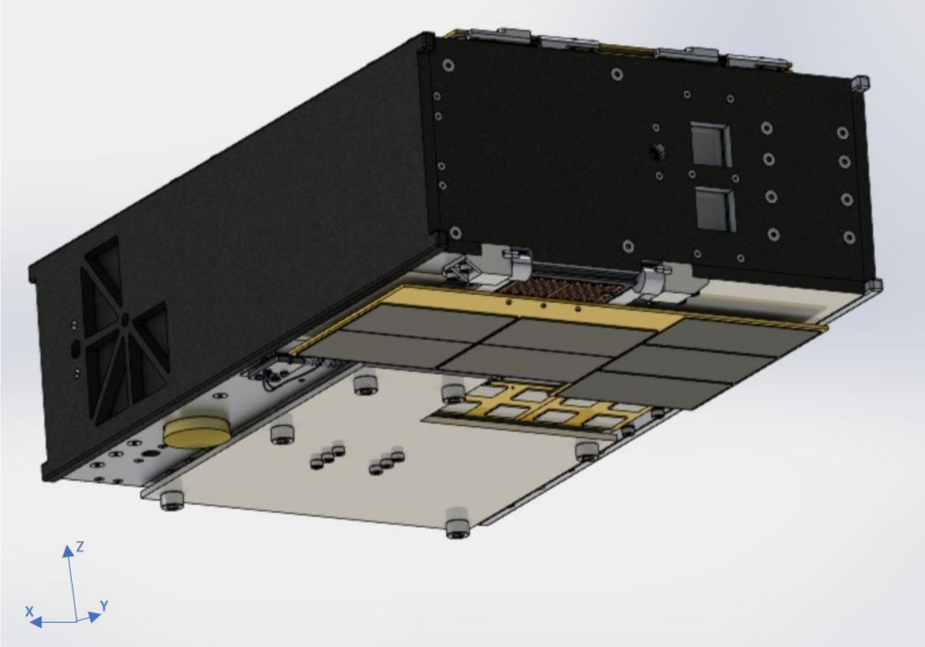

Figure 14: AEGIS Radiator View in Stowed Configuration with Coordinate System

AEGIS features three solar arrays displayed in a deployed configuration in **Figure 15**. Array A and the body-mounted arrays face the same direction, +Z. Array A only has solar cells only on the +Z face and has a high-emissivity thermal coating on the back side, discussed in Section 3.3.5. Array B faces the ±Y directions with solar cells on both surfaces. Array C is a solar array hinge technology demonstration that is deployed 135° off the -Z face. The SMA hinge technology will be presented at SciTech 2021 and is outside the scope of this work.

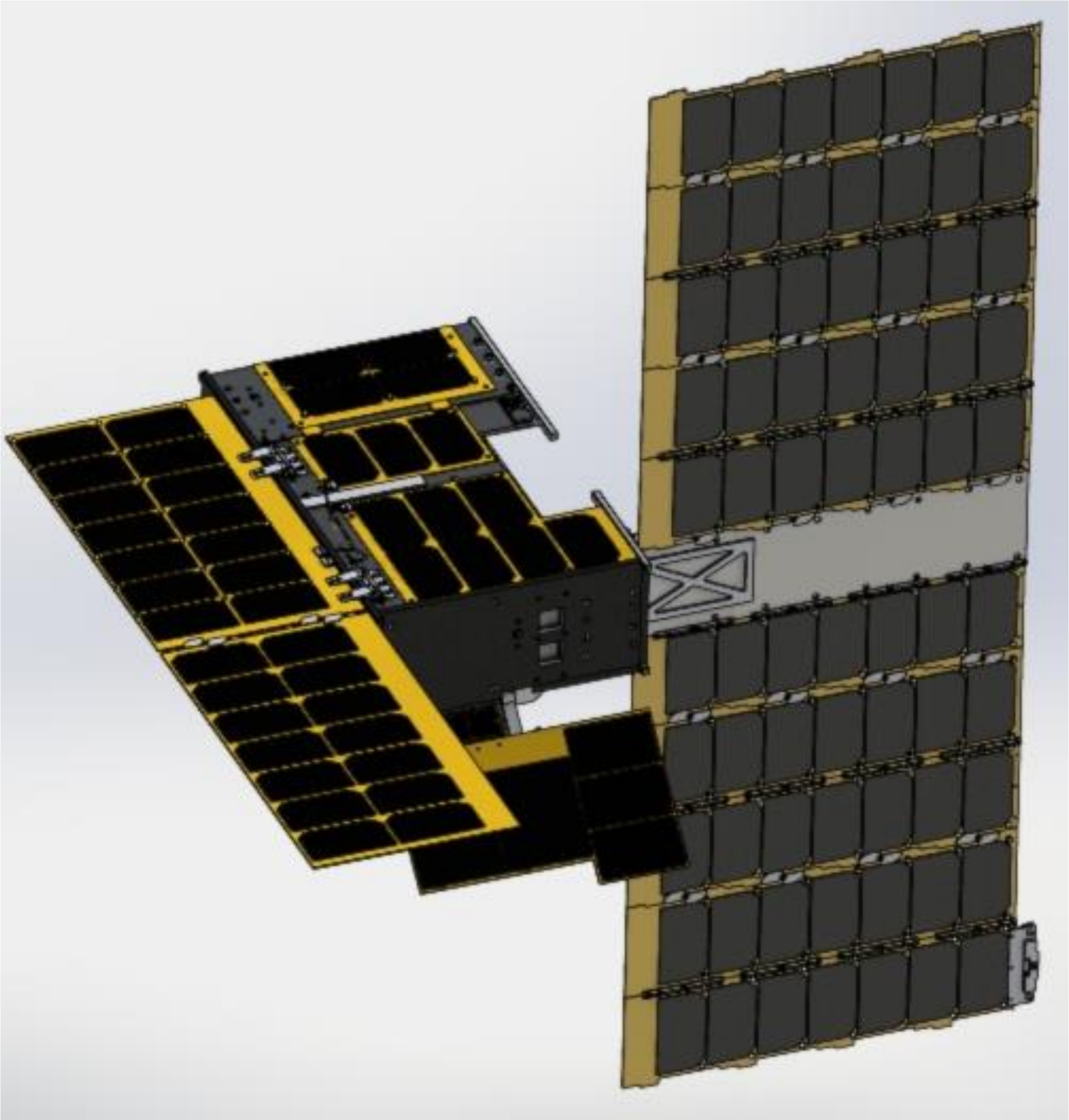

Figure 15: AEGIS Science Aperture View with Solar Arrays Deployed

Visible in **Figures 13-15** is the variety of surface coatings on AEGIS. The -Y surface, or thruster face, features a polished aluminum surface to reject thermal soakback. Black surfaces that are not solar cells are coated with Chemglaze Z306, a solar absorber. The radiator and middle panel of solar array B are coated with a solar reflector, AZ-93. The radiator, patch antenna, star tracker baffle, and HRM C are visible in **Figure 14**. A direct view of the ±Z faces is shown in **Figures 16-17**.

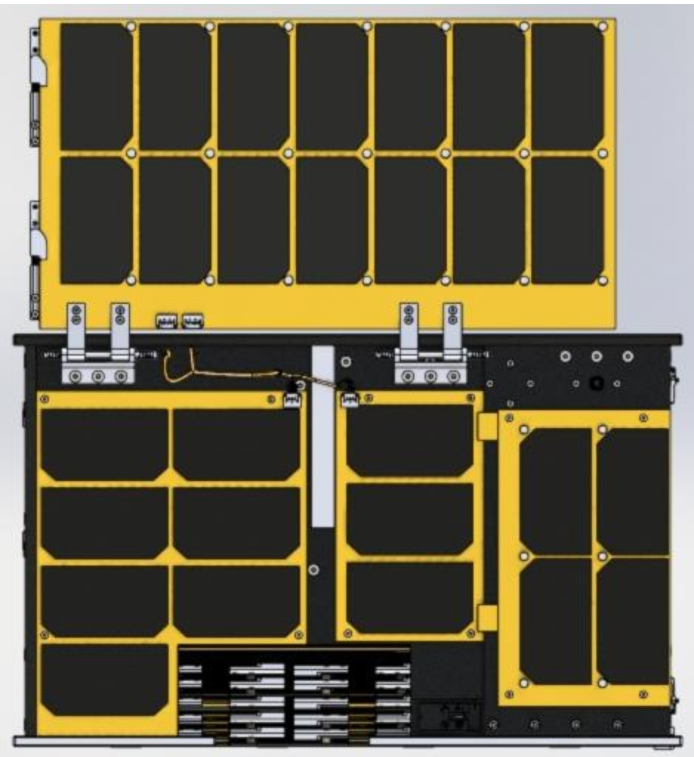

Figure 16: +Z View, Solar Array A Half-Deployed

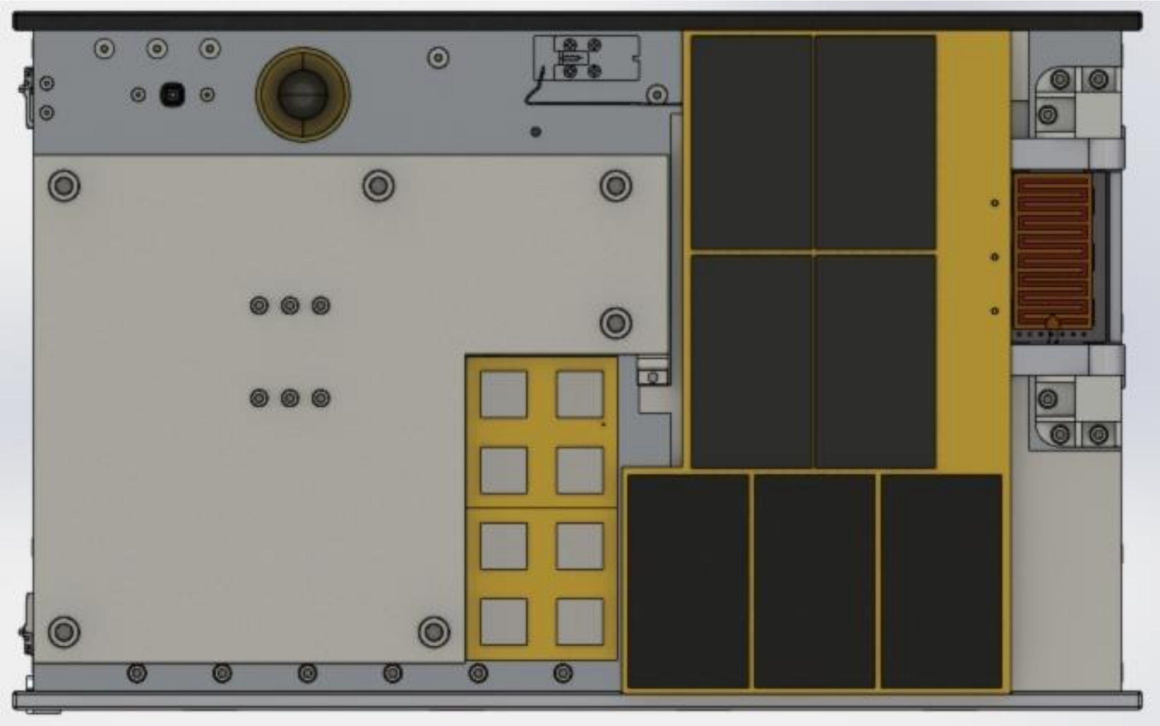

Figure 17: -Z View, Solar Array C Stowed

Additional components will be described and shown where relevant. A depiction of internal components begins in **Figures 18-19** with a view of the spacecraft interior from the +Z direction with and without interior cabling. The orange area is the back of a patch heater mounted to the +Z interior face.

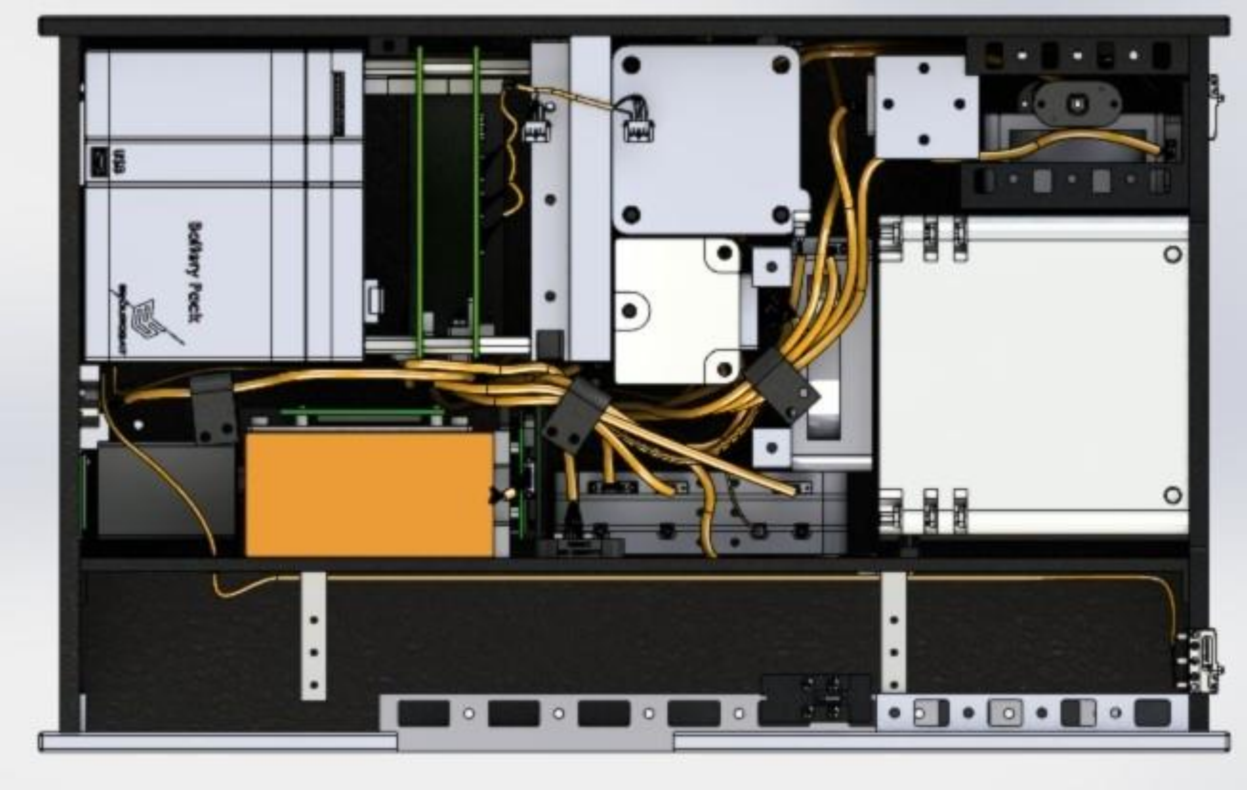
USB
Battery Pack

Figure 18: +Z View, AEGIS Interior with Kapton-Wrapped Cabling Shown

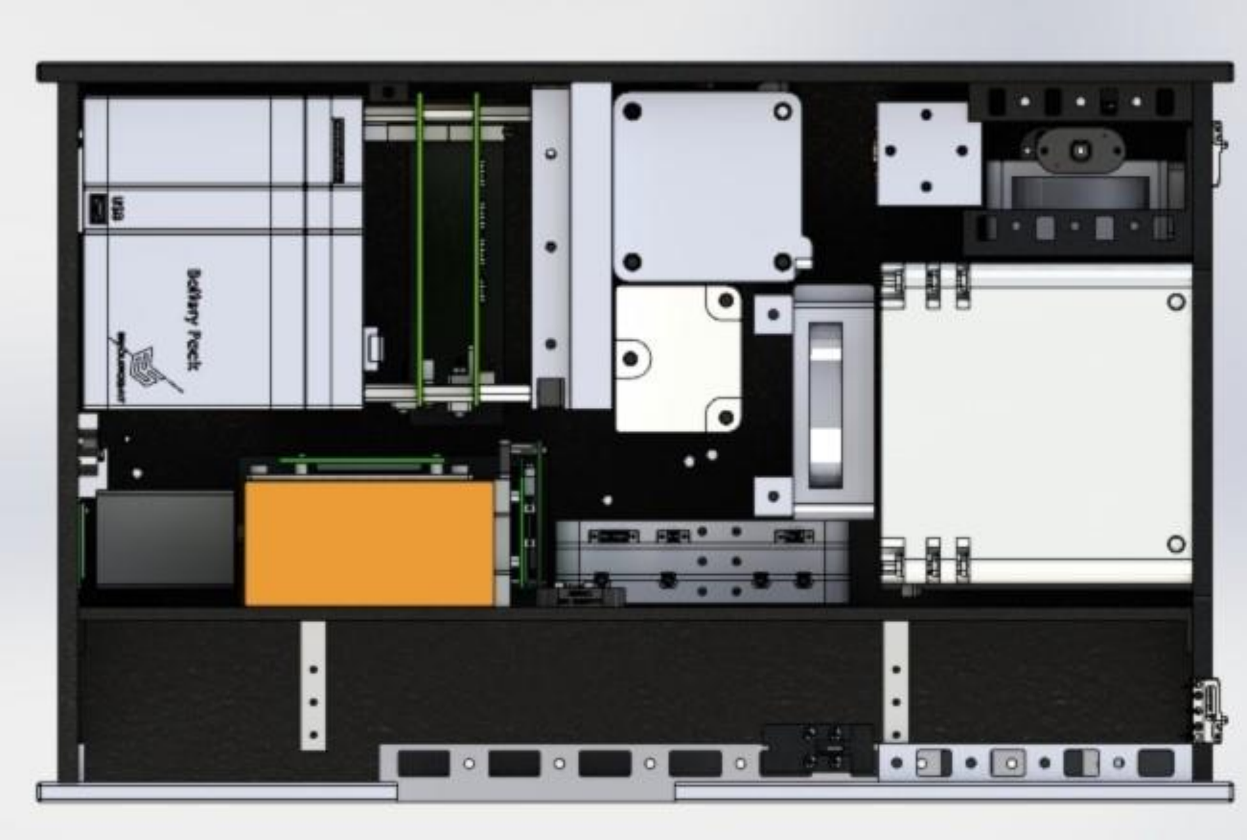
USB
Battery Pack

Figure 19: +Z View, AEGIS Interior without Cabling

The science instrument is shown in **Figure 20** with two Sun sensors and no cabling. Two radiation apertures are visible, one with lunar regolith between the aperture and science instrument and one without. A patch heater is located on the +Z chassis face. The radio is slightly visible to the left of the science instrument.

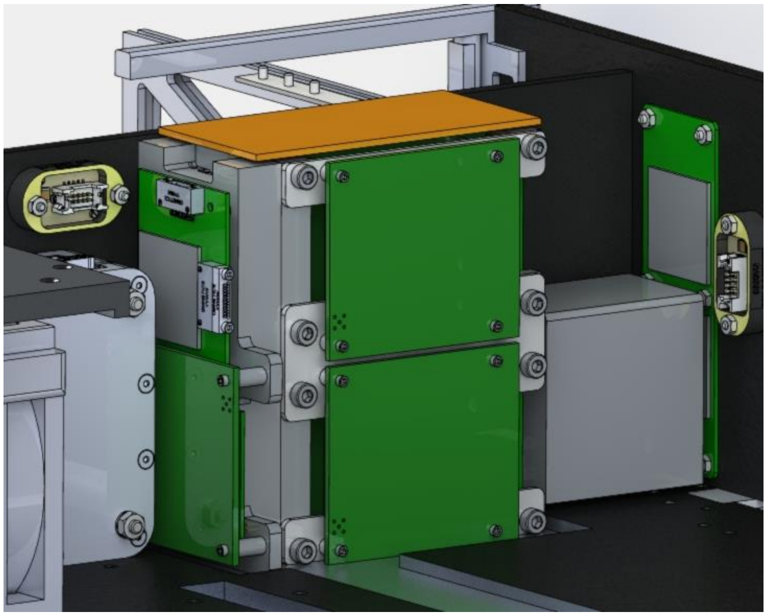

Figure 20: Science Instrument Mounting and Structure

A side view from the -X direction is provided in **Figure 21**. Pitch is described as rotation about the X-axis, roll is about the Y- axis, and yaw is about the Z-axis. The science instrument, Sun sensors, pitch and roll RWs, radio, and thruster are hidden. The primary cable management strategy involves wall-mounted cable harnesses 3D printed out of polyetherketoneketone (PEKK), a material designed to reduce Electrostatic Discharge (ESD) [41]. On the left is the battery pack and EPS stacked under the OBC and Auxiliary Board (AB), a Printed Circuit Board (PCB) for peripheral component interfacing. To the right of those is a mock-up of the DCE, both IMUs, and the yaw reaction wheels are behind the IMUs. The star tracker is to the right.

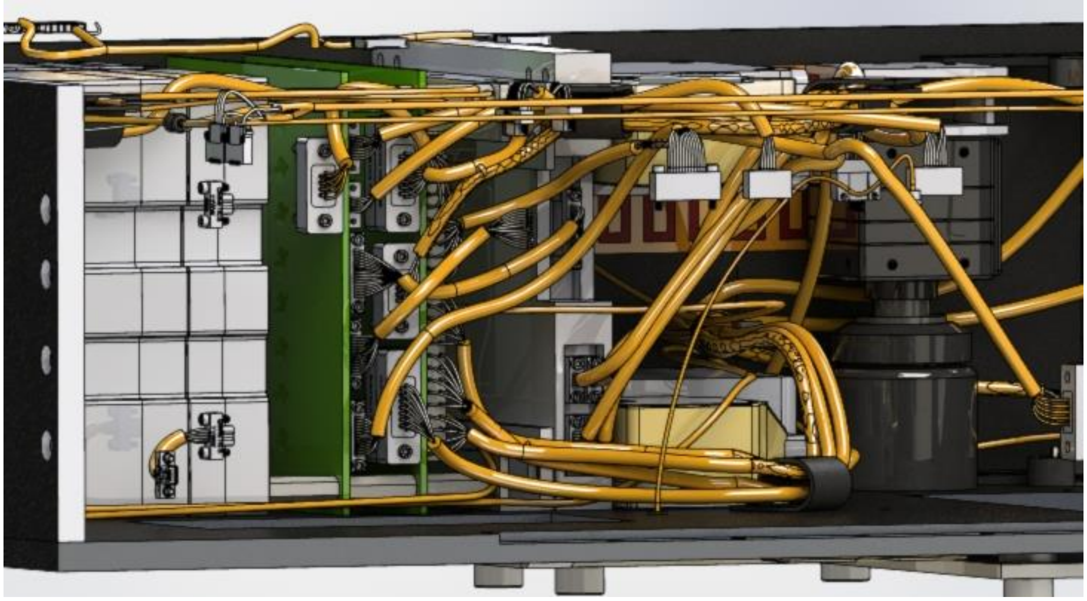

Figure 21: -X View, Interior Cable Harnessing Design

Figure 22 is from the opposite view of **Figure 21**, where all solar arrays and the patch heater at the back of **Figure 21** are hidden. The cables to the patch heater are still shown. **Figure 23** shows the same section. The pitch RW is mounted to the left of the star tracker in this view, while the two yaw RWs are on the right.

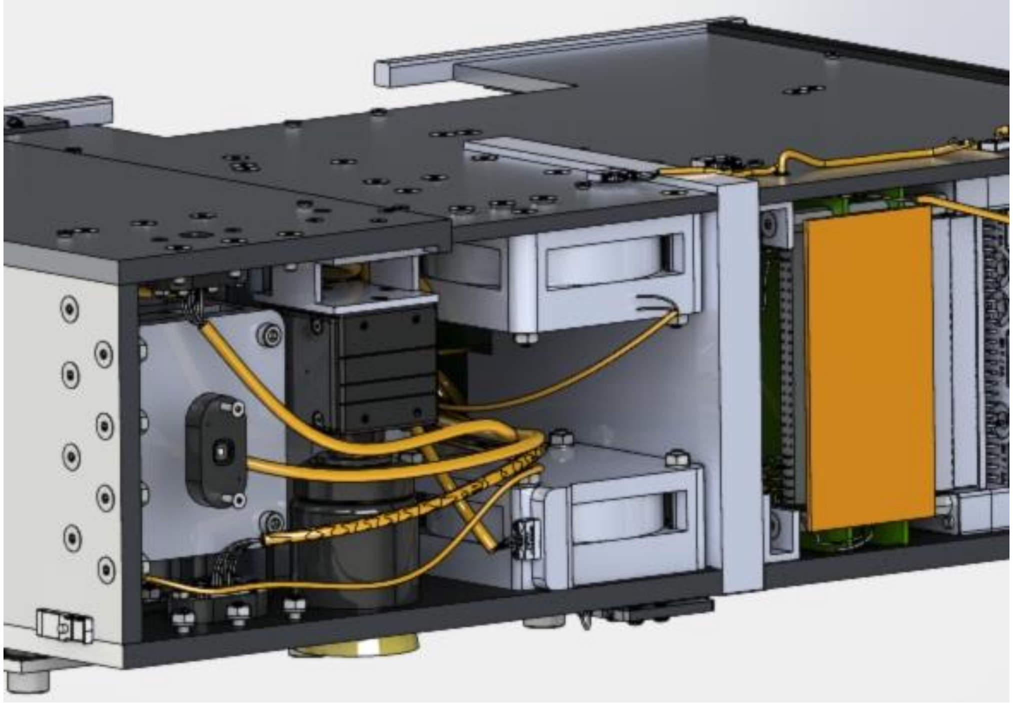

Figure 22: +X View, Interior Star Tracker View 1

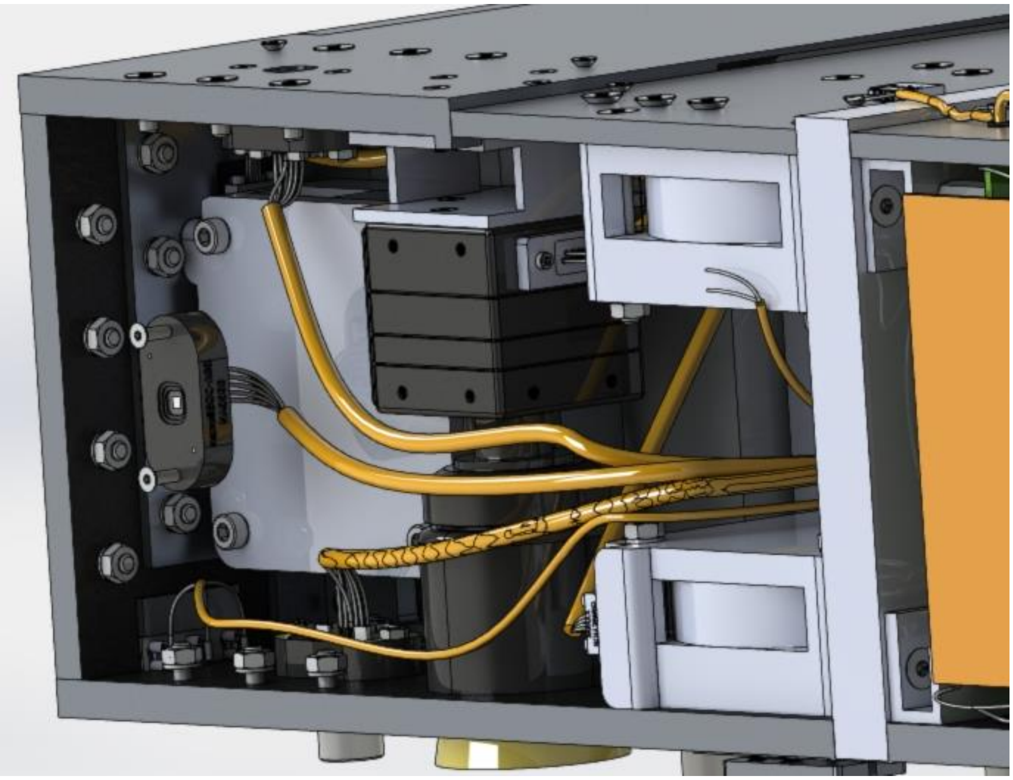

Figure 23: +X View, Interior Star Tracker View 2

One IMU, one yaw RW, and several cable harnesses are mounted directly to the +Z face, shown in **Figure 24**. The gap between the fasteners and components represents the hidden structural face. Also hidden in this view are body-mounted solar arrays. The fasteners are located underneath the body mounted arrays. **Figure 25** depicts the IMUs and yaw RWs mounted to both ±Z faces without cabling or fasteners included.

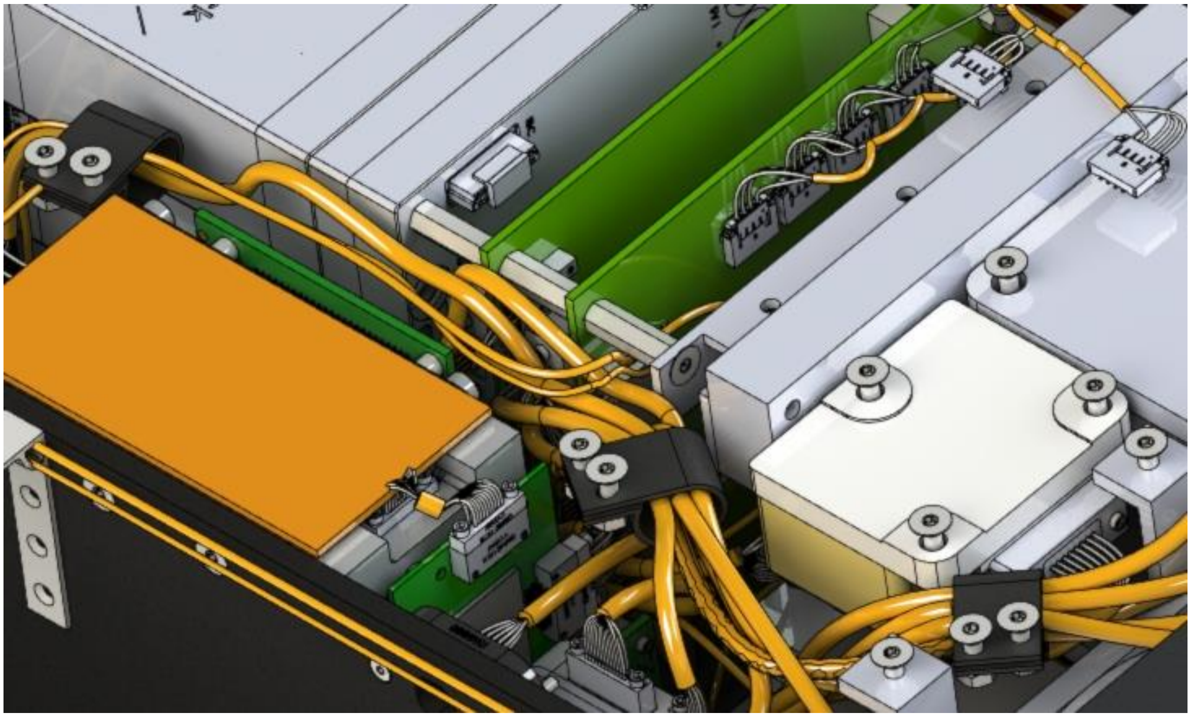

Figure 24: +Z View, Component Mounting Strategy

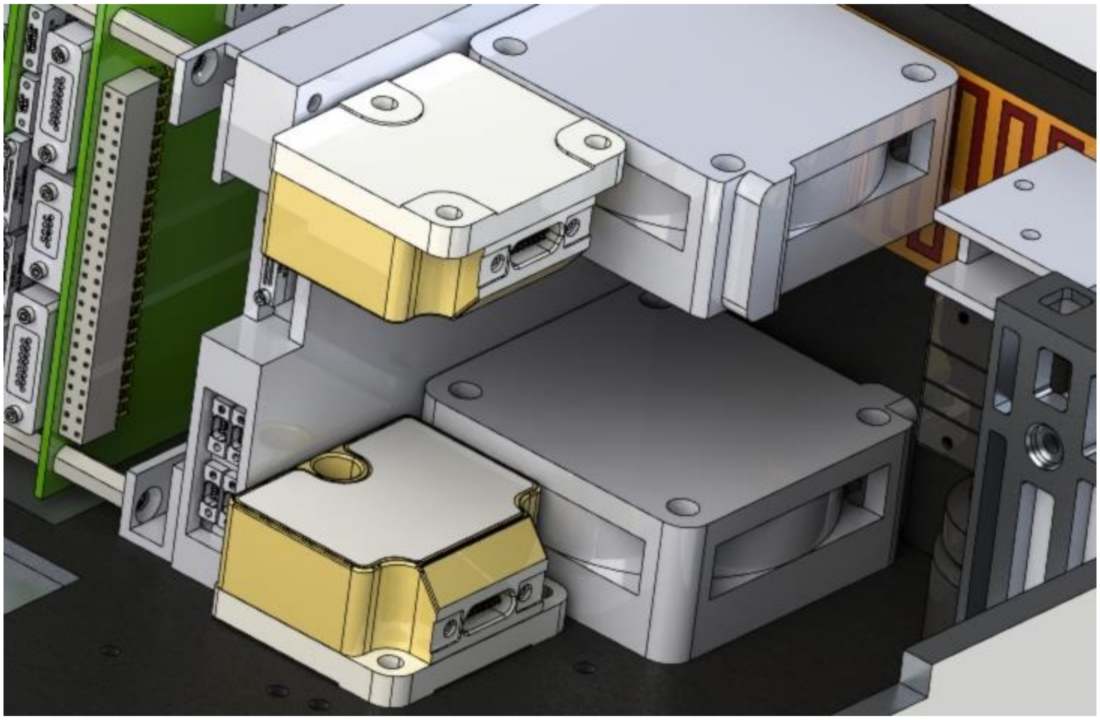

Figure 25: IMU and Yaw RW Mounting Strategy

Solar arrays and aperture components must be located such that the component Field of View (FOV) is not obscured by the arrays. The science instrument, +Y direction Sun sensor, and star tracker have a clear FOV per **Figure 26**.

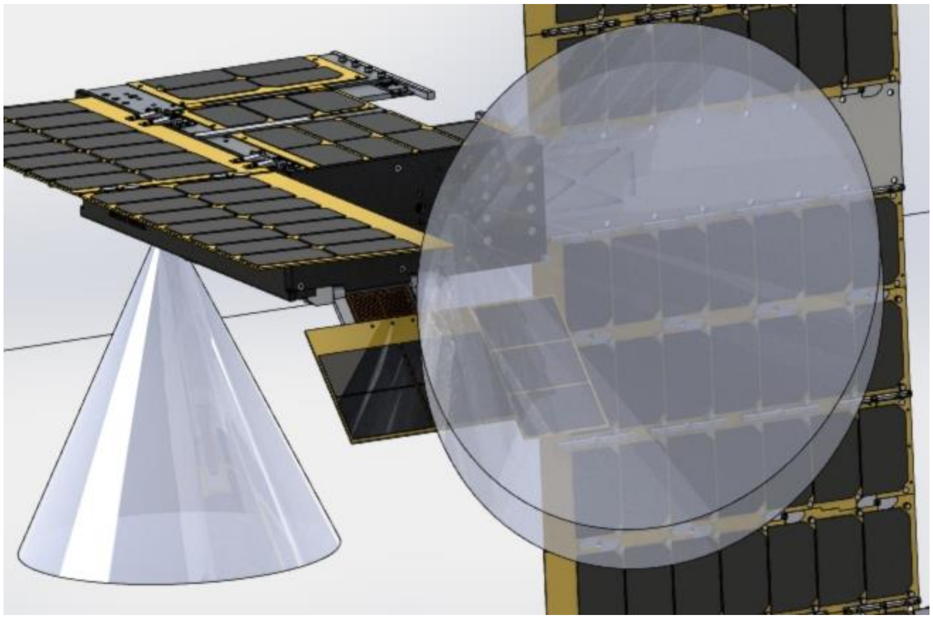

Figure 26: Science Instrument and Star Tracker FOV

Special accommodations had to be made for the -X Sun sensor, as array B is so large that nearly any location on the -X face results in some occultation, shown in **Figure 27**. Solar array B has cells on both faces, so glare is also a potential issue. It is undesirable to deploy any solar array near a thruster plume due to erosion and deposition effects.

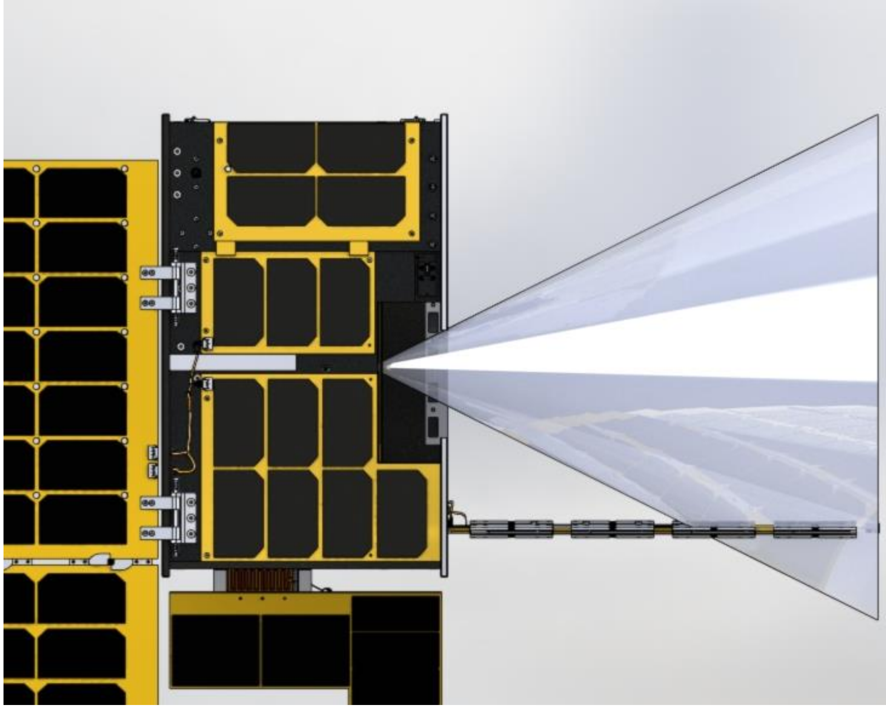

Figure 27: +Z View, -X Direction Sun Sensor FOV Occultation by Solar Array B

3.2.3 Structural Material and Fabrication

Materials for spacecraft structural fabrication range from cheap and widely available, like basic aluminums, to expensive and difficult to procure, like Stainless Steel (SS) A286. Standards MSFC-STD-3029 and NASA-STD-6016 discuss material strength and risk considerations for legacy materials, and their conclusions are parsed and expanded here specifically for deep space CubeSat design. Very hard materials, such as tungsten and tantalum, do not burn completely upon atmospheric reentry, and CubeSat disposal plans must reflect this if a satellite intends to use high-strength materials. Titanium is expensive and should not be considered for a whole chassis design, but it does have uses for structural applications requiring low thermal conductivity. Metal matrix composites and ceramic matrix composites are advanced materials with potential applications near high temperature locations due to low coefficients of thermal expansion and anisotropic thermal conductivities, but polymer matrix composites will outgas and embrittle in a vacuum and are not recommended.

3.2.3.1 Chassis Material

The premiere material for university programs who wish to move fast and break things is Al 6061-T6. It is cheap, easy to machine, and even certified, high quality stocks feature reasonable lead times. Al 6082, 5005, and 5052 with varied treatments are also used as cheap solutions. If cost is no object for a program and mission lifespan is low, Al 7075-T7 is a stronger, more reliable option than 6000 series aluminums. If additional development time and budget can be allocated or mission requirements are extreme, upgrading to Al 7075-T73 will yield a highly robust chassis.

Aluminum heat treatment temper designation T3 signifies solution treated, cold worked, and then naturally aged, T6 signifies solution heat treated and artificially aged, and T7 signifies solution heat treated and then overaged. T73 is specific to 7075 series aluminum to denote a special solution heat treatment and artificial aging process and not that T7 is applied before T3. A T73 temper reduces exfoliation corrosion and stress-corrosion cracking, but the overaging process also increases fracture toughness and reduces rates of fatigue crack propagation [42].

When machining, tolerances and specifications are not always provided for every aspect of the component. When draft considerations are not included or specified, SSTD-8070-0098-SHOP is recommended [43]. Examples of recommendations include a radius or chamfer not to exceed 0.254 mm when a sharp corner is specified on a drawing, and the radius or chamfer shall not exceed 0.762 mm. Deburring with a common deburring tool is not recommended; a series of sandpaper passes with increasing grit sizes is recommended instead. Increasing from 80 to 120 grit up to 7000 or 10000 is typical.

3.2.3.2 Fastener Material

Fastener selection is straightforward with two options: SS A286 and SS 316. A286 is a high-strength superalloy used in jet engines. It is expensive, has lead time of 6-12 months for metric sizes, and vendors willing to provide material property certifications are hard to find. If a reliable source of A286 can be identified that can provide certifications for a reasonable price and lead time, A286 should be the selection. If not, 316 is a fine downselect option as it is cheap and widely available. Fastener sizes in a CubeSat design should be no smaller than M3, though M2s are included on AEGIS near the Sun sensors due to the small size of the component. If a program is forced to use sophomoric imperial units, which are formally defined as metric units multiplied by a conversion factor, fasteners should not be smaller than #4-40.

All material purchases should come with vendor sourcing certifications. NASA-STD-8739.14, MSFC-STD-3029, and NASA-STD-6016 provide material analysis, qualifications, and test procedures to ensure the procured material is what the vendor says it is. Many predominant engineering supply companies do not perform due diligence on their suppliers, and they will lie to sell a product. Nullius in verba; test the chassis and fastener material always.

3.2.3.3 Fastener Alternatives

Bonding or welding are alternatives to fastening but neither represents as reliable a choice as a distributed set of fasteners and may not be allowed per the MI. For fasteners where a simple thread, bolt, and washer combination is not enough to ensure structural integrity and space does not exist for additional fasteners, a method called staking wherein an epoxy is applied to the threaded region can be used. Staking requires a 24-hour cure time for the epoxy and does not allow for disassembly once applied. If vibrational concerns exist for a joint, thread locking helicoils are recommended, shown in **Figure 28**. Thread locking helicoils, essentially springs for fasteners to thread into, perform almost as well as staking for tension or compression and support a stronger applied torque than in basic aluminum threads [44].

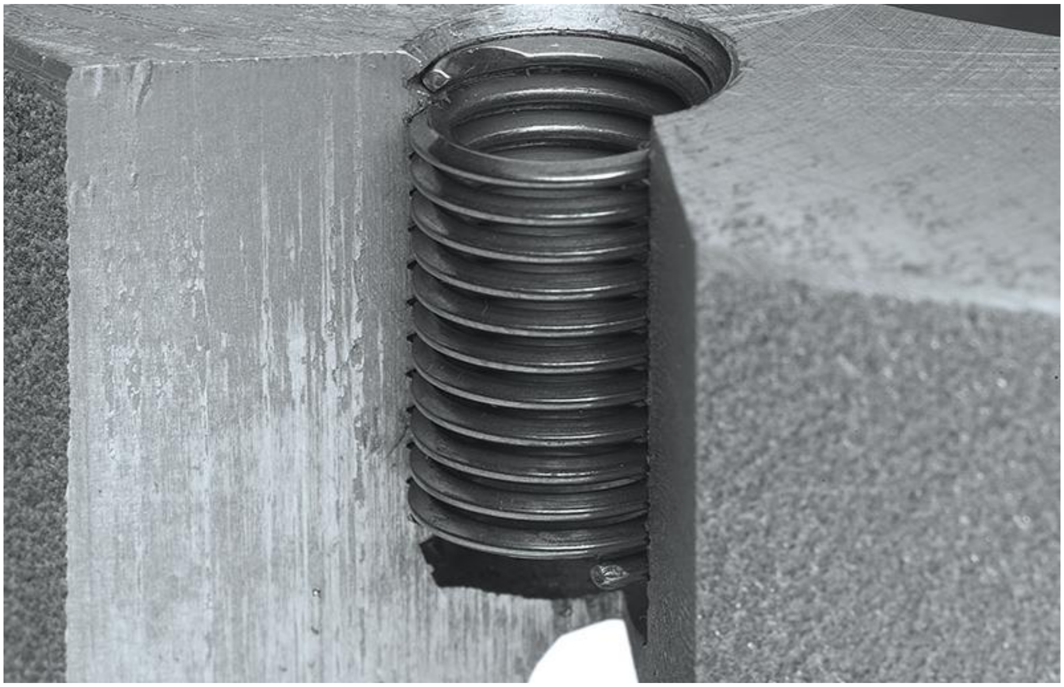

Figure 28: Thread Locking Helicoil from Boellhoff, Used with Permission [45]

Fasteners, whether bolts or helicoils, need two locking features. This could mean locking inserts or Loctite 242/243. Helicoils need a lubricant so that dust particles are not created upon application. Loctite qualifies as lubricant here. Fiber-reinforced plastics with a thermosetting matrix can be used for load transfer between chassis structures. A stable thermoset likely exists for a given application and known thermal environment, but space conditions do present risks for plastics. The low-pressure vacuum of space leads to outgassing that does not significantly degrade the properties of the plastic over short time periods but can lead to contamination of surrounding surfaces. Unreinforced plastics feature relatively large coefficients of thermal expansion, and broad thermal swings such as those in lunar orbits may lead to cracking. Atomic oxygen etches thermosetting plastics, which is not a problem outside LEO [46].

3.2.3.4 Material Surface Treatments and ESD

Surface treatments exist to reduce the electrical conductivity of a metal chassis that houses electrically sensitive equipment that cannot be repaired once in orbit. The goal is to prevent Electrostatic Discharge (ESD), or charge accumulation that causes a spark between the bus and a cable or PCB. While ESD classifications and methods of estimating surface charge accumulation are provided in Section 4.5.5, a full treatment of ESD is outside the scope of this document. Without understanding the implications of ESD characterization, designers should wrap all cables in Kapton tape, apply conductive paint over any open areas of CubeSat outer surfaces not required for solar cells, antennas, or apertures, and apply an electrical insulation material surface treatment to the bus metal. Kapton tape will reduce the electrical conductivity between cables and other components, shield the cables from radiation, and reduce Electromagnetic Interference (EMI). Conductive paint applied to the outer surface of the spacecraft will redirect accumulated surface charge to a designated location, and electrons suspended on the spacecraft outer surface will act as a Faraday cage protecting the inner component circuitry from EMI. The most common electrically insulating surface treatment is anodization, but a better option exists in Plasma Electrolytic Oxidation (PEO).

PEO is best accomplished by a proprietary process called Keronite wherein a plasma discharge surrounds a component immersed in an electrolyte bath. The oxidation and recrystallization process is complex, and the result is a surface coating of ceramic layers in both crystalline and amorphous phases with material properties exceeding those of the same material treated with hard anodization [47,48]. Some form of material electrical insulation is required for CubeSat rails; both anodization and PEO satisfy this requirement. Rails are the only component officially required to be electrically insulating, but all chassis materials should be treated including fasteners. Anodization has worked in space as intended and represents a low-cost downselect from PEO. A deep space, long-duration mission would benefit from enhanced material properties that simple anodization cannot deliver.

A final consideration regards perimeter-mounted electronics and their susceptibility to both high temperature gradients and ESD. One mitigation strategy is to apply a layer of thermally-conductive, electrically insulating elastomer filler such as CHO-THERM [34, 49]. It can provide thermal balance without impeding electrical stability. Another option is to apply Belleville washers in between mounting surfaces as shown in **Figure 29**. Belleville washers expand when hot and contract when cold, increasing the thermal conductivity when components are warm and decreasing heat flow to the exterior chassis when cold.

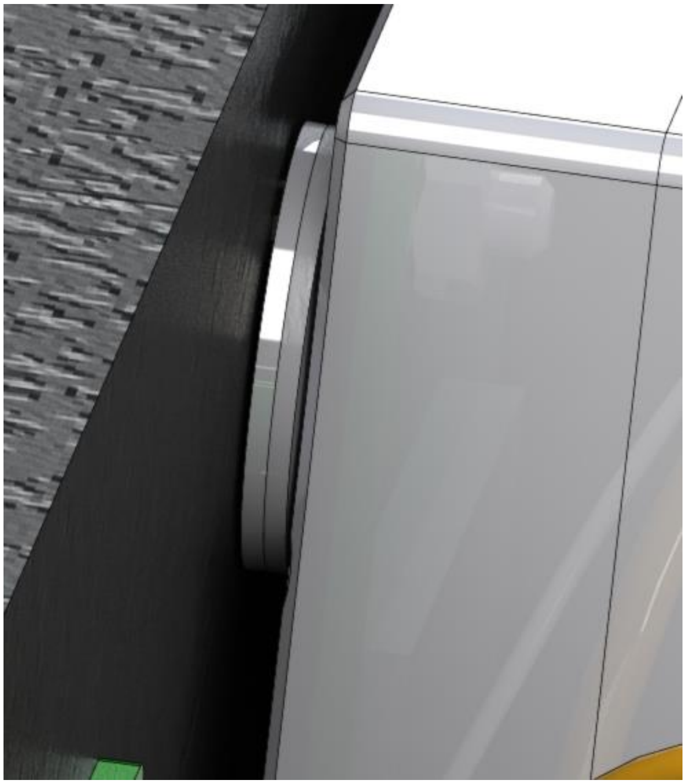

Figure 29: Belleville Washer Between Battery Pack and +Y Face

3.2.4 Rail and Dispenser Considerations

CubeSat rails feature the tightest dimensional tolerances and material requirements because they are the primary load transferring structure between the CubeSat and dispenser. A close-up of the AEGIS rails is shown in **Figure 30**. Rails are not the outermost structural component; solar arrays and surface-mounted components can extend outside the box created by the four rails. Each dispenser will have specifications for how much taller or wider than the rails surface components can be, but 10 mm is common. Launch vehicles will impose requirements that the rails be electrically insulated, moderately low friction, and that at least ~70% of the original rail length is present. Minimum rail widths are commonly no smaller than 8.5 mm with a surface roughness of less than 1.6 microns.

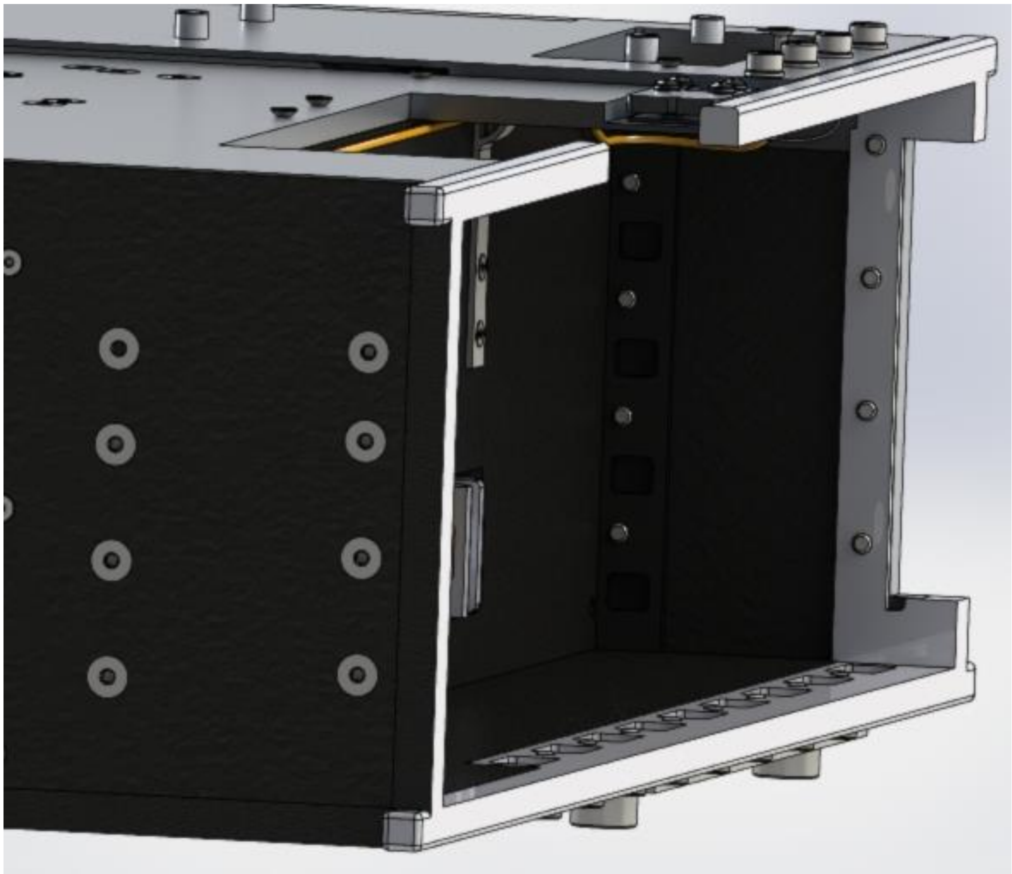

Figure 30: CubeSat Dispenser Rails on -X Direction Face

As with all other structural materials, PEO is recommended over anodization to ensure material properties are preserved during electrical insulation. A secondary benefit to PEO is the potential inclusion of low-friction additives during the process. The friction coefficient of Keronite is normally 0.5-0.6 on aluminum, but a legacy surface coating, MoS_2, can be included in the PEO process for the rails yielding a friction coefficient as low as 0.04 [48]. Cold welding between the rails and dispenser interior after PEO is not a strong risk.

3.2.4.1 Deployment Switches and RF Inhibits

Deployment switches, referred to as kill switches in Europe, are directly wired to the EPS of the spacecraft, and the EPS should have terminals for the connection. They are wired in parallel, which may be accomplished inside or outside the EPS depending on the EPS. The first set of 6U CubeSat standards released by NASA called for three switches on any given CubeSat, but this requirement has been relaxed in practice. Some dispensers only call for one switch, while the Artemis LVs originally called for two. The MI should have the final say on how many deployment switches are required. A view of one deployment switch is found in **Figure 31**.

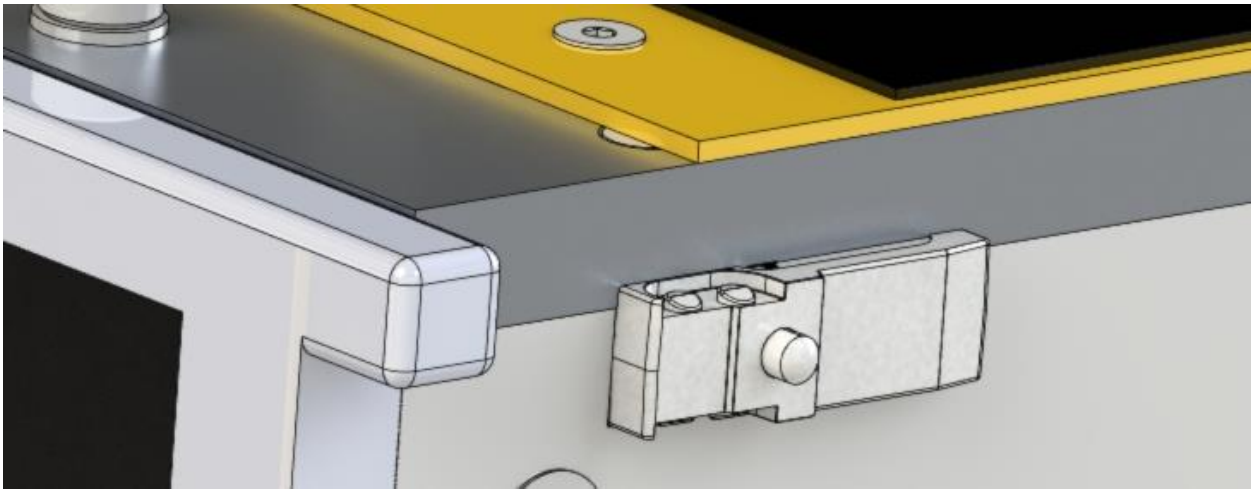

Figure 31: Plunger-Type Deployment Switch

There are three types of deployment switches: plunger, lever, and roller lever. Companies in the US that build CubeSat busses tend to prefer plunger types while European companies prefer roller. AEGIS selected the plunger-type DB2C-A1AA subminiature electromechanical switch from ZF Manufacturers, and structural housing on the thruster face was designed around the switch geometry.

Deployment switches prevent the EPS from providing power to the components of the spacecraft while in the dispenser, but LVs with multiple CubeSat payloads may require a direct line between the deployment switch or EPS and the radio. LVs do not want communications with CubeSats that are near the LV to disrupt communications between the ground station and LV, and thus a Radio Frequency (RF) Inhibit is implemented. Once all deployment switches have been un-plunged, a physical hardware timer, not a software timer, is initiated. The timer lasts anywhere between 30-60 minutes depending on the LV, and the radio may not be powered on until the timer has completed. RF Inhibits are not COTS components that can be purchased, they are cabling combinations of deployment switches, the EPS, a hardware timer somewhere in the flow, and the radio.

3.2.4.2 Dispenser Size Options

Despite almost every CubeSat paper describing CubeSats exhibiting a volume in increments of 10 cm x 10 cm x 10 cm, this is rarely the case. Two prominent 6U dispenser vendors are Tyvak and Planetary Systems Corporation. Tyvak’s 6U specification is about 119 mm x 226 mm x 340.5 or 366 mm, and Planetary Systems Corporation’s is 113 mm x 239 mm x 366 mm. Tyvak and Cal Poly are closely linked, and the CubeSat standards released by Cal Poly will be what Tyvak is designing dispensers to. Nanoracks, another company with significant CubeSat deployment experience, launches mostly 1U form factors that are, for a 3U, 119 mm x 119 mm x 340 mm. The concept of a U as 10 cm x 10 cm x 10 cm is misleading, and it should not be anticipated that companies suddenly decide on a common standard.

If a launch opportunity is selected through a non-Artemis LV, it is likely that the CubeSat program will be responsible for procuring their own dispenser. Dispensers cost between $80,000-$100,000; this cost must be factored into the overall budget by the PM if dispensers are not provided by the LV.

3.2.4.3 Access Ports, Umbilical, and RBF

CubeSats will be provided to the MI 1-4 months before launch is scheduled. LVs such as Artemis are on the 4-month end, and LVs such as the Falcon 9 would have a quicker turnaround. CubeSat batteries will be charged by the MI before placement into the dispenser, and integrators will not dismantle a CubeSat structure to access the EPS. Removing any fasteners after vibration testing will disqualify a test result, and specified access ports must be defined for the integrators to access necessary components. Components of interest are the EPS charging terminal, or umbilical, and Remove Before Flight (RBF) terminal. When the RBF pin is attached, the batteries can be charged by the umbilical cord without providing power to the rest of the spacecraft, even if the deployment switches are not depressed. Once the batteries are charged and the CubeSat is ready for integration with the dispenser, the umbilical is removed, the CubeSat is inserted into the dispenser, the deployment switches are depressed, the RBF is removed, and the access ports are plugged if desired. The extent to which an access port can be covered is dictated by the MI and dispenser but allowing any component to be exposed to space is bad practice.

3.2.5 Design Qualification

Qualifying a structural design requires benchmarks for the design to meet in the form of stress or fatigue life factors of safety. Thermal, static, and dynamic environment variables must be defined, fastener preloads must be applied, and combined stresses must be vetted in Finite Element Analysis (FEA) for performance comparison against the safety factors. NASA-STD-5001 details Factors of Safety (FOS) for use in metallic structures for a variety of mission phases such as prototyping and protoflight conditions. A single value has been selected for each of the stress evaluation criteria to streamline analysis, shown in **Table 11**.

Table 11: Material Factors of Safety for Stress Applications

Yield Stress FOS	Ultimate Stress FOS	Fatigue Life FOS
1.25	1.4	4

The goal of structural design qualification is threefold: define fastener preloads for material types, sizes, and expected thermal expansion, define static stresses such as gravity and launch vehicle thrust reaction when present, and define dynamic stresses resulting in localized stress concentrations and fatigue. Thermal, static, and dynamic loads are defined per mission phase per structural component, total stress is estimated and compared against the yield and ultimate stress FOS, and fatigue life is cumulatively summed to ensure the spacecraft will not fatigue before four times the expected mission duration. For the AEGIS science mission of 1 year, this duration amounts to 4 years. **Table 12** defines expected cycles for expected mission stresses by type. Dynamic cycles are calculated by expected frequencies of dynamic environments, found in NASA-HDBK-7005, multiplied by the expected duration.

Dynamic loads may include vibrations from ground transportation, rocket engine vibrations from both dynamic, when the rocket is first igniting, and static, when rocket momentum is fully directed, and acoustic sound pressure levels. Sound Pressure Levels (SPL) are provided by the MI and correlated to pressures by **Eq.(1)**. Dynamic loads are specific to a given launch vehicle and should not be considered mission interchangeable. Static loads are either gravity or LV-based. Thermal loads are accounted for in fastener preload calculations, and the thermal environments themselves are calculated by the procedure in Section 3.3.6. Thermal stress cycles are broken down by expected mission segment duration and sum to 365 days. Static stress cycles are singular events, and dynamic stress cycles do not sum to a meaningful value.

$$p_{rms} = \left(p_{ref} \cdot 10^{\frac{SPL}{20}} \right) \quad \textbf{Eq.(1)}$$

Table 12: Structural Mission Segment Environment

Phase	Thermal Stress Cycles Per Year	Static Stress Cycles Per Year	Dynamic Stress Cycles Per Year
Terrestrial Transport	1	1	1350000
VAB Storage	60	1	0
Pre-Launch	1	1	45000
Dynamic Ascent	1	1	360000
Static Ascent	1	1	1620000
Launch Vehicle Coast	3	0	0
CubeSat Deployment	1	1	0
Commissioning	1	0	0
Burn 1	7	0	0
On-Orbit 1	2	0	0
Burn 2	20	0	0
On-Orbit 2	2	0	0
Science Orbit	259	0	0
Reaction Wheel Desaturation	5	0	0
Disposal	1	0	0

3.2.6 Solar Array Design

Solar arrays are unique in that many programs will release a Request For Bids (RFB) where multiple companies to compete for the contract instead of vetting and selecting a component based on an array of viable options or building it themselves. When array specifications are designated in the RFB, linear stiffness and natural frequency are two important structural parameters to be supplied. Linear stiffness is best calculated in a design suite such as SolidWorks or COMSOL, but first approximations for natural frequency can be determined based on assumed geometry and hinge locations. Natural frequencies can be calculated for stowed, mid-deployment, and during deployment conditions; which natural frequency condition is relevant depends on solar array geometry. Vibrational isolators, or snubbers, can be applied at the corners of solar cells to prevent chatter between array panels, but resonance is still possible when stowed if the natural frequency of the stowed solar array is near the natural frequency of the mounting structure or dispenser. This condition can be avoided by adherence to the Octave Rule, which states component natural frequency must be greater than or equal to two times the natural frequency of the mounting structure. For CubeSats, the mounting structure is the rails of the dispenser, and the Power Spectral Density (PSD) curve of the LV must by supplied by the MI to fully vet vibrational stability. LVs such as Artemis may require vibrational isolators between the LV structure and dispenser due to strong high frequencies on the large rocket; smaller rockets such as RocketLab’s Electron will not need isolators.

An example solar panel cross-section is given in **Figure 32**, represented by a sandwich structure of outer solar cell, copper reinforcement, and FR4 substrate where the electrical traces are located. Arrays are comprised of panels.

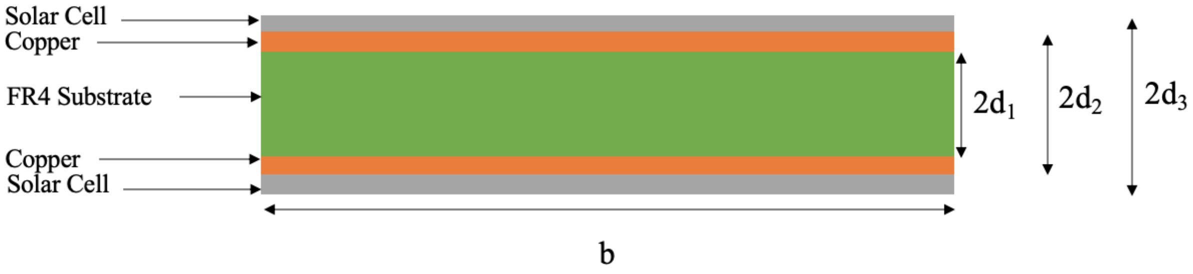

Figure 32: Solar Panel Sandwich Representation [50]

Equivalent stiffness, EI_{array}, and mass, m_{array}, can be calculated by **Eqs.(2-3)**.

$$EI_{array} = \frac{2\cdot b_{array}}{3}\cdot\sum_{\eta=1}^{3}\left[E_{\eta}\cdot\left(d_{\eta+1}^{3}-d_{\eta}^{3}\right)\right] \tag*{\textbf{Eq.(2)}}$$

$$m_{array} = 2\cdot b_{array}\cdot\sum_{\eta=1}^{3}\left[\rho_{\eta}\cdot\left(d_{\eta+1}-d_{\eta}\right)\right] \tag*{\textbf{Eq.(3)}}$$

Parameter b_{array} is width in units of meters, η represents the material layer index, d_{η} is the distance from the neutral axis of the panel to the seam between the η and η +1 layers in units of meters, E_{η} is the modulus of elasticity of the η^{th} layer in units of Pa, and ρ_{η} is the density of the η^{th} layer in units of kg/m^3. Assume material properties for the proposed solar array; materials best suited to solar panel fabrication may change over time. Material properties for this analysis are given in **Table 13**.

Table 13: Solar Panel Material Properties [50]

Material	Elastic Modulus, [GPa]	Density, [kg/m^3]
Copper	110	7764
FR4 PCB	13.8	1900
Solar Cell	70	3113

Augmentation of array linear stiffness is accomplished via increasing the thickness of the copper reinforcement. Stowed configuration natural frequency, $f_{n,stowed}$, is calculated by **Eq.(4)**.

$$f_{n,stowed} = \frac{\lambda_1}{2\cdot\pi\cdot L_{array}^{2}}\cdot\left[\frac{EI_{array}}{m_{array}}\right]^{\frac{1}{2}} \tag*{\textbf{Eq.(4)}}$$

Parameter λ_1 is dimensionless and based on boundary conditions whereas L_{array} represents beam length in units of meters. Using the procedure outlined in Blevins [50], a free-pinned and free-free boundary condition was used to find λ_1 for the deployable panels. Parameter λ_1 was calculated purely based on geometry for body mounted arrays. A rigid body assumption is made for the solar panels wherein it is assumed that the fundamental natural frequency of the solar array is driven by the relatively low stiffness of the hinges. Solar array panel mass moment of inertia is calculated by **Eq.(5)**.

$$J_{array} = \frac{m_{array}\cdot\left(L_{array}^{2}+b_{array}^{2}\right)}{12} \tag*{\textbf{Eq.(5)}}$$

Where L_{array} and b_{array} are the same length and width of the panel as in **Eqs.(2-4)**. The mass moment of inertia at the center of rotation, J, is calculated for deployable panels by **Eq.(6)**.

$$J = J_{array} + m_{array} \cdot d_{array}^2 \qquad \textbf{Eq.(6)}$$

Parameter d_{array} is the length from the solar array center of mass to CubeSat center of mass in units of meters which changes due to deployment. The natural frequency for both full deployment and mid deployment scenarios is found in **Eq.(7)**.

$$f_n = \frac{1}{2\pi} \cdot \sqrt{\frac{k_{hinge}}{J}} \qquad \textbf{Eq.(7)}$$

The parameter k_{hinge} represents the solar array spring hinge torsional stiffness, which obviously assumes a torsional spring hinge deployment method. For non-spring hinge methods such as those on solar array C, this methodology must be altered. Conclusions are provided under spring hinge assumptions regardless. A value of 10,000 N-m/rad is presented as nominal in [33]. What varies between mid and full deployment are the dimensions and geometric relations of the panels, specifically L_{array}, b_{array}, and d_{array}. The FOS metric is determined by **Eq.(8)**,

$$FOS = \frac{1}{2} \cdot \frac{f_n}{f_{min,lv}} \qquad \textbf{Eq.(8)}$$

Where f_n is the natural frequency of the solar array in units of Hz and $f_{min,lv}$ is the minimum natural frequency of the launch vehicle, assumed to be 20 Hz. If the natural frequency of the solar panel was 80 Hz, then the FOS would be 2. An example from an intermediate AEGIS solar array design is presented in **Table 14**. The configuration presented is similar but obsolete in that panel lengths, widths, and hinge locations (pin boundary conditions) are not the same as those in **Figure 15**, but an important point is communicated. Specific panel geometries are not provided because readers are encouraged to glean their conclusions from an understanding of λ_1 in [50]. There were two body panels instead of three at the time.

Table 14: Solar Panel Natural Frequency Example

Panel	Thickness, [mm]	Factor of Safety, Stowed	Configuration	Natural Frequency, [Hz]
A	1.5	3.0	Stowed	120.1
			Mid-Deployed	104.9
			Fully-Deployed	43.4
B	2.5	2.3	Stowed	91.5
			Mid-Deployed	45.1
			Fully-Deployed	42.9
C	1.5	2.9	Stowed	115.2
			Mid-Deployed	157.9
			Fully-Deployed	157.9
Body I	1	11.5	Stowed	461.2
Body II	1	6.1	Stowed	245.2

The change in natural frequency from stowed to deployed configuration in arrays A and B is not the same as the change in natural frequency for array C; this is due to panel geometry. There is a key difference in widths between sides with (the free-pinned condition) and without (the free-free condition) a hinge. Panels

A and B are wide on the side with the hinge while panel C is wide on the side without the hinge. Panel C thus has a lower λ_1 value for the stowed configuration which reduces the stowed natural frequency relative to the mid and fully deployed natural frequency for a given thickness. It is important to remember that the natural frequency to avoid is from the launch vehicle occurs when the arrays are in their stowed positions. First order estimates for solar array clearance requirements can be calculated by Miles' equation, a function of dynamic frequency, amplitude, and solar array hinge damping. Sydnee Shadoan is thanked for her assistance in organizing this material.

3.2.7 Hold and Release Mechanisms

Launch vehicles with CubeSat payload dispensers do not permit CubeSats to constrain their deployable solar arrays with the inside of the dispenser; the solar arrays must be fixed in position and released by a command to the HRM. As magnetic HRMs are high mass devices, constraining small-to-medium solar arrays is accomplished by tying arrays down with cords, usually made of Nylon or Vectran. The cords are wrapped or affixed to a burn wire, usually made of Nichrome, that heats up and severs the cord holding the array in place. When the cord is severed, the rotational spring no longer has a countertorque, and the array is rotated into the desired position. Large arrays should be held by a structural mechanism such as a door, not multiple cord-style HRMs.

Rotational spring release is a violent event akin to frangibolt actuation. Arrays will rotate until the spring hinge apparatus hits a mechanical backstop, which will impart rotational momentum to the spacecraft. A simulation performed by Shanghai Jiaotong University and repeated by MIT showed 1500 N imparted to the backstop over 0.32 seconds resulting in an angular acceleration along the rotational axis of 22.03 deg/s^2 [51, 52]. The specific volume and mass of the spacecraft are not mentioned, but the point of solar arrays causing rotations upon deployment remains. Detumbling is required between individual solar array deployments to reduce stress imparted to the hinges, and planning for these detumble maneuvers must be included in reaction wheel inertial storage estimates, described in Section 3.7.5.1.

There are three main types of HRM: edge, nut, and spring-loaded. An example of edge HRMs that AEGIS emulated for solar array B is found in [53], and generic tie down HRMs, such as the Pumpkin HRM featured on AEGIS arrays A and C, can be considered under this category. Examples of nut HRMs are found in [54,55], and spring-loaded HRM designs are found in [56, 57]. HRMs are not one size fits all, and a mix of types may be required based on solar array geometry designs. Actuation is accomplished in less than 30 seconds by providing ten or fewer watts to the nichrome wire. From a ConOps standpoint, not all HRM types have a dedicated release signal. This is shown in **Figure 116** with array C being different. Solar array deployment can be otherwise verified by measuring a change in rotation rates from the IMU or an increase in power generation from the EPS.

3.3 Thermal Control

Thermal control methodologies vary widely by spacecraft payload, orbit, and size. Some payloads require precision temperature control due to cryogenic or optically sensitive hardware; some require materials with high thermal conductivities to minimize thermal gradients across isolation structures. Operating principles of thermal components such as thermoelectric coolers, patch heaters, heat pipes, thermal straps, and deployable radiators are left to the excellent characterizations of [33,34,39]. This section will focus on advanced deep space CubeSat thermal environment definition under three assumptions: Radioisotope Heater Units (RHU) are not necessary, the spacecraft will be deployed outside the second Van Allen Belt meaning atmospheric free molecular heating and charged particle heating are negligible, and cryogenic applications, while extremely relevant for sensitive scientific instrumentation, are not required. A comprehensive Earth to Moon transfer thermal model is presented with a single denouement: both hot and cold thermal runaway can be prevented if attitude control is guaranteed.

3.3.1 Thermal Design Objectives

Table 15: Thermal Control Subsystem Design Objectives, Adapted from [28]

Design Objective	Description	Rationale	Actionable Items
Thermal Design (**TH-1**)	Thermal design produces a minimum 5°C margins, except for heater controlled elements which have a maximum 70% heater duty cycle, and two-phase flow systems which have a minimum 30% heat transport margin.	Positive temperature margins are required to account for uncertainties in power dissipations, environments, and thermal system parameters.	Determine internal generation wattage for patch heaters to reach minimum temperature requirements. Determine radiator area to expel heat during high flux mission segments.
Thermal Balance Testing (**TH-2**)	Identify thermal balance test concepts. Include thermal balance test in environmental test plan.	The test will provide verification of the system's thermal design margin. In addition, steady state temperature data from this test will be used to validate thermal math models (TMMs).	Validate thermal model in TVAC with appropriate internal generation values.
Environmental Testing Plan (**TH-3**)	Identify environmental test concept. Develop preliminary environmental test plan.	This provides workmanship/performance verifications where required environments can be achieved and reduces risk to cost during IV&T.	Identify, calibrate, and utilize a TVAC to recreate expected thermal environments as closely as possible.

3.3.2 Historical Perspective

Literature-based thermal control approaches are cross-referenced applications of texts, spacecraft lessons learned, industry test specifications, and NASA standards. The most prominent text is Gilmore [34] with the latest edition published in 2002, meaning significant technological advancements have been made since publication. The most notable shift is one of a design engineer mindset from hardware to software based thermal control solutions.

Legacy spacecraft engineers considered state-of-health hardware to be part of the TT&C subsystem [34]. FSW was not considered to be a primary subsystem, and heater units, whether patch or cartridge heater, were controlled by solid-state or bimetallic thermostats as dedicated physical units. These design notions forced control hardware to be separate from the OBC logic. Prognostic Health Management (PHM) systems are now understood to be part of the FSW subsystem where diagnostic metrics are reported and analyzed for looming thermal problems or potential subsystem errors. OBCs may now precisely control heater duty cycles based on PHM information and thermal set points. The integration of FSW with thermal control was not possible with early 2000s technology, but advancements in software state definition and processor throughput have allowed for maturation in these areas.

3.3.3 Heat Sources in Space

The principle mechanisms for spacecraft heating are direct solar heating, planetary body reflections known as a planet's albedo, planetary emission as infrared radiation (IR), and internal heat generation as both a consequence of nominal component operations and a supplemental source from heaters. If present, atmospheric and charged particle heating are non-negligible sources.

3.3.3.1 Direct Solar

The Sun can be modeled as a blackbody with temperature, T, equal to 5780 K [58]. At Earth distance, the solar heat flux is 1322 W/m^2 at aphelion and 1414 W/m^2 at perihelion with less than 1% variation between solar minima and maxima [34]. The values have been verified within 0.4% by the World Radiation Center in Davos, Switzerland [59,60]. The spectral emissive power of a hemispherical blackbody, $E_{\lambda b}$, can be calculated by **Eq.(9)**, where h_p is Planck's constant, c_0 is the speed of light in a vacuum, n is the refractive index of the medium which is unity for a vacuum, λ is the wavelength expressed in microns or nanometers as long as units are consistent, and k_B is Boltzmann's constant. The units are W/m^2-μm.

$$E_{\lambda b} = \frac{8 \cdot \pi \cdot h_p \cdot c_0^2}{n^2 \cdot \lambda^5 \cdot \left[\exp\left(\frac{h_p \cdot c_0}{n \cdot k_B \cdot \lambda \cdot T}\right) - 1\right]} \qquad \textbf{Eq.(9)}$$

Plotting **Eq.(9)** as a function of wavelength for a blackbody at 5780 K yields **Figure 33**. Wavelength dependence may be ignored as a first order approximation for heat flux calculations. The flux radiating from the Sun is calculated by the simple radiation estimate in **Eq.(10)**; blackbody emissivity, ε_b, is unity.

$$Q''_{Solar,Surf} = \varepsilon_b \cdot \sigma \cdot T^4 \qquad \textbf{Eq.(10)}$$

$$Q''_{Solar,Surf} = 1 \cdot \left(5.670374 \cdot 10^{-8} \frac{W}{m^2 \cdot K^4}\right) \cdot (5780\ K)^4 = \sim 63{,}300{,}000 \frac{W}{m^2}$$

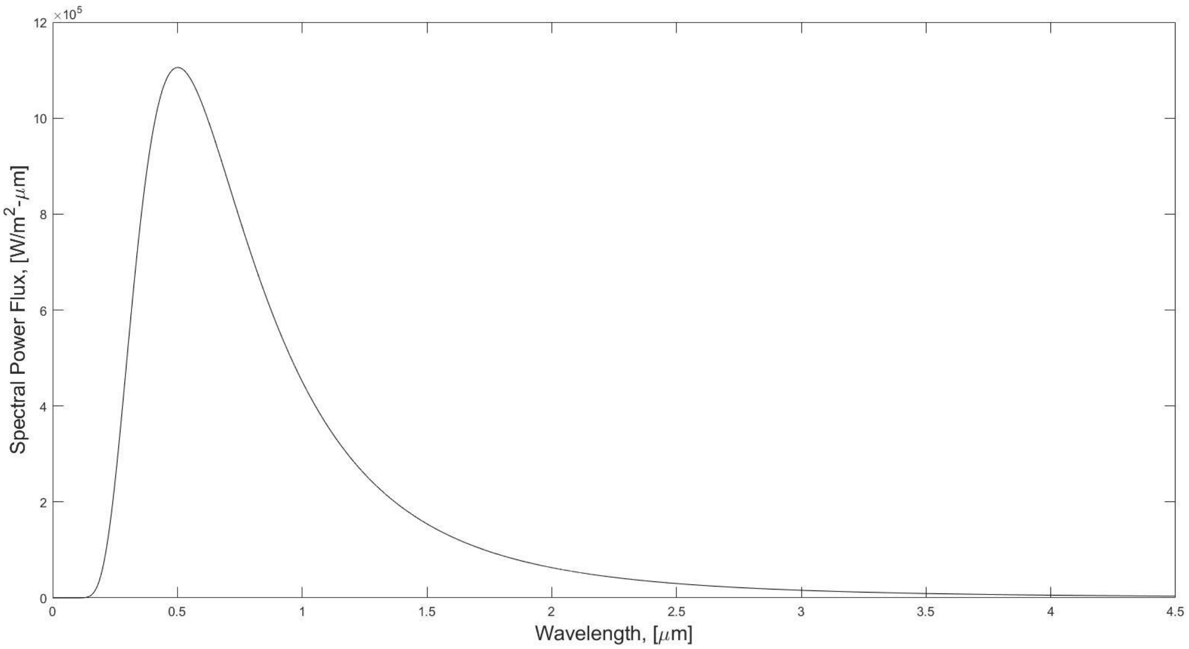

Figure 33: Spectral Emissive Power Flux from a Blackbody at 5780 K

Similarly, numerically integrating **Eq.(9)** over all wavelengths yields 63,201,000 W/m^2. The proportionality of blackbody temperature to heat flux is the nature of σ, the Stefan-Boltzmann constant.

When estimating radiation interaction with a target at a distance, radiative view factors correlating to the target geometry must be used [61]. For any small planar surface facing a sphere of radius R at a distance H to the center of the sphere, the radiative view factor, F_{rad}, in **Eq.(11)** is included.

$$F_{rad} = \frac{1}{\left(\frac{H}{R}\right)^2} \qquad \textbf{Eq.(11)}$$

Eq.(12) describes the relationship between a radiative heat source, the Sun, and the radiative heat flux from that source at a given distance, represented here as Earth. The parameter D_{Sun} is the mean distance from Earth to the Sun in units of m, and R_{Sun} is the radius of the Sun in similar units. D_{Sun} is equal to 1 AU which is formally defined from the center of the Sun. If distance is being measured from the surface of a radiative source, the radius of the sphere must be added to the distance measurement for **Eq.(11)** to be correct.

$$Q''_{Solar} = Q''_{Solar,Surf} \cdot F_{rad} = \frac{Q''_{Solar,Surf}}{\left(\frac{D_{Sun}}{R_{Sun}}\right)^2} = \frac{63{,}300{,}000\frac{W}{m^2}}{\left(\frac{1.496 \cdot 10^{11}\ m}{6.95 \cdot 10^{8}\ m}\right)^2} = \sim 1{,}366\,\frac{W}{m^2} \qquad \textbf{Eq.(12)}$$

3.3.3.2 Planetary Albedo

An albedo is the reflection of solar radiation from a planetary body. Incident radiation is either reflected or absorbed for an opaque body, and albedo represents the reflected portion. As with all radiation, the amount reflected depends on the reflectivity of the surface material, which for Earth could be desert, ice, forest, oceans, or clouds. The average albedo factor for Earth is ~0.3, with land-based albedo factors commonly ranging from 0.1 to 0.4. Values do not change significantly from one day to the next but will vary by season [34]. Albedo radiation is non-Lambertian, meaning correction factors must be applied near the terminator, polar regions, or anywhere direct reflection does not exist. There is no albedo heating during eclipse.

Albedo is dependent on latitude as well as the Sun's position. At the subsolar point where the solar zenith angle, θ_0, is equal to zero, radiation from the Sun will reflect directly back to the spacecraft from the Earth for a high local albedo. However, snow can have a reflectivity as high as 0.9, meaning the albedo factor at the poles would be higher due to surface material than the equatorial subsolar point where trees or oceans are more likely to dominate the surface. Melting ice caps would reduce Earth's albedo leading to increased planetary radiation absorption because less radiation would be reflected. Melting snow albedo factor is 0.4 and dirty snow is 0.2 [62].

Spacecraft qualification suites such as STK [32] can calculate albedo factors based on provided orbits, but a simple estimation for Earth albedo heat flux is found in **Eq.(13)**. The advanced albedo characterization work of Rickman [63] is utilized in Section 3.3.6. As in **Eq.(12)**, the radius of the emitting body R_{Earth} and the orbital altitude D_{Orbit} must be provided to obtain an account of the heat flux at a given distance. Varying hottest and coldest conditions requires only a change in solar heat flux and albedo factor, aF. The example calculation represents average albedo heat flux at 52,000 km, the edge of the VABs.

$$Q''_{Albedo} = \frac{Q''_{Solar}}{\left(\frac{D_{Orbit}+R_{Earth}}{R_{Earth}}\right)^2} \cdot aF \qquad \textbf{Eq.(13)}$$

$$Q''_{Albedo} = \frac{1{,}366\frac{W}{m^2}}{\left(\frac{52{,}000\ km+\ 6{,}378.165\ km}{6{,}378.165\ km}\right)^2} \cdot (0.3) = 4.89\,\frac{W}{m^2}$$

3.3.3.3 Planetary Emission

Earth's radiative emission is calculated in the same way the Sun's radiative emission is calculated but with low blackbody temperatures. NOAA and NASA spacecraft have flown missions that estimated the blackbody temperature of Earth is near -18 °C or 255.15 K [34]. It varies strongly with location, as deserts have a higher local temperature than ice-covered poles. IR emission does not require Lambertian radiation correction factors.

Radiation from the Earth to an orbiting spacecraft can be confusing when one considers a spacecraft may have a higher temperature than the blackbody temperature of Earth, but the view factor of the Earth must be accounted for. If the Earth were not in view, the spacecraft would be radiating directly to space with a Cosmic Microwave Background (CMB) temperature of 2.7 K [64]. It is better to assume the heat from Earth is a supplemental value because emission from the spacecraft generally assumes the spacecraft is radiating directly to space and not to a planetary body. Additionally, IR wavelengths cannot be used for power and can only cause spacecraft heating.

Planetary emission for a deep space orbit can be estimated by assuming a nominal temperature for the entire planet. This is not a realistic assumption, but one can see that both albedo and emission heat fluxes drop below 1 W/m^2 near 100,000 km. Planetary emission flux at 100,000 km is estimated in **Eq.(14)**.

$$Q''_{Emission} = \frac{\varepsilon_b \cdot \sigma \cdot T_{Earth}^4}{\left(\frac{D_{Orbit}+R_{Earth}}{R_{Earth}}\right)^2} \qquad \textbf{Eq.(14)}$$

$$Q''_{Emission} = \frac{1 \cdot \left(5.670374 \cdot 10^{-8}\frac{W}{m^2 \cdot K^4}\right) \cdot (255.15\ K)^4}{\left(\frac{100{,}000\ km+\ 6{,}378.165\ km}{6{,}378.165\ km}\right)^2} = \ 0.864\,\frac{W}{m^2}$$

3.3.3.4 Lunar Albedo and Emission

Calculations for lunar albedo and emission are non-trivial; they depend on surface temperature, regolith composition, regolith thickness, regolith disturbance, and phase of the Moon [65-69]. Legacy datasets primarily stem from Apollo 15 and 17, the only missions at the time to take simultaneous temperature and thermophysical property data at the surface [70,71]. Unfortunately, the locations of the Apollo datasets were on the edge of a unique lunar geological region known as the Procellarum KREEP Terrane, a thorium-rich area considered thermally anomalous. It is now understood that high-thorium, low density regions are warmer while high-titanium areas are cooler [65]. With measurements from Lunar Prospector, Diviner, and the Chang'E 2 Microwave Radiometer (MRM) [72-74], a better understanding of lunar albedo and emission has been formed.

The Moon is almost as absorptive as black paint, an unintuitive conclusion since human interaction with the Moon is based on lunar albedo. It will absorb solar radiation over the entire spectrum and re-emit that energy as IR; lunar IR is so powerful that spacecraft orbiting the Moon will often direct radiators toward the Sun instead of the lunar surface to keep them cool. It is important to remember that short solar radiation wavelengths can be reflected by paints or coatings while IR reflectivity is usually low. The lunar albedo varies between 0.092 and 0.129 depending on location [75], and Racca estimates lunar albedo at 0.127 ± 0.021 [66]. Apollo 11 temperature estimates placed the surface emissivity at 0.92 [76], and emissivity between 400-1000 nm wavelength has been determined to be 0.97 [66]. Because emissivity and albedo values are so dependent on surface properties, it is frequently preferable to define emissivity as a function of temperature and albedo as a function of solar zenith angle [69]. Lunar emissivity as a function of surface temperature is provided in **Eq.(15)**, and lunar albedo as a function of solar zenith angle is provided in **Eq.(16)**. **Eq.(16)** was originally calculated using JPL-sourced ephemerides [69].

$$\varepsilon_{lunar}(T_s) = 0.9696 + 0.9664 \cdot 10^{-4} \cdot T_s - 0.31674 \cdot 10^{-6} \cdot T_s^2 - 0.50691 \cdot 10^{-9} \cdot T_s^3 \qquad \textbf{Eq.(15)}$$

$$aF_{lunar}(\theta_0) = 0.12 + 0.03 \cdot \left(\frac{\theta_0}{45}\right)^3 + 0.14 \cdot \left(\frac{\theta_0}{90}\right)^8 \qquad \textbf{Eq.(16)}$$

Eqs.(15-16) are plotted against surface temperature and solar zenith angle, respectively, in **Figures 34-35**.

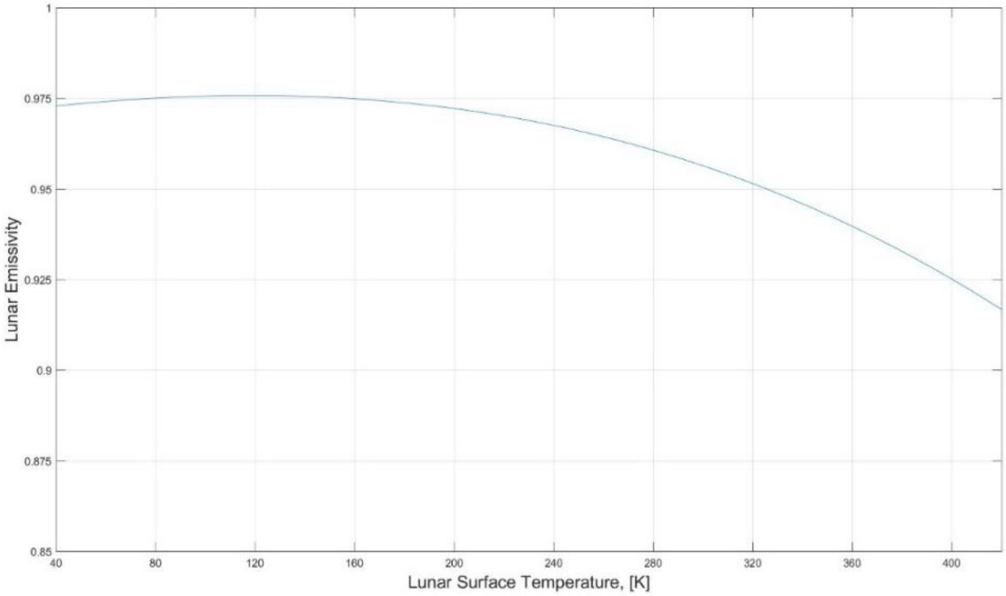

Figure 34: Lunar Emissivity as a Function of Lunar Surface Temperature

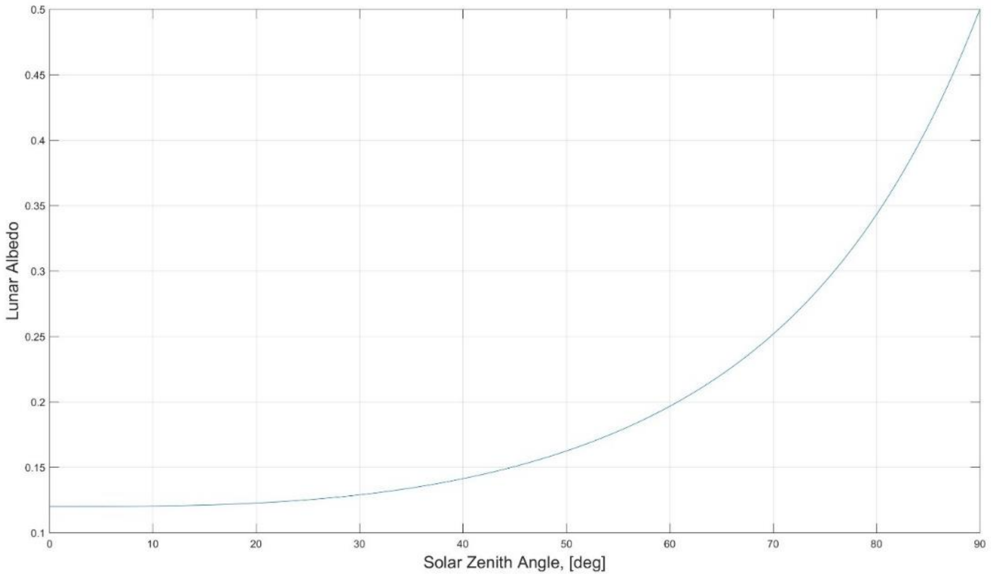

Figure 35: Lunar Albedo as a Function of Solar Zenith Angle

It is possible to apply thermal loads to a spacecraft once the lunar thermal environment is understood. The first step is to find, procure, or generate a lunar temperature map to generate heat flux distributions. Datasets from Apollo 15 and 17, Diviner, and the Chang'E 2 MRM are useful [71,73,74]; AEGIS was kindly provided lunar emission heat flux data by Stephanie Mauro at MSFC, shown in **Figure 36** and overlaid on the lunar surface in **Figure 37**. This data is meant to function as an input to Thermal Desktop models for orbiting CubeSats but is included here as a MATLAB model input. AEGIS thermal model methodology is described in Section 3.3.6. With LunIR, LunaH-Map, Lunar Flashlight, and Lunar IceCube launching in late 2020 or early 2021 on Artemis I, lunar thermal datasets should expand rapidly.

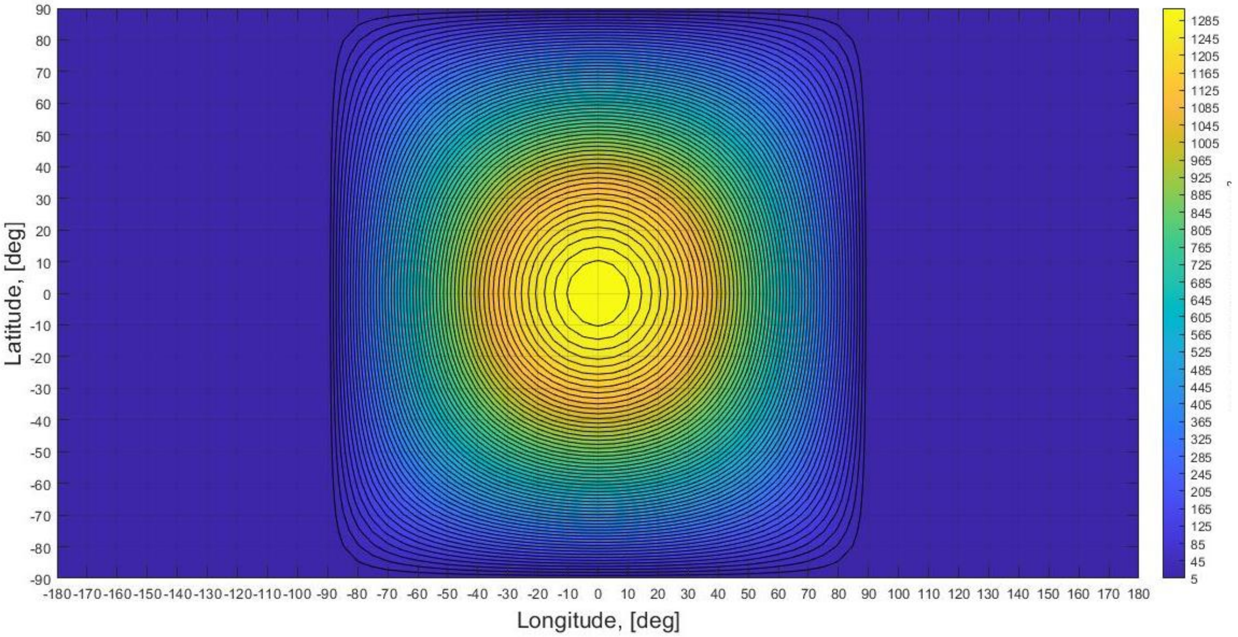

Figure 36: Lunar Emission Flux Model

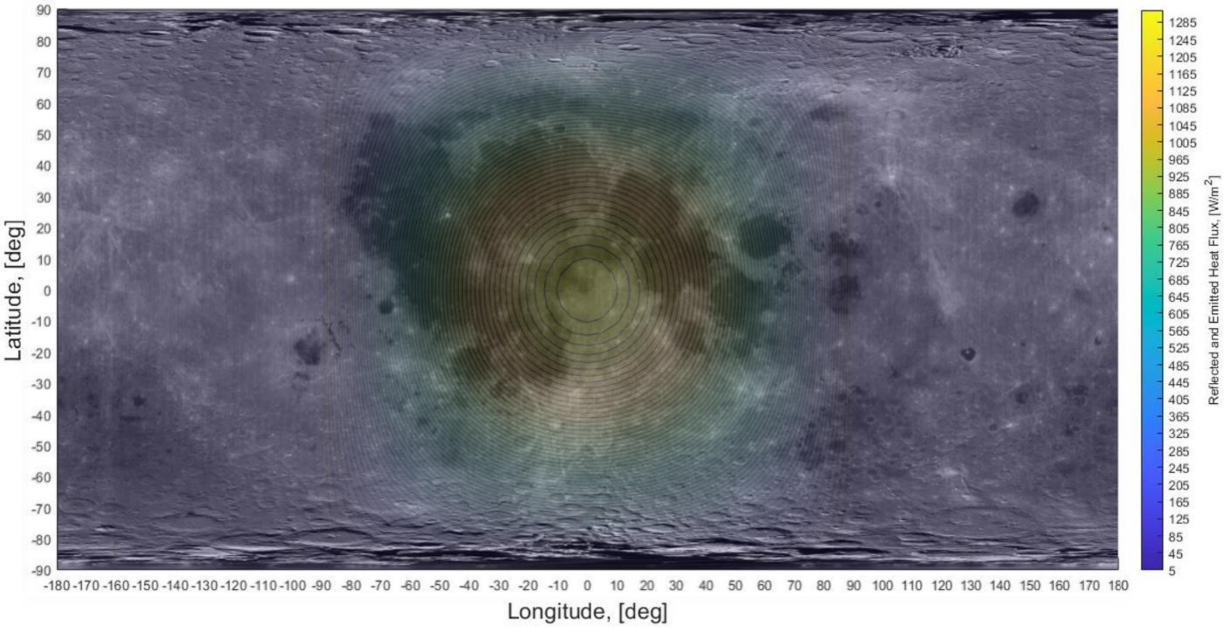
Latitude, [deg]
Longitude, [deg]
Reflected and Emitted Heat Flux, [W/m^2]
90
80
70
60
50
40
30
20
10
0
-10
-20
-30
-40
-50
-60
-70
-80
-90
-180 -170 -160 -150 -140 -130 -120 -110 -100 -90 -80 -70 -60 -50 -40 -30 -20 -10 0 10 20 30 40 50 60 70 80 90 100 110 120 130 140 150 160 170 180
1285
1245
1205
1165
1125
1085
1045
1005
965
925
885
845
805
765
725
685
645
605
565
525
485
445
405
365
325
285
245
205
165
125
85
45
5

Figure 37: Lunar Emission Flux Model Transposed Over the Lunar Surface

Spacecraft position can be defined in terms of lunar latitude and longitude, though conversion from Keplerian orbital elements will be required. If latitude and longitude are defined and related to solar zenith angle via Keplerian parameters, **Eqs.(15-16)** may be used to calculate lunar emissivity and albedo factor per orbit location. The longitude of the lunar dark side begins near ± 90° in **Figures 36-37**, but that longitude varies according to lunar phase. Lunar phase will not be known for an orbit until a launch data is set. For spacecraft anticipating lunar altitudes above 20,000 km, a simple maximum and minimum heat flux calculation will suffice for pre-PDR analysis based on equatorial lunar heat flux values. A maximum emissive heat flux of 1335 W/m^2 is present with a minimum of 5 W/m^2. These max and min values are solely viable for first order analyses and estimating the temperature of the Moon as a blackbody is bad practice.

3.3.3.5 Internal Generation

Operation of spacecraft electrical components will result in ohmic heating of the components. The amount of heat a component generates is equal to the voltage drop across the component multiplied by the current supplied to the component; this is usually described as a component Power Conversion Efficiency (PCE) or simply efficiency. If the efficiency of a component is 80% and 10 W is supplied to the component, 2 W will be released as heat. PCEs for specific components are proprietary and will not be available without a Non-Disclosure Agreement (NDA). Additionally, the thruster would draw power during the burn software state but not during the science state. Thermal engineers must sometimes estimate PCEs of many components for varied operation situations without correct or known PCEs. A limited Monte-Carlo methodology for estimating internal generation values without known PCEs is presented, but a distinction is made between operational heat generation through powered component use and intentional heat generation through dedicated heater unit operation. Heater wattage estimation is discussed in Section 3.3.7, but the current analysis pertains to operational heat generation. Operational and intentional heat generation are represented as distinct terms in the satellite energy balance.

Power generation, distribution, and consumption per software state is given a thorough description in Section 3.5; the prevailing lesson is that power consumption ergo internal thermal generation must be vetted per software state. The state with the highest power draw may not necessarily be the state with the highest internal heat generation, but it is likely. Many components are immediately powered off during a safety state, and science states generally involve waiting for an astrophysical event with components powered down, so science or safety represent assumptions for states with the lowest power draw.

Consider a set of peripheral components with varied power consumption values. A table of power supplies for AEGIS component selections is provided in **Table 16** with two software states considered, science and burn. The PCEs of the components are unknown for some early phase in spacecraft design, but they can be estimated with a nominal minimum and maximum. The minimum PCE for all components will be 70% and the maximum PCE will be 95%; these values may be altered as desired. It must first be decided which components will be operational during a given software state, which is discussed for AEGIS in Section 3.5.4.1, but the values may be more obscure than zero or non-zero. The radio may need 4.5 watts when in receive mode and 15 watts when in transmit mode, so the power draw per component per state must be defined before operational internal generation is calculated for a given state.

Table 16: Component Power Consumption Example per Software State

Component/Subsystem	Max Power Draw, [W]	Science Power Draw, [W]	Burn Power Draw, [W]
Radio	15	4.5	4.5
Science Instrument	8	8	0
OBC	2.85	2.5	2.5
Thruster	40	0	25
Star Tracker	0.65	0.65	0.65
Sun Sensors + IMU	5.16	5.16	5.16
DCE + Reaction Wheels	7.59	2	4

In a Monte-Carlo methodology, a random PCE is prescribed to each component between the min and max values. The PCE is different for each component. The power supplied to a component is multiplied by the PCE estimate for that component, and the sum of all component power supplies multiplied by their assigned PCE is taken. The internal generation value is the total power supplied to the components minus the cumulative sum of those products. This procedure is looped for 1000, 10,000, or 100,000 iterations as desired, and new PCEs are provided to the components for each iteration. A histogram of the wattage occurrences can be created per software state, and Gaussian probability metrics may be applied for operational internal generation estimates without known PCEs. Internal generation histograms for science and burn software states are shown in **Figures 38-39**.

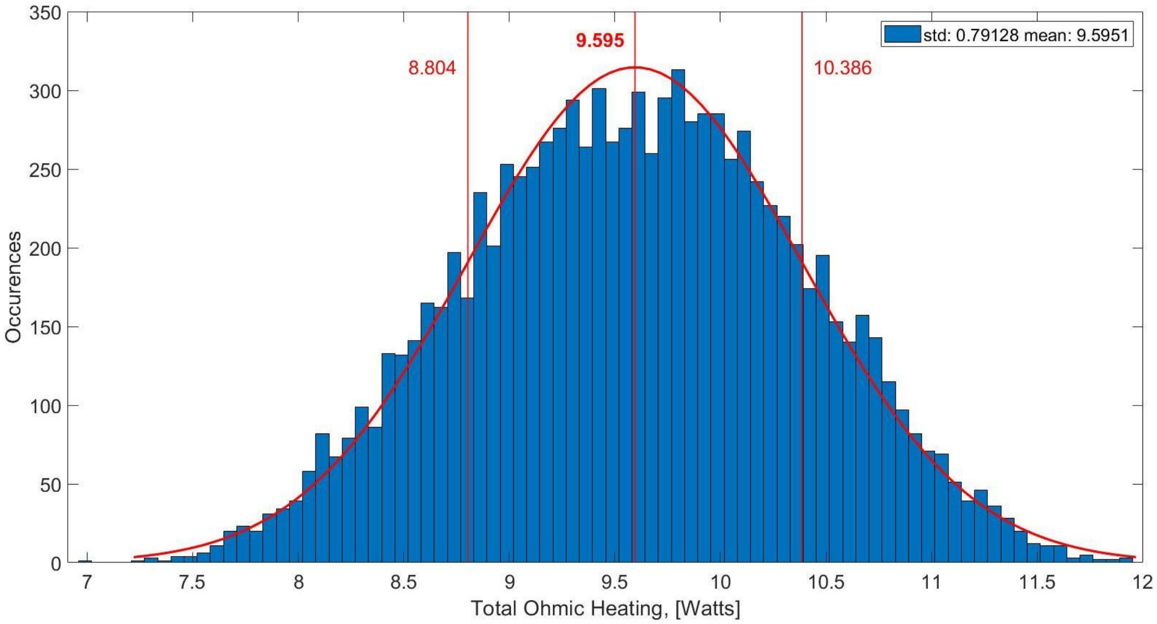

Figure 38: Histogram of Operational Internal Generation Wattage, Science State

The science power occurrences are well fit to a Gaussian distribution; the burn power occurrences are not. Any value between the upper and lower 3σ bounds has a roughly equal probability of occurring.

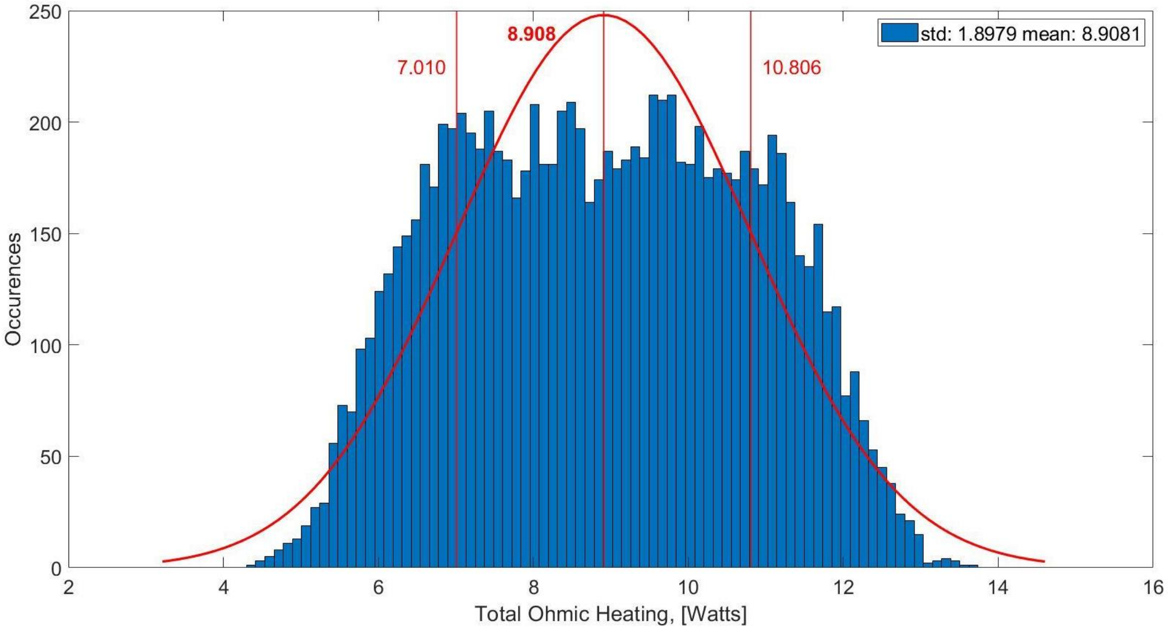

Figure 39: Histogram of Operational Internal Generation Wattage, Burn State

Obviously, the lowest generation value would be if all components were assigned 95% PCE and the highest value would be if all components were assigned 70%, but this methodology is about managing expectations for when PCEs are known. It is just as unlikely for all components to have low PCEs as it is for them to all have high PCEs, and statistical outputs are viable. Heat estimations in space result in transient spacecraft temperature distributions, so instead of placing ultra-conservative margins on heat flux or generation values, engineers frequently apply conservative margins on the temperature output itself rather than wattage inputs.

3.3.4 Orbit Beta Angle

Planetary emission will affect a spacecraft whether it is in solar view or in an eclipse umbra, but direct solar and albedo heat loads will only apply to a spacecraft not in eclipse. The β angle represents a method for spacecraft in a two-body orientation to evaluate thermal loads based on orbital position and is useful for thermal orbit visualization. It is the minimum angle between the orbit plane and the solar vector, varying from -90° to +90°. Some knowledge of orbital mechanics is required though nothing outside of an undergraduate textbook. The β angle calculation is presented in **Eq.(17)**.

$$\beta = sin^{-1}[cos(\delta_s) \cdot sin(i) \cdot sin(\Omega - \Omega_s) + sin(\delta_s) \cdot cos\,(i)] \tag{Eq.(17)}$$

Parameter δ_s is the declination of the Sun, i is the orbit inclination, Ω is the Right Ascension of the Ascending Node (RAAN), and Ω_s is the right ascension of the Sun. β can be best understood by looking at the orbit of the spacecraft around a planetary body from the point of view of the Sun. A value of 0° means the satellite appears edgewise to the Sun, has the most eclipse time out of any orbit, and experiences varied albedo loads reaching a maximum at the subsolar point [34]. A value of 90° means the orbit appears circular to the Sun, does not enter an eclipse, and receives the lowest possible albedo load. **Figure 40** illustrates these assertions.

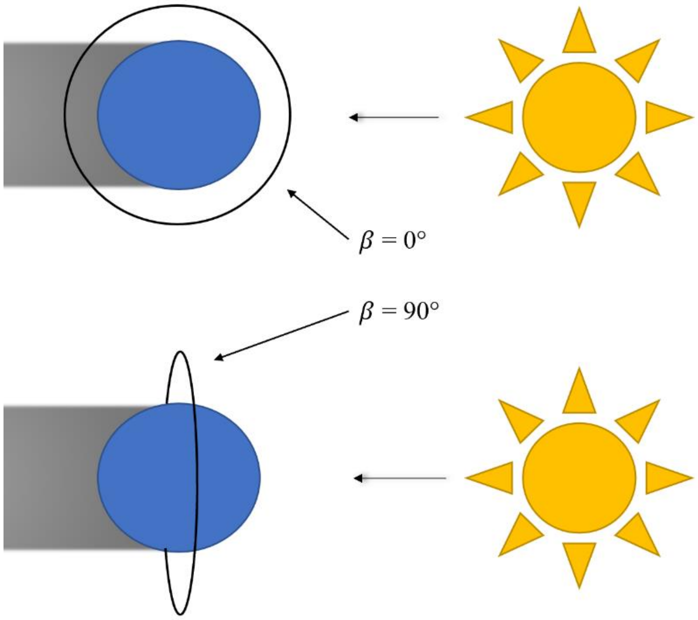

Figure 40: Beta Angle Example Diagram

For a circular orbit around a planetary body, the β angle at which eclipses begin, β^*, is calculated in **Eq.(18)**.

$$\beta^* = \sin^{-1}\left(\frac{R}{R + D_{Orbit}}\right) \;:\; 0^{\circ} \leq \beta^* \leq 90° \tag{Eq.(18)}$$

The eclipse fraction for that circular orbit is calculated by **Eq.(19)**. [34]

$$f_{Ecl} = \begin{cases} if\ |\beta| < \beta^* & \frac{1}{180^{\circ}} \cdot \cos^{-1}\left[\frac{(D_{Orbit}^2 + 2 \cdot R \cdot D_{Orbit})^{\frac{1}{2}}}{(R + D_{Orbit}) \cdot \cos(\beta)}\right] \\ if\ |\beta| \geq \beta^* & 0 \end{cases} \tag{Eq.(19)}$$

Orbits that cannot be approximated by a circular orbit should have eclipsed fractions determined evaluated in STK, Copernicus, or the Princeton Satellite Systems CubeSat Toolbox [32,77,78]. The β angle will change over time as the Sun moves, not just with satellite motion, so the eclipse fraction will also change over time. As the parameters used to calculate β are defined from a two-body perspective, the β angle is difficult to define in a three-body problem. Three-body or highly elliptical orbits should consider immediately evaluation in dedicated software suites in lieu of starting with first order approximations.

Earth-orbiting, lunar-orbiting, and transfer calculations are based on the work of Rickman [63] for a spacecraft orbiting the Earth with a nadir-facing surface that never changes attitude. Values for planetary emission per face never change because the view factor and surface temperature never change. Planetary emission values would realistically change as localized Earth surface features were hotter or colder, but a blackbody temperature is assumed for Earth. The nullification of albedo heating during eclipse is apparent.

A nuanced flaw exists in the otherwise excellent work of Rickman in that direct solar heat fluxes are modeled as variable with respect to areal exposure on the spacecraft. Rickman plots solar heat flux as variable according to which surface or combination of faces is exposed to the Sun. If one face is orthogonally exposed, the heat flux increase multiplier is unity. If two faces are exposed to the Sun at a 45° angle, the heat flux is sin(45°) + cos(45°) to approximately equal 1.41. The error is that the increase factor is applied to the heat flux estimate leading to the heat calculation instead of the areal parameter in the heat calculation. Rickman's thermal estimates are shown in **Figure 41**, and the corrected plots are shown in **Figure 42**.

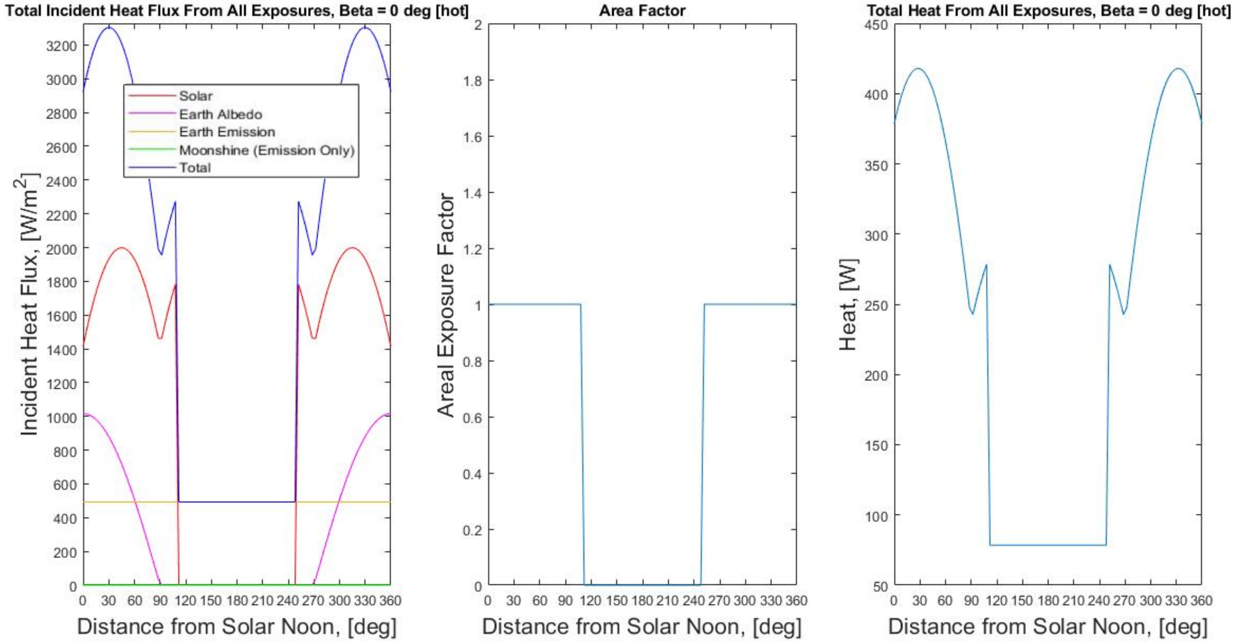

Figure 41: Scrutinized Earth Circular Orbit Solar Heat Flux Formulation, Altitude = 419 km. Atmospheric and charged particle heating not included

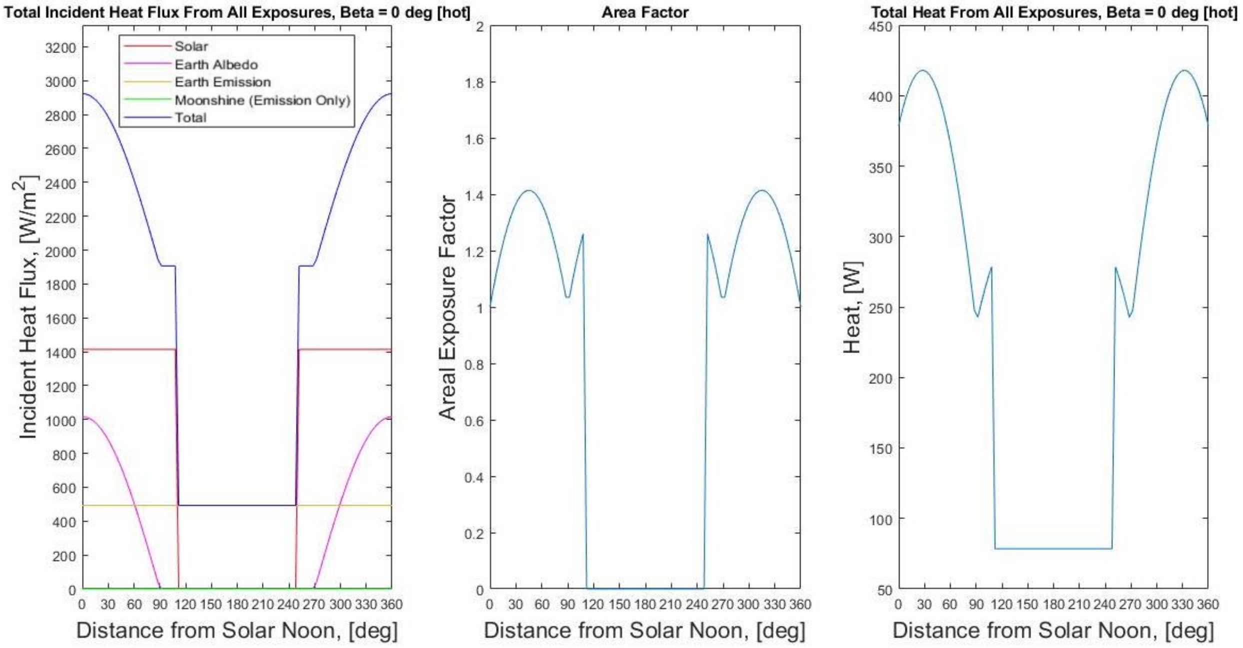

Figure 42: Corrected Earth Circular Orbit Solar Heat Flux Formulation, Altitude = 419 km. Atmospheric and charged particle heating not included

Evident is that the final heat result is the same for both procedures, but it is important that engineers understand the flux of photons from the Sun per meter squared is not changing per spacecraft orbital position.

3.3.5 Coatings and Finishes

Thermal time constants in space are on the order of minutes to hours, and localized hot or cold spots can be susceptible to thermal runaway if not designed with transient temperature profiles in mind. The application of a coating or material surface finish to control the radiative properties of the material can either passively prevent the component or surface from getting too hot or cold or extend the time constant enough to allow for active thermal control mechanisms to engage. Which coating or surface finish to use is dependent on the solar absorptance and the IR emittance.

3.3.5.1 Reflectivity, Absorptivity, and Emissivity: Wavelength Dependence

Wavelength-dependent solar radiation was introduced in Section 3.3.3.1 where the Sun, assumed to be a blackbody at 5780 K, outputs much of its radiation in the visible spectrum and some radiation in the UV and IR spectra. The peak of the Sun's radiation being in the visible spectrum is why animals on Earth evolved to see in that spectrum, and solar radiation experienced by humans as warmth instead of colors is primarily radiation in the IR spectrum. Just as humans have differing radiation absorption capabilities in different wavelengths, spacecraft coatings can be chosen to reject or receive specified wavelengths. Additionally, blackbodies at temperatures much lower than stars, such as humans, spacecraft, and even ice cubes, will emit radiation primarily in the IR spectrum, not the visible spectrum, in accordance with Wien's Displacement Law.

Emissivity and absorptivity are considered surface properties; emissivity is the ratio of the total emissive power radiated from the surface to the total emissive power radiated from a blackbody at the same temperature and is dependent on wavelength, zenith angle, azimuth angle, temperature, and time.

Absorptivity is the fraction of energy incident on a body that is absorbed by the body, and the directional and spectral characteristics of any incident radiation must also be considered with temperature. Reflectivity represents the energy fraction that is not absorbed or transmitted by a body, but it is dependent on the angle of incident radiation as well as the angles considered for that reflected energy [58]. The relationship between reflectivity and absorptivity for an opaque surface is found in **Eq.(20)** where ρ is reflectivity and α represents absorptivity.

$$\alpha = 1 - \rho$$ **Eq.(20)**

Reflectivity is calculated based on wavelength-dependent complex refractive indices, discussed below, and used with **Eq.(20)** to calculate absorptivity. Emissivity is sometimes assumed to be equal to absorptivity in a model called Kirchoff's Law, which is not a Law and states that for a surface receiving radiative energy, conservation of energy dictates the absorptivity must be equal to emissivity. This is a poor assumption for energy models being used in transient analyses, and emissivity is better assumed to be constant over a wavelength range if wavelength-dependent emissivity data is not available.

Planetary emission is in the IR spectrum, and albedo wavelengths will be at least slightly longer than direct solar wavelengths due to the energy change inherent to electromagnetic reflection. Direct solar, planetary emission, and planetary albedo all have different wavelength profiles, and radiation wavelength dependence is not effectively communicated by **Eq.(10)**. There is a more accurate way to model a spacecraft's response to radiation, primarily direct solar radiation, if a spacecraft surface material or combination of materials is known.

The following derivation assumes the reader has some knowledge of radiative transport, reflectivity, absorptivity, emissivity, and refractive indices. For a given surface material, the wavelength-dependent complex refractive index must be known. A non-comprehensive consolidation of spectral complex refractive indices for various materials can be found in [79]. The formula for complex refractive indices is shown in **Eq.(21)**, where m is the total wavelength-dependent complex refractive index, n is the refractive index, and k is the mass attenuation parameter.

$$m = n + i \cdot k$$ **Eq.(21)**

Some texts including [58] provide the mass attenuation parameter, or extinction index, as negative such that the plus sign in **Eq.(21)** is a minus sign. The difference is an ambiguous distinction in how one defines the time-harmonic factor which transforms the time-domain Maxwell equations into the frequency-domain equations. If one writes or obtains a code to work through the subsequent calculations, make sure the sign bookkeeping is performed appropriately.

Assuming the surface is flat relative to the wavelength, the complex spectral refractive indices are used to calculate surface reflectivity using modified Fresnel surface reflectivity equations, shown in **Eqs.(22-24)**. This version of the Fresnel equation calculates the reflectivity of a surface with or without a coating for varied solar Angle of Incidence (AOI) and specified coating thickness. Parameter introduction is provided in **Table 17**.

Table 17: Modified Fresnel Relation Overview

Parameter	Description
m	Base layer notation. If ms is not defined, this is the outer layer
ms	Outer coating layer notation. This could specify a paint or covering
h	Thickness of surface coating layer, ms
θ	Angle of Incidence relative to normal
R_{par}	Directional complex reflectance of parallel angle
R_{per}	Directional complex reflectance of perpendicular angle
ρ	Directional reflectivity for a surface with a layer (ms) backed by a substrate (m)

The parallel and perpendicular radiation components are calculated by **Eqs.(22-23)**, left justified for readability.

$$R_{par} = \Bigg\{-e^{\left[2\cdot i\cdot h\cdot\sqrt{1-\frac{1-(\cos\theta)^2}{(n+i\cdot k)_m}}\cdot(n+i\cdot k)_m\right]}\cdot\Bigg[\cos\theta\cdot(n+i\cdot k)_m + \sqrt{1-\frac{1-(\cos\theta)^2}{(n+i\cdot k)_m}}\Bigg]\cdot\Bigg[\sqrt{1-\frac{1-(\cos\theta)^2}{(n+i\cdot k)_{ms}}}\cdot(n+i\cdot k)_m -$$

$$\sqrt{1-\frac{1-(\cos\theta)^2}{(n+i\cdot k)_m}}\cdot(n+i\cdot k)_{ms}\Bigg] + \Bigg[\cos\theta\cdot(n+i\cdot k)_m - \sqrt{1-\frac{1-(\cos\theta)^2}{(n+i\cdot k)_m}}\Bigg]\cdot\Bigg[\sqrt{1-\frac{1-(\cos\theta)^2}{(n+i\cdot k)_{ms}}}\cdot(n+i\cdot k)_m +$$

$$\sqrt{1-\frac{1-(\cos\theta)^2}{(n+i\cdot k)_m}}\cdot(n+i\cdot k)_{ms}\Bigg]\Bigg]\Bigg\} \div \Bigg\{e^{\left[2\cdot i\cdot h\cdot\sqrt{1-\frac{1-(\cos\theta)^2}{(n+i\cdot k)_m}}\cdot(n+i\cdot k)_m\right]}\cdot\Bigg[\cos\theta\cdot(n+i\cdot k)_m - \sqrt{1-\frac{1-(\cos\theta)^2}{(n+i\cdot k)_m}}\Bigg]\cdot$$

$$\Bigg[\sqrt{1-\frac{1-(\cos\theta)^2}{(n+i\cdot k)_{ms}}}\cdot(n+i\cdot k)_m - \sqrt{1-\frac{1-(\cos\theta)^2}{(n+i\cdot k)_m}}\cdot(n+i\cdot k)_{ms}\Bigg] - \Bigg[\cos\theta\cdot(n+i\cdot k)_m + \sqrt{1-\frac{1-(\cos\theta)^2}{(n+i\cdot k)_m}}\Bigg]\cdot$$

$$\Bigg[\sqrt{1-\frac{1-(\cos\theta)^2}{(n+i\cdot k)_{ms}}}\cdot(n+i\cdot k)_m + \sqrt{1-\frac{1-(\cos\theta)^2}{(n+i\cdot k)_m}}\cdot(n+i\cdot k)_{ms}\Bigg]\Bigg\} \qquad \textbf{Eq.(22)}$$

$$R_{per} = \Bigg\{-e^{\left[2\cdot i\cdot h\cdot\sqrt{1-\frac{1-(\cos\theta)^2}{(n+i\cdot k)_m}}\cdot(n+i\cdot k)_m\right]}\cdot\Bigg[\sqrt{1-\frac{1-(\cos\theta)^2}{(n+i\cdot k)_m}}\cdot(n+i\cdot k)_m + \cos\theta\Bigg]\cdot\Bigg[\sqrt{1-\frac{1-(\cos\theta)^2}{(n+i\cdot k)_m}}\cdot(n+i\cdot k)_m -$$

$$\sqrt{1-\frac{1-(\cos\theta)^2}{(n+i\cdot k)_{ms}}}\cdot(n+i\cdot k)_{ms}\Bigg] + \Bigg[\sqrt{1-\frac{1-(\cos\theta)^2}{(n+i\cdot k)_m}}\cdot(n+i\cdot k)_m - \cos\theta\Bigg]\cdot\Bigg[\sqrt{1-\frac{1-(\cos\theta)^2}{(n+i\cdot k)_m}}\cdot(n+i\cdot k)_m +$$

$$\sqrt{1-\frac{1-(\cos\theta)^2}{(n+i\cdot k)_{ms}}}\cdot(n+i\cdot k)_{ms}\Bigg]\Bigg]\Bigg\} \div \Bigg\{e^{\left[2\cdot i\cdot h\cdot\sqrt{1-\frac{1-(\cos\theta)^2}{(n+i\cdot k)_m}}\cdot(n+i\cdot k)_m\right]}\cdot\Bigg[\sqrt{1-\frac{1-(\cos\theta)^2}{(n+i\cdot k)_m}}\cdot(n+i\cdot k)_m - \cos\theta\Bigg]\cdot$$

$$\Bigg[\sqrt{1-\frac{1-(\cos\theta)^2}{(n+i\cdot k)_m}}\cdot(n+i\cdot k)_m - \sqrt{1-\frac{1-(\cos\theta)^2}{(n+i\cdot k)_{ms}}}\cdot(n+i\cdot k)_{ms}\Bigg] - \Bigg[\sqrt{1-\frac{1-(\cos\theta)^2}{(n+i\cdot k)_m}}\cdot(n+i\cdot k)_m + \cos\theta\Bigg]\cdot$$

$$\Bigg[\sqrt{1-\frac{1-(\cos\theta)^2}{(n+i\cdot k)_m}}\cdot(n+i\cdot k)_m + \sqrt{1-\frac{1-(\cos\theta)^2}{(n+i\cdot k)_{ms}}}\cdot(n+i\cdot k)_{ms}\Bigg]\Bigg\} \qquad \textbf{Eq.(23)}$$

Parallel and perpendicular reflectivity components are combined in **Eq.(24)**.

$$\rho = \frac{\left[(|R_{par}|)^2+(|R_{per}|)^2\right]}{2} \qquad \textbf{Eq.(24)}$$

Some simplification terms are offered for ease of calculation but are not applied nor found in nomenclature.

$$kz0 = cos\theta \qquad \textbf{Eq.(25)}$$

$$S_2 = 1 - kz0^2 = 1 - (\cos\theta)^2 \qquad \textbf{Eq.(26)}$$

$$kz = \sqrt{1 - \frac{S_2}{m}} = \sqrt{1 - \frac{1-(\cos\theta)^2}{(n+i\cdot k)_m}} \qquad \textbf{Eq.(27)}$$

$$kzs = \sqrt{1 - \frac{S_2}{ms}} = \sqrt{1 - \frac{1-(\cos\theta)^2}{(n+i\cdot k)_{ms}}} \qquad \textbf{Eq.(28)}$$

There are emissivity calculations based on wavelength-dependent complex refractive indices for varied materials such as metals. If there are equations for emissivity based on wavelength-dependent complex refractive indices for a coated surface of arbitrary thickness for varied AOI, the author was not able to find them. Applications of this wavelength-dependent reflectivity calculation are provided for real surface materials.

3.3.5.2 Examples: Paint and Polish

There are four types of thermal control surfaces: solar reflectors, with high IR emissivity and very low solar absorptivity, solar absorbers, with low IR emissivity and very high solar absorptivity, flat reflectors, with moderate emissivity and low absorptivity throughout the spectral range, and flat absorbers, with low emissivity and high absorptivity throughout the spectral range. Control surfaces are often categorized by their absorptivity to emissivity ratios within a given bandwidth.

Four materials are considered: aluminum, a flat reflector, the white paint AZ-93, a solar reflector, the black paint Chemglaze Z306, a solar absorber, and Kapton, which does not fall neatly into a thermal control surface category but is often used as surface coverings of cables. **Table 18** provides the wavelength intervals over which spectral complex refractive index data was obtained; wavelength-dependent reflectivity data was provided for AZ-93 by AZ Technology and no calculation was needed. Spectral reflectivities for the four example materials are provided or calculated by **Eqs.(22-24)** and presented in **Figure 43**. Flux reflected and absorbed per wavelength are plotted in **Figure 44** and tabulated in **Table 19** as a total value integrated over the relevant spectrum. The wavelength range over which **Figures 43-44** were calculated is 0.2 – 4.5 µm for all materials because over 98% of solar radiation exists in that range [63]. A reflectivity value is assumed for all relevant wavelengths that refractive index or reflectivity data was not available, and a ramp function is used to fit the data. The slope of the ramp is assumed and represents a source of error. AOI is considered normal to the surface. For Chemglaze Z306 and Kapton, a common solar reflectivity was assumed where data was not available. For AZ-93, only the lowest UV spectrum was unaccounted for, and the first complex spectral refractive index value at 0.25 µm was assumed for wavelength values between 0.2 – 0.25 µm.

The reflectivity values assume a base material of the four example materials and not a coating of the example materials applied to a separate base material. Spectral complex refractive index values for aluminum, Chemglaze Z306, and Kapton were provided in [80-82]. It should be noted that the reflectivity of aluminum is highly dependent upon the polish and surface condition, and [80] does not describe the polish or alloy composition, if any, of the tested aluminum. Newer aluminum reflectivity data exists.

Table 18: Wavelength Range of Complex Spectral Refractive Indices for Selected Materials

Material	Wavelength Range of Data, [µm]	Assumed Reflectivity Outside Data Range
Aluminum	0.00012399 - 200	N/A
Chemglaze Z306	2.6 – 14.20	0.04
Kapton	1.667 – 20.0	0.56
AZ-93	0.25 – 21.0	0.05

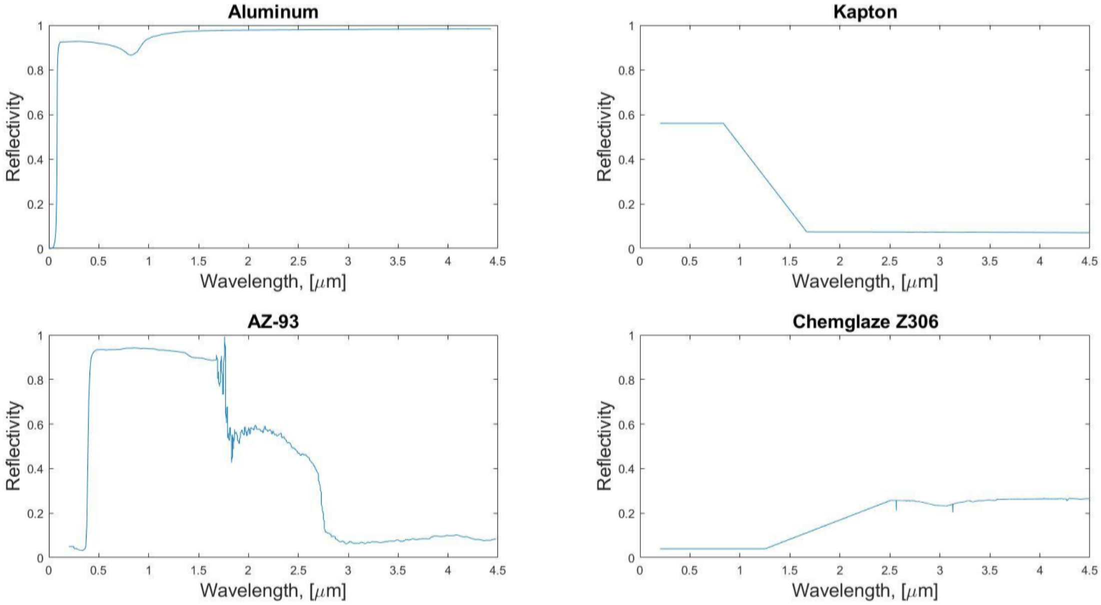

Figure 43: Spectral Reflectivity of Four Surface Materials for Solar Wavelengths

With reflectivities per wavelength calculated, the percent of radiation reflected and absorbed can be calculated per wavelength using **Eq.(9)** and **Eq.(20).** Note that the flux absorbed plus the flux reflected should equal the flux from the Sun at a given distance, namely 1366.8 W/m^2.

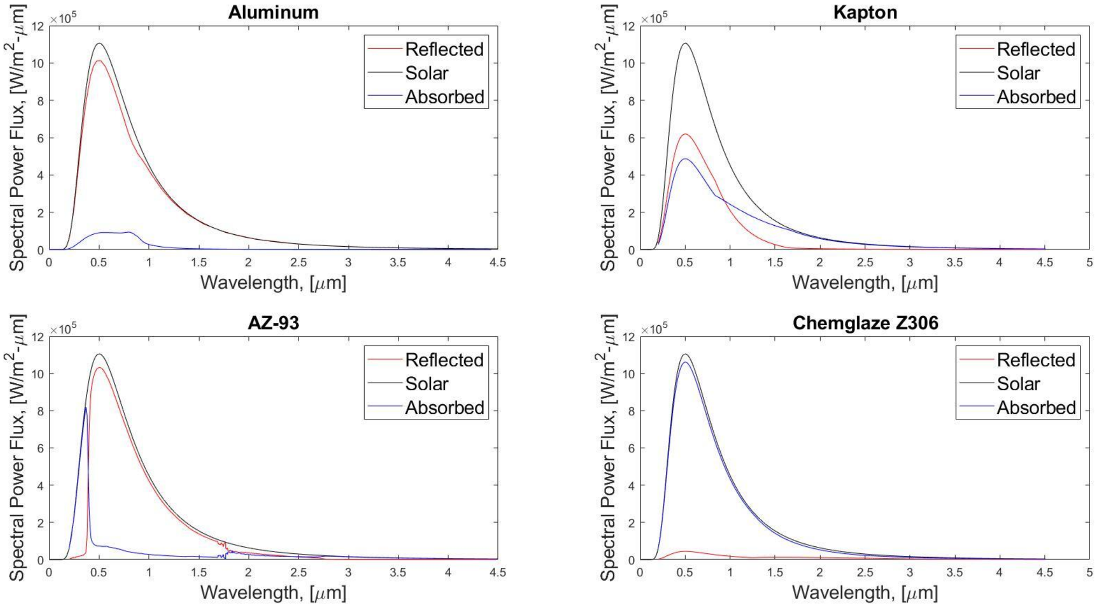

Figure 44: Reflection and Absorption of Solar Wavelengths, Four Materials

Table 19: Integrated Absorbed and Reflected Heat Flux Values per Material

Material	Heat Flux Absorbed, [W/m^2]	Heat Flux Reflected, [W/m^2]
Aluminum	101.7	1265.1
Chemglaze Z306	1312.2	54.6
Kapton	601.4	765.4
AZ-93	272.5	1094.3

Mentioned was the ability of **Eqs.(22-24)** to vary the thickness of a surface coating on a base material along with the ability the vary the AOI of solar radiation. **Figure 45** depicts the radiation absorbed and reflected by a base of aluminum with no coating for an AOI of 0°, 30°, 60°, and 90°. **Figure 46** provides the same calculations but with a 1 mm thick coating of Kapton film. Here, normal to the surface is 0° and parallel to the surface is 90°.

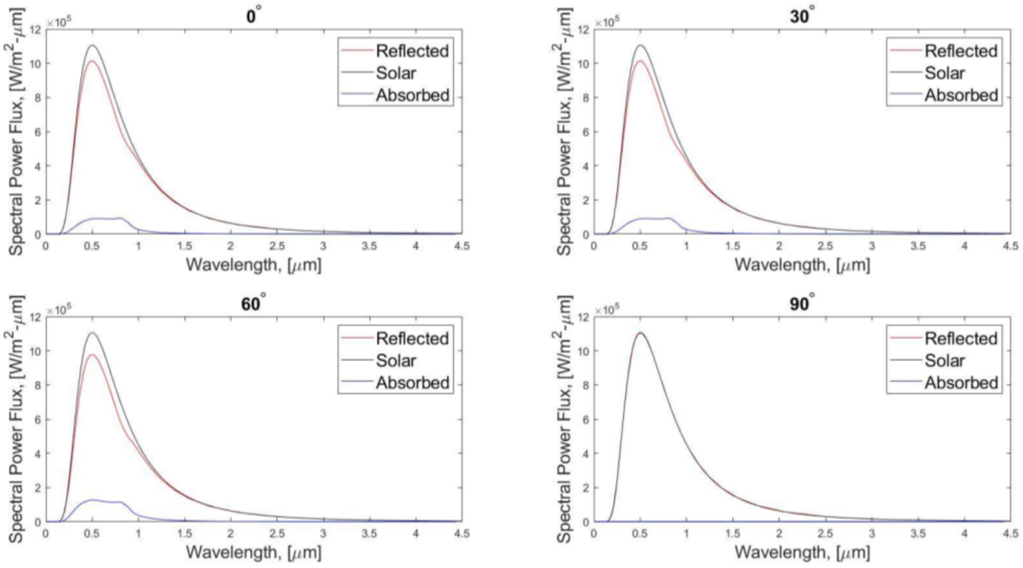

Figure 45: Varied AOI for a Surface of Bare Aluminum, No Coating

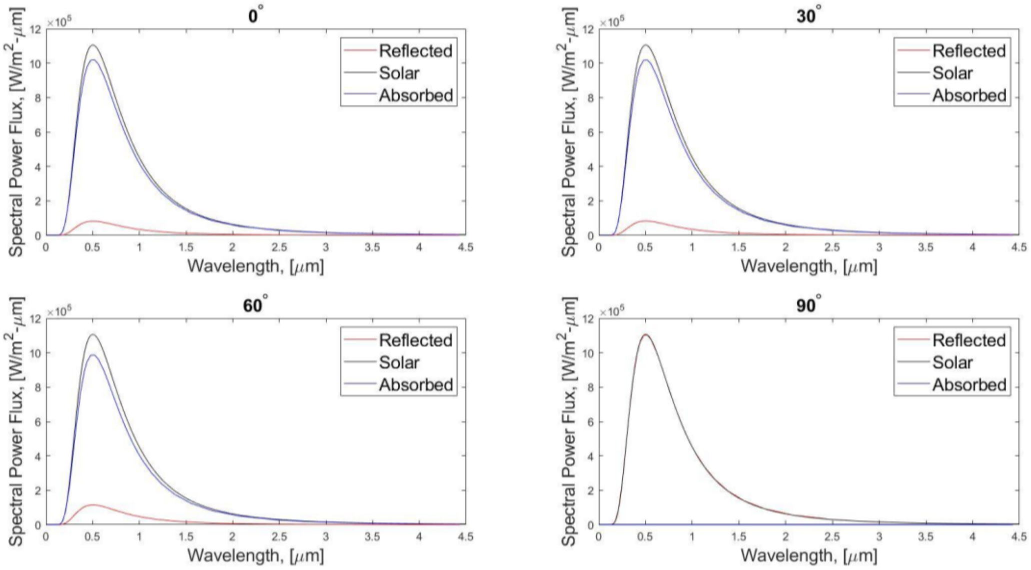

Figure 46: Varied AOI for a Surface of Kapton-Coated Aluminum, Kapton Thickness = 1 mm

A minor increase in aluminum absorptivity is present for increasing AOI, but at 90° all radiation is reflected and not absorbed. When a 1 mm layer of Kapton is applied, the surface predominantly takes on the characteristics of Kapton and not that of aluminum for all AOI except 90°. Radiation is indeed a function of material outer surface properties, but an investigation of surface layer thickness is warranted. A thickness of 1 mm is much thicker than the average layer of paint, so the dominance of Kapton surface properties over aluminum may be due more to the thickness of the layer than a simple material property switch. The ability to vary the thickness of a coating on a base material may allow advanced coating application techniques to tailor the surface properties of that surface. Kapton also features slight translucence, a factor that is not included in any of the present analyses. The transmittivity of Kapton is low but non-zero.

3.3.5.3 Variable Emissivity Phase Change Coatings

A future technology with applications for spacecraft thermal control is variable-emissivity phase change coatings, specifically VO_2. These coatings will emit more energy when the coating is above a phase transition temperature and less energy when the coating is below the phase transition. Obtaining, characterizing, and applying VO_2 are non-trivial procedures, but its use may become more prevalent with improvements in manufacturing.

The variable emissivity effect has been thoroughly studied [83-86], but the mechanism behind the transition requires an understanding of the definition of both emissivity and emittance. When VO_2 undergoes a phase transition from cold to hot, the emittance, the total amount of emitted energy per unit area per unit time for all possible wavelengths, increases [85,86], while the emissivity, the ratio of the total emissive power radiated from a surface to the total emissive power radiated from a blackbody at the same temperature, decreases [83,84]. Although the hot VO2 surface is radiating more energy than when it was below the transition temperature, the emissivity has decreased. A conjecture for why this occurs is that the VO_2 is radiating strongly in a small bandwidth above the transition temperature and radiates moderately in a wide bandwidth below the transition temperature. A wavelength-dependent emissive power model would need to be employed to mathematically characterize the increase in emittance because a reduction of emissivity in a blackbody model would produce a reduction of emissive power.

3.3.6 Energy Balance Thermal Model

There are several ways to form a Thermal Math Model (TMM) for spacecraft thermal environment characterization. The goal is to determine minimum and maximum heat flux expectations for a given orbit, correlate them to a spacecraft temperature, define required radiator area to keep maximum temperatures low, and define required heater wattage to keep minimum temperatures high. Expressly calculating the temperature distribution in a spacecraft for all times on-orbit is less useful than calculating radiator areas and heater wattage for best, worst, first, and last surface and component conditions of the spacecraft. First is what the spacecraft encounters at the mission beginning, best represents ideal or nominal conditions, worst represents the hottest or coldest conditions encountered, and last represents the spacecraft conditions after component and thermal coating degradation has occurred. The combination of worst and last conditions frames the design envelope, and radiators are often oversized due to worst and last conditions requiring much larger areas than worst and first.

A transient, numerical, isothermal model is considered for pre-PDR analysis. It is likely solar array temperatures will be underestimated and chassis temperatures overestimated for the hot case, but the goal is not to define spacecraft temperatures when an isothermal spacecraft assumption limits temperature accuracy. An isothermal model allows for environment heat fluxes to be estimated for a variety of conditions and brought over to Thermal Desktop or NX Space Systems Thermal [87,88]. Weighted averages of surface areas, component specific heats, absorptivites, and emissivities can be estimated in MATLAB for a given design, but applying calculated heat fluxes to imported CAD in Thermal Desktop or NX allows for localized areas of low or high temperatures to be discovered and addressed and geometry-specific radiative view factors to be included.

3.3.6.1 Model Formulation

Six sources of heat are present in this transient, numerical, isothermal model: direct solar radiation, planetary albedo, planetary emission, lunar emission, operational internal generation as regular component use, and intentional internal generation as heater output. Lunar albedo was not included here due to a lack of solar and CubeSat orbital position knowledge as well as lunar phase uncertainty, but deep space CubeSats should include emission and albedo by CDR from any planetary body within 100,000 km, especially very large bodies such as Jupiter. This analysis will work for CubeSats approaching any planetary body from Earth, and any number of planetary heat sources may be included.

A minimum distance to both Earth and the Moon is defined, and circular orbits of selectable beta angle about the Earth and Moon are estimated with those distances. Heat fluxes at the prescribed altitudes are calculated for all locations on the circular orbit. Hot and cold environment cases are determined for the circular Earth and lunar orbits, meaning heat fluxes must be redefined for solar, planetary emission, planetary albedo, and operational internal generation heat sources per case. Solar radiation flux will vary between 1322 and 1414 W/m^2 depending on Earth orbit location, which consequentially alters albedo calculations, but planetary blackbody temperatures and albedo factors can be varied as well. The variation of model input parameters by hot and cold cases is shown in **Table 20**.

Table 20: TMM Hot and Cold Case Parameter Input Variation

Parameter	Hot Case	Cold Case
Solar Radiation Flux, [W/m^2]	1414	1322
Earth Blackbody Temperature, [°C]	-11.81 [34]	-20.19 [34]
Earth Albedo Factor, [-]	0.35	0.3
Operational Component Heating, [W]	13	7

The Earth blackbody temperatures are 24-hour average heat flux measurements at 30 km altitude calculated back to emissive temperatures on the surface. They are 3.3σ values, meaning they will only be exceeded 0.04% of the time.

A provided lunar emissive heat flux model was used, and no lunar surface temperature variations per hot and cold case are considered. The positions along the Earth and lunar conic sections with the maximum and minimum heat flux per hot and cold case are taken and used as starting and ending points for a Hohmann transfer between Earth and the Moon. This analysis is not limited to any one type of orbit transfer; Hohmann was closest to the realistic transfer of Artemis II. If the hottest thermal case is of interest, the maximum heat flux position for the hot case set of parameters is used. If the coldest thermal case if of interest, the minimum heat flux values for the cold case set of parameters is used. The lunar emission flux values will not change per cold and hot case; the cold case applies the minimum flux value of 5 W/m^2 while the hot case applies the maximum of 1335 W/m^2. Certainly, environments in between max hot and min cold are possible.

Determination of the Earth and lunar thermal environments in those circular orbits are precursor evaluations and characterizing the spacecraft thermal balance during transfer between them is the real objective. A visual representation of the transfer is provided in **Figure 47**. It was desired for the model to be able to plot the thermal response of a spacecraft over time for any orbit, and thus orbital element assumptions were made. Assumptions regarding the Hohmann transfer are that eccentricity for starting and final orbits is zero, all inclinations are zero, and computations are performed in the ECI frame.

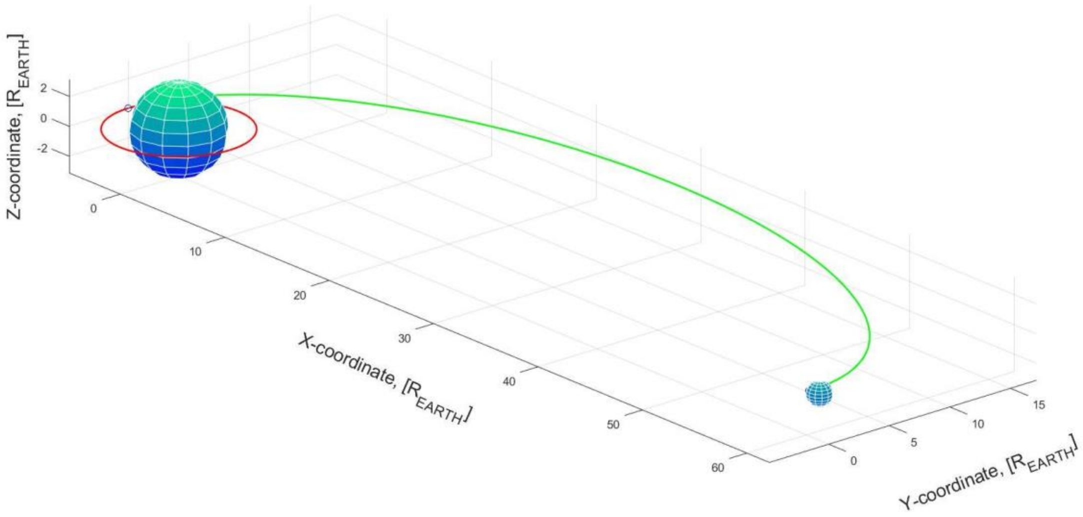

Figure 47: Hohmann Transfer for Thermal Analysis. Red represents starting circular orbit and green represents transfer orbit. Earth and Moon size scaled by a factor of π

The Hohmann transfer is described mathematically to the thermal model in terms of distance to the Earth and timestep per orbit location. The values of planetary albedo and planetary emission are calculated by **Eqs.(13-14)** at each timestep while lunar emission is calculated at each timestep using **Figure 36** and **Eq.(11)**. Each timestep-related Earth altitude is unique, but it does not have to be. The timesteps are also non-constant per distance. The Moon is assumed to be in motionless opposition to the Earth, meaning a calculated distance to the Moon for use in **Eq.(11)** would be 384,400 km less the Earth altitude distance. This aspect of the model will be mentioned as part of future work because the Moon orbits Earth anticlockwise leading to distance approximation errors from the motionless opposition assumption. The Earth also rotates anticlockwise, so the Hohmann transfer would likely originate from the negative-Y direction in **Figure 47**. Additionally, including penumbra considerations instead of only umbra will reduce expected lunar heat flux at various orbital locations but will not alter the max and min values. Erroneous orbital approximations can be overcome with sufficient effort, to be included in the next iteration.

To recap, heat sources in space are defined per Section 3.3.3. Analysis in Section 3.3.4 showed the orbital position of a spacecraft about a planet dictates the highest and lowest heat load conditions due to areal exposure of multiple faces from solar heat flux and not that heat fluxes are changing appreciably other than from eclipse conditions. If an Earth altitude of 24,582 km, the semi-major axis of a Geostationary Transfer Orbit (GTO), and a lunar altitude of 5,000 km were assumed as the starting distances, the scheme would first model circular orbits about the planetary bodies at those altitudes. The Hohmann approximation creates a transfer from 24,582 km to 384,400 km minus 5,000 km where the distance from earth per timestep is correlated with a non-constant timestep. Heat flux values are calculated per timestep with **Eq.(11)**. Maximum and minimum heat fluxes are determined for both hot and cold cases with areal exposure considerations included for the hot case. The determined max or min Earth heat flux calculations are included as parameter values for the first timestep in the transfer model. It will be shown that the numerical method employed must begin at time step j = 2.

After a full characterization of the energy balance equations, area permutations will be introduced for operational thermal envelope determination. The permutation of all possible area combinations exposed to calculated heat flux profiles represents all unique possibilities of spacecraft operational environments. Either heats or heat fluxes from the total analysis may be used as inputs to thermal CAD suites such as Thermal Desktop, NX, or STK. **Eqs.(29-33)** derive the transient, numerical model from an energy balance. **Table 21** provides a descriptive overview for the parameters without values. Fluxes are denoted with two apostrophes; the apostrophes do not represent derivatives.

Table 21: TMM Derivation Parameter Overview

Parameter	Unit	Description
$\dot{E}_{in}$	W	Incoming energy rate
$\dot{E}_{out}$	W	Outgoing energy rate
$\dot{E}_{gen}$	W	Generated energy rate
$Q_{Transient}$	W	Transient heat
Q_{Solar}	W	Heat from solar radiation
$Q_{E,Alb}$	W	Heat from Earth's albedo
$Q_{E,Ems}$	W	Heat from Earth's emission
$Q_{L,Alb}$	W	Heat from lunar albedo
$Q_{L,Ems}$	W	Heat from lunar emission
Q_{Comp}	W	Heat from operational internal generation
Q_{PH}	W	Heat from intentional internal generation, PH = Patch Heater
Q_{Rad}	W	Heat radiated from the CubeSat
α	-	Absorptivity of a given surface of the spacecraft
A	m^2	Area of a surface. Integer subscripts represent surface designations, total means all area
ε	-	Effective emissivity, weighted average of emissivities of each CubeSat face by area
σ	$W/m^2\text{-}K^4$	Stefan-Boltzmann constant
T_{surr}	K	Temperature of space = 2.7 K
T_j	K	Temperature of the entire CubeSat at time step j
Δt_j	s	Difference between time step j and time step j-1
m_{cs}	kg	Mass of entire CubeSat
c_p	J/kg-K	Effective specific heat, weighted average of c_p for all components by mass

The energy balance begins in **Eq.(29)**.

$$\Sigma\dot{E}_{in} + \Sigma\dot{E}_{gen} - \dot{E}_{out} = \frac{dE}{dt} \qquad \textbf{Eq.(29)}$$

Expanding the terms,

$$\left(Q_{Solar} + Q_{E,Alb} + Q_{E,Ems} + Q_{L,Alb} + Q_{L,Ems}\right)_{in} + \left(Q_{Comp} + Q_{PH}\right)_{gen} - (Q_{Rad})_{out} = Q_{Transient} \qquad \textbf{Eq.(30)}$$

The lunar emission dataset provided to AEGIS is hereby denoted as Moon, and lunar albedo flux is set to zero. The parameter Q_{comp} is calculated in Section 3.3.3.5. Parameter Q_{PH} refers to heat sourced from patch heaters, which will be equal to zero for all figures presented but is useful to vary in practice. It is assumed that solar radiation will affect one face of the spacecraft, radiation from Earth will affect a second, distinct face of the spacecraft, and lunar radiation will affect a third face of the spacecraft. These area terms will be used for spacecraft area permutations later. Relating terms to discernable parameters,

$$Q''_{Solar} \cdot \alpha_1 \cdot A_1 + Q''_{E,Alb} \cdot \alpha_2 \cdot A_2 + Q''_{E,Ems} \cdot \alpha_2 \cdot A_2 + Q''_{L,Moon} \cdot \alpha_3 \cdot A_3 + Q_{Comp} + Q_{PH} - \qquad \textbf{Eq.(31)}$$

$$[\varepsilon \cdot \sigma \cdot (T^4 - T_{surr}^4)] \cdot A_{total} = m_{cs} \cdot c_p \cdot \frac{dT}{dt}$$

An effective specific heat for the spacecraft can be calculated from a weighted average of expected components; aluminum is fine for a material guess of many components. Assigning a time index to temperature and timestep variables and rearranging for a numerical methodology,

$$\frac{Q''_{Solar} \cdot \alpha_1 \cdot A_1 + \left(Q''_{E,Alb} + Q''_{E,Ems}\right) \cdot \alpha_2 \cdot A_2 + Q''_{L,Moon} \cdot \alpha_3 \cdot A_3 + Q_{Comp} + Q_{PH}}{m_{CS} \cdot c_p} \cdot \Delta t_j - \qquad \textbf{Eq.(32)}$$

$$\frac{\left[\varepsilon \cdot \sigma \cdot \left(T_j^4 - T_{surr}^4\right)\right] \cdot A_{total}}{m_{cs} \cdot c_p} \cdot \Delta t_j + T_{j-1} = T_j$$

It is here that the scheme can split one of two ways. For the first route the terms T_j and T_{j-1} can be set to a target temperature value such as 10°C and the required Q_{PH} to reach that target temperature can be calculated directly. In the second method, Q_{PH} can be assumed as a constant input and T_j can be calculated iteratively. The second method is employed here, but the first method is useful for determining required heater wattage. **Eq.(32)** can be consolidated by defining $C_{1,j}$ as a constant and $C_{2,j}$ as a radiative coefficient, both requiring calculation at time step j.

$$C_{1,j} - C_{2,j} \cdot \left(T_j^4 - T_{surr}^4\right) = T_j \qquad : \qquad \textbf{Eq.(33)}$$

$$C_{1,j} = \frac{Q''_{Solar} \cdot \alpha_1 \cdot A_1 + \left(Q''_{E,Alb} + Q''_{E,Ems}\right) \cdot \alpha_2 \cdot A_2 + Q''_{L,Moon} \cdot \alpha_3 \cdot A_3 + Q_{Comp} + Q_{PH}}{m_{cs} \cdot c_p} \cdot \Delta t_j + T_{j-1}$$

$$C_{2,j} = \frac{\varepsilon \cdot \sigma \cdot A_{total} \cdot \Delta t_j}{m_{cs} \cdot c_p}$$

Eq.(33) is an explicit formulation of a numerical energy balance which can be solved iteratively for temperature, and explicit methods display stability issues with highly non-linear terms. A numerical root-finding method must be used to solve **Eq.(33)**. Newton-Raphson is the most common root-find method, but its limitations on initial guesses do not easily coincide with space temperatures and linearizing radiation equations is a less accessible approach to this problem. A review of root finding methods may be found in [89]. Dehghan and Hajarian proposed a variant of Steffensen's method that features a lower order of convergence than Newton-Raphson but displays good convergence for **Eq.(33)** [90]. Dehghan and Hajarian's Steffensen variant is described by **Eq.(34)**, and the use of **Eq.(34)** defines the need for beginning the scheme at time step j = 2.

$$x_j = x_{j-1} - \frac{f(x_{j-1})}{\frac{f\left[x_{j-1} + f(x_{j-1})\right] - f\left[x_{j-1} - f(x_{j-1})\right]}{2 \cdot f(x_{j-1})}} \qquad \textbf{Eq.(34)}$$

3.3.6.2 On-Orbit Earth Thermal Environment

Much work has been done to characterize the near-Earth thermal environment on-orbit, and a reiteration of the formulation by Rickman would be less useful to deep space CubeSat designers than a qualification and expansion of his results. Readers wishing to emulate the formulation are encouraged to see [63], but two aspects merit caution. The first is that the heat flux variation on the circular orbit is incorrect but yields correct heat values, as described in **Figures 41-42**, and the second regards thermal input on an orbital assumption. The spacecraft orbiting Earth is assumed to be nadir-pointing only; one face is always pointing directly at the Earth and no other rotation is present. The Sun is assumed stationary, and for this description assume spacecraft inclination is zero. The CubeSat has four other faces besides nadir and zenith, with two pointing ‘up’ and ‘down’ and two pointing ‘forward’ and ‘aft’, with forward being the face on the direction of travel. For an equatorial orbit, albedo and planetary emission are only assumed to impact the forward and aft faces, not the up or down faces. At first glance this can be accepted as a viable assumption that since the Earth is actually an oblate spheroid that heat fluxes affect the sides and not the top and bottom of the spacecraft because the Earth is wider than it is tall. However, this methodology works for any variation of beta angle or inclination, and a beta angle of 90° negates the two-side-only assumption entirely. For this reason, the formulation may be underestimating near-Earth heat fluxes, but as **Eq.(13)** shows the heat flux due to Earth’s emission and albedo become negligible near 60,000 km.

On-orbit heat fluxes for the International Space Station altitude of 419 km and AEGIS initial transfer altitude of 24,582 km are provided in **Figures 48-49** for both the hot and cold cases. While Artemis I’s first bus stop was outside the first VAB near 30,000 km, the AEGIS transit example will range from an initial Earth altitude of GTO distance, 24,582 km, to a 5,000 km lunar distance, or 379,400 km from Earth. It should be noted that while lunar heat flux is included for Earth-based calculations and Earth heat flux is included for lunar calculations, the values are not included twice in the transfer calculations.

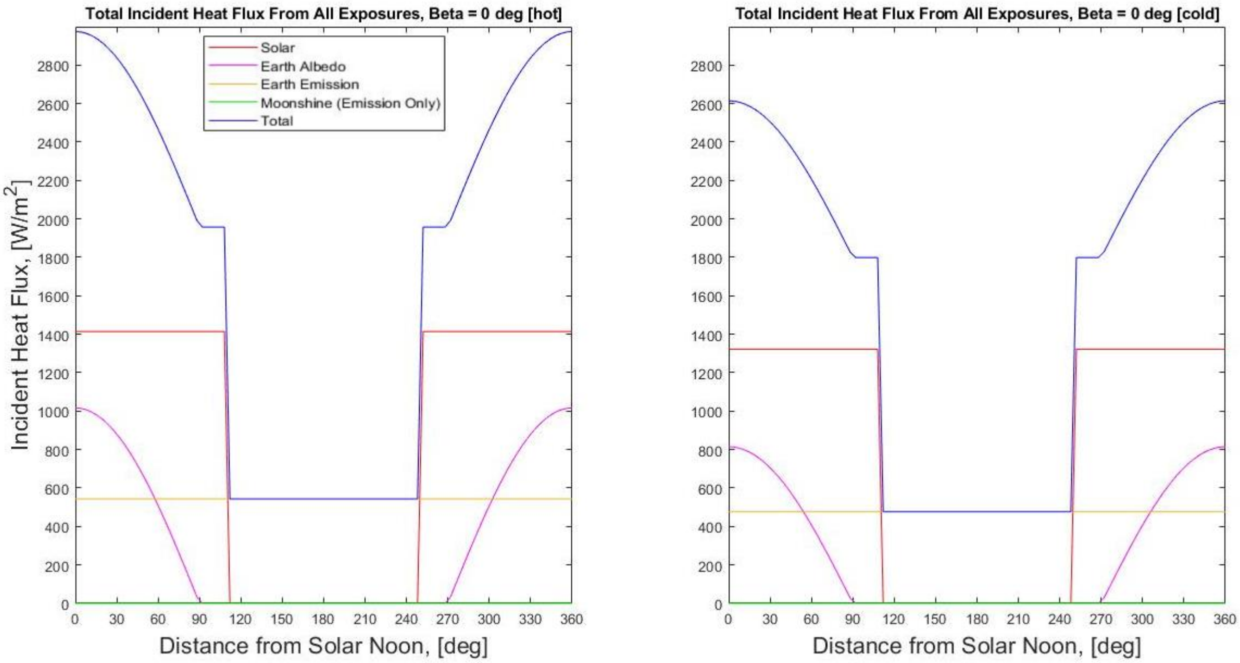

Figure 48: Heat Flux in Earth LEO, Hot and Cold Cases. Atmospheric and charged particle heating not included. Altitude = 419 km

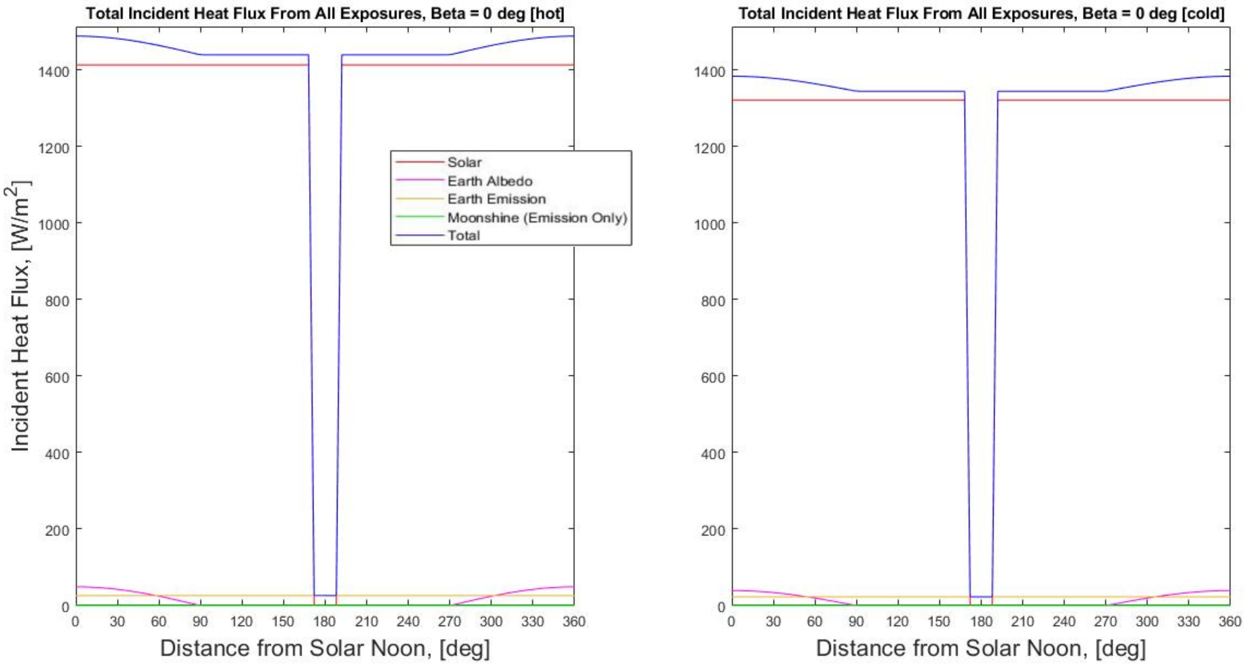

Figure 49: Heat Flux in Earth GTO, Hot and Cold Cases. Charged particle heating not included. Altitude = 24,582 km

For the transfer hot case, the highest Earth heat flux is taken. The reverse is true for the cold case. Despite the erroneous solar heat flux assumption described in **Figures 41-42**, the idea that spacecraft heating would be increased due to multiple faces being exposed to solar or planetary incidence is true. For two faces with equal areas, the maximum area factor is found in **Eq.(35)**.

$$\cos(45^\circ) + \sin(45^\circ) \cong 1.41$$ **Eq.(35)**

AEGIS does not have adjoining faces with equal areas as a 6U, but the 1.41 area factor is applied to hot case area parameters as a margin because assuming single-face exposure for incident radiation without margin is a more erroneous assumption.

Rickman's method calculates the flux on all faces per orbit angle per solar incidence angle and sums them into one term. At first it seems nonsensical to sum the heat fluxes on all faces to estimate the heat flux one should apply to a single face in a deep space calculation, but it is the dependence of the calculations on the solar zenith angle that yields correct results. When the spacecraft is at the subsolar point, the solar flux on the nadir face is zero while the solar flux on the zenith face is at maximum. Similarly, the albedo and emission terms for the nadir face are non-zero at the subsolar point while equaling zero on the zenith face. The terms for each face may be summed in total for each heat source per orbit angle because at no time does the heat flux change due to areal exposure; only the exposed areas change.

3.3.6.3 On-Orbit Lunar Thermal Environment

The lunar emission model presented in Section 3.3.3.4 works extremely well if a spacecraft can relate its expected Keplerian orbital elements to latitude and longitude values depicted in **Figures 36-37**. Unfortunately, the orbit of Artemis II was never released, and a realistic expectation of spacecraft inclination about the Moon could not be determined. Additionally, the phase of the Moon is dependent on the launch date and Time Of Flight (TOF) of the transfer, and thus the lunar albedo could not be accurately modeled. For the purposes of this evaluation, a spacecraft inclination about the Moon of 0° is assumed. An orbit angle of 0° is assumed to be the subsolar point for both the Earth and Moon circular orbits corresponding equally to a solar zenith angle of 0° for both bodies. If the Sun, Earth, and Moon were on the same ecliptic plane, this formulation would result in the Moon being eclipsed by the Earth. No eclipse of the Moon is included.

Depicted on-orbit fluxes for circular lunar orbits about the lunar equator are shown in **Figures 50-51** for an example altitude of 419 km and an AEGIS altitude of 5,000 km. Of note is the high combined flux from the Sun and Moon at 419 km and the drastic difference between maximum heat fluxes per lunar altitude.

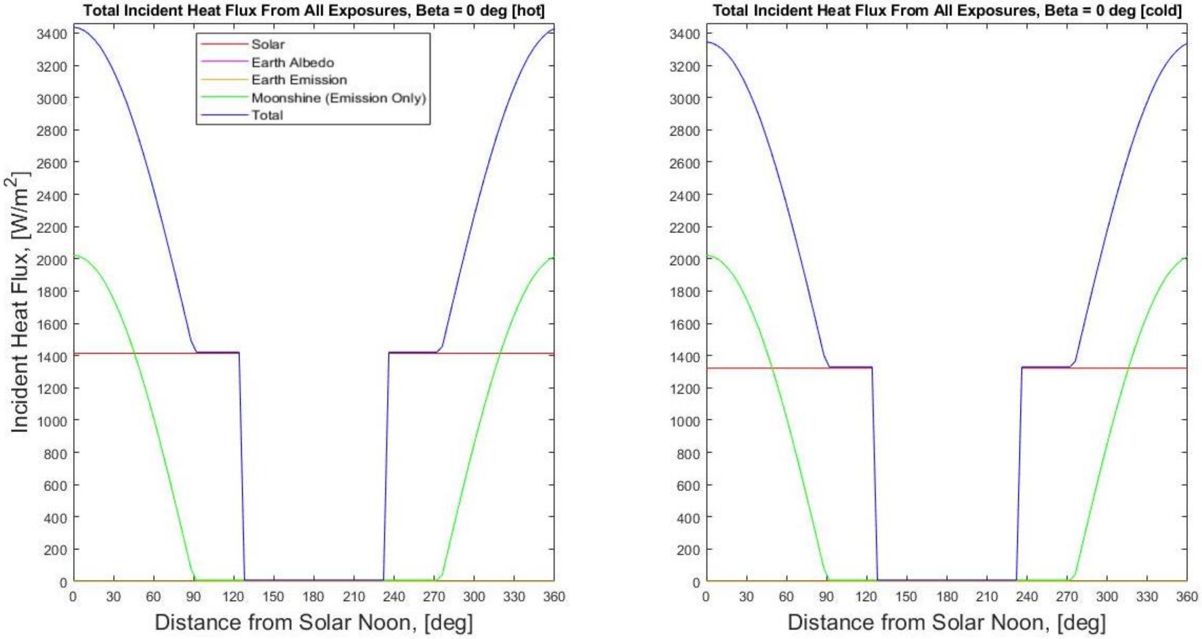

Figure 50: Heat Flux Near Equatorial Lunar Surface, Hot and Cold Cases. Altitude = 419 km

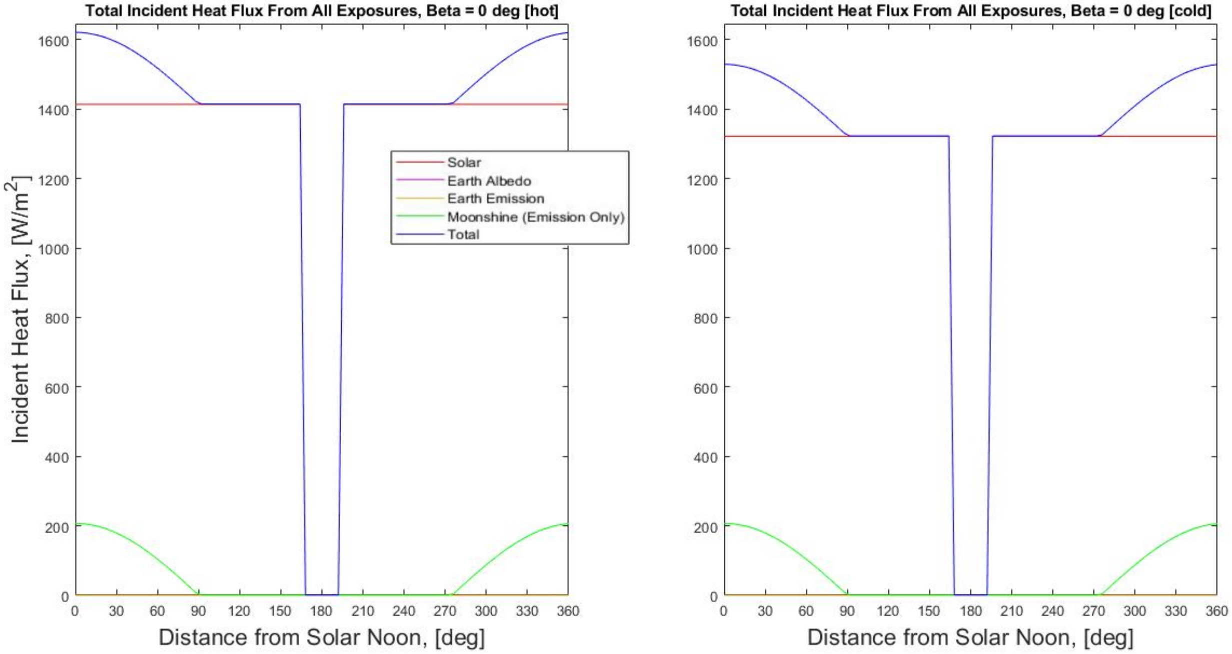

Figure 51: Heat Flux in Distant Lunar Orbit, Hot and Cold Cases. Altitude = 5,000 km

3.3.6.4 Transfer and Area Permutations

The heat flux across the entire transfer can be modeled with starting conditions from the circular Earth orbit and final conditions from the circular lunar orbit. These are shown in **Figures 52-53** for hot and cold cases.

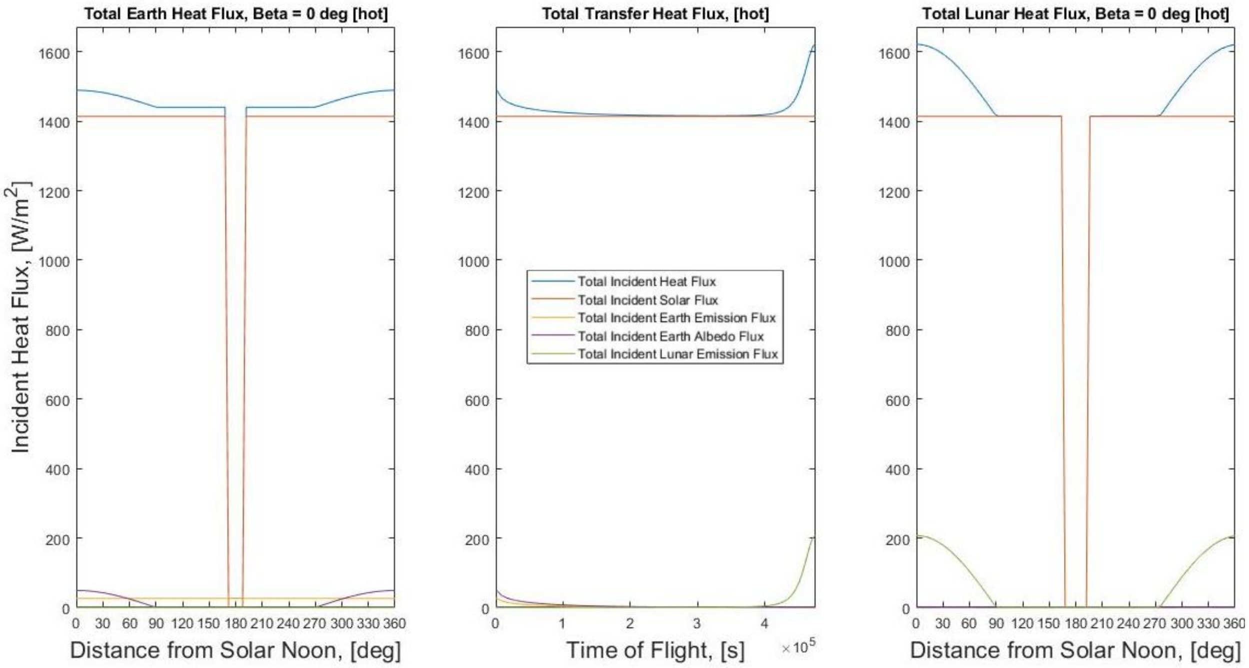

Figure 52: Heat Flux in Earth, Transfer, and Lunar Orbits. Hot Case. Earth Alt = 24,582 km, Lunar Alt = 5,000 km

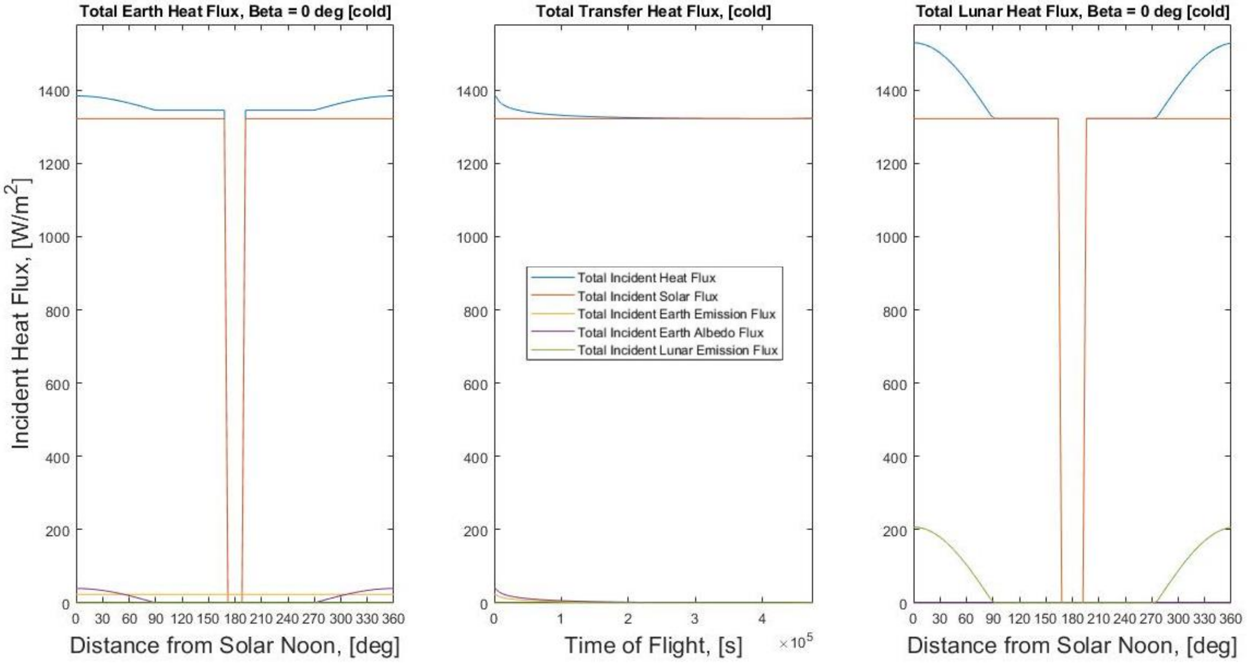

Figure 53: Heat Flux in Earth, Transfer, and Lunar Orbits. Cold Case. Earth Alt = 24,582 km, Lunar Alt = 5,000 km

Areas can be applied to the heat flux calculations to determine the heat load on the spacecraft per face, but emissivities and absorptivities per surface must first be considered for each heat source. The absorptivity of a surface material calculated by the modified Fresnel equations in Section 3.3.5 is only valid for direct solar radiation, although different wavelengths could be considered if refractive index data is available. For a blackbody at 5780 K, over 98% of the energy radiated is below 4000 nm wavelength. For a blackbody at 300 K, over 99% of the energy radiated is above 4000 nm wavelength [63]. These assertions may be verified by **Eq.(9)**, but note the IR reflectivity of the example materials shown in **Figure 43**. For materials except for the flat reflector and solar absorber, IR reflectivity is much lower than for solar wavelengths.

Solar absorptivity, IR absorptivity, and emissivity data for relevant materials are presented in **Table 22**. Kapton emissivity is highly dependent on thickness [34] and is not used as an outer surface material in this scheme. Weighted averages are used to calculate the effective emissivity of the entire spacecraft for the outgoing radiation term in **Eq.(33)**; an effective solar and IR absorptivity is calculated for each face. The areas, effective solar absorptivities, effective IR absorptivities, and effective emissivities of each surface are found in **Table 23**; solar array areas are included in projected area determinations. The effective spacecraft emissivity is 0.7817 as calculated by a weighted average of those emissivities by area. The coordinate system defined in Section 3.2.2.2 is continued.

Table 22: TMM Material Absorptivity and Emissivity Data

Material	Solar Absorptivity	IR Absorptivity	Emissivity
Aluminum	0.0879	0.0879	0.039 [92]
Kapton	0.44	0.91	0.95 [93]
AZ-93	0.05	0.9	0.92 [34]
Chemglaze Z306	0.96	0.25	0.88 [34]
Spectrolab XTE-SF Solar Cell	0.88 [91]	0.9	0.85 [91]

Table 23: TMM Surface Area, Absorptivity, and Emissivity Data

CubeSat Face	Projected Area, [m^2]	Effective Solar Absorptivity	Effective IR Absorptivity	Effective Emissivity
+X	0.0347	0.96	0.75	0.88
-X	0.0347	0.8509	0.6672	0.7748
+Y	0.3135	0.8164	0.8893	0.8581
-Y	0.3135	0.7536	0.8416	0.7976
+Z	0.1903	0.7598	0.7768	0.7270
-Z	0.1903	0.0779	0.6794	0.6676

There are 6 faces on the spacecraft with a total of 6! = 720 possible spacecraft orientations. These permutations define 6 area and absorptivity parameters: A_1, α_1, A_2, α_2, A_3, α_3. Solar radiation is assumed to impact A_1, Earth albedo and emission is assumed to impact A_2, and lunar emission is assumed to impact A_3. Which permutation is being considered defines which spacecraft faces are exposed to which radiation source, and absorptivities for α_2 and α_3 are overwritten per **Table 23** values to account for IR heating. The heat loads for all areal permutations are plotted in **Figures 54-55** for both hot and cold cases per transfer timestep.

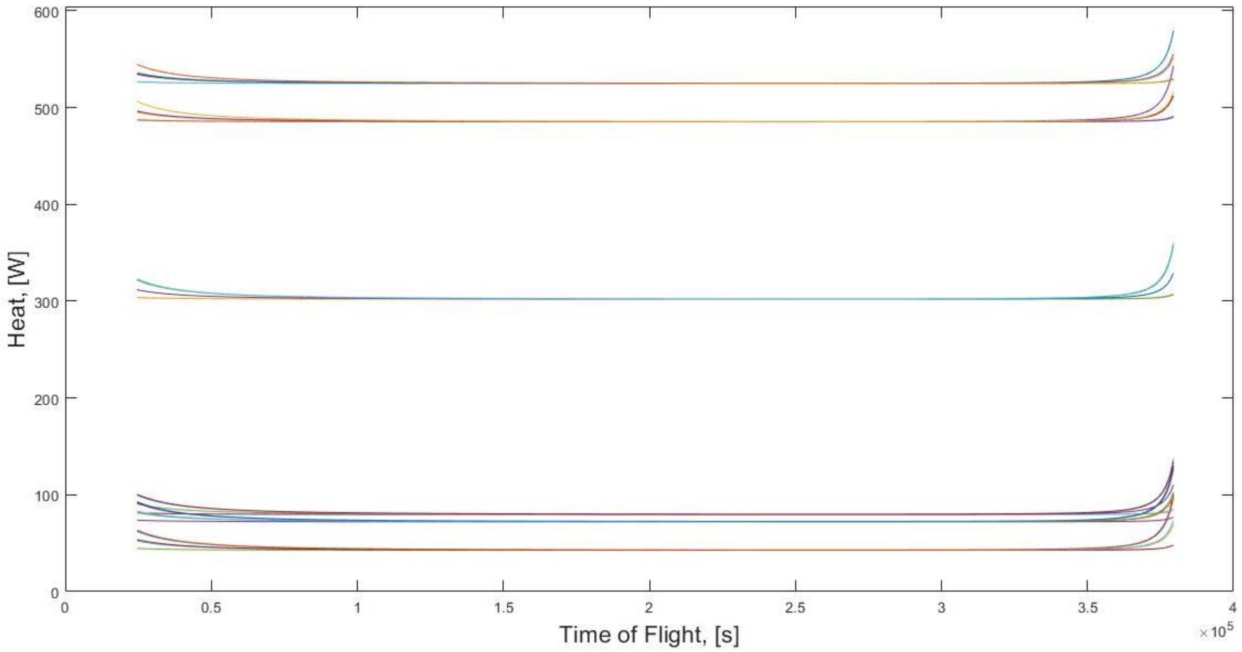

Figure 54: Heat Load, All Orbital Geometry Permutations. Hot Case. Earth Alt = 24,582 km, Lunar Alt = 5,000 km

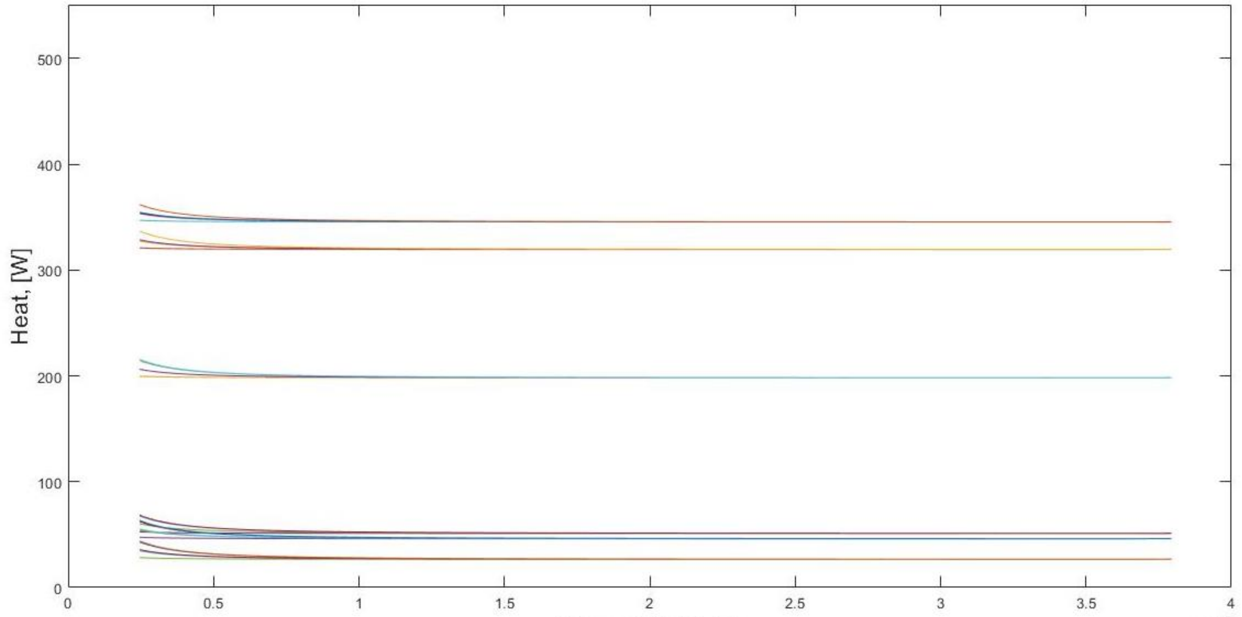

Figure 55: Heat Load, All Orbital Geometry Permutations. Cold Case. Earth Alt = 24,582 km, Lunar Alt = 5,000 km

With heat loads known at each timestep, **Eq.(33)** can be applied for temperature determination per timestep per permutation for hot and cold cases as shown in **Figures 56-57**. Temperatures are initialized to Earth temperature per **Table 20**.

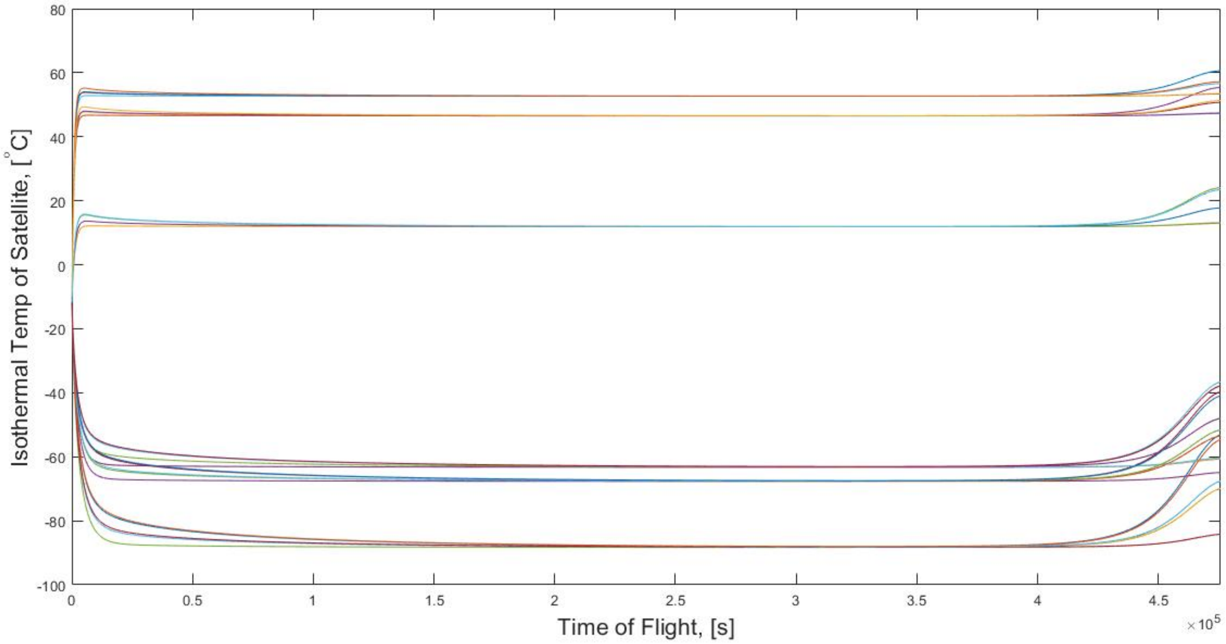

Figure 56: CubeSat Temperature, All Orbital Geometry Permutations. Hot Case, Earth Alt = 24,582 km, Lunar Alt = 5,000 km

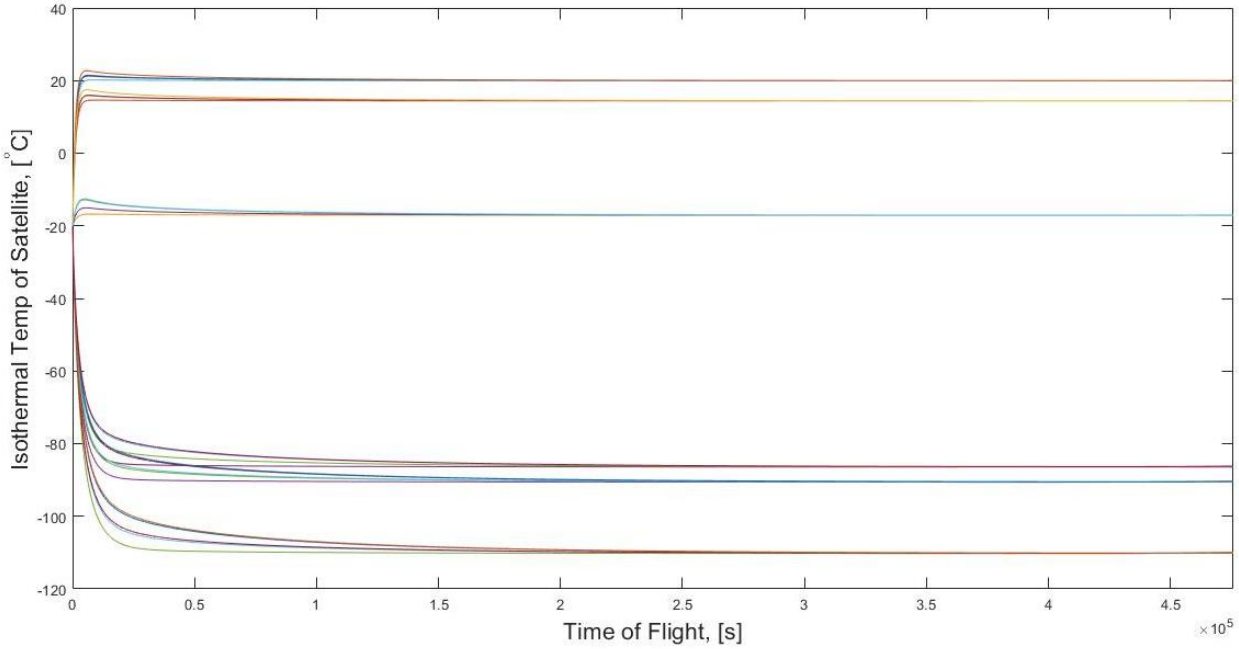

Figure 57: CubeSat Temperature, All Orbital Geometry Permutations. Cold Case. Earth Alt = 24,582 km, Lunar Alt = 5,000 km

Temperatures below 52,000 km would realistically be higher due to charged particle heating. The permutations where primary solar arrays are orthogonal to the Sun-Earth ecliptic plane can be removed because a spacecraft orientation without power generation is impractical. For AEGIS this signifies both solar arrays A and B, dropping the number of unique permutations to $2 \cdot 4! = 48$. Temperatures for power-generating CubeSat orientations are shown in **Figures 58-59**.

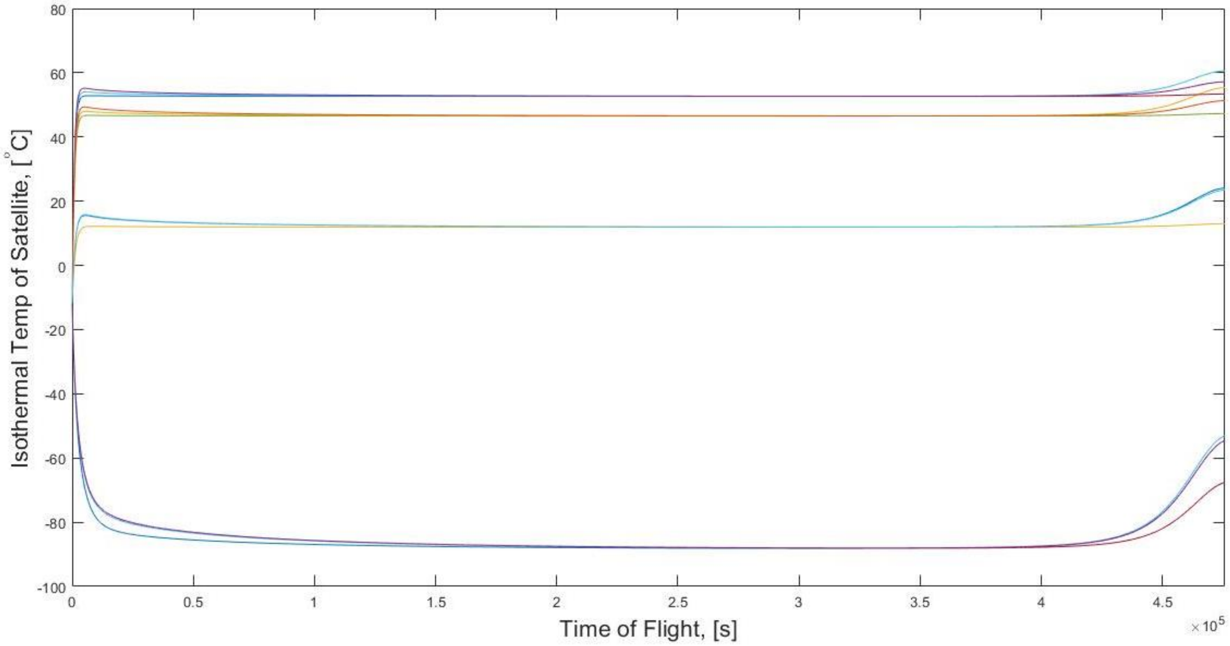

Figure 58: CubeSat Temperature, Power-Generating Orbital Geometry Permutations. Hot Case.
Earth Alt = 24,582 km, Lunar Alt = 5,000 km

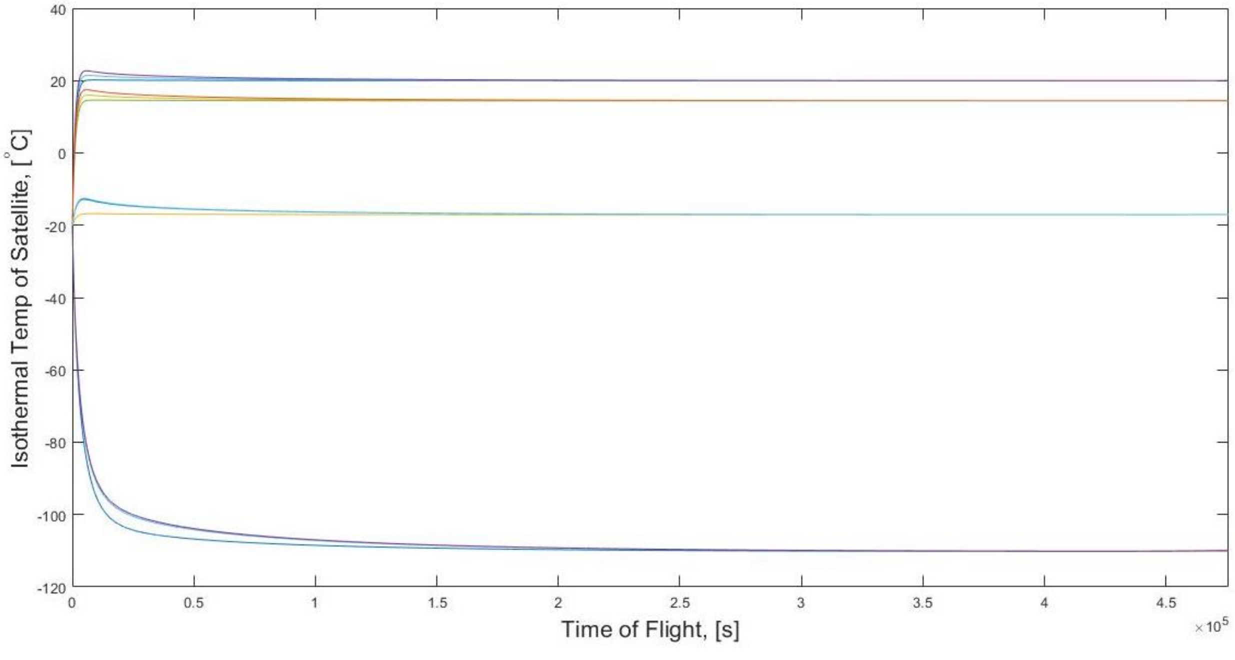

Figure 59: CubeSat Temperature, Power-Generating Orbital Geometry Permutations. Cold Case.
Earth Alt = 24,582 km, Lunar Alt = 5,000 km

The cases where the Sun is directly emitting to the radiator such that no solar flux is generating power is also unrealistic as spacecraft positioning logic would turn the solar panels toward the Sun. Removing the cases where the radiator is facing the Sun yields 36 permutation cases; temperatures are plotted in **Figures 60-61**.

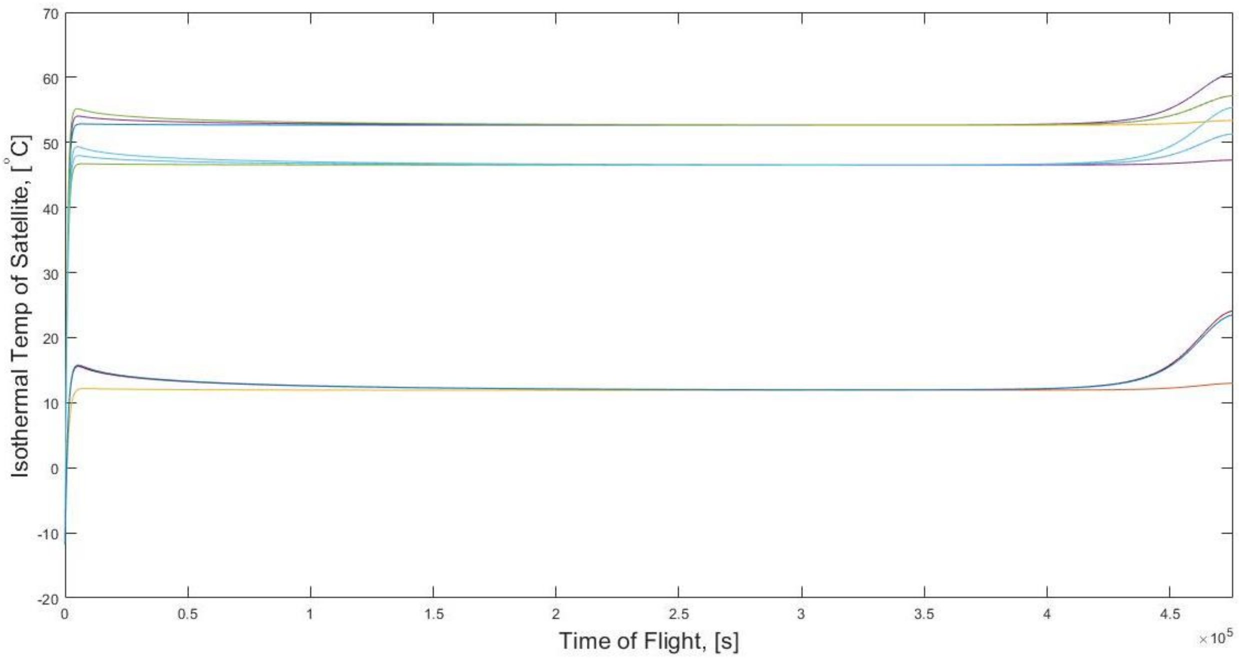

Figure 60: CubeSat Temperature, Relevant Orbital Geometry Permutations. Hot Case.
Earth Alt = 24,582 km, Lunar Alt = 5,000 km

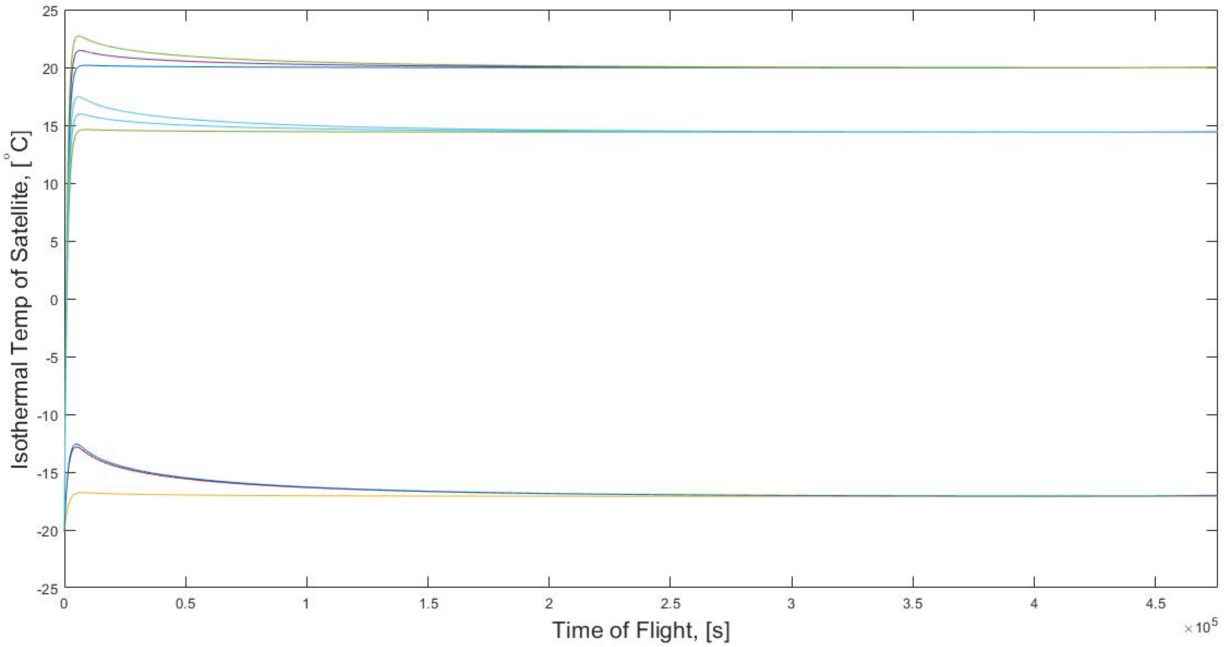

Figure 61: CubeSat Temperature, Relevant Orbital Geometry Permutations. Cold Case.
Earth Alt = 24,582 km, Lunar Alt = 5,000 km

Immediately evident is that the lowest expected temperature increases from -108 °C to -27 °C if the software and attitude control mechanisms are operating properly. Tumbling is only a condition nearest to Earth after deployment, so it is not anticipated for the spacecraft to encounter those non-relevant cases with sunlight on non-power generating surfaces. Instead of applying margins to calculated heat loads to create conservative estimates, a margin of ± 10°C is applied to the maximum and minimum temperatures of the hot and cold cases, respectively, in **Figure 62**.

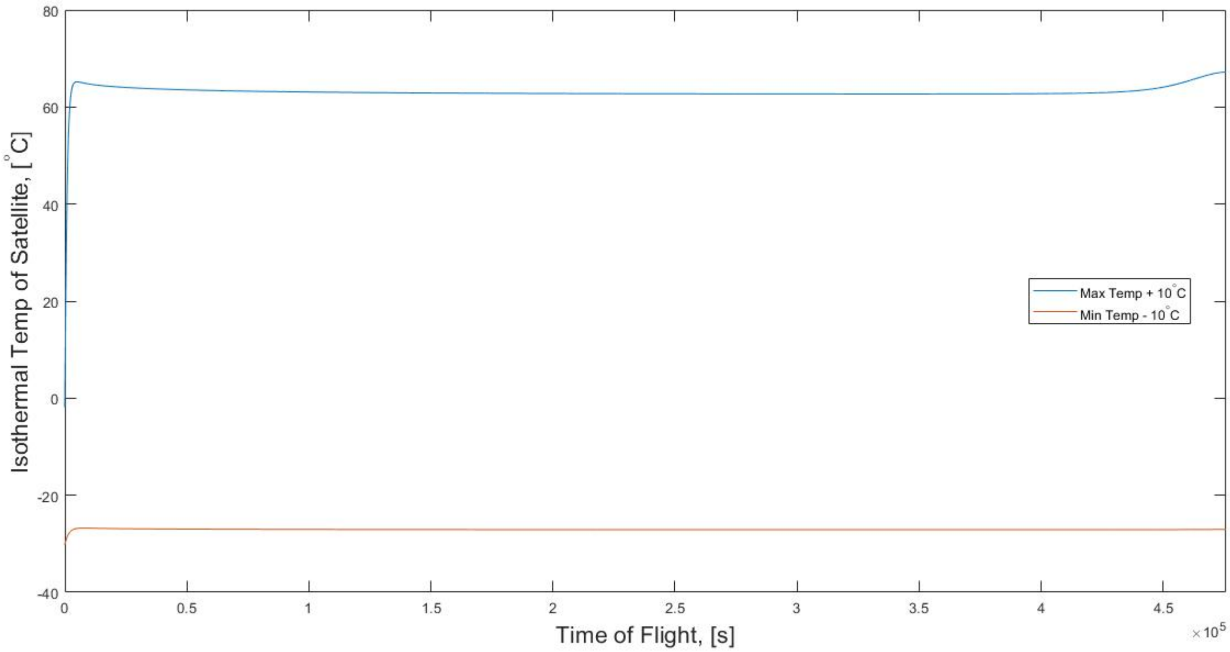

Figure 62: CubeSat Temperature Envelope, Earth Alt = 24,582 km, Lunar Alt = 5,000 km

Figure 62 represents the temperature envelope of the spacecraft between hottest and coldest cases with thermal margins applied. A designer only needs heat fluxes per face as in **Figures 52-53** for input into a CAD-specific thermal analysis suite such as Thermal Desktop or NX, but **Figure 62** dictates the absolute maximum or minimum temperature a spacecraft should encounter if it is operating properly. The maximum temperature was 67.19 °C, while the minimum temperature was the initialization temperature of -30.19 °C, which represents the cold case starting temperature from **Table 20** less 10 °C. The patch heater wattage required to keep the isothermal temperature above 0°C for this analysis is 105 W, but it should be noted this signifies keeping both the body and deployed solar arrays at 0 °C.

3.3.7 Transient Finite Difference Analyses

Isothermal analyses as first order estimates are acceptable, but real spacecraft surfaces are not isothermal. Solar arrays exposed to hot and cold conditions will undergo thermal deformation leading to stress that must be characterized. Designers must equally ensure that operating temperatures are not exceeded. Presented is a numerical heat transfer methodology for quasi-2D temperature distribution analysis on the same environmental conditions presented in Section 3.3.6 except it does not include lunar or Earth-based heat sources, only direct solar.

3.3.7.1 Radiator

The overarching goal of the method in Section 3.3.6 is to ascertain orbital heat fluxes for inclusion in a direct thermal suite, but it is also possible to reframe **Eq.(33)** as a radiator sizing tool. The parameter Q_{PH}, which is set to zero for the presented analysis, can be used to estimate how much patch heater wattage is required to keep a spacecraft within nominal temperature bounds. If Q_{PH} is set to a negative value, it can represent heat radiated away from the spacecraft. Realistically, this would alter the effective absorptivity and emissivity as well. A simple relationship depicted in **Eqs.(36-37)** and **Table 24** represents a comparison of how much radiator area is needed at a given mean temperature to radiate out a certain heat value.

$$T_{mean} = \sqrt[4]{\frac{Q_{Load}}{A_{req} \cdot \sigma \cdot \varepsilon} + T_{surr}^4}$$ **Eq.(36)**

$$A_{req} = \frac{Q_{Load}}{\sigma \cdot \varepsilon \cdot (T_{mean}^4 - T_{surr}^4)}$$ **Eq.(37)**

Table 24: Radiator Parameter Variation

Heat Radiated, [W]	Radiator Mean Temp, [K] : $A_{req} = .1\ m^2$	Area Required, [m^2] : $T_{mean} = 300\ K$
3	160.365	0.0081
6	190.708	0.0163
9	211.053	0.0244
12	226.791	0.0326
15	239.802	0.0408
18	250.986	0.0489

Thermal loads of a known wattage from components such as thrusters, radio hardware, or computational hardware can be radiated away from the spacecraft if the loads, temperatures, and radiator area is known. **Figure 63** depicts the radiator on AEGIS. It is fastened to a conductive plate designed for thermal transport and control on the underlying thruster. Titanium spacers are used to extend the radiator off the spacecraft surface and reduce conductivity between the radiator and spacecraft body. Titanium was selected because of its low thermal conductivity and high strength. A thermal load from the thruster of 8.75 W was assumed based on a conservative PCE estimate and provided power of 25 W.

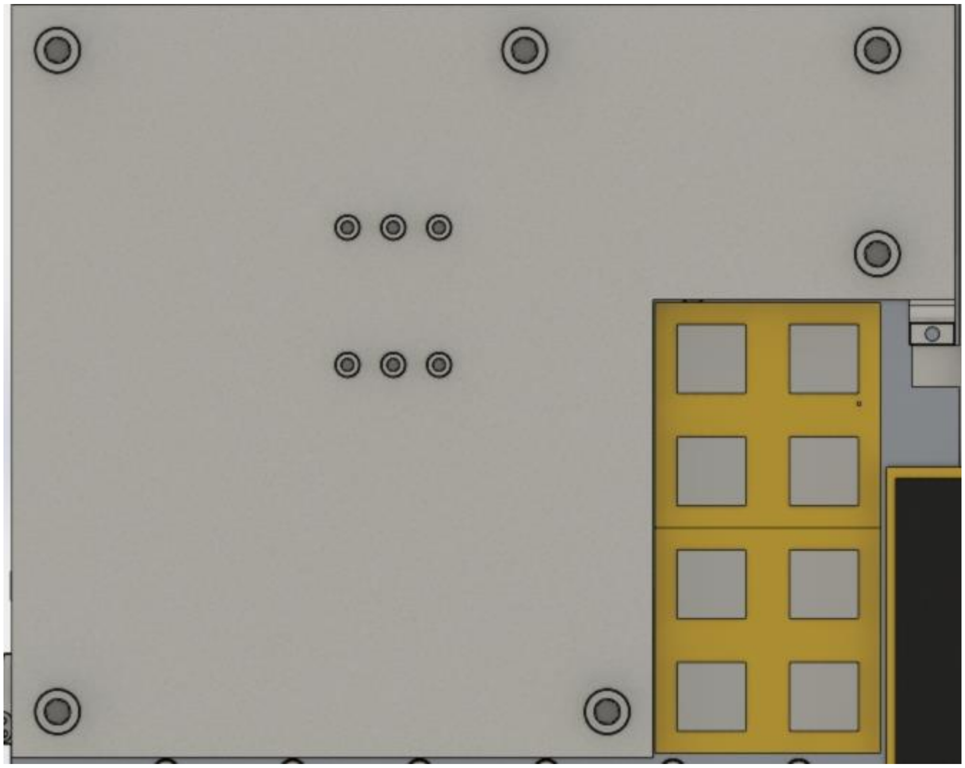

Figure 63: AEGIS Radiator Structure. Thruster mounted to section near middle six fasteners

A Gauss-Seidel numerical methodology is used to calculate temperature distributions across the Al 1050 radiator; calculation parameters are listed in **Table 25**. For all Gauss-Seidel analyses a single sheet of material is considered with no variation in the Z-direction representing thickness. The radiator is assumed to be coated in solar reflector AZ-93.

Table 25: Gauss-Seidel Model Parameters, Radiator

Parameter	Value	Unit
Nodes in X Direction	101	-
Nodes in Y Direction	101	-
ΔX	2.06	mm
ΔY	1.645	mm
ΔZ	2	mm
k_{Cond}	218	W/m-K
$c_{p,rad}$	900	J/kg-K
ρ_{rad}	2670	kg/m^3
Δt	0.1	s
ε_{AZ-93}	0.92	-
α_{AZ-93}	0.05	-

Absorptivity is included in **Table 25** but is not utilized for these examples because solar radiation is not assumed to be affecting the radiator. An example nodal condition derivation is found in **Eqs.(38-43)**. Each node location and geometry corresponds to a condition. The condition for **Eqs.(38-43)** is for internal nodes where the thruster is conducting to the radiator.

$$\Sigma \dot{E}_{in} + \Sigma \dot{E}_{gen} - \dot{E}_{out} = \frac{dE}{dT} \qquad \textbf{Eq.(38)}$$

$$\left(Q_{Cond,West} + Q_{Cond,East} + Q_{Cond,North} + Q_{Cond,South} + Q_{Cond,Thruster}\right)_{in} - \left(Q_{Rad}\right)_{out} = Q_{Transient} \qquad \textbf{Eq.(39)}$$

Directional modifiers are shortened, and an anisotropic thermal conductivity is assumed so that this analysis may be emulated with composite structures as radiator materials. Directional thermal conductivities are replaced with Fourier's law of conduction, and the thruster flux is considered a Neumann boundary condition. As with the TMM from Section 3.3.6, the subscript j denotes a time step. Because one side is assumed to be fastened to the thruster, only one side of the surface radiates. Unlike the previous TMM, the timestep in this analysis is constant.

$$\frac{k_W \cdot (T_j - T_{W,j}) \cdot \Delta Y \cdot \Delta Z}{\Delta X} + \frac{k_E \cdot (T_j - T_{E,j}) \cdot \Delta Y \cdot \Delta Z}{\Delta X} + \frac{k_N \cdot (T_j - T_{N,j}) \cdot \Delta X \cdot \Delta Z}{\Delta Y} + \frac{k_S \cdot (T_j - T_{S,j}) \cdot \Delta X \cdot \Delta Z}{\Delta Y} + Q''_{Thruster} \cdot \Delta X \cdot \Delta Y - \varepsilon_{AZ-93} \cdot \sigma \cdot \left(T_j^4 - T_{surr}^4\right) \cdot \Delta X \cdot \Delta Y = \rho_{rad} \cdot c_{p,rad} \cdot \Delta X \cdot \Delta Y \cdot \Delta Z \cdot \left(\frac{T_j - T_{j-1}}{\Delta t}\right) \qquad \textbf{Eq.(40)}$$

Each term is divided by volume as $\Delta X \cdot \Delta Y \cdot \Delta Z$, and like terms are consolidated.

$$T_j \cdot \left(\frac{k_W + k_E}{\Delta X^2} + \frac{k_N + k_S}{\Delta Y^2}\right) - \left(\frac{k_W \cdot T_{W,j} + k_E \cdot T_{E,j}}{\Delta X^2} + \frac{k_N \cdot T_{N,j} + k_S \cdot T_{S,j}}{\Delta Y^2}\right) + \frac{Q''_{Thruster}}{\Delta Z} - \frac{\varepsilon_{AZ-93} \cdot \sigma \cdot \left(T_j^4 - T_{surr}^4\right)}{\Delta Z} = \left(\frac{\rho_{rad} \cdot c_{p,rad}}{\Delta t}\right) \cdot T_j - \left(\frac{\rho_{rad} \cdot c_{p,rad}}{\Delta t}\right) \cdot T_{j-1} \qquad \textbf{Eq.(41)}$$

Non-radiative temperature terms are consolidated on the LHS.

$$T_j \cdot \left(\frac{k_W+k_E}{\Delta X^2} + \frac{k_N+k_S}{\Delta Y^2} - \frac{\rho_{rad}\cdot c_{p,rad}}{\Delta t}\right) = \frac{\varepsilon_{AA-93}\cdot\sigma\cdot\left(T_j^4 - T_{surr}^4\right)}{\Delta Z} - \frac{Q''_{Thruster}}{\Delta Z} + \left(\frac{k_W\cdot T_{W,j}+k_E\cdot T_{E,j}}{\Delta X^2} + \frac{k_N\cdot T_{N,j}+k_S\cdot T_{S,j}}{\Delta Y^2}\right) - \left(\frac{\rho_{rad}\cdot c_{p,rad}}{\Delta t}\right)\cdot T_{j-1} \qquad \textbf{Eq.(42)}$$

Terms are further consolidated and an explicit equation for the temperature at a given node at a given timestep is found.

$$T_j = \frac{\frac{\varepsilon_{az-93}\cdot\sigma\cdot\left(T_j^4 - T_{surr}^4\right) - Q''_{Thruster}}{\Delta Z} + \left(\frac{k_W\cdot T_{W,j}+k_E\cdot T_{E,j}}{\Delta X^2} + \frac{k_N\cdot T_{N,j}+k_S\cdot T_{S,j}}{\Delta Y^2}\right) - \left(\frac{\rho_{rad}\cdot c_{p,rad}}{\Delta t}\right)\cdot T_{j-1}}{\left(\frac{k_W+k_E}{\Delta X^2} + \frac{k_N+k_S}{\Delta Y^2} - \frac{\rho_{rad}\cdot c_{p,rad}}{\Delta t}\right)} \qquad \textbf{Eq.(43)}$$

This type of numerical formulation is used for each geometric condition present on the radiator and solar arrays to create the geometry of the structure. The radiator is initialized to 0°C for the hot case and -5°C for the cold case. The spacers were modeled as square sections at a constant temperature of to 5°C for the hot case and -5°C for the cold case with equal area as the real spacers. **Figure 64** shows the radiator in its hot case, when the thruster is on but the Sun is not emitting to the radiator, at four time steps: 15 seconds, 60 seconds, 300 seconds, and steady state. **Figure 65** shows the same setup for a cold case, when the thruster is off and the radiator is not receiving any heat except for the boundary conditions. The time at which the radiator reaches steady state for hot and cold cases is not the same. For all cases including solar array analyses, the relaxation parameter was set to 0.8. Maximum and minimum temperatures are tabulated later.

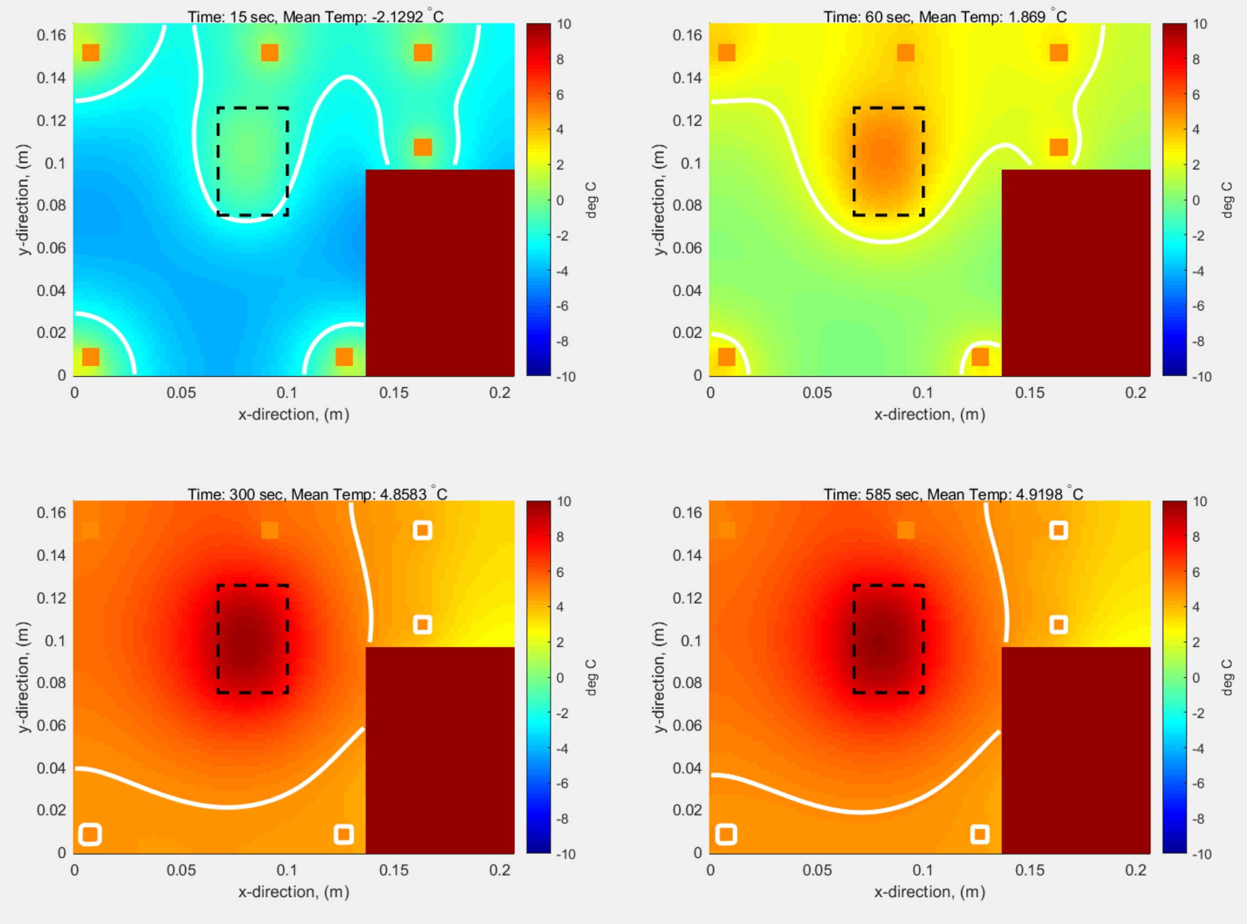

Figure 64: Transient Hot Case Temperature Distribution of the Radiator, Steady State Reached in 585 seconds

The white lines represent mean temperature isotherms with the isotherm temperature displayed at the top with the time stamp. The boxed-in location represents where the radiator is mounted to the thruster. The radiator cold case is shown in **Figure 65**.

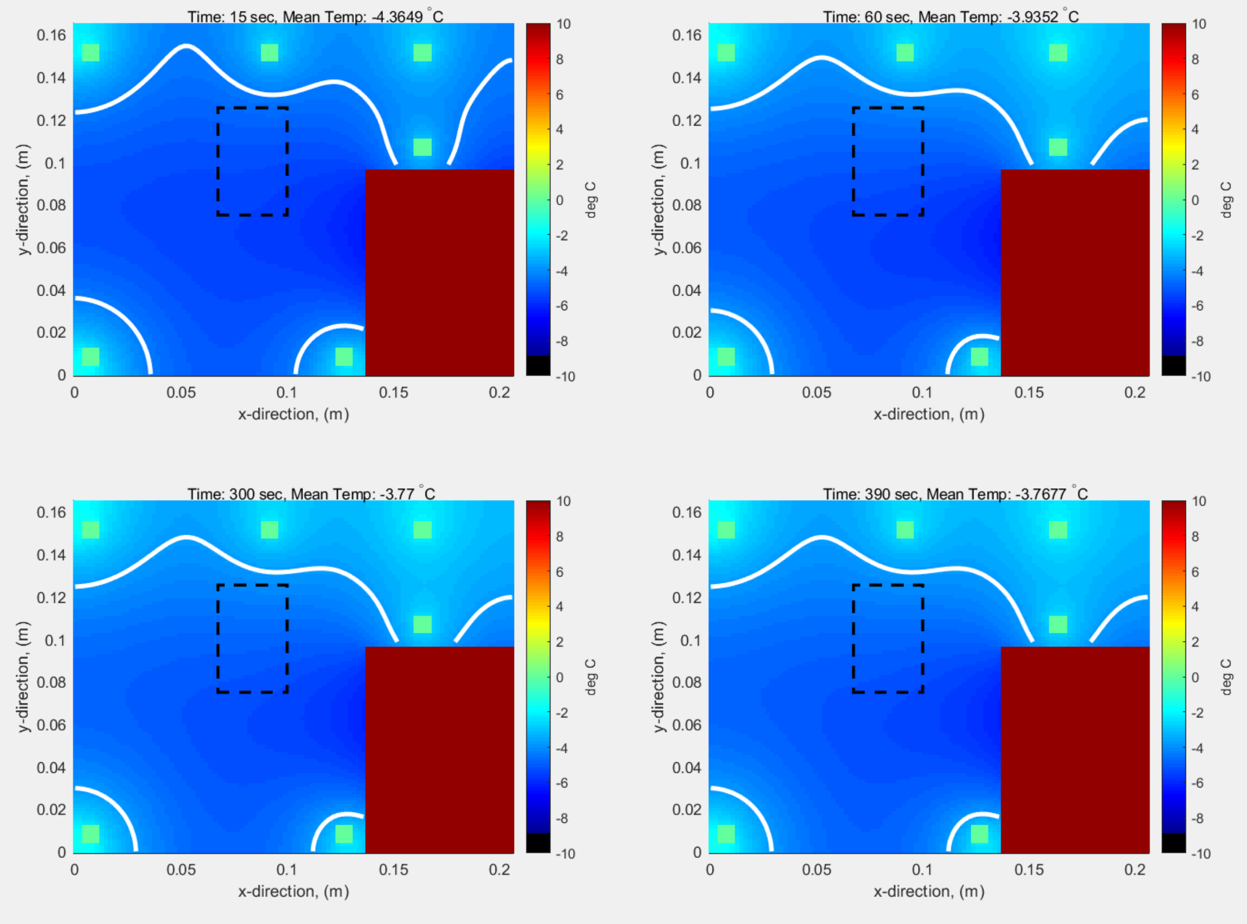

Figure 65: Transient Cold Case Temperature Distribution of the Radiator, Steady State Reached in 390 seconds

At first **Figure 65** reads as if the output is faulty, but upon closer inspection the initialization temperature of -5 °C is within 1.5 °C of the steady state value. For the hot case, the radiator must be able to reject at least 8.75 W. **Eqs.(36-37)** and **Table 24** provide the relationships between radiator area and mean temperature for a given heat load. The area of the radiator is ~0.0271 m^2 which correlates to a mean temperature of 280.56 K for the hot case with an assumed emissivity of 0.92. The mean temperature of the hot case at steady state was 278.07 K, thus the temperature of the radiator and thruster may increase marginally before equilibrium is reached. However, it will not present a large enough temperature increase to be considered a risk. The radiated power was 7.27 W for the cold case, indicating that final temperatures are a strong function of the boundary condition temperatures. It is shown that the mean temperature for the radiator in the hot case is sufficient to radiate the thruster heat load without risking material damage.

3.3.7.2 Solar Array A and B

Thermal analyses of solar arrays are for characterizing the temperature distribution across the array to determine if temperatures exceed maximum and minimum material constraints and to liken the distributions to thermal deformations in the materials. Deformations are specific to solar array material and geometry and thus will not be a focus.

As with any other thermal analysis there are hot and cold cases; the hot case is when the solar array is in direct sunlight and no radiation is being converted into electricity. This reflects when the batteries are fully charged and can no longer store additional energy. Cold case denotes when no sunlight or energy is provided to the arrays except for the boundary condition temperatures of the solar array hinges, but it will be shown that the thermal penetration depth of the Dirichlet boundary condition is limited to less than the full size of the array. **Table 26** provides the analysis parameters for solar array A.

Table 26: Gauss-Seidel Model Parameters, Solar Array A

Parameter	Value	Unit
Nodes in X Direction	101	-
Nodes in Y Direction	101	-
ΔX	6.35	mm
ΔY	1.90	mm
ΔZ	2	mm
$k_{Cond,array}$	62.395	W/m-K
$c_{p,array}$	938.5	J/kg-K
ρ_{array}	2961.5	kg/m^3
Δt	0.1	s
$\varepsilon_{front,array}$	0.85 [91]	-
$\alpha_{front,array}$	0.88 [91]	-
$\varepsilon_{back,AZ-93}$	0.92	-

An image of the physical array is shown in **Figure 66**. The transient thermal analysis for hot and cold cases are shown in **Figures 67-68**. The solar array temperature at all nodes was initialized to 0°C for both hot and cold cases. The hinge temperature was 5°C for the cold case and 25°C for the hot case. Both the initializations and hinge temperatures are the same for solar arrays A and B.

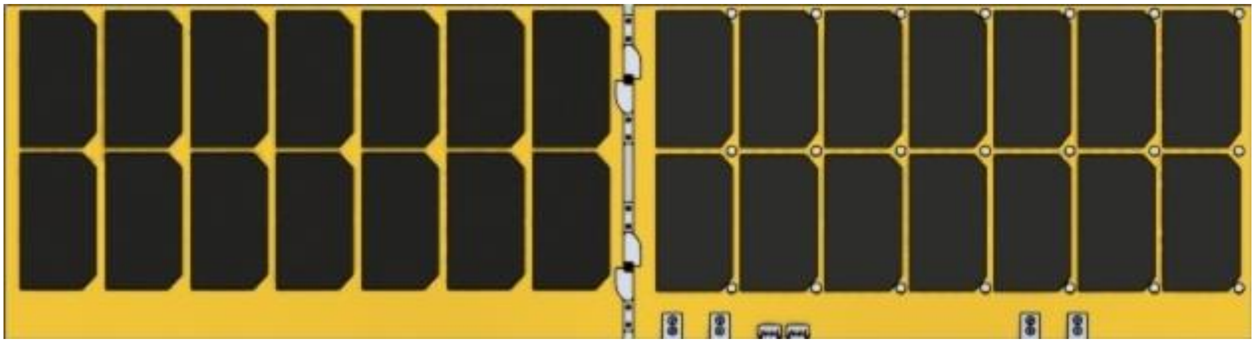

Figure 66: Geometry of Solar Array A

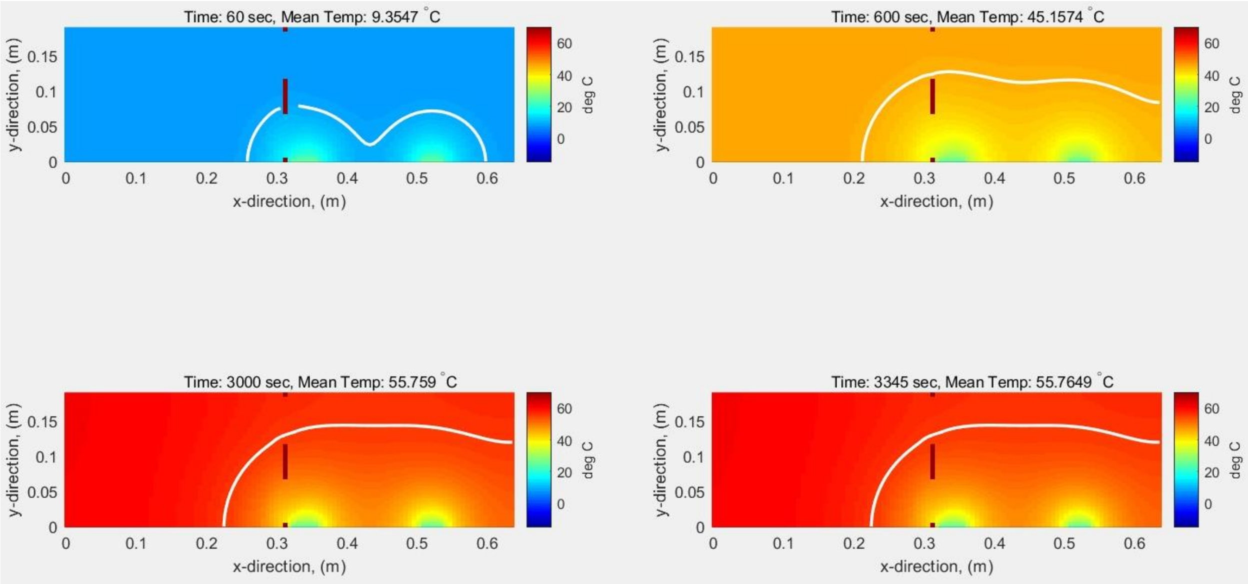
Time: 60 sec, Mean Temp: 9.3547 °C

Time: 600 sec, Mean Temp: 45.1574 °C

Time: 3000 sec, Mean Temp: 55.759 °C

Time: 3345 sec, Mean Temp: 55.7649 °C

Figure 67: Transient Hot Case Temperatures of Solar Array A, Steady-State Reached at 3345 seconds

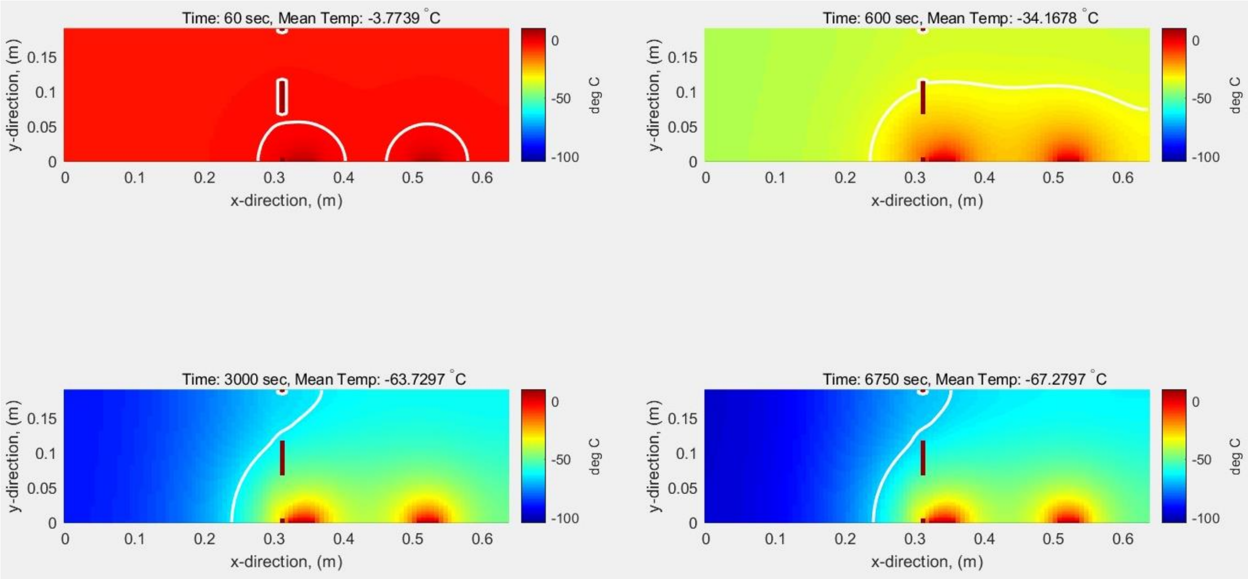
Time: 60 sec, Mean Temp: -3.7739 °C

Time: 600 sec, Mean Temp: -34.1678 °C

Time: 3000 sec, Mean Temp: -63.7297 °C

Time: 6750 sec, Mean Temp: -67.2797 °C

Figure 68: Transient Cold Case Temperatures of Solar Array A, Steady-State Reached at 6750 seconds

Compared to previous temperature distribution examples, the steady state condition of solar array A's cold case displays a sizable temperature gradient. This is the type of gradient which might result in thermal deformation or bending of the array. **Table 27** provides the model parameters for solar array B.

Table 27: Gauss-Seidel Model Parameters, Solar Array B

Parameter	Value	Unit
Nodes in X Direction	101	-
Nodes in Y Direction	101	-
ΔX	9.045	mm
ΔY	3.2	mm
ΔZ	2	mm
$k_{Cond,array}$	62.395	W/m-K
$c_{p,array}$	938.5	J/kg-K
ρ_{array}	2961.5	kg/m^3
Δt	0.1	s
ε_{array}	0.85	-
α_{array}	0.88	-

Figure 69 displays the geometry of solar array B. Transient thermal analyses for hot and cold cases are shown in **Figures 70-71**. If a solar array is facing the Sun, this type of analysis can verify how long until the solar array will exceed its maximum operational temperature or if it will at all. Of note is the drastically low temperature of solar array B during cold case. It is unrealistic for array B to be out of solar view for two and a half days, but this design point must be understood if it is to be prevented. **Table 28** provides the maximum and minimum steady-state temperature for the radiator and both arrays for both cases.

The solar array minimum temperatures are exceedingly close to the temperatures predicted by non-viable cold cases in the method described in Section 3.3.6, which is to be expected. The maximum temperatures for arrays A and B near 61 °C when calculated by the transient method while the orbital TMM calculated a maximum temperature without Earth or lunar influence around 54 °C. It was stated that the orbital method would underestimate the solar array temperatures and overestimate the body temperature due to the isothermal assumption which is verified here. It is concluded that the orbital method features an accuracy of ± 7 °C when estimating the body temperature of the spacecraft, less than the 10 °C margins applied in **Figure 62**.

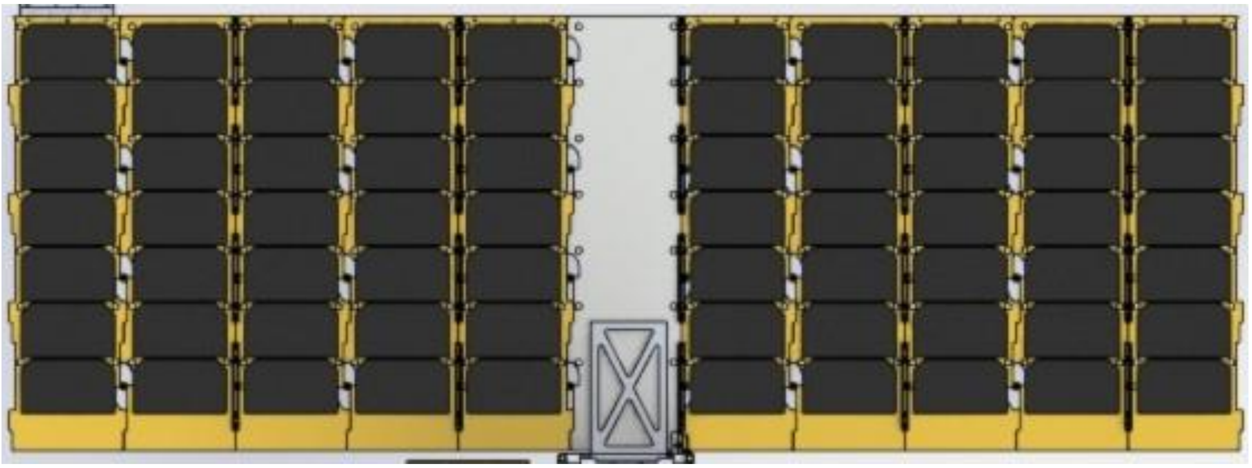

Figure 69: Geometry of Solar Array B

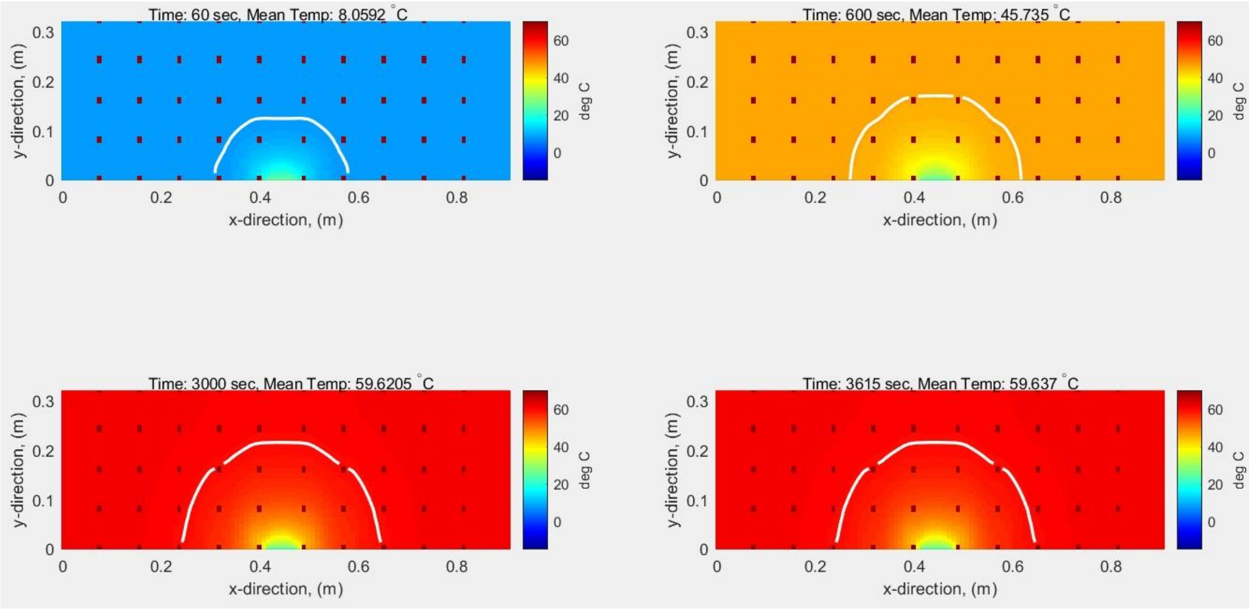

Figure 70: Transient Hot Case Temperatures of Solar Array B, Steady-State Reached at 3615 seconds

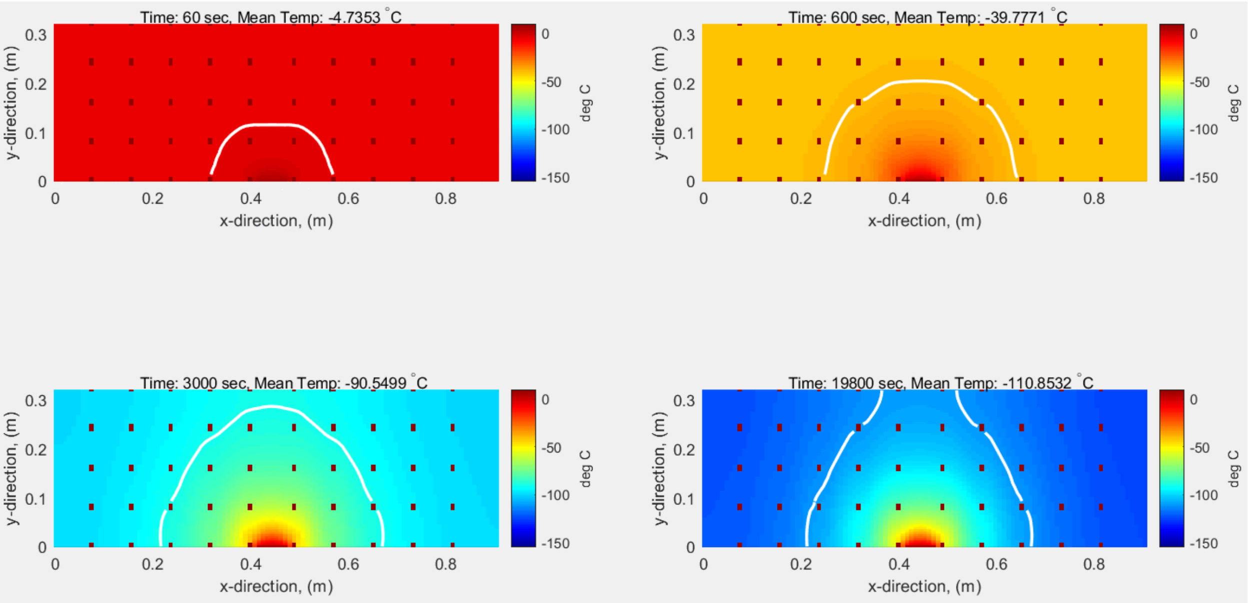

Figure 71: Transient Cold Case Temperatures of Solar Array B, Steady-State Reached at 19800 seconds

Table 28: Maximum and Minimum Temperatures per Case

Array	Hot Case Max Temperature, [°C]	Cold Case Min Temperature, [°C]
Radiator	9.86	-6.12
Solar Array A	60.8	-97.7
Solar Array B	61.4	-125.2

Mikah Abbott and Scot Carpenter are thanked for their work on these models.

3.4 Propulsion

Propulsion systems vary widely from high thrust chemical systems to high specific impulse electric propulsion systems. New propellants are consistently tested and introduced to the market, so determination of the correct thruster type for a given mission can be daunting. Rather than characterize every potential thruster type available, a system is presented to normalize and compare thrusters of varying power input, thrust, specific impulse, propellant mass, propellant volume, and burn time for a given ΔV.

3.4.1 Propulsion Design Objectives

Table 29: Propulsion Subsystem Design Objectives, Adapted from [28]

Design Objective	Description	Rationale	Actionable Items
Propulsion Electrical Safety (**PROP-1**)	An electrical disconnect "plug" and/or set of restrictive commands shall be provided to preclude inadvertent operation of propulsion system components.	Unplanned operation of propulsion system components (e.g. 'dry' cycling of valve; heating of catalyst bed in air; firing thrusters after loading propellant) can result in injury to personnel to components.	Present design and/or operational plan that preclude unplanned operation of propulsion system components.
Propulsion Fuses (**PROP-2**)	Flight fuses for wetted propulsion system components shall be selected such that overheating of propellant will not occur at the maximum current limit rating of the flight fuse	Propulsion components such as pressure transducers normally draw very low current, and therefore their fuses are usually oversized. In such cases it may be possible for malfunctioning component to overheat significantly without exceeding the rating of the fuse. Proceeding temperature limits of propellant can result in mission failure or critical/catastrophic hazard to personnel and facility.	Present fusing plan for wetted propulsion system components.

Propulsion Seal Safety (**PROP-3**)	The external leakage of hazardous propellant is a Catastrophic Hazard. Dynamics seals (e.g. solenoid valves) shall be independently verified as close to propellant loading as possible. Static seals (e.g. crush gasket, o-rings, etc.) are recognized as non-verifiable at the system level. The integrity of these seals shall be controlled by process or procedures consistent with industry standards. Components where fault tolerance is not credible or practical (e.g. tanks, lines, etc.) shall use design for minimum risk instead.	Adequate control of safety hazards is necessary in order to develop safe hardware and operations. Verification of independence of inhibits is necessary to preclude propagation of failure in safety inhibits that can result in critical or catastrophic threats to personnel, facility, and hardware. The internal volume between redundant inhibits (seal) shall be limited to the minimal practical volume and designed to limit the external leakage event of failures.	Identify proposed design inhibits that preclude hazardous condition and document in preliminary hazard analysis.
			Present compliance with range safety requirements, including fault tolerance to hazardous events.
Fuse Architecture (**PROP-4**)	A system fusing architecture shall be developed and documented for all missions, including the payloads.	Lack of a system fusing design may lead to fuse incompatibilities between the power source and the payloads, which could lead to the power source, fuse being blown prior to the payloads. The system fusing design should maximize the reliability of the system.	Identify a preliminary grounding concept.
			Complete a preliminary grounding design and communicate it to all hardware developers.
			State grounding requirements in all Electrical Interface Control Documents for the users.

3.4.2 Propulsion Overview

Propulsive thrusters and mechanisms range from high thrust, low specific impulse devices (cold gas, electrothermal), moderate thrust, moderate specific impulse devices (colloid, bipropellants, solid rockets), and low thrust, high specific impulse devices (pulsed plasma thrusters, electrospray, electromagnetic, electrostatic). Many CubeSat thruster reviews have been written [39,94-96], and a general depiction of thruster capabilities is provided in **Figure 72**. Specific impulses up to 6000 seconds are available.

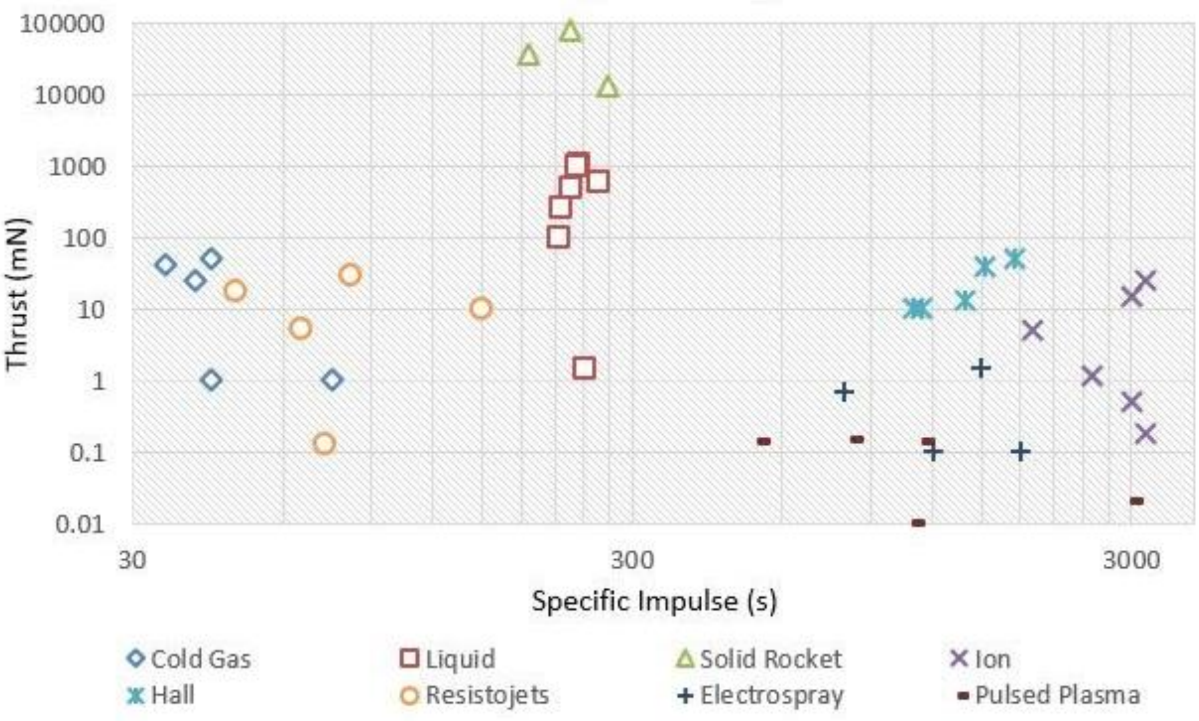

Figure 72: Thruster Capability Overview, Used with Permission [96]

Specific impulse, hereby referred to as I_{sp}, without drag or gravity can be thought of as fuel efficiency or how much ΔV can be achieved for a given amount of propellant. A high thruster I_{sp} indicates reduced propellant mass cost to achieve a desired ΔV and increased TOF. A simple reiteration of Tsiolkovsky's rocket equations is presented in **Eqs.(44-46)** without derivation.

$$\Delta V = I_{sp} \cdot g_0 \cdot \ln\left(\frac{m_0}{m_f}\right) = I_{sp} \cdot g_0 \cdot \ln\left(\frac{m_0}{m_0 - m_p}\right) \quad \textbf{Eq.(44)}$$

$$m_p = m_f \cdot \left[e^{\frac{\Delta V}{(I_{sp} \cdot g_0)}} - 1\right] \quad \textbf{Eq.(45)}$$

$$m_p = m_0 \cdot \left[1 - e^{\frac{-\Delta V}{(I_{sp} \cdot g_0)}}\right] \quad \textbf{Eq.(46)}$$

Parameter ΔV represents change in spacecraft velocity in units of m/s, I_{sp} represents specific impulse in units of seconds, m_0 represents initial spacecraft mass in units of kg, m_f represents final spacecraft mass in units of kg, and m_p represents propellant mass in units of kg. The parameter g_0 is the gravitational constant at Earth's surface, namely 9.80665 m/s^2, and it should be thought of as a conversion factor. It does not change with altitude or with changing gravitational acceleration, and it is only included to delineate whether total impulse is normalized by mass or weight [33]. If using the asinine imperial system, g_0 may not be included, and more detailed unit tracking is warranted. All units in the imperial system of measurement are formally defined as metric units multiplied by a conversion factor, and imperial units should be discarded entirely. Thrust without drag or gravity is derived by the definition of a Laval nozzle, shown in **Figure 73**.

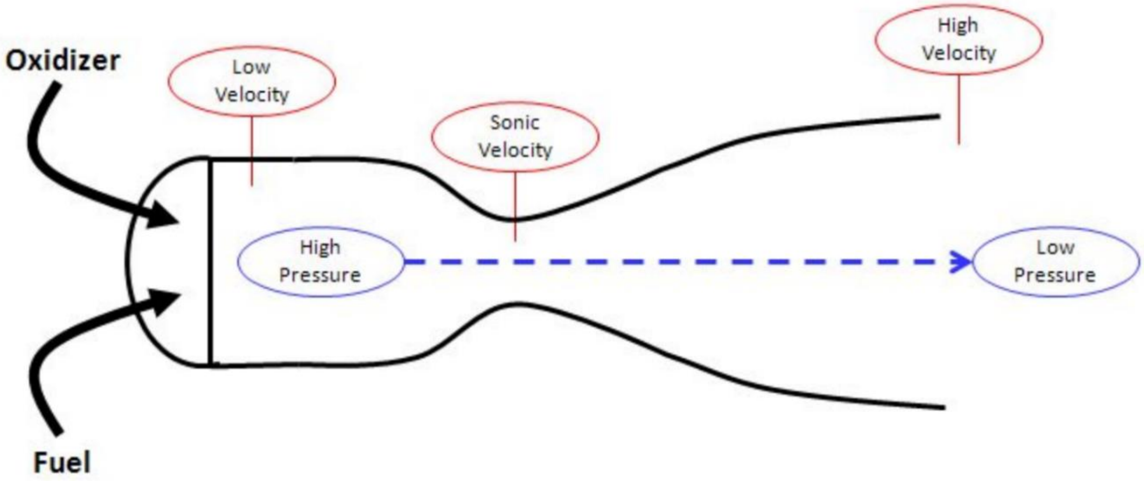

Figure 73: Bipropellant Engine Converging/Diverging De Laval Nozzle [97]

Thrust from the Laval nozzle exit on the right of **Figure 73** is equal to the mass flow rate of the exhaust multiplied by the velocity of the exhaust plus the difference in pressure at the exhaust port times the area of the exhaust port, shown in **Eq.(47)**, where T_{sc} is thrust in units of Newtons, $\dot{m}$ is mass flow rate in units of kg/s, V_e is exhaust velocity in units of m/s, A_e is the area of the thruster exit in units of m^2, p_e is pressure at the thruster exit from inside the nozzle in units of pascal, and p_a is the ambient pressure in units of pascal. A major assumption of **Eq.(47)** is that the exhaust and thrust are entirely along the horizontal axis, depicted by the blue line. **Eq.(47)** works well for exhaust plumes featuring divergence half-angles, the angle between the horizontal blue line and non-parallel thrust lines, of 15 degrees or less. This is not the case for Electric Propulsion (EP) as described below.

$$T_{sc} = \dot{m} \cdot V_e + A_e \cdot (p_e - p_a) \qquad \textbf{Eq.(47)}$$

3.4.3 Deep Space: High ΔV Maneuvers

CubeSats intended for deep space targets such as asteroids, NEOs, or other planets will either need a dedicated LV fairing with propulsive capabilities, such as Rocket Lab’s photon platform, or to include propulsive capabilities in the design. LV selection is paramount for science-type missions, but the majority of deep space CubeSats will feature propulsion with Thrust Vector Control (TVC) or a bulky Reaction Control System (RCS). At minimum, TVC and an RCS will allow for reaction wheel desaturation. Many non-LEO, near-Earth LVs will put CubeSats into GEO or GTO, and the CubeSat will require hundreds of m/s in ΔV just to get out of the VABs, which limits near-Earth science. Simple comparisons of CubeSat mass and ΔV in **Figures 74-75** depict the mathematical restrictions on thruster selections for high-ΔV maneuvers. **Figure 74** shows the drastic increase in required propellant mass for thrusters under 500 seconds I_{sp}.

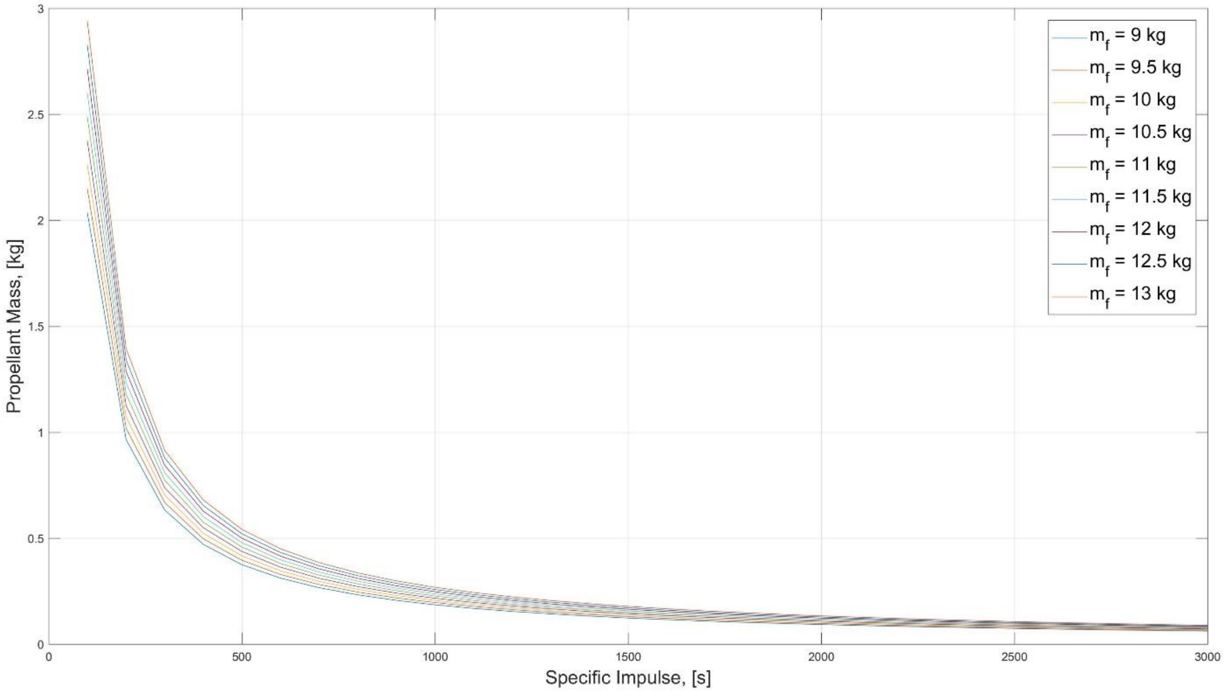

Figure 74: Basic Tsiolkovsky's Equation Comparison for 6U CubeSat Masses, ΔV = 200 m/s

Figure 74 was created with **Eq.(45)**, and some of the outputs are not realistic for a 14 kg total mass, e.g. a 13 kg final mass plus 2.5 kg of propellant mass at 200 seconds I_{sp} would sum to over 14 kg. The graph is intended to show the significant decrease in required propellant mass with increasing I_{sp} regardless of the final mass. If a hard maximum of 14 kg is desired, **Eq.(46)** can be used to graph **Figure 75** for a variety of ΔVs.

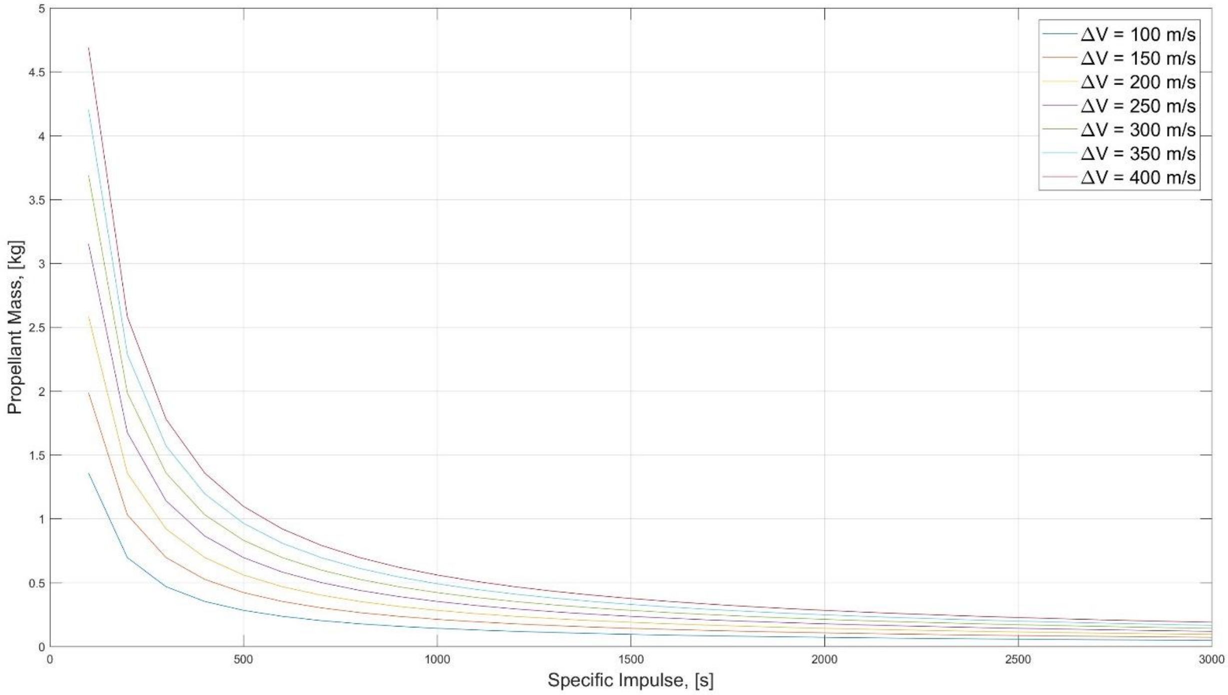

Figure 75: Basic Tsiolkovsky's Equation Comparison for varied ΔV, Total Mass = 14 kg

It is apparent that no matter the desired final mass of the spacecraft or change in velocity, the propellant mass requirement features a sharp transition before and after 500 seconds I_{sp}. Per **Figure 72**, the thruster types that can achieve such propellant mass savings are Pulsed Plasma Thrusters (PPTs), Hall effect thrusters, electrospray, and ion thrusters. All of these represent EP solutions, and there have been significant advances in each type of technology. Hall effect thrusters require much more power for less I_{sp} than electrosprays and ion thrusters, but missions that have TOF requirements should consider them for their relatively high thrust.

For any EP solution, a final consideration must be included for calculations involving ΔV, the geometric efficiency factor, λ_g. **Eq.(47)** is modified to include the geometric efficiency factor in **Eq.(48)**. The second term in **Eq.(47)** is no longer applicable as EP thrust does not stem from pressurization.

$$T_{sc} = \lambda_g \cdot \dot{m} \cdot V_e \quad : \quad \lambda_g = \frac{1+\cos(\alpha_{div})}{2} \qquad \textbf{Eq.(48)}$$

The parameter α_{div} represents the full plume divergence angle, not the divergence half-angle. Goebel and Katz handle this calculation differently [98]. EP plumes spread widely, particles can turn a full 90 degrees after exiting the thruster, and those particles can erode or be deposited on the thruster structural face. Although the particles can spread 90 degrees, the plume, usually a mix of plasma and un-ionized liquid particles, is not constant density or isothermal. An effective plume divergence angle must be assumed for generic calculations, and propulsion SMEs have stated 75 degrees as a conservative estimate. With a plume divergence angle of 75 degrees, the geometric efficiency factor is ~0.63, and the practical use of this value is to divide the required ΔV of a given orbit by the geometric efficiency factor. If the AEGIS ΔV of 134 m/s is used as an example, the EP calculations should be 134 m/s divided by 0.63, or ~212.7 m/s. It is better to alter the ΔV requirement rather than the thrust calculation because thrust calculations for EP can become cumbersome without intimate knowledge of the operations of each option. **Eqs.(49-51)** from [98] calculate the thrust of a Hall effect or ion propulsion system to prove this point, where I_b represents ion beam current, m_{ion} represents the ion mass, q_{ion} represents ion charge, and V_b is the net voltage that the ion was accelerated through. This calculation set is for singly charged ions only.

$$\dot{m} = \frac{I_b \cdot m_{ion}}{q_{ion}} \qquad \textbf{Eq.(49)}$$

$$V_e = \sqrt{\frac{2 \cdot q_{ion} \cdot V_b}{m_{ion}}} \qquad \textbf{Eq.(50)}$$

$$T_{sc} = \left[\frac{1+\cos(\alpha)}{2}\right] \cdot \sqrt{\frac{2 \cdot m_{ion}}{q_{ion}}} \cdot I_b \cdot \sqrt{V_b} \qquad \textbf{Eq.(51)}$$

3.4.4 Legacy EP Optimization Procedure

To optimize the mass of an EP propulsion system, an alteration of Tsiolkovsky's rocket equation must occur. This analysis follows the widely available logic of Oates [99] and Sutton & Biblarz [100] to minimize the mass of an electric system and optimize the specific impulse for varied payload mass and given ΔV. The payload should be understood as everything that is not the electrical system or propellant. The electrical system mass consists of the power generation system, EPS, the radiator, any heat exchangers, and the thruster, here described as the accelerator. Specific power, α', is the ratio of power provided to the accelerator, W_e, divided by the mass of the electrical system, m_e.

$$\alpha' = \frac{W_e}{m_e} \qquad \textbf{Eq.(52)}$$

The power in the exhaust stream can be modeled as **Eq.(53),** where η_α is the accelerator efficiency and c is the effective exhaust velocity. The mass flow rate is represented by $\dot{m}$. It is important to note that η_α is not the total propulsive efficiency, and the accelerator efficiency will come from a thruster datasheet or vendor. It is the thruster PCE. The term $\alpha' \cdot \eta_\alpha$ is the power per kilogram of the electrical power plant supplying power to the system.

$$\eta_\alpha \cdot W_e = \dot{m} \cdot \left(\frac{c^2}{2}\right) \qquad \textbf{Eq.(53)}$$

Rearranging to substitute for W_e and solve for m_e,

$$m_e = \frac{\dot{m}}{\alpha' \cdot \eta_\alpha} \cdot \frac{c^2}{2} \qquad \textbf{Eq.(54)}$$

Eq.(54) is an indication of power limiting. The effective exhaust velocity is a strong function of the power input and accelerator efficiency. Assuming a constant mass flow rate, common but not required for EP thrusters, the burn duration, τ, can be written with **Eq.(55)**,

$$\tau = \frac{m_p}{\dot{m}} \qquad \textbf{Eq.(55)}$$

where m_p represents propellant mass. Writing **Eq.(54)** as a ratio in terms of **Eq.(55)** yields **Eq.(56)**,

$$\frac{m_e}{m_p} = \frac{c^2}{2 \cdot \alpha' \cdot \eta_\alpha \cdot \tau} \qquad \textbf{Eq.(56)}$$

Eq.(57) represents the total mass of the system divided into electrical propulsion and power generation as m_e, propellant as m_p, and everything else in m_L as payload.

$$m_0 = m_e + m_p + m_L \qquad \textbf{Eq.(57)}$$

Dividing **Eq.(57)** by total mass and rearranging yields **Eqs.(58-59)**,

$$\frac{m_0}{m_0} = \frac{m_e}{m_0} + \frac{m_p}{m_0} + \frac{m_L}{m_0} \qquad \textbf{Eq.(58)}$$

$$\frac{m_L}{m_0} = 1 - \frac{m_p}{m_0} \cdot \left(1 + \frac{m_e}{m_0} \cdot \frac{m_0}{m_p}\right) \qquad \textbf{Eq.(59)}$$

$$\frac{m_L}{m_0} = 1 - \frac{m_p}{m_0} \cdot \left(1 + \frac{m_e}{m_p}\right)$$

Substitute **Eq.(56)** into **Eq.(59)** yields,

$$\frac{m_L}{m_0} = 1 - \frac{m_p}{m_0} \cdot \left(1 + \frac{c^2}{2 \cdot \alpha' \cdot \eta_\alpha \cdot \tau}\right) \qquad \textbf{Eq.(60)}$$

Tsiolkovsky’s equation may be written as,

$$\frac{m_p}{m_0} = 1 - e^{\frac{-\Delta V}{c}} \qquad \textbf{Eq.(61)}$$

Such that,

$$c = I_{sp} \cdot g_0 \qquad \textbf{Eq.(62)}$$

Substituting **Eq.(61)** into **Eq.(60)** yields,

$$\frac{m_L}{m_0} = 1 - \left(1 - e^{\frac{-\Delta V}{c}}\right) \cdot \left(1 + \frac{c^2}{2 \cdot \alpha' \cdot \eta_\alpha \cdot \tau}\right) \tag*{\textbf{Eq.(63)}}$$

Assume,

$$\alpha_p = \frac{\Delta V}{c} \tag*{\textbf{Eq.(64)}}$$

$$\beta_p = \frac{\Delta V}{\sqrt{2 \cdot \alpha' \cdot \eta_\alpha \cdot \tau}} \tag*{\textbf{Eq.(65)}}$$

Rewriting **Eq. (63)**,

$$\frac{m_L}{m_0} = 1 - (1 - e^{-\alpha_p}) \cdot \left[1 + \left(\frac{\beta_p}{\alpha_p}\right)^2\right] \tag*{\textbf{Eq.(66)}}$$

The optimum specific impulse or effective exhaust velocity is found by taking the derivative of **Eq.(66)** with respect to α_p [99] to obtain **Eq.(67)**. The subscript p will be dropped from α_p and β_p, but they are not the same as absorptivity or solar irradiance angle.

$$0 = \frac{2 \cdot \beta^2}{\alpha^3} - \frac{e^{-\alpha} \cdot (\alpha + 2) \cdot \beta^2}{\alpha^3} - e^{-\alpha} \tag*{\textbf{Eq.(67)}}$$

Distribute the middle term, partially distribute a common denominator, and separate β^2,

$$0 = \frac{\beta^2 \cdot (2 - e^{-\alpha} \cdot \alpha - 2 \cdot e^{-\alpha})}{\alpha^3} - e^{-\alpha} \tag*{\textbf{Eq.(68)}}$$

The goal is to solve **Eq.(68)** for $\frac{\beta^2}{\alpha^2}$,

$$0 = \frac{\beta^2}{\alpha^2} \cdot \frac{(2 - e^{-\alpha} \cdot \alpha - 2 \cdot e^{-\alpha})}{\alpha} - e^{-\alpha}$$

Rearrange,

$$\frac{\beta^2}{\alpha^2} = \frac{1}{e^\alpha} \cdot \frac{\alpha}{(2 - e^{-\alpha} \cdot \alpha - 2 \cdot e^{-\alpha})}$$

Distribute the denominator to obtain the final relationship,

$$\left(\frac{\beta}{\alpha}\right)^2 = \frac{\alpha}{2 \cdot (e^\alpha - 1) - \alpha} \tag*{\textbf{Eq.(69)}}$$

Substituting **Eq.(69)** into **Eq.(66)** yields,

$$\frac{m_L}{m_0} = 1 - (1 - e^{-\alpha}) \cdot \left[1 + \frac{\alpha}{2 \cdot (e^\alpha - 1) - \alpha}\right] \tag*{\textbf{Eq.(70)}}$$

FOIL the second term on the RHS,

$$\frac{m_L}{m_0} = 1 - \left[1 + \frac{\alpha}{2 \cdot (e^\alpha - 1) - \alpha} - e^{-\alpha} - \frac{\alpha \cdot e^{-\alpha}}{2 \cdot (e^\alpha - 1) - \alpha}\right]$$

Rearrange bracketed terms for a common denominator,

$$\frac{m_L}{m_0} = 1 - \left\{\frac{2 \cdot (e^\alpha - 1) - \alpha}{2 \cdot (e^\alpha - 1) - \alpha} + \frac{\alpha}{2 \cdot (e^\alpha - 1) - \alpha} - \frac{e^{-\alpha} \cdot [2 \cdot (e^\alpha - 1) - \alpha]}{2 \cdot (e^\alpha - 1) - \alpha} - \frac{\alpha \cdot e^{-\alpha}}{2 \cdot (e^\alpha - 1) - \alpha}\right\}$$

Simplify and revise into additive terms,

$$\frac{m_L}{m_0} = 1 + \frac{e^{-\alpha}\cdot[2\cdot(e^{\alpha}-1)-\alpha]+\alpha\cdot e^{-\alpha}-2\cdot(e^{\alpha}-1)}{2\cdot(e^{\alpha}-1)-\alpha}$$

Combine all terms over a single denominator,

$$\frac{m_L}{m_0} = \frac{[2\cdot(\,e^{\alpha}-1)-\,\alpha]+e^{-\alpha}\cdot[2\cdot(e^{\alpha}-1)-\alpha]+\alpha\cdot e^{-\alpha}-2\cdot(e^{\alpha}-1)}{[2\cdot(\,e^{\alpha}-1)-\,\alpha]}$$

Expand RHS numerator, simplify RHS numerator, and multiply denominator to LHS,

$$\frac{m_L}{m_0}\cdot[2\cdot(\,e^{\alpha}-1)-\,\alpha] = -\,\alpha + 2 - 2\cdot e^{-\alpha}$$

Divide by 2 and simplify,

$$\frac{m_L}{m_0}\cdot\left[(\,e^{\alpha}-1)-\,\frac{\alpha}{2}\right] = 1-\frac{\alpha}{2}-e^{-\alpha}$$

Rearrange to find the function F_p to be minimized,

$$F_p = 0 = 1-\frac{\alpha}{2}-e^{-\alpha}-\frac{m_L}{m_0}\cdot\left(e^{\alpha}-1-\frac{\alpha}{2}\right) \qquad \textbf{Eq.(71)}$$

Take the derivative with respect to α,

$$\frac{dF_p}{d\alpha} = 0 = -\frac{1}{2}+e^{-\alpha}-\frac{m_L}{m_0}\cdot\left(e^{\alpha}-\frac{1}{2}\right) \qquad \textbf{Eq.(72)}$$

The equations are now ready to be put into numerical iteration form. The inputs to this scheme are varied $\frac{m_L}{m_0}$, target ΔV in meters per second, and the quantity $\alpha'\cdot\eta_{\alpha}$ in watts per kilogram. The outputs are α, β, and secondary calculations yield effective exhaust velocity, optimal specific impulse, burn time, and acceleration. An initial α is needed, and time index j is used again.

$$\alpha_{j=0} = 1-\frac{m_L}{m_0} \qquad \textbf{Eq.(73)}$$

To begin the iteration, find $\alpha_{j=0}$. Use this value in **Eq.(71)** and **Eq.(72)** to get the minimizing function F and its derivative with respect to α. Plug those into **Eq.(74)** to find the next alpha. Iterate these steps until convergence. This scheme reflects a first order Taylor expansion as Newtonian iteration.

$$\alpha_{j+1} = \left(\alpha-\frac{F_p}{\frac{dF_p}{d\alpha}}\right)_j \qquad \textbf{Eq.(74)}$$

Newtonian iteration features quadratic convergence, so total iterations will be closer to 10 than 100. After α has converged, apply **Eqs.(75-79)** to obtain propulsive parameters. The order here is β, effective exhaust velocity c, optimal specific impulse $I_{sp,opt}$, burn duration τ, and acceleration a.

$$\beta = \frac{\alpha^{\frac{3}{2}}}{\sqrt{2\cdot(e^{\alpha}-1)-\alpha}} \qquad \textbf{Eq.(75)}$$

$$c = \frac{\Delta V}{\alpha} \qquad \textbf{Eq.(76)}$$

$$I_{sp,opt} = \frac{c}{g_0} \qquad \textbf{Eq.(77)}$$

$$\tau = \left(\frac{1}{2}\cdot\alpha'\cdot\eta_{\alpha}\right)\cdot\left(\frac{\Delta V}{\beta}\right)^2 \qquad \textbf{Eq.(78)}$$

$$a = \left(\frac{c}{\tau}\right) \cdot \left(1 - e^{-\alpha}\right) \qquad \textbf{Eq.(79)}$$

While **Eqs.(75-79)** can all be plotted for the optimization scheme, specific impulse and propellant ratio from **Eqs.(44-46)** recalculated with optimized inputs are of interest. **Figure 76** depicts the optimum specific impulse and payload ratio for 206 m/s ΔV, 14 kg CubeSat total mass, 25 watts power provided to the accelerator, and an accelerator efficiency of 0.8. Engine mass is calculated by later subtracting calculated propellant and payload mass from the total mass.

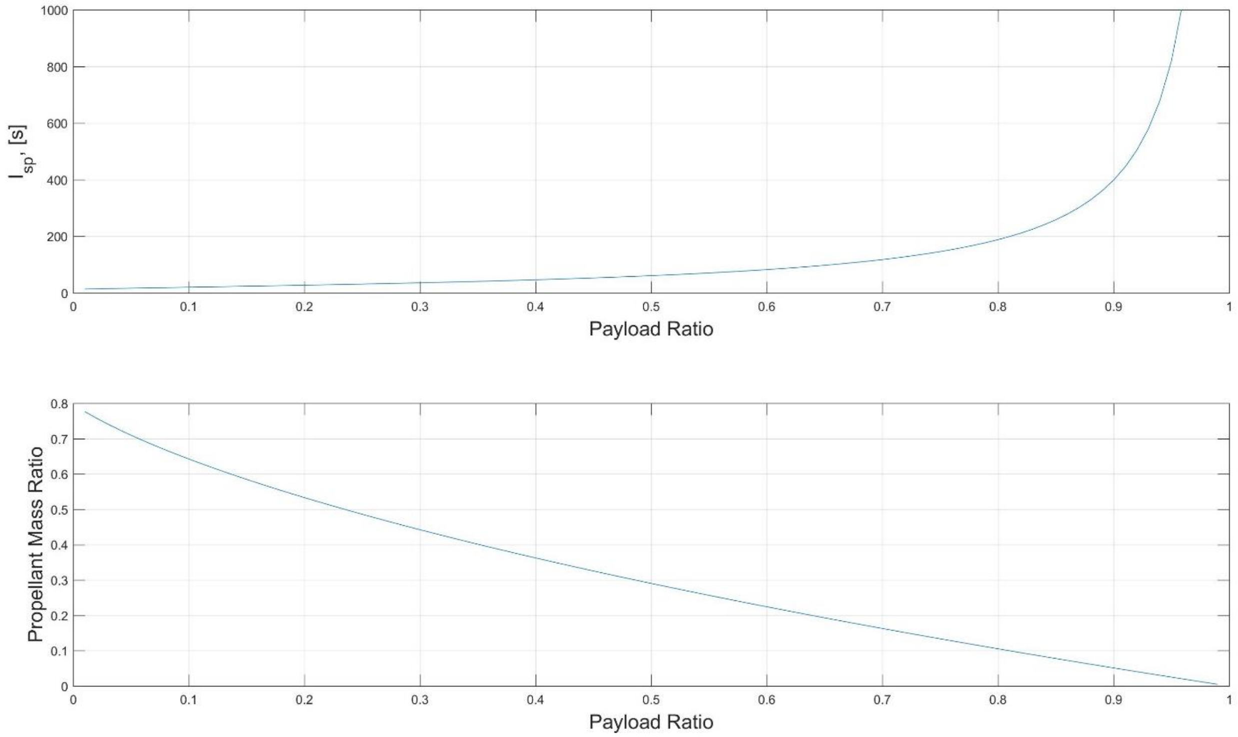

Figure 76: Legacy Optimization Output, Specific Impulse and Propellant Mass Ratio vs. Payload Ratio. ΔV = 206 m/s, m_o = 14 kg, W_e = 25 W

Immediately evident is that the optimization scheme to minimize the mass of the EP system results in a prediction of specific impulses that are featured by cold gas systems instead of EP thrusters and propellant mass ratios that are unrealistic. Even for 50% payload mass, which here means anything not directly providing power to the thruster including the radio, science payload, chassis, and thermal control components, the optimization scheme dictates over 4 kg of propellant. For a cold gas system with liquid isobutane propellant storage at 2.51 kg/m^3, the volume requirement comes out to be 1593.6 U.

When this procedure is run for a 1000 kg spacecraft with 100 W delivered to the accelerator for a ΔV of 20,000 m/s, the result is **Figure 77**. An I_{sp} of 4000 s at the same payload mass is much more aligned with the capabilities of an EP system. For an EP solid indium propellant storage density of 7025 kg/m^3, which is not the “room temperature” density value, the volume requirement of the 50% payload ratio 300 kg propellant requirement is 42.7 U. The takeaway is that the classical EP mass optimization scheme works well for large spacecraft and large ΔV requirements, but **this analysis does not work well for small spacecraft because there is no volume constraint on the propellant.**

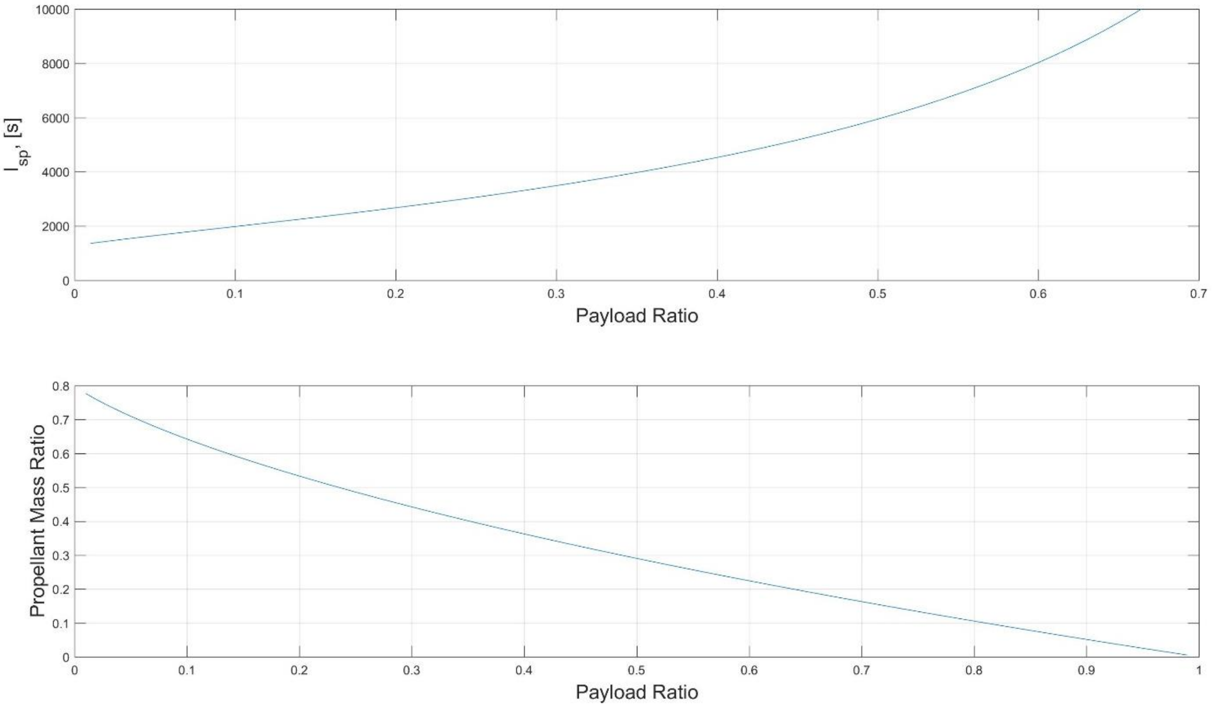

Figure 77: Legacy Optimization Output, Specific Impulse and Propellant Mass Ratio vs. Payload Ratio. ΔV = 20,000 m/s, m_o = 1,000 kg, W_e = 100 W

3.4.5 Modified EP Optimization Procedure

There are three steps to modifying the EP optimization procedure to account for a volumetric constraint: calculate the original propellant mass values as a function of payload ratio, define a new propellant mass calculation that interpolates the old values based on the volumetric constraint, and modify the effective exhaust velocity calculation to include the new propellant mass. All other steps are the same.

The modified procedure varies volume constraints applied to the spacecraft, which may be any number or fraction of U, to say that the total volume of propellant should not exceed a given constraint value. As the optimization procedure is for propellant masses, propellant densities must be included in the calculation. The inclusion of the propellant density allows this procedure to be applied to type of thrusters for comparison. A modified mass parameter μ is defined in **Eq.(80).**

$$\mu = v \cdot \rho_p + \left(\frac{m_p - m_{p_{first}}}{m_{p_{last}} - m_{p_{first}}}\right) \cdot \left(-v \cdot \rho_p\right) \qquad \textbf{Eq.(80)}$$

The parameter v is the applied volume constraint in units of m^3, ρ_p is the propellant density in units of kg/m^3, and m_p is simply the propellant mass calculated in the legacy procedure. The top left term in the numerator is the propellant mass as a function of payload ratio, and every other parameter but μ is a constant. Parameters with subscripts first and last could be the propellant masses for the first considered payload ratio of 0.01 and the last considered payload ratio of 0.99 or any values in between. After the modified mass parameter is calculated, the modified effective exhaust velocity is calculated in **Eq.(81)**.

$$c_{mod} = \frac{\Delta V}{ln\left(\frac{m_0}{m_0 - \mu}\right)} \qquad \textbf{Eq.(81)}$$

At this point c_{mod} is used in **Eq.(64)** to calculate the dimensionless parameter α, and **Eqs.(75-79)** are subsequently calculated in the same manner as the original optimization scheme. Outputs for the modified scheme are shown in **Figures 78-79** for varied volumetric constraints.

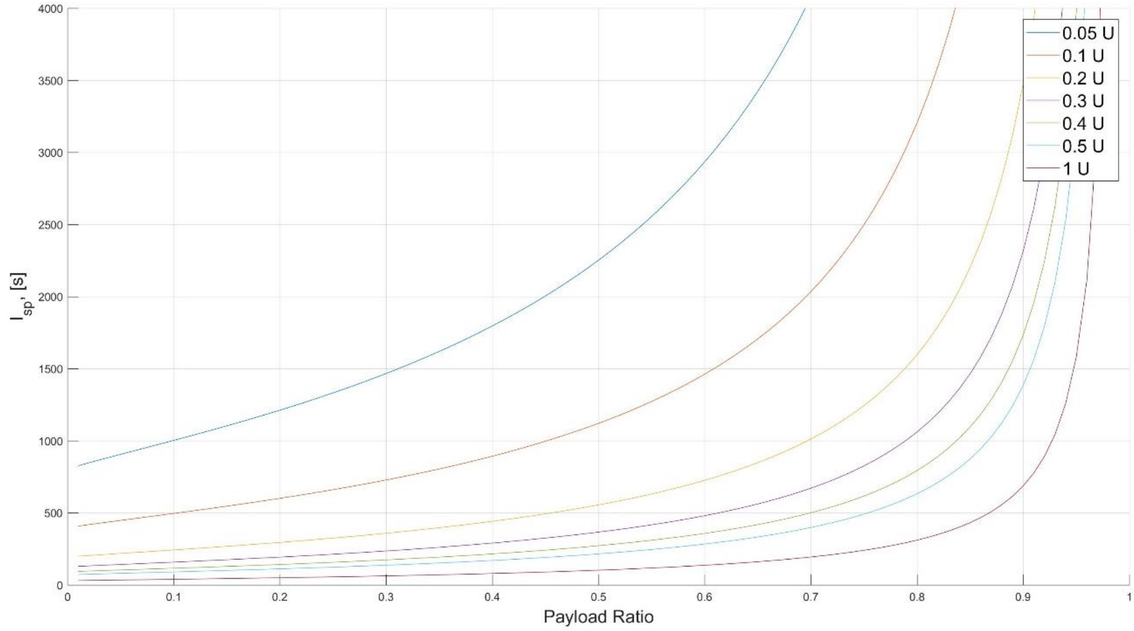

Figure 78: Modified Optimization Procedure Specific Impulse. ΔV = 206 m/s, m_0 = 14 kg, W_e = 25 W

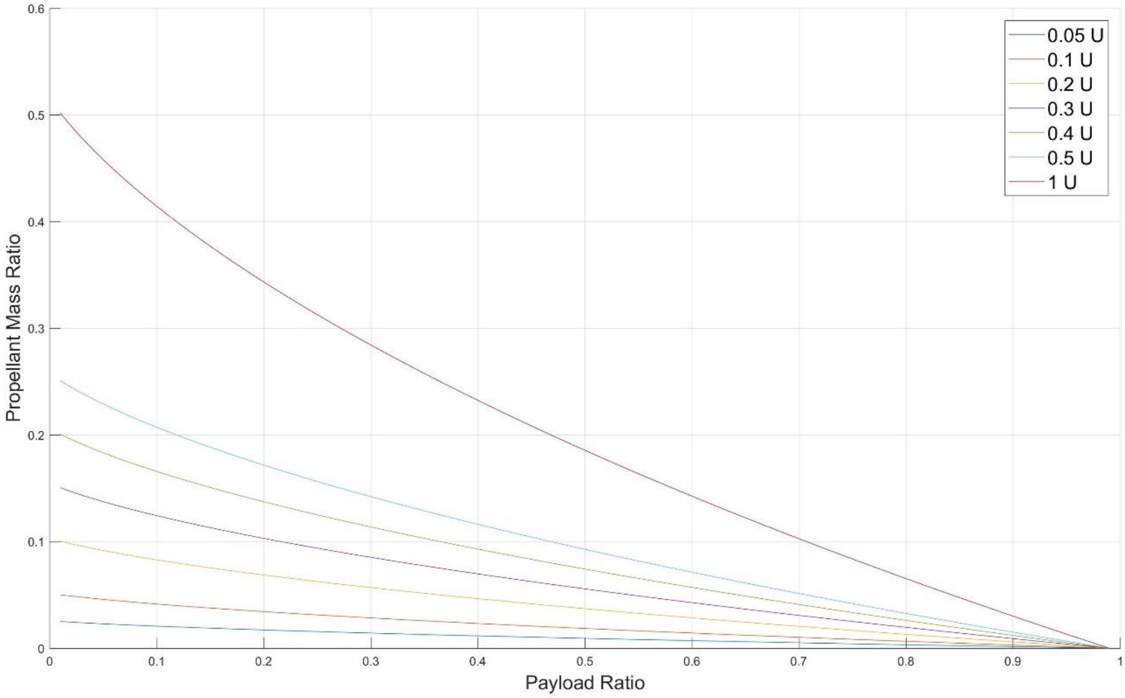

Figure 79: Modified Optimization Procedure Propellant Mass Ratio. ΔV = 206 m/s, m_0 = 14 kg, W_e = 25 W

Calculations for I_{sp} are now much more in line with realistic expectations for small spacecraft platforms, and thrusters of differing propellant types may be directly compared. Ivan Garcia is thanked for his work on this collaboration.

3.5 Electrical Power System

Written with assistance from Dr. Jaber Abu-Qahouq, University of Alabama.

An EPS is divided into power generation and processing hardware, an energy storage mechanism, output power regulation, and data collection instrumentation. The three power budgeting categories for an EPS are power generation, power distribution, and power consumption, also known as power conversion and regulation. All categories exhibit losses to be accounted for when developing a power profile for the spacecraft, and power consumption values differ per software state. Generally, burn and communication states will require the most power in deep space. Once power consumption requirements are satisfied by power generation and distribution capabilities, an analysis of Maximum Power Point Trackers (MPPTs) allows for direct comparison of COTS options. The COTS EPS that satisfies power throughput and MPPT requirements for a given mission should be the EPS selection, but modifications may be necessary if ratings or margins are exceeded.

3.5.1 EPS Design Objectives

Table 30: Electrical Power System Design Objectives, Adapted from [28]

Design Objective	Description	Rationale	Actionable Items
Electrical Supply Continuity (**EPS-1**)	Supply continuous electrical power to subsystem as needed during entire mission life including eclipses.	Lapses in power connectivity may cause unanticipated resets in the C&DH system, loss of science data, or catastrophic failure of the system.	Ensure connectivity of batteries, voltage regulators, and EPS board controls.
Distribution Control & Safety (**EPS-2**)	Safely distribute and control all power provided to subsystems.	Spikes in voltage or current from the EPS may result in component damage or failure.	Ensure proper voltage regulation and protection from voltage or current spikes by adding fuses where necessary and selecting components that are rated for higher voltage than anticipated by the design.

Power Conversion (**EPS-3**)	Provide downstream power converters with required voltage/current/power regulation for different loads/subsystems.	Power conversion at each stage of power supply results in a chain of potential faults which must be fully analyzed prior to operation.	Ensure power converters are properly connected, rated, and tested before operation.
Load Margin (**EPS-4**)	Provide enough power with margin for both average and peak loads	Solar incidence with respect to the spacecraft varies, and thus power generation with respect to solar incidence will vary.	Fully define expected peak and average loads and ensure power generation at all solar incidences complies with full power expectations with conservative margins included.
EPS Telemetry (**EPS-5**)	Provide EPS Health and Status (voltage, current, temperature, etc.)	Power telemetry may be analyzed by ground control team members to detect or characterize unanticipated faults in system operation.	Apply sensors for voltage, current, temperature, charge, and duty cycles where relevant.
EMI and Fault Mitigation (**EPS-6**)	Protect itself and others from EMI, transients, bus faults, and load faults.	EMI can cause unanticipated signals to propagate throughout the system resulting in incorrect telemetry or possible system malfunction.	Ensure cabling for power connections are properly shielded and test power supply with a digital multimeter.
Deployment Switch (**EPS-7**)	The secondary payloads shall have, at minimum, 2 deployment switches, which are actuated while integrated in the dispenser.	CubeSat must be powered down while inside the dispenser to prevent interference with the launch vehicle.	Incorporate two deployment switches.

3.5.2 Power Generation

Most satellites are powered by photovoltaic solar cells. At Earth distance, or approximately 1 AU, a 6U satellite could generate 60-150 W with a sizable solar array, and solar cell efficiencies are continually increasing. The best solar cell efficiency at time of writing is SpectroLab's XTE-SF (Standard Fluence) cell with a 32.2% BOL efficiency [101]. Solar cell manufacturers such as SpectroLab are not the companies that make the solar arrays. Cells are delivered to array manufacturers as Coverglass Interconnected Cells (CICs), and CICs are integrated onto the specified array geometry accordingly.

Alternative methods of power generation will be required as deep space CubeSats become more prevalent. **Figure 80** depicts the solar power flux available at various planetary distances based on orbit semimajor axes. If a solar array generates 100% of power at Earth distance, that power is decreased to 42% at Mars distance. There are no practical, CubeSat-sized Radioisotope Thermoelectric Generators (RTGs) and thus CubeSats may be relegated to missions focused on interior planets until this problem is resolved [102]. It is not that outer planet missions are impossible, but CubeSats would either need to bring an exceedingly large solar array or CICs intended to convert longer wavelength radiation into electrical energy. The data in **Figure 80** was calculated using **Eq.(12)**.

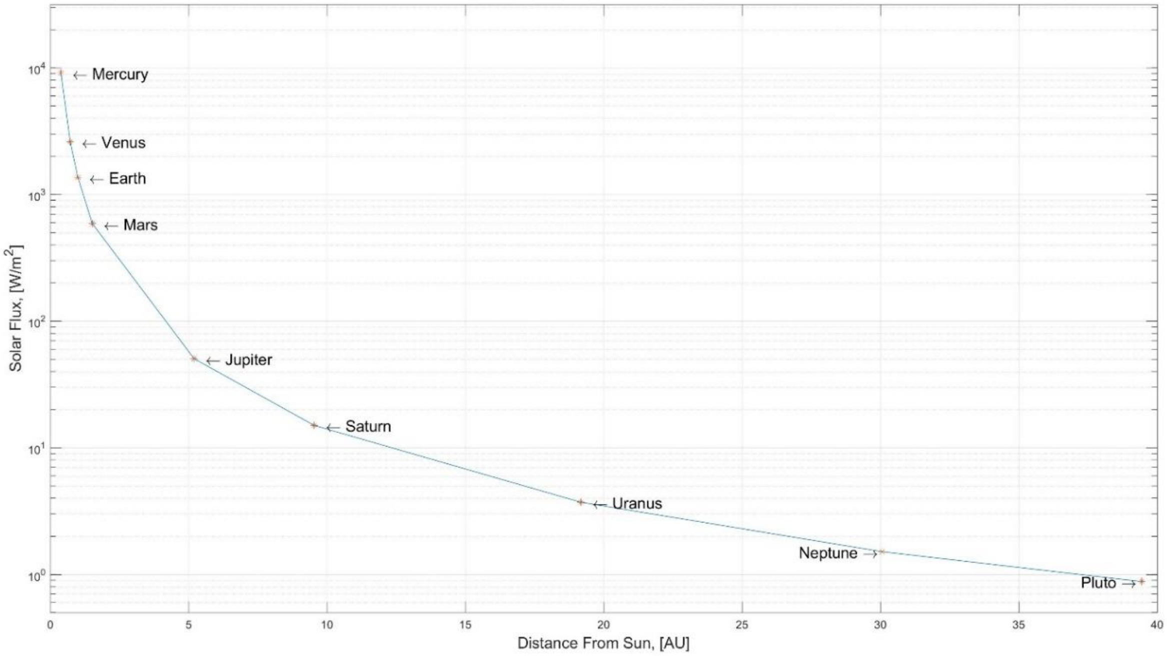

Figure 80: Available Solar Power Flux vs. Planetary Distance

Solar arrays can either be fixed in place after spring-loaded deployment or mounted on an SADA, which are extremely useful but time consuming to test and qualify. AEGIS did not employ an SADA simply due to the time constraint imposed by Artemis II's launch deadline. An SADA will decrease the overall solar array area required for a mission, leaving more room for other components, but there are drawbacks to having a single, bulky solar array. The Mars Climate Orbiter (MCO) featured a large, singular array that imposed significant stress on its reaction wheels due to the parallel axis theorem. The MCO team did not have a GN&C subsystem lead on the administrative team which ultimately resulted in the crash failure of the MCO. If a mission employs an SADA for a singular solar array, a GN&C lead on the administrative team is highly recommended.

While power generation is first described with solar array areas defined, solar array area definition is often a back and forth procedure. Subsystem teams will alter component selections which will vary the power consumption requirements. More solar array area will be required to accommodate increased power consumption which will alter internal structural configuration definition. It is highly recommended that component trade space be limited to an operational power envelope so that best and worst-case selections are described, and EPS designers will not be taken by surprise when a component is up or downselected.

A block diagram of a basic EPS is found in **Figure 81**. Power generation is on the left, distribution is in the middle, and consumption is on the right. All hardware except EPS data collection is discussed. MPPT signifies Maximum Power Point Tracker, discussed in Section 3.5.6.

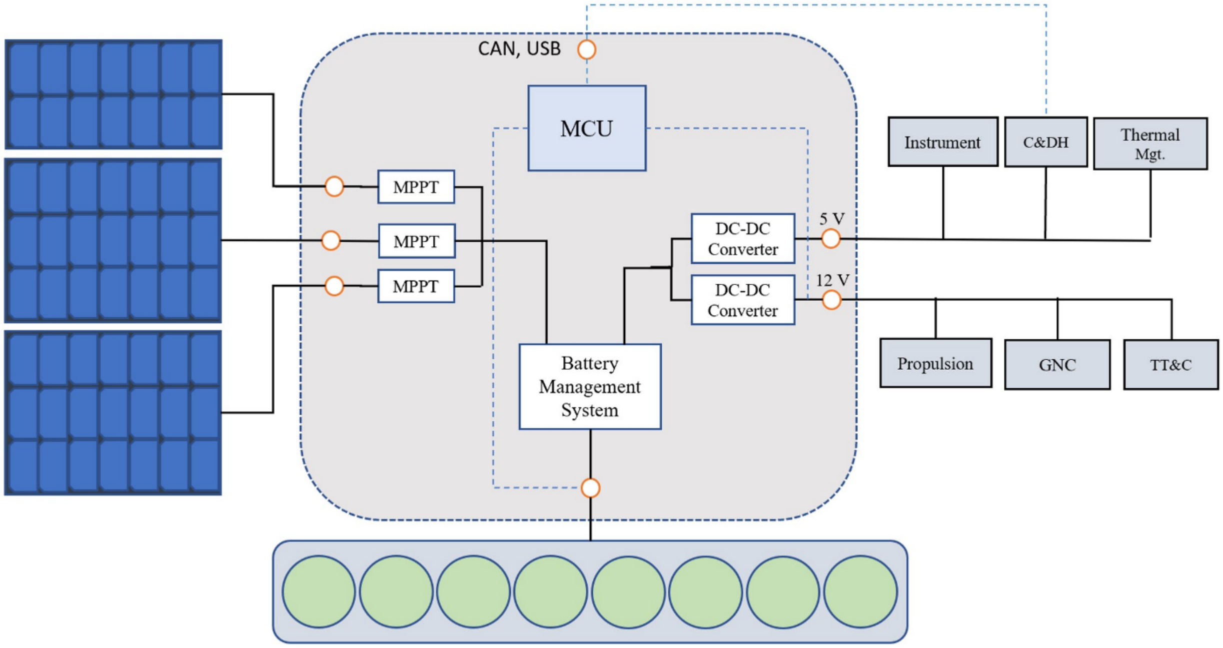

Figure 81: Basic EPS Block Diagram, Distributed MPPT System, Not All AEGIS Components Represented, Nothing to Scale.

3.5.2.1 AEGIS Solar Array Definition

AEGIS features 3 solar arrays, shown in **Figures 82-85**. Solar array A is single-sided, solar array B is double-sided, and solar array C is double-sided. The burn maneuver is the operation with the highest power draw for AEGIS, and the design team needed to ensure the spacecraft would be power-positive at all solar AOI. The Sun was always going to be on the Earth-Sun ecliptic plane which is near the satellite-Earth ecliptic plane because the orbit inclination is low. Informally, the Sun was going to be to the left, right, in front, or behind the spacecraft, never above or below. The solar arrays needed to point at the Sun even as it crossed the spacecraft ram vector from the left to the right or vice versa, but the thrust vector could not be changed. Therefore, the solar array definition strategy was to have solar array A directed to the left of the spacecraft when the Sun was on the left, and, when the Sun crossed the ram or anti-ram vector to be on the right side of the spacecraft, the spacecraft would roll about its thrust vector and position solar array A to face the right direction. When the Sun again crossed the ram or anti-ram vector during the multi-week burns, the spacecraft would roll the opposite direction as to conserve angular momentum in the roll reaction wheel.

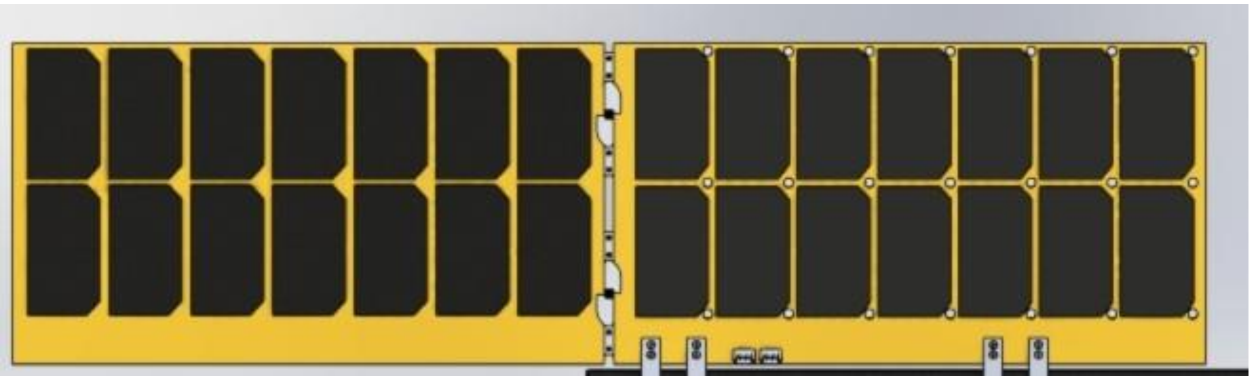

Figure 82: Solar Array A, Deployed Configuration

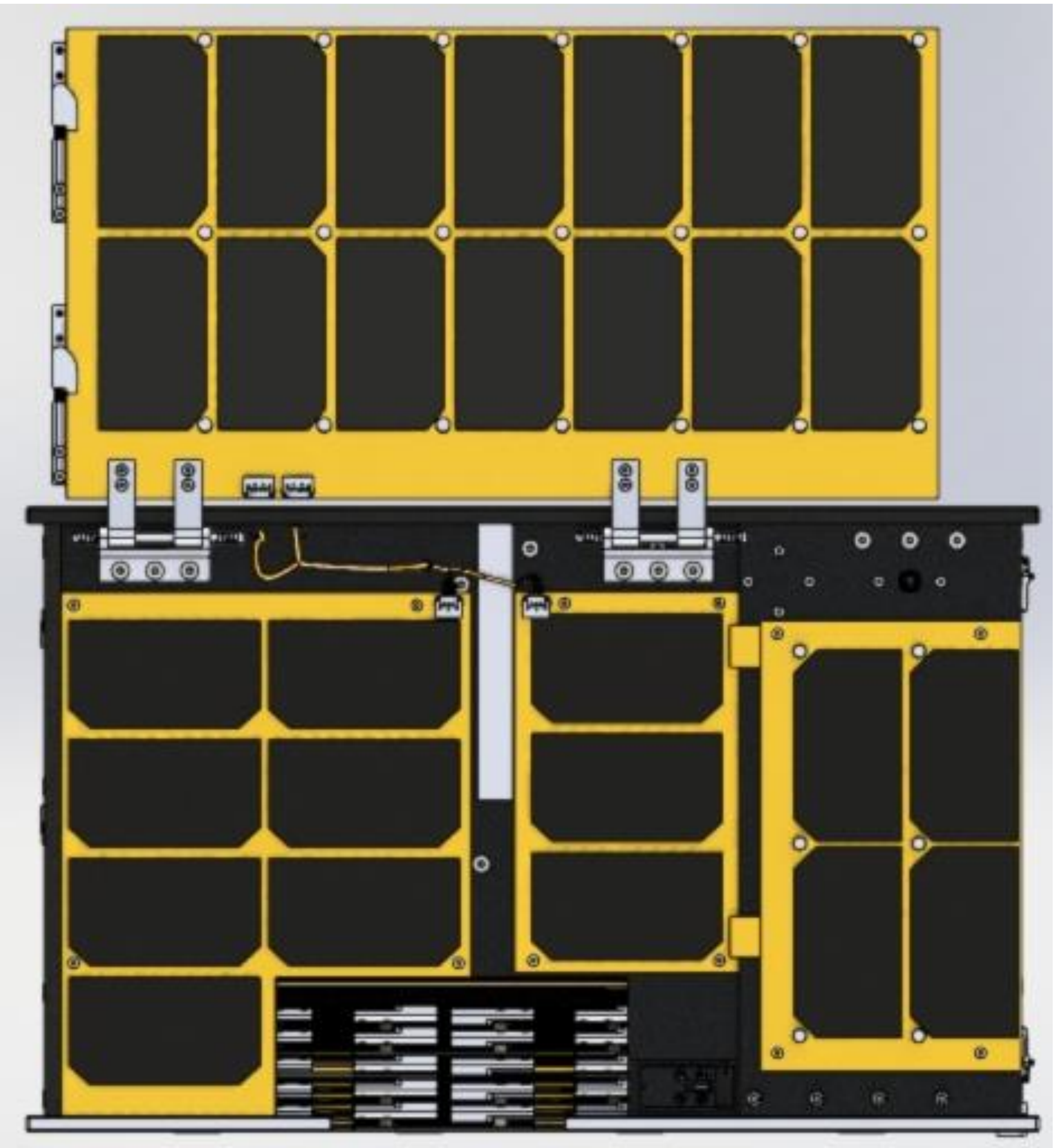

Figure 83: Body-Mounted Panels with Right Side of Solar Array A Deployed

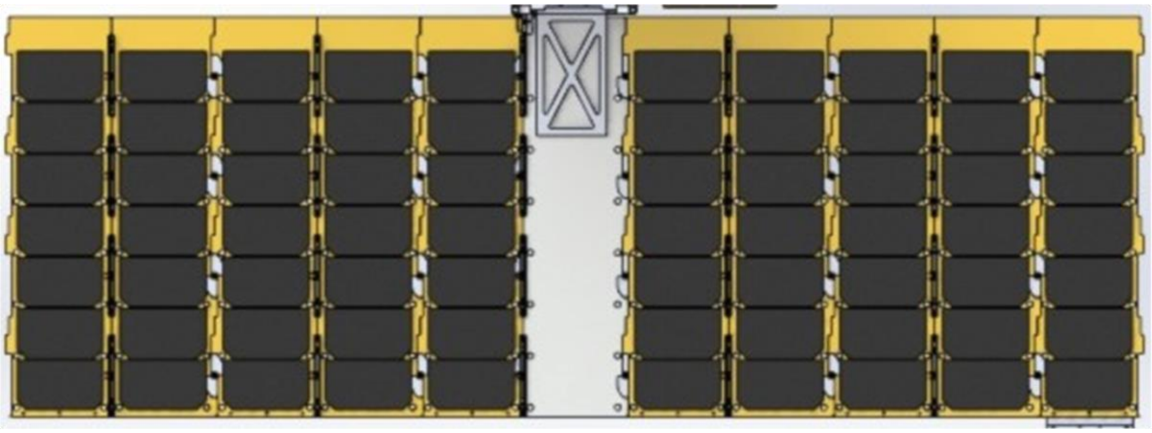

Figure 84: Solar Array B, Deployed Configuration

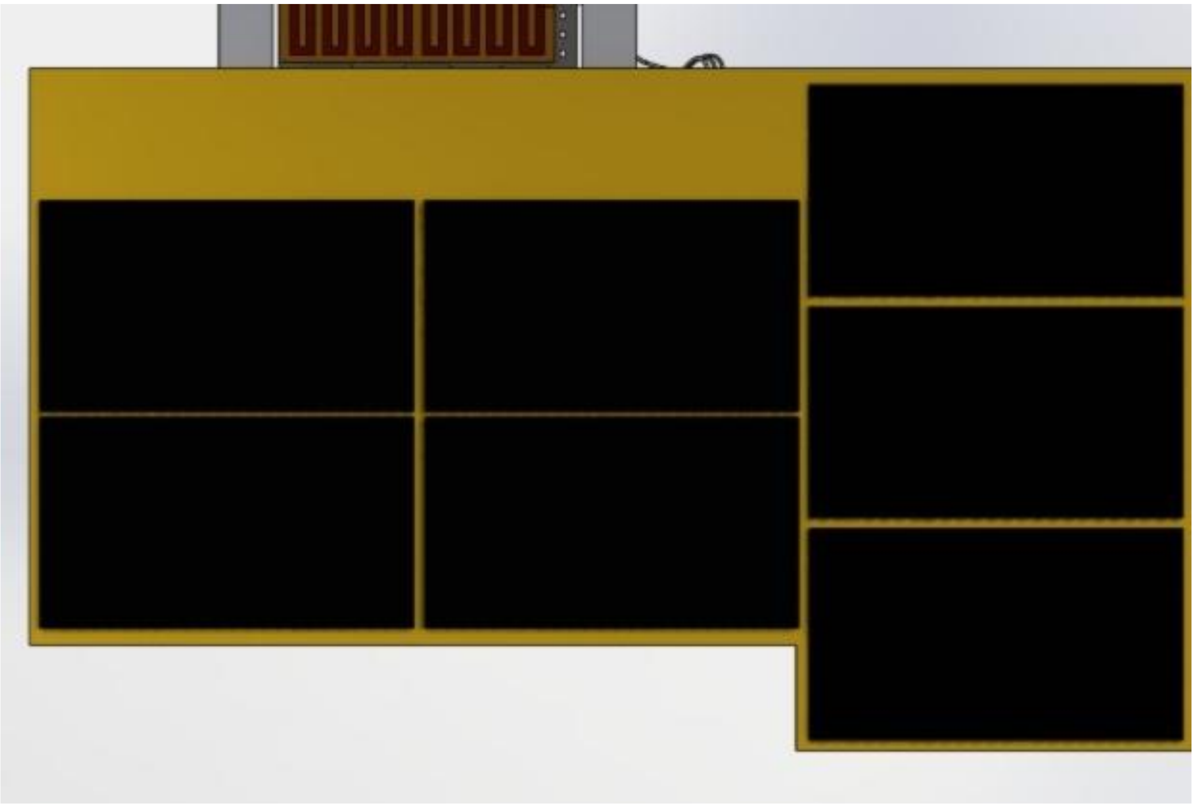

Figure 85: Solar Array C, Deployed Configuration

When the Sun was near the ram or anti-ram vector, solar array B would be the primary power generation array. When the Sun was orthogonal to the ram or anti-ram vector, solar array A would be the primary power generation array. Power generation per solar array per angle of incidence is shown in **Figure 86**. The dotted green, yellow, and red lines represent power consumption estimates, described later. Solar irradiance is considered 1366 W/m^2, BOL cell efficiency is 0.322, and absorptivity is assumed to be 0.85. Titles B2 and C2 refer to the back side of a double-sided solar array.

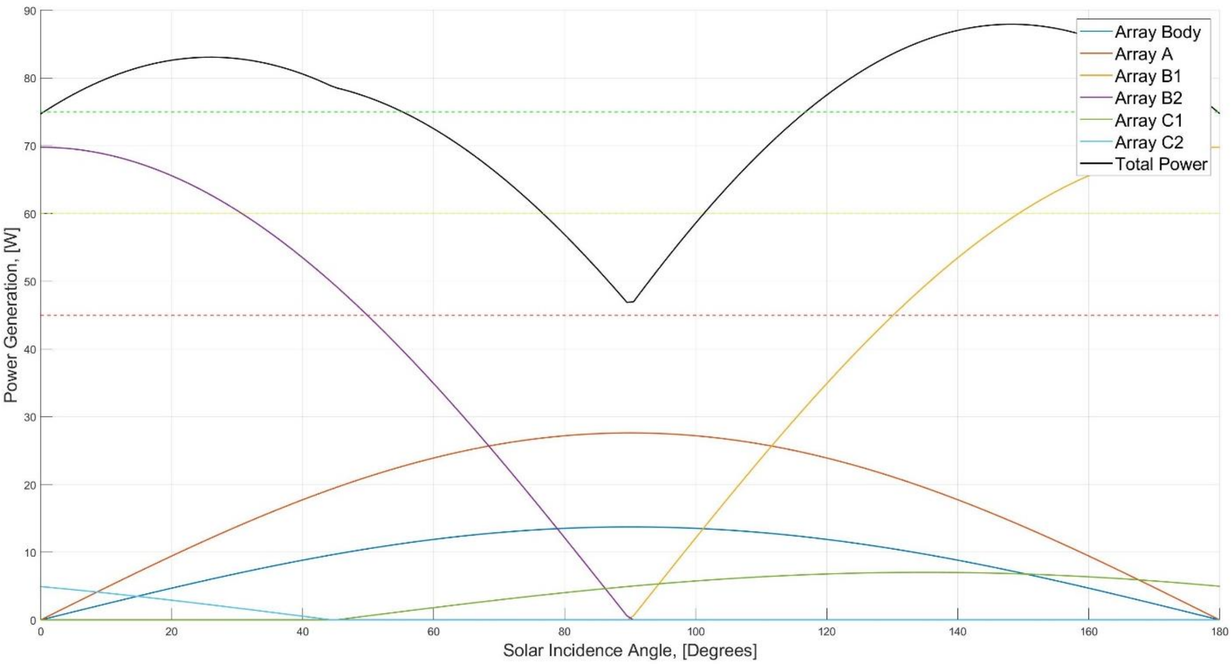

Figure 86: Power Generation Per Solar Array Per Solar Angle of Incidence

Solar array C has a different deployment mechanism than solar arrays A and B and does little for power generation. It is included to prove the capabilities of an SMA hinge rather than generate power. As seen in **Figure 86** it does not provide much for the satellite. The solar cell areas of each solar array are provided in **Table 31**. A rough estimation of usable solar cell area is 85% of the total array area, but higher percentages can be attained.

Table 31: Solar Array Areas

Solar Array	Area, [cm^2]	Note
A	742.56	-
B	1876.70	One side of B only
C	189.00	One side of C only
Body	369.32	Sum of 3 sections
Total	2988.58	One side of B, C only

3.5.2.2 Power Generation Calculations

Once an assumed area, orbital distance to the Sun, and solar cell have been identified, it is possible to estimate how much power a solar array will generate. Advanced programs exist such as STK [32] or the Princeton Satellite Systems CubeSat Toolbox for MATLAB [103] that can perform a wide variety of CubeSat calculations including power estimations for a given geometry, but those engineering suites can be cost-prohibitive for low-budget programs. **Eq.(82)** provides a method to calculate the power generation in watts of a single solar array without regard for the AOI. Highly conservative power calculations may apply a margin here, but further margins will be applied later.

$$Q_{array} = Q''_{solar} \cdot \eta_{cell} \cdot \alpha_{cell} \cdot \varphi_{temp} \cdot A_{array}$$

Eq.(82)

Q''_{solar} represents the incoming solar radiation determined by **Eq.(12)**, η_{cell} is the solar cell efficiency, α_{cell} is the absorptivity of the cell surface material, φ_{temp} is the temperature dependence coefficient of the solar cell circuitry, and A_{array} is the cumulative area of the solar cells on a given array. The solar cell efficiency, radiation absorptivity, and temperature dependence are dependent upon the specific cell used, but they are estimated at 0.322, 0.85, and 0.88 [91]. The temperature dependence factor, not included in **Figure 86**, is not always far from unity, but in extreme hot or cold environments 0.88 is possible. The value of 0.88 should be included for a conservative measure, and a solar cell distributor should be able to provide technology-specific values. The calculation of **Eq.(82)** to solar array B of AEGIS is shown in **Eq.(83)**.

$$Q_{array} = \left(1366\ \frac{W}{m^2}\right) \cdot (0.322) \cdot (0.85) \cdot (0.88) \cdot (1876.7\ cm^2) \cdot \left(\frac{0.0001 m^2}{1\ cm^2}\right) = 61.7\ W \qquad \textbf{Eq.(83)}$$

To account for AOI, a simple MATLAB script can be applied. The key is to define a coordinate system for the Sun and solar arrays to be defined within. **Eq.(84)** provides the MATLAB calculation; the subplus function is a toolbox add-on and not inherent to MATLAB. The parameter θ is the AOI defined in radians, and the parameter θ_{array} is the orthogonal angle of the solar array mounted to the spacecraft in degrees. The variation of degrees and radians is for script readability and is not required, and 90 degrees may need to be subtracted from θ_{array} depending on how the coordinate system is defined. **Eq.(84)** was used to create **Figure 86** for all arrays. It should be noted that in Section 3.3.5 AOI was defined with 0° being normal to the surface and here and in **Figure 86**, 90° represents that case.

$$Q_{array,AOI} = Q_{array} * subplus\{\sin[abs(\theta) - deg2rad(\theta_{array})]\} \qquad \textbf{Eq.(84)}$$

3.5.2.3 Solar Array Circuitry

The way a solar array is wired can have a significant effect on Size, Weight, and Power (SWaP) considerations as well as operations. One unnamed German CubeSat wired its solar arrays in a configuration that included a distinct, unmitigated loop structure. When the spacecraft began to draw power from the arrays while inside the magnetosphere, an inductive torque caused the spacecraft to tumble indefinitely, reaching a maximum angular velocity of 527 degrees per second. Proper solar array circuitry can make or break a program.

The target design for solar arrays should be a functional system of required size that, except for the power transmission cable from array to CubeSat, should not feature any external or internal wires. Solar arrays are made of strengthened PCBs with CICs mounted to the surface. The electrical terminals from the CICs connect to copper traces inside the PCB layers, and the PCB substrate class for solar arrays is FR4. Hinges connecting the CubeSat to the solar arrays are known as primary or body mounted hinges, and hinges connecting an array panel to an array panel are known as secondary or winglet hinges. Neither commonly feature locking mechanisms; the arrays are assumed to stay deployed due to the springs in the hinges. Traces in the FR4 may carry up to 4-6 A for large arrays with many CICs in series, and power across secondary hinges are not carried in distinct wires or traces. The power is transferred directly through the springs of the secondary hinges themselves, and no additional wiring exists to transfer power. An image of Pumpkin's winglet hinges on solar array B of AEGIS is shown in **Figure 87**.

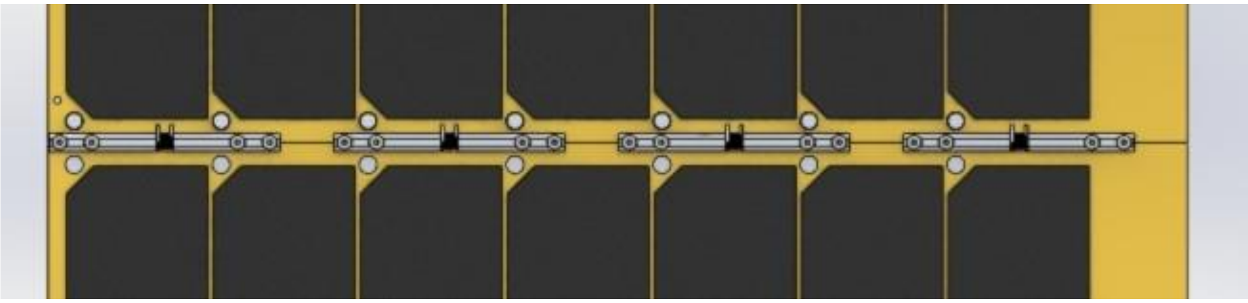

Figure 87: Power-Transferring Winglet Hinges from Pumpkin, Used with Permission

A minimum of two secondary hinges are required, but four are included for redundancy and nominal current reduction purposes. The two secondary hinges on the right are the positive current transfer lines, and the two on the left are the negatives. In this sense, it is not logical to include an odd number of secondary array hinges. The positive and negative sides should be chosen such that loop structures are avoided, though deep space CubeSats are not as concerned with magnetic induction torque effects.

3.5.3 Power Distribution

Power distribution is the simplest category between generation, distribution, and consumption. Distribution refers to the line losses and margin applications between the solar arrays, EPS, and components. A margin of 10% is applied, and an efficiency for diodes and line losses is applied. Some EPS vendors report that their diode and line loss efficiency is 99%, but all vendor data sheets must be taken with a grain of salt. Overestimating margins and losses will result in a system that generates more power than necessary at all AOIs. Solar array circuitry can be disconnected from the EPS at will to prevent overcharging but generating insufficient power while on-orbit is a much worse problem. The calculation for applying distribution margins and losses to a single solar array without AOI considerations is shown in **Eq.(85)**. Diode and line loss efficiency is estimated at 90%. It should be noted that the closer the solar arrays are to the EPS, the lower the line losses will be.

$$Q_{dist} = Q_{array} \cdot M_{dist} \cdot \eta_{diode+line} \quad \textbf{Eq.(85)}$$

M_{dist} represents the 10% margin as 0.9, and $\eta_{diode+line}$ represents the 90% diode and line loss efficiency also as 0.9. **Eq.(85)** is applied to the maximum and minimum power generations calculations from **Figure 86** in **Eqs.(86-87)** as an example; this calculation is intended for the full power generated by all solar arrays instead of one specific array.

$$Q_{dist,min} = (47.14\ W) \cdot (0.9) \cdot (0.9) = 38.13\ W \quad \textbf{Eq.(86)}$$

$$Q_{dist,max} = (88.42\ W) \cdot (0.9) \cdot (0.9) = 71.62\ W \quad \textbf{Eq.(87)}$$

3.5.4 Power Consumption

Consumption is where the PCEs of the EPS and components are applied. In the early stages of design, when Interface Control Documents (ICD) for components have not been attained because formal component selection or NDA signing has not occurred, PCEs for specific components may not be available. To make up for this, designers should underestimate the PCE of the EPS and apply additional margins to the calculations. When PCEs for components are available and mission ConOps can be related to duty cycles, more detailed analyses can be performed.

3.5.4.1 Software State Variation

Component power consumption must be summed per software state to determine the state in which the maximum power draw will occur. A power consumption table that corresponds to the software states described in Section 2.4 is shown in **Table 32**. As duty cycles are not able to be prescribed early in the design process, high, nominal, and low power values for each component are defined, and software states are related to component usage and power tranches. The power consumption summations shown in the row third from the bottom of **Table 32** are summations of selected AEGIS component power draws and represent a real spacecraft power budget. The special case under RW Desaturation indicates a potentially variable power supply to the thruster used during TVC, but the software state with the highest power requirement is the burn state at 69.46 watts. Five watts were assumed for power provided to patch heaters in the thermal category, but this value may differ significantly depending on the orbit and mission. According to **Figure 62**, five watts is likely a gross underestimation for a deep space mission.

Table 32: AEGIS Software State Power Consumption Breakdown. H = High Power Draw, N = Nominal Power Draw, L = Low Power Draw, S = Special Case, O = Off

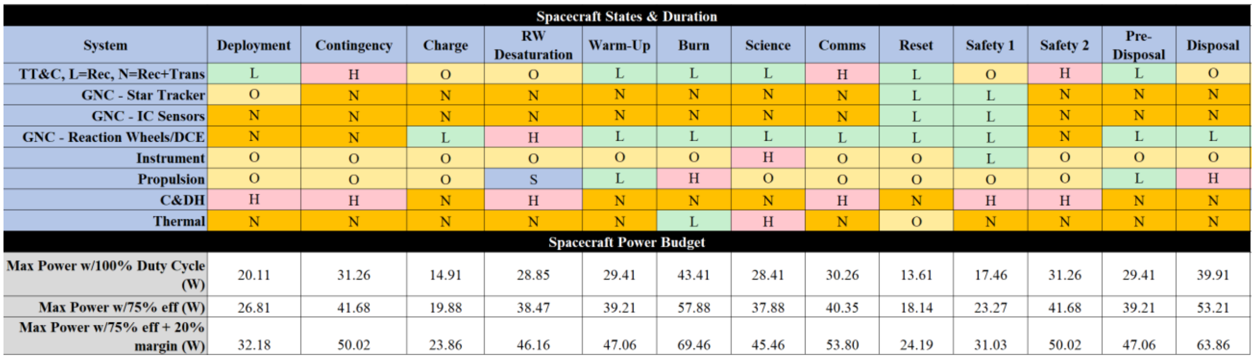

Spacecraft States & Duration													
System	Deployment	Contingency	Charge	RW Desaturation	Warm-Up	Burn	Science	Comms	Reset	Safety 1	Safety 2	Pre-Disposal	Disposal
TT&C, L=Rec, N=Rec+Trans	L	H	O	O	L	L	L	H	L	O	H	L	O
GNC - Star Tracker	O	N	N	N	N	N	N	N	L	L	N	N	N
GNC - IC Sensors	N	N	N	N	N	N	N	N	L	L	N	N	N
GNC - Reaction Wheels/DCE	N	N	L	H	L	L	L	L	L	L	N	L	L
Instrument	O	O	O	O	O	O	H	O	O	L	O	O	O
Propulsion	O	O	O	S	L	H	O	O	O	O	O	L	H
C&DH	H	H	N	H	N	N	N	H	N	H	H	N	N
Thermal	N	N	N	N	N	L	H	N	O	N	N	N	N
Spacecraft Power Budget													
Max Power w/100% Duty Cycle (W)	20.11	31.26	14.91	28.85	29.41	43.41	28.41	30.26	13.61	17.46	31.26	29.41	39.91
Max Power w/75% eff (W)	26.81	41.68	19.88	38.47	39.21	57.88	37.88	40.35	18.14	23.27	41.68	39.21	53.21
Max Power w/75% eff + 20% margin (W)	32.18	50.02	23.86	46.16	47.06	69.46	45.46	53.80	24.19	31.03	50.02	47.06	63.86

A major difference between generation and distribution versus consumption is that margins and efficiencies for generation and distribution are applied to reduce the amount of power provided to the satellite while the margin for consumption $M_{consumption}$ is applied to increase the amount of power required by the components. Therefore, the power consumption wattage should be divided by the EPS efficiency η_{EPS} rather than multiplied. This is shown in **Eq.(88)**, where the bottom row of **Table 32** corresponds to the output of **Eq.(88)**.

$$Q_{consumption} = \left(\frac{\sum Q_{component}}{\eta_{EPS}}\right) \cdot M_{consumption} \qquad \textbf{Eq.(88)}$$

The application of the consumption values for the software state with the highest power draw corresponding to **Eq.(88)** are shown in **Eq.(89)**, matching the values shown in **Table 32**. The red line in **Figure 86** denotes 45 W as a worst-case power production value over the 43.41 W consumption of burn state without margins. The yellow line represents 60 W over the 57.88 W value, and the green line represents 75 W over the value calculated in **Eq.(89)**.

$$Q_{consumption} = \left(\frac{43.41\ watts}{0.75}\right) \cdot 1.2 = 69.456\ watts \qquad \textbf{Eq.(89)}$$

3.5.4.2 Power Comparison with AOI

With considerations for power generation, distribution, and consumption defined, the worst-case power consumption software state can be compared against power generation values at a variety of AOIs in conjunction with power distribution values. The power generated and distributed across seven solar incidence values are shown in **Table 33** and compared to power consumption values to provide margins for power-positivity during the burn phase. All solar arrays are included per **Figure 86** but with worst-case temperature dependence of solar cells applied for generation, a 10% margin and line losses are included for distribution, and a component efficiency of 75% plus a 20% margin is applied for consumption.

Table 33: Comparison of Power Generation Values to Distribution and Consumption Values for Varied AOI

AOI, [deg]	**0**	**30**	**60**	**90**	**120**	**150**	**180**
Power Generated, [W]	66.10	73.39	64.50	41.48	68.34	77.77	66.14
Power Distributed, [W]	53.54	59.45	52.24	33.60	55.36	62.34	53.58
Burn Power Consumed w/Margin, [W]	69.46						
Excess Power w/Margin, [W]	-15.92	-10.01	-17.22	-35.86	-14.1	-7.12	-15.88
Burn Power Consumed w/o Margin, [W]	57.88						
Excess Power w/o Margin, [W]	-4.54	1.57	-5.64	-24.28	-2.52	5.46	-4.30

Evident from **Table 33** is that margins applied to solar power collection, distribution, and consumption rapidly add up to potentially unattainable power requirements, and this is for a relatively benign thermal power requirement estimate. It is at this point where designers would convene to discuss opportunities to either add more solar arrays, specifically to the body array or array A to improve generation near 90 deg AOI, or reduce power consumption via component downselect. According to **Figures 86**, the lossless power generation values range from 47.14 W to 88.42 W and the maximum lossless power consumption value is 43.41 W. It may be that the satellite is realistically power-positive even at 90 deg AOI, but unless it can be proven with margins and losses included, the system design must be improved before CDR.

3.5.4.3 Estimating Solar Cell Count

With the maximum power consumption state defined, it is possible to estimate the number of solar cells once eclipse time has been determined. Eclipse time calculations are dependent on orbital assumptions, and equations may be found in [104], chapter 8 of [33], or **Eq.(19)** if calculating via beta angle. A simple solar power generation requirement based on worst-case consumption and eclipse time factors is shown in **Eq.(90)**, where $\mathrm{t_{eclipse}}$ divided by $\mathrm{t_{orbit}}$ represents the fraction of time spent in eclipse. Burn may not always be the worst-case power draw state.

$$P_{min} = P_{burn} + \frac{P_{burn} \cdot t_{eclipse}}{t_{orbit}} \qquad \textbf{Eq.(90)}$$

Applying the burn power consumption value and an assumed eclipse time of 1 hour to **Eq.(99)** yields,

$$P_{min} = 69.46 \text{ watts} + \frac{(69.46 \text{ watts}) \cdot (1 \; hour)}{24 \text{ hours}} = 72.35 \; watts \qquad \textbf{Eq.(91)}$$

Dividing the watts calculated by **Eq.(91)** by the flux calculated in **Eq.(82)** without array area included, a required area can be defined.

$$A_{cell,req} = \frac{P_{min}}{Q''_{solar} \cdot \eta_{cell} \cdot \rho_{abs} \cdot \varphi_{temp}} = \frac{72.35 \; watts}{\left(1366 \frac{W}{m^2}\right) \cdot (0.322) \cdot (0.85) \cdot (0.88)} = 0.22 \; m^2 \qquad \textbf{Eq.(92)}$$

Dividing the value calculated by **Eq.(92)** by the area of the assumed solar cell will yield the number of cells required to accomplish the power needs of the mission. Spectrolab's rectangular XTE-SF cells are 3.97 cm x 6.91 cm.

$$Cell\ \# = \frac{A_{cell,req}}{A_{cell}} = \frac{0.22\ m^2}{0.00274327\ m^2} = 80.196\ cells\ \rightarrow 81\ cells \qquad \textbf{Eq.(93)}$$

3.5.5 Battery Considerations

Lithium-ion including Lithium-polymer has emerged as the premier candidate for battery type selection. Nickel Metal Hydride (NiMH) batteries have been used since the 1970s, but they exhibit self-discharging, enhanced degradation, and Li-ion batteries can charge and discharge more quickly than NiMH. Nickel-Cadmium (NiCd or "Nigh-Cad") batteries display a memory effect, where, if they are not completely discharged before recharging, they will lose charge capacity and efficiency, which is a difficult limitation for satellites to overcome. Lithium does have health hazard considerations, but with proper battery storage and handling these hazards are miniscule compared to the operational benefits.

3.5.5.1 The 18650 Li-Ion Battery

The Li-ion battery type most employed by CubeSats is the 18650 Li-ion battery, and NASA both requires this battery type for Artemis secondary payloads and provides the batteries to selected programs. The 18650 dictates a battery size of 65 mm in length and 18 mm in diameter. Other Li-ion sizes include 21700 (74 mm x 21.4 mm) and 14500 (50 mm x 14 mm). The 18650s can either be protected or unprotected, with protected meaning a circuit is included in the battery casing to prevent overcharging, overdischarging, and thermal runaway. The batteries provided by NASA are rated at 10 W-hr, and 18650s, which are 3.635 V batteries, are generally rated for at least 2 amp-hours [105]. Cycles for 18650s vary from a minimum of 300 cycles to a maximum of 2000 cycles, and there are noticeable signs of battery degradation which can be included in PHM downlink telemetry. Per one NASA SME, 18650s display 5% of output power as ohmic heating during charging and 9% of output power during discharging which can be considered part of the losses inherent to power generation. The battery has likely experienced degradation if the temperature during charging or discharging is higher than it was at the beginning of its lifespan, which can be modeled by those 5% and 9% values in a given battery housing or EPS. If the battery refuses to charge over 80% of its original capacity or recharge times, about four hours dependent on available energy and battery capacity, are much longer than anticipated, the battery is likely degraded. A list of LG's MJ1 18650 Li-ion battery characteristics is shown in **Table 34.** As a variety of ion configurations exist for Li-ion (cobalt, manganese, nickel), specific ion considerations will not be discussed. Work has been done to include graphene in Li-ion batteries to reduce mechanical stress-induced degradation [106].

Table 34: LG MJ1 18650 Li-ion Battery Specifications [105]

Parameter	Value	Unit
Mass	49.0	g
Max Surface Area	4170.07	mm^2
Max Charge Voltage	4.2 ± 0.05	V
Nominal Voltage	3.635	V
Energy	Nominal 3500 Minimum 3400	mA-hr
Max Charge Current	3400	mA
Standard Discharge	680	mA
End Voltage (Cut off)	2.5	V
Max Discharge Current	10	A
Theoretical Capacity	12.723	W-hr
Assumed/Rated Capacity by NASA	10	W-hr

A fatal flaw exists with some COTS EPS options: if one battery in the battery pack because faulty, the entire energy storage capability becomes defunct. All batteries must be assumed to be defunct, and component power must bypass the energy storage circuitry and receive power directly from the solar panels. Functionally, it is possible for nearly all COTS EPS solutions to bypass the energy storage faculties to power components directly, but the satellite will be forced to power down if the power draw exceeds the power generation. The satellite will have no choice but to continually reset itself until the solar cells generate enough power for the system to remain power positive.

3.5.5.2 Estimating Required Battery Capacity

Batteries must be able to supply power demands when power generation is insufficient to meet power consumption, a condition informally referred to as power negativity. The most common time when battery power is required is during eclipse time, and the eclipse time calculations introduced in Section 3.3.4 and 3.5.4.3 are continued here. As in power generation, distribution, and consumption, margins are applied, and some battery degradation is assumed. Across all conservative margins and estimates applied in Section 3.5, the only non-conservative parameter that assumes BOL instead of EOL is the 32.2% efficiency of the solar cells which is viable if the maximum power demand occurs during BOL. Solar radiation's effect on solar cell efficiency is discussed in Section 4.5.4. Assuming the same 1-hour eclipse time, a 20% safety margin, and a 25% degradation factor, a conservative battery capacity estimate $C_{battery}$ may be calculated in **Eq.(94)**. Note the burn power draw is $\mathrm{P_{burn}}$, not $\mathrm{P_{min}}$.

$$C_{battery} = P_{burn} \cdot t_{eclipse} \cdot M_{battery} \cdot \varphi_{degredation} \quad \textbf{Eq.(94)}$$

$$C_{battery} = (69.46 \text{ watts}) \cdot (1 \text{ hour}) \cdot (1.2) \cdot (1.25) = 104.19\ W \cdot hr \quad \textbf{Eq.(95)}$$

The EPS II from EnduroSat selected by AEGIS features eight 18650 batteries for a nominal estimate of 80 W-hr battery capacity. Without the degradation factor included, **Eq.(95)** becomes **Eq.(96).**

$$C_{battery} = (69.46 \text{ watts}) \cdot (1 \text{ hour}) \cdot (1.2) = 83.35\ W \cdot hr \quad \textbf{Eq.(96)}$$

There are several problems here. Only 70% of battery capacity is assumed usable in practice. The bottom 10-20% of capacity is reserved for safety operations, and it is assumed the battery would only charge to 80-90% after any degradation. The highest power draw phase is burn, and burn occurs at the beginning of life where no battery degradation is anticipated. Not having enough battery capacity during eclipsed high-power draws represents a risk to the spacecraft, and further research into the eclipse time, burn power draw, usable battery capacity, and useful margin is warranted.

It is possible the 3.35 W-hr deficiency in battery capacity before considering 70% usability is enough to warrant a design change but bringing more than eight batteries represents a huge shift in EPS selection and internal configuration. At a certain point, spacecraft designers are forced to draw a line in the sand and say, "This is the level of risk we are willing to accept," and this decision would have to be thoroughly characterized before CDR. The eight batteries would be configured in four rows of two in series, also known as 2s4p. Other viable series and parallel battery configurations exist.

3.5.6 Maximum Power Point Trackers

A Maximum Power Point Tracker (MPPT) is a DC-DC converter that converts the output voltage from the solar panels to a voltage that maximizes the amps provided to the batteries. Solar panels feature variable output voltages depending on the circuitry and cell temperature, and batteries do not appreciate this variability. MPPTs take a DC input from solar panels, change it to high-frequency AC, transform the AC signal, rectify the AC signal back to a DC signal, and then regulate the final DC output. Note that both the solar cells and power rails require DC-DC converters between the battery and the arrays/components, shown in **Figure 81**, but MPPTs as DC-DC converters are not performing voltage regulation at the load side.

Photovoltaic (PV) cells are connected both in parallel and in series, and the number of PV cells in series and parallel for each panel should not exceed the MPPT converter ratings in voltage, current, and power. The required number of panels must also be able to fit within the available array area. PV cells that utilize a common MPPT must be oriented in the same plane and should experience no partial shading. Dual sided panels can utilize a common MPPT if a diode is included that selects the side facing the Sun. Because the PV array configuration is interrelated to and dependent on the MPPT configuration, careful attention must be paid to the selection of an EPS that will fulfill power generation requirements, and a decoupling of PV cell and MPPT configurations is not possible.

3.5.6.1 MPPT Parameter Case Study

The EnduroSat EPS II will be considered as a case study to prove the viability of a solar array design to an EPS under consideration for trade and selection. An initial overview of the EPS II is provided in **Table 35**.

Table 35: EnduroSat EPS II Parameter Overview [107]

Parameter	Value	Unit
Number of MPPT Channels	3	N/A
MPPT Current Rating	4	A
MPPT Voltage Range	10-36	V
Voltage Output Rails	3.3 (x2), 5 (x2), 12	V
Output Current Rating	6 per Channel	A
Cost	33,500	$

The values presented in **Table 35** are threshold values, and margins should be applied as always. **Table 36** relates the initial electrical parameters to margins for use in MPPT analysis.

Table 36: EnduroSat EPS II Input Ratings [107]

Parameter	Unit	0% Margin	15% Margin	20% Margin
Max Voltage	V	36.00	31.30	30.30
Min Voltage	V	10.00	11.50	12.00
Rated Current	A	4.00	3.48	3.33
Rated Power	W	144.00	125.22	120.00

As MPPTs are directly related to and limited by PV operations, it is important to remember the PV voltage and current relationships shown in **Figure 88**.

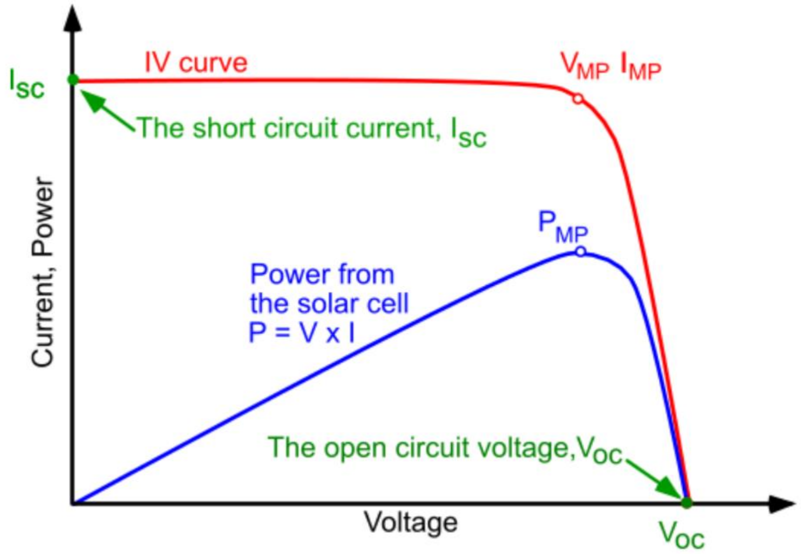

Figure 88: Photovoltaic Power and Current vs. Voltage [108]

The open circuit voltage represents the highest voltage experienced by the cells and can be used to determine the conservative maximum number of cells that can be connected in series. The short circuit current can similarly be used for estimating the conservative number of cells connected in parallel. These values would never occur at the same time and should not be used for maximum power estimations. Performing the calculations for short and open conditions as well as Maximum Power (MP) values is warranted. For the Spectrolab XTE-SF CICs used in previous calculations, the short circuit current per cell area, open circuit voltage, and maximum power values correlating to **Figure 88** are provided in **Table 37**.

Table 37: Spectrolab XTE-SF Post 1 MeV e- Retention (US Standard AIAA S-111-2005) [91]

Parameter	Value	Unit
$V_{OC,cell}$	2.750	V
$I_{SC,cell}$	0.0186	A/cm^2
$V_{MP,cell}$	2.435	V
$I_{MP,cell}$	0.0179	A/cm^2

To find the maximum number of cells configured in series, the maximum MPPT voltage is divided by the open circuit voltage, shown in **Eq.(97)**. The following calculations are performed for 0% margin.

$$N_{cells,series,max} = \frac{V_{max,MPPT}}{V_{OC,cell}} = \frac{36\ V}{2.750\ V} = 13.09 \rightarrow 13\ cells$$ **Eq.(97)**

The minimum number of cells configured in series must also be calculated using a minimum voltage, as CICs feature a voltage below which they will not generate electricity. An assumed minimum voltage of 1.5 V is applied.

$$N_{cells,series,min} = \frac{V_{min,MPPT}}{V_{min,cell}} = \frac{10\ V}{1.5\ V} = 6.66 \rightarrow 7\ cells$$ **Eq.(98)**

To determine the maximum number of cells configured in parallel, the short circuit current areal density, I_{SC}, is multiplied by the area of the cell to find the current per cell, and the maximum current rating of the MPPT is divided by the calculated amperage per cell. A rectangular cell of 3.97 cm x 6.91 cm is used.

$$N_{cells,parallel,max} = \frac{I_{max,MPPT}}{I_{SC,cell} \cdot A_{cell}} = \frac{4\ A}{\left(0.0186 \frac{A}{cm^2}\right) \cdot [(3.97\ cm) \cdot (6.91\ cm)]} = 7.84 \rightarrow 7\ cells \qquad \textbf{Eq.(99)}$$

Because all loads in series receive the same current and all loads in parallel receive the same voltage, the maximum total cells for an MPPT input channel is the maximum number of cells in parallel multiplied by the maximum number of cells in series. The values are tabulated for all margins in **Table 38**.

Table 38: EnduroSat EPS II Ratings Per MPPT Input Channel

Parameter	0% Margin	15% Margin	20% Margin
Max Cells in Series	13	11	11
Min Cells in Series	7	8	8
Max Cells in Parallel	7	6	6
Max Total Cells	91	66	66

As a quick sanity check, the maximum power voltage can be multiplied by the maximum power current per cell to find how much power is generated per cell, and that value can be multiplied by the maximum number of total cells for comparison against the rated power of the MPPT channel.

$$I_{MP,cell} \cdot A_{cell} \cdot V_{MP,cell} \cdot N_{cell,total}$$

$$= \left(0.0179 \frac{A}{cm^2}\right) \cdot [(3.97\ cm) \cdot (6.91\ cm)] \cdot (2.435\ V) \cdot (91\ cells) = 108.8\ W \qquad \textbf{Eq.(100)}$$

The calculated wattage of 108.8 W is less than the maximum wattage of 144 W, and all calculations were performed with conservative current and voltage values.

3.5.6.2 Applying MPPT Values to a Design

The maximum number of solar cells in series and parallel configurations have been calculated for a given EPS, but it is important to qualify a physical array design per the MPPT input channel ratings. Array cell configurations must be consistent across the entire system for a given MPPT. For example, both array A and the body panels on AEGIS are connected to the same MPPT by combining their power inputs in a PCB. The connections are shown in **Figure 83**. Array A features 14 cells per array panel with two panels for a total of 28 cells, and those cells are together connected in 7s4p. Array A could not have one panel with 7s2p and another in 14s1p because a current mismatch would exist when combining the power outputs of the panels. The three body panels, combined electrically as one output, must also then have the same cell configurations, and the 14 total body cells are combined in 7s2p. Array A's output of 7s4p and the body array's output of 7s2p are combined in the AB PCB, and an output of 7s6p is provided to the MPPT. Note that 7 cells in series combined in 6 parallel sets fits within the EPS parameters according to **Table 38**.

Solar array B features many more cells than array A. The central panel of the 11-panel array is strictly for structural integrity and signal routing. The five panels on either side of the central panel feature 7 cells each, and the total configuration would be 7s10p. There are cells on both sides of arrays B and C, but only one will be illuminated at a time. A diode can be included near the array power terminal so that a single MPPT may be connected to both sides of an array and only draw power from one side at a time. Array C features 7 cells on each side of a single panel for a 7s1p configuration per side.

Consider **Eqs.(101-103)** for the maximum voltage, current, and power of a PV system for a given configuration.

$$V_{max} = V_{OC,cell} \cdot N_{cells,series} \tag{101}$$

$$I_{max} = I_{SC,cell} \cdot A_{cell} \cdot N_{cells,parallel} \tag{102}$$

$$P_{max} = V_{MP,cell} \cdot I_{MP,cell} \cdot A_{cell} \cdot N_{cells,total} \tag{103}$$

These are used in the overall solar array qualification estimate found in **Table 39**. Note that cell counts only include a single side of the double-sided arrays and $P_{max} \neq V_{max} \cdot I_{max}$.

Table 39: PV Configuration MPPT Calculations

MPPT	# Cells, Series	# Cells, Parallel	# Cells, Total	V_{max}, [V]	I_{max}, [A]	P_{max}, [W]
Array A + Body	7	6	42	19.25	3.06	50.22
Array B	7	10	70	19.25	5.10	83.70
Array C	7	1	7	19.25	0.51	8.37

Looking back to **Table 35**, the maximum input voltage for the EPS II is 36 V while the maximum input amperage is only 4 A. Array B's maximum amperage is 5.1 A not including in-rush spikes. This means the qualification of solar array B fails, and some method of decreasing the input current must be utilized. From an FR4 trace circuitry standpoint it is not feasible to simply switch the parallel and series designations to a 10s7p configuration; cells on a panel like array B must be in series. The only option would be to change the EPS selection or add another EPS module with more MPPTs onto the battery pack and original EPS stack. This functionality is not currently available with the EPS II, but advanced features are expected in the early 2020s.

3.6 Telemetry, Tracking, and Command

Written with assistance from Dr. Saeed Latif, University of South Alabama.

The Telemetry, Tracking, and Command subsystem consists of the radio, one or more antennae, the radio to antenna interface, and the OBC to radio interface. Design Objectives have been defined based on functionality for evaluation and comparison. The goals of a robust TT&C subsystem are reasonable downlink speeds for payload data transfer, low power consumption, flexible transmit opportunities, reliability, and reasonable cost. At the time of writing, options for CubeSat deep space communication are severely limited. Error Detection and Correction and Error Correcting Codes are covered under the scope of radiative effect prevention in Section 4.3.3.

3.6.1 TT&C Design Objectives

Table 40: Telemetry, Tracking, and Command Subsystem Design Objectives, Adapted from [28]

Design Objective	Description	Rationale	Actionable Items
Communication Functionality (**COMM-1**)	A functional transceiver and antennas for two-way communication must be present.	Without TT&C the location of the CubeSat will not be known. The radio will be used for ranging as well.	Antennas are to be developed to be used with the radio. The DSN is currently considered for space-ground communication. A backup ground station is to be found.
Payload Data Transfer (**COMM-2**)	A robust downlink communication is required to download experimental data to the ground. Reasonable downlink speeds required.	Science data must be downloaded from the CubeSat to call the mission successful.	High gain patch antennas to be developed and tested.
Communication Redundancy (**COMM-3**)	Two bands, namely S- and X-bands are considered for redundancy purposes.	If one band of operation fails, the CubeSat can be tracked by the other communication link.	S-band antenna will be integrated with X-band patch antenna array for the redundant link.

3.6.2 Bandwidths and Frequency Selection

The bandwidth of a signal is the difference between the signal's high and low frequencies on the electromagnetic spectrum. The total range of frequencies is known as the spectrum, and the spectrum is divided into frequency bands consisting of bandwidth ranges.

3.6.2.1 Historical Bandwidth Divisions

Common spacecraft bandwidths range from the Ultra High Frequency (UHF), 300 to 3000 MHz, to the Extremely High Frequency (EHF), 30 to 300 GHz, but the "Radio Spectrum" is considered to be 3 KHz to 3000 GHz [109]. These bands are further divided into specific frequency ranges. For example, the L-band uses frequencies in the 1 to 2 GHz range, the Ku-band uses frequencies around the 12 to 18 GHz band, and the Ka-band uses the 26.5 to 40 GHz range. Which band a satellite should utilize is highly dependent upon the altitude of the satellite and the ground stations. It should be noted that variability exists in radio spectrum nomenclature, and the letters used to describe bands are not alphabetically sequential. An extended frequency spectrum breakdown is shown in **Tables 41-42**. Frequencies above 3000 GHz are considered in the optical spectrum. Optical communications systems for CubeSats are described in Section 3.6.7.

Table 41: High Level Frequency Divisions [110]

Band Name	Abbreviation	Frequency Range	Wavelength Range
Extremely Low Frequency	ELF	30 Hz – 300 Hz	10 Mm – 1 Mm
Voice Frequency	VF	300 Hz – 3 kHz	1 Mm – 100 km
Very Low Frequency	VLF	3 kHz – 30 kHz	100 km – 10 km
Low Frequency	LF	30 kHz – 300 kHz	10 km – 1km
Medium Frequency	MF	300 kHz – 3 MHz	1 km – 100 m
High Frequency	HF	3 MHz – 30 MHz	100 m – 10 m
Very High Frequency	VHF	30 MHz – 300 MHz	10 m – 1 m
Ultra High Frequency	UHF	300 MHz – 3 GHz	1 m – 10 cm
Super High Frequency	SHF	3 GHz – 30 GHz	10 cm – 1 cm
Extremely High Frequency	EHF	30 GHz – 300 GHz	1 cm – 1 mm

Table 42: Widely Accepted Frequency Divisions [110]

Band Name	Frequency Range	Wavelength Range
L-Band	1 GHz – 2 GHz	30 cm – 15 cm
S-Band	2 GHz – 4 GHz	15 cm – 7.5 cm
C-Band	4 GHz – 8 GHz	7.5 cm – 3.75 cm
X-Band	8 GHz – 12 GHz	3.75 cm – 2.5 cm
Ku-Band	12 GHz – 18 GHz	2.5 cm – 1.67 cm
K-Band	18 GHz – 26.5 GHz	1.67 cm – 1.13 cm
Ka-Band	26.5 GHz – 40 GHz	1.13 cm – 7.5 mm
Q-Band	32 GHz – 50 GHz	9.38 mm – 6 mm
U-Band	40 GHz – 60 GHz	7.5 mm – 5 mm
V-Band	50 GHz – 75 GHz	6 mm – 4 mm
W-Band	75 GHz – 100 GHz	4 mm – 3.33 mm

3.6.2.2 Initial CubeSat Use

When the concept of CubeSats was initially being developed, an amateur communication bandwidth of 437.35 +/- 0.15 MHz was identified for CubeSat use with the IARU [111]. Amateur bandwidth licensees have been required to submit pre-launch documentation to the Federal Communications Commission (FCC) since at least 2004 when the FCC started paying attention to orbital debris mitigation, but amateur bandwidths were useful in that they did not require explicit FCC approval. Satellite-based amateur radio is now handled by Amateur Radio Service, 47 C.F.R. § 97. Pragmatically, the IARU band only works for relatively low data rates at LEO altitudes. The FCC approval process is documented in Section 3.6.6.

3.6.2.3 International Telecommunication Union Designations

Deep Space Bands and Near Space Bands are bands that have been allocated to space research service by the International Telecommunication Union (ITU) for research work. They represent S-, X-, K-, and Ka-bands for spacecraft more and less than 2,000,000 km from Earth, respectively [112]. Antenna design should be specifically suited to provide enough gain to mitigate the losses induced by long distances. Information on the Deep and Near Space Bands is found in **Table 43**. Frequencies are expressed in MHz.

Table 43: ITU Allocated Frequency Bands [112]

Band Designation	**Deep Space Bands (for spacecraft greater than 2 million km from Earth)**		**Near Earth Bands (for spacecraft less than 2 million km from Earth)**	
	Uplink (Earth to Space)	Downlink (Space to Earth)	Uplink (Earth to Space)	Downlink (Space to Earth)
S-band	2110-2120*	2290-2300	2025-2110	2200-2290
X-band	7145-7190	8400-8450	7190-7235	8450-8500
K-band	**	**	**	25500-27000
Ka-band	34200-34700	31800-32300	**	**

* Deep Space S-band is not available at Madrid tracking stations due to a conflict with IMT2000 users, per agreement between NASA and Secretaria de Estado de Telecomunicaciones para la Sociedad de la Informacion (SETSI), January 2001

** No allocation or not supported by the Deep Space Network

3.6.3 Radio Hardware Evaluation

Traditional radio hardware includes preselect filters, low noise amplifiers, frequency converters, local oscillators, input multiplexers, preamplifiers, high power amplifiers, electronic power conditioners, and output multiplexers. On large-scale telecommunications satellites, these components may be massive and sizable. On CubeSats, radio hardware is generally incorporated into a PCB for inclusion into the stack. Single card radios may be transmitters, receivers, or transceivers, but a trend in satellite communications technology is the use of Software-Defined Radios (SDRs). Here, SDR discussion precedes an evaluation of three potential radio platforms for use on AEGIS.

3.6.3.1 Software-Defined Radios

SDRs were first posited by Mitola [113]. They feature the same front ends as most transceivers with low-noise amplifiers, frequency converters, and power amplifiers, but the modulation, encoding, and operating frequency are determined by software. Digital Signal Processing (DSP) has been used to give SDRs speed [114], but, per one OBC manufacturer, the programming environment for DSP is difficult to use for general OBC development. Examples of DSP and non-DSP PCBs are found in [115]. Architectures for SDR design may be found in [116,117], but the high-level design takeaway is that SDRs can reduce the volume radio hardware consumes while increasing TT&C capability.

3.6.3.2 Iris V2

The Iris radio was developed at JPL to demonstrate deep space communication with the INSPIRE CubeSat [118]. It features an RF front-end and a Field-Programmable Gate Array (FPGA) back-end for signal processing, demodulating the final intermediate frequency, and symbol generation used for RF carrier modulation. Iris is bulky, consisting of 6 PCBs in a stack. Two are antenna PCBs and the rest are radio electronics PCBs. Iris is a dependable deep space radio, but its inclusion will cost ~$1,200,000 [119].

3.6.3.3 AstroDev Lithium-2

The Astronautical Development Lithium-2 radio, not an SDR, is not commercially available at the time of writing, but its incorporation into this analysis is warranted due to the efforts of the University of Colorado Boulder's CU-E^3 program [120]. CU-E^3 recognized early that an increasing number of CubeSats desired deep space access without enormous radio hardware or high network costs, so they set about demonstrating an avenue for deep space communication. Their Artemis-1 mission, yet to launch, will feature uplink in C-Band, downlink in X-band, and a four component receive chain consisting of a C-band patch antenna, low noise amplifier, downmixer board, and the AstroDev Li-2. An XB1 central avionics unit controls the processing. Transmit does not include the AstroDev Li-2 but instead features the Blue Canyon Technologies XTX transmitter. The ATLAS ground station network was used for the communications base. The additional components required to function at lunar distance reduce radio SWaP benefits compared to standalone units, but sometimes adding bulky, cheap components is better than paying $1,200,000.

3.6.3.4 Xlink

The Xlink SDR is intended for use in LEO, but all commercial CubeSat components before 2018 were rated for LEO because nobody was building CubeSats for deep space. It features standard Consultative Committee for Space Data Systems (CCSDS) BPSK uplink, BPSK or QPSK downlink, and BCH coding. The link budget found in **Table 44** elucidates performance characteristics of the Xlink when combined with the DSN ground station, but the SwaP characteristics of the Xlink are as good as any X-band radio on the market at this time. At less than 0.2U, 200 grams, and a maximum antenna transmit power of 1 W, this radio can supply the same deep space operating capability as the Iris for a fifth of the volume and a tenth of the price, though very deep space missions may want to increase the antenna transmit power if the antenna gain is insufficient [121]. Mass and volume should be the primary trading parameters for CubeSat component selection, and these savings should not be taken lightly.

3.6.4 Antennae

The purpose of an antenna is to convert electric power into electromagnetic waves, but antenna design is complex and should be evaluated by a wireless communications expert. The two most important aspects for consideration when investigating an antenna should be the on-orbit thermal environment and the spacecraft pointing accuracy; gain comes after. Basic antenna design considerations include the gain pattern, polarization pattern, field of view, edge of coverage, efficiency, and Equivalent Isotropic Radiated Power (EIRP) [36]. This analysis will cover types of antennae and attempt to guide trade and selection efforts. Types of antennae include wire, log periodic, aperture, microstrip, reflector, lens, travelling-wave, and array, but the focus of satellite antennae evaluation should be reflector, array, travelling-wave, and microstrip. An exhaustive investigation of CubeSat antenna technology may be found in [122].

3.6.4.1 Reflector Antennae

A reflector antenna at minimum consists of a reflector and a feed. Reflectors are usually parabola or parabolic sections. Feeds may be center-fed or offset-fed. Dual-reflector, center-fed systems fall under Cassegrain or Gregorian design. These types of antenna are generally utilized by large-scale satellites such as the Cassegrain on NASA's Tracking and Data Relay Satellites (TDRS), shown in **Figure 89**. Cassegrain antennae were also used on the US military's Milstar and Advanced Extremely High Frequency (AEHF) satellites. Milstars were launched from 1994 to 2003, and the first AEHF was launch August 2010 [36]. Parabolic or deployable reflectors have been recently utilized for advanced CubeSat missions. The Radar in a CubeSat (RainCube) mission built by JPL employed a 0.5 m Ka-band parabolic deployable antenna that stows in a 1.5U volume [123]. Deployable antenna become feasible at 6U and above due to the large volume requirements.

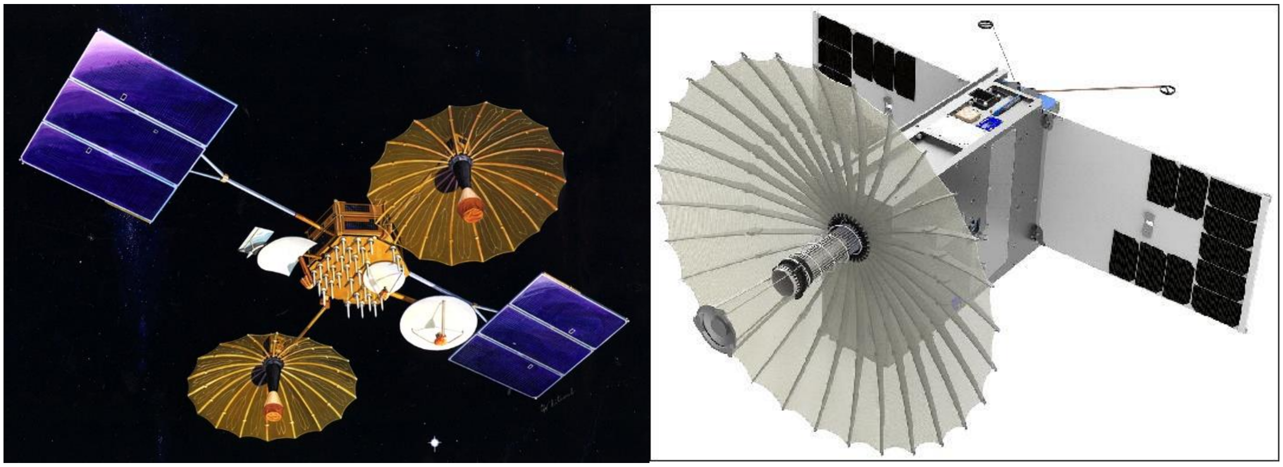

Figure 89: (a) TDRS Reflector Antenna Design [124] (b) RainCube Parabolic Reflector Antenna [123]

3.6.4.2 Antenna Array

Arrays consist of radiating elements of the same kind, laid out in a regular pattern, that form beams by combining radiating elements in particular phase or delay relationships [36]. They can be used as feeds for a reflector or comprise reflectarrays, which consist of an antenna and reflectarray surface. The 3U Integrated Solar Array and Reflectarray Antenna (ISARA) CubeSat built by JPL eponymously used reflectarrays integrated on its solar panels [125]. The MarCO satellites also carried a version of a reflectarray antenna where the high-gain, X-band antenna was a flat panel engineered to direct radio waves the way a parabolic dish antenna does [126].

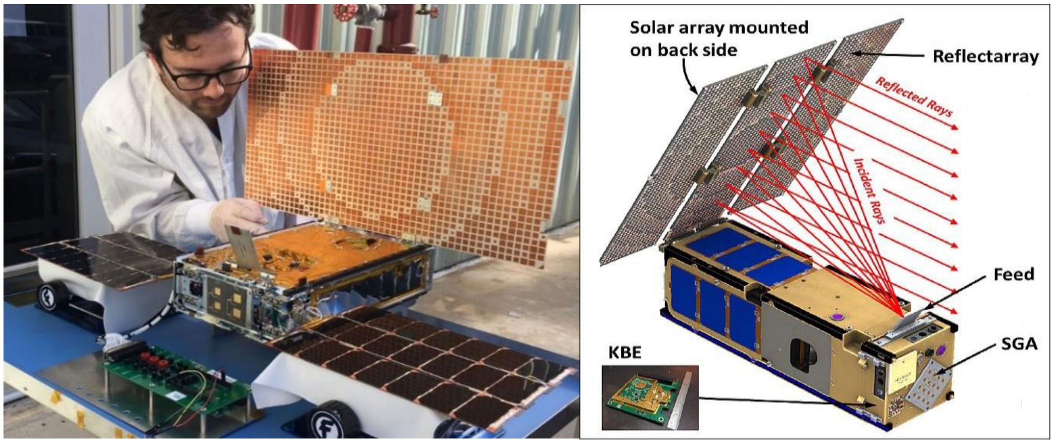

Figure 90: (a) MarCo Reflectarray Design [126] (b) ISARA Reflectarray Design [125]

On one hand, the best engineers in the satellite business are building reflectarray antennae for use in high-profile missions. On the other hand, building reflectarray antennae that fit a given mission has historically taken the best engineers in the satellite business. Reflectarray antennae should represent feasible options that take significant development time to qualify.

3.6.4.3 Travelling-Wave Antennae

The two types of travelling-wave antennae of note for CubeSat use are spiral and helical wire antennae. Specific examples of these antennae may be found in [127,128], but it is primarily the recent advances in deployment capability that should be taken into consideration. SMA may be used to construct these antennae wherein a coil of SMA wire is restricted to a small stowage volume. When the SMA is heated above its activation temperature, the coil will expand into the desired shape. This principle is depicted in **Figure 91**. These have been used for UHF uplink and downlink communications as well as V-band intersatellite communications. **Figure 91** is for 400 MHz.

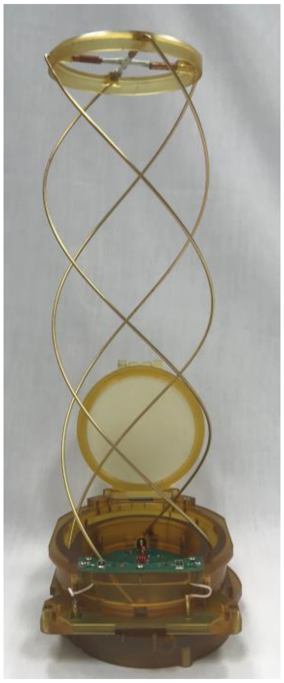

Figure 91: HCT Shape Memory Alloy Deployable Travelling-Wave Antenna, Used with Permission [132]

3.6.4.4 Microstrip Antennae

Commonly referred to as patch antennae, microstrips offer advantages in size, mass, and application potential. They are planar antennae with thicknesses on the order of 0.5 to 2 mm. They may be used as feeds for larger antennae such as reflectarray structures or as standalone antennae. A rectangular, S-band patch antenna analysis may be found in [129], and mutual coupling of multiple patch antennae may be avoided by mounting the patch antennae on adjacent surfaces [130]. A patch antenna was selected for use on AEGIS due to SwaP considerations, and an example may be seen in **Figure 92**.

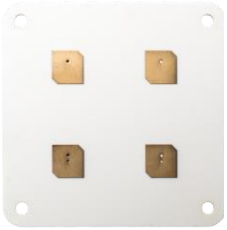

Figure 92: EnduroSat X-band 2x2 Patch Antenna array, Used with Permission, [133]

3.6.5 Link Budget and Comparison

Link budgets relate transmission power, reception power, antenna gain, beam width, free-space path loss, system noise, noise power, noise temperature, noise figure, and carrier-to-noise ratio, among other parameters, to show how capable a potential communications system would be for a given satellite altitude range. A detailed investigation of how to calculate performance parameters for a link budget may be found in [131], but an Excel version is provided in Appendix C.

3.6.5.1 AEGIS Preliminary Link Budget

A link budget analysis was performed for three frequencies considered feasible for the proposed altitude of 400,000 km. The link margin was calculated considering the DSN as the ground station for data download and telemetry. The analysis is summarized in **Table 44**.

Table 44: Link Budget Analysis for UHF, S and X-band Uplink/Downlink Considering Various Ground Station Options. Orbital Altitude Assumed at 400,000 km

Link	Freq, [GHz]	Radio	RF TX, [W]	TX Ant. Gain, [dBi]	GS	RX Ant. Gain, [dBi]	Data Rate, [kbps]	Slant Range, [km]	Link Margin, [dB]
UHF Downlink	0.4375	AstroDev Li-2	3.8	0	Various Univ.	16	128	406635	-35.59
S-band Downlink	2.30	Iris	3.8	0	DSN	63.3	128	406635	-1.53
X-band Downlink	8.45	Iris	3.8	10	DSN	74.1	128	406635	6.29
X-band Uplink	8.45	DSN	16,000	72.72	Iris	10	128	406635	65.77
X-band Downlink	8.45	Xlink	2.0	30	DSN	71	6520	406635	4.81

3.6.5.2 UHF Band Analysis

The UHF downlink displays negative margin, and Section 3.6.8 discusses how the Deep Space Network does not operate at UHF. Therefore, a much lower ground station antenna gain value is assumed where the ground stations are considered from various university receiver systems where 16 dBi is typical. This much lower antenna gain, along with the lunar distance slant range, results in negative link margin and eliminates UHF from consideration.

3.6.5.3 S-Band Analysis

The S-band downlink also has negative link margin because of the distance being cislunar in scale, which pragmatically disqualifies S-band as well. At the time of writing, S-band spectrum licenses from the FCC are considered difficult to obtain because the spectrum is crowded. S-band uplink, however, is a strong contender if a high gain ground station antenna is used.

3.6.5.4 X-Band Analysis

The X-band uplink from the DSN to the CubeSat has significant margin due to the high gain of the DSN transmit antennas and the low data rate used to command the vehicle. No issue would be expected on the uplink even if a low-gain ground station (e.g. Morehead State University, a peripheral location of the DSN) was used. The X-band downlink also looks dependable, but varied data rates may affect the margin values (data, carrier, ranging). The standard modulation indices used output a strong link margin. X-band is thereby selected as the transmission bandwidth for FCC license application, and further analysis specific to X-band is warranted.

3.6.6 FCC Licensing

The FCC and National Telecommunications and Information Administration (NTIA) have created a structured process by which satellite designers may obtain communications bandwidth approval. There is an official distinction between commercial, private, and government satellites. Only government-funded or government-operated satellites may apply through the NTIA, and all others must apply through the FCC.

3.6.6.1 Title Navigation

The Code of Federal Regulations (CFR) has many Titles, and Title 47 pertains to the FCC. In Title 47, there are three Parts that satellite designers should be aware of: Part 5, Part 25, and Part 97. Part 5 denotes *Experimental Radio Service*, Part 25 is labeled *Satellite Communications*, and Part 97 details *Amateur Radio Service*. Amateur radio will not be covered in this deep space analysis. Most of the relevant information regarding satellite communications is found in Part 25, but a pertinent question to all CubeSats travelling to deep space is whether to apply via Part 25 or Part 5.

3.6.6.2 Documentation and Guidance

There are two applicable documents when studying FCC applications apart from the CFR. In March 2013 the FCC released a public notice titled “Guidance on Obtaining Licenses for Small Satellites” (DA-13-445), which was updated in 2018 [134], and in August 2019 they published FCC-19-81 [135], “Streamlining Licensing Procedures for Small Satellites.” DA-13-445 is officially the only notice the FCC has published providing guidance concerning small satellite licensing. FCC-19-81 built upon a Notice of Proposed Rule Making to provide background on licensing practices, some of which was not included in the DA-13-445 document. The rule provisions adopted in FCC-19-81, however, did not change any of the rules for Part 5 or Part 97. It provides an optional licensing approach and is probably most useful for emerging commercial ventures. It does concern the possibility of improved interference protection, so some universities and research ventures may be interested.

There exists ambiguity when parsing these documents. For example, in Part 47 of FCC-19-81, not to be confused with Title 47 of the CFR, an arbitrary altitude of 600 km is defined as a categorizing boundary for Satellite Communications, which is located in 47 CFR § 25. FCC-19-81 reads like a discourse on whether or not small satellites which use propulsive methods to raise their altitude above 600 km should be considered Part 5 or Part 25 of Title 47. However, this should not be taken to apply directly to deep space satellites. Superseding this internal deliberation should be if the mission qualifies as experimental, which is outlined in Experimental Radio Service, 47 CFR § 5.3 and 5.51.

For the foreseeable future, science missions intended for deep space should consider Experimental Radio Service, 47 CFR § 5 to be the starting point for FCC license applications. This should continue until the FCC issues new rules eclipsing DA-13-445.

3.6.7 Optical Satellite Communication

Despite Optical Communication (OC) systems utilizing electromagnetic frequencies higher than radio frequencies, this does not translate to a bulkier subsystem. OC features advantages such as reduced SWaP, high data rates, and no tariffs or regulatory restrictions [136]. It also not a new technology, as ESA achieved regular 50 Mbit/s OC crosslinks between LEO and GEO satellites in its Semiconductor Laser Intersatellite Link Experiment (SILEX) in 2003 [137]. OC has been limited to short crosslinks or LEO downlinks for CubeSats, but this is a status in flux. Recent research by Ingersoll details LEO crosslink proliferation [138]. A deep space OC investigation is being performed by NASA GSFC and Wallops on the Science Enabling

Technologies for Heliophysics (SETH) mission [139], and the CubeSat Laser Infrared CrosslinK (CLICK) mission by NASA Ames, MIT, and the University of Florida, a three CubeSat, 10-20 Mbps downlink and crosslink experiment, is targeting a 2020-2021 launch [140]. An OC “license plate” concept is also being evaluated for satellite identification during a single pass [141]. The current holy grail, 1 Gbps data rates with angular resolution less than 1 μradian and storage capabilities over 1 TB, is still out of reach, but OC should not be discounted for ambitious mission designers. 300 GHz is the current cutoff for what the FCC considers radio versus optical. The FCC recommends that ITU filings for radio frequencies also include information on optical frequencies used.

3.6.8 Networks

Multiple public and private communications networks are available for uplink and downlink services. The three primary NASA network providers will be discussed here, but satellite networking services are now being evaluated for commercial profitability by major electronics hardware companies in the United States. Services provided by all networks include telemetry, tracking, ranging, one and two-way Doppler, and command signaling. Regardless of the network being public or private, compatibility testing will need to be performed between the network and the radio/antenna system. DSN compatibility testing costs average ~$40,000 – $50,000 [120]. This section represents GCS considerations as no other networks are usable in deep space at time of writing, though several institutions are bringing X-band capabilities online. Real time data is provided to customers via a secure internet server.

3.6.8.1 Deep Space Network

The DSN consists of three deep-space communications facilities placed approximately 120 degrees apart around the Earth. They are located outside Barstow, California, Madrid, Spain, and Canberra, Australia. The DSN is operated for NASA by JPL, and it is the largest and most sensitive scientific communications system in the world [142]. The DSN performs scientific observations, but it is also capable of transmitting and receiving data from four spacecraft at a time. Once a satellite is more than 30,000 km away from Earth, it is always able to communicate with the DSN pending a positive link margin. The DSN supports Ka-, S-, and X-band frequencies for both downlink and uplink communications.

3.6.8.2 Near Earth Network

The Near Earth Network (NEN) direct communications system provides continuous coverage to satellites up to 2 million km from Earth [143]. The direct-to-ground, NASA-operated NEN offers high-rate data services with 99.1% data proficiency through launch, early orbit, on-orbit, and disposal life cycles. Ranging services include one- and two-way Doppler and angle autotracking data. Frequencies band support includes S-, X-, L-, and Ka- bands. Operations are distributed across a range of ground control stations.

3.6.8.3 Space Network Project

The Space Network Project (SNP) provides 100% continuous coverage in near-Earth systems up to 9000 km with 99.95% data proficiency [144]. Frequency bands supported include S-, Ku-, and Ka- bands, and cross support between different telecommunications bands are possible. Services include beam forming, ranging, demodulation, data distribution, and storage capabilities. Available orbits for SNP coverage are LEO at all inclinations, geosynchronous, and highly elliptical. The central operations center for the SNP is the White Sands Complex in New Mexico. Data taken from the Guam Remote Site is piped back to White Sands. The SNP also offers cradle-to-grave service, a morbid and common expression.

3.6.8.4 Network Selection Information

If a NASA-provided network has been selected for use in a mission, deep space or otherwise, program administrators will fill out a "Customer Questionnaire" form. NASA uses the same form for the DSN, NEN, and SNP. Spacecraft designers should determine certain aspects of their mission prior to network selection. Such information for the DSN includes,

- Expected and potential mission duration
- Utilization of NASA navigation services such as FDF or MONTE python (yes, really) [145,146]
- Mission operations control center location
- Utilization of NASCOM IONet services [147]
- Coverage requirement during launch and early orbit, including post-deployment
- Coverage requirement during powered flight and critical events
- Launch site and date information
- Orbital parameters
- Applicable CCSDS standards [148]
- Frequency band (non-specific)
- Simultaneous receipt of two bands on return link utilization
- Data rate parameters
- Antenna parameters
- Tracking information
- Latency requirements for Science and Engineering data via WAN/LAN
- 24-hour contact information for interference issues
- Earth station usage and amateur band usage information

3.6.9 Signal Effects: Ranging, Tracking, and Doppler

Satellite ranging means determining the satellite's position and distance using communication signals. The range is determined by measuring the delay of signals sent from the ground to the spacecraft, received by the TT&C subsystem, and retransmitted to the ground. Velocity information is discerned by measuring the Doppler shift of the downlink signal over time [33]. If a satellite's position and velocity are known, the orbit can be directly calculated. Tracking is the opposite of ranging. It is the process of updating an object's location by first predicting where it will be based on previous state vectors and timestamps and then observing it. A satellite is tracked if its location is already known. The in-situ goal of orbit definition besides command telemetry is to provide the GN&C subsystem with orbital parameters.

3.6.9.1 Signal Definition

The transmitted uplink signal $S_T(t)$ can be written as **Eq. (104)** where f_T is the uplink carrier frequency, α_U is a function of time that accounts for the Doppler effect on the uplink, $p_c(t)$ is the ranging signal taking values of ± 1 with chip rate R_c, and θ_{mod} is the ranging modulation index [149].

$$S_T(t) = \sqrt{2}\cdot \sin\left[2\cdot\pi\cdot\alpha_U\cdot f_T\cdot t + \theta_{mod}\cdot p_c(t)\cdot sin\left(2\cdot\pi\cdot\frac{R_c}{2}\cdot t\right)\right] \qquad \textbf{Eq.(104)}$$

The range clock is $\frac{R_c}{2} = \alpha_U\cdot\beta_b\cdot f_T$ where β_b is a function of the bandwidth; more info is found in [149,150]. As the range clock also experiences the Doppler effect, the ranging signal is coherently related to the carrier frequency as discussed in the next section. **Eq.(104)** may also be written in complex form as

Eq.(105) with the use of Bessel functions. Complex signal representation allows for computational simplicity in advanced TT&C algorithms.

$$S_T(t) = \sqrt{2} \cdot J_0(\theta) \cdot \sin[2 \cdot \pi \cdot \alpha_U \cdot f_T \cdot t] + \sqrt{2} \cdot \cos[2 \cdot \pi \cdot \alpha_U \cdot f_T \cdot t] \cdot 2 \cdot J_1(\theta) \cdot p_c(t) \cdot sin\left(2 \cdot \pi \cdot \frac{R_c}{2} \cdot t\right) \qquad \textbf{Eq.(105)}$$

Signal fidelity is covered in Section 4.3.3.1 in the discussion on Error Correcting Codes (ECC). The principal signal degradations in space are due to a loss of signal energy with distance and the thermal noise in the receiving system [148]. However, data can be recovered from a noisy signal with the use of ECC.

3.6.9.2 One-Way vs. Two-Way Doppler

If a TT&C system transmits a downlink signal at a frequency which is proportional to the received frequency, that system is referred to as a coherent transponder. Coherency is important because a coherent signal allows the ground to know what frequency to expect from the spacecraft. The difference between the expected frequency and the actual frequency is the two-way Doppler shift because the signal is shifted both to and from the spacecraft [33]. If the downlink frequency is set by an internal oscillator, the spacecraft will not transmit a coherent signal. NASA networks such as the DSN can work with non-coherent (one-way Doppler) signals, but the use of one-way or two-way Doppler must be defined during the network use application. Pseudo-coherent radar also exists, also known as “coherent on receive” radar. Considerations on Doppler and clock frequency are given in Section 4.3.4.5.

3.6.9.3 AEGIS System Capabilities

The Xlink satellite transceiver has on-board processors which can be used to demodulate and correlate a pseudo-noise ranging signal and modulate this signal onto the downlink signal. As such it can be used for regenerative ranging procedure. A ranging code from JPL is provided from the DSN by default, but CCSDS T4B and T2B (CCSDS standard 414.1-B-2) may also be used [148]. Only non-coherent ranging is supported with Xlink; coherent ranging is not supported. An in-depth discussion on the Doppler and ranging services provided by the DSN may be found in [149,150].

3.6.10 System Block Diagram

A general block diagram considering the Xlink SDR for the AEGIS mission is shown in **Figure 93**. Of note is the potential for S-band to be a redundant means of uplink communication. The data between the OBC and the radio is routed via RJ-45 connectors while the power is routed from the EPS unit. The antennas are connected directly to the radio housing via SMP connectors. Also shown in **Figure 93** is the block diagram for the CU-E^3 mission with the AstroDev Li-2 radio discussed in Section 3.6.3.3. This is an experimental setup with the express purpose of testing radio hardware for deep space communication, and novel methodologies may exhibit subsystems that more closely resemble **Figure 93(b) than (a)**.

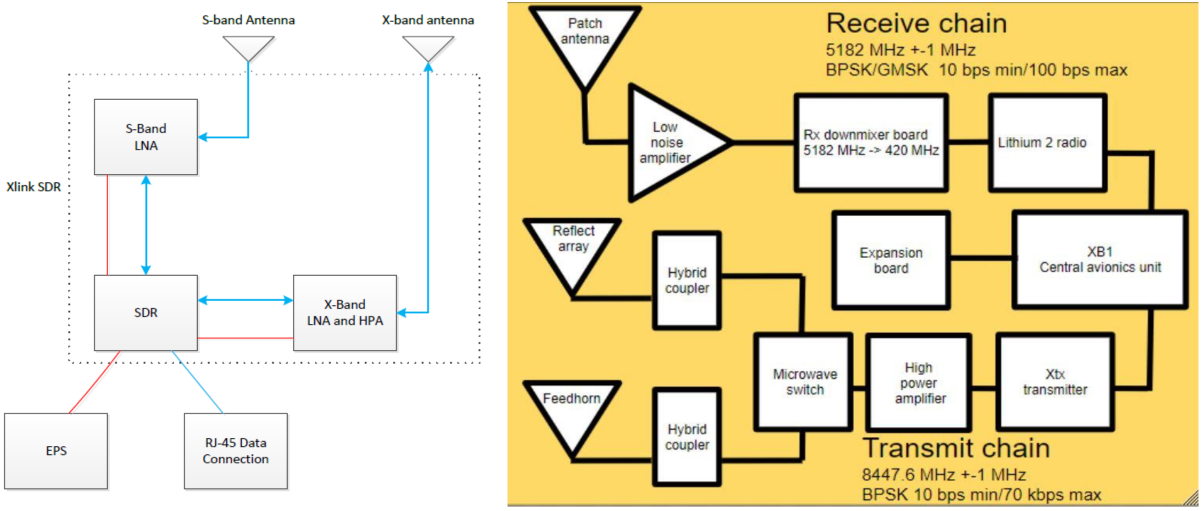
S-band Antenna
X-band antenna
S-Band LNA
Xlink SDR
SDR
X-Band LNA and HPA
EPS
RJ-45 Data Connection
Patch antenna
Receive chain
5182 MHz +-1 MHz
BPSK/GMSK 10 bps min/100 bps max
Low noise amplifier
Rx downmixer board 5182 MHz -> 420 MHz
Lithium 2 radio
Reflect array
Hybrid coupler
Expansion board
XB1 Central avionics unit
Microwave switch
High power amplifier
Xtx transmitter
Feedhorn
Hybrid coupler
Transmit chain
8447.6 MHz +-1 MHz
BPSK 10 bps min/70 kbps max

Figure 93: (a) AEGIS TT&C Block Diagram (b) CU-E3 TT&C Block Diagram, Used with Permission [120]

3.6.11 Power Interface Comparison

The power a radio consumes should be taken into consideration almost as much as the mass, volume, and performance, but the power parameters must be evaluated under the umbrella of which software state the radio is assumed to operate under. **Table 32** in Section 3.5.4.1 shows the power values per software state of each subsystem component, including the radio. Transceiver radios may operate in half-duplex (transmit or receive) or full duplex (transmit and receive) modes. An ideal scenario would be if the communications strategy only required the radio to transmit and receive during an explicit communications state. However, if the radio needs to be able to receive during a burn phase, power will be required for the thruster, OBC, GN&C components, thermal management, potentially a science instrument, and the radio. The combined power consumption of all those components plus efficiency factors and a 20% margin may result in an unrealistically large power requirement for the given state. An internal consultation on what states the radio may be partially or fully powered down is warranted. Power interface considerations are given here for the Iris V2 and Xlink radios.

3.6.11.1 Iris V2

The input voltage for the Iris is 9 – 15 VDC. For X-band half-duplex operation, 23.3 W of power is consumed while transmitting while 7.9 W of power is consumed during receiving. When the radio is in full duplex mode, a max of 25.9 W of power is consumed. While idle, the Iris radio consumes 0.5 W of power [119].

3.6.11.2 Xlink

The input voltage for the Xlink is 8 – 18 VDC with an option to differ upon request to the manufacturer. The power consumption will not exceed 15 W in duplex mode and will not exceed 5 W while receiving in half-duplex. The system does not have a standby mode and will stay in a continuous receive state, but the vendor stated that they can implement a powered on/off feature into the software. Solid state devices such as this would only need 5 seconds to boot up for operation [121]. It is important to note that while 15 W of power is provided to the radio, only 1 W is provided to the antenna. A significant amount of the 14 W disparity will be rejected as heat. AEGIS considered managing this short-term heat load by use of phase change materials, in this case paraffins, as a thermal storage mechanism.

3.7 Guidance, Navigation, and Control

Written with assistance from Dr. Carlos Montalvo, University of South Alabama.

The GN&C subsystem handles the relative localization, attitude control, and non-scientific, non-thermal sensor hardware for the satellite. Attitude is “the three-dimensional orientation of a vehicle with respect to a specified reference frame”, attitude determination is “the process of combining available sensor inputs with knowledge of the spacecraft dynamics to provide an accurate and unique solution to for the attitude state as a function of time”, and attitude control is “the combination of the prediction of and reaction to a vehicle’s rotational dynamics [33].” For LEO satellites, GN&C is often referred to as the Attitude Determination and Control Subsystem (ADCS, or ADACS). It is not until CubeSats enter the realm of deep space that GN&C nomenclature is predominant, but ambiguity exists within the CubeSat arena about the use of these terms. ADCS should be considered a subset of GN&C, and the line at which a satellite designer should reframe her or his subsystem nomenclature is **whether or not the satellite will utilize Earth’s magnetic field for primary attitude control**. If so, a satellite designer is usually operating with an ADCS without guidance or navigation coupling effects, and GPS ephemeris data is commonly involved. If not, ADCS should be considered under the umbrella of GN&C. There are satellites with highly elliptical orbits that use both reaction wheels and magnetic attitude controllers, hence the ambiguity.

3.7.1 GN&C Design Objectives

Table 45: Guidance, Navigation, and Control Subsystem Design Objectives, Adapted from [28]

Design Objective	Description	Rationale	Actionable Items
Angular Velocity (**GN&C-1**)	Angular velocity must be below 0.5 deg/s/axis.	Science payload and communications require slew rates to be lower than this threshold to get adequate data.	Reaction Wheels (RWs) are sized accordingly. An RCS or thruster with TVC is added to desaturate RWs, and an IMU will estimate angular velocity.
Pointing Accuracy (**GN&C-2**)	Vehicle must be able to point to a target within 0.5 degrees.	Science payload and communications require accurate pointing to obtain accurate data. Communications also requires basic pointing to communicate with DSN.	Star trackers and Sun sensors combined with an attitude determination algorithm are added to obtain accurate pointing estimate. The RWs and RCS are then used to control to a desired target.
Position Estimation (**GN&C-3**)	Position estimates of +-3000 km.	Science payload and communications require accurate position estimates to obtain accurate data.	The radio will communicate with DSN to obtain accurate position estimation. C&DH will then integrate orbital equations of motion to estimate position between DSN pings for GN&C.

3.7.2 Spacecraft Disturbance Sources

The total torque disturbances imparted to a CubeSat will be a summation of torques due to Solar Radiation Pressure (SRP), aerodynamic drag, gravity gradients, and residual dipoles. Between 400 and 1000 km, gravitational and magnetic torques are the two most prominent sources [151]. Above 500 km, solar radiation torques approach those generated from atmospheric drag [152]. In deep space, the disturbance torques of interest are SRP and gravity gradients, depending on a spacecraft's orbit. Magnetic field strength and atmospheric drag forces are considered negligible. SRP calculations are summarized in [151], aerodynamic forces are discussed in in [153, 35], LEO gravity gradient stabilization is outlined in [154], and residual dipole disturbance torques are detailed in [35,155,156].

3.7.3 GN&C and the Magnetosphere

All CubeSats have been launched into LEO or below except for the MarCO CubeSats and the Lucky 13 manifested on Artemis I. These CubeSats have payloads which are not, or should not be, susceptible to magnetic interference. If a CubeSat has a payload which must be outside the magnetosphere for any reason, the sensors and control hardware will differ substantially from LEO spacecraft. In many aspects, designing a CubeSat for use inside the magnetosphere is simpler than outside, which directly leads to the distinction between ADCS in LEO and GN&C everywhere else. The methodologies for time keeping and state vector acquisition are dissimilar. A depiction of Earth's magnetosphere is shown in **Figure 94**.

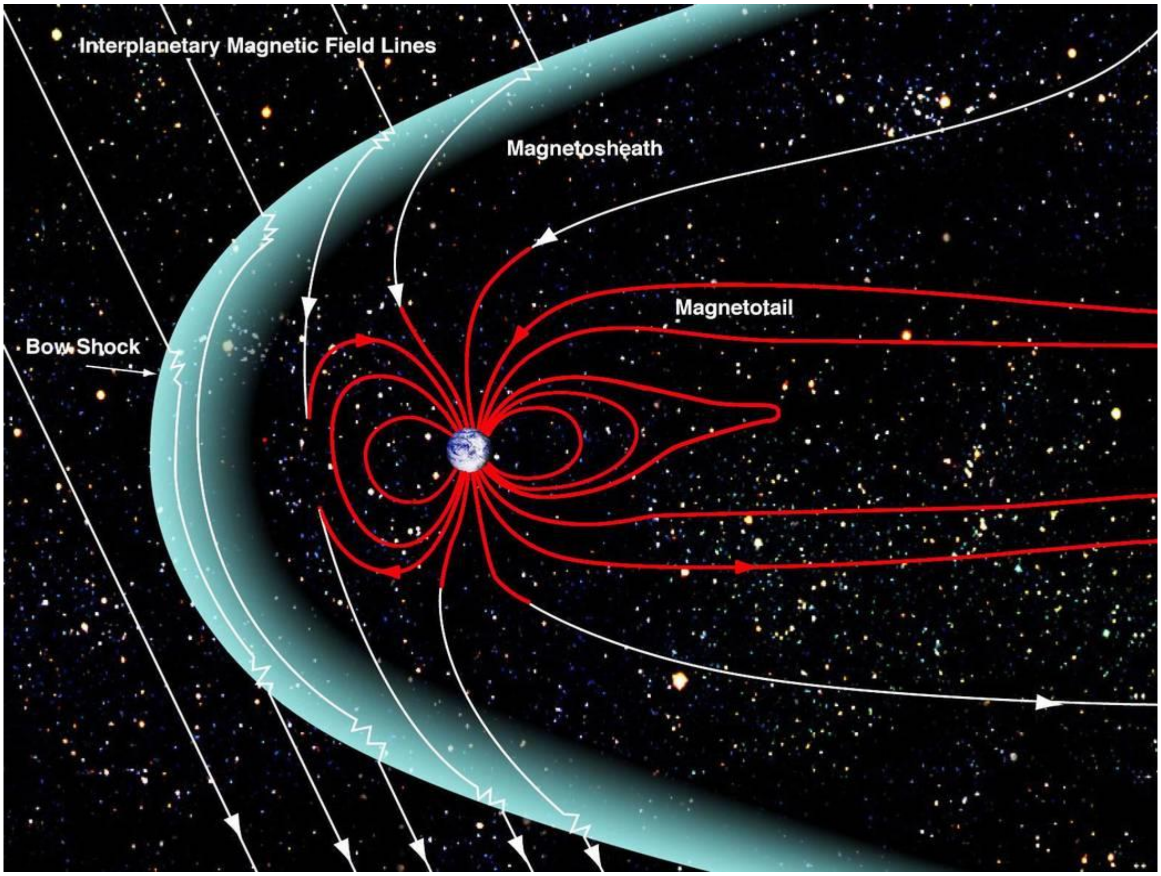

Figure 94: Magnetosphere Shape and Field Lines [157]

3.7.3.1 What is the Magnetosphere?

The magnetohydrodynamics of Earth's molten interior create a magnetic field around Earth resembling that of a dipole bar magnet. The dipole representation is accurate up to an altitude of 4 to 5 Earth radii [158]. Solar wind is a highly variable, magnetized, quasi-neutral plasma generated by the supersonic expansion of the Sun's heated outer atmosphere. At 1 AU, typical solar wind densities, flow speeds, and temperatures are on the order of 8 protons per cm^3, 440 km/s, and $1.2 \cdot 10^5$ K respectively [159]. The Earth's Magnetosphere is a teardrop-shaped geomagnetic field that is compressed on the dayside and trails off at the nightside following the solar wind's compression of Earth's dipole field.

The World Magnetic Model (WMM) is a to-scale representation of Earth's magnetic field used by NATO, the World Hydrographic Office, and the U.S. Department of Defense. Model coefficients are updated every 5 years and should be considered the standard for characterizing Earth's magnetic fields. In February 2019, a correction had to be issued for the 2015 cycle, called WMM2015v2. The current model, WMM2020, was released December 2019. All Android and iOS phones come with the WMM preloaded so that the GPS system can correct for magnetic declination. The WMM is free and may be downloaded at [160]. The International Geomagnetic Reference Field (IGRF) is also widely used and is similarly available at [161].

3.7.3.2 Magnetosphere Size

There are three primary types of plasma waves: acoustic, Alfvénic, and magnetosonic, and they are only introduced to convey that a sonic speed exists for plasma waves. The dayside of Earth's magnetosphere is characterized by solar wind decelerating from supersonic to subsonic speed causing a bow shock which terminates at approximately 10 Earth radii. Magnetic field lines on the dayside are compressed with respect to with respect to dipole shape. The magnetotail extends out to 300 Earth radii on the nightside, but in accordance with Gauss's law for magnetic fields, shown in **Eqs.(106-107)**, it does converge to a point. The magnetic field $B(r_c, t)$ as a function of generalized charge radius r_c and time t is measured in Tesla, the electric field $E_e(r_c, t)$ is measured in V/m, ρ_e is scalar charge density, and ε_0 is the permittivity of a vacuum. Regions of the magnetosphere are divided by sheets of charged particles and plasma, as air streamlines are in an atmospheric flow regime, and should be considered temporally and spatially variable.

$$\nabla \cdot E_e(r_c, t) = \frac{\rho_e(r_c, t)}{\varepsilon_0} \qquad \textbf{Eq.(106)}$$

$$\nabla \cdot B(r_c, t) = 0 \qquad \textbf{Eq.(107)}$$

3.7.3.3 The Van-Allen Belts: A Consequence of Planetary Magnetism

The magnetosphere, a magnetized shield that protects Earth's surface and low orbiting satellites from energetic charged particles, also traps particles in solid tori named the Van Allen Belts (VABs). They were predicted by Carl Størmer as early as 1930 and confirmed by James Van Allen during the Explorer I and Explorer III missions. Earth has belts of trapped radiation because, unlike the Sun's magnetic cycle which reverses every 11 years, Earth's magnetic field does not reverse nearly as often. Earth has experienced 5 magnetic reversals in a period of 1 million years and even two reversals within 50,000 years [162]. The estimates for reversal duration range from tens of thousands of years to one human lifetime [163, 164]. Earth's last magnetic reversal occurred 780,000 years ago with a duration of 22,000 years, fueling speculation that WMM2015v2 had to be released because Earth is currently entering a period of magnetic reversal [165].

Figure 95 depicts the two main VABs with distances shown for various satellites. The inner belt is relatively stable, consisting of protons, electrons, and ions such as helium and oxygen. It has a maximum density between 1.3 and 1.8 Earth radii from the Earth's center, and the proton energy is between 100 keV and 400 MeV [166]. The outer belt, with a maximum density between 3 and 4 Earth radii from the Earth's center, is more dynamic in terms of energy and flux. Its population is mostly electrons of energies between 100 keV and 5 MeV, but protons, ions, and α particles do exist. The second VAB can sometimes split into two VABs for a total of three belts, though the mechanism is not fully understood [167].

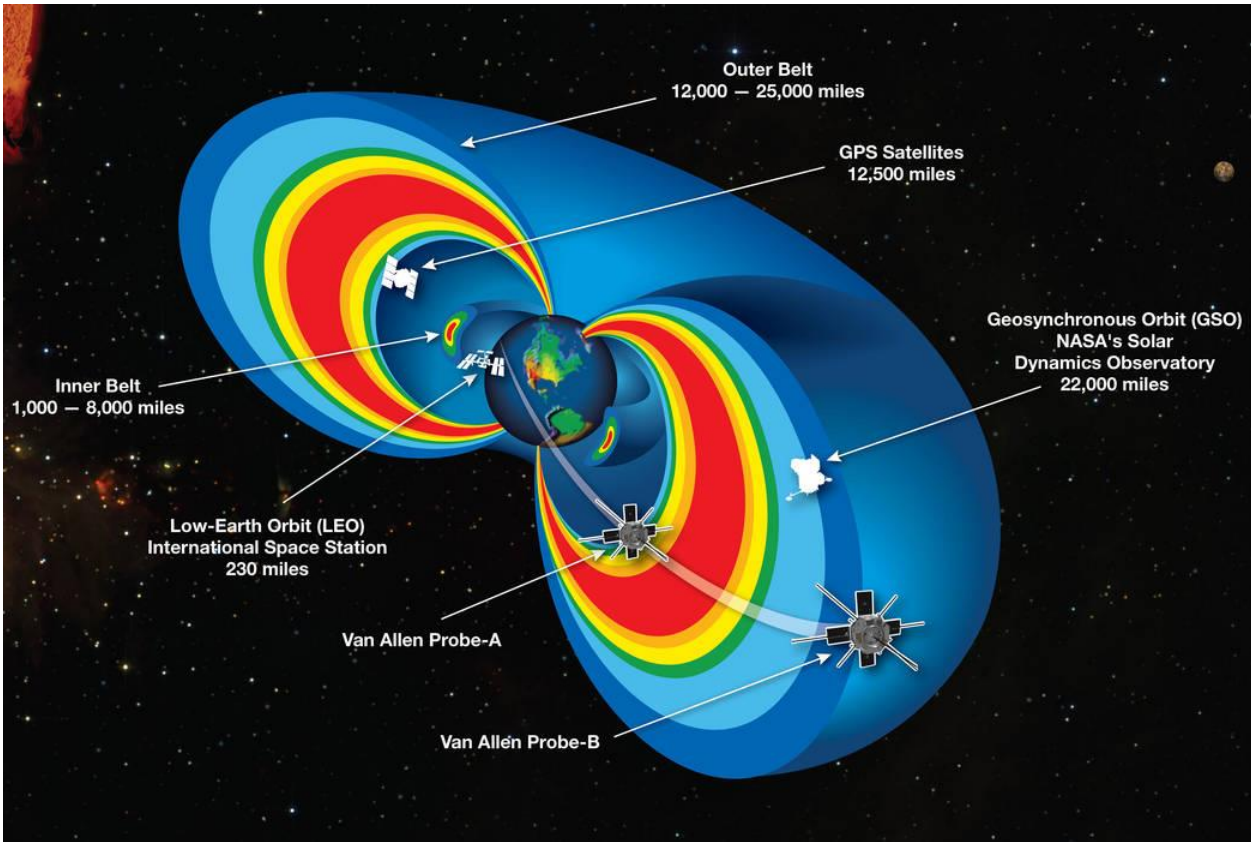
Outer Belt
12,000 — 25,000 miles
GPS Satellites
12,500 miles
Geosynchronous Orbit (GSO)
NASA's Solar
Dynamics Observatory
22,000 miles
Inner Belt
1,000 — 8,000 miles
Low-Earth Orbit (LEO)
International Space Station
230 miles
Van Allen Probe-A
Van Allen Probe-B

Figure 95: Van Allen Belts with Satellite Positioning [168]

3.7.3.4 Particle Sources: The Magnetic Disease of the Sun

Particles in the Van-Allen belts were trapped by means of charged particle confinement, as if they flew into a magnetic bottle. Incident Solar Energetic Particles (SEPs) and Galactic Cosmic Rays (GCR) in the upper atmosphere, discussed in Sections 4.1.2-3, can create nuclear reactions if outbound that result in albedo neutrons decaying to high energy protons by means of **Eq.(108)**. Low energy protons result from solar plasma and geomagnetic storms. **Eq.(108)** shows a neutron undergoing β^- decay where it is transformed into a proton p_p, electron e^-, and an electron anti-neutrino $\bar{\nu}_e$. The half-life of a free neutron n_p is 887.7 ± 2.2 seconds or 878.5 ± 0.8 seconds depending on how it is measured, which is why encountering neutrons in deep space is uncommon unless produced nearby [169,170]. Lunar surface interactions can create neutrons, but the Lunar Exploration Neutron Detector (LEND) instrument on the LRO detected only neutrons below 100 MeV. Neutrons below that threshold are thermal and feature a maximum velocity of 4,374 m/s, a function of the 100 MeV energy. That velocity multiplied by the maximum half-life of a free neutron is ~3,892 km, meaning encountering them is unlikely unless below that lunar altitude.

$$n_p \rightarrow p_p + e^- + \bar{\nu}_e \qquad \textbf{Eq.(108)}$$

The Sun primarily releases energy in the form of photonic electromagnetic radiation. However, instabilities in the magnetized plasma emerging to the Sun's photosphere lead to energetic events where hadronic particles, the vast majority of which are protons, are ejected [166]. Two main types of instabilities are of note for spacecraft: flares and Coronal Mass Ejections (CMEs). A solar flare is a brightening of any emission across the electromagnetic spectrum occurring at a time scale of minutes [171]. Highly energetic photons can damage spacecraft as electromagnetic ionizing radiation, and Section 4.2 details the mechanisms of spacecraft radiation damage. Flare spectra range from radio waves in the MHz through Gamma-ray, and flare strength is categorized by X-ray intensity measured from Earth's orbit in the spectral range of 100 to 800 pm. The five flare classes are shown in **Table 46**.

Table 46: Flare Classification System

Class	**Intensity, (W/m^2)**
A	$10^{-8} \leq S < 10^{-7}$
B	$10^{-7} \leq S < 10^{-6}$
C	$10^{-6} \leq S < 10^{-5}$
M	$10^{-5} \leq S < 10^{-4}$
X	$S > 10^{-4}$

CMEs occur when magnetic energy, stored in the form of an emerging flux rope, becomes unstable, either in the form of a kink or torus, and energy, both radiative photons and kinetic energy as particle emission, is released by magnetic reconnection. The effect of CMEs on spacecraft is mostly sensor noise, and it must be accounted for in science data if an interplanetary CME releases enough SEPs to flood the region with charged particles. Two to three CMEs are observed per day during active solar periods, and one per week is common during solar minima [166]. The Sun vacillates, following a square wave, rather than oscillates, following a sine wave, between solar minima and maxima.

If a highly energetic CME were to occur in the direction of a spacecraft, the spacecraft may die immediately. Specific particle effects on spacecraft are discussed in Sections 4.2 and 4.5, but if a CME occurs in the direction of Earth with immense, destructive energy, known as a Carrington-class storm, all spacecraft, power grids, cell towers, and anything else with a high enough voltage will fail and/or explode. In 2012, physicist Pete Riley published the probability that a Carrington-class storm would hit Earth within the next 10 years. The answer was 12% [172].

3.7.3.5 Magnetohydrodynamics and You

Spacecraft designers should evaluate whether or not they intend to use the magnetosphere for attitude control, what the effect of SEPs would be on their science payload, and if the Sun will be in solar minima or solar maxima during the mission. A detailed radiation assessment flow is provided in Section 4.5.1. If the Sun is in solar minima or the spacecraft will spend a significant amount of time eclipsed, planning for SPEs may be design overkill. If the mission is to an interior planet or a Lagrange point near the Sun, it may be prudent to take the steps in Sections 4.4-5 more seriously than the average satellite architect.

3.7.4 Guidance Sensor Overview

Guidance sensors allow a spacecraft to generate the three parameters required to define a rigid body attitude in a three-dimensional Euclidean space, namely the components of a vector. Vector rotations and transformations are commonly confused as rotation angles and Euler transformation angles are ambiguously interchanged in various texts and computational packages. In a vector rotation, the coordinate system remains unchanged and the vector points in a different direction. In a vector transformation, the coordinate system changes but the vector remains pointing in the same direction. Rotations and transformations are parameterized via three methods: Directional Cosine Matrices (DCM), Euler angles, and quaternions. DCMs and Euler angles are more computationally intense than quaternions, and thus guidance sensors aim to provide a quaternion that relates a determined vector in the guidance sensor coordinate system, e.g. which direction the Sun is, to the same vector in the spacecraft body coordinate system. That vector can then be transformed into a broader frame, such as the Earth Centered Inertial (ECI) frame, for orbital propagation and navigation. The definition and calculation of rotations and transformations for spacecraft navigation is excellently handled in [173], and major points are summarized.

Quaternions are used in parameterizing a spacecraft's attitude with respect to a reference coordinate system, propagating the attitude in time by integrating the spacecraft equations of motion, and performing coordinate transformations [173]. Their definition is based on Euler's rotational theorem which states that the relative orientation of two coordinate systems can be described by only one rotation about a fixed axis. In that sense, a quaternion is a rotation of a coordinate system along a non-principal rotation axis, but a quaternion should be considered to represent a vector transformation, not a vector rotation. The mathematical representation of a quaternion, a 4 x 1 matrix with scalar component s and vector component $\vec{v}$ is shown in **Eq.(109)**.

$$q = \begin{bmatrix} s \\ \vec{v} \end{bmatrix} = \begin{bmatrix} s \\ v_x \\ v_y \\ v_z \end{bmatrix} = \begin{bmatrix} q_s \\ q_x \\ q_y \\ q_z \end{bmatrix} \qquad \textbf{Eq.(109)}$$

The kinematic equations calculating quaternion rates of change $\dot{q}_i$ are shown in **Eq. (110)**, where q_i are the four quaternions elements such that i = {s,x,y,z} and p, q, r are the components of the angular velocity vector in the x, y, z body frame [174].

$$\begin{Bmatrix} \dot{q}_s \\ \dot{q}_x \\ \dot{q}_y \\ \dot{q}_z \end{Bmatrix} = \frac{1}{2} \begin{bmatrix} 0 & -p & -q & -r \\ p & 0 & r & -q \\ q & -r & 0 & p \\ r & q & -p & 0 \end{bmatrix} \begin{Bmatrix} q_s \\ q_x \\ q_y \\ q_z \end{Bmatrix} \qquad \textbf{Eq. (110)}$$

Further information on quaternion-based rotational dynamics may be found in [175-177]. The goal of spacecraft sensor selection is to provide a spacecraft with the ability to generate a full quaternion by calculating at least two vector measurements with respect to other objects in space. Some sensors, such as a star tracker, can make multiple vector measurements at once leading to the generation of a full quaternion within a single operation. Other sensors, such as a Sun sensor, can only generate the vector between the sensor and the Sun with azimuth and elevation components. Thus, a Sun sensor alone cannot provide adequate information about the spacecraft orientation because it lacks a secondary vector to compare the singular measurement against.

3.7.4.1 Sun Sensors

A Sun sensor detects the direction of the Sun with respect to the spacecraft and may be used both in LEO and deep space. Sun sensors can be either analog or digital; analog output is a voltage range which can be fed into an analog-to-digital converter for control logic processing. Photodetectors inside the Sun sensor can detect both the intensity of the solar radiation and the incidence angle, generating a single vector for attitude determination with azimuth and elevation components. Due to their low power consumption and high reliability, Sun sensors are often used in low-power acquisition and fault recovery modes [33]. Sun sensors should be selected based on their FOV, angular resolution, accuracy, stability, mass, volume, and radiation tolerance. Sun Sensor design analysis is covered in [178]. The AEGIS mission selected SolarMEMS Nano-SSOC-A60 and D60 Sun sensors, shown in **Figure 96**.

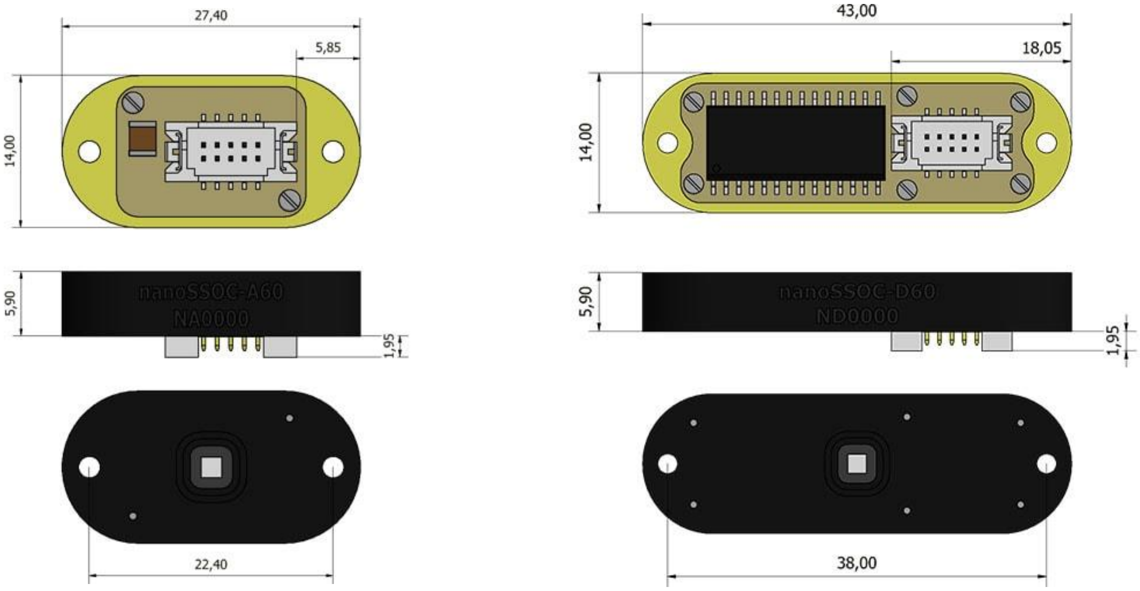

Figure 96: (a) SolarMEMS Nano-SSOC-A60 (b) SolarMEMS Nano-SSOC-D60. Used with permission [179]

3.7.4.2 Star Trackers

Star trackers operate on three basic steps: centroiding, star identification, and attitude determination. Centroiding determines the location of the stars on the image plane, star identification matches candidate stars to a catalog of known stars, and attitude determination generates vectors from the spacecraft to the identified stars [180]. The problem of star identification has been thoroughly researched [181-185], and CubeSat designers should select star trackers from commercial vendors based primarily on SWaP characteristics with regard to component FOV. Star trackers generate full quaternions without the need for additional sensors, but additional sensors may be included on the spacecraft for redundancy or safety purposes. The AEGIS mission selected Hyperion's ST200, depicted in **Figure 97**.

Figure 97: Hyperion ST200 Shown Without Baffle. Baffles are commonly 30 or 45 degrees, used with permission [186]

3.7.4.3 Horizon Sensors

Legacy infrared horizon sensors have utilized multiple single-element thermopiles to measure the Earth horizon's location. Recently it has become possible to put multiple thermopiles on a single MEMS system [187]. Future applications of this technology may lead to full quaternion generation from a single horizon sensor, but this would only be useful in LEO. Deep space CubeSats will find limited use for horizon sensors. It is worth mentioning that features of the Earth are recognizable to imaging technology through AI parsing methods, and attitude vectors can be determined with respect to those features instead of the Earth's horizon or limb. Similarly, with adequate knowledge of the features of a planetary body such as the Moon, a sensor could be created to provide attitude determination using only the surface of the planetary body. Spacecraft designed to travel to other solar systems would need the ability to create a reference frame with respect to the star, map out the surface of a planetary body, and reference that body's features to the star's location.

3.7.4.4 Inertial Measurement Units

IMUs determine rotation rates and accelerations imparted to the spacecraft. They are not used for localization or quaternion vector generation, but they are helpful in providing or corroborating rotation rate estimations from STs. Additionally, if consecutive measurements are unable to be made for whatever reason, e.g. an ST fails, the IMU measurements may be integrated for up to 12 hours for semi-accurate position estimation. A detailed evaluation of CubeSat IMU selection may be found in [188].

It is important to note that IMUs have a weakness when it comes to low thrust propulsion. As discussed in Section 3.4, many high specific impulse thrusters have low thrust values. Assuming the noise floor of an IMU is 3.5 μg, the mass m of a 6U CubeSat is 14 kg, and the thrust T_{sc} from an electrostatic thruster is 300 µN, **Eqs. (111-113)** may be used to calculate the acceleration based on Newton's second law.

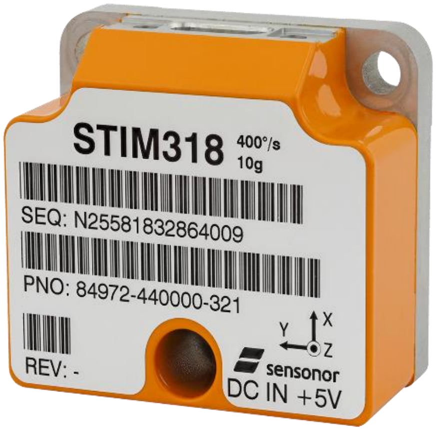

Figure 98: Sensonor STIM318, Used with Permission [189]

$$T_{sc} = m \cdot a \qquad \textbf{Eq. (111)}$$

$$a = \frac{0.0003\ N}{14\ kg} = 0.000021429\ \frac{m}{s^2} \qquad \textbf{Eq. (112)}$$

Dividing the spacecraft linear acceleration by gravity at ground level to obtain g's,

$$\frac{a}{g_0} = \frac{0.000021429\,\frac{m}{s^2}}{9.80665\,\frac{m}{s^2}} = 0.000002185 \qquad \textbf{Eq. (113)}$$

The g's imparted to the spacecraft by the low-thrust propulsion unit are not enough to register on the IMU because they are below the noise floor. Mission planners will need to decide if they need the acceleration measurement at all or if they can compensate via additional sensors. The AEGIS program selected an IMU from the Sensonor STIM300 series, shown in **Figure 98**, and is not currently planning to utilize a linear acceleration measurement for mission operations. The effective consequence of eschewing linear acceleration is that IMU measurements cannot be integrated for position estimation if the star tracker fails.

3.7.4.5 Magnetometers

Magnetometers can be used for localization and attitude determination with knowledge of the WMM or IGRF. They are often used in conjunction with magnetorquers for closed-loop attitude control algorithms. Attitude determination via Kalman filtering of magnetometer and solar cell data is accomplished in [190]. Magnetometers are of limited use in heliospheric deep space, but Voyager 2 experienced a higher magnetic field strength outside the heliosphere [191]. It is possible that magnetometers and magnetic control mechanisms may find enhanced use in interstellar space.

3.7.5 Control Mechanisms Overview

Which attitude control techniques are selected depend upon the mission and system requirements. **Table 47**, taken directly from [33] without alteration, details attitude control methods with respect to pointing requirements. **Table 47** does not provide all attitude control methods found in [33], only the ones considered relevant for deep space missions. While active magnetic control is included, it should not be considered feasible for deep space missions outside LEO and inside the heliosphere. Nuanced control methods exist, such as Gravity Gradient (GG), SRP, and pure spin stabilization, but they should not be considered the primary methods of attitude control for a deep space mission.

Table 47: Attitude Control Methods and Their Capabilities, Used with Permission [33]

Type	Pointing Options	Attitude Maneuverability	Typical Accuracy	Lifetime Limits
Rate-Damping + Target Vector Acquisition	Usually Sun (power) or Earth (communications)	Generally used as robust safe mode	±5-15 deg (2 axes)	None
Active Magnetic with Filtering	Any, but may drift over short periods	Slow (several orbits to slew); faster at lower altitudes	±1-5 deg (depends on sensors)	Life of sensors
Zero Momentum (thruster only)	No constraints	No constraints. High rates possible	±0.1-5 deg	Propellant
Zero Momentum (3 reaction wheels)	No constraints	No constraints	±0.001-1 deg (determined by sensors and processor)	Propellant (if applies). Life of sensors and wheel bearings
Zero Momentum (CMG)	No constraints. Short CMG life may require high redundancy	No constraints. High rates possible	±0.001-1 deg	Propellant (if applies). Life of sensors and wheel bearings

3.7.5.1 Reaction Wheels

RWs are low-friction flywheels with angular velocity and momentum controlled by an electrical interface. One reaction wheel can control one rotational degree of freedom. Many RW systems consist of three wheels configured perpendicularly for full rotational control. RWs are not always perpendicular to one another, and the summed operation of two or more wheels will result in a rotation along a desired spacecraft axis which is internally controlled by closed-loop algorithms provided to the DCE.

The amount of torque a reaction wheel can imbue into the satellite decreases as the wheel speed reaches its maximum limit, called the saturation limit. A RW spinning at maximum angular velocity is known to be saturated. Once saturation occurs, the angular momentum of the wheel must be unloaded by de-spinning the RW while imparting a counter torque to the spacecraft from a thruster or RCS [192]. Balancing desaturation with counter torque should result in no net change of satellite angular velocity, else the RWs will need to be used to detumble after desaturation. The AEGIS mission selected three Blue Canyon Technologies RWP50s and one RWP100 which can be controlled by the same DCE.

Sizing a RW can be done in early phases of design if an appropriate factor of safety is defined for anticipated maximum angular velocities. One should start by defining the parameters listed in **Table 48**. Estimations for masses and distances to solar array centers of mass are fine for first order analyses. As shown in **Eqs. (114-122),** the centered mass moments of inertia are defined per axis, the parallel axis theorem is applied, the maximum angular momentum is calculated, and a factor of safety is applied for reaction wheel selection. The coordinate system defined in Section 3.2.2.2 is continued and combined with length, width, and height monikers so that readers may assign axes as appropriate to their systems. It is assumed that matching solar arrays are deployed off each axis with equal centroidal distances, which is not realistic.

Table 48: Estimates for AEGIS Reaction Wheel Sizing Parameters

Parameter	**Description**	**Value**	**Unit**
m_{cs}	CubeSat Mass	14	kg
w_{cs}	Width, X-direction	0.226	m
h_{cs}	Height, Y-direction	0.366	m
l_{cs}	Length, Z-direction	0.100	m
I_{cm}	Body Mass Moment of Inertia	Variable per Axis	kg-m^2
I	Total Mass Moment of Inertia	Variable per Axis	kg-m^2
m_{array}	Mass per Solar Array (all same)	1.5	kg
d_c	Distance from Centroid (all same)	0.1	m
ω	Maximum Expected Rotation Rate	5	°/s
L_{max}	Maximum Angular Momentum	0.0183	N-m-s
FOS	Factor of Safety	2.5	-

$$I_{cm,l} = \frac{1}{12} \cdot m_{cs} \cdot (w_{cs}^2 + h_{cs}^2) = \frac{1}{12}(14\,kg) \cdot [(0.226\,m)^2 + (0.366\,m)^2)] = 0.2159\,kg \cdot m^2 \quad \textbf{(Eq. 114)}$$

$$I_{cm,w} = \frac{1}{12} \cdot m_{cs} \cdot (l_{cs}^2 + h_{cs}^2) = \frac{1}{12}(14\,kg) \cdot [(0.100\,m)^2 + (0.366\,m)^2)] = 0.1679\,kg \cdot m^2 \quad \textbf{(Eq. 115)}$$

$$I_{cm,h} = \frac{1}{12} \cdot m_{cs} \cdot (l_{cs}^2 + w_{cs}^2) = \frac{1}{12}(14\,kg) \cdot [(0.100\,m)^2 + (0.226\,m)^2)] = 0.0713\,kg \cdot m^2 \quad \textbf{(Eq. 116)}$$

Applying the parallel axis theorem,

$$I_l = I_{cm,l} + m_{array,l} \cdot d_{c,l}^2 = 0.2159\,kg \cdot m^2 + (1.5\,kg) \cdot (0.1\,m)^2 = 0.2309\,kg \cdot m^2 \quad \textbf{(Eq. 117)}$$

$$I_w = I_{cm,w} + m_{array,w} \cdot d_{c,w}^2 = 0.1679\,kg \cdot m^2 + (1.5\,kg) \cdot (0.1\,m)^2 = 0.1829\,kg \cdot m^2 \quad \textbf{(Eq. 118)}$$

$$I_h = I_{cm,h} + m_{array,h} \cdot d_{c,h}^2 = 0.0713\,kg \cdot m^2 + (1.5\,kg) \cdot (0.1\,m)^2 = 0.0863\,kg \cdot m^2 \quad \textbf{(Eq. 119)}$$

Calculate the maximum angular momentum based on an assumed rotation rate and the maximum of the calculated moments of inertia.

$$\omega = \left(5\,\frac{degree}{s}\right)\cdot\left(\frac{\pi}{180}\right) = 0.0873\,\frac{rad}{s} \qquad \textbf{(Eq. 120)}$$

$$L_{max} = \omega \cdot I_l = \left(0.0873\,\frac{rad}{s}\right)\cdot(0.2309\;kg\cdot m^2) = 0.0202\;N\cdot m\cdot s \qquad \textbf{(Eq. 121)}$$

Apply a conservative factor of safety and compare with commercial product capability.

$$Inertial\ Storage = L_{max}\cdot FOS = (0.0202\;N\cdot m\cdot s)\cdot(2.5) = 0.0504\;N\cdot m\cdot s \qquad \textbf{(Eq. 122)}$$

The RWP50 from BCT features an inertial storage of 0.05 N-m-s before requiring desaturation. Solar array masses of 1.5 kg, centroidal distances of 0.1 m, and angular velocities of 5 deg/s should be considered liberal estimates and not conservative. A second order estimate would subtract solar array mass from the total mass of the spacecraft and account for a centroid shift due to solar array deployment. Although the factor of safety allows for growth margins, AEGIS applied two RWP50s in the example axis for a total inertial storage of 0.1 N-m-s. This correlates to a maximum rotation rate reduction of ~24.8 degrees per second about the z-axis before desaturation is required, which may not be enough.

3.7.5.2 Reaction Control System

RCS are used for RW desaturation, orbital station-keeping, or any low total impulse propulsive operation. They consist of thrusters pointed in select directions with a centralized propellant storage. Thrusters do not need to be oriented in principal axes; it is common that the summation of two or more thrusters will cause a torque about a desired axis. CubeSat programs must analyze if an RCS is necessary for control or desaturation maneuvers, but the MarCO satellites and many of the Lucky 13 feature an RCS [126, 193].

RCS propellant has historically been cold gas; refrigerants such as R236fa are still used. EP methods may be considered in lieu of a cold gas system, and EP systems may be utilized for a single axis instead of a bulky COTS system that provides an RCS for all three axes. Companies such as Busek and ThrustMe have begun offering ionic liquid or solid propellant EP components for single axis control, but electrospray EP methods are also on the horizon. These components are unfortunately still too large for CubeSat platforms below 6U (they are on the order of 0.5-1.5U), but advancements in miniaturized, single-axis thrusters are expected in the 2020s.

Cold gas, EP, and microcathode arc thrusters are all options for single-axis RCS. If viewed from the -Y direction ram face, which is the thruster face because the spacecraft will be retrothrusting, the main propulsion thruster can be instructed to vector up, down, left, and right. If up/down are the pitch directions and left/right are the yaw directions, the satellite does not have the immediate ability to desaturate the roll RW by TVC. A phenomenon known as the Dzhanibekov effect may be exploited to transfer angular momentum from the roll axis to the yaw axis by applying a constant pitch countertorque and using a two-phase feedback linearization scheme to drive the roll axis down to zero during the transition periods, but no CubeSat has attempted this desaturation method [194]. If TVC exploitation of the Dzhanibekov effect is not considered a viable option for roll desaturation, a single-or-more axis RCS must be employed. If no TVC is present on the propulsion system, a three-axis RCS is required regardless.

It is important to note that a single-axis RCS will consist of two thrusters in one of two configurations shown in **Figure 99**. If thrusters are mounted on the centroid of the satellite in the Y-direction between the ram and anti-ram faces, the thrusters will only impart momentum into the roll axis. As propellant is used, that centroid will change. Thus, the thrusters will never stay exactly on the centroid, and disturbances will be imparted to the pitch or yaw axes at some point. Two thrusters in a single-axis RCS allow for desaturation of a RW in both directions.

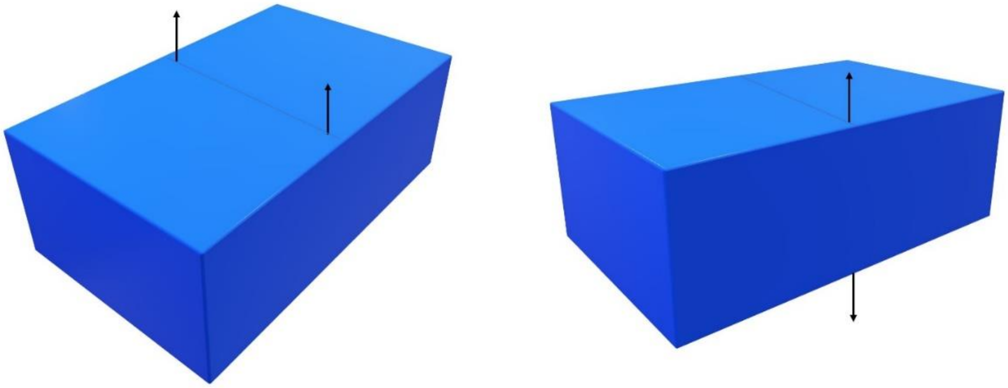

Figure 99: Single-Axis RW Desaturation Thruster Configuration Possibilities

3.7.5.3 Magnetorquers

Magnetic Torquers, or magnetorquers, are magnetic coils that generate magnetic dipole moments with magnitude proportional to a current input [33]. They are primarily used for attitude control in LEO as well as RW desaturation. The moments generated by magnetorquers are much lower than most other control mechanisms, and RW desaturation is a relatively slow process requiring multiple orbit periods. A common use of magnetorquers is to detumble LEO satellites after ejection from a dispenser. The control algorithm is known as B-dot, and B-dot application is covered in [195].

3.7.5.4 Control Moment Gyroscopes

Control Moment Gyroscopes (CMG) operate by a different principle than RWs. They are gimbaled wheels spinning at a constant rate which are controlled by turning a gimbal axis. CMGs exist in single-gimbal, dual-gimble, and variable speed configurations. They are more difficult to control than RWs, and the bearings of the wheels undergo significant stresses leading to reduced lifetimes [33]. CMGs are more power efficient than reaction wheels but require more real estate in the spacecraft. Thus, CMGs should not be used unless high-torque and fine control are required with low lifetime expectancy. An investigation into CMG operation on CubeSats may be found in [196]. The International Space Station features four CMGs designed to keep the station at a fixed attitude relative to Earth which rotate at a fixed rate of 6600 rpm, and astronauts can replace them as needed [197].

3.7.5.5 Micro-cathode Arc Thrusters

Micro-cathode Arc Thrusters (µCATs) were first developed in 2007 at the Micropropulsion and Nanotechnology Laboratory of George Washing University (GWU) under Dr. Michael Keidar. They are pulsating vacuum arc thrusters that operate by vaporizing metallic cathode material and accelerating the particles away from the satellite with electromagnetic fields [198]. µCATs are not commercially available as of this writing without working directly with GWU, but they are listed here as an exciting option for single-axis RW desaturation in the 2020s.

3.7.5.6 Active Mass Translators

Active Mass Translators (AMTs) are attitude control systems that operate by shifting a spacecraft's center of mass, thereby changing the moment arm between the thrust vector and the satellite centroid while the body undergoes a propulsive maneuver. The best example of this applied to CubeSats to date is the AMT employed by NASA's Near Earth Asteroid Scout (NEAScout) mission. NEAScout will utilize an 86 m^2 solar sail in conjunction with the AMT to control its attitude while being propelled by solar radiation pressure. The NEAScout AMT is a two-axis translation table that balances both the spacecraft's center of mass and center of pressure while also trimming disturbance torques created by off-nominal sail conditions [199]. Designers interested in applications of AMTs and solar sails should read [193] first, as [199] features lessons learned in the design presented in [193].

3.7.6 Control Accuracy

Even before SRR, a mission can define the order of magnitude of pointing requirements and use this requirement definition to narrow down the type of sensors and control mechanisms that are evaluated to fit a mission's needs. If a mission has pointing requirements of less than 0.1 deg, GG and single-axis spin stabilization may be neglected entirely because they do not offer fine control of the spacecraft compared to other methods. **Table 49**, taken directly from [33], compares pointing requirements to GN&C component selection. **Table 49** should be read to glean what should not be used rather than what should be. Material in [33] is for spacecraft design in general and is not specific to CubeSats or deep space missions. Thus, ADCS nomenclature is used in lieu of GN&C, and magnetic controls are included.

Table 49: Effects of Control Accuracy Requirements on Sensor Selection, Used with Permission [33]

Required Accuracy (3σ)	Effect on Spacecraft	Effect on ADCS
> 5 deg	• Permits major cost savings • Permits GG stabilization	Without attitude determination • No sensors required for GG stabilization • Boom motor, GG damper, and a bias momentum wheel are only required actuators With attitude determination • Sun sensors and magnetometer adequate for attitude determination at ≥ 2 deg • Higher accuracies may require star trackers or horizon sensors
1 deg to 5 deg	• GG not feasible • Spin stabilization feasible if stiff, inertially fixed attitude is acceptable • Payload needs may require despun platform on spinner • 3-axis stabilization will work	• Sun sensors and horizon sensors may be adequate, especially for spinner • Accuracy for 3-axis stabilization can be met with RCS deadband control, but reaction wheels will save propellant for long missions • Thrusters and damper adequate for spinner actuators • Magnetic torquers and magnetometer useful

Required Accuracy (3σ)	Effect on Spacecraft	Effect on ADCS
0.1 deg to 1 deg	• 3-axis and momentum-bias stabilization feasible • Dual-spin stabilization also feasible	• Need for accurate attitude reference leads to star tracker or horizon sensors and possibly gyros • Reaction wheels typical with thrusters for momentum unloading and coarse control • Magnetic torquers feasible on light vehicles (magnetometer required)
< 0.1 deg	• 3-axis stabilization is necessary • May require articulated and vibration-isolated payload platform with separate sensors	• Same as above for 0.1 deg to 1 deg but needs star tracker and better class of gyros • Control laws and computational needs are more complex • Flexible body performance very important

3.7.7 Navigation Methodology

Navigation is "the determination of the spacecraft's position and velocity relative to a specified reference frame as a function of time [33]." Navigation is used for trajectory control, which is the control of the path traveled by a spacecraft via "the determination and execution of translational commands," usually thruster firings, "required to drive the current states towards the desired states as determined by a guidance system" [33]. Additional algorithms for attitude determination may be found in [35].

AEGIS navigation is accomplished via two parallel processes, both utilizing a Nonlinear Extended-state Kalman filter (NEKF) to fuse sensor measurements with state propagation equations. The general equations for a NEKF are shown in **Eqs.(123-125)**, where K is the Kalman gain matrix, $\tilde{x}$ is the position or velocity state estimate, P is the covariance estimate, $\bar{y}$ is the sensor measurement, and h is the observation matrix such that $\bar{y} = h \cdot \tilde{x}$. The parameter w_k represents a weighting function matrix which may or may not be necessary, and I is the identity matrix. Equation dots are included to represent multiplication, but matrix multiplication should not be understood strictly as dot products.

$$K_{k+1} = P_k \cdot h_{k+1}^T \cdot [h_{k+1} \cdot P_k \cdot h_{k+1}^T + w_k^{-1}]^{-1} \qquad \textbf{Eq.(123)}$$

$$P_{k+1} = [I - K_{k+1} \cdot h_{k+1}] \cdot P_k \qquad \textbf{Eq.(124)}$$

$$\tilde{x}_{k+1} = \tilde{x}_k + K_{k+1} \cdot (\bar{y}_{k+1} - h_{k+1} \cdot \tilde{x}_k) \qquad \textbf{Eq.(125)}$$

Eqs. (123-125) are sequential and run each time a new measurement is obtained. For example, the first process, handled by C&DH and TT&C, is orbital element determination. This could mean traditional Keplerian orbital elements in a LEO TLE or cartesian state vectors, but position and velocity estimates are the goal. As described in Section 3.6.9, ranging and doppler data from the DSN will be used to determine the satellite's orbital elements. These orbital elements will then be used as initial conditions for an orbit state propagator. The equations of motion of the satellite will include gravitational forces from the Earth, Moon, and Newton's second law. A Runge-Kutta 11 (RK11) discrete numerical integration scheme, requiring an accurate clock to be updated by DSN during communications, then estimates the satellite's future position.

The second process is attitude determination. Initial conditions of the attitude will be obtained from a combination of star tracker measurements, which provide the full quaternion, and optionally the Sun sensors, which provide only azimuth and elevation to the Sun. Assume a rotation of the spacecraft is desired to point the solar panels towards the Sun in an optimal charging configuration. If a spacecraft would prefer to pre-load ephemeris data for the Sun instead of searching for the Sun to determine which way it should turn, the NASA Ancillary Information Facility (NAIF) SPICE library can be used [200]. SPICE is not a traditional acronym. This library utilizes Chebyshev polynomials to provide ephemeris data for other spacecraft, asteroids, planetary bodies, and stars. The star tracker provides the quaternion from the star tracker frame to either the body frame or J2000 ECI frame as desired. In the latter case, both the spacecraft attitude in the J2000 ECI frame from the ST and the Sun ephemeris data in the J2000 ECI frame from the SPICE library are known. The error signal to the DCE driving reaction wheel control logic is generated from the vector rotation in the known ECI coordinate system. To recap, the spacecraft uses the star tracker to determine its attitude, checks the SPICE library to find where the Sun is, and provides the difference between the original attitude and the desired attitude to the DCE to rotate the satellite to the desired orientation.

The equations of motion of the quaternion will be propagated forward in time using **Eqs.(110,123-125)**. To reiterate, q_i are the four quaternions, and p, q, r are the components of the angular velocity vector in the body frame provided by the IMU. The IMU bias will be a parameter that is estimated in the NEKF; it is anticipated that the star tracker will operate at more than 1 Hz to remove as much bias as possible. In the event the star tracker fails, the Sun sensors can be used as a backup for rough quaternion estimation. Using the star tracker at the same time as the Sun sensor will not yield greater attitude determination accuracy. The star tracker selected by AEGIS, the Hyperion ST200, operates at 5 Hz.

4. Radiation Effects, Shielding, and Redundancy

Radiation data from previous missions, analyses performed by AEGIS, and experimental validations from various textbooks are presented here; much background information in Sections 4.1, 4.2, and 4.5 stems from Christoph M. Nöldeke's book, *The Space Radiation Environment* [166], and Section 4.3 is based on the comprehensive work of Heidergott [201]. Radiation characterization begins with a description of the parameters which define radiative environments followed by the environments themselves, their effects on spacecraft, how to design spacecraft with these effects in mind, and the tools one might turn to for assistance in understanding how it all fits together. Spacecraft that supply radiation environment data are discussed in Appendix B.

4.1 Space Radiation Environment

Space is radioactive. Two types of particle sources dominate the environment: Galactic Cosmic Rays (GCRs) and Solar Energetic Particles (SEPs). Neither are comprised solely of electromagnetic radiation in the form of photons; energetic Gamma-rays are also present. GCRs are primarily heavy ions comprised of all nuclei known on Earth. Their energy spectrum ranges up to 10^{20} eV, and they are accelerated by supernovae within and without our galaxy. SEPs are comprised of protons, ions, electrons, and X-rays produced by solar flares and CMEs. Both sources are highly variable with differing fluxes and energies per particle and must be analyzed separately and then cumulatively.

4.1.1 Radiation Parameters for Spacecraft Design

Engineers characterize radiation for a variety of environment cases. The most important parameters for space radiation evaluation and mitigation are defined here, followed by a discussion of nominal values for radiative parameters and the spacecraft that ascertain them.

4.1.1.1 Flux

Flux is a generalized quantity describing the number of individual particles passing through a control area. Here, Φ is the flux defined as the number of particles dN passing per time interval dt through an area A. This could also be taken as how many particles impact the surface of a detector.

$$\varPhi = \frac{1}{A} \cdot \left[\frac{d}{dt} \cdot N(t)\right] \quad \textbf{Eq.(126)}$$

The assumptions that particles are moving in parallel, the incidence is orthogonal, and A is sufficiently small are implied, but not required. The units of flux are 1/(m^2-s), but many applications of flux take 1/(cm^2-s) or 1/(mm^2-s). If particles of the same type but varied energy are of interest, a differential flux may be defined as $\Phi_a(E)$ at energy E for a differential interval dE. Units of differential flux are 1/(m^2-s-MeV). If the goal is to define the flux of particles which exceed a given energy, **Eq.(127)** may be used to define the integral flux spectrum. Flux defined by current density is not covered.

$$\varPhi_i(E) = \int_E^{E_{max}} \varPhi_d(E') \cdot dE' \quad \textbf{Eq.(127)}$$

Deep space GCR is approximately isotropic, and the concept of sectoral flux is presented to define the particle flux unit. Sectoral flux is applicable where particles impact a detector within a sector of a solid angle. The particles are no longer travelling in parallel. The number of particles dN per unit time interval dt which pass through area A from any direction contained within a sector of solid angle $\Delta\Omega_a$ is the sectoral flux Φ_s shown in **Eq.(128)**.

$$\Phi_s = \frac{dN}{dt} \cdot \frac{1}{\Delta A \cdot \Delta\Omega_a} \qquad \textbf{Eq.(128)}$$

Sectoral flux is measured in 1/(m^2-s-sr) or 1/(cm^2-s-sr), where sr, or steradian, is the solid angle subtended at the center of a unit sphere by a unit area on its surface. The particle flux unit (pfu, intentionally lowercase) is defined by the latter unit including cm. Omnidirectional fluxes are generally reported in pfu [166].

4.1.1.2 Fluence

Fluence is flux integrated over time. For a duration exposure time t_e, the fluence F and differential fluence $F_d(E)$ are defined by **Eqs.(129-130)**.

$$F = \int_0^{t_e} \Phi(t) \cdot dt \qquad \textbf{Eq.(129)}$$

$$F_d(E) = \int_0^{t_e} \Phi_d(E,t) \cdot dt \qquad \textbf{Eq.(130)}$$

Units of fluence are 1/m^2 or 1/cm^2. Units of differential fluence are 1/(m^2-MeV) or 1/(cm^2-MeV).

4.1.1.3 Cross Section

When engineers send electronics into space, those electronics will eventually fail due to radiation-induced events. Designers must be able to compare the performance of different electronics for the same radiation environment. The cross section is a parameter which interrelates radiation events to the flux of an incident stream of particles causative of the events, regardless of the type of event or hardware. Consequently, cross section is not something that can or should be analytically determined. An integrated circuit or embedded system must be bombarded with radiation and checked for internal errors for a cross section to be generated [166]. Assuming a unidirectional flux Φ causing N events during t_e irradiation time, the cross section σ_c is defined as **Eq.(131)**. Cross section is defined in units of m^2 or cm^2. Nuclear physicists sometime use the unit barn, where 1 barn = 10^{-24} cm.

$$\sigma_c = \frac{N}{\Phi \cdot t_e} \qquad \textbf{Eq.(131)}$$

If flux is constant over the irradiation time, the cross section may be defined in terms of fluence.

$$\sigma_c = \frac{N}{F} \qquad \textbf{Eq.(132)}$$

It is important to note that the probability of a deleterious radiation interaction is directly proportional to the cross section, but a spacecraft's interaction with the surrounding radiation is a risk, meaning interactions may or may not happen at all. A spacecraft's OBC could be hit with a 5 TeV (extremely unlikely) ion and fail immediately upon satellite ejection, or deleterious radiation could miss the OBC and critical hardware entirely for 10 years in a row. Radiation exists in space and must be planned for, but risk is defined in terms of probability and impact.

4.1.1.4 Intensity

Photons are electromagnetic field particles, but they do not have mass. It is therefore more convenient to describe electromagnetic radiation in terms of power flux instead of particle flux. For a radiative power P and unit area A the intensity S in W/m^2 is defined in **Eq.(133)**.

$$S = \frac{\Delta P}{\Delta A} \qquad \textbf{Eq. (133)}.$$

Intensity as defined here is sufficient for heat transfer purposes, but intensity must be defined within a wavelength interval $[\lambda_1, \lambda_2]$. The differential intensity $\frac{dS}{d\lambda}$ must be qualified.

4.1.1.5 Activity

Activity is not explicitly needed for initial environment characterization, but it is included as an impetus to get readers thinking about nuclear power supplies for very deep space missions. Activity describes the strength of radioactivity. It is characterized by a hypothetical detector encompassing a radiating mass, and the decay mechanism, whether α, β, or γ, is not considered. For a number of nuclei N able to decay over time t the activity A_r is defined by **Eq.(134)**.

$$A_r = \frac{-dN(t)}{dt} \qquad \textbf{Eq.(134)}$$

Note the negative sign such that the number of decaying nuclei decreases over time. The unit of activity is the Becquerel (Bq), or one decay process per second. Data is usually provided as specific activity measured in Bq/kg [166].

4.1.1.6 Dose

Particle radiation is dangerous to electronics partly because it is ionizing. Electrons on a target material may be ejected from a material if ionizing radiation with sufficient energy strikes the material at the appropriate angle. This causes unanticipated materials to become charged. The measure of ion energy E_{ion} deposited by ionization per unit mass m_t of the irradiated target is the Dose.

$$D = \frac{E_{ion}}{m_t} \qquad \textbf{Eq.(135)}$$

Different types of radiation will have different effects on target materials because the energy released by ionization is depending upon radiation and material type. Transistors are particularly susceptible to ionizing radiation.

Dose is measured in Gray (Gy) outside the US and in rads inside the US, where 1 Gy = 1 J/kg and 1 rad = 0.01 Gy. This is yet another instance where ubiquitous use of metric units would be more useful. Dose applied to biological targets is known as equivalent dose and is not covered here.

The common radiation metric of interest, described more fully in Section 4.5.3, is the Total Ionizing Dose (TID). The TID evaluates the dose from protons, ions, electrons, and secondary photons and sums them into a complete measure of ionization energy provided to the target material. Neutrons are not generally of concern as primary particles in deep space because the half-life of a free neutron in space neutron is 887.7 ± 2.2 seconds or 878.5 ± 0.8 seconds depending on how it is measured, unless it is produced nearby such as a lunar surface reaction. Effects of TID in space include increased propagation delay times, lower maximum clock rates, reduced output drive, lower noise margins, increased leakage, and catastrophic failure [202].

4.1.1.7 Linear Energy Transfer

When particles strike target materials, the strike is not a single moment wherein the energy is deposited instantaneously. A charged particle moving through a semiconductor deposits a fraction of its energy in the medium by ionizing the atoms of the crystal along its path [203]. The ionizing energy loss by the ion to the material is characterized by the mass stopping power for a material, or Linear Energy Transfer (LET), which is a measure of the energy transfer per unit length of material. LET is obtained by dividing the energy loss per unit length $\frac{dE(x)}{dx}$ by the material density ρ_m [204].

$$LET(x) = \frac{1}{\rho_m} \cdot \frac{-dE(x)}{dx} \qquad \textbf{Eq.(136)}$$

In space, most heavy ions from GCR have LETs in silicon ranging from 0.01 to 40 MeV-cm^2/mg [203]. In silicon devices, where it takes an average energy of 3.6 eV for a particle to create an electron-hole pair, an LET of 1 MeV cm^2/mg roughly corresponds to a charge deposition per unit length of 10 fC/µm. Typical values of deposited charge in silicon vary from 0.1 to 400 fC/µm [203]. Assessment of upset rates in electronic devices for specific radiation scenarios cannot be done without knowledge of particle LETs [166].

4.1.1.8 Range

Residual range, or simply range, represents the distance a particle will travel through a material. Range is dependent upon the type of particle, particle energy, particle kinetics, and receiving material and is defined as a function of energy and LET in **Eq.(137)**.

$$r_p(E) = \int_0^E \frac{1}{LET(E_i)} \cdot dE_i \qquad \textbf{Eq.(137)}$$

A particle will decelerate as it traverses the medium and deposit energy in increments of dE_i [166]. Consequently, the LET will change but the change may be an increase or decrease depending on the particle and energy range.

Range has units of a dimension multiplied by the mass density of the stopping material because LET is normalized to density. The geometric range $x_p(E)$ as a common dimension is defined by **Eq.(147)**. If the geometric range of a particle is greater than the thickness of a target material, the particle will penetrate the material after depositing energy into the target's structure.

$$x_p(E) = \frac{r_p(E)}{\rho_m} \qquad \textbf{Eq.(138)}$$

4.1.1.9 Non-Ionizing Energy Loss

Non-Ionizing Energy Loss (NIEL) is the displacement damage analog of LET [205], and direct calculation is non-trivial [206]. The primary mechanism of NIEL is a perturbation of the lattice structure of the semiconductor crystal as single lattice atoms are kicked from their positions or undergo nuclear reactions [166]. Interactions are either electromagnetic, by electrical repulsion of positively charged particles, or nuclear. Individual defects such as vacancies and interstitials are generated, and cluster generation wherein more than one lattice atom is displaced is possible.

The effect of NIEL manifests as a degradation of electrical performance in semiconducting materials. Described in Appendix B, the SOHO spacecraft experienced a 2% loss in solar panel efficiency during a single SPE in the Bastille Day events of July 14th, 2000 [166]. Solar panel coverglass materials such as fused silica and lead glass are designed to mitigate radiation-induced efficiency losses in solar arrays.

NIEL is measured in MeV-cm^2/g, but it will be shown that, similar to dose, NIEL may be related to a Displacement Damage Dose (DDD) as the energy deposited per mass unit measured in J/kg as a form of lattice damage. DDD for NIEL and Dose Depth Curves (DDC) for NIEL and TID are discussed in Sections 4.5.3-4.

4.1.1.10 Parameter Unit Overview

Units for radiation parameters are generally defined in terms of SI units and then varied by order of magnitude for dimensional convenience. Strictly speaking, the SI unit for energy is the Joule and not the electronvolt; MeV and Joule are included for relevance. For each of the radiation parameters, standard SI units and commonly scaled unit variants are provided in **Table 50**. Some parameters have more than one unit variant, as values may be provided per bit or per device.

Table 50: Radiation Parameter Unit Definition

Parameter	SI Unit	Conversion	Commonly Published
Flux	1/(m^2-s)		1/(cm^2-s)
Differential Flux	1/(m^2-s-MeV)		1/(cm^2-s-MeV)
Sectoral Flux	1/(m^2-s-sr)		1/(cm^2-s-sr)
Fluence	1/(m^2)		1/(cm^2)
Differential Fluence	1/(m^2-MeV)		1/(cm^2-MeV)
Cross Section	m^2		cm^2
Intensity	W/m^2		W/m^2
Activity	-	1 Bq = 1 decay process/s	Bq
Specific Activity	-	1 Bq = 1 decay process/s	Bq/kg
Dose	J/kg	1 Gy = 1 J/kg	rad
		1 rad = 0.01 Gy	
LET	MeV-m^2/kg		MeV-cm^2/mg
Range	kg/m^2		g/cm^2
Geometric Range	m		cm
NIEL	MeV-m^2/kg		MeV-cm^2/g

4.1.2 Galactic Cosmic Rays

What radiation will be encountered on orbit is dependent upon that orbit. The orbit of AEGIS by Earth altitude may be found in **Figure 9** in Section 2.2. For the following radiation analyses, a circular orbit of 400,000 km was assumed. Figure calculations were performed in SPENVIS, a radiation model discussed in Section 4.5.2, by the AEGIS Program Manager, Jared Fuchs, for the AEGIS Radiation Environment Model. Mission duration is assumed at 6 months.

4.1.2.1 GCR Sources

GCR is a term for high energy charged particles with extrasolar origin. They were first discovered by Victor Hess in 1912 with an ionization chamber particle counter on a weather balloon but were not understood fully. Robert Millikan later introduced the term Cosmic Rays in 1920. GCR are particles accelerated by supernovae which occur on average three times per century within the Milky Way. While electrons are present in GCR, a majority of GCR particles are completely ionized nuclei of all stable elements and their isotopes from hydrogen to uranium [166]. GCR can be assumed isotropic outside of Earth's magnetosphere. Explicitly defining the GCR spectrum is critical because GCRs are the primary source of upsets in deep space electronics and the major contributor to long term degradation of electronic devices.

GCR fluxes are nominally lower than SEP fluxes, and flux for both is non-linear with increasing particle energy. As atomic proton number Z increases, the flux of ions decreases exponentially. There are fewer heavy ions in GCR than hydrogen or helium ions. Specifically, the flux of uranium ions (Z=92) could be

10 orders of magnitude smaller than the flux of hydrogen ions (Z=1). In this instance, the ionized hydrogen atoms are simply protons due to the lack of a neutron in non-deuterium hydrogen atoms. The GCR flux of protons above 1 MeV/nucleon in this example is 4.7/(cm^2-s), while the SEP flux during a Solar Particle Event (SPE) on October 29th, 2003 of the same energy is $4{\cdot}10^5$/(cm^2-s). The takeaway is that GCRs are lower flux, higher energy, and contribute more toward Single Event Upsets (SEU), discussed in Section 4.2, than SEPs. The hadronic component of GCR is ~87% ionized hydrogen, ~12% helium, and ~1% heavier nuclei [207] with kinetic energies extending beyond 10^{20} eV [208,209,166].

4.1.2.2 GCR Characterization

To numerically determine the GCR flux, a few estimations must be made in SPENVIS before the analysis is ready. SPENVIS utilizes a GCR model. The most used is called CREME96 for Cosmic Ray Effects on Microelectronics Code updated in 1996, but it is not the most accurate available. It should not be used for data sets or missions after 1997. All models have one weakness or another [209], but of note is that the example given in the prior section was calculated with CREME96. The following data was calculated with CREME2009 based on the ISO 15390 GCR standard model.

The magnetospheric shielding effects are not present at AEGIS distance; magnetospheric modulation is not included in the calculation. GCR particles are ions, so they are modulated by the heliospheric magnetic field which is frozen in and carried along with the solar wind [209,210]. The heliospheric modulation distance here is 1 AU. Higher-Z elements above 26 were not included here due to GCR model limitations. **Table 51** defines the GCR model inputs to SPENVIS. **Figure 100** displays the GCR flux in the cislunar plane. **Figure 101** denotes the combined flux per ion. Note that the units of **Figure 100** are per energy and per solid angle while the above example fluxes are not.

Table 51: GCR Model Inputs to SPENVIS

Setting	Value
Orbit	400,000 km circular
GCR Model at 1 AU	ISO 15390
Solar Activity Data	Solar Minimum (May 1996)
Magnetic Shielding	Off
Ion Range	H to Fe

Some models show higher low energy fluxes for hydrogen and helium than shown in **Figure 100**, but the amount of data available for realistic cross-referencing is insufficient. A higher particle energy is associated with higher LET and therefore a higher charge deposition in a transistor. Section 4.4 details how shielding can block out lower energy particles. An underestimation of lower energy particle flux is less concerning than Z = 3 or greater, which is most accurately modeled by BON2010 discussed in Section 4.5.2.1. As seen in **Figure 101**, the GCR combined flux decreases with increasing atomic number Z. It should be noted that the probability of encountering a high energy, high-Z particle is low, but it exists. A spacecraft could be on orbit for 10 years and never encounter such a particle near its sensitive electronics, but a spacecraft could also encounter a deleterious particle immediately upon deployment. At some point, spacecraft designers must draw a line in the sand for the risk they are willing to accept when deciding on a radiation mitigation strategy.

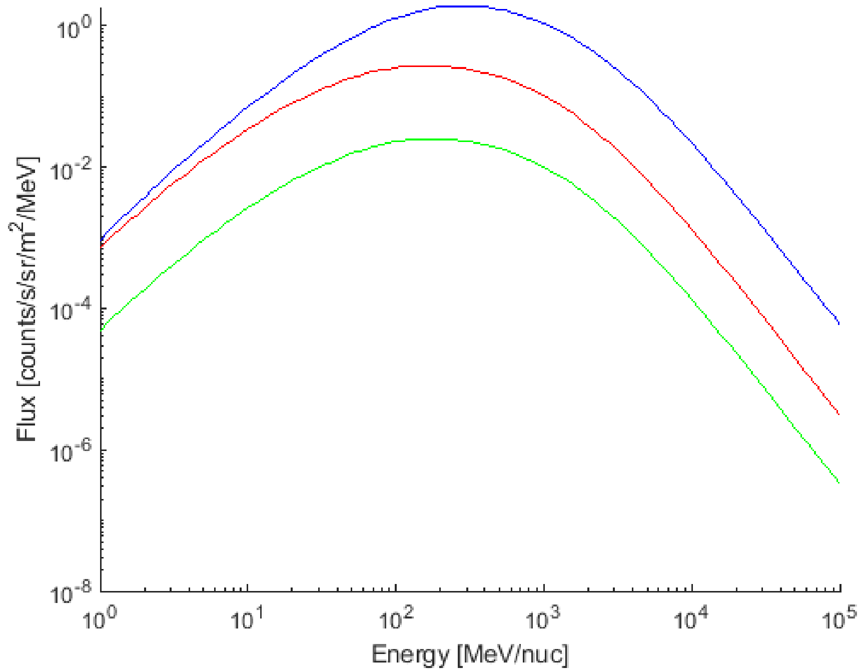

Figure 100: GCR Flux in Cislunar Space 400,000 km from Earth. Blue is H ions, red is He ions, green is heavy ion flux from Z = 3 to Z = 26

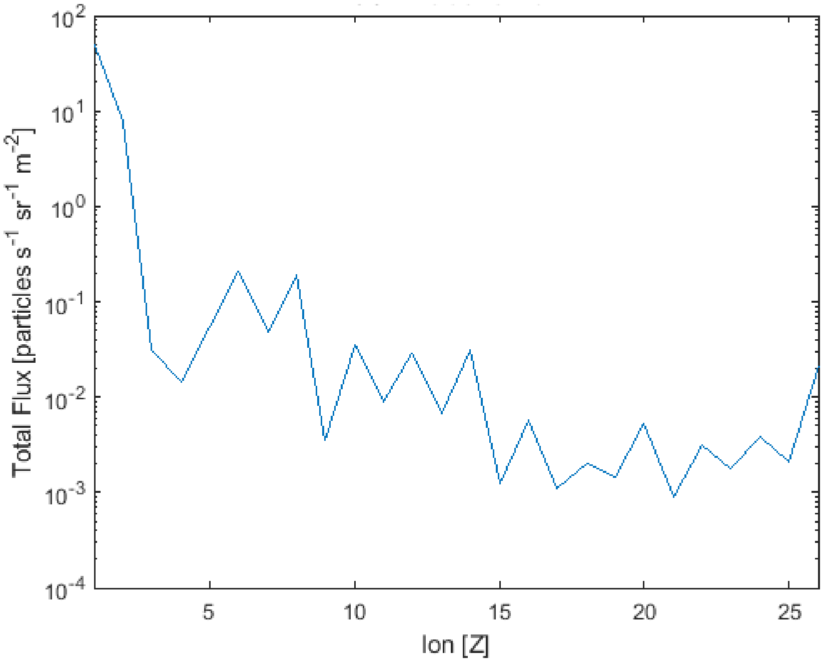

Figure 101: GCR Combined Flux per Ion Showing Relative Distribution of Flux vs. Z

4.1.3 Solar Energetic Particles

There are two components to SEPs: continuous solar wind and SPE particles. SEPs are more variable in energy and flux because they are dependent on probabilistic events linked with solar activity and the solar cycle. The next solar cycle will begin in 2020, reaching a maximum in 2025, and is expected to be relatively weak in activity [211].

4.1.3.1 SEP Sources

The solar wind is a continuous stream of particles; an approximately equal ratio of electrons to protons makes the wind electrically neutral. The proton to alpha particle ratio is approximately 22. Nuclei energies range from 0.3 to 3 keV/nucleon; here a nucleon is a baryon, either a proton or a neutron. Electron energies range from 1 to 100 eV; the fluxes for both protons and electrons range from 1 to $8 \cdot 10^8$ particles per cm^2 per second [212-214]. In comparison with the GCR data, one can see the tenets of GCR being higher energy and lower flux than SEPs hold true.

The two SPEs of note are flares and Coronal Mass Ejections, described initially in Section 3.7.3.4 Particles released from these sources will reach Earth-Moon distance in less than a day [212]. Particles from the Sun's western hemisphere that are magnetically connected with Earth may reach Earth-Moon distance in 20 minutes. Electrons with energies of 0.5-1 MeV are present as well as protons with energies of 20-80 MeV.

4.1.3.2 SEP Characterization

As SPEs are probabilistic events, probabilistic predictions for particles must be made. The two primary analyses of interest are total mission fluence and peak solar particle event flux. The SAPPHIRE model in SPENVIS is used to calculate these values [215]. SAPPHIRE calculates the expected peak flux for a specified event frequency rate, in this case 1 in 10 years. Magnetic shielding may be toggled, but it is off in this case. The SEP peak event flux model inputs may be seen in **Table 52**. The SEP peak event flux is shown in **Figure 102**.

Table 52: SEP Peak Flux Model Inputs to SPENVIS

Setting	Value
Orbit	400,000 km circular
SEP Flux Model	SAPPHIRE 1 in n year event peak flux
Event Frequency	1 in 10 Years
Magnetic Shielding	Off
Ion Range	H to Fe

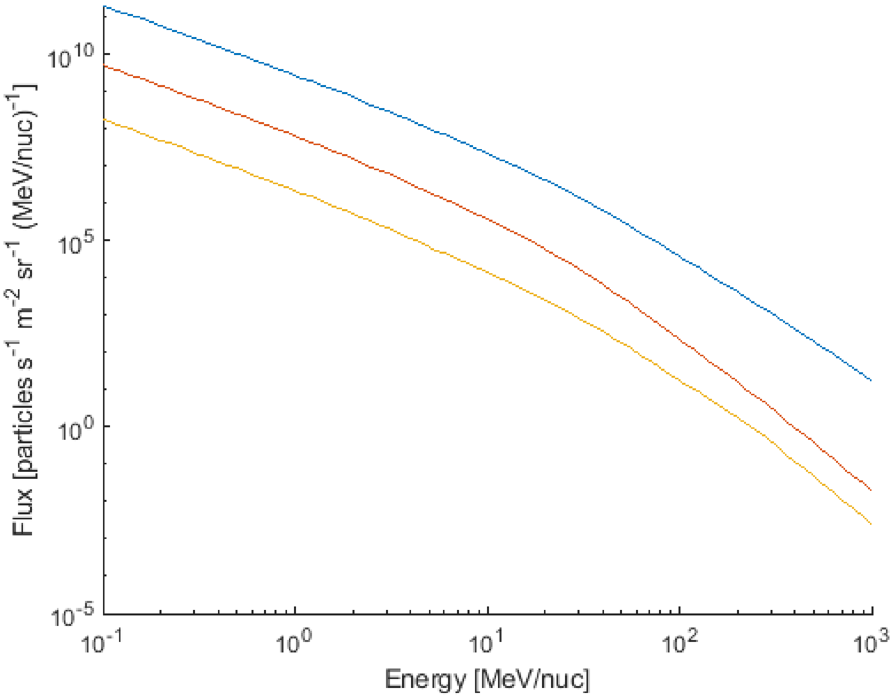

Figure 102: SEP Peak Event Flux. Blue is H ions, red is He ions, and yellow is combined heavy ion flux from Z = 3 to Z = 26

The background here is approximated as isotropic, and the SEP flux is given as a function of angular area, or inverse steradians. SEP relative flux for this case is shown in **Figure 103**.

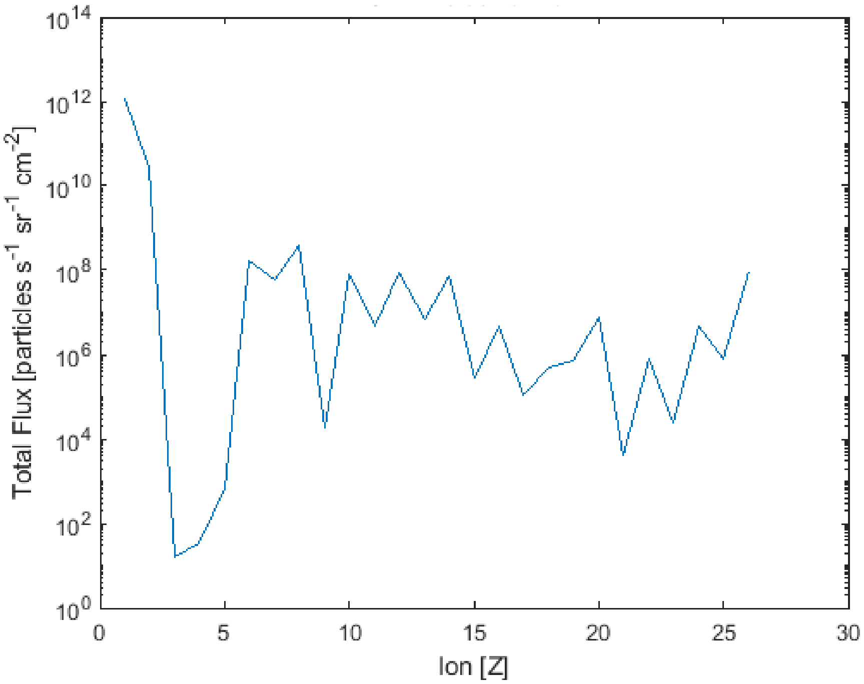

Figure 103: SEP Peak Event Relative Flux

As in **Figure 101**, ions greater than Z = 26 are ignored due to significant reduction in particle flux. Unlike **Figure 101**, data is per cm^2 instead of m^2.

One can immediately see the SEP flux is many orders of magnitude higher than GCR fluxes. This is only one assumed case, however. Specific data sets for SPE events may be found in [166]. For SEP fluence, or the total number of SEPs expected on the spacecraft per period of time, the SAPPHIRE model can again be used. SEP fluence inputs to SPENVIS may be found in **Table 53**.

Table 53: SEP Fluence Model Inputs in SPENVIS

Setting	Value
Orbit	400,000 km circular
SEP Fluence Model	SAPPHIRE (total fluence)
Prediction Period	1 Year
Confidence Level	99 %
Magnetic Shielding	Off
Ion Range	H to Fe

SEP particle fluence data for the mission is depicted in **Figure 104**.

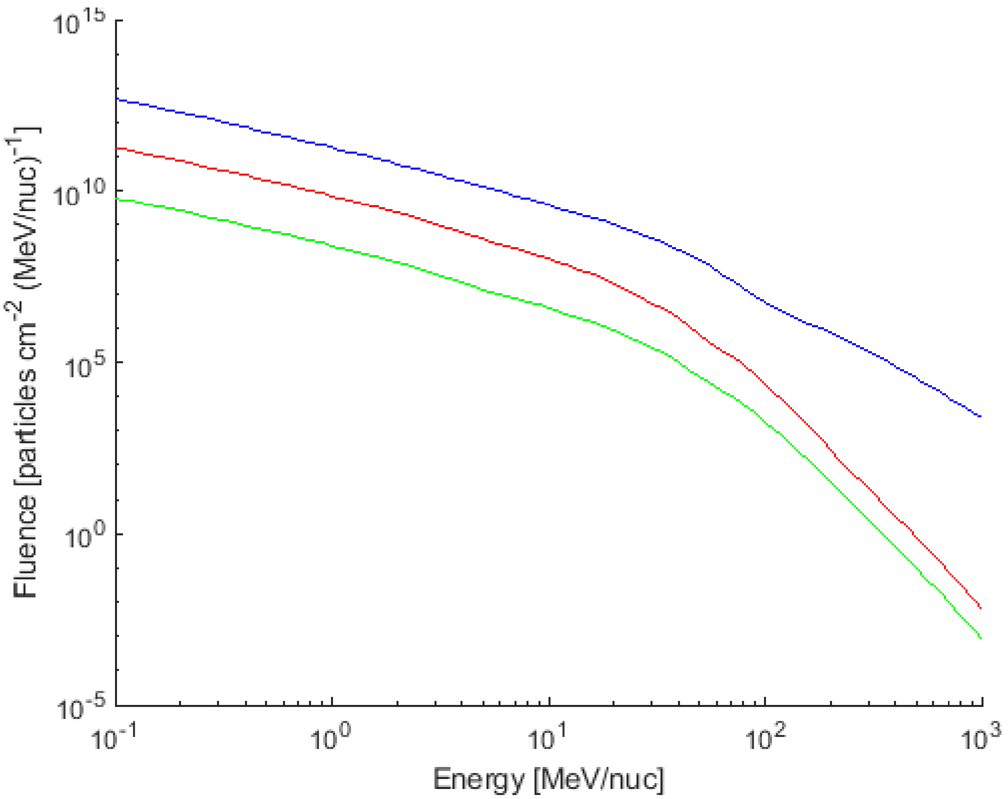

Figure 104: SEP Mission Fluence, Mission Duration 1 Year. Blue is H ions, red is He ions, and green is the combined heavy ion flux from Z=3 to Z=26

4.1.4 Electromagnetic Radiation

Electromagnetic radiation is encountered as photons, or quantized packets of light energy. Gamma-rays are the most energetic waves out of any light waves with frequencies above $3{\cdot}10^{19}$ Hz, wavelengths below 10 pm, and photon energies above 124 keV [166]. Gamma-rays, and to an extent X-rays, are forms of ionizing radiation, meaning they have enough energy to knock an electron out of its orbit or create secondary photons with material interactions. In this sense, Gamma-rays, SEPs, and GCRs are all considered deleterious to spacecraft and must be accounted for.

4.1.4.1 Gamma-ray Sources

The Gamma-ray source provided here is a composite from the Swift and Fermi data as measured from a LEO orbit [216]. It is isotropic, of extrasolar origin, and claims to experience no external shielding effects from the magnetosphere. Magnetic independence would allow for LEO data to be compared for deep space missions. The equations for modeling Gamma-ray flux as a function of energy are piecewise, described in **Eqs.(139-140).**

$$\Phi_\gamma = \frac{0.109}{\left(\frac{E}{28\,keV}\right)^{1.4} + \left(\frac{E}{28\,keV}\right)^{2.88}}$$

Eq.(139)

$$\Phi_\gamma = 0.95 \cdot 10^{-10} \cdot \left(\frac{E}{100\,MeV}\right)^{-2.32} \cdot exp\left(\frac{-E}{279{\cdot}10^{3}\,MeV}\right)$$

Eq.(140)

Eq.(139) is for energies below 890 keV, and **Eq.(140)** is for energies above or equal to 890 keV. Both equations output in units of [particles/s/sr/cm^2/keV].

4.1.4.2 Gamma-ray Characterization

Output for **Eqs.(139-140)** may be found in **Figure 105**.

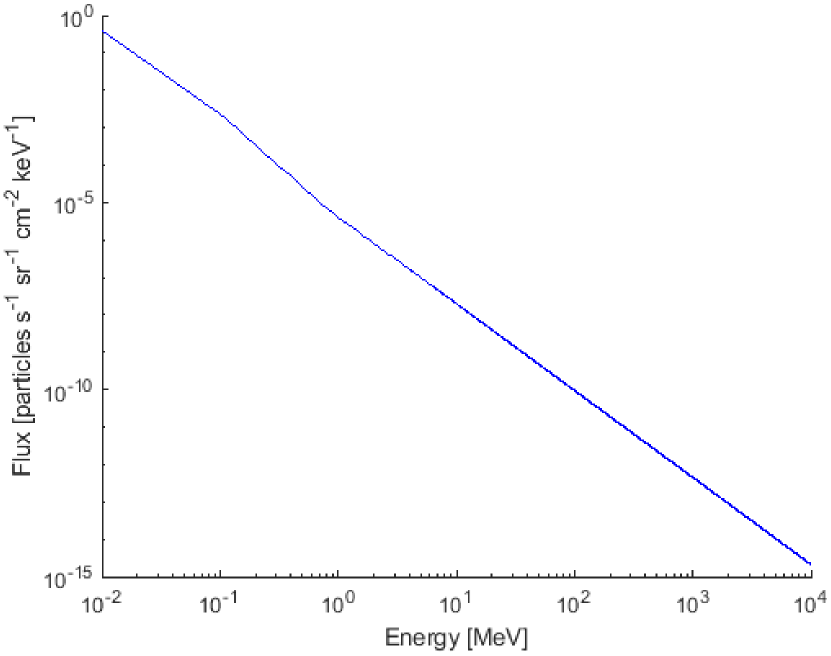

Figure 105: Gamma-ray Background Flux

Of note is that the slope trends are consistent across low energies. Unlike the GCR graph, the low energy Gamma-rays are prominent.

4.1.5 Particle Data Summary

Three primary deleterious radiation sources were described: Galactic Cosmic Rays, Solar Energetic Particles, and Gamma-rays. Albedo and planetary emission photons were not considered for radiation damage due to their lower energies. Particles trapped the Van Allen Belts, modeled by AP9 and AE9 SPENVIS models, were also not considered due to AEGIS's deployment altitude above 52,000 km.

While SEP peak event flux data is the most deleterious and energetic radiation source, it is possible the SPE will be avoided entirely. Flares and CMEs are probabilistic and directional. Even if an SPE occurs, it must be directed towards the spacecraft for the deleterious SEPs to take effect. Radiation shielding should take SEP data into account, but the LET of solar wind alone does not make the Sun a good source for baseline radiation calculations. SPEs should be viewed as worst-case scenarios for a given radiation environment.

The two consistent sources of radiation at the AEGIS target orbit are GCR and Gamma-rays. The Gamma-ray spectrum is dominant at low energies, whereas GCR takes over at high energies. Differences in model unit output, most notably the difference in cm^2 vs m^2 and keV vs MeV, make direct figure comparison somewhat cumbersome. Overall, the long-term source of high-energy ionizing radiation as a risk to electronics will be from the GCR due to increased energy and interaction potential. SEP sources, predicted to be lower probability due to reduced solar activity, represent a significant short-term particle flux. Models presented here are conservative assessments of expected event flux and total contribution.

The author would like to again thank Jared Fuchs for his work on producing **Figures 100-105**.

4.2 Single Event Effects

When singular, high-energy particles impact electronic components and circuits, various detrimental effects may occur in the components, known as Single Event Effects (SEE). These include recoverable effects such as Single Event Transients (SET), Single Event Upsets (SEU), sensor noise, Single Event Hard Errors (SEHE), and Single Event Functional Interrupts (SEFI), as well as destructive effects such as Single Event Latch-Ups (SEL), Single Event Snap-Backs (SESB), Single Event Burnout (SEB), Single Event Gate Ruptures (SEGR), and Single Event Dielectric Ruptures (SEDR) [166]. Recoverable event effects in satellites are termed soft errors while destructive event effects are termed hard errors. The goal of a satellite radiation mitigation strategy is to minimize the damage caused by hard errors while planning for the effects of soft errors, which may be corrected with meticulous flight software foresight.

Unlike displacement damage effects, SEEs are not related to the cumulative effects of radiation. They occur via a stochastic process caused by random interactions of a device with ions of various energies, species, and angles of incidence [204]. If the energy deposition by the ionizing particle is not sufficient to cause a malfunction, whether recoverable or destructive, a single event has occurred, but an SEE has not. The stochastic nature of the problem illuminates how not all ionized particle impacts cause faults or errors.

SEEs in global signals such as clocks, bias voltages, and reference voltages can create errors throughout the entire system. Critical nodes and signal paths must be thoroughly understood because methods of selectively hardening sensitive components can result in significant improvements in system radiation hardness with minimal penalties for hardware footprint, power, and processor throughput [217].

4.2.1 Recoverable Effects

Recoverable effects are reversible. The primary method of identifying soft errors and fixing them involves a technique originally known as Majority Voting and Scrubbing (MV&S) which has been expanded into

Temporal Triple Modular Redundancy (TTMR) with demand and patrol scrubbing. Much detail will be provided on how to invoke these strategies.

4.2.1.1 Single Event Transients

SETs are transient signals caused by charge collection and distribution from ionizing radiation, specifically SPEs, GCRs, and proton-induced reactions in LEO. They will manifest in the form of specious outputs from any analog or digital instrumentation, which could be described as a radiation-induced pulse. From a microelectronics standpoint, the energy transfer is a strongly localized generation of electron-hole pairs along the path taken by the impacting particle [203]. It is important to be aware of SETs when analyzing diagnostic data, as an error in operation may simply be a transient signal. SETs may lead to spurious signals, information loss, physical failures, or total loss of control of the spacecraft. In III-V semiconductors such as GaN or System On Insulator (SoI) devices, parasitic bipolar effects are possible. One example of a component affected by SETs would be an inverting operational amplifier.

Conditions for errors induced by SETs are highly dependent upon the target device, but the energy (deposition depth), location, and time scale of the impact relative to nearby circuitry may be analyzed specifically. Strikes are assumed to take place among nodes, or junctions, of electrical signals, and transistors are highly susceptible. A transient charge collected due to an impact will produce a current pulse at the junction due to the electron-hole pairs. Generally, the farther away from the junction that the event occurs, or if the ionization track does not cross the junction, the less charge is collected, and the less likely a soft error is to occur [218].

SETs occur by radiation strikes lasting on the order of 1 ps, but effects may be felt over hundreds of picoseconds depending on the type of ion, its initial energy, and the process technology [166]. For sub-micron Complementary Metal Oxide Semiconductor (CMOS) technologies, an SET typically lasts 200 picoseconds with the bulk of the charge collection occurring within 2-3 microns of the junction region [218]. With increasing deposition depth in semiconductors, the charge-collection transient assumes a slower profile due to the source-drain current and gives rise to charge amplification [204].

How fast and across what distance an SET propagates is dependent upon the capacitance and resistance of the circuit's internal nodes, and low capacitances featured in modern technologies are not effective in attenuating SETs [203]. However, the spatial characteristics of an SET are less important than the temporal profile upon introducing the concept of a Window of Vulnerability (WoV). Setting aside physical failures and catastrophic spacecraft loss, which may be mitigated by derating, or selecting a component with a higher voltage rating that what is required for operation, an SET may cause a processor to output an incorrect bit (0 or 1) or a similar bit flip in a latch-up, flip-flop, or other physical memory unit. The WoV is the time interval during which the SET can be latched into a register, and it is proportional to the temporal extent of the SET and the clock speed of the device. The temporal extent is a function of the deposited charge which is a function of the ion LET. Therefore, ions with high LET values may cause SETs with large WoVs and are more likely to produce said bit-flips [203].

The time period wherein a memory cell is able to be intentionally written to is defined by the clock speed, and increasing operating frequencies increases the probability that SETs will arrive at a latch during that time as a forced value for the cell. When analyzing processor speed and throughput, clock frequencies in the GHz range may lead to a significant increase in SET-induced errors due to the picosecond SET profiles, though space-rated OBCs usually operate in the hundreds of MHz. SET rates will likely increase with future, faster technologies.

SETs occurring in analog devices are potentially more dangerous because methods used to mitigate SETs in digital devices do not work for analog signals. SETs are analog in nature, and analog devices will respond significantly when a parasitic signal exceeds the analog noise characteristics. Digital devices are generally downstream from analog devices, and if 1) an SETs propagation distance is above the distance required to disrupt a digital circuit 2) the signal arrives during the WoV, the analog SET will cause a bit error in a downstream digital device [203]. The waveform of an analog SET may be positive, negative, or bipolar with a variety of amplitudes and pulse widths.

Testing may be done on a device to measure the duration of a WoV by using an external signal to both trigger the firing of a laser and to provide the clock signal for a logic circuit [203]. A pulse of laser light focused on a semiconductor can induce a localized transient generation of electron-hole pairs if the photon energy is greater than the semiconductor bandgap energy.

4.2.1.2 Single Event Upsets

SEUs are the most common adverse radiative effects that occur in spacecraft digital systems, such that a 1 becomes a 0 or a 0 becomes a 1 in a latch or register of the component when impacted by ionizing radiation [166]. Effectively, any bit of boot, configuration, or working memory may be incorrect when read by the system, leading to unknown faults. Early observations of SETs were static bit errors in combinatorial logic gates leading to sequential logic elements, which could be a memory cell. SETs that propagate to and are captured by data storage elements cannot be distinguished from SEUs occurring when particles directly strike the data storage elements. Therefore, the Soft Error Rate (SER) must include radiation-induced errors with both SET and SEU contributions.

An unnamed 2000’s silicon process technology exhibited a typical Failure-in-Time (FIT) rate of 10-100 for the hard reliability mechanisms, while the SER exceeded 50,000 FIT. A FIT is equivalent to one failure in a billion device hours [218]. Without detection and correction, it is apparent that soft errors will dominate the total Bit Error Rate (BER).

The concepts of spatial, temporal, and informational redundancy are applied here; descriptions of redundancy strategies are deferred to Sections 4.3-4.4. Reiterated then but of consequence to SEU characterization is the concept of bit adjacency. In modern memory circuits, four bits of memory may comprise a word to the computer addressing system. The four bits comprise a coherent piece of information, but those bits are not *physically adjacent* to one another due to a bit handling concept called interleaving. Therefore, if an ion strike causes faults in multiple, physically adjacent bits on a memory chip, only minor, singular faults will be introduced to words in computer memory.

4.2.1.3 Sensor Noise

Sensor noise is predominantly prevalent in imaging devices such as a Charge Coupled Device (CCD). If the radiation environment’s effect on susceptible sensors is characterized pre-launch, post-processing filtering methods may be able to remove unwanted sensor noise from downlinked data.

4.2.1.5 Single Event Functional Interrupts

The mechanism for SEFIs differs across memory types, but generally a SEFI is a special case of SEU where the control signal rather than the memory is corrupted. SEFIs will likely result in multiple faults and errors, and, if the faults are not masked by redundancy strategies, a hard reset must occur to reset the memory signals [201].

4.2.1.4 Single Event Hard Errors

SEHEs, sometimes written as SHEs, refer to a permanent alteration of the memory cell where the incorrect bit cannot be overwritten, but the component is still operational as a whole. The bit flip is a hard error, but SEHEs are considered soft errors in total. Utilizing Magnetoresistive Random Access Memory (MRAM) negates the effects of SEHEs. If the memory chip is comprised of Configurable Logic Blocks (CLB) on a Field-Programmable Gate Array (FPGA), the FPGA may be reconfigured to avoid bits that are suspected to be corrupted by SEHEs. The other side of this coin is that unused gates now included in the CLBs could have been corrupted while unused, and the fault went unnoticed before the gate was reconfigured.

4.2.2 Destructive Effects

Destructive effects are irreversible. If a destructive event occurs in a critical component, the entire satellite may be compromised. Most destructive events occur in III-V semiconducting transistors [166]. Therefore, it is advisable to provide redundant transistors where possible or selectively increase the radiation hardness of the target area. If the operation of a component is dependent upon a single transistor, it will likely be the cause of a catastrophic failure when ionizing radiation is encountered. Certain III-V semiconductors such as GaN have shown resistance to radiation strike-induced failures. Implementing SoI techniques has proven successful at mitigating radiative effects as well [166].

4.2.2.1 Single Event Latch-Ups

SELs may occur in semiconductor components where regions of differing doping types are adjacent to one another. Bipolar PN transitions can form parasitic thyristors upon ionization, meaning they have a PNPN doping sequence. A heavy ion or proton which passes through one of the two inner transistor junctions can turn on the thyristor-like structure, which is then latched-up or shorted. CMOS logical circuits and semiconductors are the most susceptible, but a version of SoI called System On Sapphire (SoS) has demonstrated latch-up free operation [166]. SoS also provides lower parasitic capacitance and higher speed compared to most CMOS technology.

4.2.2.2 Single Event Snap-Backs

SESBs are similar to latch-ups but affect N-type Metal Oxide Semiconductor (NMOS) devices and parasitic PN junctions, forming an unwanted, bipolar NPN transistor. An ionizing particle will create electron-hole pairs, and minority carriers, or holes, are injected from the drain junction causing increasing drain voltage [166]. When operations dictate that the parasitic NPN transistor be turned on, the drain voltage “snaps back,” and an avalanche current is generated at the drain. This is amplified by the bipolar transistor, and the device is thermally overwhelmed.

4.2.2.3 Single Event Burnouts

SEBs are also caused by parasitic NPN bipolar transistors. They are formed between the n- doped epitaxial layer, which acts as the collector, and the n+ doped region, which is connected to the source [166]. If an energetic particle hits the p-doped layer, an electron-hole plasma will form. Minority carriers, electrons in this case, are injected into the base, and the transistor is turned on. The following burnout current will destroy the component.

SEBs were first noticed in Europe during the 1990s when burnout failures of newly developed devices were experience on trains. It was found that the key to SEB susceptibility is the operating voltage. The minimum operating voltage for SEB susceptibility is ~270 V, so SEBs will be less of an issue for deep space CubeSats. Where CubeSats should be careful, however, is the PPU of any gridded ion thruster. There are localized areas on EP power modules which exceed 1000 V, and SEB susceptibility at those areas may become a problem in deep space exploration. Hopefully, data will be provided on the operation of the NEXT-C engine regarding SEB prevention. Derating is particularly useful as a prevention mechanism for SEBs.

4.2.2.4 Single Event Gate Ruptures

SEGRs are caused by ionization in the gate oxide. An energetic particle colliding with the gate will create an electron-hole plasma in the gate oxide. Minority carriers, in this case holes, become trapped in the epitaxial layer and majority carriers, electrons, will be sent to the drain electrode. This causes the electric field across the gate oxide to increase until dielectric breakdown occurs [166]. The leakage current coming from the gate will then destroy the device.

4.2.2.5 Single Event Dielectric Ruptures

SEDRs happen in CMOS devices with high field regions of a dielectric layer. The deposited charge of an energetic particle in the oxide layer of the gate will break down the dielectric displacement field. The isolating layer is obliterated, and deposited charge carriers will be swept out. The transistor is then no longer functional [166].

4.3 Radiation-Tolerant Electronics Design

Radiation tolerance in electronics can take many forms. A system can be built out of inherently radiation resistant materials or designed to have many aspects of the system fail without errors. This section will cover the appropriate way to communicate faults and errors, major strategies of radiation-tolerant design, and radiation effect mitigation strategies for both hardware and software. The most important maxim to remember is that a fault tolerant system design makes dedicated use of fault avoidance, fault masking, detection of compromised system operation, containment of error propagation, and recovery to normal system operations [219]. Much credit goes to Heidergott [201] for excellent attention to detail in this field.

4.3.1 Faults, Errors, and Tolerance

Before addressing what a fault is, one must understand from where a fault may originate. Faults may arise from incorrect specifications in documentation or vendor materials, design errors, undetected manufacturing defects, human operator actions, component damage or failure, or interaction with the operating environment [201]. Radiation-induced faults are common to an extent, but loss of spacecraft function on-orbit should not immediately be attributed to radiation-induced error.

4.3.1.1 Faults vs. Errors

Faults are characterized by their nature, duration, and extent. The nature is the location of the fault origination including the root cause, the duration may be transient, intermittent, or permanent, and the extent is classified by induced errors and their functional propagation. A fault is the initiating defect. This may be an energetic particle event inducing an SEU or SET. An error is an undesired system state caused by the fault, which could be loss of subsystem function or the inability to provide a service.

4.3.1.2 Fault Tolerance

Fault tolerance is the capability of a system to recover from a fault or error without exhibiting failure or compromised availability [201]. Not all faults result in errors. Spacecraft with significant error containment capabilities may be able to deal with unwanted, radiation-induced effects before an error occurs.

Conversely, a fault may be latent in that it exists but has not resulted in an error. In the latter case, a particular system state or state transition must be realized before the fault results in an error.

4.3.2 Fault Avoidance

Fault avoidance takes two forms. A spacecraft can seek to reduce the severity of the energetic radiation environment through orbit considerations and shielding, or a spacecraft can reduce the impact the radiation has on the system circuitry by selectively hardening or shielding sensitive components from charge collection or accumulation effects. Orbit and system-level effects are discussed first with semiconductor charge collection effects following. Radiation shielding, while under the umbrella of fault avoidance, is given dedicated characterization in Section 4.4.3.

4.3.2.1 Orbit Design and System-Level Avoidance

Certain SEEs, including but not limited to SETs, SEUs, SEFIs, SESBs, and SEBs, predominantly occur when the component containing the memory register, bit, or transistor is powered on. High energy particles can still damage PCBs when they are powered off, but those types of radiation effects require power for the fault to immediately result in an error. Powering down a faulty component on orbit and rebooting it later has had success in previous missions [220], so there is merit to assessing operations recovery with power considerations.

If a spacecraft is going to traverse a particularly deleterious region of space such as the VABs, South Atlantic Anomaly (SAA), or anywhere remotely near Jupiter and hardware operations are critical for mission success but not necessarily required at that moment in time, a viable strategy is to power down all non-essential hardware during the deleterious orbit segment. Elevated particle flux levels are a marker of space that may result in enhanced SEE rates.

When designing an orbit, it is worth asking if the altitude and inclination may be altered if it is anticipated to spend considerable time in one of the aforementioned deleterious environments. If the orbit requires the transit of a dangerous region of space and no orbital corrections can be made, that is a good indicator that enhanced shielding provisions should be used. Proton events typically dominate upset events in the VABs.

4.3.2.2 SEEs in III-V Semiconductors

III-V (three-five) semiconductors have gained notoriety as space-rated semiconductors with some exhibiting natural radiation tolerance. GaN has shown aptitude for satellite applications [221-224]. They are named III-V semiconductors due to the valence electrons, not the fact that they are group 13 and 15, respectively, on the periodic table. III-V semiconductors are used to create Heterojunction Bipolar Transistors (HBTs), High Electron Mobility Transistors (HEMTs), tunnel diodes, and Multi-Quantum-Wells (MQWs). They can be found in conventional electronics, optoelectronics, nano-electronics, photovoltaics, high-power, and ultra-low-power applications [204].

SEEs in semiconductors are not related to TID or cumulative effects of radiation. It is the effect of energetic, ionizing particles that causes SEEs. A diagram of this concept may be found in **Figure 106**. When ionizing particles impact an integrated circuit with a semiconductor, charge deposition occurs in a funnel-shaped region, and charge collection occurs at the electrodes of a device. Investigation of the phenomena involves an understanding of charge transport, recombination, and collection mechanisms at the single transistor level. Charge collection duration is on the order of hundreds of picoseconds, and the deeper the charge funnel, or particle deposition depth, the slower the character of the charge-collection transient.

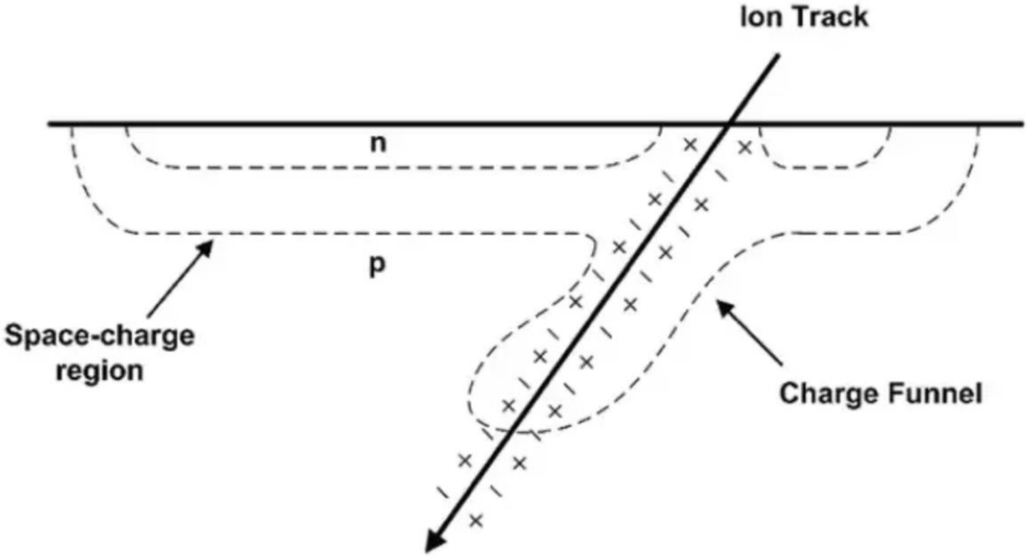

Figure 106: Charged Particle Strike Example in a PN Junction

To mitigate recoverable and destructive SEEs in semiconductor circuitry without redundancy considerations, device-level hardening approaches have been utilized. Mitigation techniques originally focused on reducing the charge collection at the device level, but this strategy failed to realize the primary source of charge collection is associated with enhanced source-drain current and not mitigation of the ionized funnel itself [204]. One successful technique with substantial literature support is placing a layer of III-V semiconductor material underneath the original layer where the underlayer was grown at lower temperatures than the upper layer. The charge carrier concentration produced by the ionizing event is lowered, leading to a ~100x reduction in total collected charge [225]. It should be noted that these considerations were for GaAs-based Field Effect Transistors.

Here is where the strategy of SoI is reinforced. Underlayers of insulating material, such as the SoS discussed in Section 4.2.2.1, can be used to enhance the radiation tolerance of susceptible electronics in space. If a PCB is being designed in-house or a custom PCB is being fabricated by a vendor, it is worth asking if SoI is a possibility during the fabrication procedure. The distinction is between SoI device isolation and reverse-biased junction isolation.

4.3.3 Fault Masking and Redundancy

There are hardware and software approaches to fault masking and redundancy, but the lines between them become blurred when specific hardware is required to enact software operations such as Error Correcting Codes (ECC). Software relates to bit handling rather than storage. The basic techniques for hardware fault masking are informational redundancy, a software technique where redundant data structures are used on the same device, spatial redundancy, a hardware technique where information is stored on redundant hardware devices, and temporal redundancy, a software technique where redundant operations are performed sequentially to see if the output changes. Majority voting is applied to the output of these techniques to increase output fidelity. All techniques are meritorious, and the best fault masking strategies utilize them concurrently.

Software fault masking strategies include Error Detection and Correction (EDAC) implementations, ECC, and scrubbing techniques. EDAC implementations verify that bits already stored on memory devices are not corrupted. ECC is commonly used for data storage systems, but here it is predominantly used in space communications systems to ensure signal bits are understood in the appropriate order without error. Some EDAC strategies are implemented as ECC. Scrubbing is how EDAC is physically implemented and takes various forms. EDAC is discussed as a precursor to scrubbing followed by the history and current use of ECC. The three primary redundancy strategies are characterized, and a combination of the strategies is presented last. Engineers interested in defining TT&C encoding and decoding should follow the ECC section closely and read the cited literature.

4.3.3.1 Error Detection and Correction

If an error exists, informational structures will have some internal inconsistency such as a bit flip. Encoding the bits in a word gives a monitoring system the ability to detect where an error has occurred. EDAC varies in detection and correction capabilities, code efficiency, and complexity of encoding circuitry [201].

The simplest method is to check to see what the parity of the bit word is. A parity bit is added to the word to match the sum of the encoded data as 0 or 1, usually in the first bit location. If a bit flip has occurred, parity is lost, and an error is detected. This method cannot localize where the error has occurred in one pass, and, if two bits in a word are corrupted, parity checking cannot identify an error at all. All EDAC will involve encoding by adding bits to words, but some implementations do not have the ability to localize single errors.

As SEEs strike a localized area, it follows that several bits in a given area may be corrupted by the SEE. This does not translate to multiple bits in a word becoming corrupted because physically adjacent bits do not usually comprise a word. Bits in a word are physically dispersed, and a given SEE will likely induce a single error in multiple words [218].

EDAC on OBCs is handled by a Memory Management Unit (MMU) designed specifically for this purpose. The MMU may perform simple parity checks, cyclic redundancy checks, or a more advanced ECC algorithm as described below, but a dedicated device must be available to perform EDAC. The MMU will perform EDAC on stored memory to check for errors in a word. A single bit in a word can be located and corrected with multiple parity checks, but two-bit errors in a word cannot with simple parity checking. More advanced EDAC applications exist which can correct multiple errors. Thus, it is important to check the stored data frequently, which introduces patrol and demand scrubbing.

A final consideration is that of the three types of non-volatile memory, boot, configuration, and science data storage, the boot and configuration memory hardware will likely be radiation-tolerant or radiation-hardened. The assumption is that bits in the boot and configuration memory are less susceptible to errors. It is not always this way, but in this instance the EDAC is performed on science storage memory or persisting RAM bits, if desired. The overall effect of EDAC or ECC for stored memory is that the SER for a system is no longer dominated by memory upsets.

4.3.3.2 Patrol and Demand Scrubbing

Scrubbing is the act of checking a word for bit errors and re-writing the faulty bit to its correct form. It is the physical implementation of EDAC. Demand scrubbing is checking the bit for errors when the bit is called. Whenever the science data is prepared for downlink, or whenever a stored value for an LUT or Chebyshev polynomial is called, the MMU will check for errors in the word before passing the bit. This action does increase latency in memory retrieval, but it is better to know the data is correct rather than assume it is. Demand scrubbing is manageable to implement with the OBC ICD and with all Xilinx FPGAs.

Patrol scrubbing is more difficult than demand scrubbing and represents distributed demand scrubbing wherein the bits are called and scrubbed but not passed anywhere. Patrol scrubbing is a continuous read and write action over all of a given memory component as the lowest priority action a scheduler can take. Whenever no other action, process, or state change is queued in the OS scheduler, the default action the OBC should take is to scrub the memory for errors. Bit by bit, the MMU will read and write the memory into place, which could be considered lowest-priority, democratized demand scrubbing.

4.3.3.3 Error Correcting Codes and Reed-Solomon

ECC is a subset of EDAC, and many more subsets exist. EDAC can vary widely in detection and correction capabilities, efficiency, and circuit complexity. ECC can involve cyclic redundancy checks and convolutional schemes in serial data transfer interfaces or storage media, and these codes are commonly termed block codes or convolutional codes [201]. An MMU may use ECC as EDAC for stored memory, but the discussion of ECC presented here is primarily in terms of communications channels or data transfers.

The first class of linear block codes devised for error correction were the Hamming codes, the most common of which is the single-error correcting, double-error detecting (SECDED) Hamming codes [201]. SECDED is common in memory storage EDAC but requires 8 check bits for 64 information bits. A faster and more efficient subclass of linear codes are cyclic codes, and a common group of those are the Bose, Chaudhuri, and Hocquenghem (BCH) codes. BCH codes are generalized Hamming codes that can correct multiple errors, and the most important subclass of non-binary BCH codes are the Reed-Solomon (RS) codes. RS codes will be the primary topic of discussion and should garner the most attention. RS codes are byte-oriented and previously required 64 and 128 bit information lengths, but Kaneda and Fujiwara have developed a class of RS codes with arbitrary code and byte definitions.

RS can be used as a standalone ECC, but it is usually used as a concatenated coding system consisting of a convolutional inner code and an RS outer code. Convolutional codes are specified by a constraint length and rate. Convolutional codes will not be covered here except to say that nominal performance is achieved through a constraint length of 7 and a rate of ½, otherwise called a (7,½) convolution. Telemetry identified in this manner is best described in [148] and [226] but is summarized thusly. Downlink data begins in storage, undergoes packetization, optionally undergoes segmentation, becomes a transfer frame, is coded into a telemetry bit stream, and becomes a physical waveform via digital signal processing and modulation before being emitted by the antenna. Channel coding means signal processing so that data can be downlinked or uplinked through a noisy channel, but distinct messages can be distinguished. Data can then be reconstructed from a noisy channel reliably.

Telemetry synchronization and channel coding protects the transfer frames against channel noise-induced errors. If the channel and coding scheme are chosen appropriately, the data can be transmitted with a higher throughput and same quality as uncoded data for less energy expended per information bit. Conversely, it can be thought of as having a lower BER than uncoded data for the same energy per bit. SER details the operation of an entire system in units of FIT or Mean Time Between Failures (MTBF); BER details the bit errors in a communication channel.

RS codes are characterized by a block length n_b defined by **Eq.(141)**, where q_a is the alphabet size and J_{bit} is the symbol size.

$$n_b = q_a - 1 \therefore q_a = 2^{J_{bit}} \quad \textbf{Eq.(141)}$$

The multi-bit symbols in an outer RS code are what is being further encoded by an inner convolutional code. The error probability is an exponentially decreasing function of block length. As each value in the block represents a byte or symbol, the values can be prescribed as alphanumeric values or other information symbols. An arbitrarily chosen odd minimum distance d_b must be selected. For a given distance d_b, the number of information symbols k_b may be specified by **Eq.(142)**, and any combination of the number of errors in k_b, E_b, may be corrected by **Eq.(143).**

$$k_b = n_b - d_b + 1 \quad \textbf{Eq.(142)}$$

$$E_b = \frac{d_b - 1}{2} = \frac{n_b - k_b}{2} \quad \textbf{Eq.(143)}$$

Assigning some values to this nebulous summary, consider symbol size J_{bit} = 8 bits, alphabet size q_a = 256, and block length n_b = 255. A minimum distance d_b = 33 is selected which makes the number of information symbols k_b = 223 and maximum correctable errors E_b = 16. Thus, an RS block code exhibiting these values can host 223 information symbols, defined as elements of a finite field rather than 0 or 1, and correct 16 errors within k_b. Each element of the symbols is comprised of 8 bits, so the output of the encoder still looks like binary data. This RS code would be termed a (255,223) code.

AEGIS will be using a concatenated convolutional code with RS encoding and QPSK modulation. The convolutional code will have a rate ½ and constraint length 7. The RS outer layer will be a (255,233). Next generation SDR hardware, including the Xlink radio, will be able to take packetized data, apply RS as an outer layer, perform symbol interleaving, insert a frame sync pattern, apply a convolutional inner layer, apply QPSK modulation, and transmit that waveform to the antenna. Voyager utilized a concatenation with the (255,223) RS code and a (7,½) convolutional code. The Cassini/Pathfinder ECC consisted of the same RS code concatenated with a (15, 1/6) convolutional code. It should be noted that all of these utilize the same decoder, namely the Viterbi decoder [148]. The bit overhead for AEGIS RS encoding was a 14.2% increase. The total bit overhead increase after (255,223) RS encoding, interleaving, frame sync attachment, and (7,1/2) convolutional encoding was ~229% before QPSK.

4.3.3.4 Spatial Redundancy

Spatial redundancy can refer to bit storage on physically separate memory devices, but it can equally refer to redundant processors performing the same calculation or process. For memory storage, three memory units may have the same information stored, and, if those bits are called, the bits are called from all three memory units and compared. The requested bits will usually be the same because demand scrubbing can be implemented on all three before the bits are called, but sometimes bit errors persist. A majority voting structure is then implemented to compare the three bits and take the majority value. This is sometimes called modular redundancy. For processors, the tenet of majority voting structures remains the same. This can be accomplished by entirely separate processors or multiple cores on a single processor.

The hardware for majority voting operations may be D-flip-flops, latches, state machines, complete processing functional blocks, or entire subsystems [201]. FPGA CLBs are also included. The most common form of this MV&S technique is Triple Modular Redundancy (TMR). OBC vendors will have proprietary versions of TMR for specific hardware, and TMR enaction may be characterized by the OBC ICD. TMR significantly increases the ability to detect a single fault, and delivery of a correct value after MV&S is almost equally reliable. A full characterization of how to test SEEs in FPGAs with TMR is found in [227].

The primary issue for TMR implementations is recovery of component operations after an error is detected. General operations recovery is discussed in Section 4.3.6, but the question of how to identify if a faulty memory unit or processor is usable has been widely studied. For memory units, a test function may be applied to determine if the error-inducing fault was caused by a recoverable or destructive SEE. If it was recoverable, the memory unit can be re-synchronized with TMR by a hard reset. If the SEE was destructive, continued bit calls from the faulty memory device may induce additional errors. For faulty processors, the recovery operation requires recovery of data and software control states in addition to resynchronization processes [201]. For TMR to be implemented in multiple processors or multicore processors, they must be in lockstep with the clock signal with or without a set delay in increments of the clock speed, discussed further in the next section. If a processor produces an erroneous value, that lockstep must be broken for recovery operations and resynchronization to commence. The tradeoffs between complexity and operations fidelity in OBCs is fluently characterized in [228]. Known MRAM bits may be read to determine if a processor error was due to a spurious SET signal or if the processor itself has been corrupted.

A destructive event in a TMR memory unit causing that unit to become inoperable brings about the question of what do about that unit once it is no longer useful. Here the concept of n-modular redundancy is introduced in that the number of hardware devices for spatially redundant applications is not limited to three. Four, five, or more units could be used where only three are queried for output at a time. If one unit displays an error during TMR, the unit breaks lockstep and the next unit value is queried. In the case of n-modular redundancy, ceasing the use of a faulty memory unit is non-problematic for TMR because another unit can be easily utilized if it was already running the process but not being queried for output. There is a significant power cost to running a redundant processor in lockstep but not querying the output, and there is no guarantee a fault has not occurred in the unqueried processor. If only three units are available and one fails, TMR cannot be implemented with only two units. In this scenario, temporal redundancy must be implemented.

SpaceX has utilized the concept of n-modular redundancy on its engines during launch. In 2012, a Falcon 9 rocket was launched to send a Dragon capsule up to the ISS. One of the 9 Merlin engines failed during launch, and the redundancy scheme reconfigured the other 8 engine outputs to make up for the failure [229]. As one can see, n-modular redundancy is scalable from chip-scale processes to entire subsystems.

4.3.3.5 Temporal Redundancy

Temporal redundancy can mean sampling the same memory unit or processor output three or more times and passing each output through voting circuitry, or it can mean adding a delay to the output sampling of distinct units where the delay is an integer multiple of the clock cycle. Temporal redundancy has an advantage over spatial and information redundancy in that temporal redundancy resists SETs. If the pulse occurs during the sampling of a memory unit or processor output, a value that was originally a zero would be construed as a one, or vice versa if it occurs before a NOR gate. Many instances of signal corruption can be imagined based on a variety of circuitry configurations and SET locations. If temporal redundancy is utilized, the odds of SETs occurring in the same circuit location during the subsequent polling operations is extremely low. An SET would only induce an error in one of the three, or more, queries, and majority voting would rule out the spurious output.

In the case that TMR is utilized for three memory or processor units, one becomes faulty, and only two functional units remain, temporal redundancy is the fallback strategy. Instead of applying a majority voting structure to two units, which would not provide a resolution in the outputs differed, the strategy would shift to sampling one or both of the units three times. This strategy does not invoke the clock delay. If one of the units is sampled three times, the majority voting structure compares the three outputs. If both of the units are sampled three times, majority voting could be applied to the six outputs. Hardware infrastructure will need to be in place to implement this secondary redundancy strategy if TMR fails.

A common strategy in modern OBCs is Temporal TMR, or TTMR. TTMR can take on both temporal redundancy meanings, i.e. multiple sampling of single units at the same time or individual sampling of multiple units at varied clock signal integers. In the former case, the triplicate query undergoes a voting operation, and the voted output from an individual unit is passed to be compared against two or more other units that have undergone the same triplicate query operation. In the latter case, a sampling delay is implemented wherein the samples are taken at different clock signals but the output is held for concurrent comparison. Hardware must be in place for this to occur and is easily implemented as an FPGA CLB. The primary penalty of both types of temporal redundancy is the inherent latency of waiting an additional two clock cycles for an operation to be completed. Below operating frequencies of 50 MHz, this latency is relatively insignificant. However, the delay becomes a non-negligible percentage of the overall circuit latency as clock signals approach multiple GHz [201]. If a 200-picosecond value is placed on the two-cycle clock latency, an upper limit of 2.5 GHz on the maximum operating frequency of a signal path or data latch exists [217]. Some OBCs can operate at 5 GHz or higher, so it is important to perform latency tradeoffs for a given redundancy strategy. An analysis of SET pulse time characterization is warranted; the clock cycle integer multiple strategy will only work if the clock cycle time is longer than the SET pulse time. If sampling a DDR SDRAM unit, the memory output is passed at both the rising and falling edge of the clock signal and must be handled appropriately.

A final consideration for temporal, and to an extent spatial, redundancy is that this usually only works for digital circuits. At the time of writing there is not a CubeSat OBC-sized method of constructing a voting circuit to compare analog outputs, but SETs can affect analog signals, nonetheless.

4.3.3.6 Informational Redundancy

Informational redundancy is the easiest strategy to implement, and the increase in hardware mass is typically less than spatial redundancy [201]. Redundant data structures can be set up so that TMR may be implemented on a single memory unit, but this strategy means the overall memory capacity is cut to a third before EDAC check bits are implemented. As radiation-tolerant memory units have significantly less storage capacity than ground-based COTS hardware, implementing informational redundancy with EDAC on rad-tolerant hardware will result in exceedingly small data capacity.

A benefit to redundant informational data structures is that EDAC on one data structure can be compared against another data structure on the same hardware unit, reducing the latency time it would take to compare the data structure to the same data structure on a spatially redundant memory unit. In this case, it is assumed the EDAC implementation is a simple one, such as SECDED Hamming, and not a robust ECC. Two-bit errors in a single bit word would not be able to be corrected without comparison to a ‘correct’ data structure. Instead of labeling the data as corrupted, the MMU could compare the data structure to the informationally redundant structure. The odds of the same bit word in the informationally redundant structure being corrupted are exceedingly low if patrol and demand scrubbing are utilized efficiently.

4.3.3.7 Combining the Strategies

At this point, one can imagine the strategies being combined effectively. Informationally redundant data structures can be applied to the same memory unit for EDAC fidelity. Demand scrubbing vets the bit values before the bits are output to a query, and patrol scrubbing scrutinizes memory bits when dormant. Spatially redundant memory units and processors are queried in triplicate for temporal redundancy, and the output is passed to majority voting hardware. SEUs in memory and processors are no longer a cause for BER concern, and SETs can only corrupt one of the triplicate queries if the time between queries is greater than the SET pulse duration. With the exception of scrubbing and EDAC, all of these strategies can be implemented as FPGA CLBs. For this reason, spacecraft designers can expect to see increased and sustained use of FPGAs on spacecraft OBCs as System on Chip (SoC) configurations.

4.3.4 Process Error Detection

The previous discussions on faults and errors have assumed the faults to be caused by SEEs, but this is not always the case. Errors can manifest as faults in the OBC manufacturing process, code structure, or OS scheduler errors such as priority inversion. The error could be caused by a physical design flaw, such as the current loop structure in the solar arrays described in Section 3.5.2.3, or it could be damage from a micrometeoroid impact. Short of a hard failure where the satellite recognizes it has lost the ability to complete basic tasks or functions, fault detection and thus error detection becomes incredibly difficult without well-defined diagnostics downlinks. Defining how software recognizes its diagnostics then becomes paramount for error detection. If error detection were simple, no satellite would be lost prematurely.

Detection and recovery may be concurrent with normal system operation, or it may be preemptive where system operation is suspended until completion of the recovery operations [201]. The most important aspect no matter what strategy is chosen is that detection and recovery are decoupled. They should be two distinct processes that are not contingent upon each other. Recovery should be based upon previously saved states or data structures, not the output of an error detection operation.

It is tempting to define detection and recovery in a way that allows resumption of a software process wherein an error was detected. This is incorrect because one can almost never assume the state of the process is what it was prior to the pause for recovery operations, no matter if they are concurrent or preemptive. The best way to address this issue is Application-Oriented Programming (AOP) where processes are divided into intermediate steps, and recovery becomes a simple routine of finding the latest intermediate step without a failure-inducing error.

4.3.4.1 Application-Oriented Software Solutions

The software components of AOP are called assertions where rules are defined for a given process. The type of calculation, hardware involved, and software state will determine what those rules are. Assertions are metrics defined for a given process and are included in the process itself. The logic would read if not ASSERTION then ERROR [201]. The assertions themselves are only as good as the characterizations of the Failure Modes and Effects Analysis (FMEA) of the FSW. The goal is to detect a compromised state of program execution.

There are two aspects of AOP worth considering. The first is that the strategy is predicated on the assumption that if the intermediate step results are all correct, then the final result will be correct. If this assumption does not hold true for the determined assertions, then the assertions are incorrect. This is a testable aspect of AOP, and simulated fault injection analysis should be performed to test the assertions. The second is that AOP does not care about every single fault. If the fault does not manifest in a failure of operations, the fault is inconsequential and can be ignored.

For example, an intermediate step might check to see if a data structure was a 2x3 matrix, as it should be. A value in the data structure might determine the desired deployment angle of a locking solar array hinge mechanism. The structure size is checked and is fine. The process continues, and the solar array mechanism would begin to actuate. If the value determining the deployment angle was overestimated due to a fault, the mechanism might think it was actuating to 270 degrees when the locking mechanism is set to lock at 180 degrees. The mechanism would deploy, lock, and register successful deployment despite the erroneous target value. This is an instance of a fault that that does not result in an error, and the software would not register any failure or error diagnostics. Separately, value checks can be applied on top of data structure checks. There could be a check on the target value before actuation to ensure it was below 181 degrees.

There are a variety of acceptance test techniques for validating AOP assertions. The ones discussed below are N-version programming, self-checking software, recovery blocks, and watchdog coprocessors. Several surveys of fault tolerant software techniques are available which go into more detail [230,231].

4.3.4.2 N-Version Programming

The concept of N-Version Programming (NVP) was created by Liming Chen and Algirdas Avizienis in 1977 with the conjecture that "independence of programming efforts will greatly reduce the probability of identical software faults occurring in two or more versions of the program" [232,233]. The idea is that, for a given program with defined inputs, there are multiple ways the program could be computed or realized, and independent teams who create independent solutions to a program would not make the same mistakes in their computation. One team might make one type of mistake in coding, but it is unlikely that multiple independent teams will make the same mistake. Therefore, if three independent process codes are utilized for the same program, the output can be put through a majority voting structure as in the radiation tolerance hardware. The NVP process can be seen in **Figure 107**.

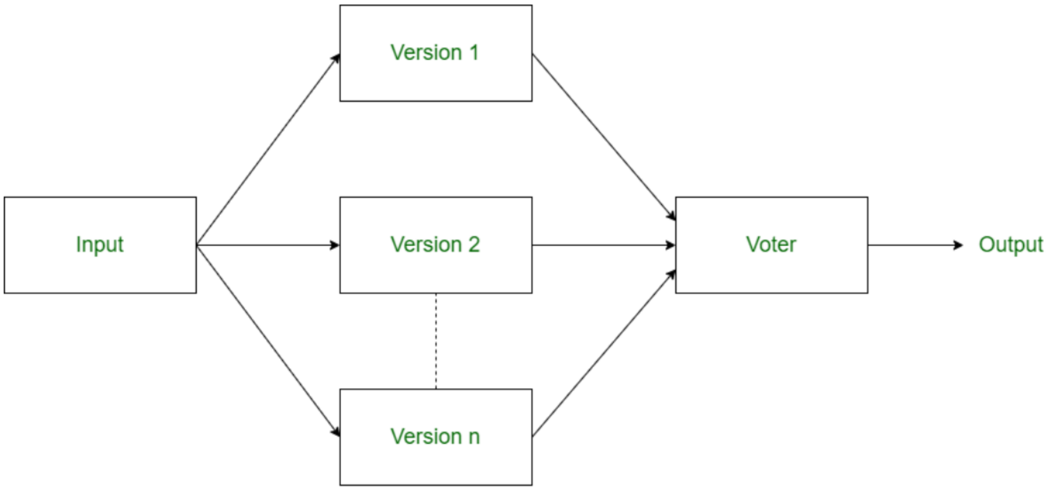

Figure 107: N-Version Programming Procedure [234]

Redundant copies of the same general algorithm are run concurrently. Acceptance tests, or assertions, are not specifically run on an output that has undergone majority voting. There exists a statistical correlation to failure, but NVP has experienced criticism in practice. Knight and Leveson performed an experiment to test the original conjecture that independent teams would not produce similar computing errors and found it to be flawed [235,236]. The primary downside of NVP, not including the potentially flawed original conjecture, is increased development time and resources. Three teams must make independent code versions without regard for other teams' work, which is difficult to realize for streamlined programs.

4.3.4.3 Self-Checking Software

Self-Checking Software (SCS) is accomplished by verifying the correctness of the operation of the system during execution time [237]. SCS can detect software errors, locate them, verify the integrity of the system, and help the system recover from those errors. This is only possible if the system is outputting abnormal data or executing in a way that is abnormal from the originally planned process. SCS can provide functional checking, where the reasonableness of the results is considered based on the size and value of the output, control sequence checking, where the path of a process is vetted for improper paths such as an incorrect number of loop executions, and data checking, where concepts such as expected variance and data mean are applied to the output.

A useful approach to SCS is to apply structure labelling embedded in the syntax of the program text [201]. Path tags are introduced to check the block sequencing validity, and block tags are introduced to verify that the execution of the blocks proceeded from entry to the expected exit. The key is that each block in a program contains a unique signature. Upon block entry, the block tag is set to that signature. Checking block tags after each block in a program verifies that the block was not entered from anywhere except the expected entry point. The path tag is set to the value of the next block signature, which is checked on entry for each block.

4.3.4.4 Recovery Blocks

Recovery blocks are for reusable calculations or data retrieval processes that employ acceptance tests to determine the validity of the output. The acceptance tests may be in the form of AOP assertions. Unlike NVP, recovery blocks cannot be used for mission-critical processes such as a boot procedure or desaturation maneuver pre-calculation. The process of recovery block applications is shown in **Figure 108**.

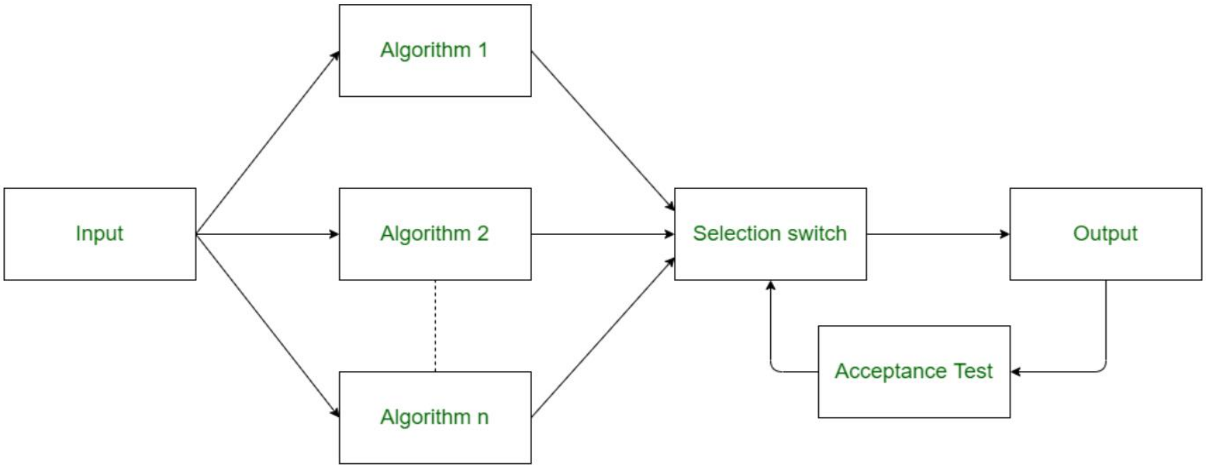

Figure 108: Recovery Block Procedure [234]

There is no majority voting, and the application of recovery blocks is restricted to processes where there are distinct, plausible methods of calculating or retrieving a desired output value. To revisit an example in Section 3.7.7, there are several ways of calculating Earth and Sun ephemeris data. One is to have the data pre-programmed as a Look-Up Table (LUT), and the other is to utilize a Chebyshev polynomial such as the SPICE library [200]. If the Chebyshev polynomial was attempted first, and the acceptance test flagged an issue with the output data, data format, checksum, or path tag if SCS is used, the selection switch would then assign the scheduler the secondary algorithm for calculating the same value. In this case, the secondary value is the LUT retrieval.

Recovery blocks are not run concurrently as in NVP. They are run individually and only if the deadline for the calculation is greater than the computation time of all possible algorithms. This is a major reason why they are not used in critical processes requiring hard deadlines.

4.3.4.5 Watchdog Coprocessor

Watchdog coprocessors, or timers, are the only strategy the author is recommending to be utilized regardless of any other error detection strategy inclusion. Watchdog coprocessors are a must for reliable space systems. The previous section introduced the concept of calculation deadlines, and this document does not go into proper detail on real-time versus general-purpose operating systems for FSW or C&DH considerations due to International Traffic in Arms Regulations (ITAR) concerns. Nearly all processes can be prescribed a calculation time, where the successful completion of a calculation can raise a flag to 'kick' or 'nibble' the timer. If the process fails to complete before the prescribed time, the watchdog coprocessor is not kicked, and the timer initiates a hard reset of the entire system. The entire satellite will turn off and back on. While turning off the satellite completely seems like an unreasonable strategy, it is always safer to panic, reset, and resume previous operations than to allow a process to loop indefinitely.

Watchdog timers are simple timers connected to the power system of a spacecraft. The circuitry difference that makes them so useful is that they are a separate processor that is on a separate clock signal than the rest of the spacecraft. If they were on the same clock signal as the equipment they were monitoring, an SEE that damages the clock line of the suspect hardware would similarly damage the watchdog timer's ability to monitor that hardware, and induced SET pulses could be registered as a false-positive for a kick or nibble. False positives make it difficult for pre-shutdown diagnostics to find the process that featured an error. Multicore processors can become locked in FSW scheduler issues such as race conditions and priority inversions, which is why the processor for the watchdog timer should be independent of the primary OBC.

One strategy for the separate clock signal is to utilize a Chip-Scale Atomic Clock (CSAC) for both the watchdog timers and radio signal clock. The ground station uplinks a signal to the spacecraft for both ranging and Doppler operations. The accuracy of the state vector measurements is dependent upon the precision of the clock signal, and coherency is a major consideration. Many deep space radios under $1,000,000 will not feature coherency, and coherency advantages include Doppler measurements on smaller phase shifts as well as lower signal-to-noise ratios than non-coherent systems. An accurate state vector measurement then becomes dependent on the precision of the clock, and the CSAC utilized for this purpose can equally be used for the watchdog timer.

As watchdog timers are capable of halting mission operations and ConOps flows, the frequency of allowed resets is worth consideration. The Dellingr mission experienced a "potentially thermal-related issue" that caused the spacecraft to reset every 63 seconds indefinitely, rendering communications with the spacecraft impossible [238]. In their lessons learned, they note a planned daily reset allows for flexibility in software diagnostics, but the number of resets experienced is far greater than anticipated. Reset considerations must be thoroughly vetted, and operations plans must be developed for hardware that is working intermittently instead of a hard failure.

4.3.4.6 AEGIS Error Detection Strategy

The recommended error detection strategy is a combination of SCS for path and block identification, recovery blocks for non-critical processes having independent calculation methods, and watchdog coprocessors for timing and scheduler verification. Data value reasonableness, structure size, and calculation path will be vetted by AOP assertions. In the event of watchdog-initiated resets, timestamped scheduler processes will be logged for downlink post-issue diagnostics. Diagnostics registered in this manner will be automatically queued for downlink. Diagnostic report size must be included in potential downlink time estimates and link budgets. Much, much more work went into AEGIS FSW and C&DH operations than is being reported, and the author is happy to discuss upon request and proof of ITAR compliance.

4.3.5 Containment of Error Propagation

The greatest strength and Achilles heel of CubeSats is their modularity. Many systems are, in a sense, plug and play. If an error is propagated through that plug, it becomes difficult to say if the error originated local to a fault or upstream of it. Containment of error propagation is embodied by the strategy of limiting errors to the module or subsystem in which the fault occurred. If the error originated in memory, the error is corrected before the data is passed to the next subsystem. If output from the IMU does not meet checks for reasonableness, a diagnostics query is initiated for the IMU before using the suspect data.

The physical action which contains the errors to modules or subsystems is a boundary definition. To liken this example to a real system, consider the FSW architecture. The AEGIS FSW architecture, F Prime, is comprised of connections, ports, and topologies. The connections may be the physical data transfer line, and ports would define the boundary to that data connection for both input and output. Checks such as data structure, data reasonableness, and path identification can be applied at those port locations, and the information in the checks is set in the driver for the component. Error detection methodologies without error recovery operations will result in process halting, error diagnostics, single component hardware power cycling, and total system power cycling.

4.3.6 Recovery of Operations

The recovery sequence begins with the identification and removal of errors, proceeds to restoration of valid subsystem states, and terminates with validation of a complete and successful operation [201]. System operators worry that unmasked faults will propagate within a system and manifest in ways that are not identifiable via standard boundary checks. If an error is detected, diagnostics are logged, and the recovery sequence is given the green light to proceed as a decoupled procedure from the error detection sequence. A recovery operation timer is initiated while the PHM operates. If the recovery sequence can complete within the timer, the erroneous process will be re-initialized and satellite operations will continue. If the prescribed time for recovery operations is exceeded, the watchdog timer will initiate a hard reset.

Many recovery strategies will restore system operation to some previous state or checkpoint that was analyzed and deemed correct. This is a usable strategy but a dangerous one. It is always safer to shut down and re-initialize than to pick up at an assumed safe state, but mission ConOps may not allow for such caution. The act of saving the acceptable previous state involves forcing cache data to be restored from protected main memory [201]. This means that, periodically, an operation should be saving intermediate process information to some memory location that is assumed either incorruptible or frequently scrubbed. Frequent scrubbing of the save state may involve a higher priority designation for the patrol scrubbing of those memory registers. If a processor is to be rolled back to a recovery point, the processor state and key variables are restored to a known good condition, the cache memory is invalidated, and the cache data is similarly restored to that of the recovery point. The recovery point must be defined, the processor state variables, key variables, and cache data must be saved for that recovery point, and any error, likely in the cache memory, may again cause an error and induce this process. Recovery operation counters may be included to ensure that cyclical recovery operations are not being performed on the same erroneous process. The methodology described here is a backward error recovery scheme. Forward error recovery, where the output is assumed but not calculated due to the error, is a dangerous strategy and should be avoided in critical processes.

4.3.7 Additional Embedded System Design Guidance

Several strategies have been discussed regarding the fidelity of embedded system operation, but alpha particle environments, PCB surface treatments, Enhanced Low Dose Radiation Sensitivity (ELDRS), and physical component selection are worth consideration from a fabrication standpoint.

Alpha particles are composite particles comprised of two protons and two neutrons. They are relatively slow and heavy with high ionization potential. The high ionization potential means that they can cause damage to electronic circuits, but it also means they can be stopped easily by shielding. The problem is that components in embedded systems can emit alpha particles, so there is no shielding to prevent embedded systems from damaging themselves. Alpha particle environment severity can be reduced by carefully selecting the materials used in device manufacture, including low alpha-emitting solder and plastic encapsulate materials [217]. Another method is to apply the concept of exclusion zones where highly emitting materials, such as solder bumps, are physically separated from sensitive components. SEEs in global signals such as the clock, bias voltage, or reference voltage can create errors throughout the entire system, so those global signal paths must be handled with additional care.

As alpha particles are easily stopped by any material, careful selection of a CubeSat PCB surface coating material may result in a lower alpha particle environment severity. There is no literature on this conjecture; it is an informed guess based on previous research. The most common PCB surface treatment is Electroless Nickel Immersion Gold (ENIG), but a recent advancement in surface treatment technology called Electroless Nickel Electroless Palladium Immersion Gold (ENEPIG) offers a harder trace coating material (i.e. Palladium) over ENIG. ENEPIG can also be used for advanced PCB design techniques such as Through-Hole Technology (THT). The application of low alpha-emitting solder on an ENEPIG-coated trace may provide enhanced protection for internal III-V semiconductors from alpha particles. When combined with SoI technology on a Class 3 PCB for an OBC in a shielded electronics box, the PCB could potentially survive for decades. If mission life is short, these additional considerations may not be necessary, and many LEO missions have attained success without them.

ELDRS is when low dose radiation causes ionizing effects in semiconducting devices in the same way high dose energy processes would without the theoretical energy required to cause a fault. Radiation dose at a very low dose rate would have a greater cumulative effect than the same dose at a much higher rate. It was first discovered in a bipolar linear process [239], and it similarly involves electron-hole pair production, transport, and trapping in the dielectric regions. ELDRS is not well understood, and a postulate for the physical mechanism of ELDRS in bipolar devices was presented in 2020 [240]. MIL-STD-883 1019.8 discusses test procedures for ionizing radiation susceptibility in microelectronics, and OBC procurement should include a question to vendors regarding ELDRS susceptibility according to this standard. There is not much a spacecraft designer can do to prepare for ELDRS other than asking a vendor about it in relation to a given OBC design. The presence of ELDRS does not mean a mission will fail regardless of radiation environment, more so that faults and errors could occur regardless of environment.

A final consideration is physical component selection. Certain components, such as pinched resistors, diffused resistors, MOS capacitors, surface Zener diodes, and lateral PNP transistors display inherent vulnerability to radiation effects [217]. These components, if used on an OBC or science instrument, should be considered for replacement, perhaps by polysilicon capacitors in poly-poly or poly-metal configurations, or not used at all. There are strategies to cancel or balance radiation-induced offset voltages in amplifiers and comparators, such as charge pump circuits and build-source biasing circuits, but these techniques compensate for the symptoms of TID, not prevent radiation damage itself. If a program decides to purchase a COTS OBC, specific circuitry information should be acquired so that sensitive regions may be vetted for additional shielding or radiation effect prevention mechanisms.

4.4 Radiation-Tolerant Structural Design

It may seem a simple tradeoff: denser shielding material leads to a lower geometric range for a particle of a given energy per **Eq.(138)**, and the most dense material would be the best shield for a given mass allowance. However, as all things in spacecraft design, it is not so simple, and the reason is spallation.

Spallation is when a high energy particle such as GCR or SEP impacts dense matter, i.e. as almost all radiation shielding, and the shield material interactions with the incident particle cause a blast of secondary nucleons, such as protons and neutrons, in the general direction that the high energy particle was originally travelling. The matter in the shield is being broken apart, becoming atomic shrapnel. If the shield was protecting sensitive electronics, the single high energy particle may be blocked, but potentially hundreds of protons and neutrons are ejected towards the same sensitive electronics. Therefore, it is not always best to put a single slab of thick material between space and the device of interest.

Radiation shielding application is a cat and mouse game of what is worse for a given device in a given radiation environment, high energy particles or spallation products. This section will begin with a discussion of the spallation products, called secondary particles, followed by a review of modern shielding techniques and their spallation-mitigation strategies.

4.4.1 Secondary Particles

An incident cosmic ray encounters a solid shield or atmospheric gas, and the energetic particle collision generates secondary particles. Those secondary particles may in turn have enough energy to create spallation products when they encounter matter, generating tertiary particles. The energy of the particles at each subsequent spallation event decreases, and accounting for tertiary events alone proves difficult. Three secondary cosmic rays can induce SEUs in electronics: neutrons, protons, and pions [241]. Pions are pi-meson particles, part of the hadron classification, with a rest mass of ~140 MeV. SEEs in general can be caused by any high energy particle with ionization potential. More specifically, the interaction of hadrons with a semiconductor lattice can produce nuclear reactions that cause spallation products or secondary particles which can damage sensitive electronics. It was noted that neutrons in space have are not frequently encountered in the void unless generated nearby. Neutrons as secondary particles are taking part in picosecond-scale reactions and must be considered.

An additional consideration to the conversion of primary particle interactions to secondary particle interactions is Bremsstrahlung, or ‘braking radiation’. Bremsstrahlung is when a charged particle, usually an electron, interacts with the nuclei of matter, in this case shielding, and produces electromagnetic radiation in the form of photons as the particle slows down. Photons cannot be ignored as high energy photons have ionization potential.

4.4.2 Characterizing Secondary Particles

Outside of spallation textbooks [242], spacecraft engineers may find useful characterization of secondary particle interactions with electronic components difficult, but resources exist in the form of radiation transport codes. A study was performed on the Space Shuttle where the energy spectrum of secondary particles generated by GCR interactions with the Space Shuttle shielding was directly measured [243]. Protons, deuterons, tritons, ^{3}He and ^{4}He were identified. The transport code the direct measurement was compared against was the HZETRN radiation transport model developed by NASA. The Space Shuttle study was performed in 1995, but the latest version of HZETRN came out in 2015. Primary observations of the study were that HZETRN was underestimating the flux of many light ions. HZETRN is a deterministic code, but a stochastic radiation transport code called MCNPX was developed by Jun [244]. Section 4.5.2 elaborates on which codes to use for what purpose, but spallation and Bremsstrahlung products may be accurately modeled by these codes.

4.4.3 Types of Radiation Shielding

Radiation shielding has been studied for nuclear fission and fusion reactors as well as dental patients undergoing X-rays. Shielding is generally thick, dense, and heavy. On spacecraft, mass budgets severely limit the density and thickness possibilities of shielding, and spallation products cause dense, thick shields to potentially worsen SEEs in microelectronics. Several types of radiation shields are presented that converge in different ways upon the same conclusion: **it is better to characterize the radiation environment and protect against specifically anticipated particles in the order they will be encountered than to generalize the radiation environment and attempt to resist everything at once**.

4.4.3.1 Single Layers

Single layers of radiation shielding are the most common analyses performed in radiation transport codes because a simple correlation of dose vs. shielding depth can be attained for a given environment. Specific particles or environment-dependent particles may be analyzed individually and then cumulatively, such as electrons trapped in the VABs and solar protons. It is straightforward to couple single-layer analyses with environment or particle generation codes. The single layers are modeled as either semi-infinite media or solid spheres, where the solid sphere analysis, something likely not practical until SphereSats become popular, can be taken as a conservative, worst-case scenario [166]. Even if a different shielding type is planned for use, performing a single-layer analysis can provide nominal, conservative data for comparison against more advanced analyses.

Single layers may be foils or plates, and high-Z materials are preferred. Aluminum is widely considered due to its common use as structural bus material, and it would be cheap to utilize a thicker section of the already-included bus material as radiation shielding. Unfortunately, aluminum alone in GEO would not reduce the dose of a 15-year mission below 1,000 rads until 5 cm thickness was attained [166]. That analysis was performed with OMERE, described with other radiation codes in Section 4.5.2, and included trapped electrons, solar protons, and Bremsstrahlung. As a substitute material, tantalum (Z=73), tungsten (Z=74), and titanium (Z=22) are frequently used, but high-Z materials also do not burn completely upon atmospheric re-entry, making disposal plans more complex.

4.4.3.2 Layered Shielding

The future of CubeSat radiation shielding is layered shielding, which must be introduce generally before specifically. The relevant questions for layered shielding applications are what the shield layers are made of, how the layers are bonded together, and where the layers are applied.

Material selection for the layers may be aluminum, titanium, tantalum, nickel, or any combination of materials including nonmetals, and transport codes have material models for use with radiation environment codes. Transport codes can also vet layers of shielding instead of single-layer shields, with users specifying the layer material and thickness per layer. Not all materials bond cleanly with other materials. The common method of bonding metals has been heat treatment or press fits, which are two sides of the same energy coin. When energy is introduced to the interface between dissimilar metals, it is common for oxides and carbides to form at the interface. An excellent description of this process may be found in [245], and a depiction of the interface material is shown in **Figure 109**. Oxides and carbides worsen the structural integrity and shielding capacity of the layered shield. A better way to bond the materials is Ultrasonic Additive Manufacturing (UAM), where metal ‘tape’ is friction-bonded to a substrate material ultrasonically [246]. The process happens in such a short time scale that the material interface does not have time to heat up, and the materials are bonded without oxides or carbides forming. Verification of the existence or absence of oxides and carbides in bonded structures may be accomplished by a scanning electron microscope. If oxides or carbides are present in a layered shielding interface, the performance of radiation attenuation and shielding will be less than what is predicted by the models.

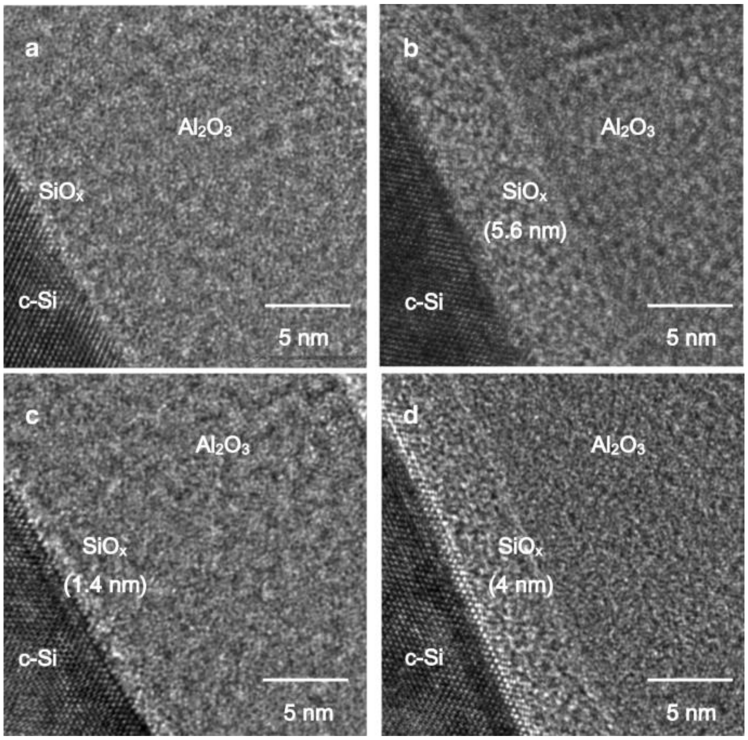

Figure 109: Oxide Formation Between Dissimilar Bonded Materials [247]

Selection of layer position cements layered shielding as the future of physical CubeSat fault avoidance by means of positioning material layers to protect against particle interactions as the particles are generated in the shielding itself. It has been noted that alpha particles emitted by packaging materials in electronics had limited energy and range near those sensitive circuits [201]. A thin polyamide material deposited on the PCB die surface resulted in significant reduction of the population of alpha particles reaching those sensitive devices. The concept of placing specific types of shielding where it was most useful was expanded to the layered outer shielding itself, known as Z-Graded radiation shielding.

4.4.3.3 Z-Graded Radiation Shielding

The Z in Z-Graded radiation shielding represents atomic number, and the grading of the atomic numbers refers to placing the highest-Z materials on the spacecraft shield exterior and lower-Z materials on the spacecraft shield interior. There are also versions where high-Z materials are sandwiched between low-Z materials. For a single shielding component with atomic number Z and atomic mass $m_{A,shield}$, the energy loss by ionization $dE_{particle}$ of one incident particle per area A_{shield} in cm^2 per unit mass m_{shield} is proportional to the electrons per atom and inversely proportional to the density of the material ρ_{shield}, as described in **Eq.(144)** [248].

$$\frac{-dE_{particle}}{A_{shield} \cdot m_{shield}} \approx \frac{Z}{\rho_{shield} \cdot m_{A,shield}} \qquad \textbf{Eq.(144)}$$

In practice **Eq.(144)** signifies higher-Z shielding materials will have a higher stopping power for higher energy particles, which is in line with the “denser is better” mantra, but it also means that lower-Z particles resist lower energy particles better than a high-Z shield because the Z/A ratio is highest for hydrogen and other low-Z matter. Interactions are highly dependent on particle type and energy; consider what happens after the high energy particle is encountered. The spallation products of the high energy particle impacting the high-Z shield will continue past the high-Z shield and encounter a lower-Z shield material. The idea is to tailor the layering strategy to resist particles as they are generated. There may be several layers of differing low-Z materials after the initial high-Z material is encountered and then another high-Z layer to block any high energy particles that may have traversed the first high-Z layers without spallation.

Any number and order of layers may be evaluated for dose resistance in SPENVIS, but only a few have been attempted in space. The Shields-1 mission was a technology demonstration CubeSat developed by NASA Langley [249]. They demonstrated that a Z-Graded radiation shield comprised of aluminum and tantalum increased the resistance to electrons by ~30% while reducing the overall thickness of the shielding by half compared to a shield of just aluminum. Additional demonstration of initial operations including a titanium layer were provided at the Small Satellite Conference 2019 but are not readily available. After further research is complete, it may be that vital missions to deep space include shielding that is a layered combination of aluminum, titanium, tantalum, nickel, chromium, molybdenum, and copper. Tapes layered by UAM may be thinner than a quarter of a millimeter, so a broad potential set of combinations exist for a given shield thickness.

It is important to note that while metals are commonly discussed here, thermoplastics have shown excellent resistance to protons because proton shielding in solid matter is achieved by inelastic scattering with shield electrons [248,250]. Electron shielding is achieved by both elastic and inelastic scattering as well as bremsstrahlung. Polyethylene specifically could be considered as a final, inner layer, potentially mounted between final layers, but it may be difficult to structurally incorporate and vet for outgassing. Modeling by

Wesley showed low-Z materials, such as polypropylene, displayed a reduction in proton dose of half when compared with the same areal density of tantalum [251].

4.4.3.4 Versatile Structural Radiation Shielding

Z-Graded radiation shielding has proven effective as an external shielding strategy, but it is also viable as a shielding strategy mounted directly to the OBC. Versatile Structural Radiation Shielding (VSRS™) was developed by Tethers Unlimited as a fault avoidance structural technique that can be applied to any sensitive electronics regardless of geometry. A depiction of VSRS is shown in **Figure 110**.

VSRS represents the ability to shield specific electronics from an anticipated space environment, be that an OBC or science instrument, but the true utilization of VSRS will come when the shielding strategy is democratized between outer Z-graded shielding on the spacecraft bus and inner Z-graded shielding on the sensitive electronics as VSRS or a future derivative of it.

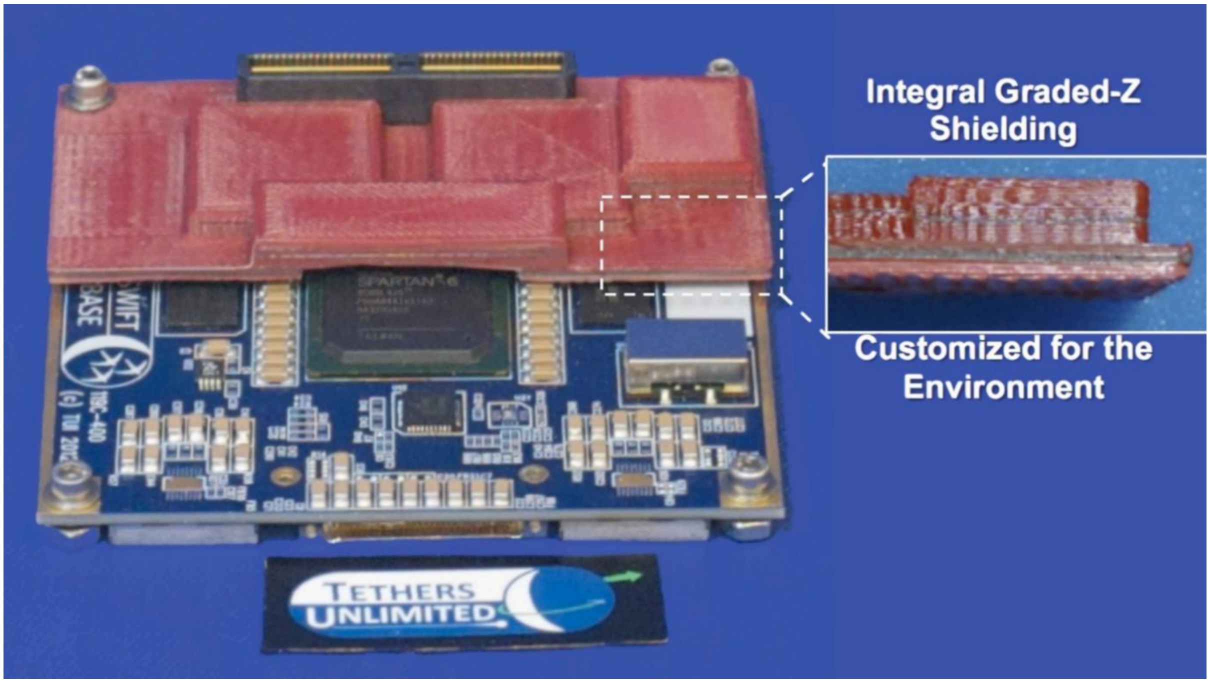

Figure 110: VSRS Multi-Layer Conformal Shielding. Low-Z PEEK polymer (red) with layers containing high-Z tungsten (gray). Used with permission from Tethers Unlimited, Inc. [250]

To elaborate, an experiment was performed on tungsten/polyetheretherketone (PEEK) VSRS with an areal density of 1 g/cm^2 where a 1.13 MeV beam of electrons with a raw beam flux of ~$1.55 \cdot 10^{11}$ e/cm^2-s irradiated the sample. The sample was designed to resist 99% of electrons, modeled and predicted in GEANT4, discussed momentarily, and there was no measurable transmission of electrons through the sample [250].

If external shielding was designed to resist high energy heavy ions and internal shielding was designed to resist any remaining protons and electrons, nearly all radiation-induced SEEs may be prevented. This includes direct strikes resulting in quantum wells and charge collection, secondary particles due to heavy ion spallation, bremsstrahlung, and potentially even ELDRS. The single-shield solution should become discretized into system of dissimilar shields intended to reduce the impact of a given radiation environment on sensitive electronics as the particles themselves are altered by shielding locations. Additionally, nanoscale shield fabrication processes will offer greater control and fidelity of shield specifications to all forms of Z-graded shielding [252]. Plastic shielding placed directly on OBC devices should be scrutinized for melting and long-term deformation considerations. Covering heat-generating devices will result in increased thermal insulation and higher temperatures, but layers of metallic shielding may also provide electronics thermal management solutions via thermal spreading.

4.4.3.5 Cable Shielding

Cables are the final individually shielded component of note. Interface or power cables can be ordered with shielding materials, but those materials are generally for EMI protection and Electromagnetic Compatibility (EMC) considerations. All cables should be carefully wrapped in electrically insulating Kapton to prevent charge buildup. In high power cables, charge accumulation may still occur on the outer surface of the cable shield material. Harnessing those cables with electrically insulating structural materials, such as the PEKK described in Section 3.2.2.2, will offer additional protection against unanticipated, radiation-induced events in the cables themselves that may translate to ESD events outside the cable. A classical overview of radiation-induced signals in cables may be found in [253].

4.5 Radiation Effect Assessment

With considerations for the space radiation environment, SEEs, published spacecraft radiation data, radiation-tolerant electronics design, and radiation-tolerant structural design understood, one can begin to synthesize a plan for characterizing a CubeSat's response to a given environment. There are four primary radiation damage interaction mechanisms in semiconductor devices.

The first interaction mechanism is ionization, causing gradual degradation by parameter shift. This could mean reduction of gain in a circuit or bias voltage drift, and ionization is measured by TID. The second is displacement damage, which can refer to displacement of lattice atoms, formation of vacancies and interstitials, or changes of species by nuclear reactions. Displacement damage is measured by NIEL. Third is internal dielectric charging, which refers to charge accumulation in space and manifests as arc discharge or an electromagnetic pulse. Plasma energy, density, and voltage levels are defined. Fourth is the classic SEE, described in Section 4.2. The parameters of interest for SEE environment definitions are particle flux and LET spectrum [166].

4.5.1 Radiation Characterization Flow

The operations for assessing a spacecraft's response to a radiation environment are shown in **Figure 111**. Operations with light circles in the upper right corner are near-Earth operations and can be excluded for spacecraft outside the magnetosphere. Final operations will be given explicit consideration after the simulation tools are introduced. Near-Earth operations, such as the conversion of orbital elements and geomagnetic field models to McIlwain coordinates, are widely available and will not be given additional consideration. The WMM and IGRF geomagnetic field models are introduced and described in Section 3.7.3.1 [160,161]. The difference between the WMM and IGRF is that the WMM is a predictive model valid for a 5-year epoch while the IGRF is retrospectively updated. IGRF-12 is valid for 1900-2020, and IGRF-13 was recently released.

The flow begins by modeling the orbit and trajectory from science and communications requirements. If the spacecraft will traverse the VABs, trajectory coordinates must be mapped to the McIlwain coordinates for inclusion to the proton and electron models. McIlwain coordinates are dependent upon the magnetic field as well as a spacecraft's position. Trapped electrons and protons refer to charged particles trapped in the VABs. Once VAB particles, SEPs, and GCRs are accounted for, shielding models can be applied to analyze three of the four interaction mechanisms. Surface charging and internal dielectric charging can also be modeled by a different code in the same simulation suite.

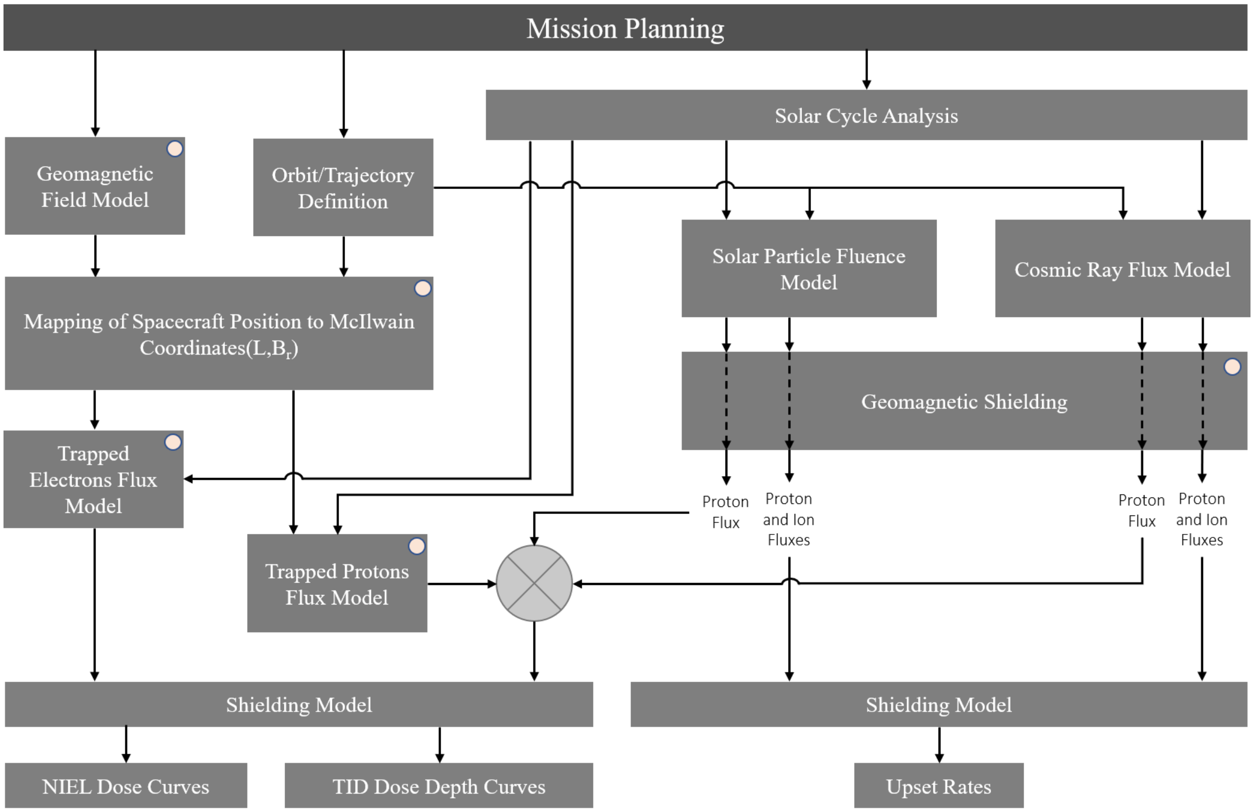

Mission Planning
Solar Cycle Analysis
Geomagnetic Field Model
Orbit/Trajectory Definition
Solar Particle Fluence Model
Cosmic Ray Flux Model
Mapping of Spacecraft Position to McIlwain Coordinates(L,B$_r$)
Geomagnetic Shielding
Trapped Electrons Flux Model
Proton Flux
Proton and Ion Fluxes
Proton Flux
Proton and Ion Fluxes
Trapped Protons Flux Model
Shielding Model
Shielding Model
NIEL Dose Curves
TID Dose Depth Curves
Upset Rates

Figure 111: Radiation Assessment Flow, Adapted with Permission from [166]

4.5.2 Simulation Tools

The primary tools for predicting the space radiation environment for a given mission will be the Space Environment Information System, known as SPENVIS [254], and OMERE [255]. SPENVIS and OMERE are composite space radiation models that include models from many sources. Both are free and require an account online. Particle data must either be generated in SPENVIS/OMERE or imported for use in the shielding and charge models. The model packages in SPENVIS are broken into coordinate generators, radiation sources and effects, spacecraft charging, atmosphere and ionosphere, magnetic field, meteoroids and debris, GEANT4, and a miscellaneous category. Models for calculating GCR and SEP are presented, followed by a description of other simulation tools. Not all of them are inherent to SPENVIS/OMERE, but all feature data sets that can be imported.

4.5.2.1 Galactic Cosmic Ray Models

An excellent comparison of GCR models is handled by [209] and summarized here. There are four GCR models of merit: CREME96, CREME2009, Badhwar-O’Niell 2010 (BON2010), and Burger-Usoskin. CREME96 was the best model for a while, but in 2010 it was proven that the model should not be used for data sets after 1997. This negated significant research, including a lunar TID assessment comparison with CRaTER data [256]. CREME2009 reproduces empirical data from the Advanced Composition Explorer (ACE) fairly well, but it overestimates hydrogen flux by 40-70% and helium 25-40%. Burger-Usoskin and BON2010 both derive their models differently than the CREME models do; details are omitted for the sake of brevity. The conclusion is that BON2010 is the best fit for Z = 3 and greater, and no single GCR model is valid over the entire spectrum. There is, unfortunately, a dearth of data for hydrogen and helium fluxes in the last decade, so care must be taken in estimating what is effectively 99% of the hadronic GCR with any one model. CREME2009 as ISO15390 should be sufficient for most programs to create predictive GCR environment data, and overestimation is always better than underestimation.

A BON2020 model does exist, but one must contact O'Neill to obtain it. It is written in FORTRAN, so it is likely not as user-friendly as SPENVIS/OMERE with an ISO model. Hopefully, the model will be translated.

4.5.2.2 Solar Energetic Particle Models

A direct comparison of SEP models does not exist, but models exist in both SPENVIS and OMERE that include protons and ions. A detailed description of solar particle models may be found in [257]. The most common proton models include ESP, JPL91 Extended, SPOF, and SAPPHIRE. For ions, PSYCHIC and SAPPHIRE are both widely used. SAPPHIRE can also be used to model solar flare events. As with the GCR models, these are simply data sets to characterize particle environments for a given orbit. Geomagnetic shielding for both GCR and SEP is a setting that may be toggled and requires nothing other than the orbit.

4.5.2.3 Trapped Particles

Models for trapped protons, electrons, and plasma are the AP8, AE8, and SPM models [258]. Except for SPM, which stands for Standard Plasma Model, they are not acronyms. AP8 is for protons and AE8 is for electrons. They are widely used and are included in both SPENVIS and OMERE. Parameters for AE8 and AP8 are solar min or max, particle energy range, McIlwain L-shell range, relative magnetic field strength range, and integral or differential flux.

The newest versions, AP9 and AE9, have been approved for public release but are not in SPENVIS or OMERE yet. They are comprised of 37 satellite data sets. Given satellite orbital elements or an ephemeris, the model returns specified quantities of flux, fluence, or dose, and chosen statistics for these quantities are available from run modes of mean, perturbed mean, or Monte-Carlo scenarios in either omnidirectional or unidirectional formats [258]. The data can be imported to SPENVIS or OMERE. Soon, the AP9, AE9, and SPM models will receive international collaborators at which point the entire model system will be renamed IRENE for International Radiation Environment Near Earth. An example comparison between the AP8/AE8 (left) and AP9/AE9 (right) models can be seen in **Figure 112**.

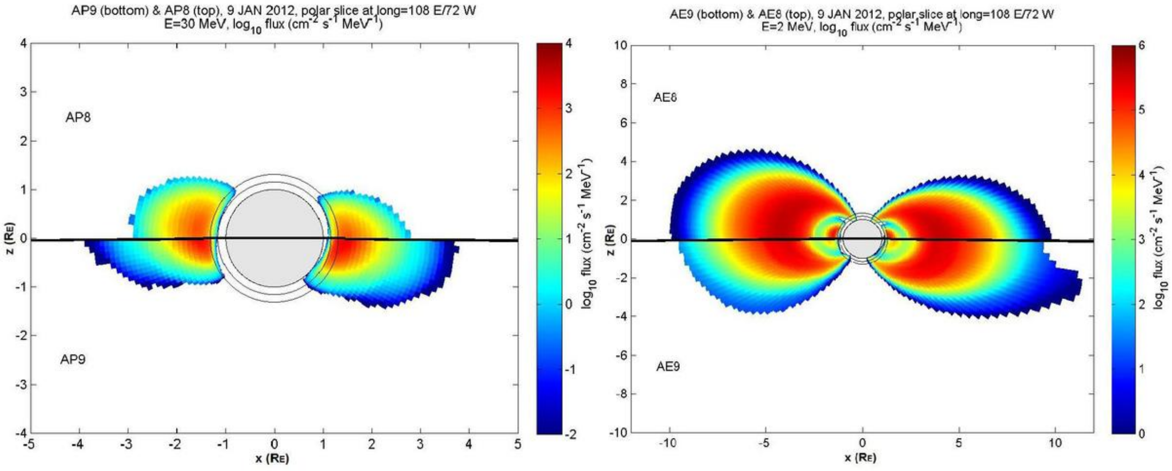

Figure 112: Differences in AP8/AE8 and AP9/AE9 [259]

4.5.2.4 Shielding Programs

GEANT4 is a toolkit for the simulation of the passage of particles through matter [260]. There are three main reference papers for GEANT4, Nuclear Instruments and Methods in Physics Research A 506 (2003) 250-303, IEEE Transactions on Nuclear Science 53 No. 1 (2006) 270-278 and Nuclear Instruments and Methods in Physics Research A 835 (2016) 186-225. The comparison of spacecraft shield thickness to a given particle environment is accomplished in GEANT4.

SHIELDOSE2, developed by NASA, determines the absorbed dose as a function of depth in aluminum shielding material of spacecraft given the electron and proton fluences encountered in orbit. It makes use of precalculated, mono-energetic depth-dose data for an isotropic, broad-beam fluence of radiation incident on uniform aluminum plane media [261]. Aluminum may not be the only shielding material of interest to spacecraft but using SHIELDOSE2 is simple. It is limited to 1-D.

MULASSIS is a more advanced tool for multi-layer shielding analysis [262]. It was developed by ESA as part of the GEANT4 collaboration, and it is not restricted to aluminum. It was built atop the capabilities of GEANT4, and both SHIELDOSE2 and MULASSIS are integrated into SPENVIS. SHIELDOSE2 is integrated into OMERE as well.

A widely used suite for determining heavy ion stopping power in shielding is the Stopping and Range of Ions in Matter (SRIM) website [263]. The advantage of SRIM lies in its customizability. Pre-defined or custom materials may be input as well as a variety of high energy particles. Shielding comparisons for specific particles without orbital considerations are best accomplished in SRIM.

If individual dose for equipment mounted within the satellite is of interest, a technique called sector shielding is available. Integrated software tools such as FASTRAD and ESABASE utilize effective shielding depth inputs present for a given direction with CAD considerations.

4.5.3 Finding Total Ionizing Dose

TID is caused by protons, ions, electrons, and secondary photons and will result in gradual degradation of the spacecraft which manifests as drifting parameters. Dose in rads in the common unit, and TID is graphically conveyed in Dose Depth Curves (DDC). The DDC is defined as the TID of the various radiation components as a function of the shielding depth [166]. SHIELDOSE2, GEANT4, and MULASSIS can all generate DDCs, but the particle index P, shielding type and geometry S, and target material T must be specified. The total dose for the chosen shielding geometry, mission lifespan, and energy range can be calculated by **Eq.(145)**.

$$DDC_{PST,TID}(z) = GF_S \cdot K \cdot \int_{E_{min}}^{E_{max}} F_{d,p}(E) \cdot LET_{PST}[E, z_p(z,E)] \cdot dE \qquad \textbf{Eq.(145)}$$

The function $F_{d,p}(E)$ is the omnidirectional differential fluence measured in units of 1/(cm^2-MeV) over the mission lifespan per **Eq.(130)**. GF_S is a dimensionless geometry factor specific to the shielding geometry, S, which may be a semi-infinite medium or solid sphere. For a semi-infinite medium, GF_S = ½. The quantity K is a constant conversion factor between the energy unit MeV and rad·g, or erg, and is equal to $1.6023\cdot10^{-8}$ (rad·g/MeV).

The parameter $LET_{PST}[E, z_p(z,E)]$, or stopping power, is a conditional LET available in the target, not the shielding, at energy E after the particle has penetrated the shielding to depth z [166]. TID in shielded electronics itself is simply the conditional LET multiplied by the omnidirectional differential fluence integrated over the energy range. Parameter $z_p(z, E)$, the depth of the target normalized to $r_p(E)$, the range of the particle of type P at energy E, is defined in **Eq.(146)**.

$$z_p = \begin{cases} \frac{z}{r_p(E)} \; if \; \frac{z}{r_p(E)} \leq 1 \\ else = 1 \end{cases} \qquad \textbf{Eq.(146)}$$

To accomplish these steps, spacecraft designers will determine the radiation environment with GCR, SEP, and trapped particle models, calculate the omnidirectional differential fluence, determine the energy levels of interest (greater than 1 MeV is nominal), calculate the range of the particles in a supposed shielding material and thickness, calculate the normalized target depth, calculate the LET, decide on a shielding geometry (solid sphere is conservative), and generate the DDC. All steps are possible in the SPENVIS/OMERE software suites, but newer particle models, such as the BON2020 GCR model, may be imported if desired. An example TID DDC is shown in **Figure 113**.

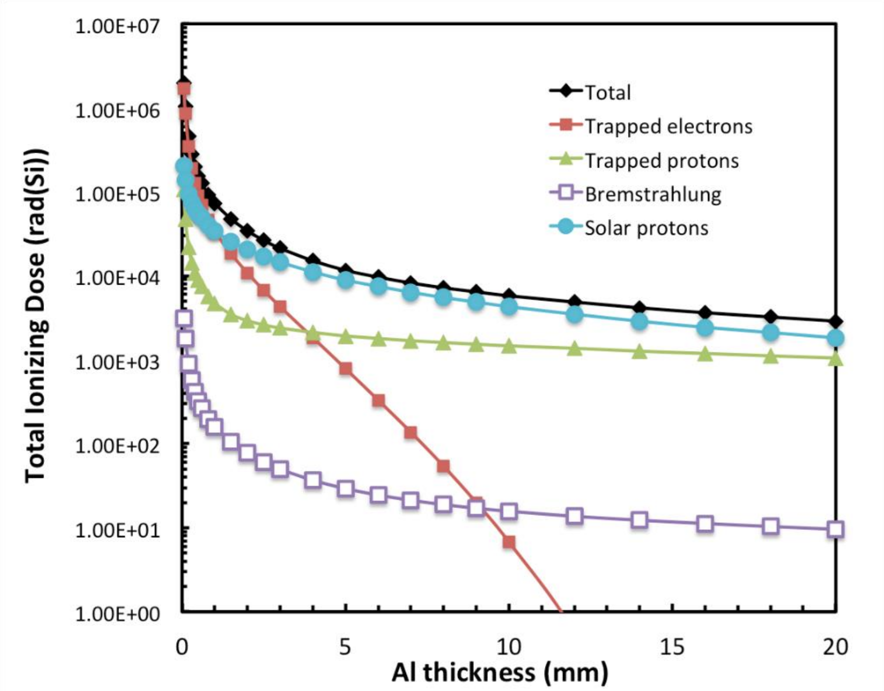

Figure 113: TID Dose Depth Curve Example, Target Material Si, Shield Material Al, GCR Not Included. GEO 1 year. Used with permission from Zero-g Radiation

4.5.4 Finding Non-Ionizing Energy Loss

NIEL describes the rate of energy loss due to atomic displacements as a particle traverses a material. There are dedicated NIEL characterizations for protons [264], electrons [265], alpha particles [266], and heavy ions [267]. It is measured by the same units as LET in MeV-cm^2/g, and a corollary dose calculation, the Displacement Damage Dose (DDD), may be calculated by **Eq.(147)** in units of J/kg, gray, or rads [166].

$$DDD = \int_{E_{min}}^{E_{max}} F_p(E) \cdot NIEL[E, Z_p(z, E)] \cdot dE \qquad \textbf{Eq.(147)}$$

The quantity $F_p(E)$ is calculated the same as in **Eq.(130)**, but the quantity $NIEL(E)$ must be calculated with a tool such as the Screened Relativistic Nuclear Stopping Power Calculator [268]. This tool can be embedded in GEANT4, MULASSIS, and thus SPENVIS. Once $NIEL[E, Z_p(z, E)]$is calculated for a given energy range and target material, **Eq.(148)** may be used to calculate the DDC. The only difference between **Eq.(145)** and **Eq.(148)** is that $LET_{PST}[E, Z_p(z,E)]$ is substituted for $NIEL[E, Z_p(z,E)]$, but not all NIEL calculations involve shielding, so a normalized range may not be necessary.

$$DDC_{PST,NIEL}(z) = GF_S \cdot K \cdot \int_{E_{min}}^{E_{max}} f_p(E) \cdot NIEL[E, Z_p(z,E)]dE \qquad \textbf{Eq.(148)}$$

An example proton-specific DDC for NIEL DDD in silicon is shown in **Figure 114**. Of note is the total dependence of DDD on trapped protons.

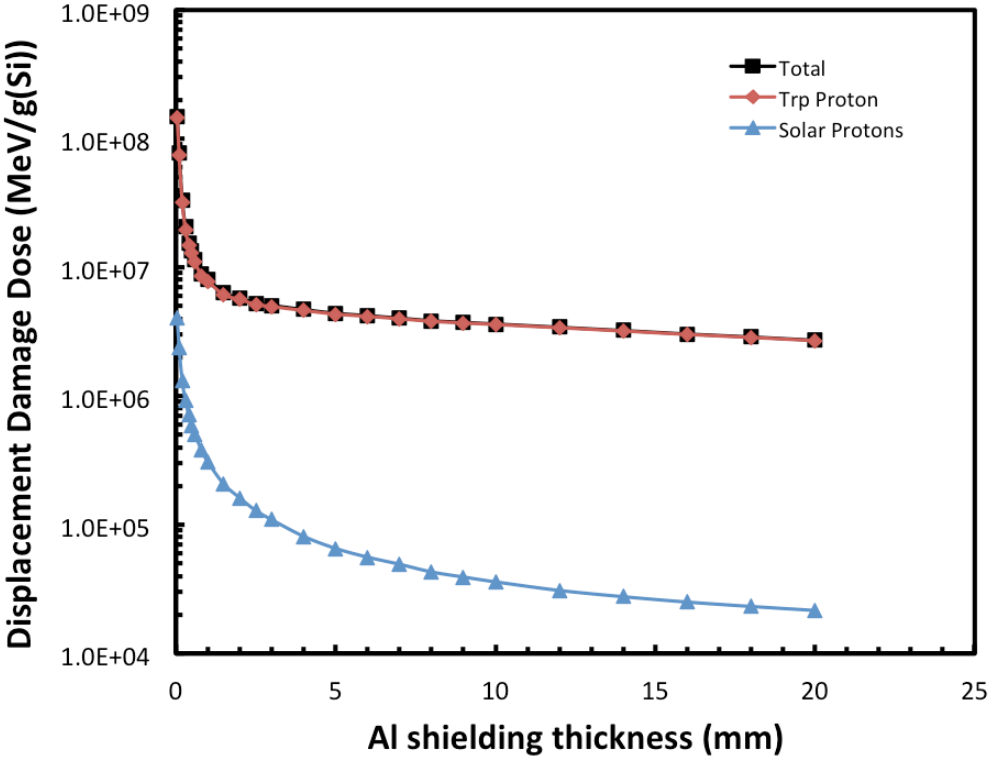

Figure 114: NIEL Dose Depth Curve Example, Target Material Si, Shield Material Al, GCR Not Included. ISS Orbit 3 year. Used with permission from Zero-g Radiation

NIEL manifests in optoelectronics much more strongly than in structural or computing components. The primary mechanism will be a decrease in solar panel efficiency in high particle fluence periods. For the Solar and Heliophysics Observatory (SOHO) spacecraft described in Appendix B, the spacecraft experienced a ~2% degradation in solar panel efficiency in a single day during the Bastille Day SPE on July 14th, 2000. While overall NIEL DDD is generally less than TID, it cannot be neglected. The lesser magnitude only indicates that interactions of energetic particles with electrons of crystal lattice atoms are more efficient than interactions with the lattice atoms themselves [166].

4.5.5 Finding Surface Charge

Surface charge is not included in **Figure 111** because, while the particle environment definition remains largely the same, calculation methods are less straightforward than TID, NIEL, or upset rate determination. Four useful charging codes are readily available: the Japanese Multi Utility Spacecraft Charging Analysis Tool (MUSCAT) [269], the NASCAP codes [270], the SEE Interactive Spacecraft Charging Handbook [271], and the Spacecraft Plasma Interaction System (SPIS) [272]. The physics of internal dielectric charging are non-trivial and outside the scope of this document, so beginners should start with the SEE Interactive Spacecraft Charging Handbook, which can be obtained through the website [271].

If more detailed analysis with a CAD-based, three-dimensional model is desired, NASCAP-2K [270] is recommended. Surface charging in interplanetary orbits, material databases, finite element visualization, and Particle-In-Cell capabilities are available. NASCAP-2K can be obtained by request through the website.

Three ESD models are described in NASA-HDBK-8739.21, the Workmanship Manual for Electrostatic Discharge Control: the Human Body Model (HBM), the Machine Model (MM), and the Charged-Device Model (CDM). The HBM simulates discharge from the fingertip of the operator in contact with the device wherein a 100-pF capacitor is discharged through a 1500-ohm resistor. The MM replicates a worst case HBM wherein a 200-pF capacitor is discharged directly to ground. The CDM considers a charged device that is discharged to ground through one pin or connector and likely represents the most applicable classification. ESD component sensitivity classes are provided in **Tables 54-56**.

Table 54: ESD Component Sensitivity Classes, HBM

Class	Voltage Range, [V]
0	< 250
1A	250 - < 500
1B	500 - < 1,000
1C	1,000 - < 2,000
2	2,000 - < 4,000
3A	4,000 - < 8,000
3B	≥ 8,000

Table 55: ESD Component Sensitivity Classes, MM

Class	Voltage Range, [V]
M1	< 100
M2	100 - < 200
M3	200 - < 400
M4	≥ 400

Table 56: ESD Component Sensitivity Classes, CDM

Class	Voltage Range, [V]
C1	< 125
C2	125 - < 250
C3	250 - < 500
C4	500 - < 1,000
C5	1,000 - < 1,500
C6	1,500 - < 2,000
C7	≥ 2,000

4.5.6 Finding SEE-Induced Upset Rates

SEE primary effects are memory content corruption and logical gate status changes leading to loss of scientific data, OBC errors, telemetry data corruption, and temporary loss of spacecraft status visibility, among more serious errors such as spurious command generation and thruster misfiring [166]. The simplest descriptor parameter of SEUs is the cross section, defined in **Eq.(131)**. This characterization does not include different particle types or target materials because vendors will test and report their cross sections for a given particle type, usually protons or heavy ions. SPENVIS and OMERE can calculate more advanced predictions of upset rates given the proper inputs.

SEUs from GCR ions, GCR protons, and SEP protons must be evaluated differently because the LET is different, and the LET spectrum is a direct measure of the ionization efficiency of a particular species of radiation onto a specific target material at a given energy [166]. For an unshielded spacecraft without geomagnetic shielding, GCR protons have an LET below 0.2 MeV-cm^2/mg in silicon, meaning they cannot directly cause SEUs. To cause upsets in that target, interactions with the lattice as inelastic scattering and nuclear reactions must occur. SEEs in general could occur due to direct ionization, and ionization energy considerations for common semiconductors is shown in **Table 57**. Note the high ionization energy of GaN.

Table 57: Band Gap and Ionization Energy of Semiconductors at Room Temperature, Used with Permission [166]

Material	Band Gap, [eV]	Ionization Energy, [eV]
Ge	0.68	2.96
Si	1.12	3.6
GaAs	1.42	4.8
GaN	3.39	8.9
SiC	2.9	6.88

The SRIM website offers tools for calculating SER due to GCR. If cross-section for relevant particle types is not vendor-provided, methods exist to estimate the cross-section and upset rates for a given device. These include the Rectangular Parallelepiped (RPP) model and the Integrated Rectangular Parallelepiped model, the latter of which is integrated into both OMERE and SPENVIS.

After defining distinct particle environments and device cross sections, LET-based upset rates may be produced in the software suites. Weibull distributions are used to estimate proton, neutron, and heavy ion upset rate data. A Bendel distribution can also be used. Example data sets for various proton environments on a semi-infinite shielding geometry are depicted in **Table 58**. Parameters given in the table description are for Weibull and Bendel distributions. Summing upset rates for all particle types and sources will yield a cumulative upset rate expectation.

Table 58: Proton Upset Rate Predictions $\sigma_0 = 1.0 \cdot 10^{-12}\ cm^2, E_0 = 20\ MeV, W = 50\ MeV,\ S = 2$. Used with permission [166].

Proton Source	Shielding	Flux Data Reference	Upset Rate/(bit-day)	
			Weibull Fit	Bendel Fit
GCR, solar minimum	none	No Geomagnetic Shielding	$3.83 \cdot 10^{-7}$	$3.62 \cdot 10^{-7}$
	10 mm Al		$3.80 \cdot 10^{-7}$	$3.60 \cdot 10^{-7}$
SEP Protons, "Halloween" worst day	none	GEO Orbit	$1.88 \cdot 10^{-3}$	$9.32 \cdot 10^{-4}$
	10 mm Al		$8.05 \cdot 10^{-4}$	$3.88 \cdot 10^{-4}$
SEP Protons, average values	none	SPOF Model, GEO Orbit	$1.50 \cdot 10^{-6}$	$8.17 \cdot 10^{-7}$
	10 mm Al		$1.92 \cdot 10^{-7}$	$9.69 \cdot 10^{-8}$

5. Conclusion

Many assertions have been made regarding CubeSat design, and many of the analysis results presented in this work are calculations that can be revised, improved, and expanded. As the author is first and foremost a thermal engineer, the thermal orbit model will be augmented to more appropriately include lunar orbit motion, Beta angle variation, penumbra effects in addition to the already included umbra, forward and aft radiative view factors instead of only top and bottom face view factors, lunar albedo, and patch heater/radiator area. The MATLAB model will be compared against STK and published as a standalone work.

Sadly, the AEGIS CAD will be shelved and will not proceed to PDR, but CAD development for the next ASGC mission, the Alabama Burst Energetics eXplorer (ABEX), has already begun. PDR is expected to occur in the Fall of 2021.

Thank you to all who made it to the end of this document. The author plans to release an updated version as a textbook after a few more years of CubeSat design under his belt. If you would like to suggest a change, revision, or comment to this work, or feel an aspect was insufficiently characterized, please email michael.c.halvorson@gmail.com.

Ad Astra.

REFERENCES

SECTION 1: INTRODUCTION

[1] Kovo, Yael. “Integration, Launch and Deployment.” NASA, NASA, 30 Mar. 2020, www.nasa.gov/smallsat-institute/sst-soa/integration-launch-and-deployment.

[2] Swartwout, Michael. CubeSat Database, sites.google.com/a/slu.edu/186wartwout/home/cubesat-database.

[3] Jung, Jaewoo, Naoki Kuzuya, and Robert J. Twiggs. “The design of the OPAL attitude control system(Orbiting Picosatellite Automatic Launcher).” AIAA/USU Conference on Small Satellites, 10 th, Utah State Univ, Logan, UT. 1996.

[4] Puig-Suari, Jordi, Clark Turner, and William Ahlgren. “Development of the standard CubeSat deployer and a CubeSat class PicoSatellite.” 2001 IEEE aerospace conference proceedings (cat. No. 01TH8542). Vol. 1. IEEE, 2001.

[5] Funase, Ryu, et al. “On-orbit operation results of the world’s first CubeSat XI-IV-lessons learned from its successful 15-years space flight.” (2019).

[6] “Cost of the Mars Reconnaissance Orbiter.” The Planetary Society, www.planetary.org/space-policy/cost-of-the-mars-reconnaissance-orbiter.

[7] Harwood, William. “Atlas 5 Rocket Launches NASA Moon Mission.” *CNET*, CNET, 24 Sept. 2009, www.cnet.com/news/atlas-5-rocket-launches-nasa-moon-mission/.

[8] Elliott, Dan. “Next-Generation of GPS Satellites Are Headed to Space.” Phys.org, Phys.org, 17 Dec. 2018, phys.org/news/2018-12-next-generation-gps-satellites-space.html

[9] Clark, Stephen. “NASA’s First Interplanetary CubeSats Fall Silent beyond Mars.” Spaceflight Now, 6 Feb. 2019, spaceflightnow.com/2019/02/06/nasas-first-interplanetary-cubesats-fall-silent-beyond-mars/.

[10] Chin, Gordon, and Craig Tooley. “Lunar Reconnaissance Orbiter (LRO).” NASA Space Science Data Coordinate Archive, NASA, nssdc.gsfc.nasa.gov/nmc/spacecraft/display.action?id=2009-031A.

[11] “About the Lander.” NASA, NASA, 21 May 2020, mars.nasa.gov/insight/spacecraft/about-the-lander/.

[12] “Satellite Solutions.” Rocket Lab, www.rocketlabusa.com/satellites/.

[13] McIntosh, Dawn M., John D. Baker, and Joseph A. Matus. “The NASA Cubesat Missions Flying on Artemis-1.” (2020).

[14] “Rocket Lab Completes Fit Check for NASA VCLS ElaNa XIX Mission.” Rocket Lab, www.rocketlabusa.com/news/updates/rocket-lab-completes-fit-check-for-nasa-vcls-elana-xix-mission/.

[15] Bruhn, Fredrik. “TechEdSat-CubeSat Technology demonstration mission featuring Plug-and-play and radiation hardened electronics.” 9th Annual Spring CubeSat Developer’s Workshop, Cal Poly State University, San Luis Obispo, CA, USA. 2012.

[16] Twiggs, Robert, et al. “The ThinSat program: flight opportunities for education, research and industry.” (2018).

[17] “One-Stop Webshop for CubeSats & Nanosats.” CubeSatShop.com, 4 June 2020, www.cubesatshop.com/.

[18] “S3VI – Small Spacecraft Systems Virtual Institute.” NASA, NASA, s3vi.ndc.nasa.gov/.

[19] CubeSat, Gunter's Space Page, space.skyrocket.de/doc_sat/cubesat.htm.

[20] “Small Satellite Conference: Conferences and Events: Utah State University.” Small Satellite Conference | Conferences and Events | Utah State University, digitalcommons.usu.edu/smallsat/.

[21] Artemis-1 – Satellite Missions – EoPortal Directory, directory.eoportal.org/web/eoportal/satellite-missions/a/artemis-1.

[22] Garner, Rob. “OSIRIS-Rex.” NASA, NASA, 20 Feb. 2015, www.nasa.gov/osiris-rex.

[23] “Asteroid Explorer Hayabusa2: Spacecraft.” ISAS, www.isas.jaxa.jp/en/missions/spacecraft/current/hayabusa2.html.

[24] Talbert, Tricia. “Double Asteroid Redirection Test (DART) Mission.” NASA, NASA, 30 June 2017, www.nasa.gov/planetarydefense/dart.

[25] J. Banik, S. Kiefer, M. LaPointe and P. LaCorte, “On-orbit validation of the roll-out solar array,” 2018 IEEE Aerospace Conference, Big Sky, MT, 2018, pp. 1-9, doi: 10.1109/AERO.2018.8396390.
[26] Goldberg, Hannah, et al. “The Juventas CubeSat in Support of ESA’s Hera Mission to the Asteroid Didymos.” Small Satellite Conference, Logan, Utah. 2019.
[27] Toorian, Armen, Ken Diaz, and Simon Lee. “The cubesat approach to space access.” 2008 IEEE Aerospace Conference. IEEE, 2008.
[28] United States, GSFC. NASA Technical Standards System, 30 June 2016. Standards.nasa.gov/standard/gsfc/gsfc-std-1000.
[29] “Our Process.” Process, universitynanosat.org/process/.
[30] NASA Strategic Plan 2018, 2018. www.nasa.gov/sites/default/files/atoms/files/nasa_2018_strategic_plan.pdf.

SECTION 2: MISSION AND SPACECRAFT CONOPS

[31] Artemis-1 – Satellite Missions – EoPortal Directory, directory.eoportal.org/web/eoportal/satellite-missions/a/artemis-1.
[32] “Systems Tool Kit (STK).” *Agi*, www.agi.com/products/stk.

SECTION 3: ARCHITECTURE AND SUBSYSTEM DESIGN

[33] Wertz, James R, David F. Everett, and Jeffery J. Puschell. *Space Mission Engineering: The New Smad*. Hawthorne, CA: Microcosm Press, 2011. Print.
[34] Gilmore, David G., and Martin Donabedian. Spacecraft Thermal Control Handbook. American Institute of Aeronautics and Astronautics, 2003.
[35] Wertz, James R. Spacecraft Attitude Determination and Control. Kluwer Academic Pub, 1999.
[36] Braun, T. M. Satellite Payload in Digital Communication Systems Design, Technology, and Analysis. Wiley, 2012.
[37] Shishko, Robert, et al. NASA Systems Engineering Handbook. 1995.
[38] Lambert, Tyler Ross, Austin Gurley, and David Beale. “SMA actuator material model with self-sensing and sliding-mode control; experiment and multibody dynamics model.” *Smart Materials and Structures* 26.3 (2017): 035004.
[39] Kovo, Yael. “State of the Art of Small Spacecraft Technology.” NASA, NASA, 6 Mar. 2020, www.nasa.gov/smallsat-institute/sst-soa.
[40] “NASA Technical Standards.” NASA, NASA, standards.nasa.gov/nasa-technical-standards.
[41] Jones, Justin S. “Additive Manufacturing (AM) Activities and Non-Destructive Evaluation (NDE) at GSFC.” (2017).
[42] ASM Handbook: Heat Treating of Aluminum Alloys. Vol. 4, American Society for Metals, 1991.
[43] “SSTD-8070-0098-SHOP.” NASA, NASA, standards.nasa.gov/standard/ssc/sstd-8070-0098-shop.
[44] Miller, Daniel G. Vibrational Analysis of a 12U Chassis. AIR FORCE INSTITUTE OF TECHNOLOGY WRIGHT-PATTERSON AFB OH WRIGHT-PATTERSON AFB United States, 2016.
[45] Wilhelm Böllhoff GmbH & Co. KG. “Products and Services.” Thread Inserts for Metals HELICOIL® | Böllhoff, www.boellhoff.com/de-en/products-and-services/special-fasteners/thread-inserts-helicoil.php.
[46] “Space Materials Database: Thermoset Plastics.” SPACEMATDB, www.spacematdb.com/spacemat/datasearch.php?name=18: Thermoset plastics.
[47] Malayoglu, Ugur, et al. “An investigation into the mechanical and tribological properties of plasma electrolytic oxidation and hard-anodized coatings on 6082 aluminum alloy.” Materials science and Engineering: A 528.24 (2011): 7451-7460.
[48] Shrestha, S., and B. D. Dunn. “Advanced plasma electrolytic oxidation treatment for protection of light weight materials and structures in a space environment.” Advanced Surface Treatment (2007): 40-44.

[49] “CHO THERM 1671.” Thermally Conductive Elastomer Insulators, SPACEMATDB, www.spacematdb.com/spacemat/manudatasheets/cho-therm1671.

[50] Blevins, Robert D. Formulas for Natural Frequency and Mode Shape. R.E. Krieger, 2001.

[51] Gao, Er-wei, Xue-ping Zhang, and Zhen-qiang Yao. “Simulation and analysis of flexible solar panels’ deployment and locking processes.” Journal of Shanghai Jiaotong University (Science) 13.3 (2008): 275-279.

[52] Peters, Eric David. Dynamic instabilities imparted by CubeSat deployable solar panels. Diss. Massachusetts Institute of Technology, 2014.

[53] Park, Tae-Yong, Bong-Geon Chae, and Hyun-Ung Oh. “Development of 6 U CubeSat’s Deployable Solar Panel with Burn Wire Triggering Holding and Release Mechanism.” International Journal of Aerospace Engineering 2019 (2019).

[54] Oh, Hyun-Ung, and Myoung-Jae Lee. “Development of a non-explosive segmented nut-type holding and release mechanism for cube satellite applications.” Transactions of the Japan Society for Aeronautical and Space Sciences 58.1 (2015): 1-6.

[55] Lee, Myeong-Jae, Yong-Keun Lee, and Hyun-Ung Oh. “Performance evaluation of hinge driving separation nut-type holding and releasing mechanism triggered by nichrome burn wire.” International Journal of Aeronautical and Space Sciences 16.4 (2015): 602-613.

[56] Park, Tae-Yong, et al. “Experimental investigation on the feasibility of using spring-loaded pogo pin as a holding and release mechanism for CubeSat’s deployable solar panels.” International Journal of Aerospace Engineering 2018 (2018).

[57] Thurn, Adam, et al. “A nichrome burn wire release mechanism for CubeSats.” The 41st Aerospace Mechanisms Symposium, Jet Propulsion Laboratory. 2012.

[58] Howell, John R., et al. Thermal Radiation Heat Transfer. 6th ed., CRC Press, 2016.

[59] Fröhlich, C., and R. W. Brusa. “Solar radiation and its variation in time.” Solar Physics 74.1 (1981): 209-215.

[60] Fröhlich, C., and C. Wehrli. “Spectral distribution of solar irradiance from 25000 nm to 250 nm.” World Radiation Center, Davos, Switzerland, private communication (1981).

[61] Martinez, Isidoro. “Radiative View Factors. 2013.”

[62] Hall, Dorothy. *Remote sensing of ice and snow*. Springer Science & Business Media, 2012.

[63] Rickman, Steven L. “Introduction to on-orbit thermal environments.” Thermal and Fluids Analysis Workshop. 2014.

[64] Fixsen, D. J. “The temperature of the cosmic microwave background.” The Astrophysical Journal 707.2 (2009): 916.

[65] Siegler, Matt, et al. “Lunar Global Heat Flow: Predictions and Constraints.” Nasa.gov, Lunar-Landing.arc, 5 Feb. 2019, 18:47 GMT, lunar-landing.arc.nasa.gov/sites/default/files/presentations/57-Siegler_Landed_Mission_Workshop%20copy.pdf.

[66] Racca, Giuseppe D. “Moon Surface Thermal Characteristics for Moon Orbiting Spacecraft Thermal Analysis.” Planetary and Space Science, vol. 43, no. 6, 30 Mar. 1995, pp. 835–842., doi:10.1016/0032-0633(95)00067-f.

[67] Williams, J.-P., et al. “The Global Surface Temperatures of the Moon as Measured by the Diviner Lunar Radiometer Experiment.” Icarus, vol. 283, 2017, pp. 300–325., doi:10.1016/j.icarus.2016.08.012.

[68] Keihm, Stephen J. “Interpretation of the Lunar Microwave Brightness Temperature Spectrum: Feasibility of Orbital Heat Flow Mapping.” Icarus, vol. 60, no. 3, 1984, pp. 568–589., doi:10.1016/0019-1035(84)90165-9.

[69] Miyahara, Hiroko, et al. “Deriving Historical Total Solar Irradiance from Lunar Borehole Temperatures.” AGU Journals, John Wiley & Sons, Ltd, 29 Jan. 2008, agupubs.onlinelibrary.wiley.com/doi/full/10.1029/2007GL032171.

[70] Langseth, Marcus G., Stephen J. Keihm, and Kenneth Peters. “Revised lunar heat-flow values.” Lunar and Planetary Science Conference Proceedings. Vol. 7. 1976.

[71] Keihm, S. J., and M. G. Langseth Jr. “Surface brightness temperatures at the Apollo 17 heat flow site: Thermal conductivity of the upper 15 cm of regolith.” Lunar and Planetary Science Conference Proceedings. Vol. 4. 1973.

[72] Little, R. C., et al. “Latitude variation of the subsurface lunar temperature: Lunar Prospector thermal neutrons.” Journal of Geophysical Research: Planets 108.E5 (2003).

[73] Williams, J-P., et al. “The global surface temperatures of the Moon as measured by the Diviner Lunar Radiometer Experiment.” Icarus 283 (2017): 300-325.

[74] Cai, Zhanchuan, and Ting Lan. “Lunar brightness temperature model based on the microwave radiometer data of Chang’E-2.” IEEE Transactions on Geoscience and Remote Sensing 55.10 (2017): 5944-5955.

[75] Apollo 15 Preliminary Science Report NASA SP-289, 1972.

[76] Cremers, C. J., R. C. Birkebak, and J. E. White. “Lunar surface temperatures at tranquillity base.” AIAA Journal 9.10 (1971): 1899-1903.

[77] Williams, Jacob. “Copernicus Trajectory Design and Optimization System.” NASA, NASA, 8 Aug. 2016, www.nasa.gov/centers/johnson/copernicus/index.html.

[78] “CubeSat Toolbox.” *Princeton Satellite Systems*, 12 May 2020, www.psatellite.com/products/sct/cubesat-toolbox/.

[79] “RefractiveIndex.INFO.” RefractiveIndex.INFO – Refractive Index Database, refractiveindex.info/.

[80] Rakić, Aleksandar D. “Algorithm for the determination of intrinsic optical constants of metal films: application to aluminum.” Applied optics 34.22 (1995): 4755-4767.

[81] Wood, B. E., et al. “Surface effects of satellite material outgassing products.” Journal of Thermophysics and Heat Transfer 2.4 (1988): 289-295.

[82] Zhang, Z. M., G. Lefever-Button, and F. R. Powell. “Infrared refractive index and extinction coefficient of polyimide films.” International journal of thermophysics 19.3 (1998): 905-916.

[83] Guinneton, F., et al “Comparative study between nanocrystalline powder and thin film of vanadium dioxide VO2: electrical and infrared properties.” Journal of Physics and Chemistry of Solids 62.7 (2001): 1229-1238.

[84] Gomez-Heredia, C. L., et al. “Thermal hysteresis measurement of the VO 2 emissivity and its application in thermal rectification.” Scientific reports 8.1 (2018): 1-11.

[85] Hendaoui, A., et al. “VO2-based smart coatings with improved emittance-switching properties for an energy-efficient near room-temperature thermal control of spacecrafts.” Solar energy materials and solar cells 117 (2013): 494-498.

[86] Hendaoui, A., et al. “Enhancement of the positive emittance-switching performance of thermochromic VO2 films deposited on Al substrate for an efficient passive thermal control of spacecrafts.” Current Applied Physics 13.5 (2013): 875-879.

[87] “Thermal Desktop.” Thermal Desktop: Modeling Software - FEM, FD & FNM Methods, 1 Jan. 1970, www.crtech.com/products/thermal-desktop.

[88] “NX Space Systems Thermal.” Mechanical Engineering : University of Rochester, www2.me.rochester.edu/courses/ME204/nx_help/index.html#uid:id1246054.

[89] Ren, Hongmin, Qingbiao Wu, and Weihong Bi. "A class of two-step Steffensen type methods with fourth-order convergence." Applied Mathematics and Computation 209.2 (2009): 206-210.

[90] Dehghan, Mehdi, and Masoud Hajarian. "A variant of Steffensen’s method with a better approximation to the derivative." Appl. Math. Comput (2008).

[91] “Photovoltaics.” Spectrolab, www.spectrolab.com/photovoltaics.html.

[92] Bergman, T. L., et al. Fundamentals of Heat and Mass Transfer. John Wiley & Sons, Inc., 2019.

[93] Titus, Jon. “Engineers Warm up to IR Vision.” EDN, 1 Nov. 2007, www.edn.com/engineers-warm-up-to-ir-vision/.

[94] Mueller, Juergen, Richard Hofer, and John Ziemer. "Survey of propulsion technologies applicable to cubesats." (2010).

[95] Pascoa, Jose C., Odelma Teixeira, and Gustavo Filipe. "A review of propulsion systems for cubesats." ASME International Mechanical Engineering Congress and Exposition. Vol. 52002. American Society of Mechanical Engineers, 2018.

[96] Tummala, Akshay Reddy, and Atri Dutta. "An overview of cube-satellite propulsion technologies and trends." Aerospace 4.4 (2017): 58.

[97] Greene, W.D. "Convergent-Divergent Nozzle – Liquid Rocket Engines (J-2X, RS-25, General)." NASA, NASA, 3 Feb. 2012, blogs.nasa.gov/J2X/tag/convergent-divergent-nozzle/.

[98] Goebel, Dan M., and Ira Katz. Fundamentals of Electric Propulsion: Ion and Hall Thrusters. Wiley, 2008.

[99] Oates, Gordon C. Aircraft Propulsion Systems Technology and Design. American Institute of Aeronautics and Astronautics, 1989.

[100] Sutton, George Paul, and Oscar Biblarz. Rocket Propulsion Elements. Wiley., 2017.

[101] Chiu, Philip T., et al. "Qualification of 32% BOL and 28% EOL Efficient XTE Solar Cells." *2019 IEEE 46th Photovoltaic Specialists Conference (PVSC)*. IEEE, 2019.

[102] Cataldo, Robert L., and Gary L. Bennett. "US space radioisotope power systems and applications: past, present and future." *Radioisotopes-Applications in Physical Sciences* (2011).

[103] "CubeSat Toolbox." *Princeton Satellite Systems*, 12 May 2020, www.psatellite.com/products/sct/cubesat-toolbox/.

[104] Curtis, Howard D. Orbital Mechanics for Engineering Students. Elsevier, Butterworth-Heinemann, 2020.

[105] "LG Chem MJ1 3500mAh 10A Discharge 18650 Rechargeable Li-Ion Cell - Original - INR18650 MJ1." RareComponents.com, rarecomponents.com/store/LG-MJ1-INR18650.

[106] Kucinskis, Gints, Gunars Bajars, and Janis Kleperis. "Graphene in lithium ion battery cathode materials: A review." *Journal of Power Sources* 240 (2013): 66-79.

[107] "EPS - Power Module II Battery Pack." CubeSat by EnduroSat, www.endurosat.com/cubesat-store/cubesat-power-modules/eps-power-module-ii/.

[108] Lindholm, F. A. "IV Curve." PVEducation, www.pveducation.org/pvcdrom/solar-cell-operation/iv-curve.

[109] Wallace, Megan. "Radio Spectrum." NASA, NASA, 11 Apr. 2018, www.nasa.gov/directorates/heo/scan/spectrum/radio_spectrum/.

[110] RF Cafe, Kirt Blattenberger. "Radio Electromagnetic Spectrum Frequency Bands." RF Cafe, www.rfcafe.com/references/electrical/freq-bands.htm.

[111] Toorian, Armen, Ken Diaz, and Simon Lee. "The cubesat approach to space access." 2008 IEEE Aerospace Conference. IEEE, 2008.

[112] Shin, Dong K. 201 Frequency and Channel Assignments, JPL, 2014.

[113] Mitola, Joseph. "The software radio architecture." IEEE Communications magazine 33.5 (1995): 26-38.

[114] Cruz, Pedro, and Nuno Borges Carvalho. "Multi-Mode Receiver for Software Defined Radio." Pnd gongress of ortuguese gommittee of s,(Lisbon, Portugal) (2008).

[115] "Digital Slices." Digital Slices | Space Micro, www.spacemicro.com/products/digital-slices.html.

[116] Akos, Dennis M., et al. "Direct bandpass sampling of multiple distinct RF signals." IEEE Transactions on communications 47.7 (1999): 983-988.

[117] Sarraf, Steven, and Lisa Rulli. "Low cost, broadband tunable ferroelectric filters for jtrs cluster 5 applications." Ferroelectrics 342.1 (2006): 129-140.

[118] Klesh, Andrew T., et al. "Inspire: Interplanetary nanospacecraft pathfinder in relevant environment." AIAA SPACE 2013 Conference and Exposition. 2013.

[119] "Iris V2.1 CubeSat Deep Space Transponder." National Aeronautics and Space Administration Jet Propulsion Laborator, 2016, https://www.jpl.nasa.gov/cubesat/pdf/Brochure_IrisV2.1_201611-URS_Approved_CL16-5469.pdf.

[120] Sobtzak, John, et al. "A Deep Space Radio Communications Link for Cubesats: The CU-E^3 Communication Subsystem." (2017).

[121] "X Band Transceiver SDR for Small Satellites." IQ Spacecom, June 2019, https://www.iq-spacecom.com/images/downloads/XLink_Datasheet_06.2019.pdf.

[122] Imbriale, William A., Steven Shichang Gao, and Luigi Boccia. Space antenna handbook. John Wiley & Sons, 2012.

[123] Peral, Eva, et al. "The radar-in-a-Cubesat (RAINCUBE) and measurement results." IGARSS 2018-2018 IEEE International Geoscience and Remote Sensing Symposium. IEEE, 2018.

[124] Dunbar, Brian. “Tracking and Data Relay Satellite (TDRS).” NASA, NASA, 28 Apr. 2015, www.nasa.gov/directorates/heo/scan/services/networks/tdrs_main.

[125] Hodges, Richard E., et al. "ISARA-integrated solar array and reflectarray CubeSat deployable Ka-band antenna." 2015 IEEE International Symposium on Antennas and Propagation & USNC/URSI National Radio Science Meeting. IEEE, 2015.

[126] “MARCO.” JPL, NASA, www.jpl.nasa.gov/cubesat/missions/marco.php.

[127] Ochoa, Daniel, Kenny Hummer, and Mike Ciffone. "Deployable helical antenna for nano-satellites." (2014).

[128] Vourch, Clement J., and Timothy D. Drysdale. "V-band “bull's eye” antenna for cubesat applications." IEEE Antennas and Wireless Propagation Letters 13 (2014): 1092-1095.

[129] Nascetti, Augusto, et al. "High-gain S-band patch antenna system for earth-observation CubeSat satellites." IEEE antennas and wireless propagation letters 14 (2014): 434-437.

[130] Islam, Mohammad Tariqul, et al. "Compact antenna for small satellite applications [Antenna Applications Corner]." IEEE Antennas and Propagation magazine 57.2 (2015): 30-36.

[131] N. Ya'acob, J. Johari, M. Zolkapli, A. L. Yusof, S. S. Sarnin and N. F. Naim, "Link budget calculator system for satellite communication," 2017 International Conference on Electrical, Electronics and System Engineering

[132] O'Neill, Greg. "Quadrifilar Helical Antenna." 2016 International Workshop on Antenna Technology (iWAT). IEEE.

[133] “X-Band Patch Antenna - CubeSat Antenna.” CubeSat by EnduroSat, www.endurosat.com/cubesat-store/all-cubesat-modules/x-band-patch-antenna/. (ICEESE), Kanazawa, 2017, pp. 115-119, doi: 10.1109/ICEESE.2017.8298397.

[134] “Guidance On Obtaining Licenses For Small Satellites.” Federal Communications Commission, 15 Oct. 2018, www.fcc.gov/document/guidance-obtaining-licenses-small-satellites. DA-13-445.

[135] “Streamlining Licensing Procedures for Small Satellites.” Federal Communications Commission, 5 Mar. 2020, www.fcc.gov/document/streamlining-licensing-procedures-small-satellites-1. FCC-19-81.

[136] B. M. Folio and J. M. P. Armengol, “Radio frequency and optical inter satellite links comparison for future identified scenarios,” presented at CNES Workshop on Intersatellite Links, Toulouse (27–28 November 2003).

[137] Planche, Gilles, and Vincent Chorvalli. "SILEX in-orbit performances." International Conference on Space Optics—ICSO 2004. Vol. 10568. International Society for Optics and Photonics, 2018.

[138] Ingersoll, Joshua. "A Technical Evaluation of Integrating Optical Inter-Satellite Links into Proliferated Polar LEO Constellations." (2020).

[139] Shelton, Marta, et al. "SETH Technology Demonstration of Small Satellite Deep Space Optical Communications to aid Heliophysics Science and Space Weather Forecasting." Proceedings of the AIAA/USU Conference on Small Satellites], SSC19-P3-17. 2019.

[140] Cahoy, Kerri, et al. "The CubeSat Laser Infrared CrosslinK Mission (CLICK)." International Conference on Space Optics—ICSO 2018. Vol. 11180. International Society for Optics and Photonics, 2019.

[141] Holmes, Rebecca M., et al. "Status of ELROI satellite license plate demonstration on the CubeSat NMTSat." Advanced Photon Counting Techniques XIII. Vol. 10978. International Society for Optics and Photonics, 2019.

[142] JPL, NASA, deepspace.jpl.nasa.gov/.

[143] Dunbar, Brian. “Near Earth Network.” NASA, NASA, 24 Apr. 2015, www.nasa.gov/directorates/heo/scan/services/networks/nen.

[144] NASA, NASA, spacenetwork.gsfc.nasa.gov/.

[145] “Navigation.” Flight Dynamics Facility, NASA, fdf.gsfc.nasa.gov/services/navigation.

[146] "MONTE." Mission Analysis, Operations, and Navigation Toolkit Environment, NASA, montepy.jpl.nasa.gov/.

[147] Solomon, Joseph B. "Communications Program Services Document." NASA Communications Program, 3 Aug. 2020, nasasitebuilder.nasawestprime.com/cso/wp-content/uploads/sites/24/2020/08/CP-001-Rev5-CSD_approved-August-2020-by-CSB-1.pdf.

[148] Consultative Committee on Space Data Systems, CCSDS Secretariat. TM Synchronization and Channel Coding - Summary of Concept and Rationale, 130.1-G-3 ed., CCSDS, 2020.

[149] Cheung, Kar-Ming, Dariush Divsalar, and Scott Bryant. "Two-way ranging and Doppler for multiple orbiting spacecraft at Mars." 2018 IEEE Aerospace Conference. IEEE, 2018.

[150] Berner, Jeff B., Scott H. Bryant, and Peter W. Kinman. "Range measurement as practiced in the deep space network." Proceedings of the IEEE 95.11 (2007): 2202-2214.

[151] Ibrahim, Syahrim Azhan, and Eiki Yamaguchi. "Comparison of Solar Radiation Torque and Power Generation of Deployable Solar Panel Configurations on Nanosatellites." Aerospace 6.5 (2019): 50.

[152] Meyer, Rudolph X. Elements of Space Technology for Aerospace Engineers. Academic Press, 1999.

[153] Anderson, John D. Fundamentals of Aerodynamics. McGraw Hill Education, 2017.

[154] Bender, Erich. "An Analysis of Stabilizing 3U CubeSats Using Gravity Gradient Techniques and a Low Power Reaction Wheel." (2011).

[155] Paluszek, Michael, et al. Spacecraft Attitude and Orbit Control Volume 1: A Systems Approach, 3rd ed.; Princeton Satellite Systems: Plainsboro Township, NJ, USA, 2012.

[156] Springmann, John, James Cutler, and Hasan Bahcivan. "Magnetic sensor calibration and residual dipole characterization for application to nanosatellites." AIAA/AAS Astrodynamics Specialist Conference. 2010.

[157] Zell, Holly. "Earth's Magnetosphere." NASA, NASA, 2 Mar. 2015, www.nasa.gov/mission_pages/sunearth/multimedia/magnetosphere.html.

[158] Barth, Janet L. "Space and atmospheric environments: from low earth orbits to deep space." Protection of Materials and Structures from Space Environment. Springer, Dordrecht, 2004. 7-29.

[159] Gosling, J. "The solar wind, Encyclopedia of the Solar System." Academic, San Deigo (1999).

[160] Meyer, Brian. "Home." World Magnetic Model - Software Download, www.ngdc.noaa.gov/geomag/WMM/soft.shtml.

[161] Nair, Manoj. IAGA V-MOD Geomagnetic Field Modeling: International Geomagnetic Reference Field IGRF-13, www.ngdc.noaa.gov/IAGA/vmod/igrf.html.

[162] Banerjee, Subir K. "When the compass stopped reversing its poles." Science 291.5509 (2001): 1714-1715.

[163] McElhinny, M. W., and Phillip L. McFadden. The magnetic field of the earth: paleomagnetism, the core, and the deep mantle. Vol. 63. Academic Press, 1998.

[164] Sagnotti, Leonardo, et al. "Extremely rapid directional change during Matuyama-Brunhes geomagnetic polarity reversal." Geophysical Journal International 199.2 (2014): 1110-1124.

[165] Singer, Brad S., et al. "Synchronizing volcanic, sedimentary, and ice core records of Earth's last magnetic polarity reversal." Science advances 5.8 (2019): eaaw4621.

[166] Nöldeke Christoph M. The Space Radiation Environment. Monsenstein Und Vannerdat, 2015

[167] Mann, Ian Robert, et al. "Explaining the dynamics of the ultra-relativistic third Van Allen radiation belt." Nature Physics 12.10 (2016): 978-983.

[168] Zell, Holly. "Radiation Belts with Satellites." NASA, NASA, 23 Mar. 2015, www.nasa.gov/mission_pages/sunearth/news/gallery/20130228-radiationbelts.html.

[169] Ramram, Adam. "Programmatic Thermal Neutron Flux Calibration for Neutron Generators." (2020).

[170] Vasiliev, Boris V. "Effect of Reactor Neutrinos on Beta-Decay." Journal of Modern Physics 11.01 (2020): 91.

[171] Benz, Arnold O. "Flare observations." Living Reviews in Solar Physics 14.1 (2017): 2.

[172] Riley, Pete. "On the probability of occurrence of extreme space weather events." Space Weather 10.2 (2012): 1-12.

[173] Großekatthöfer, Karsten, and Zizung Yoon. "Introduction into quaternions for spacecraft attitude representation." TU Berlin 16 (2012).

[174] Montalvo, Carlos, and Bruce Wiegmann. "Electric sail space flight dynamics and controls." Acta Astronautica 148 (2018): 268-275.

[175] B. Etkins, Dynamics of Atmospheric Flight, Dover, Mineola, New York, 2000 pages 9-13,134-151,196–318.

[176] Filipe, Nuno, and Panagiotis Tsiotras. "Adaptive position and attitude-tracking controller for satellite proximity operations using dual quaternions." Journal of Guidance, Control, and Dynamics 38.4 (2015): 566-577.

[177] Lin, Arthur KL, and Regina Lee. "Attitude control for small spacecraft with sensor errors." AIAA SPACE 2015 Conference and Exposition. 2015.

[178] Allgeier, Shawn, Matt Mahin, and Norman Fitz-Coy. "Design and analysis of a coarse sun sensor for pico-satellites." AIAA Infotech@ Aerospace Conference and AIAA Unmanned. Unlimited Conference. 2009.

[179] “NanoSSOC: Space Equipment: Solar MEMS Solar Sensor.” Solar MEMS, 10 Sept. 2020, www.solar-mems.com/nanossoc/.

[180] McBryde, Christopher Ryan, and E. Glenn Lightsey. "A star tracker design for CubeSats." 2012 IEEE Aerospace Conference. IEEE, 2012.

[181] Padgett, Curtis, and Kenneth Kreutz-Delgado. "A grid algorithm for autonomous star identification." IEEE Transactions on Aerospace and Electronic Systems 33.1 (1997): 202-213.

[182] Cole, Craig L., and John L. Crassidis. "Fast star-pattern recognition using planar triangles." Journal of guidance, control, and dynamics 29.1 (2006): 64-71.

[183] Mortari, Daniele, et al. "The pyramid star identification technique." Navigation 51.3 (2004): 171-183.

[184] Kolomenkin, Michael, et al. "Geometric voting algorithm for star trackers." IEEE Transactions on Aerospace and Electronic Systems 44.2 (2008): 441-456.

[185] Mortari, Daniele. "Search-less algorithm for star pattern recognition." The Journal of the Astronautical Sciences 45.2 (1997): 179-194.

[186] “ST200.” Hyperion Technologies B.V., 3 Jan. 2020, hyperiontechnologies.nl/products/miniaturised-star-tracker/.

[187] Wessels, Jurie Hendrik. Infrared horizon sensor for CubeSat implementation. Diss. Stellenbosch: Stellenbosch University, 2018.

[188] Sorgenfrei, Matt, Matt Nehrenz, and Dayne Kemp. "Selection of an inertial measurement unit for high accuracy CubeSat attitude determination." 54th AIAA Aerospace Sciences Meeting. 2016.

[189] “STIM318.” Sensonor.no, www.sensonor.com/products/inertial-measurement-units/stim318/.

[190] Babcock, Erik. "CubeSat attitude determination via Kalman filtering of magnetometer and solar cell data." (2011).

[191] Izmodenov, Vladislav V., and Dmitry B. Alexashov. "Magnitude and direction of the local interstellar magnetic field inferred from Voyager 1 and 2 interstellar data and global heliospheric model." Astronomy & Astrophysics 633 (2020): L12.

[192] Peters, Eric David. Dynamic instabilities imparted by CubeSat deployable solar panels. Diss. Massachusetts Institute of Technology, 2014.

[193] Stiltner, Brandon C., et al. "Cold Gas Reaction Control System for the Near-Earth Asteroid Scout CubeSat." AIAA SPACE and Astronautics Forum and Exposition. 2017.

[194] TRIVAILO, Pavel M., and Hirohisa KOJIMA. "Discovering Method of Control of the" Dzhanibekov's Effect" and Proposing its Applications for the Possible Future Space Missions." TRANSACTIONS OF THE JAPAN SOCIETY FOR AERONAUTICAL AND SPACE SCIENCES, AEROSPACE TECHNOLOGY JAPAN 17.1 (2019): 72-81.

[195] Juchnikowski, G., T. Barcinski, and J. Lisowski. "Optimal control gain for satellite detumbling using B-dot algorithm." 2nd CEAS Specialist Conference on Guidance, Navigation and Control. 2013.

[196] S. P. Viswanathan and A. Sanyal, "Design of an Adaptive Singularity-free Control Moment Gyroscope (ASCMG) actuator for agile and precise attitude control of cubesat," 2016 Indian Control Conference (ICC), Hyderabad, 2016, pp. 284-291.

[197] “Space Station Control Moment Gyroscope Lessons Learned.” NASA, NASA, ntrs.nasa.gov/search.jsp?R=20100021932.

[198] Hurley, Samantha, Denis Zolotukhin, and Michael Keidar. "Advancing the microcathode arc thruster: effect of the ablative anode." Journal of Propulsion and Power 35.5 (2019): 917-921.

[199] Few, Alex, et al. "Testing and maturing a mass translating mechanism for a deep space CubeSat." (2018).

[200] “SPICE Toolkit.” NASA, NASA, naif.jpl.nasa.gov/naif/toolkit.html.

SECTION 4: RADIATION EFFECTS, SHIELDING, AND REDUNDANCY

[201] Heidergott, W. F. "System Level Single Event Upset Mitigation Strategies." International journal of high speed electronics and systems 14.02 (2004): 341-352.

[202] Nowlin, Nathan, et al. "A total-dose hardening-by-design approach for high-speed mixed-signal CMOS integrated circuits." International journal of high speed electronics and systems 14.02 (2004): 367-378.

[203] Fouillat, P., et al. "Investigation of single-event transients in fast integrated circuits with a pulsed laser." International journal of high speed electronics and systems 14.02 (2004): 327-339.

[204] McMORROW, Dale, Joseph S. Melinger, and Alvin R. Knudson. "Single-event effects in III-V semiconductor electronics." Radiation Effects And Soft Errors In Integrated Circuits And Electronic Devices. 2004. 27-41.

[205] Dale, C. J., et al. "Displacement damage equivalent to dose in silicon devices." Applied physics letters 54.5 (1989): 451-453.

[206] Messenger, S. R., et al. "Nonionizing energy loss (NIEL) for heavy ions." IEEE Transactions on Nuclear Science 46.6 (1999): 1595-1602.

[207] Simpson, J. A. (1983), Elemental and isotopic composition of the galactic cosmic rays, Annu. Rev. Nucl. Part. Sci., 33, 323–382, doi:10.1146/ annurev.ns.33.120183.001543

[208] Hörandel, J. R. (2008), The origin of galactic cosmic rays, Nucl. Instrum. Methods Phys. Res., Sect. A, 588, 181–188, doi:10.1016/j.nima.2008. 01.036.

[209] Mrigakshi, Alankrita Isha, et al. "Assessment of galactic cosmic ray models." Journal of Geophysical Research: Space Physics 117.A8 (2012).

[210] Heber, B. (2001), Modulation of galactic and anomalous cosmic rays in the inner heliosphere, Adv. Space Res., 27, 451–460, doi:10.1016/S02731177(01)00083-7.

[211] Kitiashvili, Irina N., Bay Area Environmental Research Institute, and. Solar Activity Forecast for the Next Decade

[212] Feldman W.C., Ashbridge J.R., Bame S.J., and Gosling J.T. (1977) Plasma and magnetic fields from the Sun. In The Solar Output and its Variation (O.R. White, ed.), 351-382. Colorado Assoc. Univ. Boulder.

[213] Bame S.J., Feldman W.C., Gosling J.T., Young D.T., and Zwickl R.D. (1983) What magnetospheric workers should know about solar wind composition. In Energetic Ion Composition in the Earth's Magnetosphere (R.G. Johnson, ed.), 73-98, Terra, Tokyo.

[214] McGuire R.E., von Rosenvinge T.T., and McDonald F.B. (1986) The composition of solar energetic particles. Astrophys. J. 301, 938-961.

[215] Jiggens, Piers, et al. "Updated model of the solar energetic proton environment in space." Journal of Space Weather and Space Climate 8 (2018): A31.

[216] Cumani, P., et al. "Background for a gamma-ray satellite on a low-Earth orbit." Experimental Astronomy 47.3 (2019): 273-302.

[217] Holman, W. T. "Radiation-tolerant design for high performance mixed-signal circuits." International journal of high speed electronics and systems 14.02 (2004): 353-366.

[218] Baumann, Robert C. "Soft errors in commercial integrated circuits." International Journal of High Speed Electronics and Systems 14.02 (2004): 299-309.

[219] Somani, Arun K., and Nitin H. Vaidya. "Understanding fault tolerance and reliability." Computer 4 (1997): 45-50.

[220] “GEOTAIL Magnetosphere Tail Observation Satellite: Spacecraft.” ISAS,

[221] Cook, Thomas, et al. “Radiation-Tolerant, GaN-based Point of Load Converters for Small Spacecraft Missions .” 2018, Small Satellite Conference. digitalcommons.usu.edu/cgi/viewcontent.cgi?article=4138&context=smallsat.

[222] Mahmud, Sadab, et al. "A GaN-Based Four-Switch Buck-Boost Converter Using Ripple Correlation Control for Maximum Power Point Tracking in Dynamic Deep Space Environments." (2020).

[223] Barchowsky, Ansel, et al. "GaN-Based, Ultra-Compact Power Conversion System for the PUFFER Autonomous Mobility Platform." (2020).

[224] Cook, Thomas, et al. "Soft-Switching GaN-Based Isolated Power Conversion System for Small Satellites with Wide Input Voltage Range." (2020).

[225] McMorrow, Dale, et al. "Charge-collection characteristics of GaAs MESFETs fabricated with a low-temperature grown GaAs buffer layer: Computer simulation." IEEE Transactions on Nuclear Science 43.6 (1996): 2904-2912.

[226] NASA, JSPC, and William A Geisel. Tutorial on Reed-Solomon Error Correction Coding, 1990.

[227] Allen, Gregory, et al. "Single event test methodologies and system error rate analysis for triple modular redundant field programmable gate arrays." IEEE Transactions on Nuclear Science 58.3 (2011): 1040-1046.

[228] Fuchs, Christian M., et al. "Fault-tolerant nanosatellite computing on a budget." arXiv preprint arXiv:1903.08781 (2019).

[229] Doglio, Fernando. “Fault Tolerance Is Not High Availability.” DZone: Performance Zone, Devada Media, 3 June 2018, dzone.com/articles/fault-tolerance-is-not-high-availability.

[230] Xie, Zaipeng, Hongyu Sun, and Kewal Saluja. "A survey of software fault tolerance techniques." University of Wisconsin-Madison, Department of Electrical and Computer Engineering (2006).

[231] Abaei, Golnoush, and Ali Selamat. "A survey on software fault detection based on different prediction approaches." Vietnam Journal of Computer Science 1.2 (2014): 79-95.

[232] Chen, Liming, and Algirdas Avizienis. "N-version programming: A fault-tolerance approach to reliability of software operation." Proc. 8th IEEE Int. Symp. on Fault-Tolerant Computing (FTCS-8). Vol. 1. 1978.

[233] Avizienis, Algirdas. "The methodology of n-version programming." Software fault tolerance 3 (1995): 23-46.

[234] Patel, Pankaj. “Difference between N-Version Programming and Recovery Blocks Techniques.” GeeksforGeeks, 4 May 2020, www.geeksforgeeks.org/difference-between-n-version-programming-and-recovery-blocks-techniques/.

[235] Knight, John C., and Nancy G. Leveson. "An experimental evaluation of the assumption of independence in multiversion programming." IEEE Transactions on software engineering 1 (1986): 96-109.

[236] Knight, John C., and Nancy G. Leveson. "A reply to the criticisms of the Knight & Leveson experiment." ACM SIGSOFT Software Engineering Notes 15.1 (1990): 24-35.

[237] Yau, Stephen S., and Ray C. Cheung. "Design of self-checking software." ACM SIGPLAN Notices 10.6 (1975): 450-455.

[238] Kepko, Larry, et al. "Dellingr: Reliability Lessons Learned from On-Orbit." (2018).

[239] E. W. Enlow, R. L. Pease, W. Combs, R. D. Schrimpf and R. N. Nowlin, "Response of advanced bipolar processes to ionizing radiation," in IEEE Transactions on Nuclear Science, vol. 38, no. 6, pp. 1342-1351, Dec. 1991, doi: 10.1109/23.124115.

[240] Pershenkov, Vyacheslav, et al. "Enhanced low dose rate sensitivity (ELDRS) and reduced low dose rate sensitivity (RLDRS) in bipolar devices." Facta Universitatis, Series: Electronics and Energetics 33.2 (2020): 303-316.

[241] Normand, Eugene. "Single event effects in avionics and on the ground." Radiation Effects And Soft Errors In Integrated Circuits And Electronic Devices. 2004. 1-14.

[242] Filges, Detlef, and Frank Goldenbaum. Handbook of Spallation Research Theory, Experiments and Applications. Wiley-VCH-Verl., 2009.

[243] Badhwar, Gautam D., et al. "Measurements of the secondary particle energy spectra in the space shuttle." Radiation measurements 24.2 (1995): 129-138.

[244] Jun, Insoo. "Effects of secondary particles on the total dose and the displacement damage in space proton environments." IEEE Transactions on Nuclear science 48.1 (2001): 162-175.

[245] Cuevas, Antonio Contreras, et al. Metal Matrix Composites: Wetting and Infiltration. Springer, 2018.

[246] Friel, Ross J., and Russell A. Harris. "Ultrasonic additive manufacturing–a hybrid production process for novel functional products." Procedia CIRP 6 (2013): 35-40.

[247] Hsu, Chia-Hsun, et al. "Enhanced Si Passivation and PERC Solar Cell Efficiency by Atomic Layer Deposited Aluminum Oxide with Two-step Post Annealing." Nanoscale Research Letters 14.1 (2019): 1-10.

[248] United States, Congress, Cucinotta, Francis A, et al. Evaluating Shielding Approaches to Reduce Space Radiation Cancer Risks, 2012. TM-2012-217361.

[249] Thomsen, Donald, Wousik Kim, and James Cutler. "Shields-1, A SmallSat radiation shielding technology demonstration." (2015).

[250] Wrobel, Jonathan, et al. "Versatile Structural Radiation Shielding and Thermal Insulation through Additive Manufacturing." (2013).

[251] Fan, Wesley C., et al. "Shielding considerations for satellite microelectronics." IEEE Transactions on nuclear science 43.6 (1996): 2790-2796.

[252] Thibeault, Sheila A., et al. "Nanomaterials for radiation shielding." Mrs Bulletin 40.10 (2015): 836-841.

[253] Chadsey, W. L., et al. "Radiation-induced signals in cables." IEEE Transactions on Nuclear Science 23.6 (1976): 1933-1941.

[254] “Space Environment, Effects, and Education System.” SPENVIS, www.spenvis.oma.be/.

[255] “Our Radiation Software.” TRAD, www.trad.fr/en/space/omere-software/.

[256] Mazur, J. E., et al. "New measurements of total ionizing dose in the lunar environment." Space Weather 9.7 (2011).

[257] Help: Solar Proton Models, www.spenvis.oma.be/help/background/flare/flare.html.

[258] “AE9/AP9/SPM: Radiation Belt and Space Plasma Specification Models Air Force Research Laboratory (AFRL).” AE9/AP9/SPM Factsheet, www.vdl.afrl.af.mil/programs/ae9ap9/factsheet.php.

[259] Johnston, W. Robert, et al. "AE9/AP9/SPM: New models for radiation belt and space plasma specification." Sensors and Systems for Space Applications VII. Vol. 9085. International Society for Optics and Photonics, 2014.

[260] Overview, geant4.web.cern.ch/.

[261] ShielDose2 Model - Space Monitoring Data Center, smdc.sinp.msu.ru/index.py?nav=model-shieldose2.

[262] Lei, F., et al. "MULASSIS: A Geant4-based multilayered shielding simulation tool." IEEE Transactions on Nuclear Science 49.6 (2002): 2788-2793.

[263] “INTERACTIONS OF IONS WITH MATTER.” James Ziegler - SRIM & TRIM, srim.org/.

[264] Jun, Insoo, et al. "Proton nonionizing energy loss (NIEL) for device applications." IEEE Transactions on Nuclear Science 50.6 (2003): 1924-1928.

[265] Jun, Insoo, Wousik Kim, and Robin Evans. "Electron nonionizing energy loss for device applications." IEEE Transactions on nuclear science 56.6 (2009): 3229-3235.

[266] Jun, Insoo, Michael A. Xapsos, and Edward A. Burke. "Alpha particle nonionizing energy loss (NIEL)." IEEE transactions on nuclear science 51.6 (2004): 3207-3210.

[267] Messenger, S. R., et al. "Nonionizing energy loss (NIEL) for heavy ions." IEEE Transactions on Nuclear Science 46.6 (1999): 1595-1602.

[268] “Home.” Screened Relativistic Nuclear Stopping Power Calculator, www.sr-niel.org/.

[269] MUSCAT Space Engineering Co., Ltd., astro-muse.com/contents_en_products.html.

[270] “Software Details.” NASA, NASA, software.nasa.gov/software/MFS-32056-1.

[271] “Software Details.” NASA, NASA, software.nasa.gov/software/MFS-31675-1.

[272] “About SPIS.” SPIS, www.spis-services.eu/software/about-spis/.

APPENDIX B

[273] Dunbar, Brian. “NASA's SAMPEX Mission: A Space Weather Warrior.” NASA, NASA, www.nasa.gov/mission_pages/sunearth/news/sampex-deorbit.html.

[274] “Solar and Heliospheric Observatory Homepage.” NASA, NASA, sohowww.nascom.nasa.gov/

[275] “WIND Spacecraft.” NASA, NASA, wind.nasa.gov/.

[276] Cluster - EoPortal Directory - Satellite Missions, earth.esa.int/web/eoportal/satellite-missions/c-missions/cluster.

[277] Zell, Holly. “SDO Spacecraft & Instruments.” NASA, NASA, 2 Apr. 2015, www.nasa.gov/mission_pages/sdo/spacecraft/index.html.

[278] Zell, Holly. “STEREO Spacecraft & Instruments.” NASA, NASA, 14 Apr. 2015, www.nasa.gov/mission_pages/stereo/spacecraft/index.html.

[279] Parker Solar Probe, parkersolarprobe.jhuapl.edu/.

[280] Jones, Drew Ryan, et al. "Orbit Determination Covariance Analyses for the Parker Solar Probe Mission." (2017).

[281] Alibay, Farah, et al. “Sun Radio Interferometer Space Experiment (SunRISE) Proposal: Status Update.” Utah State University, digitalcommons.usu.edu/cgi/viewcontent.cgi?article=3662&context=smallsat.

[282] “Lunar Reconnaissance Orbiter.” NASA, NASA, lunar.gsfc.nasa.gov/about.html.

[283] “Welcome to the Planetary Data System.” NASA, NASA, pds.nasa.gov/.

[284] Dunbar, Brian. “LCROSS.” NASA, NASA, www.nasa.gov/mission_pages/LCROSS/main/index.html.

[285] Jenner, Lynn. “GOES - Geostationary Operational Environmental Satellite Network.” NASA, NASA, 18 Feb. 2015, www.nasa.gov/content/goes.

[286] “ACE In Depth.” NASA, NASA, solarsystem.nasa.gov/missions/ace/in-depth/.

www.isas.jaxa.jp/en/missions/spacecraft/current/geotail.html.

[287] “Mars Reconnaissance Orbiter.” NASA, NASA, www.jpl.nasa.gov/missions/mars-reconnaissance-orbiter-mro/.

[288] “Mars As Art.” NASA, NASA, 14 Sept. 2017, mars.nasa.gov/multimedia/images/?page=0&per_page=25&order=pub_date desc&search=&condition_1=1:is_in_resource_list&category=51:189.

NOMENCLATURE

A	Area of a surface
A_1	Area of first considered face, solar flux direction
A_2	Area of second considered face, Earth flux direction
A_3	Area of third considered face, lunar flux direction
A_{array}	Area of the cells on a solar array
A_{cell}	Area of a solar cell
$A_{cell,req}$	Required total solar cell area
A_e	Thruster nozzle exit area
A_r	Radioactive activity
A_{req}	Required radiator area
A_{shield}	Area of a radiation shield
A_{total}	Total CubeSat surface area
a	Spacecraft acceleration
aF	Albedo factor
aF_{lunar}	Lunar albedo factor
B	Magnetic field strength
b_{array}	Solar array width
$C_{1,j}$	Constant for Thermal Math Model
$C_{2,j}$	Coefficient for Thermal Math Model
$C_{battery}$	Battery energy storage capacity
c	Thruster effective exhaust velocity
c_0	Speed of light in a vacuum
c_{mod}	Modified thruster effective exhaust velocity
c_p	Specific heat of the entire CubeSat
$c_{p,rad}$	Specific heat of the radiator material
$c_{p,array}$	Specific heat of composite solar array
D	Dose
D_{Orbit}	Orbit altitude
D_{Sun}	Mean distance from the Earth to the center of the Sun
$DDC_{PST,TID}$	Dosage Depth Curve for a given particle, shielding geometry, and target material

DDD	Displacement Damage Dose
d_{array}	Distance from solar array mass centroid to satellite mass centroid
d_b	Reed-Solomon odd symbol distance
d_c	Solar array distance from CubeSat center of mass
$d_{c,h}$	Solar array distance from CubeSat center of mass in the y-direction
$d_{c,l}$	Solar array distance from CubeSat center of mass in the z-direction
$d_{c,w}$	Solar array distance from CubeSat center of mass in the x-direction
d_η	Distance from the neutral axis of the solar panel layer to the seam between the η and η +1 layers
E	Energy
E_b	Number of Reed-Solomon errors that can be corrected
E_e	Electric field strength
$\dot{E}_{gen}$	Generated energy rate
$\dot{E}_{in}$	Incoming energy rate
E_{ion}	Ion energy
E_{max}	Maximum particle energy
E_{min}	Minimum particle energy
$\dot{E}_{out}$	Outgoing energy rate
$E_{particle}$	Particle energy
EI_{array}	Solar array equivalent stiffness
E_η	Modulus of elasticity of the ηth solar panel layer
$E_{\lambda b}$	Spectral emissive power of a hemispherical blackbody
e^-	Electron representation
F	Fluence
F_d	Differential fluence
$F_{d,p}$	Omnidirectional differential fluence per particle type
F_p	Propulsion optimization minimizing function
F_{rad}	Radiative View Factor
FOS	Factor of Safety
f_{Ecl}	Circular orbit eclipse fraction
$f_{min,lv}$	Minimum natural frequency of the launch vehicle
f_n	Deployed solar array natural frequency
$f_{n,stowed}$	Stowed solar array natural frequency

f_T	Carrier uplink frequency
GF_S	Geometry factor for a given radiation shielding DDC
g_0	Gravitational constant
H	Distance to the center of a sphere
h	Thickness of material surface coating layer, ms
h_{cs}	CubeSat height dimension
h_p	Planck’s constant
I	Total mass moment of inertia with parallel axis theorem included
I_b	Ion beam current
I_{cm}	Body mass moment of inertia
$I_{cm,h}$	Body mass moment of inertia about the y-axis
$I_{cm,l}$	Body mass moment of inertia about the z-axis
$I_{cm,w}$	Body mass moment of inertia about the x-axis
I_h	Total mass moment of inertia about the y-axis
I_l	Total mass moment of inertia about the z-axis
I_{max}	Maximum current provided to MPPT from array
$I_{max,MPPT}$	Maximum MPPT specification input current
$I_{MP,cell}$	Solar cell maximum power areal current density
$I_{SC,cell}$	Solar cell short circuit areal current density
I_{sp}	Specific impulse
$I_{sp,opt}$	Optimum specific impulse
I_w	Total mass moment of inertia about the x-axis
i	Orbit inclination
J	Center of rotation mass moment of inertia
J_{array}	Solar array mass moment of inertia
J_{bit}	Reed-Solomon symbol size
J_n	Bessel function, n = 0, 1, 2 …
j	Time index
K	Conversion factor between MeV and rad·g
k	Mass attenuation parameter
k_B	Boltzmann’s constant
k_b	Reed-Solomon number of information symbols

k_{Cond}	Thermal conductivity
$k_{Cond,array}$	Thermal conductivity of composite solar array
k_E	Thermal conductivity of East direction node
k_{hinge}	Torsional hinge spring constant
k_N	Thermal conductivity of North direction node
k_S	Thermal conductivity of South direction node
k_W	Thermal conductivity of West direction node
L_{array}	Solar array length
LET	Linear energy transfer
LET_{PST}	LET in a target at energy E after penetrating the shielding to depth
L_{max}	Maximum angular momentum required to reduce a rotation rate to zero
l_{cs}	CubeSat length dimension
$M_{battery}$	Battery capacity margin
$M_{consumption}$	Power consumption margin
M_{dist}	Power distribution margin
m	Total wavelength-dependent complex refractive index, base layer notation
$\dot{m}$	Thruster exhaust mass flow rate
m_0	Initial CubeSat mass
$m_{A,shield}$	Atomic mass of a radiation shield material
m_{array}	Solar array mass
$m_{array,h}$	Solar array mass in the y-direction
$m_{array,l}$	Solar array mass in the z-direction
$m_{array,w}$	Solar array mass in the x-direction
m_{cs}	Total CubeSat mass
m_e	Mass of the CubeSat electrical system
m_f	Final CubeSat mass
m_{ion}	Ion mass
m_p	Propellant mass
$m_{p_{first}}$	Propellant mass at first considered payload ratio
$m_{p_{last}}$	Propellant mass at last considered payload ratio
m_t	Ionization target mass
ms	Total wavelength-dependent complex refractive index, surface layer notation

m_{shield}	Mass of a radiation shield
N	Number, could refer to number of particles, number of events, etc.
$N_{cells,parallel,max}$	Maximum number of cells linked in parallel
$N_{cells,series,max}$	Maximum number of cells linked in series
$N_{cells,series,min}$	Minimum number of cells linked in series
$N_{cell,total}$	Total number of solar cells
$NIEL$	Non-Ionizing Energy Loss, non-trivial calculation
n	Refractive index of a medium
n_b	Reed-Solomon block length
n_p	Free neutron representation
P	Radiative power
P_{burn}	Burn power generation requirement
P_{max}	Maximum power provided to MPPT from array
P_{min}	Minimum total power generation requirement
p	Angular velocity component about the body x-direction
p_a	Ambient pressure
p_c	Ranging signal
p_e	Pressure at the thruster exit from inside the nozzle
p_p	Proton representation
p_{ref}	Reference pressure, usually 20 μPa
p_{rms}	Root mean square value of LV acoustic pressure
Q''_{Albedo}	Flux radiating from the Earth due to the Earth's albedo at satellite distance
Q_{array}	Power generated by a solar array
$Q_{array,AOI}$	Power generated by solar array with AOI accounted for
Q_{Comp}	Heat from operational internal generation
$Q_{component}$	Power from an individual component
$Q_{Cond,East}$	Heat conducted from the West direction
$Q_{Cond,North}$	Heat conducted from the North direction
$Q_{Cond,South}$	Heat conducted from the South direction
$Q_{Cond,Thruster}$	Heat conducted from the thruster
$Q_{Cond,West}$	Heat conducted from the West direction
$Q_{consumption}$	Power consumed by satellite components for a given software state

Q_{dist}	Power distributed by the EPS
$Q_{dist,max}$	Maximum power distributed by the EPS
$Q_{dist,min}$	Minimum power distributed by the EPS
$Q_{E,Alb}$	Heat from the Earth’s albedo
$Q''_{E,Alb}$	Heat flux from the Earth’s albedo
$Q_{E,Ems}$	Heat from the Earth’s emission
$Q''_{E,Ems}$	Heat flux from the Earth’s emission
$Q''_{Emission}$	Flux radiating from the Earth as IR at satellite distance
$Q_{L,Alb}$	Heat from lunar albedo
$Q_{L,Ems}$	Heat from lunar emission
$Q''_{L,Moon}$	Heat flux from lunar emission
Q_{Load}	Heat load applied to radiator
Q_{PH}	Heat from intentional internal generation
Q_{Rad}	Heat radiating from the CubeSat
Q_{Solar}	Heat radiating from the Sun at target distance
Q''_{Solar}	Heat flux radiating from the Sun at target distance
$Q''_{Solar,Surf}$	Heat flux radiating from the surface of the Sun
$Q''_{Thruster}$	Heat flux conducting from the thruster
$Q_{Transient}$	Transient heat
q	Angular velocity component about the body y-direction
q_a	Reed-Solomon alphabet length
q_i	Quaternion elements
$\dot{q}_i$	Quaternion rates of change
q_{ion}	Ion charge
q_s	Quaternion scalar component
q_x	Quaternion vector component in the body x-direction
$\dot{q}_x$	Quaternion rate of change vector component in the body x-direction
q_y	Quaternion vector component in the body y-direction
$\dot{q}_y$	Quaternion rate of change vector component in the body y-direction
q_z	Quaternion vector component in the body z-direction
$\dot{q}_z$	Quaternion rate of change vector component in the body z-direction
R	Radius of a sphere

R_c	Signal chip rate
R_{Earth}	Radius of the Earth
R_{par}	Directional complex reflectance of parallel angle
R_{per}	Directional complex reflectance of perpendicular angle
R_{Sun}	Radius of the Sun
r	Angular velocity component about the body z-direction
r_c	Charge radius
r_p	Particle range
S	Radiative intensity
S_T	Transmitted uplink signal
s	Quaternion scalar component
T	Temperature
T_{Earth}	Temperature of the Earth
$T_{E,j}$	Temperature of the East direction node at time j
T_j	Isothermal temperature of the CubeSat at time j
T_{mean}	Mean temperature of the radiator
$T_{N,j}$	Temperature of the North direction node at time j
T_{sc}	Thrust
$T_{S,j}$	Temperature of the South direction node at time j
T_{surr}	Radiative surrounding temperature of space
$T_{W,j}$	Temperature of the West direction node at time j
t	Time
t_e	Exposure time
$t_{eclipse}$	Time spent in eclipse, arbitrary time scale
t_{orbit}	Orbital period, arbitrary time scale
V_e	Thruster exhaust velocity
V_{max}	Maximum voltage provided to MPPT from array
$V_{max,MPPT}$	Maximum MPPT specification input voltage
$V_{min,cell}$	Minimum voltage for a solar cell to generate a current
$V_{min,MPPT}$	Minimum MPPT input voltage
$V_{MP,cell}$	Solar cell maximum power voltage
$V_{OC,cell}$	Solar cell open circuit voltage

$\vec{v}$	Quaternion vector component
$\bar{\nu}_e$	Electron anti-neutrino representation
v_x	Quaternion vector component in the body x-direction
v_y	Quaternion vector component in the body y-direction
v_z	Quaternion vector component in the body z-direction
W_e	Power provided to accelerator
w_{cs}	CubeSat width dimension
x	Distance, usually wall thickness
x_p	Geometric range
Z	Atomic number
z	Distance, usually shielding depth
z_p	Depth of the target normalized to r_p
α	Absorptivity
α'	Specific accelerator power
α_1	Absorptivity of first considered face, solar flux direction
α_2	Absorptivity of second considered face, Earth flux direction
α_3	Absorptivity of third considered face, lunar flux direction
α_{AZ-93}	Absorptivity of thermal coating AZ-93
α_{cell}	Absorptivity of a solar cell
α_{div}	Electric propulsion plume divergence angle
$\alpha_{front,array}$	Absorptivity of solar array front, equal to photovoltaic cell absorptiivty
α_p	Electric propulsion optimization parameter
α_U	Doppler effect coefficient
β	Solar view angle
β^*	The angle β when eclipses will begin for a circular orbit
β_b	Signal bandwidth function
β_p	Electric propulsion optimization parameter
ΔV	Change in spacecraft velocity
ΔX	Discretized X-direction distance
ΔY	Discretized Y-direction distance
ΔZ	Discretized Z-direction distance
Δt_j	Time step between times j and j-1

δ_s	Declination of the Sun
ε_0	Permittivity of a vacuum
ε_{AZ-93}	Emissivity of thermal coating AZ-93
ε_b	Emissivity of a blackbody
$\varepsilon_{back,AZ-93}$	Emissivity of solar array A back, equal to AZ-93 emissivity
$\varepsilon_{front,array}$	Emissivity of solar array front, equal to photovoltaic cell emissivity
ε_{lunar}	Lunar emissivity
η	Solar array layer index
η_{cell}	Solar cell efficiency
$\eta_{diode+line}$	EPS diode and line loss efficiency
η_{EPS}	EPS component efficiency
η_α	Accelerator efficiency
θ	Solar Angle of Incidence
θ_{array}	Solar array mounting angle
θ_{mod}	Ranging modulation index
λ	Wavelength of a light wave
λ_1	Vibrational parameter, consult [50]
λ_g	Geometric efficiency factor
μ	Modified propellant mass parameter
υ	Propellant volume constraint
ρ	Reflectivity
ρ_{array}	Density of the composite solar array
ρ_e	Scalar charge density
ρ_m	Material density
ρ_p	Propellant density
ρ_{rad}	Density of the radiator material
ρ_{shield}	Density of a radiation shield material
ρ_η	Density of the η^{th} solar panel layer
σ	Stefan-Boltzmann constant
σ_c	Radiation cross-section
τ	Thruster burn duration
Φ	Particle flux

Φ_d	Differential particle flux
Φ_s	Sectoral flux
Φ_γ	Gamma-ray flux
$\varphi_{degredation}$	Battery degradation factor
φ_{temp}	Solar cell temperature dependence coefficient
Ω	Right Ascension of the Ascending Node (RAAN)
Ω_a	Solid angle
Ω_s	RAAN of the Sun
ω	Maximum expected rotation rate of the CubeSat, no specific axis

ACRONYMS

AA&M	Alabama Agriculture & Mechanical
AB	Auxiliary Board
ABEX	Alabama Burst Energetics eXplorer
ACE	Advanced Composition Explorer
ADCS	Attitude Determination and Control Subsystem, sometimes ADACS
AEGIS	Alabama Experiment on Galactic-ray In-situ Shielding
AEHF	Advanced Extremely High Frequency
AFOSR	Air Force Office of Scientific Research
AFRL	Air Force Research Laboratory
AIAA	American Institute of Aeronautics and Astronautics
AIDA	Asteroid Impact and Deflection Assessment
AMT	Active Mass Translator
AOI	Angle of Incidence
AOP	Application-Oriented Programming
ASGC	Alabama Space Grant Consortium
AU	Auburn University
BCH	Bose, Chaudhuri, and Hocquenghem
BER	Bit Error Rate
BOL	Beginning of Life
BON2010	Badhwar-O’Niell 2010
BPSK	Binary Phase Shift Keying
CAD	Computer-Aided Design
CCD	Charge Coupled Device
C&DH	Command & Data Handling
CDM	Charged-Device Model
CDR	Critical Design Review
CE	Chief Engineer
CFR	Code of Federal Regulations
CIC	Coverglass-Interconnected Cell
CLB	Configurable Logic Block
CLICK	CubeSat Laser Infrared CrosslinK

CMB	Cosmic Microwave Background
CME	Coronal Mass Ejection
CMG	Control Moment Gyroscope
CMOS	Complementary Metal Oxide Semiconductor
ConOps	Concept of Operations
CRaTER	Cosmic Ray Telescope for the Effects of Radiation
CRISM	Compact Reconnaissance Imaging Spectrometer for Mars
CTX	Context Camera
DART	Double Asteroid Redirection Test
DCE	Drive Control Electronics
DCM	Directional Cosine Matrix
DDC	Dosage Depth Curve
DDD	Displacement Damage Dose
DLRE	Diviner Lunar Radiometer Experiment
DO	Design Objective
DoD	Depth of Discharge
DSN	Deep Space Network
DSP	Digital Signal Processing
ECC	Error Correcting Code
ECI	Earth-Centered Inertial
EDAC	Error Correction And Detection
EHF	Extremely High Frequency
EIRP	Equivalent Isotropic Radiated Power
ELDRS	Enhanced Low Dose Radiation Sensitivity
ELF	Extremely Low Frequency
EMC	Electromagnetic Compatibility
EMI	Electromagnetic Interference
ENEPIG	Electroless Nickel Electroless Palladium Immersion Gold
ENIG	Electroless Nickel Immersion Gold
EOL	End of Life
EOR	Early Operations Review
EP	Electric Propulsion
EPS	Electrical Power System

ESA	European Space Agency
ESD	Electrostatic Discharge
FEA	Finite Element Analysis
FCC	Federal Communications Commission
FDF	Flight Dynamics Facility
FIT	Failure-In-Time
FMEA	Failure Modes and Effects Analysis
FOS	Factor of Safety
FOV	Field of View
FPGA	Field-Programmable Gate Array
FRR	Flight Readiness Review
FSR	Flight Selection Review
FSW	Flight Software
GCR	Galactic Cosmic Rays
GCS	Ground Control Station
GEO	Geosynchronous Equatorial Orbit
GG	Gravity Gradient
GGS	Global Geospace Science
GN&C	Guidance, Navigation, & Control
GOES	Geostationary Operational Environment Satellite
GSFC	Goddard Space Flight Center
GTO	Geostationary Transfer Orbit
GWU	George Washington University
HBM	Human Body Model
HBT	Heterojunction Bipolar Transistors
HEMT	High Electron Mobility Transistors
HEO	High Earth Orbit, sometimes Highly Elliptical Orbit but not here
HF	High Frequency
HiRISE	High Resolution Imaging Science Experiment
HRM	Hold and Release Mechanism
ICD	Interface Control Document
ICPS	Interim Cryogenic Propulsion Stage
ICR	Initial Confirmation Review

IGRF	International Geomagnetic Reference Field
IMP	Integrated Master Plan
IONet	Internet protocol Operations Network
IR	Infrared Radiation
IRENE	International Radiation Environment Near Earth
ISARA	Integrated Solar Array and Reflectarray Antenna
ISTP	International Solar Terrestrial Physics
ITU	International Telecommunication Union
IV&T	Integration, Verification, and Testing
JAXA	Japan Aerospace Exploration Agency
JPL	Jet Propulsion Laboratory
KPP	Key Performance Parameter
LAMP	Lyman Alpha Mapping Project
LCROSS	Lunar Crater Observation and Sensing Satellite
LEND	Lunar Exploration Neutron Detector
LEO	Low Earth Orbit
LET	Linear Energy Transfer
LF	Low Frequency
LOLA	Lunar Orbiter Laser Altimeter
LRO	Lunar Reconnaissance Orbiter
LROC	Lunar Reconnaissance Orbiter Camera
LSE	Lead Systems Engineer
LUT	Look-Up Table
LV	Launch Vehicle
LWS	Living With a Star
MARCI	Mars Color Imager
MarCO	Mars Cube One
MCO	Mars Climate Orbiter
MCR	Mission Concept Review
MCS	Mars Climate Sounder
MDR	Mission Definition Review
MF	Medium Frequency
MFR	Merit and Feasibility Review

MI	Mission Integrator
MIT	Massachusetts Institute of Technology
MM	Machine Model
MMU	Memory Management Unit
MONTE	Mission analysis, Operations, Navigations, and Navigation Toolkit Environment
MP	Maximum Power
MPPT	Maximum Power Point Tracker
MQW	Multi-Quantum Well
MRAM	Magnetoresistive Random Access Memory
MRM	Microwave Radiometer
MRO	Mars Reconnaissance Orbiter
MRR	Mission Readiness Review
MSFC	Marshall Space Flight Center
MTBF	Mean Time Between Failures, sometimes Mean Time To Failure
MUSCAT	Multi Utility Spacecraft Charging Analysis Tool
MV&S	Majority Vote & Scrub
NAIF	Navigation and Ancillary Information Facility
NASA	National Aeronautics and Space Administration
NASCOM	NASA Communications System
NATO	North Atlantic Treaty Organization
NDA	Non-Disclosure Agreement
NEAScout	Near-Earth Asteroid Scout
NEKF	Nonlinear Extended-state Kalman Filter
NEN	Near Earth Network
NEO	Near-Earth Object
NIEL	Non-Ionizing Energy Loss
NiMH	Nickel Metal Hydride
NMOS	N-type Metal Oxide Semiconductor
NRE	Non-Recurring Engineering
NTIA	National Telecommunications and Information Administration
NVP	N-Version Programming
OC	Optical Communications
ORR	Operational Readiness Review

OSA	Orion Stage Adapter
PCB	Printed Circuit Board
PCE	Power Conversion Efficiency
PDR	Preliminary Design Review
PEEK	Polyetheretherketone
PEKK	Polyetherketoneketone
PEO	Plasma Electrolytic Oxidation
PER	Pre-Environmental Review
PHM	Prognostic Health Management
PI	Principal Investigator
PIR	Pre-Integration Review
PM	Program Manager
PMP	Project Management Plan
PMR	Program Management Review
P-POD	Poly Picosatellite Orbital Deployer
PPT	Pulsed Plasma Thruster
PRM	Panel Release Mechanism
PSD	Power Spectral Density
PSP	Parker Solar Probe
PSR	Pre-Ship Review
QPSK	Quadrature Phase Shift Keying
RAAN	Right Ascension of the Ascending Node
RBF	Remove Before Flight
RCS	Reaction Control Subsystem
RF	Radio Frequency
RFB	Request For Bids
RFP	Request For Proposals
RHU	Radioisotope Heater Unit
RK	Runge-Kutta
ROSA	Roll Out Solar Array
RPP	Rectangular Parallelepiped
RS	Reed-Solomon
RTG	Radioisotope Thermoelectric Generator

RW	Reaction Wheel
SAA	South Atlantic Anomaly
SaaS	Software as a Service
SADA	Solar Array Drive Assembly
SCR	System Concept Review
SCS	Self-Checking Software
SDO	Solar Dynamics Observatory
SDR	Software-Defined Radio
SEB	Single Event Burnout
SECDED	Single Error Correction Double Error Detection
SEDR	Single Event Dielectric Rupture
SEE	Single Event Effect
SEFI	Single Event Functional Interrupt
SEGR	Single Event Gate Rupture
SEHE	Single Event Hard Error
SEL	Single Event Latch-up
SEMP	Systems Engineering Management Plan
SEP	Solar Energetic Particles
SER	Soft Error Rate
SESB	Single Event Snap-Back
SET	Single Event Transient
SETH	Science Enabling Technologies for Heliophysics
SETSI	Secretaria de Estado de Telecomunicaciones para la Sociedad de la Información
SEU	Single Event Upset
SGC	Space Grant Consortium
SHARAD	Shallow Radar
SHF	Super High Frequency
SILEX	Semiconductor Laser Intersatellite Link Experiment
SLS	Space Launch System
SMA	Shape Memory Alloy
SME	Subject Matter Expert
SNP	Space Network Project
SoC	System on Chip

SoI	System on Insulator
SoS	System on Sapphire
SOHO	Solar and Heliophysics Observatory
SPE	Solar Particle Event
SPIS	Spacecraft Plasma Interaction System
SPL	Sound Pressure Level
SPM	Standard Plasma Model
SRIM	Stopping and Range of Ions in Matter
SRP	Solar Radiation Pressure
SRR	System Requirements Review
SS	Stainless Steel
S3VI	Small Satellite Systems Virtual Institute
STEM	Science, Technology, Engineering, and Mathematics
STEREO	Solar Terrestrial Relations Observatory
SunRISE	Sun Radio Interferometer Space Experiment
SWaP	Size, Weight, and Power
TDRS	Tracking and Data Relay Satellites
TechEdSat	Technology Education Satellite
THT	Through-Hole Technology
TID	Total Ionizing Dose
TMM	Thermal Math Model
TMR	Triple Modular Redundancy
TOF	Time of Flight
TRL	Technology Readiness Level
TRR	Test Readiness Review
T&S	Trade & Selection
TT&C	Telemetry, Tracking & Command
TTMR	Temporal Triple Modular Redundancy
TU	Tuskegee University
TVC	Thrust Vector Control
UA	University of Alabama
UAB	University of Alabama at Birmingham
UAH	University of Alabama in Huntsville

UAM	Ultrasonic Additive Manufacturing
UHF	Ultra High Frequency
USA	University of South Alabama
VAB	Van Allen Belt
VF	Voice Frequency
VHF	Very High Frequency
VLF	Very Low Frequency
VSRS	Versatile Structural Radiation Shielding
WBS	Work Breakdown Structure
WMM	World Magnetic Model
WoV	Window of Vulnerability
μCAT	Microcathode Arc Thruster

APPENDIX A: SOFTWARE STATE LOGIC FLOWS

Software state logic flows describe how a satellite accomplishes mission tasks and objectives through the enaction of smaller, singular tasks such as turning components on, turning components off, checking the state of parameters before moving to a subsequent task, or saving data after communicating with Earth. AEGIS utilized a framework from JPL, F Prime, to create the satellite software, but logic flows are independent of any single software framework. Satellite software is ideally autonomous, and **Figure 115** describes how the software states can logically proceed from one to the next as well as proceed back and forth as necessary. The software topology is broken into subsystems, and software states are given control of relevant subsystems. This not only prevents unwanted activity, e.g. thruster operation is not possible in the science state, but it also allows for ease of component resets.

The most important thing to understand about the software states is that they are selected via a State Queue. The State Queue is not a stack or a list, and its operation is governed by queue logic. Thus, whichever state is on the bottom of the list when the State Queue is checked for subsequent operations is the state the software will transition into and remove from the queue. States may be added to the top or the bottom of the State Queue, but usually they are added to the bottom. For example, the Warmup state must happen before the Burn state, so to get to Burn the software would add Burn to the bottom of the State Queue first and then add Warmup to the bottom of the State Queue. When the State Queue is checked, Warmup will be the next state because it was added to the bottom of State Queue second. When the software switches into Warmup, Warmup is removed from the State Queue and Burn would come next.

Four types of superclasses are shown in the software logic: Thermal Control, Attitude Control, Communications, and the Prognostic Health Management (PHM) system. Thermal Control is always initialized first. When this superclass, visually a large, colorful block, is initialized, it simply means a process is running in the background. For Thermal Control, this means the patch heaters have a set point that their duty cycle error signal will be based on. Attitude Control may be shown as "Detumble," "Point at Earth," or "Point at Sun." These represent closed-loop DCE control algorithms that are enacted via the reaction wheels for differing target vectors. Communications superclasses indicate transmission is possible, and the PHM superclass and corresponding subsystem is the most important. In normal operations, the logic diamonds will compare some parameter, either a battery charge, angular velocity, or timer value, to a target value. These values are shown in the "Control Parameters" tables. When operations are occurring inside a PHM superclass, if a value exceeds the values provided in the "PHM Thresholds" tables, the spacecraft will stop what it is doing, put the current state at the bottom of the State Queue, put Safety 1 at the bottom of the State Queue, and check the State Queue. This will effectively put the spacecraft into the Safety 1 state where diagnostics can be performed. If the spacecraft cannot come to a resolution, the Safety 2 state is entered and ground communications are required. The most important aspect to understand is that if the PHM superclass box is around the logic flow, it is possible for the spacecraft to enter Safety 1. Brandon Molyneaux is thanked for his assistance organizing these software states.

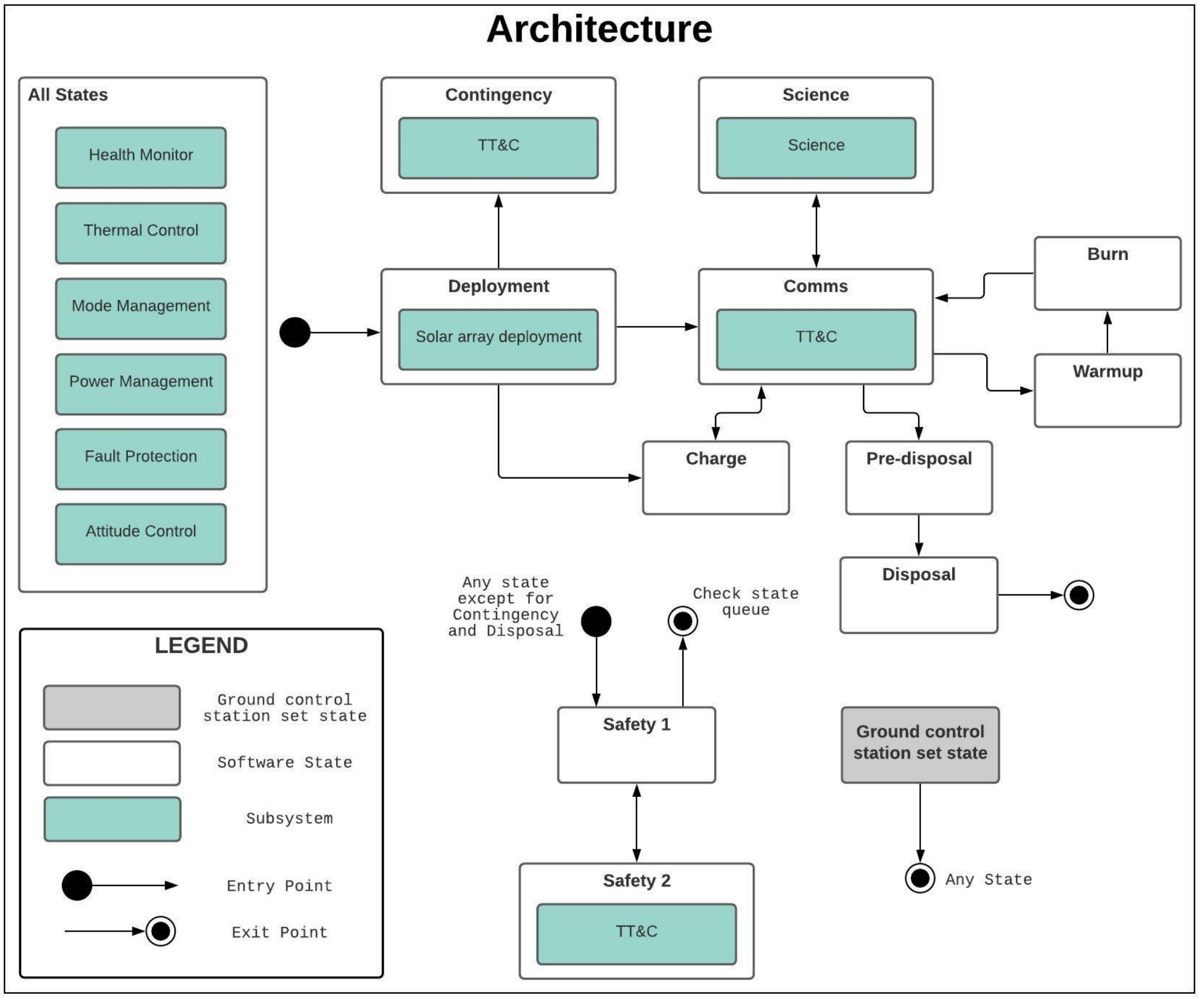
Architecture
All States
Health Monitor
Thermal Control
Mode Management
Power Management
Fault Protection
Attitude Control
Contingency
TT&C
Science
Science
Deployment
Solar array deployment
Comms
TT&C
Burn
Warmup
Charge
Pre-disposal
Disposal
Any state except for Contingency and Disposal
Check state queue
Safety 1
Safety 2
TT&C
Ground control station set state
Any State
LEGEND
Ground control station set state
Software State
Subsystem
Entry Point
Exit Point

Figure 115: Software State Architecture Flow

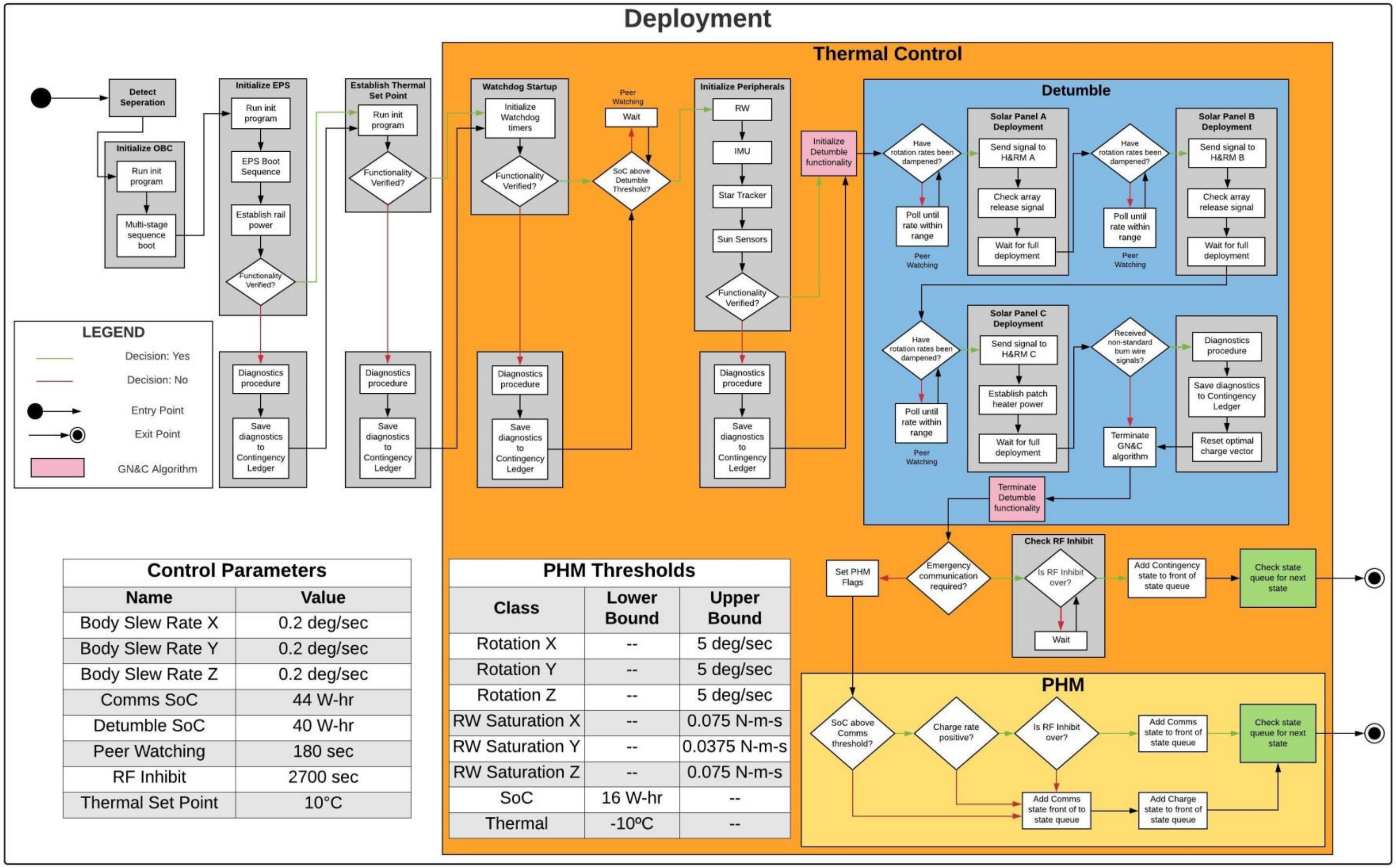
Deployment
Thermal Control
Detect Seperation
Initialize OBC
Run init program
Multi-stage sequence boot
Initialize EPS
Run init program
EPS Boot Sequence
Establish rail power
Functionality Verified?
Diagnostics procedure
Save diagnostics to Contingency Ledger
Establish Thermal Set Point
Run init program
Functionality Verified?
Diagnostics procedure
Save diagnostics to Contingency Ledger
Watchdog Startup
Initialize Watchdog timers
Functionality Verified?
Diagnostics procedure
Save diagnostics to Contingency Ledger
Peer Watching
Wait
SoC above Detumble Threshold?
Initialize Peripherals
RW
IMU
Star Tracker
Sun Sensors
Functionality Verified?
Diagnostics procedure
Save diagnostics to Contingency Ledger
Initialize Detumble functionality
Detumble
Have rotation rates been dampened?
Poll until rate within range
Peer Watching
Solar Panel A Deployment
Send signal to H&RM A
Check array release signal
Wait for full deployment
Have rotation rates been dampened?
Poll until rate within range
Peer Watching
Solar Panel B Deployment
Send signal to H&RM B
Check array release signal
Wait for full deployment
Have rotation rates been dampened?
Poll until rate within range
Peer Watching
Solar Panel C Deployment
Send signal to H&RM C
Establish patch heater power
Wait for full deployment
Received non-standard burn wire signals?
Diagnostics procedure
Save diagnostics to Contingency Ledger
Reset optimal charge vector
Terminate GN&C algorithm
Terminate Detumble functionality
Emergency communication required?
Set PHM Flags
Check RF Inhibit
Is RF Inhibit over?
Wait
Add Contingency state to front of state queue
Check state queue for next state
PHM
SoC above Comms threshold?
Charge rate positive?
Is RF Inhibit over?
Add Comms state to front of state queue
Check state queue for next state
Add Comms state front of to state queue
Add Charge state to front of state queue
LEGEND
Decision: Yes
Decision: No
Entry Point
Exit Point
GN&C Algorithm

Control Parameters	
Name	**Value**
Body Slew Rate X	0.2 deg/sec
Body Slew Rate Y	0.2 deg/sec
Body Slew Rate Z	0.2 deg/sec
Comms SoC	44 W-hr
Detumble SoC	40 W-hr
Peer Watching	180 sec
RF Inhibit	2700 sec
Thermal Set Point	10°C

PHM Thresholds		
Class	**Lower Bound**	**Upper Bound**
Rotation X	--	5 deg/sec
Rotation Y	--	5 deg/sec
Rotation Z	--	5 deg/sec
RW Saturation X	--	0.075 N-m-s
RW Saturation Y	--	0.0375 N-m-s
RW Saturation Z	--	0.075 N-m-s
SoC	16 W-hr	--
Thermal	-10ºC	--

Figure 116: Deployment Software State Logic

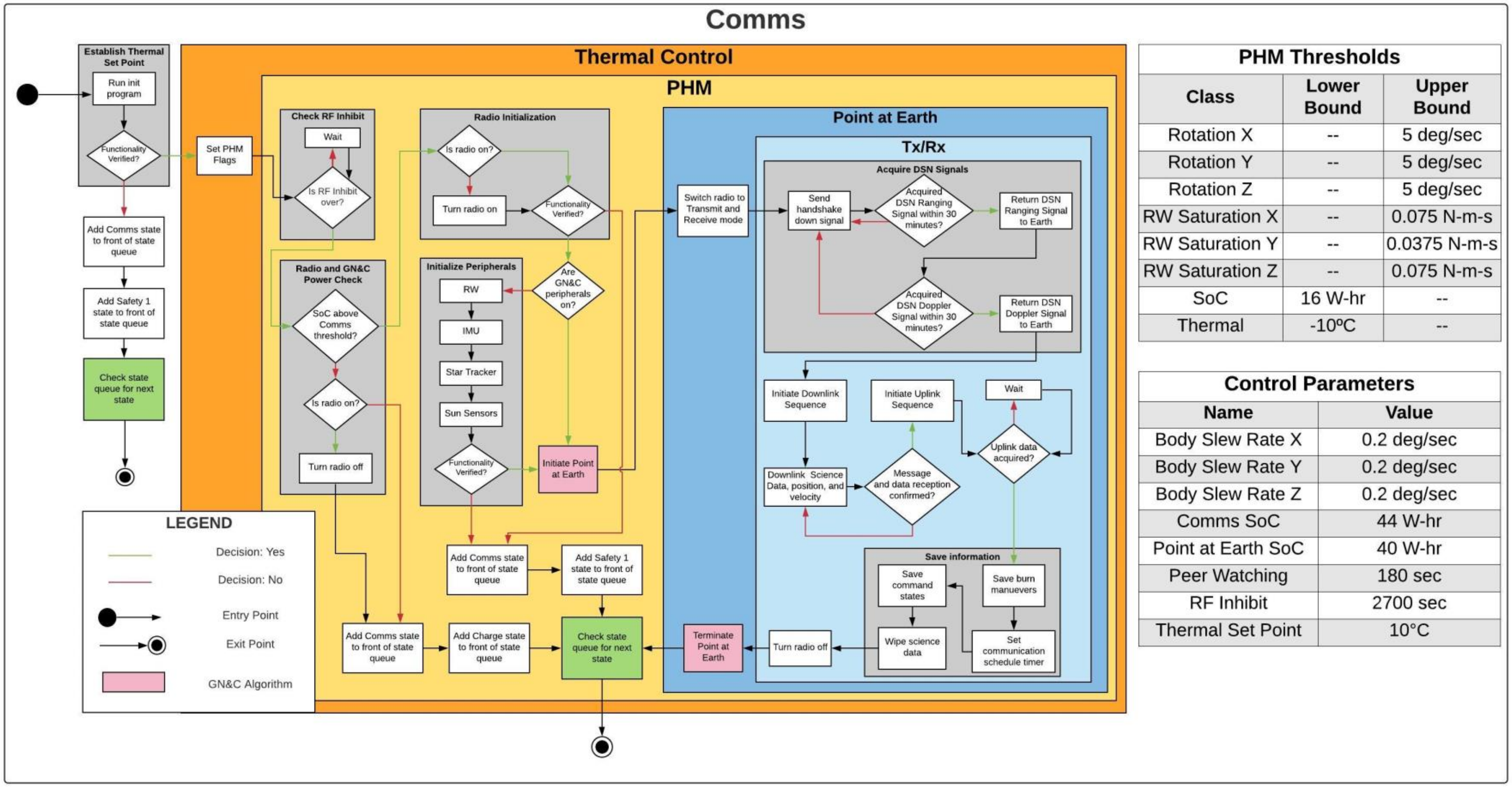
Comms
Thermal Control
PHM
Establish Thermal Set Point
Run init program
Functionality Verified?
Add Comms state to front of state queue
Add Safety 1 state to front of state queue
Check state queue for next state
Set PHM Flags
Check RF Inhibit
Wait
Is RF Inhibit over?
Radio and GN&C Power Check
SoC above Comms threshold?
Is radio on?
Turn radio off
Radio Initialization
Is radio on?
Turn radio on
Functionality Verified?
Initialize Peripherals
RW
IMU
Star Tracker
Sun Sensors
Functionality Verified?
Are GN&C peripherals on?
Initiate Point at Earth
Add Comms state to front of state queue
Add Safety 1 state to front of state queue
Add Comms state to front of state queue
Add Charge state to front of state queue
Check state queue for next state
Point at Earth
Switch radio to Transmit and Receive mode
Tx/Rx
Acquire DSN Signals
Send handshake down signal
Acquired DSN Ranging Signal within 30 minutes?
Return DSN Ranging Signal to Earth
Acquired DSN Doppler Signal within 30 minutes?
Return DSN Doppler Signal to Earth
Initiate Downlink Sequence
Initiate Uplink Sequence
Wait
Uplink data acquired?
Downlink Science Data, position, and velocity
Message and data reception confirmed?
Save information
Save command states
Save burn manuevers
Wipe science data
Set communication schedule timer
Turn radio off
Terminate Point at Earth
LEGEND
Decision: Yes
Decision: No
Entry Point
Exit Point
GN&C Algorithm

PHM Thresholds

Class	Lower Bound	Upper Bound
Rotation X	--	5 deg/sec
Rotation Y	--	5 deg/sec
Rotation Z	--	5 deg/sec
RW Saturation X	--	0.075 N-m-s
RW Saturation Y	--	0.0375 N-m-s
RW Saturation Z	--	0.075 N-m-s
SoC	16 W-hr	--
Thermal	-10ºC	--

Control Parameters

Name	Value
Body Slew Rate X	0.2 deg/sec
Body Slew Rate Y	0.2 deg/sec
Body Slew Rate Z	0.2 deg/sec
Comms SoC	44 W-hr
Point at Earth SoC	40 W-hr
Peer Watching	180 sec
RF Inhibit	2700 sec
Thermal Set Point	10°C

Figure 117: Communications Software State Logic

Charge

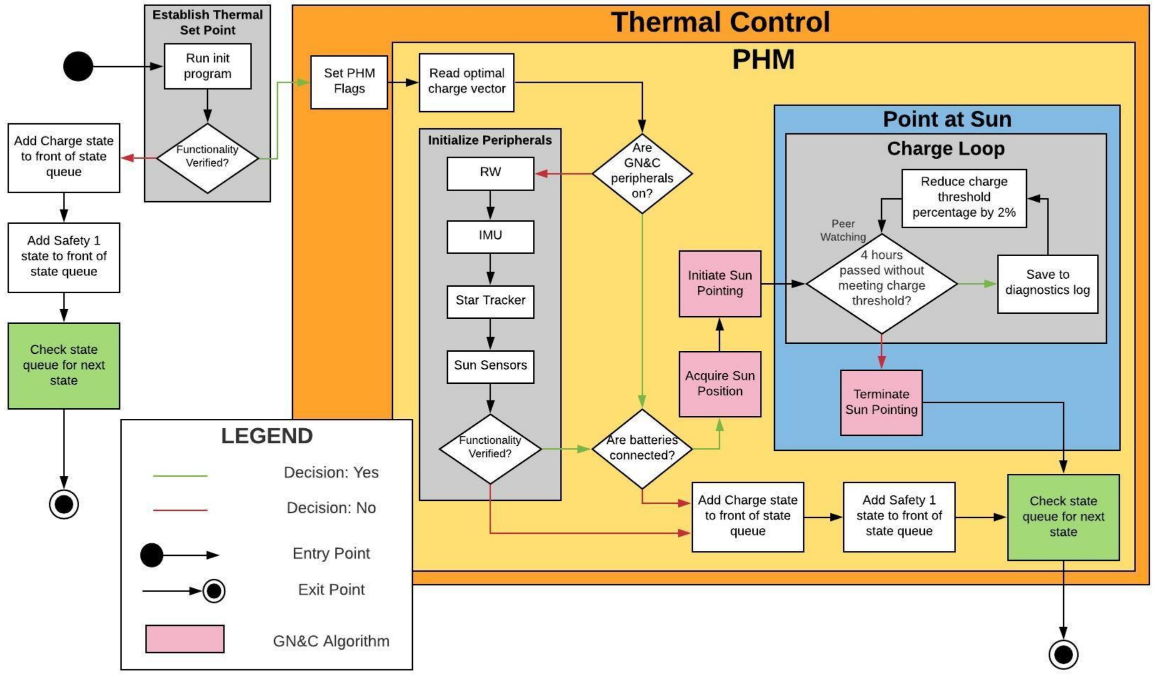
Establish Thermal Set Point
Run init program
Functionality Verified?
Add Charge state to front of state queue
Add Safety 1 state to front of state queue
Check state queue for next state
Thermal Control
PHM
Set PHM Flags
Read optimal charge vector
Initialize Peripherals
RW
IMU
Star Tracker
Sun Sensors
Functionality Verified?
Are GN&C peripherals on?
Are batteries connected?
Initiate Sun Pointing
Acquire Sun Position
Point at Sun
Charge Loop
Reduce charge threshold percentage by 2%
Peer Watching
4 hours passed without meeting charge threshold?
Save to diagnostics log
Terminate Sun Pointing
Add Charge state to front of state queue
Add Safety 1 state to front of state queue
Check state queue for next state
LEGEND
Decision: Yes
Decision: No
Entry Point
Exit Point
GN&C Algorithm

PHM Thresholds

Class	Lower Bound	Upper Bound
Rotation X	--	5 deg/sec
Rotation Y	--	5 deg/sec
Rotation Z	--	5 deg/sec
RW Saturation X	--	0.075 N-m-s
RW Saturation Y	--	0.0375 N-m-s
RW Saturation Z	--	0.075 N-m-s
SoC	16 W-hr	--
Thermal	-10ºC	--

Control Parameters

Name	Value
Angular Position X	0.025 deg
Angular Position Y	0.167 deg
Angular Position Z	0.025 deg
Peer Watching	14,400 sec
Thermal Set Point	10°C

Figure 118: Charge Software State Logic

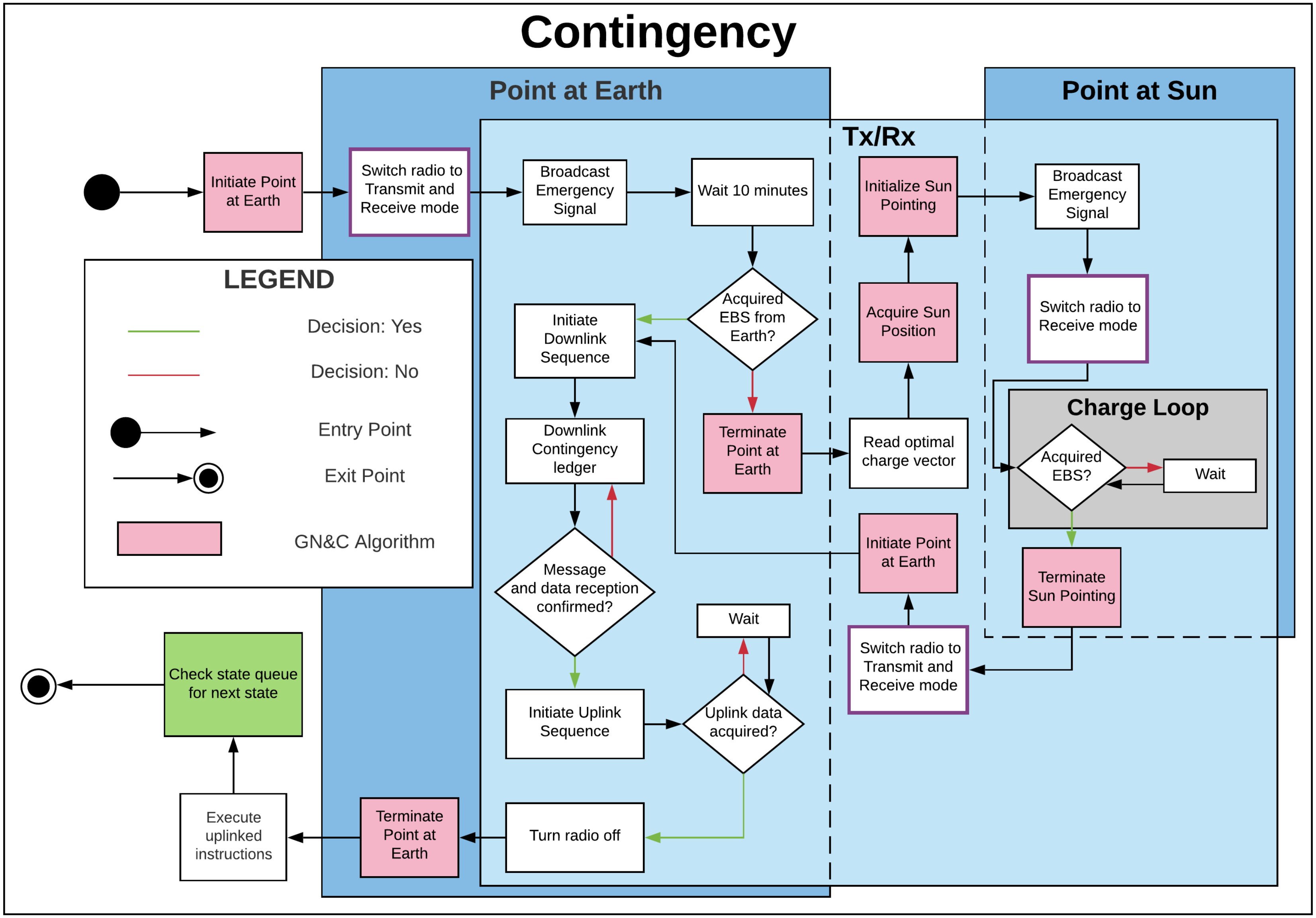
Contingency
Point at Earth
Point at Sun
Tx/Rx
Initiate Point at Earth
Switch radio to Transmit and Receive mode
Broadcast Emergency Signal
Wait 10 minutes
Acquired EBS from Earth?
Initiate Downlink Sequence
Downlink Contingency ledger
Terminate Point at Earth
Message and data reception confirmed?
Initiate Uplink Sequence
Wait
Uplink data acquired?
Turn radio off
Terminate Point at Earth
Execute uplinked instructions
Check state queue for next state
Initialize Sun Pointing
Acquire Sun Position
Read optimal charge vector
Initiate Point at Earth
Switch radio to Transmit and Receive mode
Broadcast Emergency Signal
Switch radio to Receive mode
Charge Loop
Acquired EBS?
Wait
Terminate Sun Pointing
LEGEND
Decision: Yes
Decision: No
Entry Point
Exit Point
GN&C Algorithm

Figure 119: Contingency Software State Logic

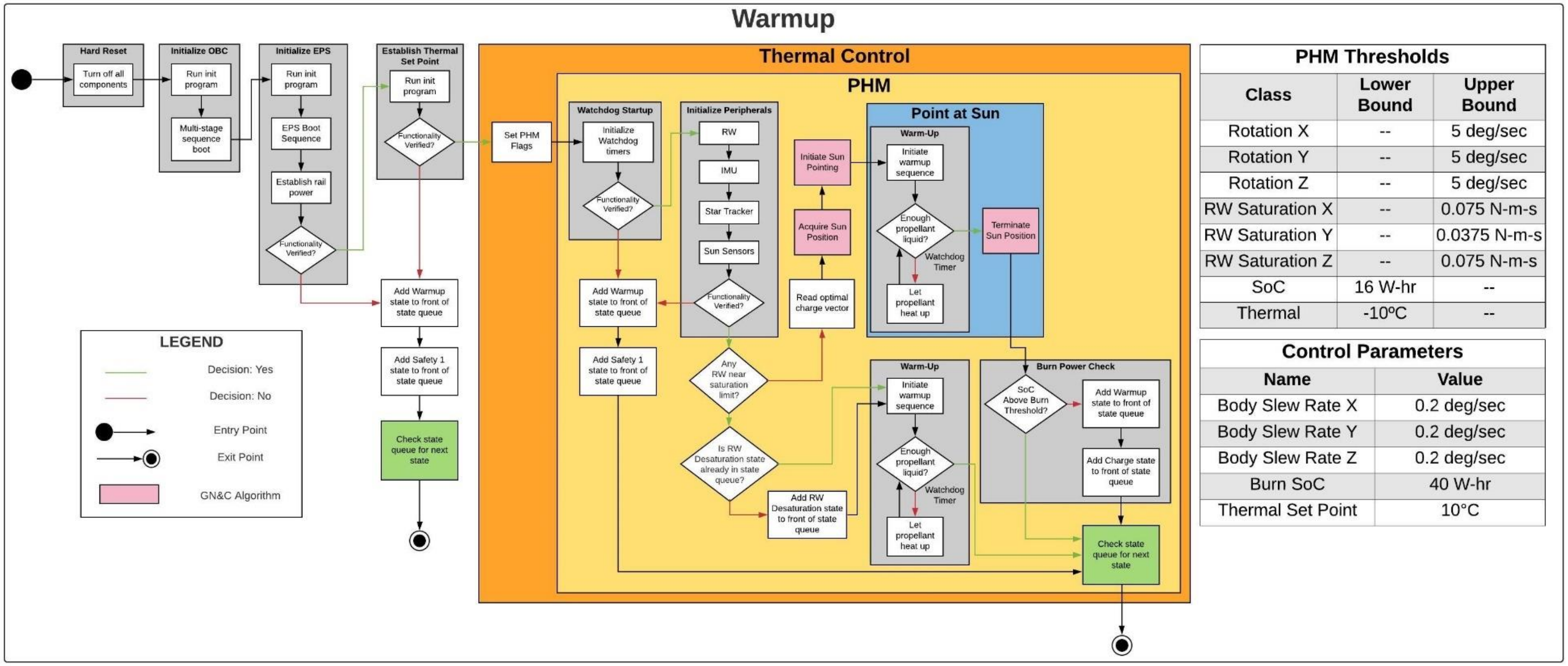
Warmup
Hard Reset
Turn off all components
Initialize OBC
Run init program
Multi-stage sequence boot
Initialize EPS
Run init program
EPS Boot Sequence
Establish rail power
Functionality Verified?
Establish Thermal Set Point
Run init program
Functionality Verified?
Add Warmup state to front of state queue
Add Safety 1 state to front of state queue
Check state queue for next state
LEGEND
Decision: Yes
Decision: No
Entry Point
Exit Point
GN&C Algorithm
Thermal Control
PHM
Set PHM Flags
Watchdog Startup
Initialize Watchdog timers
Functionality Verified?
Add Warmup state to front of state queue
Add Safety 1 state to front of state queue
Initialize Peripherals
RW
IMU
Star Tracker
Sun Sensors
Functionality Verified?
Any RW near saturation limit?
Is RW Desaturation state already in state queue?
Add RW Desaturation state to front of state queue
Read optimal charge vector
Acquire Sun Position
Initiate Sun Pointing
Point at Sun
Warm-Up
Initiate warmup sequence
Enough propellant liquid?
Watchdog Timer
Let propellant heat up
Terminate Sun Position
Warm-Up
Initiate warmup sequence
Enough propellant liquid?
Watchdog Timer
Let propellant heat up
Burn Power Check
SoC Above Burn Threshold?
Add Warmup state to front of state queue
Add Charge state to front of state queue
Check state queue for next state

PHM Thresholds

Class	Lower Bound	Upper Bound
Rotation X	--	5 deg/sec
Rotation Y	--	5 deg/sec
Rotation Z	--	5 deg/sec
RW Saturation X	--	0.075 N-m-s
RW Saturation Y	--	0.0375 N-m-s
RW Saturation Z	--	0.075 N-m-s
SoC	16 W-hr	--
Thermal	-10ºC	--

Control Parameters

Name	Value
Body Slew Rate X	0.2 deg/sec
Body Slew Rate Y	0.2 deg/sec
Body Slew Rate Z	0.2 deg/sec
Burn SoC	40 W-hr
Thermal Set Point	10°C

Figure 120: Warmup Software State Logic

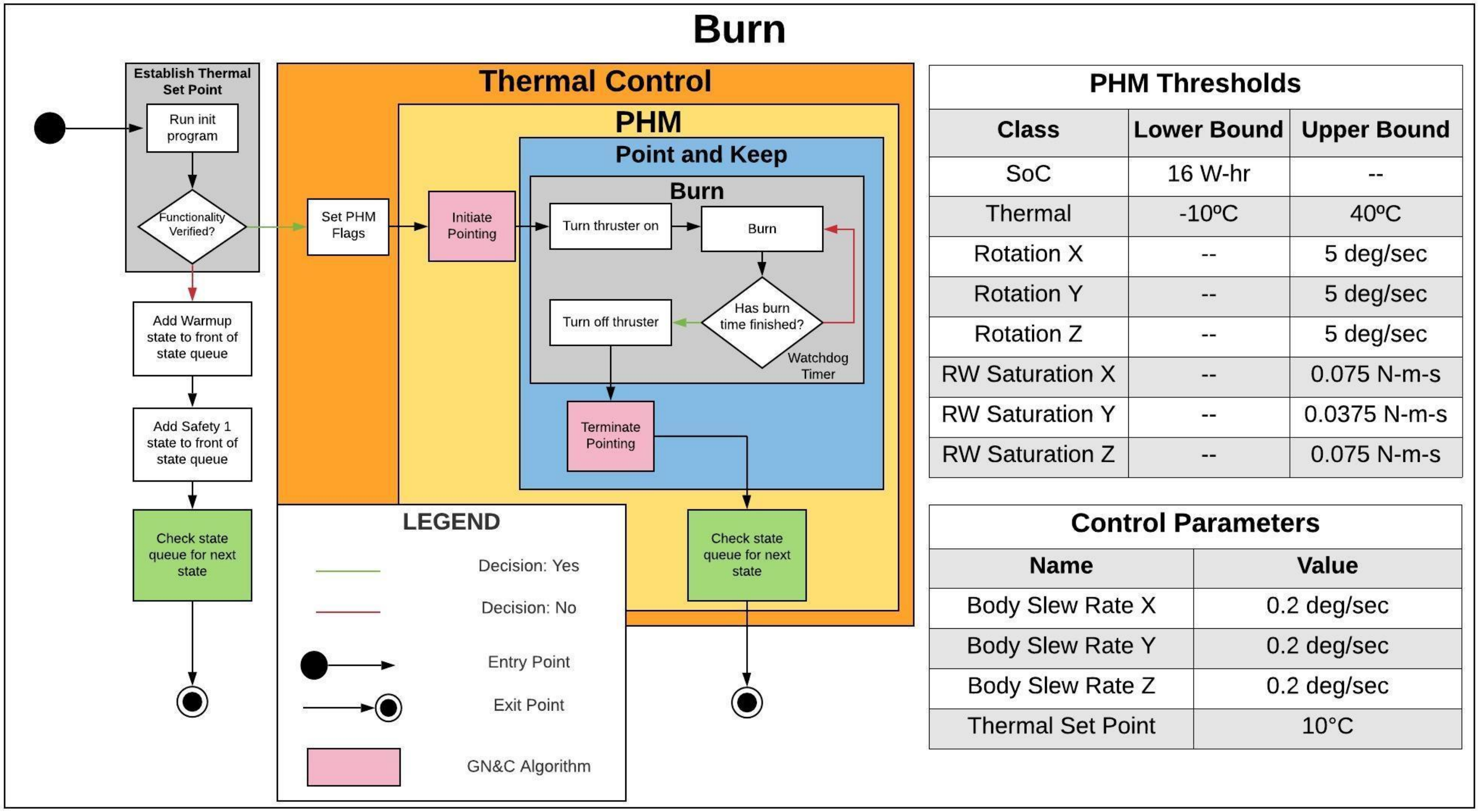
Burn
Establish Thermal Set Point
Run init program
Functionality Verified?
Add Warmup state to front of state queue
Add Safety 1 state to front of state queue
Check state queue for next state
Thermal Control
PHM
Point and Keep
Burn
Set PHM Flags
Initiate Pointing
Turn thruster on
Burn
Has burn time finished?
Watchdog Timer
Turn off thruster
Terminate Pointing
Check state queue for next state
LEGEND
Decision: Yes
Decision: No
Entry Point
Exit Point
GN&C Algorithm

PHM Thresholds

Class	Lower Bound	Upper Bound
SoC	16 W-hr	--
Thermal	-10ºC	40ºC
Rotation X	--	5 deg/sec
Rotation Y	--	5 deg/sec
Rotation Z	--	5 deg/sec
RW Saturation X	--	0.075 N-m-s
RW Saturation Y	--	0.0375 N-m-s
RW Saturation Z	--	0.075 N-m-s

Control Parameters

Name	Value
Body Slew Rate X	0.2 deg/sec
Body Slew Rate Y	0.2 deg/sec
Body Slew Rate Z	0.2 deg/sec
Thermal Set Point	10°C

Figure 121: Burn Software State Logic

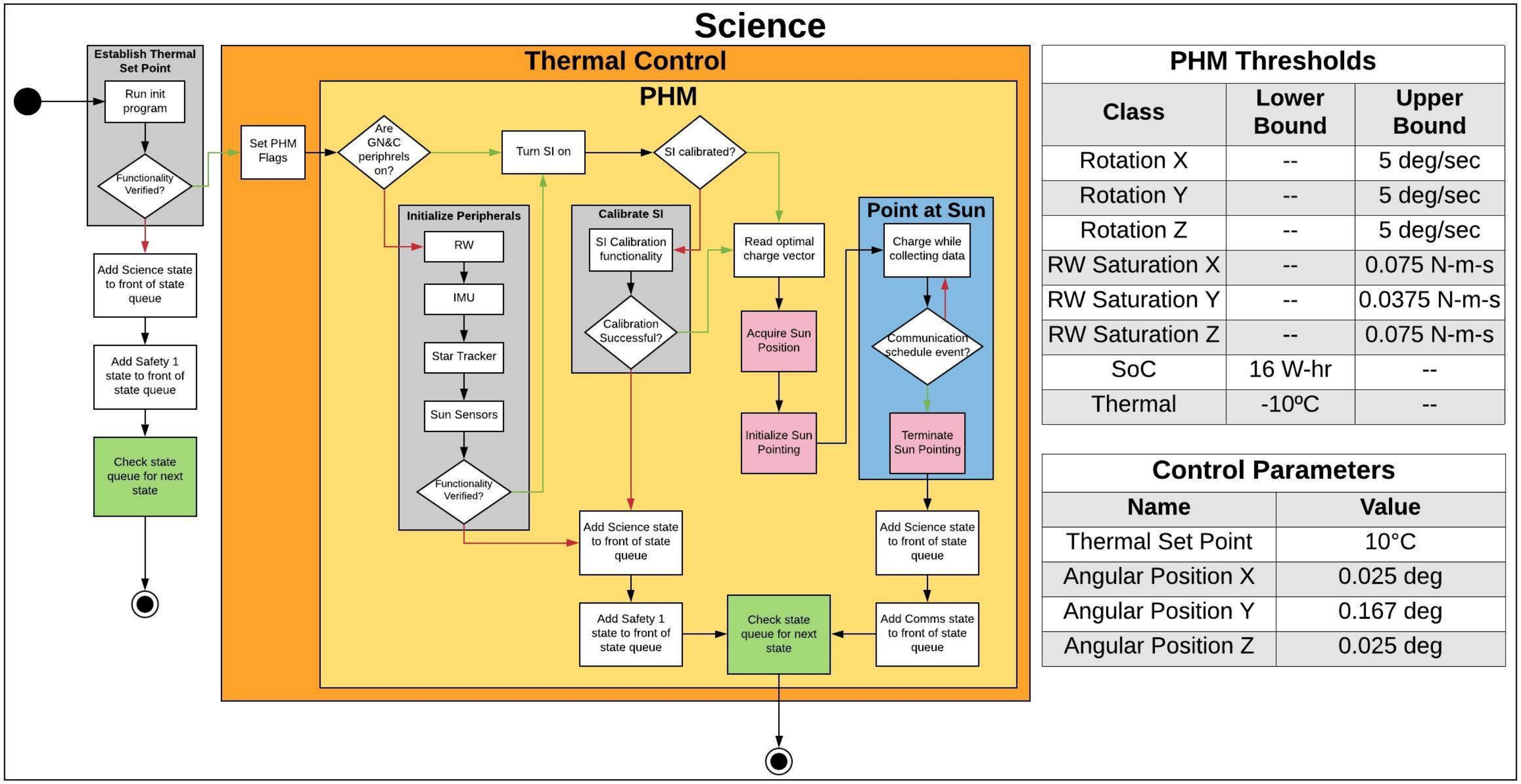
Science
Establish Thermal Set Point
Run init program
Functionality Verified?
Add Science state to front of state queue
Add Safety 1 state to front of state queue
Check state queue for next state
Thermal Control
PHM
Set PHM Flags
Are GN&C periphrels on?
Turn SI on
SI calibrated?
Initialize Peripherals
RW
IMU
Star Tracker
Sun Sensors
Functionality Verified?
Calibrate SI
SI Calibration functionality
Calibration Successful?
Read optimal charge vector
Acquire Sun Position
Initialize Sun Pointing
Point at Sun
Charge while collecting data
Communication schedule event?
Terminate Sun Pointing
Add Science state to front of state queue
Add Safety 1 state to front of state queue
Check state queue for next state
Add Science state to front of state queue
Add Comms state to front of state queue

PHM Thresholds

Class	Lower Bound	Upper Bound
Rotation X	--	5 deg/sec
Rotation Y	--	5 deg/sec
Rotation Z	--	5 deg/sec
RW Saturation X	--	0.075 N-m-s
RW Saturation Y	--	0.0375 N-m-s
RW Saturation Z	--	0.075 N-m-s
SoC	16 W-hr	--
Thermal	-10ºC	--

Control Parameters

Name	Value
Thermal Set Point	10°C
Angular Position X	0.025 deg
Angular Position Y	0.167 deg
Angular Position Z	0.025 deg

Figure 122: Science Software State Logic

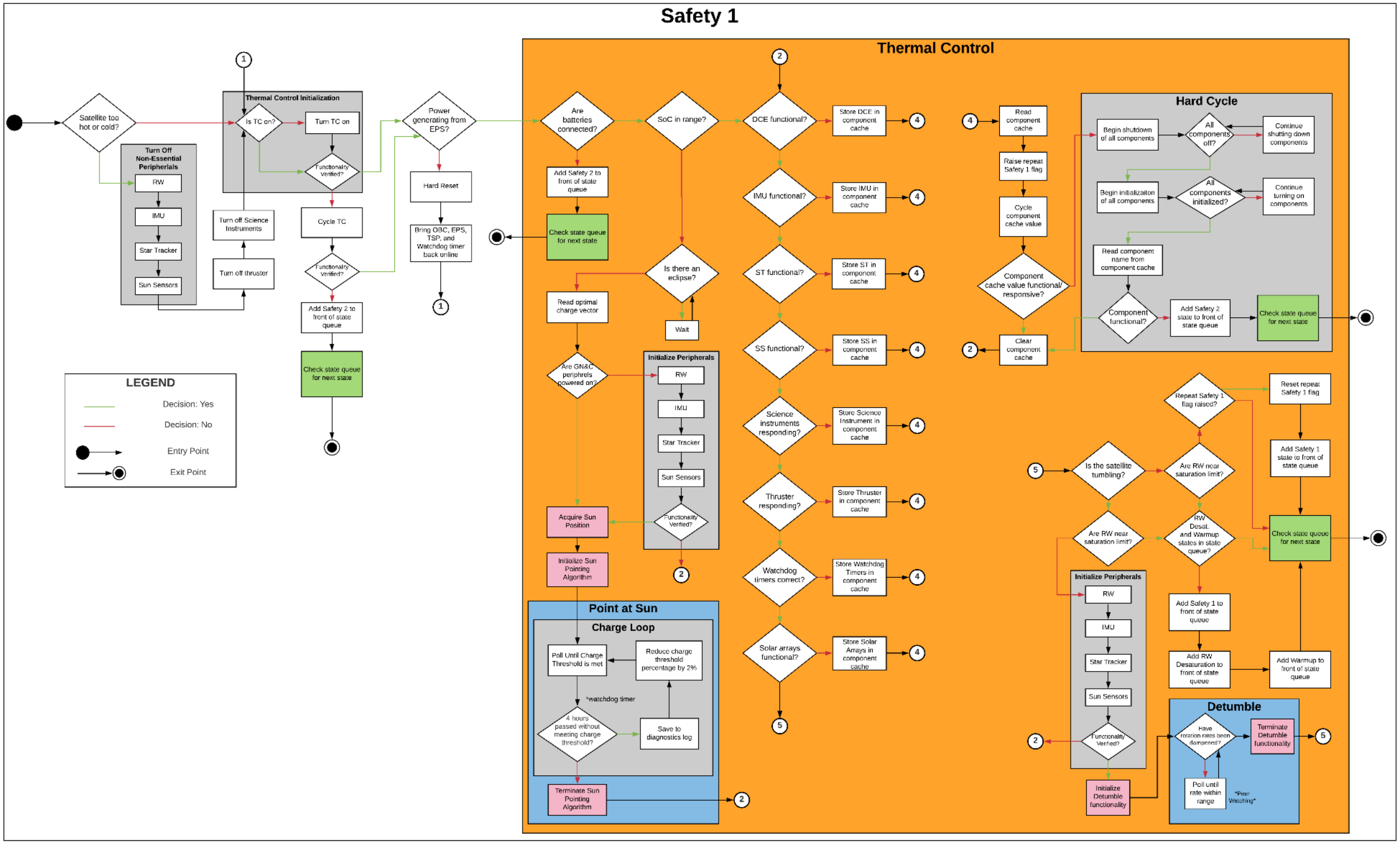
Safety 1
Thermal Control
Satellite too hot or cold?
Turn Off Non-Essential Peripherals
RW
IMU
Star Tracker
Sun Sensors
Thermal Control Initialization
Is TC on?
Turn TC on
Functionality Verified?
Turn off Science Instruments
Turn off thruster
Cycle TC
Functionality Verified?
Add Safety 2 to front of state queue
Check state queue for next state
Power generating from EPS?
Hard Reset
Bring OBC, EPS, TSP, and Watchdog timer back online
1
1
LEGEND
Decision: Yes
Decision: No
Entry Point
Exit Point
Are batteries connected?
Add Safety 2 to front of state queue
Check state queue for next state
SoC in range?
Is there an eclipse?
Wait
Read optimal charge vector
Are GN&C periphrels powered on?
Initialize Peripherals
RW
IMU
Star Tracker
Sun Sensors
Functionality Verified?
2
Acquire Sun Position
Initialize Sun Pointing Algorithm
Point at Sun
Charge Loop
Poll Until Charge Threshold is met
Reduce charge threshold percentage by 2%
*watchdog timer
4 hours passed without meeting charge threshold?
Save to diagnostics log
Terminate Sun Pointing Algorithm
2
2
DCE functional?
Store DCE in component cache
4
IMU functional?
Store IMU in component cache
4
ST functional?
Store ST in component cache
4
SS functional?
Store SS in component cache
4
Science instruments responding?
Store Science Instrument in component cache
4
Thruster responding?
Store Thruster in component cache
4
Watchdog timers correct?
Store Watchdog Timers in component cache
4
Solar arrays functional?
Store Solar Arrays in component cache
4
5
4
Read component cache
Raise repeat Safety 1 flag
Cycle component cache value
Component cache value functional/ responsive?
Clear component cache
2
Hard Cycle
Begin shutdown of all components
All components off?
Continue shutting down components
Begin initializaiton of all components
All components initialized?
Continue turning on components
Read component name from component cache
Component functional?
Add Safety 2 state to front of state queue
Check state queue for next state
Repeat Safety 1 flag raised?
Reset repeat Safety 1 flag
Add Safety 1 state to front of state queue
5
Is the satellite tumbling?
Are RW near saturation limit?
Are RW near saturation limit?
RW Desat. and Warmup states in state queue?
Check state queue for next state
Initialize Peripherals
RW
IMU
Star Tracker
Sun Sensors
Functionality Verified?
2
Add Safety 1 to front of state queue
Add RW Desaturation to front of state queue
Add Warmup to front of state queue
Initialize Detumble functionality
Detumble
Have rotation rates been dampened?
Poll until rate within range
Peer Watching
Terminate Detumble functionality
5

Figure 123: Safety 1 Software State Logic

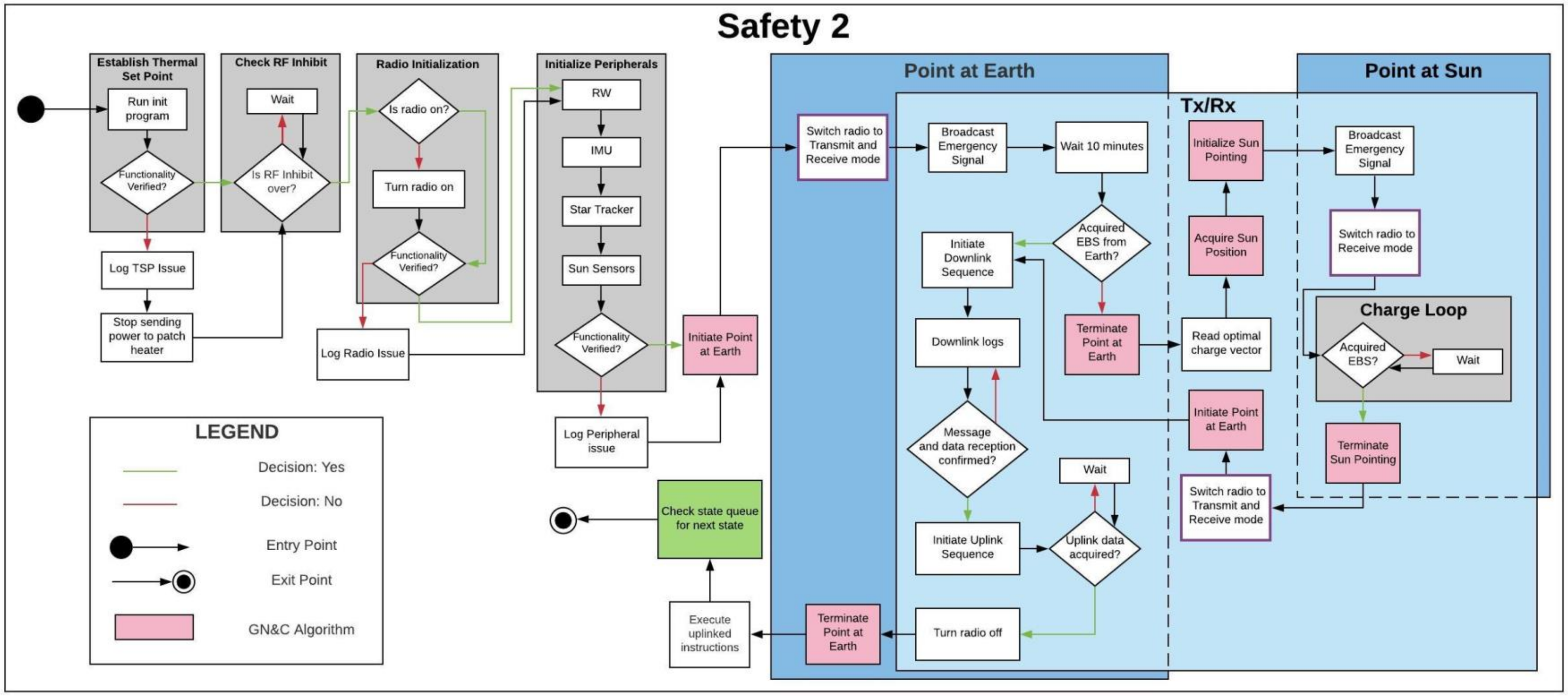
Safety 2
Establish Thermal Set Point
Run init program
Functionality Verified?
Log TSP Issue
Stop sending power to patch heater
Check RF Inhibit
Wait
Is RF Inhibit over?
Radio Initialization
Is radio on?
Turn radio on
Functionality Verified?
Log Radio Issue
Initialize Peripherals
RW
IMU
Star Tracker
Sun Sensors
Functionality Verified?
Log Peripheral issue
Initiate Point at Earth
Point at Earth
Tx/Rx
Switch radio to Transmit and Receive mode
Broadcast Emergency Signal
Wait 10 minutes
Acquired EBS from Earth?
Initiate Downlink Sequence
Terminate Point at Earth
Downlink logs
Message and data reception confirmed?
Wait
Initiate Uplink Sequence
Uplink data acquired?
Turn radio off
Terminate Point at Earth
Execute uplinked instructions
Check state queue for next state
Point at Sun
Initialize Sun Pointing
Acquire Sun Position
Read optimal charge vector
Initiate Point at Earth
Switch radio to Transmit and Receive mode
Broadcast Emergency Signal
Switch radio to Receive mode
Charge Loop
Acquired EBS?
Wait
Terminate Sun Pointing
LEGEND
Decision: Yes
Decision: No
Entry Point
Exit Point
GN&C Algorithm

Figure 124: Safety 2 Software State Logic

APPENDIX B: SPACECRAFT FOR RADIATION CHARACTERIZATION

A variety of conclusions are presented about space radiation in Section 4; without knowledge of the spacecraft that provide data from which to draw conclusions, readers are forced to take authors at their word. Presented here are the spacecraft relevant deep space CubeSat designers who wish to vet a given radiation environment. If a reader's satellite is intended for any of these solar system regions, investigation should be done into the most recent data provided by the following spacecraft. Older missions, such as SAMPEX [273] are not covered, but the data sets provided by those missions are included in many radiation models. The space radiation environment is highly variable, and new data is emerging constantly.

B.1 Solar Observation Spacecraft

Many satellites have multiple purposes with secondary or tertiary science payloads in addition to their primary instrument. The following are satellites with primary payloads for solar observation but may have additional instrumentation. An orbit alone does not necessarily define the purpose of a spacecraft, as some satellites with varying purposes share orbits.

B.1.1 Solar and Heliophysics Observatory

The Solar and Heliophysics Observatory (SOHO) was launched in 1995 with twelve instruments and is still operational. It was built by what is now EADS Astrium under ESA but is managed by NASA at GSFC. It resides in a halo orbit around the ES-L1 Lagrange point. Its primary investigation pertains to high energy particles, solar wind, and magnetic fields. The International Solar Terrestrial Physics (ISTP) program, of which SOHO is a part, is also responsible for WIND, Geotail, and Cluster [274].

B.1.2 Comprehensive Solar Wind Laboratory

WIND is not an acronym. The original name was the Interplanetary Physics Laboratory as part of the Global Geospace Science (GGS) program, a subset of the ISTP. The GGS had another program, the Polar Plasma Laboratory, which was combined with the physics platform as WIND. WIND is also at ES-L1, and its primary science objectives are to provide baseline ecliptic plane observations and characterize plasma, energetic particles, and magnetic field variations in the solar wind. It was launched in 1994 and recently celebrated 25 years in orbit [275].

B.1.3 Cluster

The distinctions between solar vs. non-solar observation become ambiguous with Cluster because the cluster of four satellites monitor the interaction between solar wind and Earth's magnetosphere. Cluster I was a four-spacecraft mission that died on the failed Ariane-5 launch vehicle. Cluster II was a full recovery mission of all four satellites launched in two increments of two satellites each on Soyuz launch vehicles in 2000. The primary of the four spacecraft was humorously deemed Phoenix after rising from the ashes of failure in only 18 months. Phoenix and its three identical spacecraft are in an elliptical HEO which traverses all sections of the magnetosphere in a tetrahedral configuration. Differential plasma measurements were taken for the first time to map VAB shape and size, solar wind turbulence effects, and magnetic recombination of the magnetotail [276].

B.1.4 Solar Dynamics Observatory

The Solar Dynamics Observatory (SDO), launched in 2010 into a geosynchronous inclined orbit, is the first mission under NASA's Living With a Star (LWS) program. Its primary motivation is to study how the Sun's magnetic field is generated and structured in addition to how that stored energy is converted and released into the heliosphere. It is a powerful imaging satellite capable of high-definition images in 13 wavelengths [277].

B.1.5 Solar Terrestrial Relations Observatory

The Solar Terrestrial Relations Observatory (STEREO) is comprised of two spacecraft, STEREO A and STEREO B, colloquially "Ahead" and "Behind". Launched in 2006, the primary mission goal is to image the Sun from angles that many spacecraft can't reach. Following a heliosynchronous orbit, these angles provide comprehensive data for the magnetic field, plasma properties, energetic particles, and radio waves from the Sun. CME transient data is also captured by STEREO [278].

B.1.6 Parker Solar Probe

The Parker Solar Probe (PSP) out of the Applied Physics Laboratory at Johns Hopkins is likely performing what no CubeSat could do due to the orbit and material constraints. Coming seven times closer to the Sun than any spacecraft before and reaching temperatures up to 1377 °C, its mission is to understand the solar corona and why it is hotter than the surface itself. The PSP has instruments for imaging, particle counting, spectroscopy, and field strength measurement. The PSP should be the first source of solar data when investigating the most recent discoveries in solar science [279]. An image of the PSP design and instrumentation may be found in **Figure 125**.

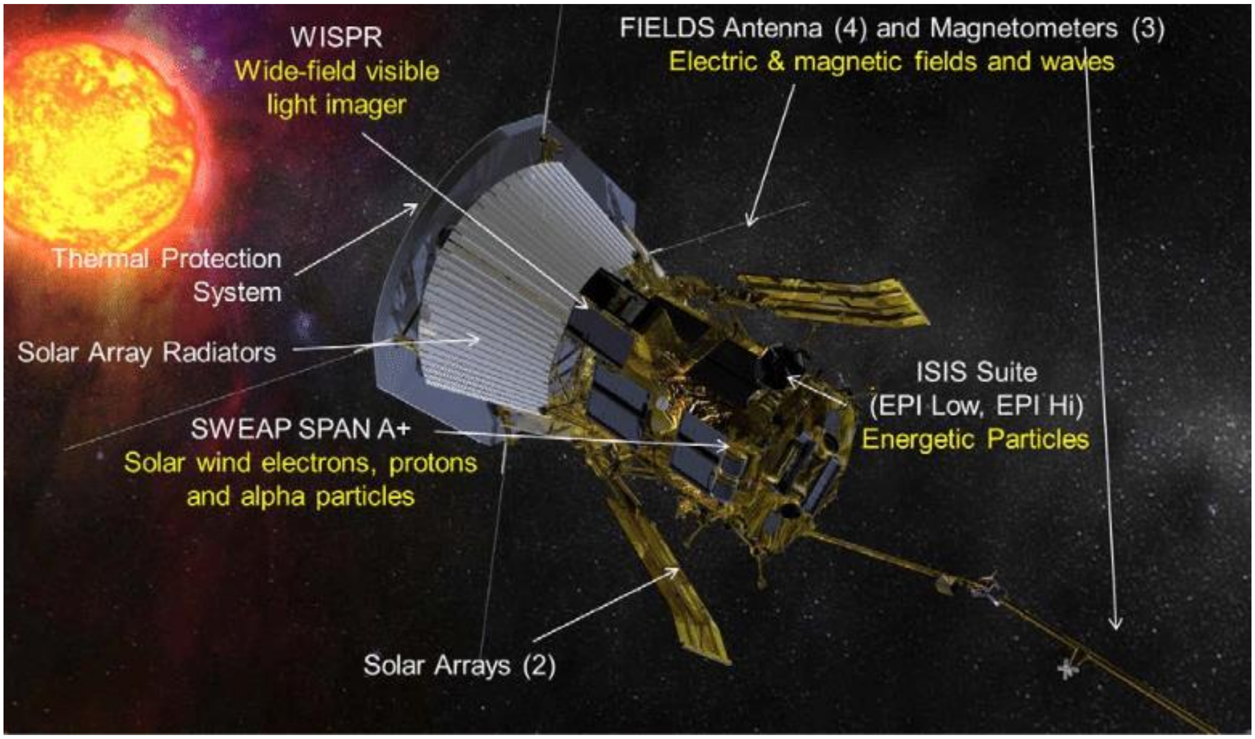
WISPR
Wide-field visible light imager
FIELDS Antenna (4) and Magnetometers (3)
Electric & magnetic fields and waves
Thermal Protection System
Solar Array Radiators
ISIS Suite
(EPI Low, EPI Hi)
Energetic Particles
SWEAP SPAN A+
Solar wind electrons, protons and alpha particles
Solar Arrays (2)

Figure 125: Parker Solar Probe Design and Instrumentation [280]

B.1.7 SunRISE

The Sun Radio Interferometer Space Experiment (SunRISE), a collaboration between JPL and the University of Michigan at Ann Arbor, was recently awarded a contract for six CubeSats to map the magnetic field lines between the Sun and interplanetary space. While the PSP will face extreme temperatures and radiation, SunRISE is a much better candidate for CubeSat-based heliophysics. The program is expected to deliver no later than July 1, 2023. SunRISE represents the first CubeSat constellation intended exclusively for solar science data [281].

B.2 Cislunar Observation Spacecraft

There is a long list of spacecraft which have performed lunar observations, including WIND, STEREO, and GEOTAIL (discussed momentarily in the interplanetary section), but attention is paid to the most recent and comprehensive dataset published from the Lunar Reconnaissance Orbiter (LRO) and its companion spacecraft, the Lunar Crater Observation and Sensing Satellite (LCROSS).

B.2.1 Lunar Reconnaissance Orbiter

The LRO was launched June 18, 2009 on an Atlas V rocket. The LRO maps the lunar surface, evaluates terrain for human presence, creates day-night temperature maps, provides a global geodetic grid, returns high resolution color imaging, and investigates the Moon's UV albedo [282]. Polar regions have received more attention than others. Data sets from the LRO are compiled and deposited in the Planetary Data System every three months [283].

The LRO contains six dedicated science instruments and a technology demonstration. Of primary interest to AEGIS is the Cosmic Ray Telescope for the Effects of Radiation (CRaTER), which characterizes the lunar radiation environment. Many of the anticipated radiation values for the AEGIS mission were published observations by CRaTER. The Diviner Lunar Radiometer Experiment (DLRE) focuses on mapping surface and subsurface temperatures. The Lyman Alpha Mapping Project (LAMP) searches for surface ice and frost as well as maps the entire lunar surface in UV. The Lunar Exploration Neutron Detector (LEND) maps hydrogen distributions and is likely to be complemented by LunaH-map CubeSat discoveries. The Lunar Orbiter Laser Altimeter (LOLA) discovers permanently illuminated and shadowed areas based on elevation as well as vetting potential landing site slopes. The Lunar Reconnaissance Orbiter Camera (LROC) captures images of the lunar poles with resolutions down to one meter in black and white. It can also image in color and UV. The technology demonstration is the Mini-RF radar which searches for water ice deposits. If a mission is looking to perform lunar science, the LRO instrument data should be the first place a Principal Investigator (PI) looks.

B.2.2 LCROSS

LCROSS launched with the LRO on the same Atlas V rocket as a companion mission to the LRO but kept the Atlas V upper stage attached, known as the Centaur. The Centaur detached on October 9, 2009 and acted as a lunar impactor. LCROSS was to fly through the impact debris field and perform measurements on the material. A sensor malfunction caused LCROSS to deplete over half its fuel reserves, but LCROSS was still able to perform its baseline mission. Water was detected in the plume ejected from the lunar surface, but contrary to apocryphal reports the impactor plume ejecta was not visible from Earth [284].

B.3 Interplanetary Observation Spacecraft

While of immeasurable importance to the field of deep space scientific discovery, spacecraft programs such as Venera, Cassini, Mariner, Pioneer, and Voyager will not be discussed. The spacecraft chosen for discussion were intended as datasets for future CubeSat endeavors. CubeSats going past Mars will need innovative power generation mechanisms that are not sufficiently miniaturized yet to be considered relevant.

B.3.1 Geostationary Operational Environment Satellite

The Geostationary Operational Environment Satellite (GOES) mission is a satellite program rather than a single spacecraft, beginning in 1966 and extending through 2036 at the time of writing. Its primary goal is to surveil space weather with magnetic field measurements, energetic particle detection, and X-ray imaging. At least two spacecraft are operating at any given time. The GOES-12 satellite features a Solar X-ray Imager. GOES has had a storied launch past, as GOES-7, designed to replace GOES-4, was lost when the launch vehicle was struck by lightning shortly after liftoff in 1986. As the name implies, GOES satellites are geostationary [285].

B.3.2 Advanced Composition Explorer

The Advanced Composition Explorer (ACE), launched in 1997 into the same ES-L1 orbit as SOHO and WIND, is one of the dual-purpose spacecraft that characterize both the interplanetary medium as well as the solar corona. ACE also evaluates matter of extrasolar origin. ACE can provide near-real-time solar wind information given the appropriate downlink position, and warnings of geomagnetic storms can be provided within an hour of the storm beginning. If a Carrington-Class storm, discussed in Section 3.7.3.4, were to occur, ACE would be one of Earth's only warning systems [286].

B.3.3 Geotail

Geotail was launched on a Delta-II rocket on July 24th, 1992. Its purpose was to discover how magnetic field energy changed in the magnetosphere tail, or magnetotail, and the corresponding implications for ion and electron acceleration. The orbit of Geotail has varied widely outside of the second VAB to study a wide range of magnetotail sections. Geotail includes magnetic and electric field monitors, two sets of plasma monitors, two sets of high-energy particle monitors, and a plasma wave instrument. Interestingly, the computer controlling the plasma monitors failed in 1993, and attempts to reset it were unsuccessful. When the satellite passed through the lunar shadow later that year, all power was intentionally cut from the batteries. When the spacecraft was rebooted, the computer was functional [220].

B.3.4 Mars Reconnaissance Orbiter

The MarCO CubeSats may have been the first CubeSats to visit Mars, but they will not be the last. All CubeSats destined for the red planet will utilize the Mars Reconnaissance Orbiter (MRO) in one way or another, be that building on scientific discoveries or using the MRO to relay data back to Earth. Launched August 12th, 2005 on an Atlas V rocket, the MRO achieved Mars orbit insertion on March 10th, 2006. The orbit was successively refined, making exemplary use of aerobraking. The MRO maps the surface, atmosphere, and climate of Mars while providing data relay capabilities for rovers and landers using seven scientific instruments, not including the TT&C instrumentation.

The High Resolution Imaging Science Experiment (HiRISE) offered the most advanced camera ever sent to another planet at the time. The Compact Reconnaissance Imaging Spectrometer for Mars (CRISM) maps mineral residue indicating previous water reservoirs. The Mars Color Imager (MARCI) characterizes the

Martian climate ranging from days to years as well as observing dust storms. The Context Camera (CTX) takes grayscale images at 6 meters per pixel scale over 30 km per image to monitor planet geography changes. The Shallow Radar (SHARAD) looks for subsurface ice deposits. The Mars Climate Sounder (MCS) measures the atmospheric temperature, humidity, and dust content in visible and infrared light, and accelerometers are included on the MRO for dramatic effect [287].

There is no doubt that future CubeSat missions will utilize the MRO for science or communication acuity. An image from the *Mars As Art* campaign has been included in **Figure 126** directly from the MRO.

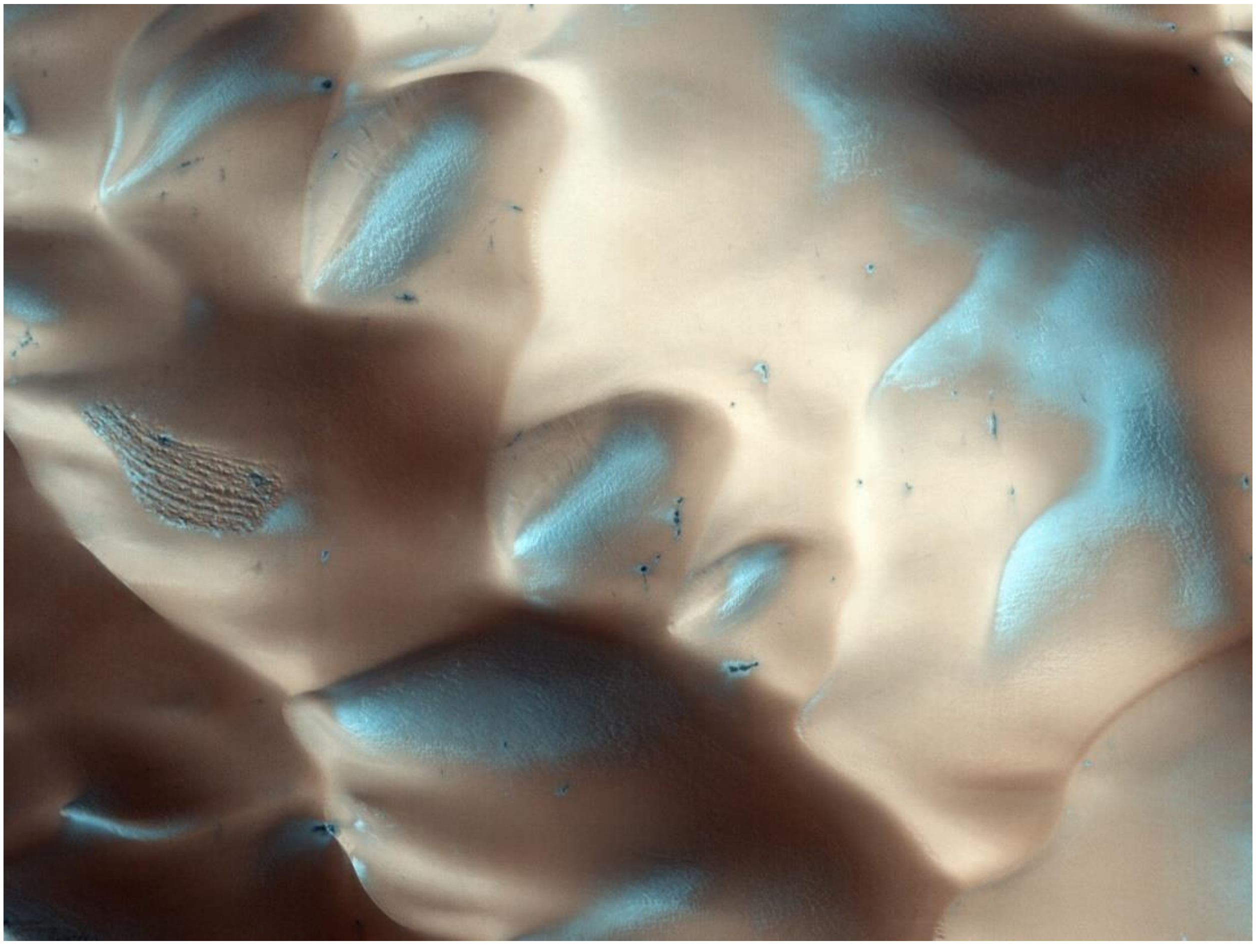

Figure 126: Frost-covered Dunes on the Martian Surface [288]

APPENDIX C: LINK BUDGET EXCEL CALCULATOR

There are many link budget calculators available; a detailed version is provided in [33]. Many values labeled "Estimate" will require further reading to fully understand for a given orbit or radio system. DSN documentation, [33], and [36] have copious information on these topics.

Table 59: Link Budget Excel Calculator

Row	Parameter	Value	Units	Equation
4	Frequency	8.425	GHz	Input
5	Speed of light	299792458	m/s	-
6	Radius of Earth	6370	Km	-
7	Altitude	400000	km	Input
8	Elevation Angle	10	degree	-
9	X1 (Intermediate Calculation Value)	0.188830185		SIN(RADIANS(C8+DEGREES(ASIN(COS(RADIANS(C8))*(C6/(C7+C6))))))
10	Wavelength	0.035583675	m	C5/(C4*1000000000)
11	Slant Range	405215.4376	Km	SQRT((C6+C7)^2+C6^2-(2*C6*(C6+C7)*C9))
12	Free Path Loss	223.1129011	dB	20*LOG(4*PI()*C11*1000/C10)
13	**Antenna**			
14	Transmitting Antenna Gain	14	dBi	Input
15	DC Transmitter Power	2		Input
16	Transmitter Power Efficiency	0.5		Input
17	Transmitter Output Power	1	W	C15*C16
18	Transmitter Output Power in dB	0	dB	10*LOG(C17)
19	Line Loss/Transmitter System Loss	1.2	dB	Estimate
20	CubeSat (Transmit) Antenna Pointing Accuracy	5	degree	Input
21	CubeSat (Transmit) Antenna Beamwidth	120	degree	Input
22	CubeSat (Transmit) Antenna Pointing Loss	0.020833333	dB	12*(C20/C21)^2
23	EIRP	12.77916667	dBW	C18+C14-C19-C22
24	**Ground Effects**			
25	Atmospheric loss	0.1	dB	Estimate
26	Polarization Loss	1	dB	Estimate
27	Ground Station (Receive) Antenna Gain	74.1	dBi	GCS Specified
28	Ground Station (Receive) Antenna Beamwidth	21	degree	GCS Specified
29	Ground Station (Receive) Antenna Pointing Accuracy	4	degree	GCS Specified
30	Ground Station (Receive) Antenna Pointing Loss	0.43537415	dB	12*(C29/C28)^2
31	Received Power at Ground Staion Antenna	-137.7691085	dB	C23+C27-C25-C26-C30-C12
32	Ground Station Receiver Passive Loss	1.5	dB	GCS Specified
33	Received Power at Ground Staion Receiver	-139.2691085		C31-C32
34	**Noise in receiving System**			

35	Receiver System Noise Temperature	40	K	GCS Specified
36	Boltzman's Constant	1.38E-23	W/Hz.K	-
37	Receiver System Power Noise	-212.58	dBW/Hz	10*LOG10(C35*C36)
38	Receiver Figure of Merit, G/T	58.08	dB/K	C27-10*LOG(C35)
39	**Data and Signal Effects**			
40	Data Rate	256000	bps	Input
41	Required Bit Energy to Noise Ratio	3	dB	Input
42	Carrier to Noise Ratio Density	57.08239965	dB-Hz	10*LOG(C40)+C41
43	Required Design Margin	2.67	dB	Estimate
44	Minimum Pr/No	59.75239965	dB-Hz	C42+C43
45	Implementation Loss	3	dB	Estimate
46	Final Carrier to Noise Ratio Density	70.31	dB-Hz	C33-C37-C45
47	**Link Margin**	10.56	dB	Output